

AD-A253 472



OSA Proceedings on

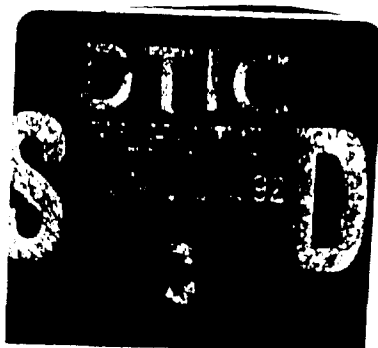
PICOSECOND ELECTRONICS AND OPTOELECTRONICS

Volume 9

Edited by

T. C. L. Gerhard Sollner and Jagdeep Shah

Proceedings of the Topical Meeting
March 13-15, 1991
Salt Lake City, Utah



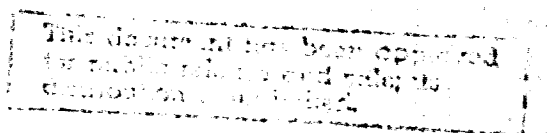
Cosponsored by

Optical Society of America
IEEE/Lasers and Electro-Optics Society

Supported by

Air Force Office of Scientific Research
National Science Foundation

Optical Society of America
2010 Massachusetts Avenue, NW
Washington, DC 20036
(202) 223-8130



OSA Proceedings on
PICOSECOND ELECTRONICS AND OPTOELECTRONICS

92 6 16 098

92-15740



Accession For	
NTSC	Serial
NTSC	Print
User Requested	
Classification	
By	
Distribution/	
Availability Codes	
Email and/or	
Dist	Special
A-1	
	5

Technical Program Committee

T. C. L. Gerhard Sollner, General Chair
MIT Lincoln Laboratory

Jagdeep Shah, Program Chair
AT&T Bell Laboratories

David H. Auston
Columbia University

David M. Bloom
Stanford University

Daniel R. Grischkowsky
IBM T. J. Watson Research Center

Chi H. Lee
University of Maryland

Umesh Mishra
University of California, Santa Barbara

Hiroyuki Sakaki
University of Tokyo, Japan

Janis Veldmanis
University of Michigan

Claude Weisbuch
Thomson CSF, France

Jerry Woodall
IBM T. J. Watson Research Center

Naoki Yokoyama
Fujitsu Laboratories, Japan

REPORT DOCUMENTATION PAGE

Form Approved
OMB No. 0204-0188

Public reporting burden for this collection of information is estimated to average 1.75 hours per response, including the time for reviewing instructions, gathering and maintaining the data needed, and completing and reviewing the collection of information. Send comments regarding this burden estimate or any other aspect of this collection of information, including suggestions for reducing this burden, to Washington Headquarters Services, Directorate for Information Operations and Reports, 1215 Jefferson Davis Highway, Suite 1204, Arlington, VA 22202-4302, and to the Office of Management and Budget, Paperwork Reduction Project (0704-0188), Washington, DC 20503.

1. AGENCY USE ONLY (Leave blank)	2. REPORT DATE	3. REPORT TYPE AND DATES COVERED
	May 22, 1992	Final 1/1/91-12/31/91
4. TITLE AND SUBTITLE		5. FUNDING NUMBERS
Organization of the 1991 Optical Society of America Photonic Science Topical Meeting Series		G - AFOSR-91-0176
6. AUTHOR(S)		
Jarus W. Quinn		
7. PERFORMING ORGANIZATION NAME(S) AND ADDRESS(ES)		8. PERFORMING ORGANIZATION REPORT NUMBER
Optical Society of America 2010 Massachusetts Ave. NW Washington, DC 20036		AFOSR-TR- 02 05 20
9. SPONSORING/MONITORING AGENCY NAME(S) AND ADDRESS(ES)		10. SPONSORING / MONITORING AGENCY REPORT NUMBER
US Air Force Office of Scientific Research Department of the Air Force Bolling Air Force Base Washington, DC 20332-6448 <i>Schlossberg</i>		NE 2305/A1
11. SUPPLEMENTARY NOTES		
12a. DISTRIBUTION / AVAILABILITY STATEMENT		12b. DISTRIBUTION CODE
Approved for public release Distribution unlimited		
13. ABSTRACT (Maximum 200 words)		
<p>Attach list of reports supported by Optical Society of America</p> <p>Photorefractive Materials, Effects, and Devices</p> <p>Integrated Photonics Research</p> <p>Nonlinear Guided Wave Phenomena</p> <p>Optical Amplifiers and Their Applications</p> <p>Optical computing</p> <p>Picosecond Electronics and Optoelectronics</p> <p>Quantum Optoelectronics</p> <p>Photonic Switching</p> <p>Microphysics of Surfaces: Beam Induced Processes</p> <p>Soft X-ray Projection Lithography</p> <p>Short Wavelength Coherent Radiation, Generation & Applications</p> <p>Persistent Spectral Hole-Buring: Science & Applications</p>		
14. SUBJECT TERMS		15. NUMBER OF PAGES
16. PRICE CODE		17. LIMITATION OF ABSTRACT
18. SECURITY CLASSIFICATION	19. SECURITY CLASSIFICATION	20. SECURITY CLASSIFICATION
21. FUNDING SOURCE	22. FUNDING SOURCE	23. FUNDING SOURCE

OSA Proceedings on
**PICOSECOND ELECTRONICS AND
OPTOELECTRONICS**

Volume 9

Edited by
T. C. L. Gerhard Sollner and Jagdeep Shah

**Proceedings of the Topical Meeting
March 13-15, 1991
Salt Lake City, Utah**

Cosponsored by
**Optical Society of America
IEEE/Lasers and Electro-Optics Society**

Supported by
**Air Force Office of Scientific Research
National Science Foundation**

**Optical Society of America
2010 Massachusetts Avenue, NW
Washington, DC 20036
(202) 223-8130**

Articles in this publication may be cited in other publications. In order to facilitate access to the original publication source, the following form for the citation is suggested:

Name of Author(s), Title of Paper, OSA Proceedings on Picosecond Electronics and Optoelectronics, T. C. L. Gerhard Sollner, Jagdeep Shah, eds. (Optical Society of America, Washington, DC 1991), Vol. 9, pp. xx-xx.

ISBN Number 1-55752-177-8

LC Number 90-63015

Copyright © 1991, Optical Society of America

Individual readers of this proceedings and libraries acting for them are permitted to make fair use of the material in it, such as to copy an article for use in teaching or research, without payment of fee, provided that such copies are not sold. Copying for sale is subject to payment of copying fees. The code 1-55752-177-8/91/\$2.00 gives the per-article copying fee for each copy of the article made beyond the free copying permitted under Sections 107 and 108 of the U.S. Copyright Law. The fee should be paid through the Copyright Clearance Center, Inc., 21 Congress Street, Salem, MA 01970.

Permission is granted to quote excerpts from articles in this proceedings in scientific works with the customary acknowledgment of the source, including the author's name, name of the digest, page, year, and name of the Society. Reproduction of figures and tables is likewise permitted in other articles and books provided that the same information is printed with them and notification is given to the Optical Society of America. Republication or systematic or multiple reproduction of any material in this proceedings is permitted only under license from the Optical Society of America; in addition, the Optical Society may require that permission also be obtained from one of the authors. Address inquiries and notices to the Director of Publications, Optical Society of America, 2010 Massachusetts Avenue, NW, Washington, DC 20036. In the case of articles whose authors are employees of the United States Government or its contractors or grantees, the Optical Society of America recognizes the right of the United States Government to retain a nonexclusive, royalty-free license to use the author's copyrighted article for United States Government purposes.

The views and conclusions in this proceedings are those of the author(s) and should not be interpreted as necessarily representing endorsements, either expressed or implied, of the editors or the Optical Society of America.

Printed in the U.S.A.

Contents

Preface	xiii
--------------------------	-------------

Terahertz Sources and Spectroscopy

Large-Aperture Photoconducting Antennas	2
<i>D. H. Auston and X. -C. Zhang</i>	

Femtosecond Pulses of Terahertz Radiation: Physics and Applications	9
<i>D. Grischkowsky and N. Katzenellenbogen</i>	

Low-Temperature Epitaxially Grown GaAs as a High-Speed Photoconductor for Terahertz Spectroscopy	15
<i>James M. Chwalek, John F. Whitaker, and Gerard A. Mourou</i>	

Broadband Periodic Antennas for Detecting Picosecond Terahertz Radiation	20
<i>D. R. Dykaar, B. I. Greene, J. F. Federici, A. F. J. Levi, L. N. Pfeiffer, and R. F. Kopf</i>	

Terahertz Absorption Between Split Subbands in Coupled Quantum Wells	24
<i>Hartmut Roskos, Martin C. Nuss, Jagdeep Shah, Ben Tell, Jack Cunningham, and Klaus Köhler</i>	

Terahertz Time-Domain Transmission of Superconductors	31
<i>Martin C. Nuss, Paul M. Mankiewich, Megan O'Malley, Keith W. Goossen, Hartmut Roskos, Ben Tell, and Manjul Bhushan</i>	

Ultrafast Optoelectronics

GaAs-Based, Very Fast Integrated Optoelectronics	36
<i>Takeshi Kamiya</i>	
Femtosecond Spatiotemporal Field Measurements in GaAs Quantum Wells	40
<i>W. H. Knox, G. E. Doran, J. Cunningham, M. Ramaswamy, and S. M. Goodnick</i>	
Propagation of Picosecond Electrical Pulses in GaAs for Velocity-Matched Modulators	46
<i>Yi Chen, John Nees, and Steve Williamson</i>	
Picosecond High-Voltage Photoconductive Switching	49
<i>T. Motet, J. Nees, S. Williamson, and G. Mourou</i>	

Electro-Optic Sampling

Two-Dimensional Field Mapping of GaAs Microstrip Circuit by Electro-Optic Sensing	54
<i>Ming G. Li, Eve A. Chauchard, Chi H. Lee, and Hing-Loi A. Hung</i>	
Modeling of an Electro-Optically Probed Photoconductive Switching Experiment	59
<i>K. M. Connolly, R. O. Grondin, S. M. El-Ghazaly, and R. P. Joshi</i>	
Improvement of the Minimum Detectability of Electro-Optic Sampling by Using a Structurally New Probe	64
<i>Shinichiro Aoshima, Hironori Takahashi, Isuke Hirano, and Yutaka Tsuchiya</i>	
Improvement of Space-Dependent Sensitivity and Absolute Voltage Measurement in Noncontact Picosecond Electro-Optic Sampling	70
<i>H. Takahashi, S. Aoshima, and Y. Tsuchiya</i>	
New Scheme of Electro-Optic Sampling by Probe-Beam Polarization Modulation	75
<i>Ryo Takahashi and Takeshi Kamiya</i>	

Electro-Optic Sampling for the Measurement of the Response of Fast Oscilloscopes	79
<i>D. Henderson, A. G. Roddie, and A. J. A. Smith</i>	

Ultrafast Photodetectors

Limitations of the Impulse Response of GaAs Metal-Semiconductor-Metal Photodetectors	86
<i>J. Kuhl, M. Klingenstein, M. Lambsdorff, C. Moglestue, J. Rosenzweig, A. Axmann, Jo. Schneider, and A. Hülsmann</i>	
Ultrafast Graded Double-Heterostructure p-i-n Photodiode	92
<i>D. L. Crawford, Y. G. Wey, K. Giboney, J. E. Bowers, M. J. Rodwell, P. M. Sylvestre, M. J. Hafich, and G. Y. Robinson</i>	
Picosecond Metal-Semiconductor-Metal Photodetectors with Sub-100-nm Finger Spacing and Finger Width in GaAs	97
<i>Yue Liu, Paul B. Fischer, and Stephen Y. Chou</i>	
2.0 ps GaAs Monolithic Photodiode and All-Electronic Sampler	101
<i>E. Özbay, K. D. Li, and D. M. Bloom</i>	
Picosecond GaAs Photodetector Monolithically Integrated with a High-Speed Sampling Circuit	104
<i>Masayuki Kamegawa, K. Giboney, J. Karin, S. Allen, M. Case, R. Yu, M. J. W. Rodwell, and J. E. Bowers</i>	

High-Speed Transistors and Electronics

75-GHz SiGe Heterojunction Bipolar Transistors: GaAs Performance in Si Technology?	110
<i>J. M. C. Stork, J. H. Comfort, G. L. Patton, E. F. Crabbé, and B. S. Meyerson</i>	
Recent Advances in Ultrafast High-Electron-Mobility Transistor Technology	116
<i>Loi D. Nguyen</i>	

Picosecond Radiation-Induced Current Transients in Digital GaAs MESFETs	119
<i>Dale McMorrow, Arthur B. Campbell, Alvin R. Knudson, and Todd R. Weatherford</i>	
Transient Simulation of Ultrasmall GaAs MESFET Using Quantum Moment Equations	126
<i>J.-R. Zhou, A. M. Kriman, and D. K. Ferry</i>	
Theoretical Model of the Photon Transport Transistor	131
<i>A. K. Chu, Y. Gigase, and B. Van Zeghbroeck</i>	
Subpicosecond Jitter Triggering Using Resonant Tunneling Diodes	136
<i>Ekmel Özbay and David M. Bloom</i>	
Impulse Generation and Frequency Multiplication Using Soliton Effects in Monolithic GaAs Circuits	140
<i>Michael Case, Eric Carman, Masayuki Kamegawa, Kirk Giboney, Ruai Yu, Kathryn Abe, M. J. W. Rodwell, and Jeff Franklin</i>	

Millimeter-Wave Circuits

100-GHz Electro-Optic S-Parameter Characterization of High-Electron-Mobility Transistors	146
<i>M. Y. Frankel, J. F. Whitaker, G. A. Mourou, J. A. Valdmanis, and P. M. Smith</i>	
Display of Microwave Waveform Through a Low-Frequency Replica Using an Optical Phase-Locking and Sampling Technique	151
<i>Ming G. Li, Sheng-lung L. Huang, Chi H. Lee, and Hing-Loi A. Hung</i>	
All-Optical Microwave Gain Measurements on MMIC Amplifiers	156
<i>Kurt J. Weingarten and Majid Riazat</i>	
Propagation of 100-GHz Bandwidth Electrical Pulses on a Silicon-Based Microstrip Line with Buried CoSi ₂ Groundplane	161
<i>Hartmut Roskos, Martin C. Nuss, Keith W. Goossen, David W. Kisker, Ben Tell, Alice E. White, Ken T. Short, Dale C. Jacobson, and John M. Poate</i>	

High-Frequency Analog Signal Processing with High-Temperature Superconductors	167
<i>W. G. Lyons, R. S. Withers, J. M. Hamm, R. H. Mathews, B. J. Clifton, P. M. Mankiewich, M. L. O'Malley, and N. Newman</i>	

Ultrafast Lasers

Femtosecond Monolithic Colliding-Pulse Mode-Locked Quantum-Well Lasers	176
<i>M. C. Wu, Y. K. Chen, T. Tanbun-Ek, and R. A. Logan</i>	
Optimization of Packaged, Actively Mode-locked 1.5- μ m InGaAsP Diode Laser for >10 Gb/s OTDM Transmission Systems	181
<i>I. W. Marshall, A. J. Lowery, P. D. Constantine, D. J. Cooper, and D. Elton</i>	
Generation of High-Power Femtosecond Optical Pulses from a Semiconductor Diode Laser System	185
<i>P. J. Delfyett, L. Florez, N. Stoffel, T. Gmitter, N. Andreadakis, and G. A. Alphonse</i>	
Numerical Simulations of an Actively Q-Switched Semiconductor Laser	188
<i>Björn Jonsson and Sverre T. Eng</i>	
Injection Seeding of a Gain-Switched Semiconductor Laser with a Mode-Locked Master Oscillator	194
<i>E. A. Chauchard, L. G. Joneckis, J. S. Wey, Chi H. Lee, and G. Burdge</i>	

Tunneling

Electron Transport in Double-Barrier Diodes Studied by Differential Absorption Spectroscopy	198
<i>T. K. Woodward, D. S. Chemla, I. Bar-Joseph, D. L. Sivco, and A. Y. Cho</i>	

Coherent Oscillations of a Wave Packet in a Semiconductor Double Quantum-Well Structure	204
<i>Karl Leo, Jagdeep Shah, Ernst O. Göbel, T. C. Damen, Stefan Schmitt-Rink, Wilfried Schäfer, and Klaus Köhler</i>	
Carrier Sweep-Out from Quantum Wells in an Electric Field	210
<i>A. M. Fox, D. A. B. Miller, G. Livescu, J. E. Cunningham, and W. Y. Jan</i>	
Temperature Dependence of the Resonant Tunneling Process	214
<i>I. Bar-Joseph, Y. Gedalyahu, A. Yacoby, T. K. Woodward, D. S. Chemla, D. L. Sivco, and A. Y. Cho</i>	
Tunneling and Relaxation in Coupled Quantum Wells	218
<i>B. Deveaud, A. Chomette, F. Clérot, A. Regreny, S. Gurvitz, and I. Bar-Joseph</i>	
Competition Between Tunneling and Exciton Formation for Photoexcited Carriers in Asymmetric Double Quantum Wells	223
<i>J. Kuhl, R. Strobel, R. Eccleston, and K. Köhler</i>	
Quantum Transport of an Electron Wave Packet Across a Heterostructure Discontinuity: Applications in the GaAs/Al _x Ga _{1-x} As Heterosystem	229
<i>Vasu Sankaran and Jasprit Singh</i>	

Materials

Strained-Layers for Electronics and Optoelectronics	236
<i>David R. Myers</i>	
Characterization of Terahertz Optoelectronic Behavior of GaAs Epilayers Containing Arsenic Precipitates	242
<i>A. C. Warren, N. Katzenellenbogen, D. Grischkowsky, J. M. Woodall, M. R. Melloch, and N. Otsuka</i>	
Transient Absorption of Low-Temperature Molecular-Beam Epitaxy Grown GaAs	244
<i>T. B. Norris, W. Sha, W. J. Schaff, X. J. Song, Z. Liliental-Weber, and E. R. Weber</i>	

Comparison of Oxygen Ion- and Proton-Implanted GaAs Photoconductive Switches	248
<i>Sheng-lung L. Huang, Eve A. Chauchard, Chi H. Lee, Thane Smith, Timothy T. Lee, and Thomas R. Joseph</i>	
Femtosecond Refractive and Absorptive Nonlinearities Due to Real Carriers in GaAs	253
<i>T. Gong and P. M. Fauchet</i>	
<hr/> Digest Summaries <hr/>	
Picosecond Superconductive Electronics	262
<i>T. Van Duzer</i>	
High-Capacity Lightwave Transmission: Ultra-High Speed or Wavelength Multiplexing	265
<i>Tingye Li</i>	
Photon-Assisted Resonant Tunneling Through a GaAs/AlGaAs Multiple Quantum Well Structure	267
<i>Bjorn Jonsson, Ingemar Andersson, Anders Larsson, Thorwald Andersson, and Johan Westin</i>	
Index	271

Preface

This volume is a collection of papers that were presented at the fourth Picosecond Electronics and Optoelectronics Topical Meeting of the Optical Society of America. The purpose of this topical meeting, since its inception in 1985, has been to foster greater interaction between those segments of the electronics and optics communities that have been pushing the frontiers toward ever higher speeds. The following pages reveal some of the successful results of these efforts. This preface is meant to serve as an introduction and summary of the meeting and as a guide to these proceedings.

Chapter I summarizes the state of the art in the relatively new field studying the generation and propagation of electromagnetic pulses with terahertz bandwidths. These pulses have significant implications for far-infrared spectroscopy and fundamental materials studies.

Chapter II contains recent advances in techniques used for ultrafast optoelectronics. This includes the measurement of picosecond pulse propagation in one and two dimensions.

Chapter III describes the sensing of rapidly varying electric fields by picosecond optical pulses. These techniques exploit the dependence of the index of refraction, and hence the optical path length, on electric field. For GaAs, the electric fields in the substrate can be probed directly, but some techniques move nonlinear material in to sample the fields.

Chapter IV covers improvements in the ultrafast detectors needed for high-speed optical communication. The emphasis is on speed as well as quantum efficiency.

Chapter V contains several papers on high-speed electronic devices. The fastest transistors are presented, both those based on silicon as well as III-V devices, and some unique applications of fast, two-terminal devices are also discussed.

Chapter VI concentrates on the measurement of performance of millimeter-wave circuits using optical sampling techniques. These techniques achieve in the time domain what is traditionally accomplished at lower frequencies in the frequency domain.

Chapter VII reports advances in the technology of ultrafast lasers. Short, well-controlled pulses are needed for optical communications, and one paper describes a mode-locked laser with up to a 350-GHz repetition rate.

In Chapter VIII papers on tunneling and resonant tunneling are presented. Charge storage in the well of a resonant-tunneling diode has been measured, and tunneling between two wells coupled by a tunneling barrier is examined in several papers.

Chapter IX collects all the papers with a strong emphasis on materials development. Devices that use strained layers, gallium arsenide grown by molecular beam epitaxy at low temperatures, and nonlinear materials are examined.

Finally, Chapter X contains digest summaries from those authors who did not wish to write an extended paper for this proceedings volume.

We would especially like to thank the Air Force Office of Scientific Research and the National Science Foundation for their generous support of this meeting. The advice of the Technical Program Committee was essential in selecting papers that represented the current state of the art, and their efforts to insure the highest quality are greatly appreciated. Finally, the tireless attention of Monica Malouf of the OSA to the many details of organizing a meeting of over 200 attendees made the experience a pleasant one.

T. C. L. Gerhard Sollner
MIT Lincoln Laboratory

Jagdeep Shah
AT&T Bell Laboratories

Terahertz Sources and Spectroscopy

Large-Aperture Photoconducting Antennas

D. H. Auston and X. -C. Zhang

*Electrical Engineering Department and Center for Telecommunications Research,
Columbia University, New York, New York 10027*

Abstract

We describe a novel optoelectronic technique to generate and detect THz electromagnetic waves by using large-aperture planar photoconducting antennas and antenna arrays. This approach is an effective method of producing directional and steerable sub-millimeter wave pulses.

1. Introduction

Various approaches have been used for generating and detecting ultrafast electromagnetic pulses [1]. These include elementary Hertzian dipoles, resonant dipoles, tapered antennas, transmission lines [2-5]. Large-aperture photoconducting antennas developed recently provide an alternative source to generate and detect directional submillimeter electromagnetic pulses with a terahertz bandwidth [6,7].

The physical mechanism for the generation of subpicosecond electromagnetic pulses from large aperture photoconducting antennas is the radiation from a fast time varying photocurrent. By large aperture, we mean one whose transverse dimensions are large relative to the spatial duration of the submillimeter-wave pulse. The technique is based on the following concept. When illuminated by ultrashort optical pulses, as shown in Figure 1, a large aperture planar photoconductor produces a transient current. The current pulse sweeps across the photoconductor and radiates a directional electromagnetic pulse

which can be steered by varying the angle of incidence of the optical beam [1]. The submillimeter-wave radiates in both the forward and backward directions (θ_1 and θ_2). If the angle of incidence of the optical pulse is θ_{op} , the angles of the radiated electromagnetic pulses satisfy the generalized Fresnel's law equations:

$$\begin{aligned} n_1(\omega_{op}) \sin \theta_{op} &= n_1(\omega_{el}) \sin \theta_1 \\ &= n_2(\omega_{el}) \sin \theta_2 \end{aligned} \quad (1.1)$$

where $n_1(\omega_{op})$, $n_1(\omega_{el})$, are the indices of refraction of the optical and electromagnetic pulses outside the photoconductor, and $n_2(\omega_{el})$ is the index of refraction of the electrical pulse in the photoconductor. If $n_1(\omega_{op}) = n_1(\omega_{el}) = 1$, as is true for the case where air is medium 1, the angle of the backward radiated electromagnetic pulse is equal to the angle of the incident optical pulse. Since the aperture size of the photoconductor is larger than the spatial pulse duration of the electromagnetic radiation, the electromagnetic wave is directional and diffraction-limited.

We can estimate the behavior of the electric

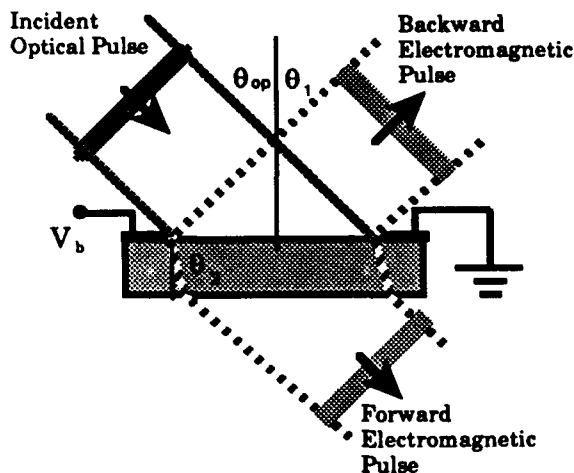


Figure 1

field by the following arguments. Near the transmitter, we expect the field to be approximated by a plane wave whose amplitude can be derived by simple boundary value conditions at the surface of the photoconductor. This gives us the following approximate expression for the electric field close to the transmitter (TM polarization of the radiated pulse):

$$E = -E_b \frac{\sigma_s \eta_0}{\cos \theta_{op}} \left[\sigma_s \eta_0 + \frac{1}{\cos \theta_{op}} + \frac{\sqrt{\epsilon}}{\cos \theta_2} \right]^{-1} \quad (1.2)$$

where E_b is the bias field, η_0 is the characteristic impedance of free space, ϵ is the dielectric constant of the photoconductor, and σ_s is the surface photoconductivity, given by the expression:

$$\sigma_s(t) = \frac{e\mu(1-R)\cos\theta_{op}}{\hbar\omega} \int_{-\infty}^t dt' I_{op}(t') e^{-(t-t')/\tau_r} \quad (1.3)$$

where μ is the carrier mobility of the photoconductor, R is the optical reflectivity, $\hbar\omega$ is the photon energy, I_{op} is the incident optical intensity and τ_r is photocarrier decay time. From expressions (1.2), we see that at low optical excitations, the electric field is proportional to the incident optical intensity. Note, however, that its sign is opposite to the applied bias field.

2. Generation and Detection

A number of semiconductor materials, including InP, GaAs, CdTe, polysilicon and radiation-damaged silicon-on-sapphire were evaluated, for use as large aperture photoconductors to generate submillimeter-waves. They were chosen because all have strong absorption at the wavelength of our femtosecond laser (625 nm) and high dark resistivities. The

later requirement was necessary to hold off the high electric field used to bias them. Electrode spacings varying from 2 to 10 mm and voltages ranging from 100 to 3000 Volts were used.

The source of optical pulses in our experiments was a balanced colliding pulse, mode-locked rhodamine 6G dye laser. The pulse duration was 75 fs and the wavelength was 625 nm. Approximately 10 mW of average optical power was used for the pump beam and 5 mW for the probe beam. The pump beam was used to illuminate the large area transmitting antenna with a defocused Gaussian beam which had a 1/e beam diameter comparable to the electrode spacing of the photoconductor.

The radiated field was detected with a photoconducting dipole antenna. It consisted of a 100 μ m dipole having a radiation-damaged silicon-on-sapphire photoconductor at its feed point. A 3.2 mm sapphire ball lens was placed over the dipole to improve its collection efficiency. The small size and high speed of the detecting antenna permitted its use as a movable probe to measure both the temporal and spatial distribution of the radiation field of the large aperture photoconductors. Due to its small size, the dipole antenna could also be scanned in space to measure the spatial distribution of the field.

The field strength as a function of time was obtained by recording the gated output current from the dipole detector while varying the relative time delay between the pump pulses which illuminated the large aperture antenna and the probe pulse which gated the detector. The current signal from the detector was amplified and digitized by a lock-in amplifier and a computer.

The amplitude of the radiated electromagnetic waves at far field is proportional to the first time derivative of the photocurrent in the photoconductor. If the fall-time of the photocurrent is much longer than the rise-time, the rise-time is found to be more important than the fall-time in determining the relative sensitivity of photoconducting materials[7]. Indium phosphide is found to be more sensitive than the other semiconductors used.

Figure. 2 shows the detected electric field waveform from an InP planar photoconductor having an electrode spacing of 10 mm. This waveform was measured in the far field using a 5 cm focal length fused silica lens to focus the electromagnetic pulse onto the dipole detector which was aligned in the specular direction of the emitted radiation. The radiated electric field

was found to be linearly proportional to the bias voltage and optical power. The observed waveform was strongly influenced by the response of the dipole detector and does not correspond to the true electric field waveform. The waveforms generated by the other photoconducting materials were similar, suggesting that in each case, the true waveform is substantially shorter, and that we are measuring the impulse response of the detector in each case. What was surprising is that the relatively "slow" material, Indium phosphide produced a signal that was comparable in speed to the radiation-damaged silicon-on-sapphire sample, and was almost 10 times larger. The relative sensitivities (normalized to silicon-on-sapphire) of the other materials ranged from 0.2 (polysilicon) to 7.5 (semi-insulating GaAs:Cr).

The electric field radiated by the each antenna was probed in the transverse direction to measure its directionality. This was achieved by scanning the dipole detector in the far field of the large aperture photoconductor and recording the time domain waveform for each angle. An example of the angular variation of the radiated signal is plotted in Figure 3. This shows the variation of the peak amplitude of the radiated

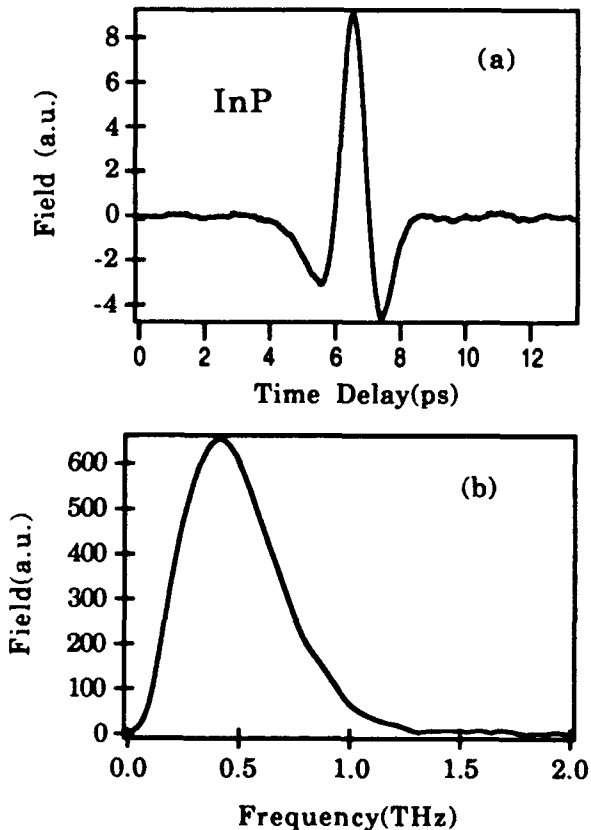


Figure 2.

signal from a 10 mm InP antenna. The data was taken at a distance of 16 cm between the transmitter and the detector. In this case, no lens was used. The radiated field had a beam-width that measured only 6° at the 3 db points. The maximum signal was observed at an angle corresponding to the specular reflection of the optical beam, which was at 30° relative to the normal. The pulse width was observed to broaden off axis, and became more flat-topped as the angle increased, consistent with a theoretical model of the radiation field.

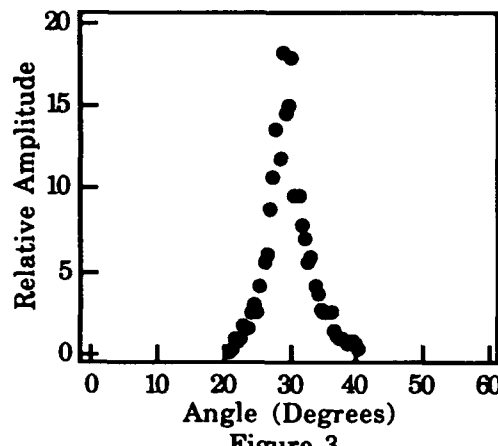


Figure 3.

3. Power Scaling

The large aperture photoconducting antennas show power scaling and saturation properties [8]. At high optical fluences, the radiated electric field (near field) saturates at a value comparable to the bias field.

At normal incidence, the radiation field (near field) from equation (1.2) can be rewritten as:

$$E = -E_b \frac{\sigma_s \eta_0}{\sigma_s \eta_0 + (1 + \sqrt{\epsilon})} \quad (3.1)$$

With the increase of the optical power, the number of the photocarriers increases, causing an increase of the surface conductivity σ_s (equation 1.3). When the surface photoconductivity σ_s becomes comparable to the radiation admittance of the antenna, the radiated near field E is expected to saturate at a value comparable to the applied bias field E_b . Therefore we have the equation

$$\lim_{\sigma_s \rightarrow \infty} E = -E_b \quad (3.2)$$

Figure 4 shows the Experimental setup for the study of the saturation behavior in the GaAs emitter. The source of the optical pulses is a balanced colliding pulse, mode-locked ring dye laser amplified by a copper vapor laser pumped amplifier. It provides a pulse energy of a few

microjoule at a repetition rate of 8 kHz and a 70 fs pulse duration at a center wavelength of 625 nm. The GaAs emitter has a photoconducting gap of 1 mm. A 0.5 mm gap radiation-damaged silicon-on-sapphire detector placed 10 mm from the emitter with a maximum optical excitation fluence $400 \mu\text{J}/\text{cm}^2$.

When the surface photoconductivity becomes greater than the reciprocal of the radiation resistance which requires approximately $1 \text{ mJ}/\text{cm}^2$ optical energy density, we expect the peak electric field amplitude of the submillimeter pulse in the near field to saturate at a value comparable to the bias field.

Figure 5 shows the experimental data of the radiated electric field from the GaAs emitter as a function of pump optical fluence at 2000 V/cm bias field. When the divergence and Fresnel losses are considered, the radiated field is estimated to be 1750 V/cm, close to the bias field of 2000 V/cm. We have also observed similar saturation properties from InP and CdTe photoconductors.

Because the depolarization field due to the charge distribution builds up at a later time scale, the model used here does not include the contribution of the space charge effect. For a detail analysis of the radiation, the space charge contribution should be considered.

With appropriate power scaling, it should be possible to generate electromagnetic pulses with

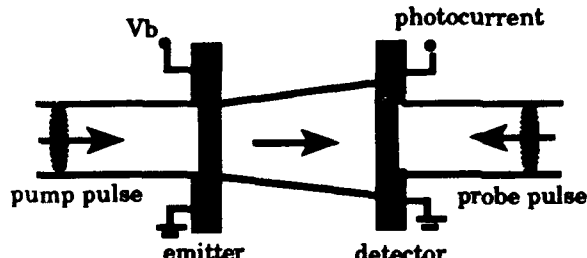


Figure 4.

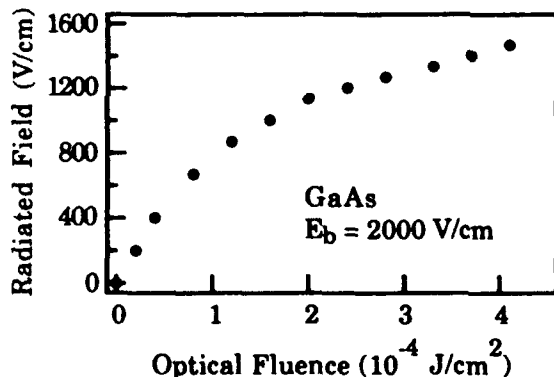


Figure 5.

peak powers up to 1 GW and local electric fields greater than 10 MV/cm. Figure 6 schematically illustrates the experimental set up for the generation of very high electromagnetic fields. Two off-axis parabolic mirrors are used to collect the radiation and to focus the radiation to the detector. If the emitter area is 100 cm^2 with a pulsed bias field of 100 KV/cm, the radiated power from the emitter is over 1 GW. Assuming the radiation is focused to 1 mm^2 , the local electric field can be as high as 10 MV/cm. Such field strength can be used for the study of nonlinear properties of the dielectric materials at submillimeter wave region.

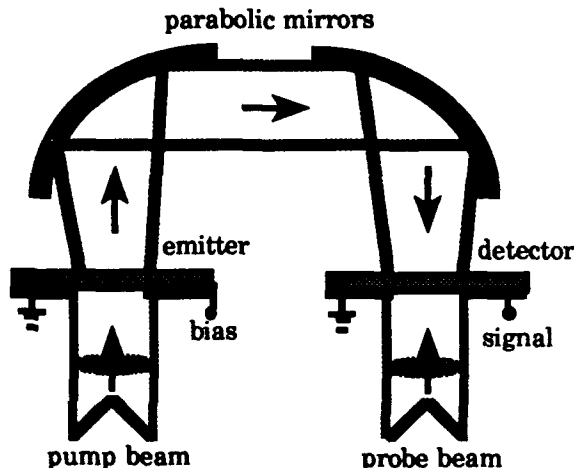


Figure 6.

4. Antenna Arrays

The concept of a single photoconducting antenna can be easily extended to an antenna array [9,10]. The direction of the emitted radiation from the array can be electrically controlled by varying the static bias applied to the individual antenna elements.

The array of photoconducting antennas is created by a pattern of parallel electrodes, each independently biased, on a semi-insulating GaAs substrate as illustrated in Figure 7. By setting the bias voltage on the electrodes appropriately, the amplitude of the photocurrent between every two adjacent electrodes can be controlled. When an optical pump pulse illuminates the structure, each current element acts roughly like a short dipole antenna. The far-field pattern of the array can be calculated according to conventional antenna theory and is given by the approximate expression:

$$E(\theta) = \frac{A \cos \theta}{4\pi\epsilon_0 c^2 r} \left[\frac{\mu e}{\hbar \omega} \right] \sum_{n=1}^{N-1} \left(\frac{V_n - V_{n-1}}{d} \right) \cdot I_n(\Omega) e^{-inKd \sin \theta} \quad (4.1)$$

where A is the optically illuminated area of the array, θ is the angle defined from the array normal as in Figure 8, r is the radial distance, N is the number of electrodes under the illumination, V_n is the bias voltage on the n th electrode, d is the spacing between the photoconductor elements, $I_n(\Omega)$ is the optical intensity at the n th electrode, modulated at the microwave frequency Ω , and K is the microwave free space propagation constant. If the strengths of the static bias voltage on each antenna element are made to vary periodically with respect to one another, the array will act like an amplitude grating, steering the beam in a direction which can be controlled by varying the bias period. Specifically, if the static bias voltages vary sinusoidally in space, with period Λ_{bias} , as:

$$V_n = \frac{E_0}{\kappa} \cos(nkd + \phi) \quad (4.2)$$

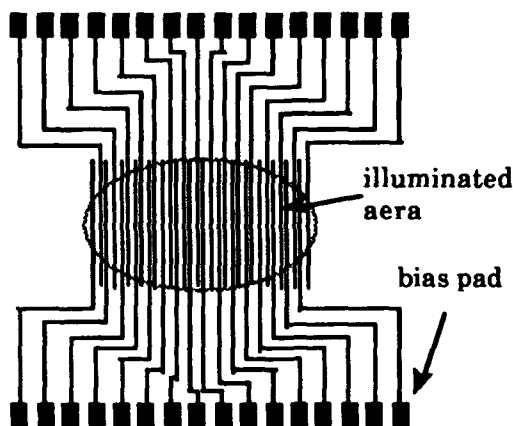


Figure 7.

where E_0 is the maximum static field between adjacent electrodes, $\kappa = (2\pi/\Lambda_{\text{bias}})$, ϕ is the phase which can be set to zero and the optical intensity is uniform, then the radiated signal in the far-field can be approximated by the expression:

$$E(\theta) \sim \cos\theta \left[\frac{4\mu E_0 I(\Omega)}{4\pi\epsilon_0 c^2 r\hbar\omega} \right] \frac{\sin\left(\frac{Nd(\kappa \pm K\sin\theta)}{2}\right)}{\sin\left(\frac{d(\kappa \pm K\sin\theta)}{2}\right)} \quad (4.3)$$

where K is the microwave free space propagation constant, which can be written as $K = (2\pi/\lambda)$ where λ is the center wavelength of the radiation. Four main lobes are expected, one pair inside and one pair outside the semiconductor. In free space, the maxima are at angles where $\sin\theta = \pm\kappa/K$. Clearly, by varying the periodicity of the voltage bias, the emission angle of these lobes can be steered continuously over a range from zero to nearly

$\pm\pi/2$. The concept is illustrated in Figure 8.

Ideally, the temporal modulation on the optical illumination should be sinusoidal at the frequency of the emitted radiation. To approximate this condition, we have used a train of ultrashort optical pulses spaced by 2 ps to produce a burst at 500 GHz. A dual-jet, hybrid mode-locked dye laser, synchronously pumped at 78 MHz by a frequency-doubled YLF laser (Coherent Antares-Satori system), generated optical pulses at 640 nm with a duration of approximately 150 femtoseconds. The unfocussed beam, having a Gaussian profile 3 mm wide and an average power of 130 mW, was used to illuminate the antenna array. A train of four optical pulses of equal intensity, each spaced 2 psec apart, was generated by passing a single optical pulse through two calcite crystals having birefringent delays of two and four picoseconds.

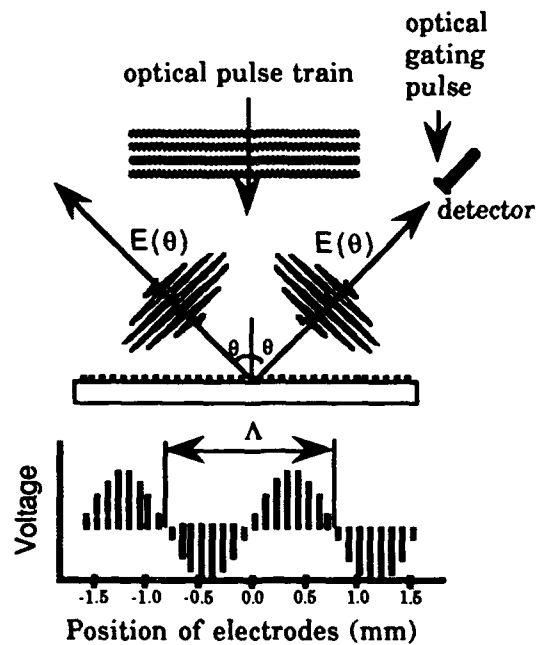


Figure 8

The antenna array used in our experiments (figure 7) consisted of 32 parallel electrodes, each 2 mm long and 25 microns wide, spaced 100 microns apart center to center. The electrodes, on a semi-insulating GaAs substrate, were made of gold germanium with a top layer of pure gold to facilitate wire bonding, giving a total thickness of about 2000 angstroms. The electrodes in the array were biased sinusoidally with respect to one another, as shown in figure 8, using slide potentiometers so that the bias period could be easily varied. The voltages were scaled so that the maximum E field between elements was kept constant at 1.25 kV/cm for all bias periods,

ensuring that the amplitude of the emitted radiation was constant. Due to the relatively low transient mobility of this material, we expect the photocurrent to be proportional to the product of the applied field and the absorbed optical flux.

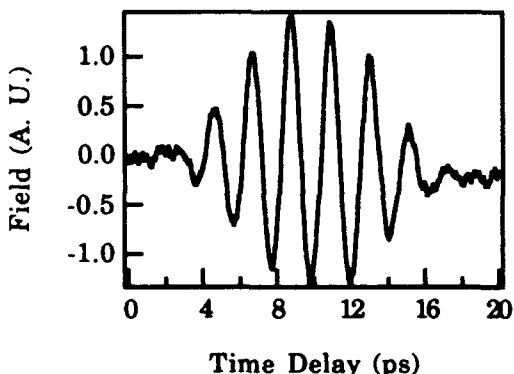


Figure 9.

The detected waveform at an angle of 45 degrees off normal and 3 cm from the array is shown in Figure 9. The periodicity of the voltage bias in this case was adjusted to be 0.9 mm to produce a maximum signal in the direction of the detector (equation 4.3). The 500 GHz burst is clearly resolved. Because the radiation from different antenna elements experiences different delay times, the emitted pulse train is broadened in time with respect to the optical pulse train.

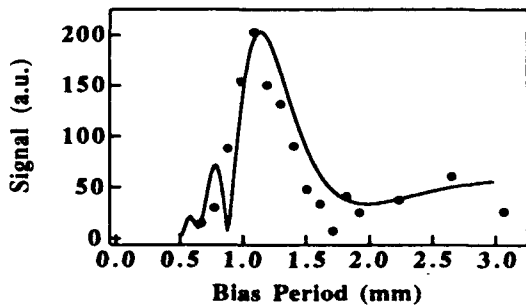


Figure 10.

To test the steerable property of the array, the detector was kept fixed at 45° and the periodicity of the voltage bias was varied to sweep the angle of the emitted beam across the detector. The bias voltage amplitude was changed with period to maintain a constant maximum electric field, as in equation 4.2. The time traces obtained for each bias period were Fourier transformed so that the signal amplitude at 500 GHz could be measured. The 500 GHz signal is plotted as a function of bias

period in figure 10. The signal peaks for a bias period close to the expected value. A theoretical curve of the variation in the signal is also plotted in figure 10. It is based on the simple model of equation (4.1), assuming that the optical intensity profile is Gaussian. The width of the scanning beam at the 3 db points was approximately 10°. This width is determined by the overall length of the array (3.2 mm) and could be much narrower if a larger array were used.

The array structure has also been used for frequency tuning the submillimeter-waves. A single optical pulse with a 150 fs pulse duration illuminated the array at a normal incident angle. The center electrode (No. 16) of the array was always biased at the highest voltage. The dipole detector was placed 30 mm away from the emitting array at a detection angle of θ .

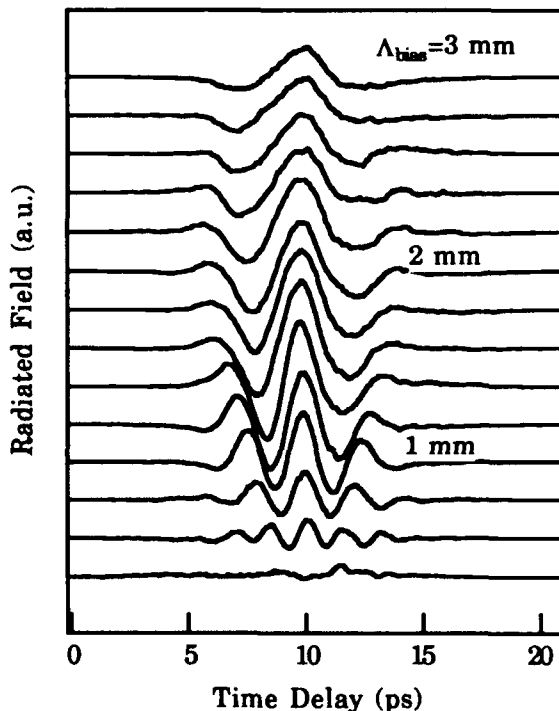


Figure 11.

From equation (4.3), the maxima radiation is at the condition of $\kappa = \pm K \sin \theta$. This condition can be rewritten as $\lambda = \pm \Lambda_{bias} \sin \theta$. It is clear that for a fixed angle θ , the center wavelength λ is proportional to Λ_{bias} . Therefore by varying the bias period Λ_{bias} , the radiation wavelength λ (or radiation frequency f) can be electrically tuned at a defined direction.

To illustrate the tuning properties of the photoconducting antenna array, we plot the

temporal waveforms of the radiated fields versus the bias period Λ_{bias} , as shown in Figure 11. The number of the pulses in a wave packet is proportional to the number of the bias cycles across the array. For a better vision, the curves have been offset. The bias period Λ_{bias} was varied from 0.4 mm to 3 mm while the No. 16 electrode was kept at the highest voltage. Since the center wavelength λ of the radiation is proportional to the bias period, increasing the bias period Λ_{bias} , causes the radiation wavelength to increase and the pulse width to broaden.

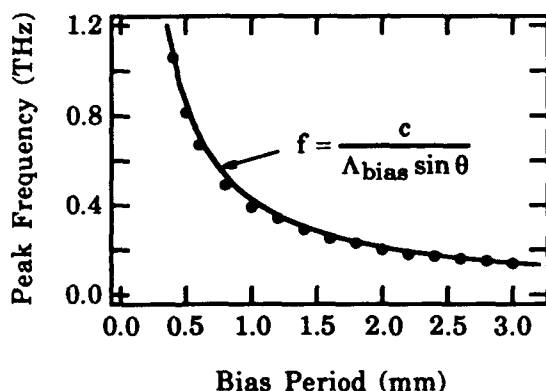


Figure 12.

The temporal waveforms have been transformed into a frequency spectrum. The center carrier frequency of each waveform has been plotted versus the bias period Λ_{bias} , as shown in Figure 12. The solid dots are the measured values and the curve is the calculation from the equation $f = c / (\Lambda_{\text{bias}} \sin \theta)^{-1}$. When the bias period increases from 0.4 mm to 3 mm, the main peak of the frequency decreases from 1.06 THz to 140 GHz. The experimental data and the theoretical calculation are in good agreement. When the frequency was tuned over 1 THz, the measured amplitude of the radiation decreased, due to the frequency response of the dipole detector and the frequency response of the radiation from a single antenna. No radiated signal was measured when the bias had a linear distribution ($V_n = nE_0$). In this case, the radiation direction satisfies Fresnel's law equation [1]. The tuning bandwidth and resolution is largely determined by the size of the array and the number of the antenna elements. For an array size of 10×10 cm² with 50 μm photoconducting gaps, we expect that the tuning range can cover from 3 GHz to over 1 THz. The upper limit of the tuning range is comparable with the bandwidth of the radiation from a single antenna.

With an ultrafast optical pulse excitation (assuming the pulse width of the radiated field from a single antenna is much less than the array retardation time τ_a), the temporally spread radiation waveform reflects the spatial distribution of the bias across the array, because the radiation from different antenna elements experiences different delay times. For example, the voltage of the center electrode (No. 16) was kept at the highest value when the periodicity of the bias was changed. This made the waveforms in Figure 11 have a symmetry about their centers (approximately at 10 ps position). Also when the bias phase ϕ in equation (4.2) varied, pulses within the wave package shifted in time. The amount of the shift was $(\phi \sin \theta) / (c \kappa)$. The direction of the shift depended on the sign of the phase ϕ , and the shift was confined within the duration of the array retardation time τ_a .

5. Acknowledgment

This research was sponsored by the Air Force Office of Scientific Research under grant #F49620-88-C-0109.

References:

- [1] For example, see chapter 5 in "Ultrashort Laser Pulses and Applications", W. Kaiser, Ed. New York: Springer-Verlag, (1987).
- [2] D.H. Auston, K.P. Cheung, and P.R. Smith, *Appl. Phys. Lett.* **45**, 284 (1984).
- [3] P.R. Smith, D.H. Auston, and M.C. Nuss, *IEEE J. Quantum Electron.*, **24**, 255 (1988).
- [4] A. P. DeFonzo and C. R. Lutz, *Appl. Phys. Lett.*, **51**, 212 (1987).
- [5] Ch. Fattinger and D. Grischkowsky, *Appl. Phys. Lett.* **54**, 490 (1989).
- [6] B.B. Hu, J.T. Darrow, X.-C. Zhang, D.H. Auston and P.R. Smith, *Appl. Phys. Lett.* **56**, 886 (1990).
- [7] J.T. Darrow, B.B. Hu, X.-C. Zhang and D.H. Auston, *Opt. Lett.*, **15**, 323 (1990).
- [8] J.T. Darrow, X.-C. Zhang and D.H. Auston, *Appl. Phys. Lett.* **58**, Jan 7, (1991)
- [9] N. Froberg, M. Mack, B.B. Hu, X.-C. Zhang and D.H. Auston, *Appl. Phys. Lett.* **58**, 446 (1991)
- [10] B.B. Hu, N. Froberg, M. Mack, X.-C. Zhang and D.H. Auston, *Appl. Phys. Lett.* **58**, Apr., 1 (1991)

Femtosecond Pulses of Terahertz Radiation: Physics and Applications

D. Grischkowsky and N. Katzenellenbogen

*IBM T. J. Watson Research Center, P.O. Box 218,
Yorktown Heights, New York 10598*

ABSTRACT

The use of high-performance, Hertzian-dipole antennas has enabled us to extend the operation of our optoelectronic, pulsed THz beam system to beyond 3 THz and to thereby, determine the limiting time-domain response function of the photoconductive switch. Via this capability, we have characterized a new type of THz source producing 380 fsec pulses, the shortest directly measured THz pulses in free space to date.

A high-brightness pulsed THz beam system has been recently developed (1). This optoelectronic system is based on repetitive, fsec optical excitation of a Hertzian dipole antenna (1,2) embedded in a charged coplanar transmission line structure. The resulting synchronous bursts of radiation are collimated by a THz optical system into a diffraction-limited beam and focused onto a similar receiver. The THz system has quite tight coupling between the transmitter and receiver, while the good focusing properties preserve the ultrafast time dependence of the source. Transmitted waveforms have been measured with subpsec resolution and with signal-to-noise ratios of more than 10,000:1.

In this paper we extend the work of Ref. (1) to smaller antennas and thereby, increase the frequency response to 3 THz. From the calculated THz optical transfer function together with the known THz absorption, we extract the limiting bandwidth of the system. Because the transmit-

ter and receiver are identical, identical transmitter and receiver bandwidths are obtained. This result is compared to the calculated radiation spectrum from a Hertzian dipole (2,3) driven by the current pulse determined by the laser pulsewidth, the current risetime, and the carrier lifetime. From this comparison, the time-domain response function for the antenna current is obtained. We then use the receiver response function to extract the true bandwidth of a novel source of relatively powerful and extremely short pulses of freely propagating THz radiation (4). These pulses, having a measured (full-width-at-half-maximum) pulsewidth of 380 fsec with no deconvolution, are the shortest directly-measured, freely-propagating THz pulses in free space to date.

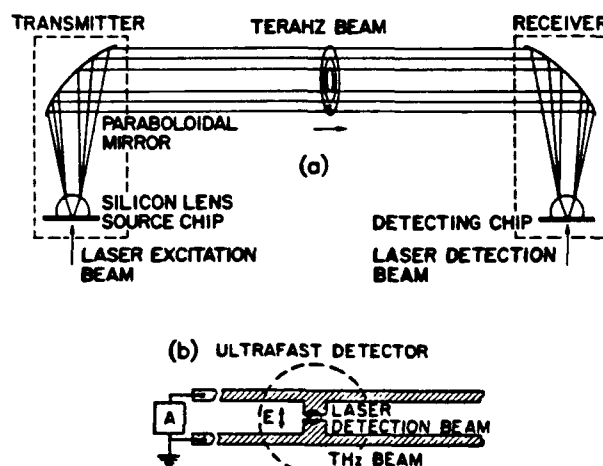


Fig. 1 (a) THz optics, (b) Receiving antenna.

The optoelectronic THz beam system (1) is shown in Fig. 1a. In general, laser excitation of the source chip produces a burst of THz radiation. A large fraction of the radiation is emitted into the substrate in a cone normal to the interface and is then collected and collimated by a high-resistivity (10 k Ω cm) crystalline silicon lens attached to the back side of the chip (5). A colliding-pulse, mode-locked (CPM) dye laser provides the 623 nm, 60 fsec excitation pulses at a 100 MHz repetition rate in a beam with an average power of 7 mW on the excitation spot. After collimation by the lens, the beam of THz pulses propagates and diffracts to a paraboloidal mirror, where the THz radiation is recollimated into a highly directional beam. After further propagating 50 cm the THz beam is incident upon the receiver, where a second matched paraboloidal mirror focuses the beam onto a second identical silicon lens, which in turn focuses it onto an ion-implanted SOS detection chip with the antenna geometry shown in Fig. 1b. The antenna structure is located in the middle of a 20-mm-long coplanar transmission line consisting of two parallel 5- μ m-wide aluminum lines separated from each other by 10 μ m. The electric field of the focused incoming THz radiation induces a transient bias voltage across the 5 μ m gap between the two arms of this receiving antenna, directly connected to a low-noise current amplifier. The amplitude and time dependence of this transient voltage is obtained by measuring the collected charge (average current) versus the time delay between the THz pulses and the delayed CPM laser pulses in the 5 mW detection beam. These pulses synchronously gate the receiver, by driving the photoconductive switch defined by the 5 μ m antenna gap.

For the transmitting antenna shown in Fig. 2a, identical to the receiving antenna and also fabricated on ion-implanted SOS, we measure the transmitted THz pulse shown in Fig. 2b. This pulse is shown on an expanded time scale in Fig. 2c, where the measured FWHM pulselength of 420 fsec (with no deconvolution) is indicated. This pulselength is significantly shorter than the 540 fsec pulse obtained from the same experimental arrangement, but with 30- μ m-long antennas (1). The use of antennas smaller than Fig. 2a did not significantly shorten the THz pulses. The numerical Fourier transform of Fig. 2b is shown in Fig.

2d, where the amplitude spectrum is seen to extend beyond 3 THz. The sharp spectral features are water lines (6), from the residual water vapor present in the apparatus.

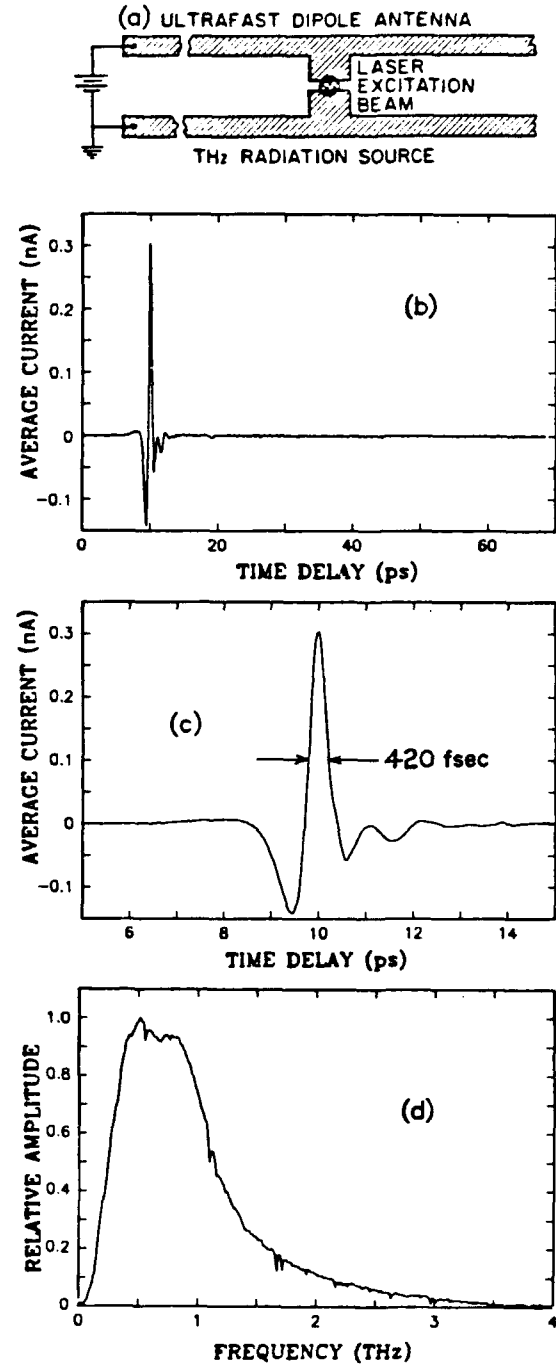


Fig. 2 (a) Transmitting antenna, (b) Measured THz pulse, (c) Measured THz pulse on expanded time scale, (d) Amplitude spectrum of Fig. 2b.

Two effects reduce the spectral extent of the measured pulse (Fig. 2d). These are the frequency-dependent transfer function (7) of the THz optical system (Fig. 1a) and the THz absorption in the sapphire (SOS) chips (5). The transmission function describing these two effects is presented in Fig. 3a. Dividing the measured spectrum in Fig. 2d by this transmission function we obtain Fig. 3b. Here, the spectral extent is determined only by the product of the receiver response and the transmitted spectrum. Because the transmitter and receiver are identical, by the reciprocity theorem (8), the transmitted spectrum is identical to the receiver response, and is given by the square root of Fig. 3b shown in Fig. 3c.

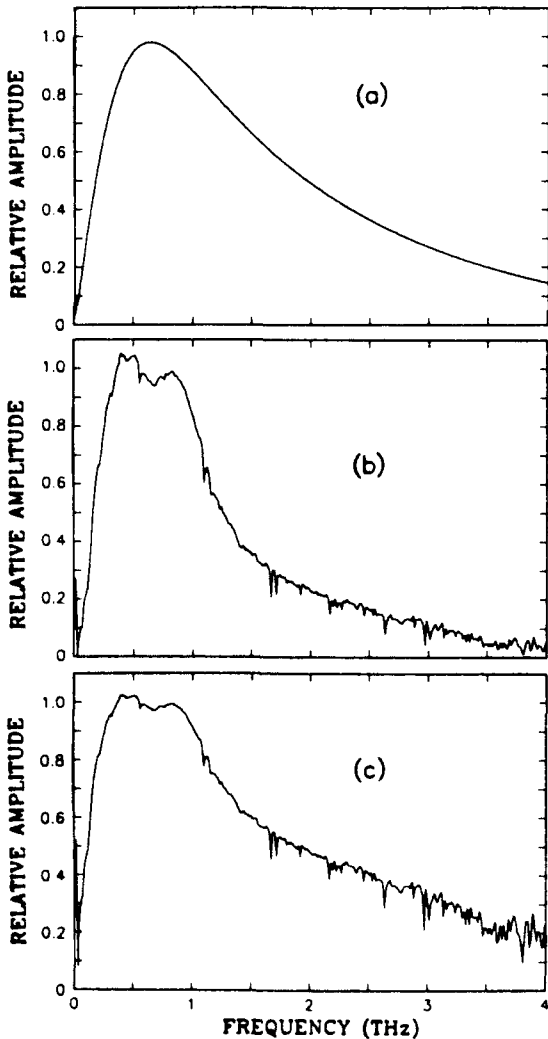


Fig.3 (a) Transmission function, (b) Amplitude spectrum of Fig. 2c divided by transmission function, (c) Amplitude spectral response of transmitter and receiver.

In the small antenna limit corresponding to the Hertzian dipole (2,3), the generated radiation field is proportional to the time-derivative of the current pulse. Based on our results we conclude that the current in the antenna is mainly determined by the intrinsic response of the semiconductor itself. We will now briefly derive the intrinsic time-domain response function for a semiconductor described by the simple Drude formalism. For this case the free carriers are considered as classical point charges subject to random collisions. Here we use the simplest version of this model for which the collision damping is independent of the carrier energy and for which the frequency dependent complex conductivity $\sigma(\omega)$ is given by (9)

$$\sigma(\omega) = \sigma_{dc} \frac{i\Gamma}{\omega + i\Gamma}, \quad (1)$$

where $\Gamma=1/\tau$ is the damping rate and τ is the average collision time. This relationship is in good agreement with recent time-domain spectroscopy measurements on lightly doped silicon from low frequencies to beyond 2 THz (9). The dc conductivity is given by $\sigma_{dc} = e\mu_{dc}N$, where e is the electron charge, μ_{dc} is the dc mobility and N is the carrier density. In the following discussion it is helpful to cast the formalism into a frequency dependent mobility as

$$\mu(\omega) = \mu_{dc} \frac{i\Gamma}{\omega + i\Gamma}, \quad (2)$$

The dc current density is given by $J_{dc} = \sigma_{dc}E$, or equivalently $J_{dc} = eE\mu_{dc}N$, where E is a constant electric field. Because of the linearity of the current in N , for a time dependent carrier density $N(t)$, the time dependent current density can be written as

$$J(t) = eE \int_{-\infty}^t \mu(t-t')N(t')dt', \quad (3)$$

where $\mu(t-t')$ is the time-domain response function for the mobility. This function is determined by the inverse transform of the frequency dependent mobility to be the causal function

$$\mu(t-t') = \mu_{dc}\Gamma e^{-\Gamma(t-t')} \quad (4)$$

which vanishes for negative $(t-t')$.

In order to facilitate the understanding of the photoconductive switch it is useful to rewrite the basic Eq. (3) in the equivalent form,

$$J(t) = eEA \int_{-\infty}^t \mu(t-t') \int_{-\infty}^{t'} R_c(t'-t'') I(t'') dt'' dt', \quad (5)$$

where $I(t'')$ is the normalized intensity envelope function of the laser pulse, A is a constant giving the conversion to absorbed photons/volume and R_c describes the decay of the photogenerated carriers. By defining a new photocurrent response function $j_{pc}(t-t')$, we can rewrite Eq.(5) in the following form

$$J(t) = \int_{-\infty}^t j_{pc}(t-t') I(t') dt', \quad (6)$$

where $j_{pc}(t-t')$ is obtained by evaluating Eq.(5) with a delta function $\delta(t'')$ laser pulse. Assuming the causal function $R_c(t'-t'') = \exp(-(t'-t'')/\tau_c)$, describing a simple exponential decay of the carriers with the carrier lifetime τ_c (significantly longer than the average collision time τ) for positive $(t'-t'')$ and vanishing for negative $(t'-t'')$, and that $\mu(t-t')$ is given by the Drude response of Eq. (4), the causal response function $j_{pc}(t-t')$ is then evaluated to be

$$j_{pc}(t) = \frac{\mu_{dc} eEA\Gamma}{\Gamma - 1/\tau_c} (e^{-t/\tau_c} - e^{-t/\Gamma}) \quad (7)$$

for positive $t = (t-t')$ and shown to vanish for negative t . In the short pulse limit of the ultrafast excitation pulses, the time dependence of the photocurrent $J(t)$ is approximately equal to that of the photocurrent response function $j_{pc}(t)$ for positive t . For a long carrier lifetime, the time dependence of $j_{pc}(t)$ is described by a simple exponential rise with a risetime of the order of $\tau = 1/\Gamma$, which is equal to 270 fsec and 150 fsec for the electrons and holes, respectively, in lightly doped silicon (9). As these results show, the material response can be slow compared to the duration of the ultrafast laser excitation pulses which can be as short as 10 fsec, but is more typically of the order of 60 fsec.

For the photoconductive switches considered here, we assume the time-domain response

function $j_{pc}(t)$ to have the time dependence described by Eq. (7). This response function is

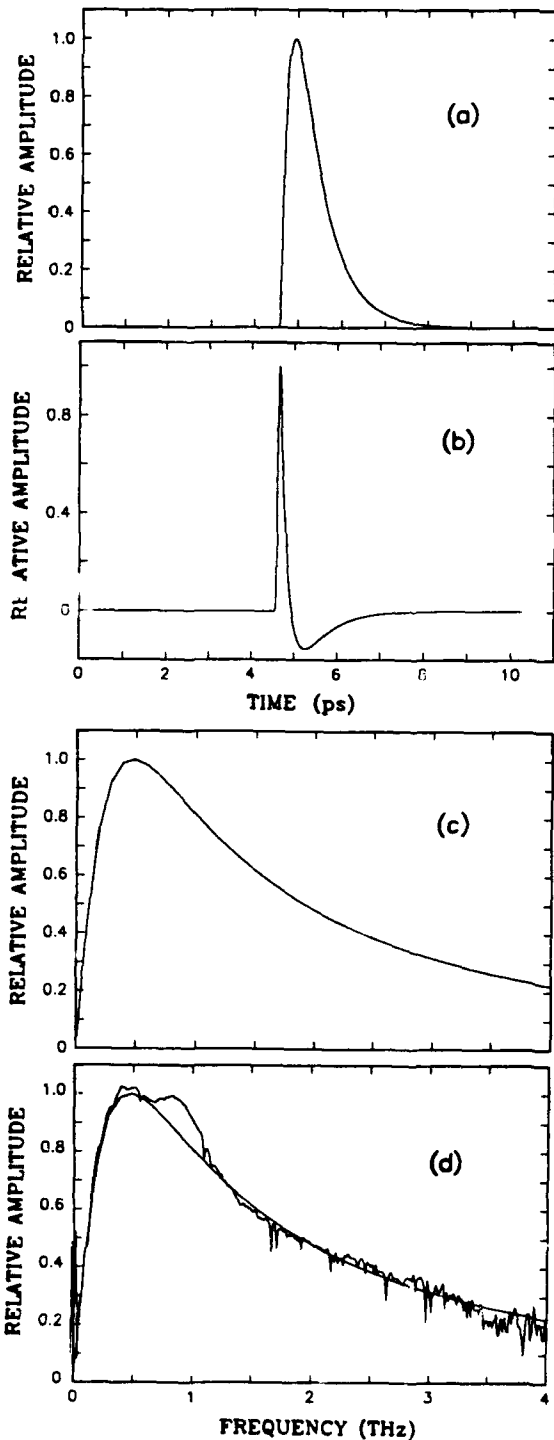


Fig.4 (a) Calculated current pulse in antenna, (b) Time-derivative of current pulse, (c) Amplitude spectrum of Fig. 4b, (d) Comparison of Figs. 4c and 3c.

then correlated with a Gaussian shaped laser pulse with a FWHM of 60 fsec. The carrier lifetime τ_c has been measured to be 600 fsec for ion-implanted SOS (10). As demonstrated above good agreement with experiment is obtained with the average collision time $\tau = 190$ fsec. With these parameters the calculated shape of the current pulse in the photoconductive switch and the Hertzian dipole antenna is presented in Fig. 4a. The time derivative of this pulse is given in Fig. 4b, where an extremely fast transient, corresponding to the rising edge of the current pulse, is seen. The numerical Fourier transform of Fig. 4b, presented in Fig. 4c, is the predicted amplitude spectrum of the transmitter. In Fig. 4d, this spectrum is compared with the amplitude spectrum of the transmitter from Fig. 3c; the agreement is excellent. Thus, we have determined an experimentally self-consistent time-domain response function describing the current in the dipole antenna, although the 190 fsec risetime (collision time) seems too slow for ion-implanted SOS.

The well-characterized THz beam system and ultrafast detector of Fig. 1 can now be used to determine the spectral response of a new source of extremely short pulses of THz radiation (4). The operation of this source is based on a recently discovered optoelectronic effect (11), initially used to generate 350 fsec electrical pulses on a coplanar transmission line by focusing ultrafast laser pulses on the interface (edge) of the positively biased line. Here, as illustrated in Fig. 5a, we use the same technique with a different line geometry and together with the THz beam system to capture the radiation emitted into the substrate from the point of excitation. The 20-mm long coplanar transmission line structure consists of two 10- μm -wide, Ni-Ge-Au metal lines separated by 80 μm and fabricated on intrinsic, high-resistivity GaAs. Irradiating the edge of the positively biased line with focused 10 μm -diameter, ultrafast laser pulses produces synchronous bursts of electromagnetic radiation. This source is completely compatible with the THz beam system and merely replaces the source chip.

The measured THz pulse emitted from the laser excited metal-GaAs interface with +60V bias across the transmission line is shown in Fig. 5b, and on an expanded time scale in Fig. 5c. The feature (dip) on the falling edge of the THz pulse

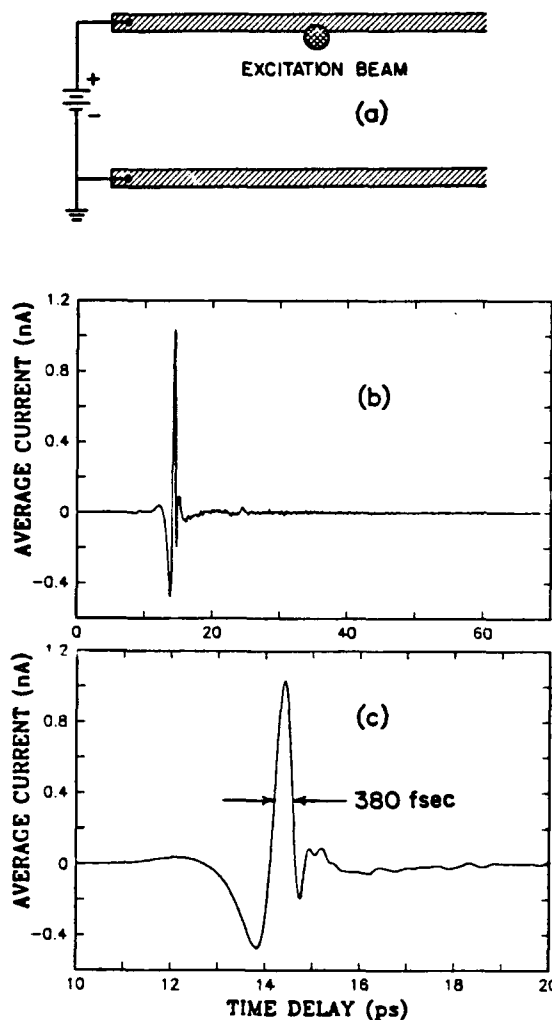


Fig. 5 (a) New method to generate pulses of THz radiation, (b) Measured THz pulse, (c) Measured THz pulse on an expanded time scale.

is the sharpest feature ever measured with an ion-implanted, SOS detector. The dip is caused by the pulse reshaping due to the dispersive (5) propagation of the ultrashort THz pulse through the 0.46-mm-thick GaAs generation chip and the 0.46-mm-thick sapphire substrate of the SOS detection chip. Because of the exceptionally low dispersion and absorption of silicon (5), the 13.5 mm propagation through the silicon lenses does not significantly effect the pulseshape. The measured 190 fsec time delay from the minimum of the dip to the next later maximum, demonstrates an exceptionally fast receiver

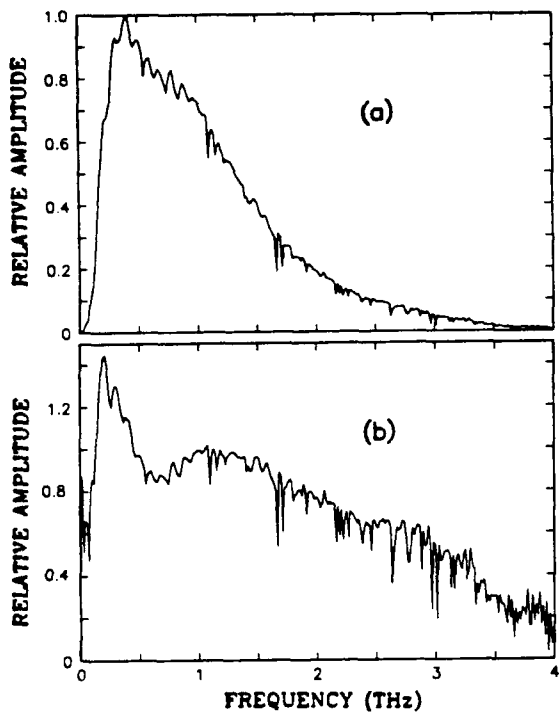


Fig.6 (a) Amplitude spectrum of Fig.5b, (b) Amplitude spectrum (Fig. 6a) divided by the transmission function (Fig.3a) and by the receiver response (Fig. 4c).

response time, consistent with the time-domain response function describing the current in the receiving antenna as given by Eq. (7).

The numerical Fourier transform of the pulse of Fig. 5b, as presented in Fig. 6a, is only a lower limit to the true spectral extent. However, by using the above information characterizing the THz beam system, we can now access the true spectral response of this source. Accordingly, the spectrum in Fig. 6a is divided by the transmission function (Fig. 3a) and then divided by the receiver frequency response (Fig. 4c). The result shown in Fig. 6b illustrates the broad spectrum of this source. Again, the sharp line structure is due to water absorption lines (6).

ACKNOWLEDGMENTS

We acknowledge stimulating and informative conversations with Stephen Ralph and Joshua Rothenberg. Martin van Exter initially calculated the THz optical transfer function and an early version of the time-domain response function. Søren Keiding made some preliminary measurements on the GaAs based source. The excellent masks and wafer fabrications were done by Hoi Chan.

REFERENCES

1. Ch. Fattiger and D. Grischkowsky, *Appl. Phys. Lett.*, Vol. 53, 1480 (1988); Vol. 54, 490 (1989); Proc. Picosecond Electronics and Optoelectronics Topical Meeting (Salt Lake City, UT), Mar. 8-10, 1989, p225; M. van Exter, Ch. Fattiger, and D. Grischkowsky, *Appl. Phys. Lett.*, Vol. 55, 337 (1989); M. van Exter and D. Grischkowsky, *IEEE Trans. Microwave Theory Tech.*, Vol.38, 1684 (1990).
2. P.R. Smith, D.H. Auston, and M.C. Nuss, *IEEE J. Quantum Elect.* Vol. 24, 255 (1988).
3. D.H. Auston, K.P. Cheung, and P.R. Smith, *Appl. Phys. Lett.*, Vol. 45, 284 (1984).
4. N. Katzenellenbogen and D. Grischkowsky, *Appl. Phys. Lett.*, Vol. 58, 222 (1991).
5. D. Grischkowsky, S. Keiding, M. van Exter and Ch. Fattiger, *J. Opt. Soc. Am. B*, Vol.7, 2006 (1990).
6. M. van Exter, Ch. Fattiger, and D. Grischkowsky, *Optics Lett.*, Vol.14, 1128, (1989).
7. J.C.G. Lesurf, "Millimetre-Wave Optics, Devices & Systems", (Adam Hilger, Bristol, England, 1990).
8. G.D. Monteath, "Applications of the Electromagnetic Reciprocity Principle", (Pergamon Press, Oxford, 1973).
9. Martin van Exter and D. Grischkowsky, *Phys. Rev. B*, Vol. 41, 12 140 (1990)
10. F.E. Doany, D. Grischkowsky, and C.-C. Chi, *Appl. Phys. Lett.*, Vol. 50, 460 (1987).
11. D. Krökel, D. Grischkowsky, and M.B. Ketchen, *Appl. Phys. Lett.*, Vol. 54, 1046 (1989).

Low-Temperature Epitaxially Grown GaAs as a High-Speed Photoconductor for Terahertz Spectroscopy

James M. Chwalek, John F. Whitaker, and Gerard A. Mourou

Ultrafast Science Laboratory, University of Michigan, Ann Arbor, Michigan 48109-2099

I. Introduction

Photoconductive elements have been employed to generate and detect ultrafast electrical signals in many areas of optical electronics.[1,2] One outstanding application of these structures, when they are fabricated on substrates with rapid recombination times, is as transmitting and receiving antennas that can be used for millimeter-wave and submillimeter-wave spectroscopy. Experiments which characterize a terahertz radiation system using dipole-like antennas have been carried out,[3] and the system has been applied to the spectroscopy of dielectrics [4] and semiconductors.[5]

Assuming that short laser pulses and a high-quality imaging system are available, the fidelity of the broadcast signals and the resolution attainable for a spectroscopy system depend primarily on the photoconductor material and antenna system. The best photoconductive-switch substrates combine an extremely short photoexcited carrier-response lifetime (< 200 fs) with adequate carrier mobility ($\sim 100 \text{ cm}^2/\text{V}\cdot\text{s}$), and they possess ultrafast response speed, high responsivity, high dielectric-breakdown field ($> 200 \text{ kV/cm}$), and a high resistivity ($\sim 10^7 \Omega\cdot\text{cm}$). Under the correct growth conditions, the material system that has been found to surpass semi-insulating, amorphous, and radiation-damaged semiconductors in these respects is low-temperature, MBE-grown GaAs (LT GaAs).[6-7] We demonstrate, for the first time, the advantages of the use of optimized LT-grown materials as they are applied to the photoconductive generation and detection of radiated terahertz bursts. In this investigation, dipole-like antennas fabricated on LT-grown materials with the cleanest photoconductive response have been found to generate the shortest, and thus widest bandwidth, radiation bursts. Measurements were made using antennas fabricated on radiation-damaged silicon-on-sapphire (SOS) and LT GaAs layers grown at

different temperatures so that the performance of each could be compared and the optimum growth temperature of the latter determined.

We also explore alternative antenna structures - in the form of logarithmically-periodic planar antennas - in order to increase the bandwidth and the radiation efficiency over conventional dipole antennas.

Lastly, we extend the coherent time-domain spectroscopy technique to the measurement of thin absorbing films. In this case the transmission of terahertz radiation through a thin-film of a high-temperature superconductor, $\text{YBa}_2\text{Cu}_3\text{O}_{7-x}$ (YBCO), was measured above and below the critical temperature. From these measurements, the complex conductivity was directly obtained without the use of a Kramers-Kronig analysis.

II. LT-GaAs layers

The higher responsivity of the LT GaAs layers allows larger signals to be generated by the transmitter, as well as a larger response to be induced in the receiver for the same detected field. Furthermore, the higher breakdown of the LT GaAs materials allows higher bias voltages and larger photogenerated signals, so that the overall signal-to-noise ratio is found to be approximately 20 times greater than for a comparable system employing dipole-like antennas fabricated on radiation-damaged silicon-on-sapphire (SOS).

Figure 1 shows photoconductively generated pulses using a gap in a coplanar transmission line fabricated on different samples of LT GaAs grown at two different temperatures at MIT-Lincoln Laboratory. Until now, it was believed that a 200°C growth temperature would yield a photoconductive material with the fastest response. However, using external electro-optic measurement techniques, the material that was grown at 190°C was found to yield a pulse with an

unconvolved FWHM of 480 fs with no persistent tail. This would thus represent an upper limit to the response time of this material. The LT GaAs grown at 200°C responded with a FWHM of 630 fs, due partly to the presence of prolonged photoconductivity. Although the accuracy of the absolute growth temperature is questionable at these low growth temperatures, the distinguishing factor is the crystalline structure of the material during growth. In the case of the 190°C material, it is on the verge of becoming polycrystalline during growth (as indicated by the RHEED pattern). The material grown at 200°C is crystalline during growth. In both cases the material is post-annealed in situ at 600°C in an arsenic over-pressure. Measurements on a material grown at an intermediate temperature indicated improvement over the 200°C material, but still exhibited a tail on the response. The existence of this tail, seriously inhibits an accurate frequency domain analysis as artifacts are introduced during truncation when a numerical fast Fourier transform (FFT) is applied.

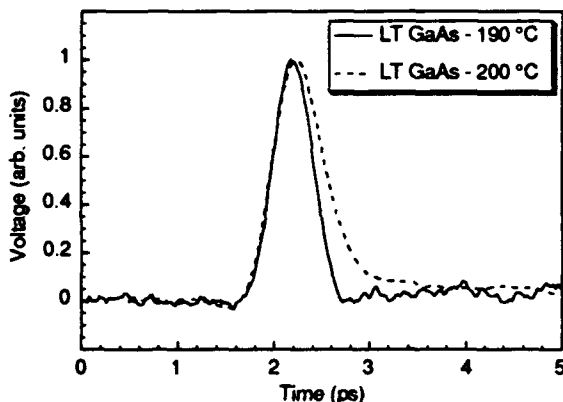


Figure 1. Electrical pulses photoconductively generated using LT GaAs substrates at 190°C and 200°C growth temperatures and measured via electro-optic sampling.

Next, coplanar striplines which have been shown to behave as dipole-like-antenna radiators [3] were fabricated on the same LT-grown GaAs materials and mounted on hyperhemispherical-dome lenses made of high-resistivity silicon. The dc-biased transmitter was positioned several centimeters from an identical receiving antenna, allowing a nearly-collimated radiation beam to be broadcast and detected. The signals were triggered by 150-fs laser pulses at the transmitter and then measured via photoconductive sampling at the receiver. The measured radiation was a convolution of the broadcast signal and the receiver response, so the result using the 190°C material was far superior to that using the 200°C material. The FWHM as determined by a Gaussian fit to the central spike of the time-domain waveform was found to be 0.44 ps (Fig. 2). This is only an upper limit to the response which is limited by the antenna bandwidth and the laser pulse duration. The spectrum generated using this optimized

(190°C) material extends beyond 2.5 THz, allowing spectroscopic measurements to be made on low-loss materials at frequencies in excess of 2 THz (Fig. 3).

III. Log-periodic Antennas

In order to increase both the bandwidth and the amplitude of the radiated signals, logarithmically-periodic planar antennas fabricated on the LT GaAs have also been tested (Fig. 4). [8] The antenna design uses a ratio of 0.5 for the distance of successive teeth from the center with an arm angle of 45°. The temporal characteristics of these broadband, efficient radiators display an oscillatory behavior exhibiting a variable period, with a correlation noted between this performance and the spacing of the stub-gap pairs on the log-periodic structure (Fig. 5). The antenna can be modeled as a series of resonant structures periodically placed along a transmission line. Upon creation and subsequent propagation of an electrical transient originating at the center of the antenna, each one of the resonant teeth in turn is encountered and radiates at the corresponding resonant frequency. This gives rise to

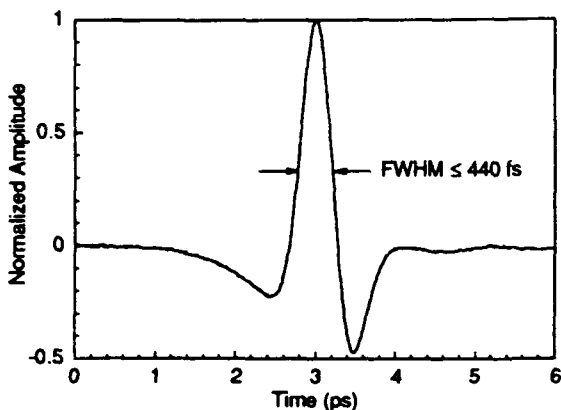


Figure 2. Radiation burst photoconductively generated and detected using dipole-like antennas fabricated on LT GaAs grown at 190°C

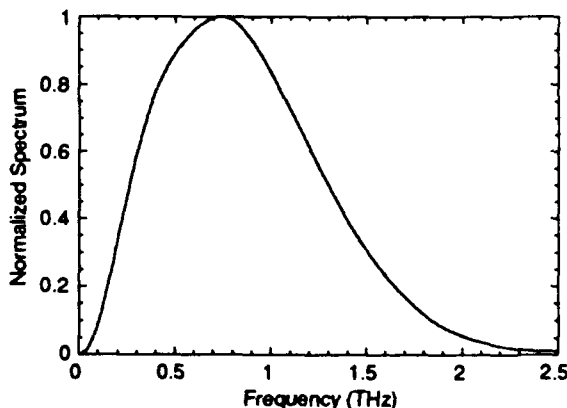


Figure 3. Spectrum of the time-domain waveform of Fig. 2

the chirp-like temporal characteristics seen in Fig. 5. An experimental comparison has been made between photoconductively excited log-periodic and the coplanar-stripline dipole-like antennas, with the amplitude of the radiated field of the former found to be at least 10 times greater than that of the latter. This was combined with a log-periodic receiver and the overall amplitude increase scaled roughly as the square of the amplitude increase seen with just the transmitter replaced by a log-periodic antenna (*i.e.*, ~100 times increase).

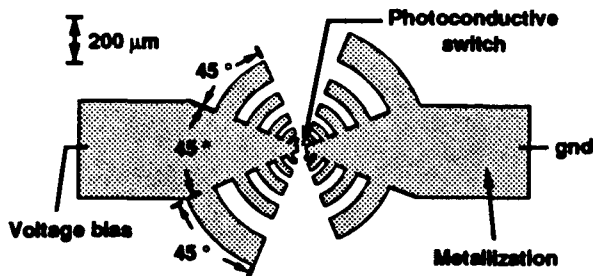


Figure 4. A logarithmically-periodic antenna structure.

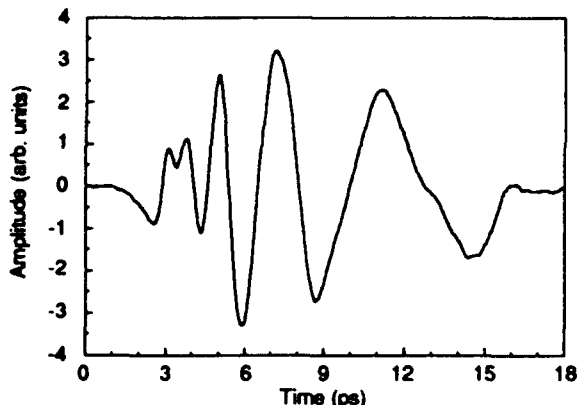


Figure 5. The time-domain response of a transmitter using the antenna shown in Fig. 4. The receiver was a dipole-like antenna.

Despite this large increase in efficiency over a more conventional dipole-like antenna design, the discrete nature of the antenna makes applications to terahertz spectroscopy less desirable than using dipole-like antennas. However, this antenna may have other uses which take advantage of its broadband, high efficiency nature, such as pulsed radar.

IV. High- T_c Superconducting Thin-Films

Studies of the high-frequency properties of superconducting materials based on their response to millimeter- and submillimeter-wave electromagnetic perturbations are of special interest. They give insight into the nature of quasiparticle excitations and pairing mechanisms, as well as a direct assessment of how the materials would perform as passive microwave devices

(*e.g.*, interconnects, resonators, filters, *etc.*). The latter is found via measurements of the complex conductivity or surface impedance. In the past, time-domain techniques have been used to assess the high-frequency response of YBCO thin films by measuring the dispersion characteristics of short electrical pulses (~1 ps) propagating on transmission line structures patterned from these films.[9,10] In one such study (Ref. 10) the surface impedance was obtained for frequencies extending to 500 GHz. The coherent time-domain spectroscopy technique offers a nondestructive, noncontact way to study the complex conductivity of a thin-film, a fundamental quantity which may be directly compared to theories, BCS-based or otherwise.

We first apply the terahertz spectroscopy technique to assess the characteristics of a MgO substrate on which the high- T_c thin films are later deposited. From a measurement of the transmission function the complex index, N can be directly obtained. The results are shown in Fig. 6. The real part of the index increases only slightly with frequency. Indeed this demonstrates the ability to accurately measure index changes of less than 2% over a bandwidth exceeding 2 THz in thin samples (0.5 mm). From the imaginary part of the index the power absorption was within experimental error having an upper limit of ~4 cm⁻¹ at room temperature over the entire measured frequency range. At lower temperatures this value decreases even further.[11] These properties make this substrate an excellent choice as a microwave substrate for circuit applications.

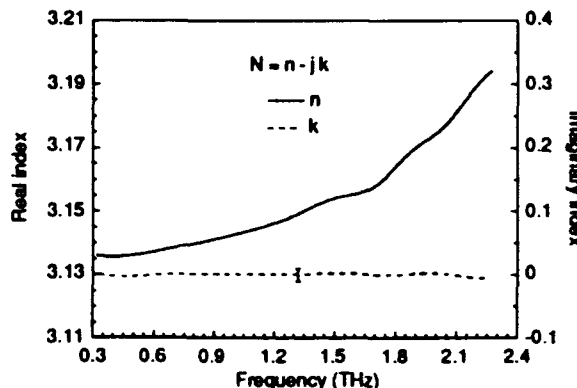


Figure 6. The measured complex index for a 500-μm thick magnesium oxide substrate.

Next a superconducting YBCO thin film (~1000-Å thickness) deposited on a MgO substrate was placed between the antennas. The epitaxial *c*-axis oriented film was produced using a standard laser-ablation process.[12] Figure 7 shows the time-domain response in transmission for temperatures above and below the critical temperature (~80 K). The changes associated with the onset to superconductivity can be directly seen. A dramatic decrease in the transmitted signal amplitude occurred mainly as a result of the increase in

the reflection of the incident wave. An even more dramatic change can be seen for temperatures below $-T_c/2$. A phase shift and an accompanying change in pulse shape are also identified. This is a direct result of the presence of superconducting electrons.

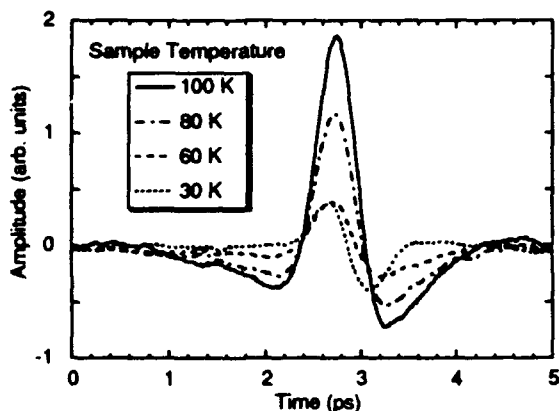


Figure 7. Transmitted time domain waveforms through a $\sim 1000 \text{ \AA}$ thick YBCO thin-film above and below the transition temperature.

From the measured transmission function (in this case the frequency response of the film-on-substrate divided by the response of the substrate alone) and the standard thin-film transmission formula,[13] the complex index as well as the complex conductivity were obtained.[14] A plot of the normalized complex conductivity versus frequency for sample temperatures above and below the critical temperature is shown in Fig. 8. The small undulations in some of the values is an artifact due to the noise present in the time domain waveforms (see Fig. 7). The conductivities were normalized to the normal state conductivity just above T_c . A number of dramatic effects can be seen. The imaginary part of the conductivity, σ_2 , nearly zero in the normal state, increases greatly at low frequencies exhibiting a $1/\omega$ frequency dependence, as expected from theory.[15] This behavior of σ_2 is primarily from superconducting pairs. The real part of the conductivity, σ_1 , decreases below the normal state value for low temperatures. However this reduction in σ_1 is not as great as would be expected, a sign of residual loss which is associated with the depressed T_c of the film. Further optimization of the films are needed for this non-lattice matched substrate.

V. Conclusions

We have demonstrated a coherent time-domain spectroscopy system which employs low-temperature MBE grown GaAs. Due to the superior material properties of LT GaAs it can out perform

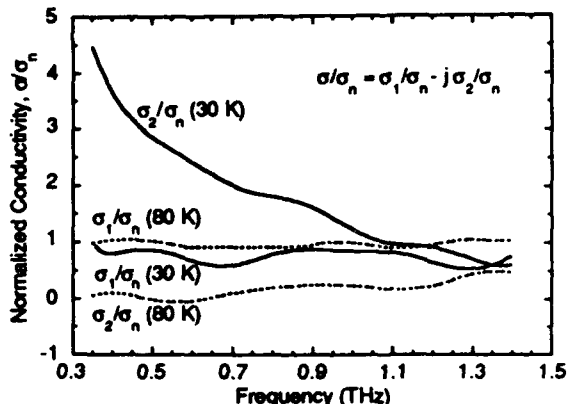


Figure 8. The complex conductivity obtained from the transmitted waveforms of Fig. 7.

conventional photoconductive materials such as radiation damaged silicon-on-sapphire. A log-periodic antenna was demonstrated which had a measured increase in radiation efficiency of ~ 10 times over a conventional dipole-like antenna. We have also shown that the terahertz spectroscopy technique can be used to nondestructively measure fundamental ac properties of thin superconducting high- T_c films.

Acknowledgments

We wish to thank F.W. Smith and A.R. Calawa of MIT-Lincoln Laboratory for growing and supplying the LT-grown GaAs materials, G. Rebeiz of the University of Michigan for aid in the design of the log-periodic antennas, and J. A. Agostinelli of the Eastman Kodak Co. for supplying the superconducting films measured. This work has been supported by the AFOSR, University Research Initiative under contract number AFOSR-90-0214 and NASA under contract number NCC3-130.

References

1. for instance, see chapters within *Picosecond Optoelectronic Devices*, Edited by Chi H. Lee, Academic Press, Orlando, 1984.
2. C. H. Lee, "Picosecond optics and microwave technology," *IEEE Trans. on Microwave Theory Tech.*, vol. 38, pp. 596-607, May 1990.
3. Martin van Exter and D. Grischkowsky, "Characterization of an optoelectronic terahertz beam system," *IEEE Trans. on Microwave Theory Tech.*, vol. 38, pp. 1684-1691, November 1990.
4. D. Grischkowsky, Søren Keiding, Martin van Exter, and Ch. Fattinger "Far-infrared time-domain spectroscopy with terahertz beams of dielectrics and semiconductors," *J. Opt. Soc. Am. B*, vol. 7, pp. 2006-2014, October 1990.

5. Martin van Exter and D. Grischkowsky, "Optical and electronic properties of doped silicon from 0.1 to 2 THz," *Appl. Phys. Lett.*, vol. 56, pp. 1694-1696, 23 April, 1990.
6. F. W. Smith, H. Q. Le, V. Diadiuk, M. A. Hollis, A. R. Calawa, S. Gupta, M. Frankel, D. R. Dykaar, G. A. Mourou, and T. Y. Hsiang, "Picosecond GaAs-based photoconductive optoelectronic detectors," *Appl. Phys. Lett.*, vol. 54, pp. 890-892, 6 March 1989.
7. J.F. Whitaker, J.A. Valdmanis, M.Y. Frankel, S. Gupta, J.M. Chwalek, and G.A. Mourou, "External electro-optic integrated circuit probing," *Microelectronic Engineering*, vol. 12, pp. 369-379, 1990.
8. *Antenna Theory and Design*, W. L. Stutzman and G. A. Thiele, John Wiley & Sons, New York, 1981, p.288.
9. D.R. Dykaar, R. Sobolewski, J. M. Chwalek, J. F. Whitaker, T. Y. Hsiang, and G. A. Mourou, "High-frequency characterization of thin-film Y-Ba-Cu oxide superconducting transmission lines," *Appl. Phys. Lett.*, vol. 52, pp. 1444-1446, 25 April, 1988.
10. M. C. Nuss, K. W. Goossen, P. M. Mankiewich, R. E. Howard, B. L. Straughn, G. W. Berkstresser, and C. D. Brandle, "YBa₂Cu₃O₇ superconductors for high-speed interconnects," *IEEE Electron Device Lett.*, vol. 11, pp. 200-202, May 1990.
11. D. Grischkowsky and Søren Keiding, "THz time-domain spectroscopy of high T_c substrates," *Appl. Phys. Lett.*, vol. 57, pp. 1055-1057, 3 September 1990.
12. X. D. Wu, A. Inam, T. Venkatesan, C. C. Chang, P. Barboux, J. M. Tarascon, and B. Wilkens, *Appl. Phys. Lett.*, vol. 52, pp. 754-756, 1988.
13. *Advance Optical Techniques*, edited by A. C. S. Van Heel, North-Holland, Amsterdam, p. 268.
14. J. M. Chwalek, J. F. Whitaker, and G. A. Mourou, "Submillimeter wave response of superconducting YBa₂Cu₃O_{7-x} using coherent time-domain spectroscopy," *Electronics Letters*, vol. 27, pp. 447-448, 28 February 1991.
15. *Applied Superconductivity*, edited by V. L. Newhouse, Academic Press, New York, 1975, Vol. II, ch. 8.

Broadband Periodic Antennas for Detecting Picosecond Terahertz Radiation

D. R. Dykaar, B. I. Greene, J. F. Federici, A. F. J. Levi, L. N. Pfeiffer, and R. F. Kopf

AT&T Bell Laboratories, 600 Mountain Avenue, Murray Hill, New Jersey 07974-2070

ABSTRACT

A new type of log-periodic antenna, the wire log-spiral, has been designed and implemented on low temperature grown GaAs substrates. The new antenna is compared to two traditional antenna designs (log-periodic and dipole) for the detection of pulsed THz radiation.

INTRODUCTION

Microwave pulses, with terahertz bandwidth and picosecond duration can be generated using standard femtosecond laser techniques, and detected using a 1/2 wave dipole antenna [1,2]. This antenna is typically 100 μm long and fabricated on a short carrier lifetime substrate, such as ion-implanted silicon on sapphire. The received signal is then electrically gated with the same femtosecond laser that is used to generate the RF. Gates are photolithographically defined at the center or feed point of the antenna.

This paper reports on the design, fabrication and initial performance demonstration of a new type of antenna for detection of broadband pulsed THz radiation, the log periodic antenna. In addition, a new kind of log periodic structure, the Wire Log Spiral (WLS), is presented. The new design is compared experimentally with a dipole and a standard log-periodic design, also fabricated for this purpose.

PERIODIC ANTENNAS

Unlike a 1/2 wave dipole which is resonant at a single frequency, logarithmically, or Log Periodic (LP) antennas are a family of frequency

independent antennas [3]. Their large bandwidth is due to the repetition of a pattern or cell. One advantage of this design is that it is resonant at $\approx 1/4$ wavelength excitation for *both* the longest and shortest teeth. As was shown in Ref. [3], this structure can be reduced to wire outlines, as the currents flow at the outer edges of the conductors. This approximation greatly simplifies the layout. An outline of the LP antenna electrodes used in this work is shown as an inset in Fig 2(b). In addition, non-planar implementations can narrow the beam pattern of a given antenna, but are not considered here for practical reasons. For a given design the number of elements in an antenna can be varied. This reduces the impedance for symmetrically connected arms, as long as the electrodes do not overlap. The requirements for good antenna performance are the avoidance of edge effects and near constant impedance (at the feed point) over the entire frequency band.

Edge effects can be avoided by making the antenna large relative to the lowest frequency, or about 1/2 of the longest wavelength [4]. Both designs considered here are ≈ 1 mm across the longest dimension. The increasing impedance of the antenna with radius causes a resonant section to propagate any received energy toward the feed point in a backward wave configuration. This also tends to eliminate edge effects.

The requirement of constant impedance is critical for antennas which are fed by $50\ \Omega$ feed lines. In the original implementations operating at < 1 GHz great care was taken to integrate the coaxial feed cable into the structure (structures ranged in size from a few centimeters to several meters) [4]. For antennas which are gated at the

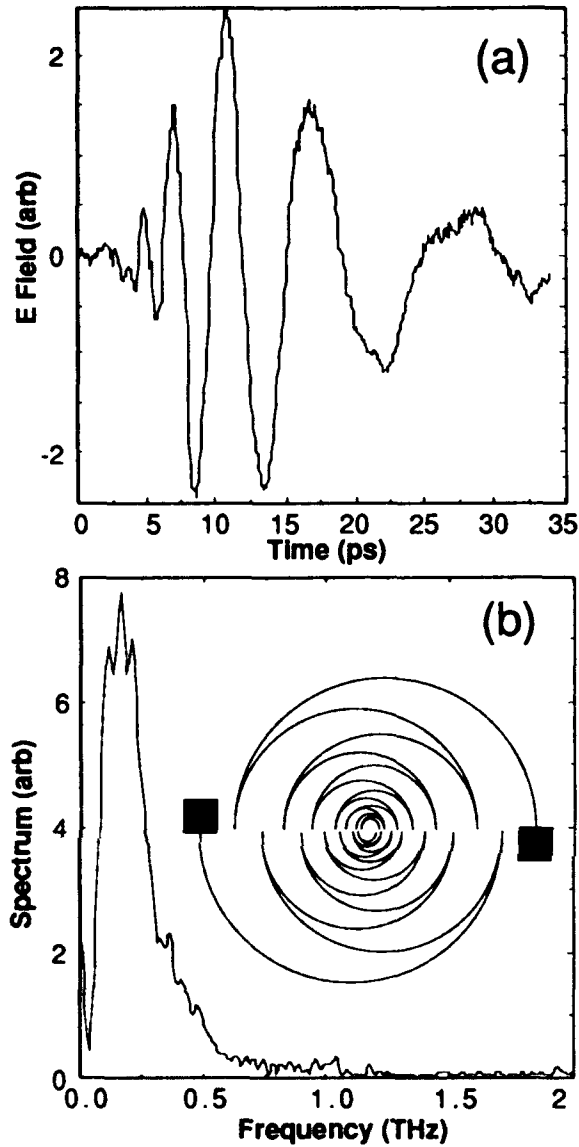


Figure 1. Wire Log-spiral antenna. (a) Measured time waveform, $E(t)$. (b) Fourier transform of $E(t)$. Inset shows electrode pattern. Line width is 5 μm and contact pads are 100x100 μm .

feed point, this requirement does not appear to be important (the switch effectively mixes the RF down to either the laser repetition rate or alternatively, the lock-in frequency). In these structures the gated, low frequency signals are read from the contact pads, using the antenna simply as a wire connecting the pad and feed point. Detected reflections were found to come from the backside of the wafer on which the antenna was fabricated, rather than the antenna edge.

Another antenna type is the LP-sinuous spiral, where the electrode pattern is generated by a more complicated mathematical expression [5]. The sinuous design is expected to offer better

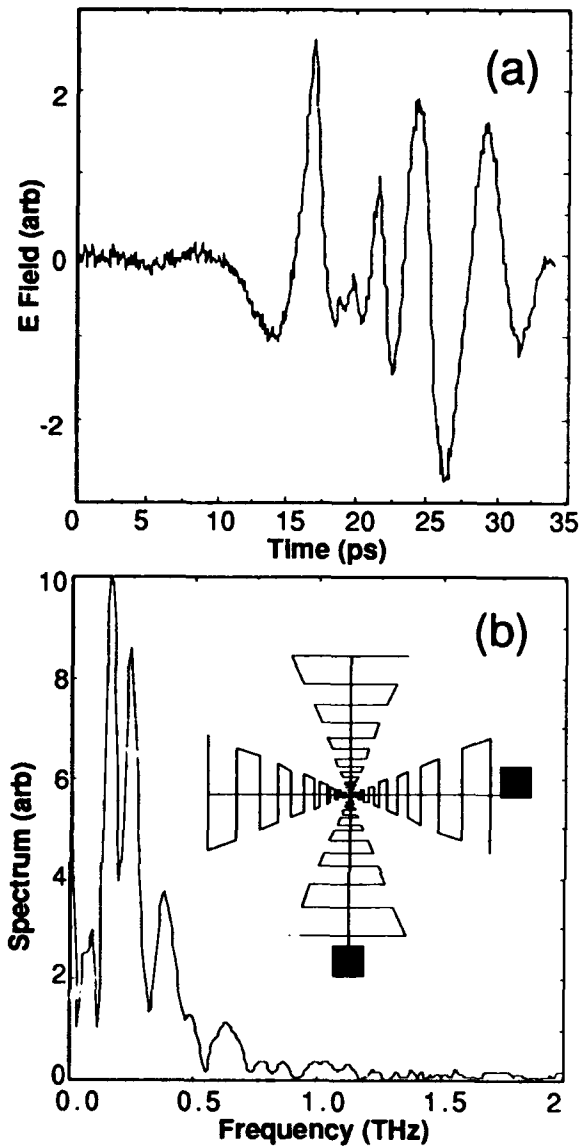


Figure 2. Log periodic antenna. (a) Measured time waveform, $E(t)$. (b) Fourier transform of $E(t)$. Inset shows electrode pattern. Line width is 5 μm and contact pads are 100x100 μm .

frequency coverage since the circular nature of the antenna produces a continuous range of resonances, while preserving the LP nature of the antenna.

By applying a similar reduction of the pattern to a wire outline with this design, the WLS structure results and is shown in the inset of Fig. 1(b). However, in this approximation, the antenna pattern is reduced to a series of *non-concentric* half circles whose radii scale in the same way as the LP antenna elements. The individual half circles are offset along the axis to alternately join and form a continuous path.

With both structures, the wire approximation violates the self complementary nature of the

antenna. We note that the LP design presented here is polarization independent, since it contains four arms. The WLS design has two arms, and manifests a polarization dependent response. Both antennas are fabricated by deposition of 1 μm thick by 5 μm wide gold electrodes on Low Temperature (LT) grown GaAs photoconductors [6].

EXPERIMENT

The THz RF pulse is derived by illuminating an InP wafer with $\sim 50 \mu\text{J}$, 70 fs Full Width at Half Maximum (FWHM) visible optical pulses derived from a 10 Hz amplified CPM dye laser system [1, 7]. Peak detected signals were several hundred millivolts at a current gain of 10^8 A/V . Signals were acquired using a current preamp and boxcar averager because of the low (10 Hz) repetition rate. The RF pulse is strongly polarized due to the orientation of the InP wafer, requiring correct antenna orientation. This was confirmed using a wire grid polarizer. A single experimental scan (acquisition time of ~ 1 minute) of the electric field, $E(t)$, incident on the WLS antenna as a function of gate delay time is shown in Fig. 1(a).

Analogous $E(t)$ data for the log periodic antenna is shown in Figs. 2(a) and 2(b). Unlike the WLS, peaks appear in the frequency spectrum. These are due to the discrete nature of the antenna which behaves as a series of resonant dipoles distributed along a transmission line.

The frequency dispersion (chirp) observed for both antennas is a consequence of the propagation time required for longer wavelength signals to reach the feed point of the antenna, and has been previously observed in another antenna type [8]. This dispersion can be advantageous when analyzing spectral response, as the time axis of Figs. 1(a) can also be viewed as the frequency axis since the phase of the Fourier transform is nearly linear (not shown).

By setting the phase of the transform to zero and performing an inverse Fourier transform, the chirp is removed and a short pulse similar to the dipole response (but symmetric) is produced, shown in Fig. 3 (a), with a FWHM about equal to the photoconductive switch response. The dipole antenna (100 μm elements) produces the same transformed response and is shown in Fig 3 (b). The qualitative accuracy of this approximation is seen by the small amount of energy in the wings. In comparison Fig. 4 shows the same zero phase transformation for the log periodic, with clearly poorer results due to the poor spectral overlap of the individual elements.

Both periodic antennas have been used as detectors in linear and nonlinear spectroscopic measurements on Pb [9] and GaAs [7].

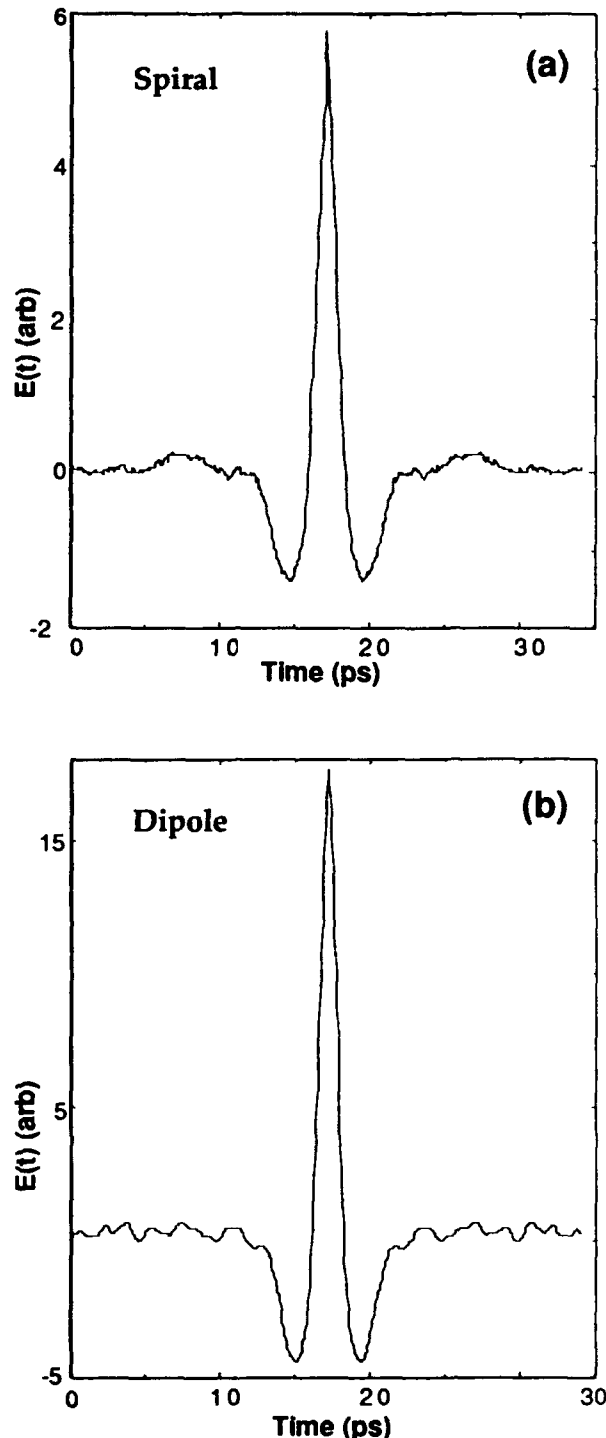


Figure 3. (a) Spiral antenna response with phase of transform set to zero and transformed back into the time domain. (b) Dipole antenna response after identical transformation.

Using etch techniques it should be possible to reduce the amount of dispersion for a given antenna [10]. Both designs produce peak amplitudes similar to a dipole antenna, but an order of magnitude larger total energies are detected due to the broader spectral coverage.

As these preliminary results were obtained using a photoconductor with a carrier recombination time of ~ 1 ps, the upper frequency detectable by these antennas was limited to ~ 1 THz. As our understanding of LT GaAs improves [11] these broadband, periodic structures will provide improved sensitivity and greater bandwidth. The smallest feature size is 10 - 20 μ m, so the highest *received* (as distinguished from detected) frequencies could be > 10 THz.

CONCLUSION

In conclusion, we have demonstrated two LP antenna designs for use with pulsed terahertz light sources. The wire log-spiral, a new design, is a simplification of a sinuous spiral which produces a smooth spectral response. Both types

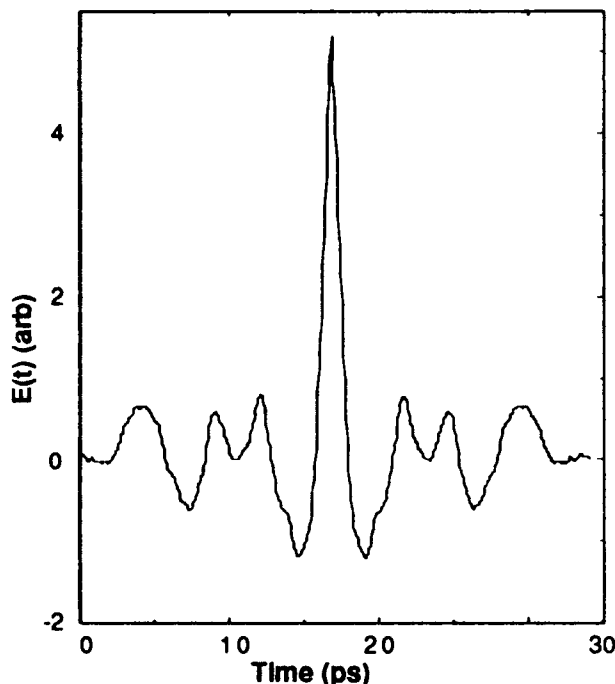


Figure 4. Log periodic response with zero phase transformation showing poor chirp linearity.

have an order of magnitude better overall response than dipole antennas presently in use. The wire log-spiral exhibits a smooth chirp which can be used directly for spectroscopic measurements or removed through Fourier transform manipulations, resulting in a short pulse limited by the photoconductive switch response.

REFERENCES

1. J.T. Darrow, B.B. Hu, X.-C. Zhang, and D.H. Auston, *Optics Letters*, **15**, (6), 223 (1989).
2. M. van Exter, Ch. Fattinger, and D. Grischkowsky, *Optics Letters*, **14**, 1128 (1989).
3. R.H. DuHamel and F.R. Ore, *Proceedings I.R.E. National Convention Record*, 139 (1959).
4. Y.T. Lo and S.W. Lee, *Antenna Handbook, Theory Applications and Design*, Van Nostrand Reinhold Co., New York (1988).
5. R.H. DuHamel, U.S. Patent #4658262, April 14, 1987. *and*, T.T. Chu and H.G. Oltman, Jr., *Microwave Systems News & Communications Technology*, **18**, (6), 40 (1988).
6. F. W. Smith, H. Q. Lee, V. Diadiuk, M. A. Hollis, A. R. Calawa, S. Gupta, M. Frankel, D.R. Dykaar, G.A. Mourou, and T.Y. Hsiang, *Applied Physics Letters*, **54**, (10), 890 (1989).
7. B.I. Greene, J.F. Federici, D.R. Dykaar, A.F.J. Levi, and L. N. Pfeiffer, *Optics Letters*, **16** (1), 48 (1990).
8. Y. Pastol, G. Arjavalasingam, and J.M. Halbout, *Elec. Lett.* **26**, (2), 133 (1990).
9. B.I. Greene, J.F. Federici, D.R. Dykaar, R. Dynes, and F. Sharifi, *Submitted to Applied Physics Letters*, 1991.
10. D.R. Dykaar, A.F.J. Levi, and M. Anzlowar, *Applied Physics Letters*, **57** (11), 1123, (1990).
11. D.J. Eaglesham, L.N. Pfeiffer, K.W. West, and D.R. Dykaar, *Applied Physics Letters*, **58** (1), 65 (1991).

Terahertz Absorption Between Split Subbands in Coupled Quantum Wells

Hartmut Roskos, Martin C. Nuss, Jagdeep Shah, Ben Tell, and Jack Cunningham

AT&T Bell Laboratories, Crawfords Corner Road, Holmdel, New Jersey 07733

Klaus Köhler

*Fraunhofer-Institut für angewandte Festkörperphysik, 7800 Freiburg,
Federal Republic of Germany*

ABSTRACT

The transition between split subbands (design splitting: 5 meV) in n-doped coupled quantum wells is investigated by time-domain spectroscopy with ultrafast pulses of far-infrared radiation. This very strong transition has a linewidth of 2.5 meV. The maximum absorption is observed at 4.2 meV photon energy, lower than the design splitting. We attribute this down-shift of the peak absorption tentatively to the influence of many-body interactions which lead to correction terms for the calculated transition energy in the same order of magnitude as the transition energy itself.

INTRODUCTION

Two quantum systems with energy levels in resonance with each other experience a splitting of these levels when the wavefunctions of the systems overlap. In semiconductor structures consisting of pairs of closely spaced quantum wells the wavefunction overlap of charge carriers in the wells leads to a novel kind of intersubband transition. To date, this transition has been studied by interband absorption and luminescence [1-5] and, most recently, by four-wave-mixing experiments [6]. Here, we report of the first direct absorption measurements of the split-subband transition in coupled quantum wells.

SAMPLE

The results discussed here are obtained with a sample consisting of 50 periods of pairs of identical square potential quantum wells grown by gas-source molecular-beam-epitaxy. Each pair is formed by two

80 Å thick GaAs layers separated by a 31 Å (11 monolayers) wide $\text{Al}_{0.3}\text{Ga}_{0.7}\text{As}$ barrier. 200 Å thick $\text{Al}_{0.3}\text{Ga}_{0.7}\text{As}$ buffer layers isolate the double quantum wells from each other. The buffer layers are n-doped providing modulation-doping ($n_{\text{well}} = 1.2 \times 10^{17} \text{ cm}^{-3}$) to the quantum wells. The whole stack of quantum wells is sandwiched between 500 Å thick layers of undoped $\text{Al}_{0.3}\text{Ga}_{0.7}\text{As}$. 5000 Å thick n-doped $\text{Al}_{0.3}\text{Ga}_{0.7}\text{As}$ layers ($n = 1.5 \times 10^{17} \text{ cm}^{-3}$) on the top and the bottom of the stack prevent the formation of a depletion zone in the well region ensuring flatband conditions. The back-side of the sample is polished to allow transmission measurements.

The amount of splitting of the resonant levels can be estimated by solving the eigenvalue equation for coupled square wells. For the parameters of our sample we calculate a design splitting of 5 meV (corresponding to a frequency of 1.25 THz). Bandbending by the dopants and many-particle effects are not included in this calculation. At our doping densities we expect the bandbending effects to be of minor importance [7].

MEASUREMENT TECHNIQUE

We measure the absorption spectrum of the split-subband transition by time-domain spectroscopy. Information about the dispersion and absorption properties of the sample is extracted by Fourier analysis from the change of the shape of an ultrashort light pulse propagating through the sample.

Fig. 1 gives a schematic representation of the setup of our time-domain spectrometer (similar to that of [8]). The far-infrared pulses needed for our experiment are

generated in a photoconducting dipole antenna [9]. The dipole consists of a 50 μm long, 5 μm wide and 0.25 μm thick gold strip on a sapphire wafer. A 5 μm wide gap in the middle of the strip is centered on a 0.6 μm thick photoconducting silicon mesa that has been radiation damaged with 350 keV silicon ions at a dose of $5 \times 10^{14} \text{ cm}^{-2}$ to obtain a subpicosecond photocurrent decay time. The antenna is biased with 9 V across the gap. Optical generation of carriers in the photoconductor with 100 fs long light pulses from a balanced colliding pulse mode-locked (CPM) dye laser produces an ultrashort burst of electrical current in the antenna which radiates off a terahertz bandwidth electromagnetic pulse. Most of the power is directed into the sapphire substrate. This part of the radiation is coupled into free space by a hyper-hemispherical silicon lens glued on the backside of the sapphire substrate. The emerging beam forms a cone with a full angle of about 25°. The radiation is first collimated by an off-axis paraboloidal mirror, then focused onto the sample by a second paraboloidal mirror. The diameter of the focal spot is 600 - 700 μm . Another set of paraboloidal mirrors focuses the transmitted beam onto a second dipole antenna used to detect the waveform of the terahertz radiation via photoconductive sampling. The terahertz segment of the experimental setup is placed in a chamber flooded with nitrogen gas to eliminate background absorption by the water vapor in the air [10].

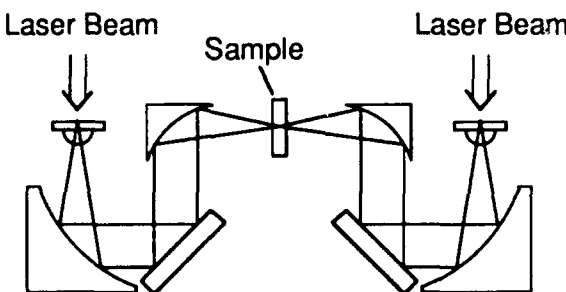


Fig. 1 Time-domain far-infrared spectrometer setup covering the photon energy range 0 - 9 meV. The terahertz beam, generated in photoconducting dipole antennas, can be focused with paraboloidal mirrors to the diffraction limit of several hundred micrometers.

The sample is mounted on the cold-finger of a continuous-flow helium cryostat equipped with 3 mm thick high-resistivity (10 k Ωcm) silicon windows. To observe the split-subband absorption, the sample is placed under Brewster's angle. We also perform control measurements with the sample rotated to a position perpendicular to the beam. In this geometry, with the polarization of the radiation perpendicular to the growth direction of the quantum well stack, polarization selection rules forbid split-subband absorption.

EXPERIMENTAL RESULTS

In Fig. 2, the waveforms of terahertz bandwidth far-infrared pulses detected after propagation through the sample under Brewster's angle are shown for sample temperatures of 10 K (solid line), 30 K (dashed line) and 100 K (dotted line), respectively. Room temperature data are not shown explicitly, because the waveform at 300 K closely follows that for 100 K. At 300 K, the far-infrared pulse suffers hardly any attenuation resulting from the excitation of intersubband transitions because the electrons populate the lower and the higher subband nearly equally. The split-subband absorption is compensated to a great extent (theoretically about 95 %) by stimulated

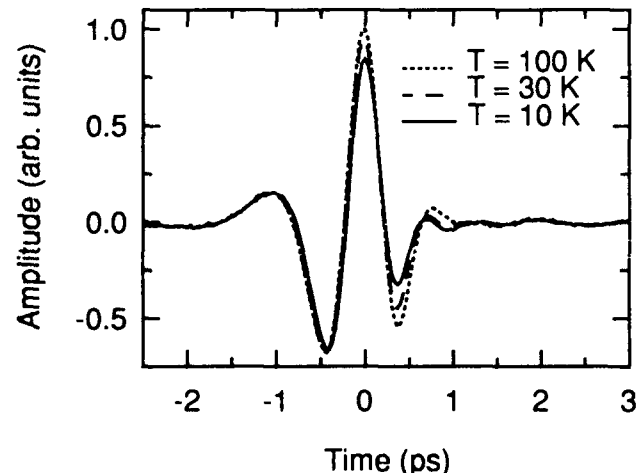


Fig. 2 Time dependence of the detected amplitude of the far-infrared light pulse after propagation through the sample under Brewster's angle. Sample temperatures: 100 K (dotted line), 30 K (dashed line) and 10 K (solid line).

emission. For temperatures below 100 K, we observe a reduced amplitude in the trailing part of the transmitted terahertz pulse and a strongly damped ringing at the tail of the pulse. Both the attenuation and the ringing are attributed to the intersubband excitation of electrons that now occupy mostly states in the lower subband.

Fig. 3 shows the Fourier transforms of the terahertz pulses of Fig. 2 revealing the spectral dependence of the intersubband absorption. As discussed above, the pulse spectrum without absorption is given by the curve for a sample temperature of 100 K. For lower temperatures, the amplitude of the Fourier transforms is reduced in the frequency range around 1 THz, but remains unchanged for very high and very low frequencies. The frequency dependence of the absorption does not seem to change with temperature.

In Fig. 4, results of a control measurement with the sample rotated to a position perpendicular to the beam are displayed. The Fourier transforms of pulses transmitted through the sample at temperatures of 100 K (solid line), 30 K (dashed line) and 10 K (dotted line) hardly differ from each other. This corroborates the theoretical prediction that no intersubband absorption can be obtained if the polarization of the terahertz radiation lies in the plane of the quantum wells. Another important conclusion concerns the free-carrier absorption by the

electrons in the quantum wells and the doped layers sandwiching the quantum wells. From our experiments we are not able to determine the absolute contribution of the free-carrier absorption to the attenuation of the terahertz radiation. With the results of Fig. 4 we can, however, rule out that free-carrier absorption impedes the interpretation of the temperature dependence of our data as caused by the split-level absorption. Free-carrier absorption does not vanish when the sample is rotated. If free-carrier absorption would significantly contribute to the attenuation of the terahertz radiation and would change noticeably with temperature as has been found under certain conditions [11], we should observe a change of absorption with temperature also if the polarization of the radiation is parallel to the plane of the quantum wells.

From the data for 100 K (or 300 K) and 10 K plotted in Fig. 3, we deduce the lineshape of the absorption. Fig. 5 shows the absorbance of the sample, i.e. the quantity $-\log_{10}(T)$. T is the power transmission, $T = |\hat{E}(L, \omega)|^2 / |\hat{E}(0, \omega)|^2$, of a terahertz pulse $E(0, t)$ propagating through the quantum well stack. To calculate the absorbance, we use the Fourier transforms of the data for 100 K and 10 K as $\hat{E}(0, \omega)$ and $\hat{E}(L, \omega)$, respectively. The absorption line peaks at a photon energy of 4.2 meV ($\nu = 1.05$ THz), 0.8 meV lower than the design

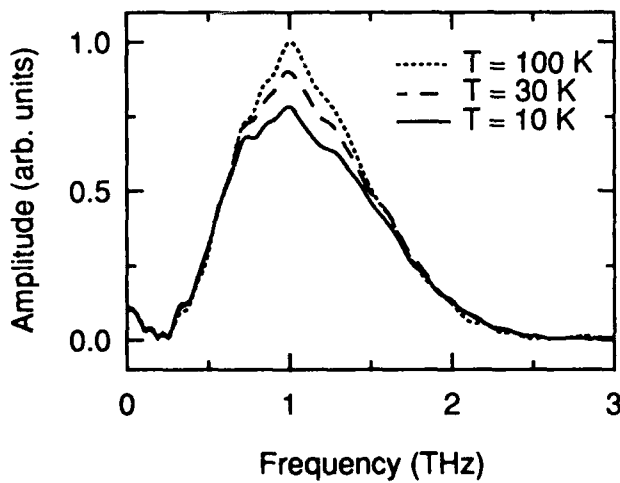


Fig. 3 Fourier transforms of the far-infrared light pulse after propagation through the sample placed under Brewster's angle. Sample temperatures: 100 K (dotted line), 30 K (dashed line) and 10 K (solid line).

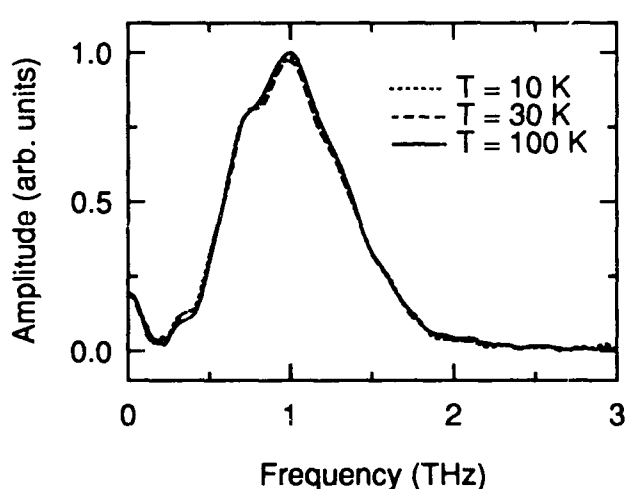


Fig. 4 Control measurement: Fourier transforms of the far-infrared light pulse after propagation through the sample placed perpendicular to the beam. Sample temperatures: 100 K (dotted line), 30 K (dashed line) and 10 K (solid line).

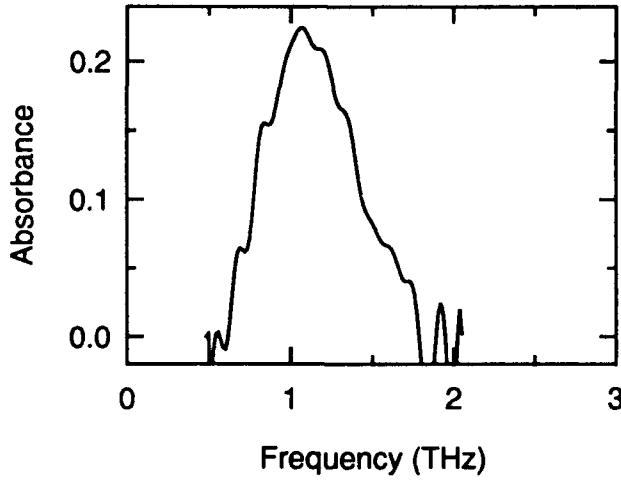


Fig. 5 Lineshape of the split-subband absorption

splitting. The width of the line is 2.5 meV, its shape is asymmetric extending to the high frequency side.

THEORY

A theoretical description of the absorption process can closely follow the approach developed for the modeling of the intersubband absorption in interface accumulation layers [12,13] and in single quantum wells [14]. The quantum well region in the sample is described as an ensemble of two-level systems. The lower level is significantly populated making it necessary to include many-particle interactions into the theory. The ensemble is characterized by a dielectric tensor with vanishing non-diagonal components. The diagonal components for the directions parallel to the surface are identical. They consist of the background dielectric constant ϵ_0 plus a Drude term for the plasma contribution:

$$\begin{aligned}\epsilon_{xx}(\omega) &= \epsilon_{yy}(\omega) = \epsilon_{||}(\omega) = \\ &= \epsilon_0 \left(1 - \frac{\omega_{p||}^2}{\omega^2 + i\omega\Gamma_{||}}\right).\end{aligned}\quad (1)$$

$\Gamma_{||} = 1/\tau_{||}$ is the damping constant for plasma oscillations parallel to the surface and $\omega_{p||}$ is the corresponding plasma frequency. The component ϵ_{\perp} of the dielectric tensor for the direction perpendicular to the surface describes the intersubband absorption under the presence of the plasma:

$$\epsilon_{zz}(\omega) = \epsilon_{\perp}(\omega) = \epsilon_0 \left(1 + \frac{\omega_0^2(\alpha - \beta)}{\omega_0^2 - \omega^2 - i\Gamma_{\perp}\omega}\right).\quad (2)$$

$\hbar\omega_0$ is the intersubband transition energy. Γ_{\perp} is the homogeneous linewidth of the intersubband transition describing the relaxation of the oscillation of a wavepacket from one quantum well to the other. In the context here, Γ_{\perp} determines the damping of the perpendicular plasma oscillations coupled to the intersubband absorption. The term α contains the frequency of the plasma oscillations:

$$\alpha = \frac{\omega_{pl\perp}^2}{\omega_0^2}.\quad (3)$$

The plasma frequency $\omega_{pl\perp}$ is given by:

$$\omega_{pl\perp}^2 = \frac{4\pi Ne^2 f}{\epsilon_0 m d_{eff}},\quad (4)$$

where N is the sheet density of the electrons and m is the effective electron mass. The oscillator strength f and the effective thickness d_{eff} of the charge layer are calculated with the following relations [15]:

$$f = \frac{2m}{\hbar} \omega_0 \langle z \rangle^2,\quad (5)$$

$$d_{eff} = \frac{\hbar f}{2m\omega_0 L_{11}},\quad (6)$$

$$L_{11} = \int_{-\infty}^{\infty} dz \left[\int_{-\infty}^z da \zeta_0(a) \zeta_1(a) \right]^2.\quad (7)$$

$e \langle z \rangle$ is the dipole moment of the transition. $\zeta_{0,1}(z)$ denotes the envelope of the wave function of the lower and upper split level, respectively.

The term β in Eqn. (2) is a many-particle correction for the collective intersubband excitation. It results from the so called excitonlike or final-state interaction of the electrons. β is given by:

$$\beta = \frac{-2N}{\hbar\omega_0} \times \int_0^{\infty} dz \zeta_1^2(z) \zeta_0^2(z) \frac{\partial v_{xc}(n(z), z)}{\partial n(z)}.\quad (8)$$

Here, v_{xc} is the exchange-correlation potential as a function of the density $n(z)$ of the electrons.

To determine the attenuation and the phase shift of a pulse propagating through the quantum well stack we model the sample as a slab consisting of the thick non-absorbing semiconductor substrate and a thin uniaxial absorbing layer on top of it. We treat the sample as a Fabry-Perot-system taking into account multiple reflections of the electromagnetic wave from the interfaces of the quantum well region. We can neglect the interfaces within the quantum well region because the

wavelength of our pulses is much bigger than the separation of any two interfaces. We also neglect reflections from the backside of the substrate because the reflected pulses do not temporally overlap with the main pulse. The transmission coefficient $t(\omega)$ of the sample is then given by:

$$t(\omega) = \sqrt{\epsilon_0} \frac{t_{12} t_{23}}{1 + r_{12} r_{23} \exp(2ik_{\perp} L)} \exp(ik_{\perp} L). \quad (9)$$

t_{ij} and r_{ij} are the transmission and reflection coefficients of the two interfaces of the quantum well region. L is the effective thickness of the quantum well region ($L = 50 \times 191 \text{ \AA}$). k_{\perp} is the perpendicular component of the \vec{k} -vector. It is given by $k_{\perp} = (\omega/c) \sqrt{\epsilon(\omega)}$, with the effective dielectric function $\epsilon(\omega)$:

$$\epsilon(\omega) = \epsilon_{\parallel}(\omega) \left[1 - \frac{\epsilon_i}{\epsilon_{\perp}(\omega)} \sin^2 \theta_i \right]. \quad (10)$$

θ_i is the angle between the propagation direction of the incident wave and the normal to the surface of the sample. Using Eqns. (1) and (2), we obtain from Eqn. (10):

$$\epsilon(\omega) = \epsilon_{\parallel} \left[1 - \frac{\epsilon_i \sin^2 \theta_i}{\epsilon_{\infty}} \times \right. \\ \left. \times \frac{\omega_0^2 - \omega^2 - i\Gamma_{\perp} \omega}{\omega_0^2 (1 + \alpha - \beta) - \omega^2 - i\Gamma_{\perp} \omega} \right]. \quad (11)$$

The absorption resonance is given by the pole of $\epsilon(\omega)$. The resonance occurs at a frequency ω_{res} , determined by:

$$\omega_{res}^2 = \omega_0^2 (1 + \alpha - \beta). \quad (12)$$

The remarkable result here is that the resonance frequency is not given by ω_0 . On one hand, the resonance is shifted by term α from ω_0 to higher energies. $\sqrt{\alpha}$ is the plasma frequency normalized by ω_0 . The up-shift of the absorption resonance has been shown to be a consequence of the screening of the electric field by the carrier plasma [12,16] and is known as resonant screening or depolarization effect. The exchange-correlation of the electrons, on the other hand, pushes the resonance via term β back towards ω_0 .

RESONANCE ENERGY

It is instructive to estimate the shift of the absorption resonance due to both the exchange-correlation effect and the depolarization effect. The depolarization-induced shift of the resonance energy is evaluated with

Eqn. (3). For the envelope functions ζ_0 and ζ_1 of the first and the second sublevel we use as a simple approximation the wavefunctions for two infinitely deep square potential wells separated by an infinitesimally thin barrier. The thickness of each well is assumed to be equal to the thickness $w = 80 \text{ \AA}$ of the quantum wells of our experiment plus half the barrier width $b = 31 \text{ \AA}$. The wavefunctions are given by:

$$\zeta_0 = \sqrt{\frac{2}{2w+b}} \left| \sin(kz) \right|, \quad (13)$$

$$\zeta_1 = \sqrt{\frac{2}{2w+b}} \sin(kz). \quad (14)$$

The wavevector k is equal to $2\pi/(2w+b)$. With these expressions the effective plasma frequency $\omega_{pl\perp}$ of Eqn. (4) is calculated to be $2\pi \times 1.5 \text{ THz}$ ($\hbar\omega_{pl\perp} = 1.5 \text{ meV}$). For the shift term α we obtain a value of 1.42.

It should be mentioned here, that we have omitted to include the coupling of the collective intersubband excitations with the phonons into the theory. Pinczuk et al. have shown that the inclusion of this effect can be important for the interpretation of the resonance shift of intersubband transitions in single quantum wells [14]. The screening of the electric field within the quantum wells by the polar GaAs lattice strongly influences the resonance position for energies close to the LO and TO phonon energies. Far away from the phonon resonances, the coupling to the phonons becomes weak. In our case we obtain for the shift term α a value of 1.54 instead of 1.42 if we take the screening by the polar lattice into account.

The exchange-correlation effect can be evaluated with the help of Eqn. (8). For the exchange-correlation potential in Eqn. (8), Ando gives a parameterized expression [17]:

$$v_{xc} = \frac{me^4}{\pi \alpha r_s \epsilon_0^2 \hbar^2} \times \\ \times \left[1 + 0.0545 r_s \ln \left(1 + \frac{11.4}{r_s} \right) \right], \quad (15)$$

with $r_s = (3/(4\pi n))^{1/3} me^2/(\hbar^2 \epsilon_0)$ and $\alpha^3 = 4/(9\pi)$. Assuming that all electrons are in the lower subband, the electron density $n(z)$ is given by $N |\zeta_0(z)|^2$. With these expressions we can calculate the shift β in Eqn. (12). For a sheet density of the electrons of $2.3 \times 10^{11} \text{ cm}^{-2}$ we obtain for β a value of 1.29.

Both many-particle effects shift the resonance energy by sizable amounts. The depolarization effect alone - without the exchange-correlation correction - would push the resonance from the design splitting energy $\hbar\omega_0$ for the undoped sample of 5.0 meV up to 8.0 meV, producing a 60 % increase. The exchange-correlation effect, however, counteracts this increase and nearly compensates it by reducing the resonance energy again to 5.6 meV. In the experiment the absorption peaks at 4.2 meV, somewhat lower than the design splitting energy. Recent measurements of α and β in single quantum wells yield similar values for α and β as those calculated here [18].

MODEL CALCULATIONS

Using Eqn. (9) we perform calculations to model the change of amplitude and shape of a terahertz pulse propagating through the sample. Results of such calculations are shown in Fig. 6. In this time-domain plot, a pulse transmitted through the quantum well region is displayed. The solid and the dashed line represent the situation with and without intersubband absorption, respectively. In the calculation we use for N , ω_0 and Γ_{\perp} the experimentally relevant values. For the sheet density of the electrons we assume $N = 2.3 \times 10^{11} \text{ cm}^{-2}$ ($= n_{\text{wells}} \times (2w + b)$), for ω_0 we use the calculated value $\hbar\omega_0 = 5.0 \text{ meV}$, and the perpendicular damping constant Γ_{\perp} we determine from the full width at half maximum of the measured absorbance: $\hbar\Gamma_{\perp} = 2.5 \text{ meV}$. For the envelope wavefunctions ζ_0 and ζ_1 we use the approximations described above. For the plasma frequency $\omega_{pl\perp}$ and the resonance shift terms α and β we then obtain the values given earlier: $\hbar\omega_{pl\perp} = 1.5 \text{ meV}$, $\alpha = 1.54$, and $\beta = 1.29$. $\hbar\omega_{pl\perp}$ is assumed to be negligibly small. The incident pulse is the experimentally obtained pulse plotted as dotted line in Fig. 1. For its angle of incidence, θ_i , we assume $\theta_i = 73^\circ$, and for L , the effective interaction length of the light in the quantum well region, we use $L = 15 \mu\text{m}$.

In Fig. 6, the intersubband absorption leads to a reduction of the pulse amplitude in the trailing part of the pulse. A strongly damped ringing at the end of the pulse results from the polarization oscillations of the electrons which have been excited by the terahertz pulse. These oscillations decay with a time constant $T_2 = 2/\Gamma_{\perp}$ which for a linewidth of 640 GHz is $T_2 = 0.5 \text{ ps}$. Hence, the damping is faster than even a single oscillation period $1/(2\pi\omega_{res}) = 0.8 \text{ ps}$. For a smaller value of Γ_{\perp} the polarization oscillations would produce a ringing at the end of the pulse which would last distinctly longer

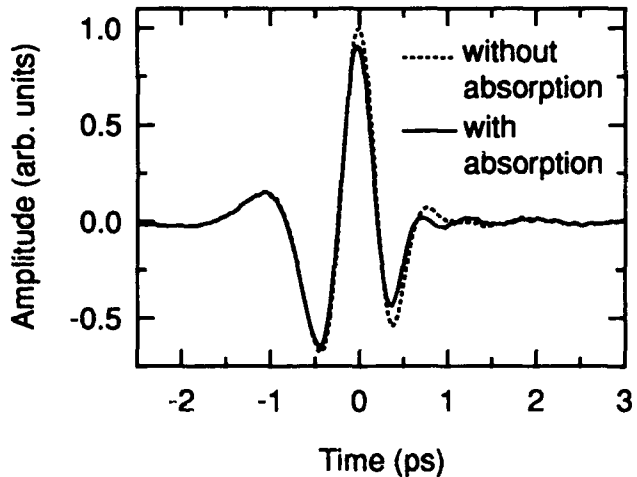


Fig. 6 Calculated time dependence of a terahertz light pulse after propagation through the sample. Solid line: with intersubband absorption, dotted line: no intersubband absorption.

than the original pulse [10]. Comparing Fig. 6 with Fig. 2, the change of the pulse shape obtained in the model calculation is very similar to that observed in the experiment.

LINE BROADENING MECHANISMS

In the calculations for Fig. 6 we assume that the absorption line is purely homogeneously broadened. We have also performed model calculations which assume a predominantly inhomogeneously broadened line (width: 600 GHz) with only a small contribution of homogeneous broadening ($\Gamma_{\perp} = 50 \text{ GHz}$). Comparing the results of these calculations we find no significant difference in both the time-domain and the frequency-domain data. From this we conclude that we are not able to decide which type of line broadening prevails in our experiment.

The model calculations predict, however, that for a much longer interaction length the shape of the transmitted pulse should be different for homogeneous and inhomogeneous line broadening. In the case of homogeneous broadening we should be able to observe a phase shift in the trailing part of the transmitted pulse which is not present in the calculations for an inhomogeneously broadened line. This phase shift over the length of the pulse requires a strong attenuation of the pulse which can only be obtained after a sufficiently long propagation

in the absorbing medium. Experimentally such a situation can be realized with a waveguide geometry for the sample, e.g. a zigzag structure as has been used for the measurement of the intersubband absorption in single quantum wells [19]. Preliminary data obtained for such a structure show no obvious phase-shift of the transmitted pulse suggesting that inhomogeneous broadening of the absorption line is predominant. More careful measurements are needed, however, because the Fourier analysis of data obtained with waveguide structures is difficult. For waveguides fabricated from typical semiconductor wafers, the wavelength of our terahertz pulses is on the order of the width of the waveguide (i.e. the thickness of the semiconductor substrate). Diffraction of the terahertz beam can severely distort the shape of the pulse and cause changes of the pulse spectrum which do not result from absorption.

SUMMARY

In summary, we have performed the first direct absorption measurements on the split subband transition in coupled quantum wells by time domain spectroscopy with a beam of far-infrared pulses. We observe a 2.5 meV wide absorption line which peaks at an energy of 4 meV, somewhat smaller than the design splitting energy of 5 meV. Our model calculations suggest that this down-shift of the resonance may be caused by many-body effects.

ACKNOWLEDGMENT

We are pleased to acknowledge helpful discussions with K. Goossen. F. Baumann advised us in the preparation of waveguide structures. During this work, H. Roskos was partially supported by the Deutsche Forschungsgemeinschaft.

REFERENCES

1. T. Furuta, K. Hirakawa, J. Yoshino, and H. Sakaki, *Jap. J. Appl. Phys.*, 25, L151-L154 (1986).
2. Y. J. Chen, E. S. Koteles, B. S. Elman, and C. A. Armieto, *Phys. Rev.* b36, 4562-4565 (1987).
3. H. Q. Le, J. J. Zayhowski, and W. D. Goodhue, *Appl. Phys. Lett.*, 1518-1520 (1987).
4. J. W. Little, and R. P. Leavitt, *Phys. Rev.*, B39, 1365-1368 (1989).
5. A. M. Fox, D. A. B. Miller, G. Livescu, J. E. Cunningham, J. E. Henry, and W. Y. Jan, *Phys. Rev.* B42, 1841-1844 (1990).
6. K. Leo, K., J. Shah, E. O. Göbel, T. C. Damen, S. Schmitt-Rink, W. Schäfer, K. Köhler, *Phys. Rev. Lett.* 66, 201 (1991).
7. G. Livescu, D. A. B. Miller, D. S. Chemla, M. Ramaswamy, T. Y. Chang, N. Sauer, A. C. Gossard, and J. H. English, *IEEE J. Quantum Electron.* QE-24, 1677-1689 (1988).
8. M. van Exter, and D. Grischkowsky, *IEEE Trans. Microwave Theory Tech.* 38, 1684-1691 (1990).
9. P. R. Smith, D. H. Auston, and M. C. Nuss, *IEEE J. Quantum Electron.* QE-24, 255-260 (1988).
10. M. van Exter, C. Fattinger, and D. Grischkowsky, *Opt. Lett.* 14, 1128-1130 (1989).
11. M. van Exter, and D. Grischkowsky, *Phys. Rev.* B41, 12140-12149 (1990).
12. W. P. Chen, Y. J. Chen, and E. Burstein, *Surf. Sci.*, 263-265 (1976).
13. T. Ando, A. B. Fowler, and F. Stern, *Rev. Mod. Phys.* 54, 437-672 (1982).
14. A. Pinczuk, and J. M. Worlock, *Surf. Sci.* 113, 69-84 (1982).
15. S. J. Allen, Jr., D. C. Tsui, and B. Vinter, *Solid State Commun.* 20, 425-428 (1976).
16. D. A. Dahl, and L. J. Sham, *Phys. Rev.* B16, 651-661 (1977).
17. T. Ando, and S. Mori, *J. Phys. Soc. Jpn.* 47, 1518-1527 (1979).
18. A. Pinczuk, S. Schmitt-Rink, G. Danan, J. P. Villaldares, L. N. Pfeiffer, and K. W. West, *Phys. Rev. Lett.* 63, 1633-1636 (1989).
19. B. F. Levine, R. J. Malik, J. Walker, K. K. Choi, C. G. Bethea, D. A. Kleinman, and J. M. Vandenberg, *Appl. Phys. Lett.* 50, 273-275 (1987).

Terahertz Time-Domain Transmission of Superconductors

Martin C. Nuss, Paul M. Mankiewich, Megan O'Malley, Keith W. Goossen,
Hartmut Roskos, and Ben Tell

AT&T Bell Laboratories, Crawfords Corner Road, Holmdel, New Jersey 07733

Manjul Bhushan*

*Lincoln Laboratory, Massachusetts Institute of Technology,
Lexington, Massachusetts 02173-9108*

ABSTRACT

The conductivity σ of superconducting films is studied with collimated terahertz radiation from photoconductive dipole antennas. We measure both real and imaginary part of the conductivity directly without using the Kramers-Kronig relations.

INTRODUCTION

The optoelectronic generation and coherent detection of extremely short electrical pulses with bandwidths in excess of several terahertz^{1,2} have made possible the study of materials and electronic transport phenomena in a previously hardly accessible region of the electromagnetic spectrum. These electrical pulses can be propagated in free space and collimated as well as focussed like optical pulses using lenses and mirrors.² The extremely high signal-to-noise ratio of the electrical pulses generated by the photoconductive dipole antennas together with the phase sensitive detection scheme outperforms conventional Fourier-transform infrared spectrometers in the terahertz range by a large margin. Here, we use collimated terahertz radiation from photoconductive dipoles to study the electronic response of the Cooper pairs and of thermally excited quasiparticles in thin superconducting films. Historically, far-infrared studies of superconductors have been a crucial factor for the theoretical description of superconductivity and the agreement of these studies with BCS theory has been seen as a validity proof of the BCS theory.³⁻⁵

In our studies, we investigate the transmission of terahertz bandwidth radiation of high temperature $\text{YBa}_2\text{Cu}_3\text{O}_7$ as well as conventional niobium superconducting films. A significant distinction between niobium and $\text{YBa}_2\text{Cu}_3\text{O}_7$ is the magnitude of the superconducting bandgap 2Δ in these materials. Whereas the 660 GHz bandgap of niobium is right in the middle of the frequency range covered by the terahertz radiation and pair breaking can be observed, the bandgap of $\text{YBa}_2\text{Cu}_3\text{O}_7$ is well above this range ($3.52 \cdot kT_c = 6.7$ THz). However, we will show that the subbandgap response of the Cooper pairs provides information about such important quantities as the coupling strength of the electron-electron interaction and the magnetic penetration depth.

PHENOMENOLOGY

Superconductors below the superconducting transition temperature T_c are characterized by the bandgap 2Δ , the magnetic penetration depth $\lambda(T)$, a coherence length ξ_0 and the electron mean-free-path l . Whereas above the critical temperature T_c the conductivity can be described by the Drude formula with frequency dependent effective mass m^* and momentum scattering time τ^* ,⁶ the condensation of the Cooper pairs below T_c introduces a large imaginary component σ_2 of the conductivity. This imaginary part of the conductivity is intimately related with the condensation of the Cooper pairs and is in fact an immediate consequence of superconductivity.⁷ Most important, the expression for the imaginary part of the

* Lincoln Laboratory work was conducted under the auspices of the Consortium for Superconducting Electronics with full support by the Defense Advanced Research Projects Agency.

conductivity can be derived from elementary sum rules and therefore is independent of the theoretical model for the superconductor:⁷

$$\sigma_2 = 2A/\pi\omega \quad (1)$$

Here A is the famous "missing area" in the normal-state conductivity when the Cooper pairs condensate.⁷ The missing area A is correlated with the coupling strength of the superconducting pairs and it can be shown that $A = \pi/2\mu_0\lambda^2$, where λ is the magnetic penetration depth.⁷ In $\text{YBa}_2\text{Cu}_3\text{O}_7$, the Drude conductivity has almost its entire oscillator strength below the gap value 2Δ ,⁸ in which case λ acquires the full London value $\lambda_L = (m^*/\mu_0ne^2)^{1/2}$.

Dipole Antennas

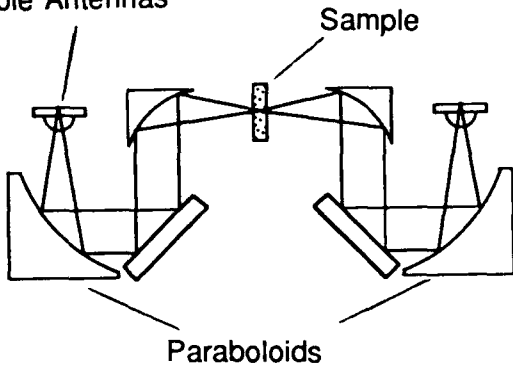


Fig. 1 Schematic of the time domain terahertz spectrometer

EXPERIMENTS

Figure 1 shows the experimental setup of our time-domain terahertz spectrometer, which is similar to the one described by van Exter et al² with the addition of the intermediate focusing optics used to focus the terahertz beam to a diffraction limited spot size at the location of the sample. Terahertz radiation is generated by a 100 μm half-wave dipole antenna on a radiation-damaged silicon-on-sapphire substrate.¹ The radiation is coupled into free space by a hyperhemispherical silicon substrate lens.^{9,2} The full angle of the electro-magnetic radiation is roughly 25°. This radiation cone is subsequently collimated to a 25 mm diameter beam by an off-axis paraboloidal mirror. This arrangement is repeated on the detector side, where a second photoconductive dipole serves as a receiver for the terahertz radiation. The superconducting films are placed in a continuous-flow cryostat equipped with 3-mm thick fused quartz windows placed at the focus in the center of the setup. The temperature in the cryostat can be continuously varied

between 300 K and 2 K. The spectrum of the radiation from the 100 μm antennas extends to roughly 1.2 THz with a peak at 600 GHz.¹

Figure 2 shows the time domain data for the 500 Å $\text{YBa}_2\text{Cu}_3\text{O}_7$ film for four temperatures just above and below T_c . Besides the reduction in amplitude due to the increased reflectivity of the sample below the superconducting transition, the most apparent change is a phase shift below T_c that increases with decreasing temperatures. This phase shift is the signature of the superconductor and is proportional to the imaginary (inductive) component of the conductivity. For a thin conducting layer much thinner than the wavelength of the terahertz radiation, the boundary conditions at the superconducting film can be solved quite easily and both real and imaginary part of the conductivity can be extracted from the transmitted spectra:

$$E(\omega) = \frac{Y_+}{Y_+ + \sigma_s(\omega)} \cdot E_0(\omega) \quad (2)$$

In Eq. 2, $Y_+ = 1/Z_0 + 1/Z_1$, where Z_0 is the impedance of free space and Z_1 the impedance of the substrate, and σ_s is the sheet conductivity in units of Ω^{-1} . $E(\omega)$ is the transmitted electric field and $E_0(\omega)$ is the field transmitted through the substrate alone without the superconducting film. Solving Eq. 2 for $\sigma_s(\omega)$, both the real and the imaginary part of the conductivity are obtained. In Fig. 3 we plot the real part of the conductivity σ_1 as a function of frequency with temperature as a parameter.

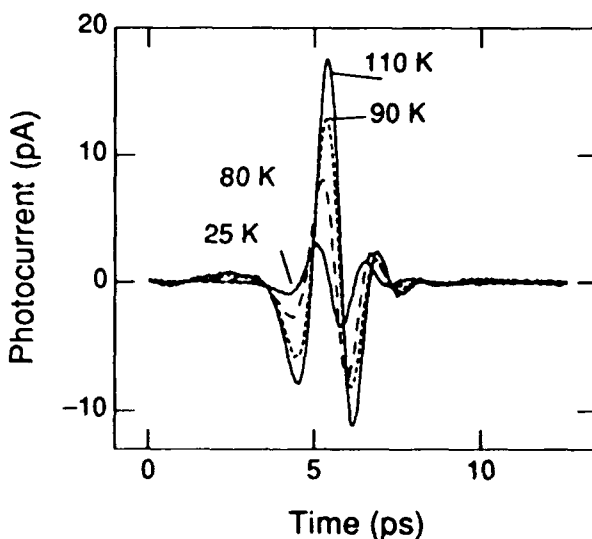


Fig. 2 Time domain waveforms for 110 K (solid), 90 K (dotted), 80 K (dashed) and 25 K (solid).

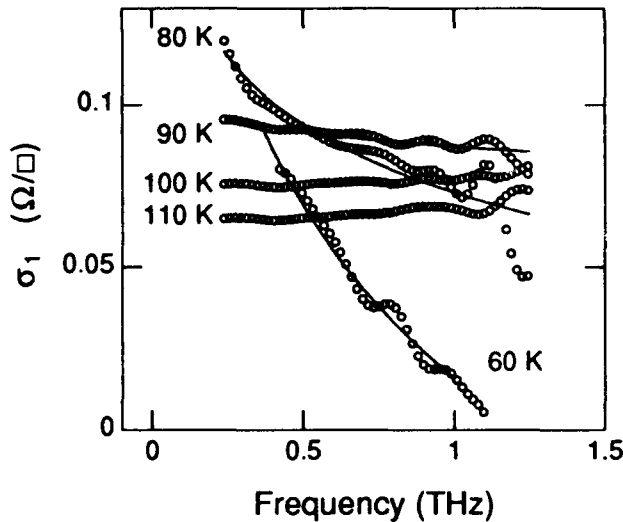


Fig. 3 Real part σ_1 of the conductivity. The open circles show the experimental curves, the solid lines are fits to the $\ln(\Delta/kT)$ dependence expected from the BCS theory.

The graph includes the experimental data as well as theoretical curves using the frequency dependence expected from the BCS theory:^{10, 11}

$$\frac{\sigma_1}{\sigma_n} \sim \frac{2\Delta}{kT} \frac{e^{\Delta/kT}}{(1 + e^{\Delta/kT})^2} \ln[q(T)\Delta/\hbar\omega], \quad (3)$$

with

$$q(T) = 2.3kT/\Delta + 6(kT/\Delta)^3. \quad (4)$$

Above T_c , $\sigma_1/\sigma_n = 1$ by definition, which is fulfilled very well for our data above T_c . Below T_c , σ_1 initially actually rises above σ_n and increases as $\omega \rightarrow 0$. This behavior is anticipated from the logarithmic divergence in Eq. (3). For 50 K, the magnitude of σ_1 becomes smaller again due to the exponential freeze-out of the electrons. Although the fact that the conductivity is highest at 70 K and exceeds the normal state conductivity is predicted for pure BCS superconductors,¹² but is unexpected for $\text{YBa}_2\text{Cu}_3\text{O}_7$ with their smeared out density of states.

In Fig. 4, we plot the imaginary part $\sigma_2(\omega)$ of the conductivity normalized to the normal-state conductivity. Clearly, at the lowest temperature, σ_2 shows the $1/\omega$ divergence predicted from the sum rule (Eq. 1). Even above T_c , σ_2 is not zero because of the long inelastic scattering times in $\text{YBa}_2\text{Cu}_3\text{O}_7$, which lead to an appreciable imaginary part of the Drude conductivity.

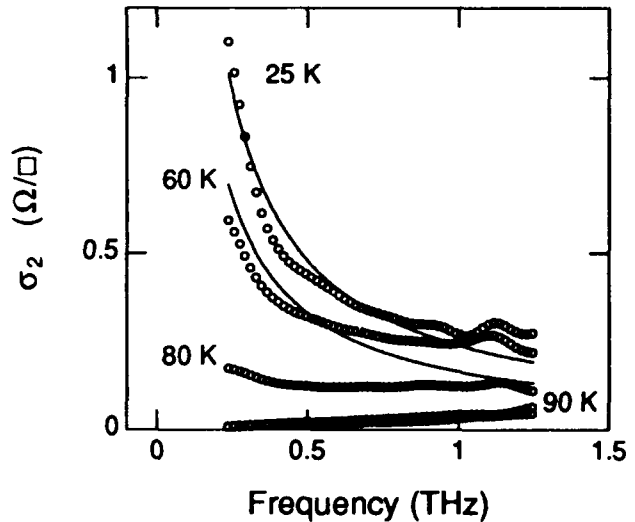


Fig. 4 Imaginary part σ_2 of the conductivity. Open circles are experimental results, solid lines are fits to $\sigma_2 = 1/\omega\mu_0\lambda^2$.

At the lowest temperature, we derive $\lambda = 1600 \text{ \AA}$ from Fig. 4 with the aid of Eq. 1, a value for the magnetic penetration depth that is close to the one measured by other techniques on thin superconducting $\text{YBa}_2\text{Cu}_3\text{O}_7$ films.

MEASUREMENTS ON NIOBIUM

As a comparison, we also measure the terahertz transmission of superconducting niobium films above and below the transition temperature. In Fig. 5, we display results on 100 Å thick niobium films deposited on a sapphire substrate at Lincoln Laboratories.

As the temperature is lowered below the transition temperature $T_c = 6.25 \text{ K}$, the waveform changes its shape significantly. Most important, unlike in $\text{YBa}_2\text{Cu}_3\text{O}_7$ films, the transmitted signal below the transition temperature below T_c is actually higher than in the normal state. Palmer and Tinkham³ in their pioneering work on far-infrared transmission of ultrathin lead films have shown that this is a consequence of the superconducting bandgap: at the frequency of the superconducting gap 2Δ , the transmission coefficient exhibits a peak and the ratio T_s/T_n exceeds unity.

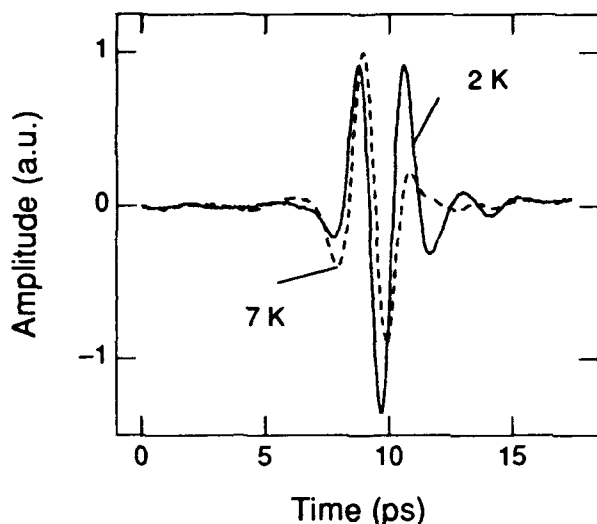


Fig. 5 Time-domain terahertz transmission data for a niobium film at 7 K (dashed) and at 2 K (solid).

This behavior is confirmed by our terahertz transmission experiments. Figure 6 plots the ratio of the power transmission coefficient in the superconducting and normal state. A peak appears at 470 GHz, extremely close to the BCS value for the gap frequency $2\Delta=3.52 kT_c$.

In this context, we would like to remark that this peak in the transmission is only present in the extreme

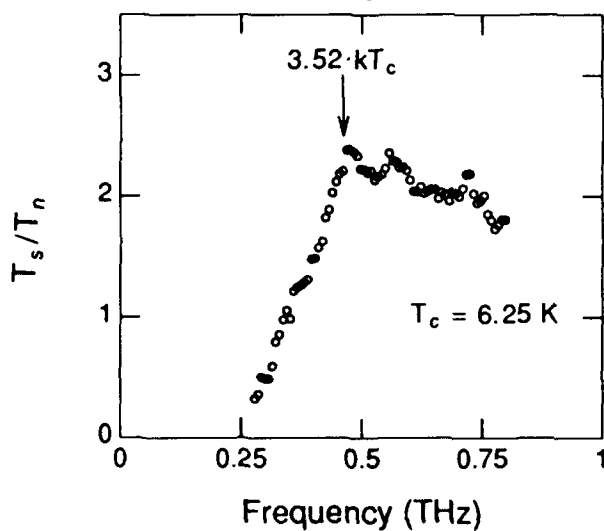


Fig. 6 Ratio T_s/T_n of the transmission coefficient above and below the transition temperature.

anomalous or extremely dirty limit of superconductivity. In the London limit, which is applicable to $\text{YBa}_2\text{Cu}_3\text{O}_7$, the full London value of σ_2 dominates the transmission (and reflection), and no peak is observed, even if the bandwidth of the electrical pulses was high enough to reach the superconducting bandgap.

REFERENCES

- [1] P. R. Smith, D. H. Auston, and M. C. Nuss, *IEEE Journ. Quantum Electr.*, Vol. 24, p. 255, 1988.
- [2] M. van Exter, C. Fattiger, and D. Grischkowsky, *Optics Lett.*, Vol. 14, p. 1128, 1989.
- [3] L. H. Palmer and M. Tinkham, *Phys. Rev.*, Vol. 165, p. 588, 1968.
- [4] M. Tinkham, in *Far Infrared Properties of Solids*, S. S. Mitra and S. Nudelman, Eds., Plenum, New York, 1970, p. 223.
- [5] D. R. Karecki, G. L. Carr, S. Perkowitz, D. U. Gubser, and S. A. Wolf, *Phys. Rev.*, B 27, p. 5460, 1983.
- [6] C. M. Varma, P. B. Littlewood, S. Schmitt-Rink, E. Abrahams, and A. E. Ruckenstein, *Phys. Rev. Lett.*, Vol. 63, p. 1996, 1989.
- [7] M. Tinkham and R. A. Ferrell, *Phys. Rev. Lett.*, Vol. 2, p. 331, 1959.
- [8] K. Kamaras, S. L. Herr, C. D. Porter, N. Tache, D. B. Tanner, S. Etemad, T. Venkatesan, E. Chase, A. Inam, X. D. Wu, M. S. Hedge, and B. Dutta, *Phys. Rev. Lett.*, Vol. 64, p. 84, 1990.
- [9] D. B. Rutledge, D. P. Neikirk, and D. P. Kasilingham, in *Infrared and Millimeter Waves*, Vol. 10, K. J. Button, Ed., Academic, New York, 1983, pp. 1-90.
- [10] D. C. Mattis and J. Bardeen, *Phys. Rev.*, Vol. 111, No. 2, p. 412, 1958.
- [11] K. W. Goossen and M. C. Nuss, *J. Appl. Phys.*, Vol. 67, p. 6568, 1990.
- [12] M. Tinkham, *Introduction to Superconductivity*, Krieger, Malabar, Florida, 1980.

Ultrafast Optoelectronics

GaAs-Based, Very Fast Integrated Optoelectronics

Takeshi Kamiya

*Department of Electronic Engineering, University of Tokyo, 7-3-1, Hongo,
Bunkyo-ku, Tokyo 113, Japan*

I. INTRODUCTION

Adding to the success of optoelectronics in fiber-optic transmission and optical recording, there still remains a challenging peak of optical information processing. Introduction of optical technology in the field of information processing will be justified when the intrinsic properties of optical media such as very fast response (1) and parallelism (2) are fully exploited. A series of fundamental researches have been made along the line of all optical processing, where replacement of all the electronic devices with optical devices should help getting rid of RC time constant constraints. This approach, however, turned out to be rather futuristic, in the sense that there still remain too many premature components yet to be developed before the total ultrafast pure optical signal processing system will be brought to reality.

In comparison, a partial introduction of optical technology into electronic integrated circuits sounds more realistic because a number of important peripheral technologies so far developed in the past can be utilized. This we call as optoelectronic processing. One of the optoelectronic approaches is the realization of optically controlled optical switches where the device principle involves electronic processes. As the most successful example the self-electrooptic device (SEED) utilizes the photovoltaic action to induce the quantum confined Stark effect by optical addressing, thus giving rise to the switching of optical signal (optically three terminal device). Leaving the description of SEED to the recent review (3), the present paper deals with our alternative approach where EO and OE conversion devices will be assembled on a hybrid circuit. Then some discussions on the inspection of GaAs IC by electrooptic sampling will follow.

II. VERY SHORT OPTICAL PULSE GENERATION

The semiconductor laser is by far the most practical light source for electronics in comparison with other

laser systems. Highly repetitive ultrashort pulses can be obtained from actively modelocked lasers successfully (4). Only disadvantage of this scheme is the fixed repetition frequency which makes it somewhat difficult to use it with digital circuits operating with an independent clock source. Gain switched semiconductor lasers are the alternative options capable of arbitrary repetition, on which we have made several trials. Use of multi-quantum well (MQW) lasers was found to be favorable (5) for their high gain when they are driven to upper sub-level ($n=2$), though the carrier leakage at high density excitation must be carefully treated for optimization (6). Advantage of MQW laser was also demonstrated at 1.3 micron, achieving the pulse width less than 4 ps (7). Various compression techniques are also applicable to semiconductor laser pulses (8),(9). Recently we have examined the pulse shaping effect of nonlinear gain in semiconductor laser amplifiers. The depletion of population inversion after the passage of large amplitude signal pulse leaves only low gain at the tail part of the pulse, thus very effective to suppress the optical energy residing at the tail part. This effect was demonstrated to be very much pronounced when reflected wave amplifier (RWA) configuration was employed for a InGaAsP laser (10).

III. VERY SHORT ELECTRICAL PULSE GENERATION

Photodiodes and fast photoconductors are useful as optically triggered electrical switches. Photoconductive switches with reduced recombination lifetime was used as the sampling gate by Austin (11). GaAs based integrated optoelectronic circuits were implemented with optical triggering technique by Leonberger (12). The present author's group has been trying to use GaAs MSM photodiodes as the very short electrical pulse generator. Composite photodiode configuration as had been tried for InP by Hori et al. (13), was applied to high mobility GaAs homoepitaxial structure (14). Delayed optical pulse excitation was used for the generation of electrical pulse less than

30 ps wide with reasonably high efficiency. Excitation of twin photodiodes which are connected to a pair of transmission lines with different lengths was proven to act similarly effective (15).

IV. INTEGRATED OPTOELECTRONIC LOGIC

If an array of photoelectric switches with high speed and efficiency and high speed are integrated to form a logic unit with patterned optical address, there are possibilities of combining parallel and high speed features in optoelectronic digital processing. A new configuration of logic unit for "exclusive OR = EOR" was proposed and was implemented by a combination of GaAs MSM photodiodes (Fig.1 and 2) (16).

Typical results of photoelectric response are shown in Fig.3 ($X = 1, Y = 0$) and Fig.4 ($X = 1, Y = 1$). For the case of Fig.4 the positive partial current supplied by the voltage sources V_1 and V_2 is compensated by the negative partial current from V_3 , thus giving rise to null output. Full width at half maximum was between 80 and 100 ps. The clock frequency around 5 GHz should be feasible. One problem arising from connecting two photodiodes in series such as in AND unit or in a part of EOR unit is the pattern effect due to the charge up process when only one photodiode was illuminated. To solve this shunt resistors were provided to individual photodiodes so that discharging process will become faster. Shunt resistivity ranging 200 and 500 Ω was found to be effective.

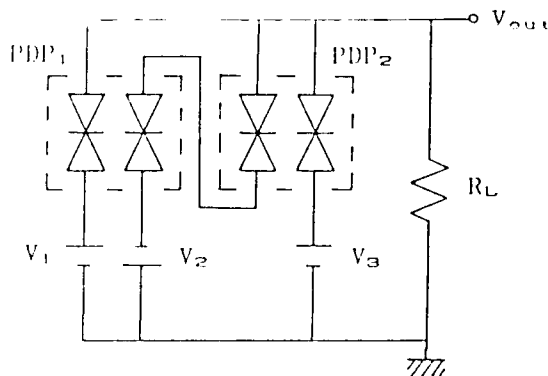


Fig.1 Proposed exclusive OR composed of GaAs MSM photodiode switches.

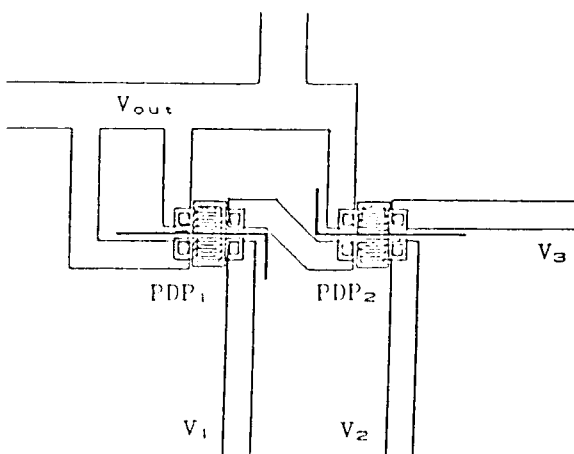


Fig.2 A part of mask pattern accomodating two pairs of MSM photodiodes with trench isolation of closely placed PD's.

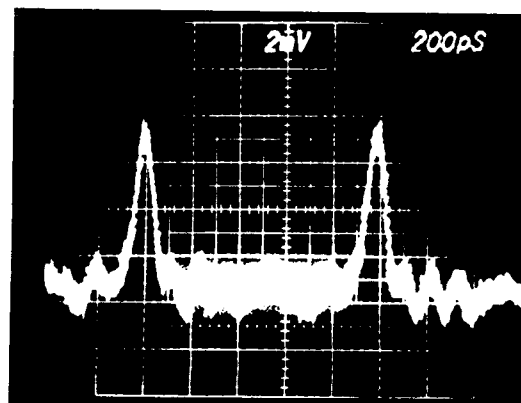


Fig.3 Experimental result of EOR for $X=1, Y=0$ input.

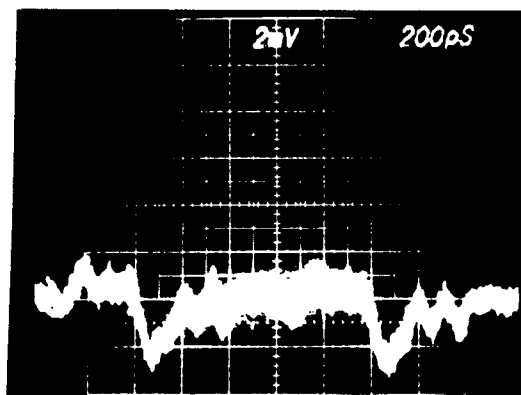


Fig.4 Experimental result of EOR for $X=1, Y=1$ input.

Figure 5 shows a concept of hybrid construction of 4 bit full adder. It is assumed that 4 bit signals X and Y are encoded into dot pattern and duplicated by a lens array, forming a pair of 8 dot images $[X, Y]$. The output current from each logic unit will be amplified by integrated transistors and will drive the surface emitting diode laser array. Then the output optical patterns are fed to the photoelectric logic units again with beam splitter arrangement. After some iterative operation of OE and EO units, the output patterns $Z = X + Y$ will be extracted.

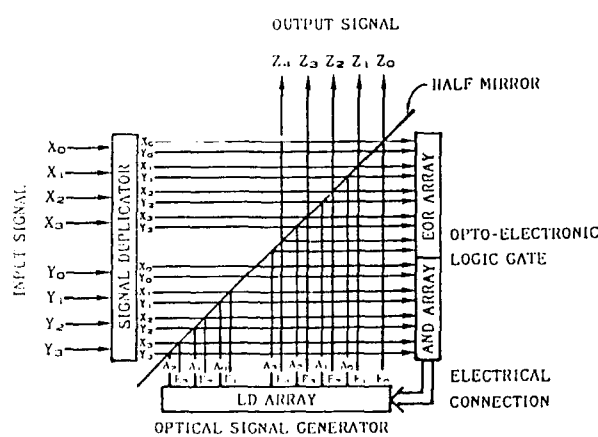


Fig.5 Basic concept of hybrid configuration of Four bit full adder.

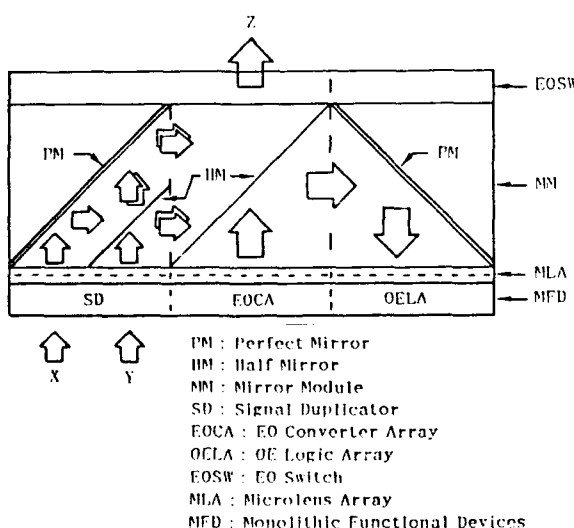


Fig.6 A projection of monolithically integrated optoelectronic logic array (OELA) and electrooptic converter array (EOCA).

Implementing the construction of Fig.5 requires some addition of new technologies. Important items to be solved are (1) power amplification of PD output by a booster transistor to drive LD, (2) high band width electrical connection of OELA and EOCA by non wire bonding techniques, (3) electrooptic switching (EOS) plate for the extraction of output signal pattern by rotating the axis of polarization. In Fig.6 another projection is depicted where a monolithic assembly of surface emitting diode laser array and optoelectronic logic array is assumed. Microoptic components are also essential constituents for the assembly of this logic unit(17). To be specific we have studied experimentally close loop gain condition of PD-Transistor-LD (18). We have designed and fabricated an MSM PD- single stage 2DEGFET inverter combination (Fig.8) by the courtesy of the Hitachi Central Research Laboratory GaAs integrated circuit group. Voltage gain of 6dB with 140ps pulse was confirmed. With some extrapolation of the potential performance in lasers and transistors by referring to the recent reports, power budget diagram was drawn in Fig.8.

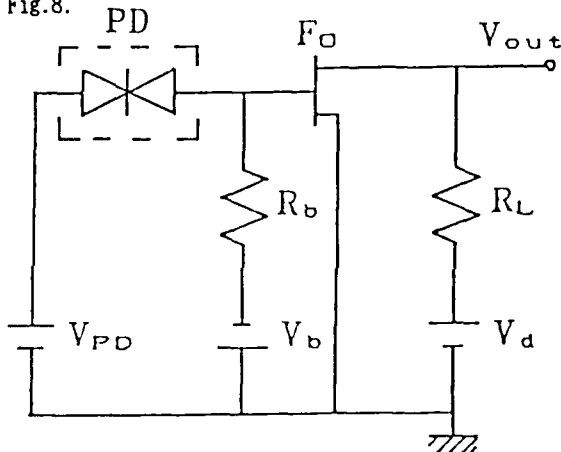


Fig.7 Circuit connection scheme of MSM-PD = 2DEGFET inverter.

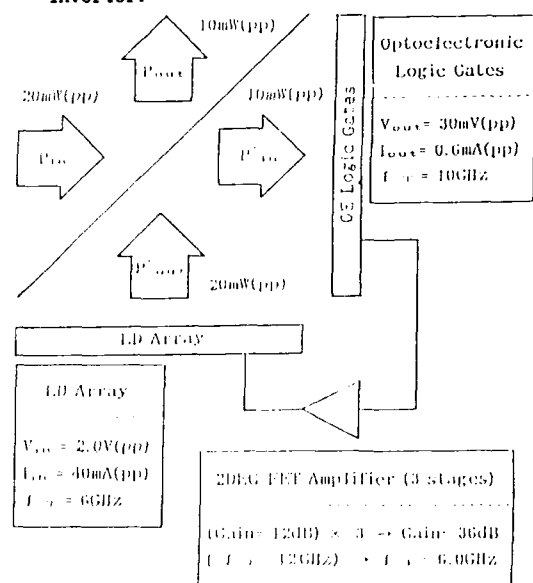


Fig.8 Power budget estimation of PD-Transistor-LD loop.

V. PRACTICAL E-O SAMPLING By SEMICONDUCTOR LASER FOR GaAs IC TESTING

To bridge the present technology of picosecond optoelectronics concentrating mostly on discrete or small scale integrated devices and the future technology of multi-Gbit/s optoelectronic signal processing, it would be very favorable if any kind of industrial products using picosecond optoelectronic technology will start to be on sale. One of the most promising candidates would be the product of metrological instruments with high temporal definition. For example the electrooptic sampling system offers capability of devices and integrated circuit inspection with picosec resolution (19),(20). Especially semiconductor laser based system (21) will be more and more attractive from practical point of view. We have made efforts to further improve the performance by the introduction of diode laser amplifier into the desk-top electrooptic sampling apparatus for GaAs IC inspection (22). Also it was devised that low noise signal detection by lock-in technique become applicable without modulating the electrical signal by the introduction of polarization modulation of probe optical beam (23).

VI. SUMMARY

In summary, (a) it was claimed that gain-switched semiconductor lasers are suitable source for high repetition triggering of electronic circuits; (b) For testing GaAs IC's by optical means with low jitter, optically triggered electrical pulse generation was tried; (c) A novel integrated optoelectronic logic unit based on photodiode gates was proposed and examined experimentally; (d) a consideration was made on PD-2DEG FET-LD close loop gain condition based on some preliminary experiments on PD-FET inverter; (e) Semiconductor laser based electrooptic sampling systems were improved in the hope of bridging the present technological needs and the future target of picosecond industry.

The author thanks the laboratory colleagues for their helps in the preparation of the paper. He would like to express his sincere gratitude to many Japanese industry researchers for their generous helps both in experimental means and in open minded discussions.

REFERENCES

- (1)Chi H. Lee ed., "Picosecond Optoelectronic Devices" Academic Press, New York (1984).
- (2)S.Ishihara ed. "Optical Computing in Japan" NOVA Scientific Publishers (1990).
- (3)D.A.B.Miller, Intern. J. High Speed Electronics vol.1 (1990) 19.
- (4)J.E.Bowers, P.A.Morton, A.Mar, S.W.Corzine, IEEE J. Quantum electron. vol.25 (1989) 1426.
- (5)R.Nagarajan, M.Fukazawa, T.Kamiya, MRS-JSAP Proc. Intern. Conf. Electronic Materials (1988) 217.
- (6)R.Nagarajan, T.Kamiya, A.Kurobe, IEEE J. Quantum Electronics vol.25 (1989) 1161.
- (7)R.Nagarajan, T.Kamiya, A.Kasukawa, H.Okamoto, Appl. Phys. Lett. vol.55 (1989) 1273.
- (8)Y.T.Lee, R.Takahashi, T.Kamiya, Jap. J. appl. Phys. vol.29 (1990) L89.
- (9)H.F.Liu, et al., 12th IEEE Intern. Semiconductor Laser Conf. (1990) Post deadline paper.
- (10)M.Tohyama, T.Kamiya, 12th IEEE International Semiconductor Laser Conf. (1990) 224.
- (11)D.H.Auston, in "Picosecond Optoelectronic Devices" ref.(1).
- (12)F.J.Leonberger, in "Picosecond Optoelectronic Devices" ref. (1).
- (13)Y.Hori, J.Paslaski, M.Yi, A.Yariv, Appl.Phys. Lett. vol.46 (1985) 749.
- (14)H.Kamiyama, Y.Kobayashi, T.Nagatsuma, T.Kamiya, Jap. J. appl. Phys. vol.29 (1990) 1717.
- (15)H.Kamiyama: Doctoral Thesis at Univ. Tokyo (1991).
- (16)H.Kamiyama, A.Shouno, Y.Umemoto, T.Kamiya, Jap. J. appl. Phys. vol.29 (1990) L1248.
- (17)J.L.Chen, K.Kodate, T.Kamiya, Jap. J. appl. Phys. vol.29 (1990) L1539.
- (18)Y.Kobayashi, H.Kamiyama, T.Kamiya, Proc. MRS Intern. Conf. Electronic Materials (ICEM-90) to be published.
- (19)J.A.Valdmanis, G.Mourou, C.W.Gabel, Appl. Phys. Lett. vol.41 (1982) 211.
- (20)B.H.Kolner, D.M.Bloom, IEEE J. Quantum Electron. vol.22 (1986) 79.
- (21)J.M.Wiesenfeld, R.K.Jain, in "Semiconductors & Semimetals" (Academic Press) vol.28 (1990) 221.
- (22)R.Takahashi, H.F.Liu, T.Kamiya, Tech. Digest Topical Meeting on Optical Amplifiers and their Applications vol.13 (1990) 272.
- (23)R.Takahashi, T.Kamiya, Proc. Topical Meeting on Picosecond Electronics and Optoelectronics (1991) Paper WE 4.

Femtosecond Spatiotemporal Field Measurements in GaAs Quantum Wells

W. H. Knox, G. E. Doran, and J. Cunningham

AT&T Bell Laboratories, Holmdel, New Jersey 07733

M. Ramaswamy

Massachusetts Institute of Technology, Cambridge, Massachusetts 02139

S. M. Goodnick

Oregon State University, Corvallis, Oregon 97731

Introduction

Excitonic electroabsorption has been used recently to detect ultrafast electrical transients in ultra-thin quantum well coplanar striplines with time resolution as fast as 180 fs [1]. The use of thin films of quantum wells as both generator and detector of electrical signals with coplanar stripline interconnection results in several interesting capabilities. First, since the exciton exhibits a sensitive saturation response with resonant excitation, it can be used as an in-situ calibration of the excitation and probing response functions. This nonlinear response is instantaneous, since it is based on excitonic phase space filling [2]. Second, the exciton exhibits sensitive electroabsorption in either parallel (field ionization mode) or perpendicular (quantum-confined stark effect - field ionization inhibited mode) electric fields [3]. In the present case, we use the parallel field effect because it easily adapts to high speed geometries like the coplanar stripline (CPS). By focusing the probe beam to a 1 micron spot, we can make space and time resolving electroabsorption measurements with 150 fs time resolution which provide information about the microscopic internal electric fields. We can also determine the static field profile at the generation and detection points. In the present paper, we show several examples of these points and demonstrate full 2-d space-time mappings of propagating femtosecond electrical signals.

Nonlinear Optical and Electrical Response Time

In the experiments, we use an infrared colliding pulse modelocked dye laser producing 85 fs pulses at 820 nm at 160 MHz repetition rate [4] with high frequency phase sensitive detection. The samples are grown by molecular beam epitaxy, consisting of 0.4 microns of quantum wells on a 0.35 micron AlGaAs stop-etch layer. A 10 micron gold coplanar stripline is patterned on the sample and the substrate is etched away with a selective chemical etch, leaving a free-standing membrane of about 1 by 2 mm. First, the pump-probe response is measured with the beams overlapped (Figure 1a). Then the pump beam is focused into the stripline. With an applied bias voltage, the resulting carrier injection creates an electrical signal which propagates in the coplanar stripline. The electrical signal is measured by passing the probe beam through the stripline further down the line (50 microns propagation distance in this case) and detecting the change in absorption of the exciton which results from the changing potential as the electrical signal passes by.

We find that the response time of this optoelectronic technique is comparable to the pulsedwidths in the experiment, therefore we use a simple model to determine the total optoelectronic response time of the circuit. We fit the signals using a simple three-level model with a single exponential rise and a single exponential decay. First, the pump-probe signal is fit to

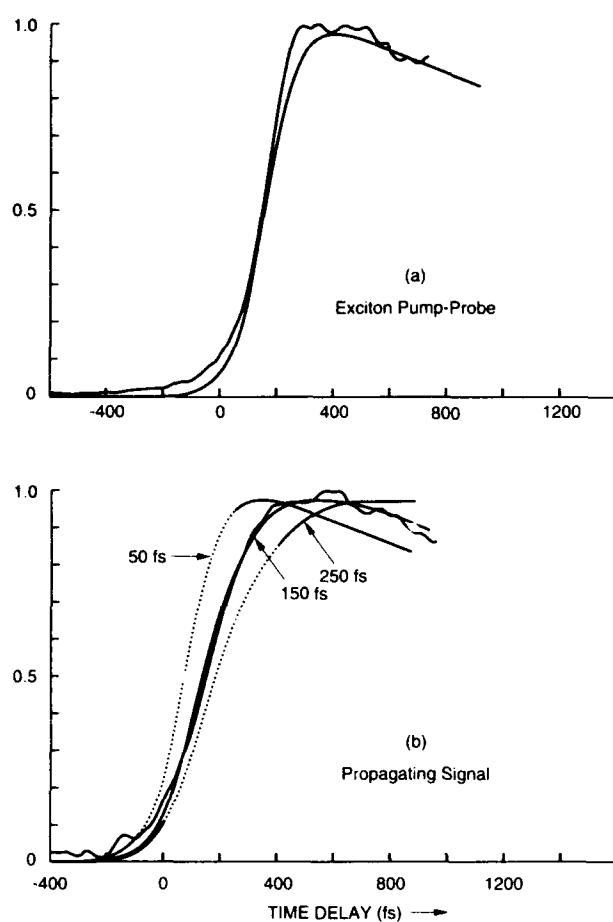


Figure 1. (a) pump-probe excitonic saturation signal, and fit to model, (b) propagating signal and fit to 150 fs rise function.

an instantaneous rise with a decay of a few ps by adjusting the excitation function. A 200 fs FWHM excitation function is obtained. This accounts for the pump and probe pulsewidths and for significant dispersion in the acousto-optic modulator in the pump beam. Then, the electrical signal (1b) is fit using rise functions of 50,

150 and 250 fs. The 150 fs rise function fits best. This result indicates that the entire process of electrical pulse generation by excitonic field ionization, propagation in a thin film a distance of 50 microns on a coplanar stripline, and detection by excitonic electroabsorption is all accomplished with a 150 fs time constant. Further experiments with higher time resolution are required to determine the origin of this response time, but it is likely that the generation mechanism is approaching a physical limit, as we discuss later. Dispersion in the thin film is not enough to explain this result. We have calculated

the high frequency dielectric properties of such geometries [5] and further experiments show that a 300 fs risetime electrical signal at 50 microns distance broadens to only 500 fs after an additional 700 microns of propagation. Also, the excitonic electroabsorption is unlikely to limit the speed of detection in the present experiments, as theory indicates a response time of 40 fs or so for the present conditions [6].

DC Electroabsorption Mapping

In nearly all semiconductor devices with metal contacts, the electric fields are non-uniform as a result of the formation of depletion regions. In the present case, proton-implanted quantum wells having very high resistivity ($> 10^7 \Omega \cdot cm$) are used in order to avoid ohmic dissipation under high bias fields. In addition, dielectric dissipation for THz frequency components of the propagating electrical signal is minimized in semi-insulating materials. This material contains a range of defects from shallow to deep impurities. Upon the application of a DC bias, the impurities which are ionized release carriers which migrate and are trapped at deep level impurities, producing a space charge which opposes the bias field. The DC electroabsorption gives a measure of the internal field in such a device, as shown in Figure 2. This data was obtained by illuminating the

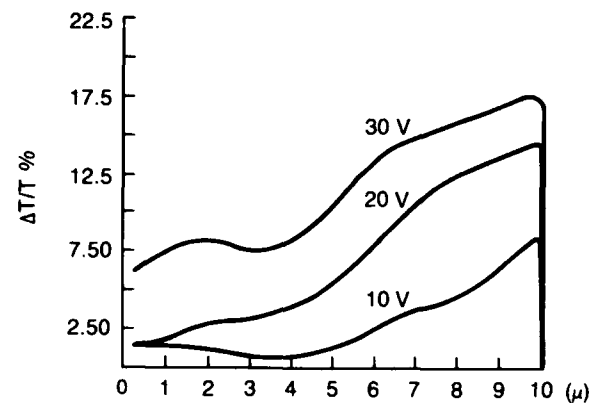


Figure 2. DC electroabsorption mapping of a 10 micron CPS at three different voltages. The lateral depletion length depends on the voltage.

device uniformly with narrow-band CW light from a laser diode at the exciton peak wavelength and digitizing the transmitted image with a frame-grabber and CCD camera [7]. Having a very low effective free electron concentration, the lateral depletion extends to 5-10 microns and depends on the bias voltage. This profile can be further modified by carrier injection and space charge fields at high densities, but this represents the low-density limit.

1-Dimensional Femtosecond Mapping

In the first experiment, the pump beam is focused into the gap and generates an electrical transient, and the probe beam is focused to a small spot (1-2 microns). The probe beam is scanned through the device and the detected electrical signal is recorded (Figure 3). Such an experiment would seem trivial, since the propagating signal is a TE mode, and the detected signal should not depend on the position of the probe beam. The excitonic electroabsorption detector has a bias-dependent detection sensitivity [1], however, and in addition it is important to show that overshoot effects are not due to a field relaxation at the detection point. Although the magnitude of the detected signal varies with position, its shape does not. Therefore, the overshoot recorded in the detected transient does not depend on the probe beam position. The amplitude of the detected signal follows generally the profiles which were measured by DC techniques (Figure 2).

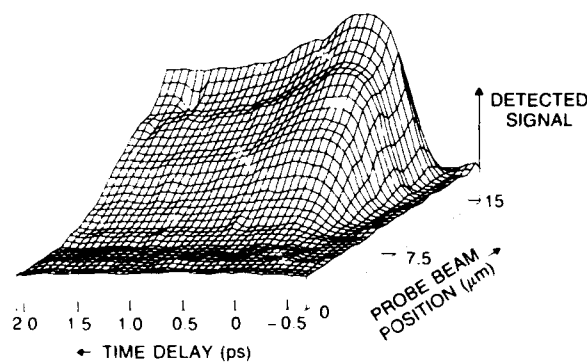


Figure 3. 1-D spatially resolved electroabsorption in 10 micron CPS.

Space-Resolved Generation of Femtosecond Transients

The generation of femtosecond electrical transients in micron-scale structures is a very complex and important problem. Many unresolved issues remain at present. In particular, velocity overshoot effects [8] have been reported in electro-optic sampling measurements [9], however alternative explanations have been given involving space-charge effects, particularly for the case of high excess initial carrier energy [10]. In the present case, we excite carriers of zero excess energy initially in the form of excitons therefore giving the maximum contribution to velocity overshoot. Secondly, using the spatial resolution of the excitonic electroabsorption, we characterize the DC field profile. This new additional information

as well as carrier density-dependent studies may resolve the controversy about velocity overshoot - vs - space charge field relaxation effects. The field non-uniformity in the CPS should cause the shape of the generated electrical signal to depend on the pump beam position, since both velocity overshoot and space charge effects exhibit field-dependent dynamics. Figure 4 shows an experiment in which the photoconductivity overshoot is space-resolved at high excitation density. We focus the pump beam to a small spot (about 2 microns diameter) and scan its position through the device while measuring the electrical signal with a probe beam 50

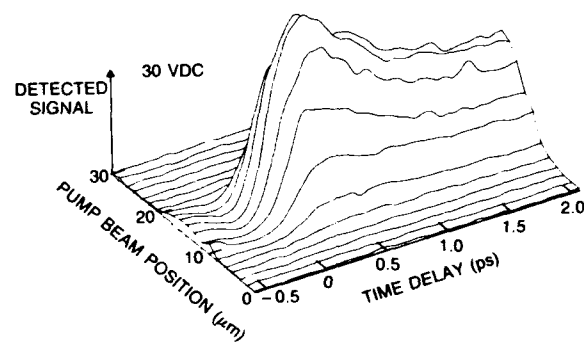


Figure 4. Space-resolved generation of femtosecond electrical signal.

microns away. We find that when the pump beam is scanned across the stripline, the risetime and decay time of the electrical signal change. At one point, the signal rises rapidly and exhibits a large overshoot. When exciting in other regions, the signal rises more slowly and exhibits less of an overshoot. This is shown more clearly in Figure 5, which is a contour plot of the data in Figure 4. The point of maximum overshoot is clearly shown. This picture does not exactly fit the DC field profile shown in Fig. 2 or the detected signal cross-section shown in Fig. 3. Clearly, the static field profile is modified by the presence of the pump beam, and we would expect the overshoot transient to contain strong space-charge contributions. The excitation density is above 10^{18} cm^{-3} for this case.

The essential difficulty with the understanding of these signals is summarized: when the pump beam is focused weakly so that it fills the device uniformly (a 10 micron spot) each region of the device generates a different electrical signal with a different rise and decay time. The total displacement current is approximately the sum of the individual current sources. The net result is an initial photocurrent transient which is averaged over

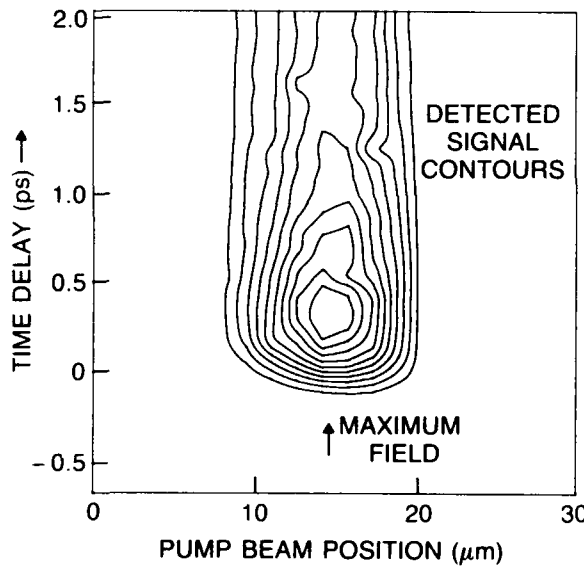


Figure 5. Time-space contours of data of Fig. 4 obtained by moving the focused pump beam through the CPS and recording the generated signal.

all the fields of the device. If the pump beam is focused to a spot size which is smaller than the scale of the field non-uniformity (1-2 microns in the present case) the DC field is uniform across the generation region, but the excited density is high enough so that space charge effects modify the dynamics of the carrier velocities. Thus, low density large-spot size signals exhibit essentially density-independent signals which appear to be an indication of excitonic velocity overshoot, but they are field-averaged. Of course, the velocity overshoot effect critically depends on the field, therefore nonuniform fields smear out the effect substantially.

Ensemble Monte Carlo Modeling

We have simulated our experiments with a real-space Ensemble Monte Carlo (EMC) simulation of our experiment. We include polar optical phonon scattering, electron-electron and electron-hole scattering and intervalley scattering with a nonuniform electric field and nonuniform carrier injection in one dimension.

We take a field profile of $E(x) = E_{\max} \left(\frac{x_d}{x+x_d} \right)^2$, where x_d

is the depletion scale length, here taken to be 5μ . We use a very short (6 fs) excitation pulse with a corresponding wide initial distribution around $k=0$ to illustrate the initial current transient clearly. We assume for simplicity that the field profile linearly decreases from one side of the device to the other, and inject carriers with a 2 micron gaussian spot. Fig. 6a shows the generated signals for two different pump beam positions and Fig. 6b shows the generated signal with uniform excitation of the device. Clearly, non-uniform fields play a significant role in these experiments. We note that at fields of 40 kV/cm as in Fig. 6, even if a 6 fs optical pulse is used to excite the device, the photocurrent requires 100-200 fs to rise to its maximum value. This is simply limited by the effective mass of the electron. Therefore, in the experiment shown in Fig. 1, the 150 fs response time results most likely from the initial acceleration of charge.

In the present case, our EMC model does not account for space charge effects, and we obtain good qualitative agreement with low density experiments. We are extending our EMC modeling to include space-charge effects as in [10] for conditions appropriate to our experiments with tightly focused pump beams at high densities.

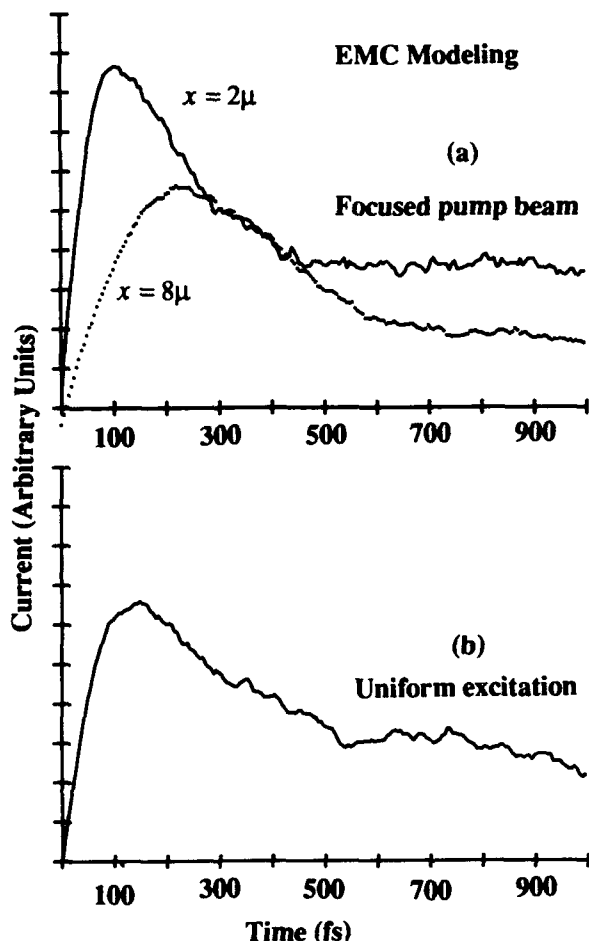


Figure 6. (a) 1-D EMC simulation of pulse generation with linearly decreasing field across 10 micron CPS. A 2 micron pump beam is placed at two different positions. (b) corresponding case of uniform excitation, showing averaging effect.

One indication of the complexity of this problem is that the generated signals in the small pump beam high-density conditions does not simply follow the DC field profile measured at low density. It is clear that at high densities the injected carriers modify the field profile in a complex, dynamical manner, as suggested in [10]. Screening processes are somewhat difficult to take into account in EMC in a precise way, especially at high densities. In any case, it is clear that excitonic velocity overshoot (velocity overshoot starting at $k=0$) plays a significant role in the initial transient, but at high densities

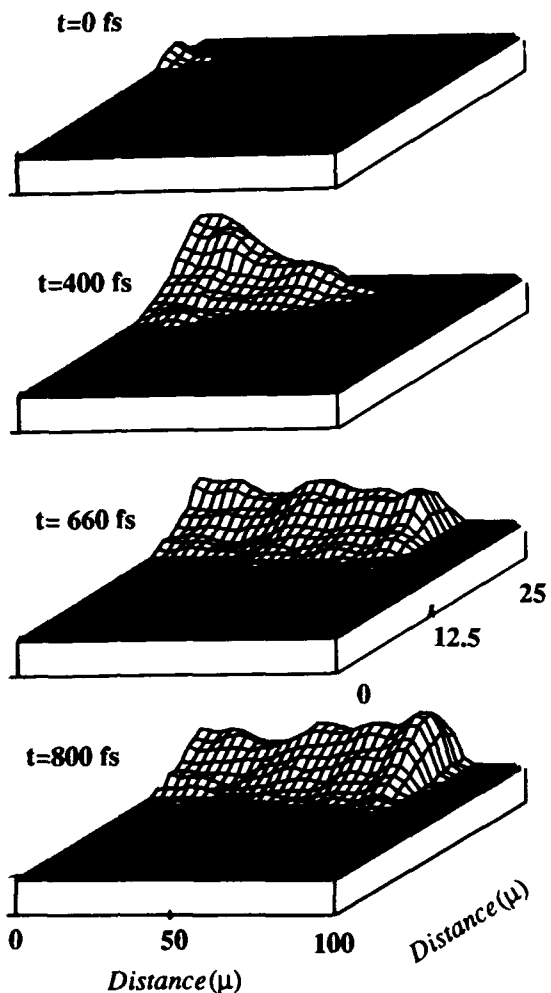


Figure 7. 2-dimensionally resolved propagating electrical signal in 25 micron CPS. An open termination is encountered.

space charge effects also contribute. Nonuniform fields serve to further complicate the situation, however excitonic effects of electroabsorption and saturation may provide key new information. In addition, the picture of Fig. 5 should be excitation density and bias dependent.

2-Dimensional Femtosecond Field Mapping

The technique of field-mapping can be easily extended to a full two-dimensional format. In this case, the probe lens is attached to an orthogonal 0.1 micron resolution stepper motor and for each time delay a full 32x32 raster scan of the probe beam is made. With the probe beam focused to a 1 micron diameter spot, the detected signal is recorded at each point. We typically record 10 time frames. Figure 7 shows four successive time frames of a pulse which propagates in a 25 micron stripline and encounters an open termination consisting of a 25 micron gap in the CPS. The capability of full two-dimensional field mapping with femtosecond time resolution should provide additional new information, and particularly in the case of complex devices.

Summary

In summary, we have used the excitonic nonlinear saturation response to measure the impulse excitation of quantum well coplanar stripline structures in thin films. We use excitonic electroabsorption to measure DC field profiles and 1 and 2 dimensionally resolved propagating femtosecond electrical signals. In addition, we have investigated the effects of excitonic velocity overshoot and its relation to space charge effects. Clearly much more work is required for a full understanding of these processes.

Acknowledgments

The authors would like to thank J. Shah, M.C. Nuss, G.W. 'tHooft and D.A.B. Miller for stimulating discussions regarding this work.

References

- [1] W.H. Knox, J.E. Henry, K.W. Goossen, K.D. Li, B.Tell, D.A.B. Miller, D.S. Chemla, A.C. Gossard, J. English and S. Schmitt-Rink, *IEEE J. Quant. Electron.* **25**, 12 (1989).
- [2] W.H. Knox, R.L. Fork, M.C. Downer, D.A.B. Miller, D.S. Chemla, C.V. Shank, A.C. Gossard and W. Weigmann, *Phys. Rev. Lett.* **54**, 1306 (1985).
- [3] D.A.B. Miller, D.S. Chemla, T.C. Damen, A.C. Gossard, W. Weigmann, T.H. Wood and C.A. Burrus, *Phys. Rev.* **B32**, 1043 (1985).
- [4] W.H. Knox and F.A. Beisser, *Proc. Ultrafast Phenomena VII*, Springer Verlag, NY p. 20, 1990.
- [5] G. Hasnain, K.W. Goossen and W.H. Knox, *Appl. Phys. Lett.* **56**, 515 (1990).
- [6] S. Schmitt-Rink, D.S. Chemla, W.H. Knox and D.A.B. Miller, *Opt. Lett.* **1**, 60 (1990).
- [7] M. Ramaswamy, W.H. Knox, T. Sizer, B. Tell, J.E. Henry, G.E. Doran, IQEC, 1990 paper QTUH24; to be published.
- [8] "The Physics of Submicron Semiconductor Devices", ed. H.L. Grubin, D.K. Ferry and C. Jacoboni, *Proc. 1983 NATO ADV. Study Inst.* Plenum Press, NY (1988).
- [9] K. Meyer, M. Pessot, G. Mourou, R. Grondin and S. Chamoun, *Appl. Phys. Lett.* **53**, 2254 (1988).
- [10] A.E. Iverson, G.M. Wysin, D.L. Smith and A. Redondo, *Appl. Phys. Lett.* **52**, 2148 (1988); R.P. Joshi and R.O. Grondin, *Solid State Electronics* **32**, 1813 (1989).

Propagation of Picosecond Electrical Pulses in GaAs for Velocity-Matched Modulators

Yi Chen, John Nees, and Steve Williamson

*Ultrafast Science Laboratory, University of Michigan, 2200 Bonisteel Boulevard,
Room 1006, Ann Arbor, Michigan 48109-2099*

Abstract

We report on propagation of picosecond step pulses over 10 millimeters with a GaAs-encapsulated transmission line. The effective dielectric constant matches the optical value to within 0.1%.

Introduction

A traveling-wave electro-optic modulator fabricated from GaAs can, in principle, be fabricated having a modulation bandwidth exceeding 500 GHz. To approach such performance will require the elimination of not only velocity mismatch, which now limits the

state-of-the-art to ~40 GHz,[1] but also modal dispersion of the microwave signal, radiation loss, free carrier absorption, and losses due to skin effect absorption.

The major source of dispersion, velocity mismatch, can be practically eliminated by fully encapsulating the transmission lines in a uniform GaAs medium.[2] GaAs possesses the unique property of having bulk dielectric constants in the near infrared- and millimeter-wave radiation regimes that are essentially equal.[3] If the radiation fields for the optical and electrical signals are completely enclosed within GaAs, velocity mismatch between the two will be eliminated. Encapsulating the transmission line also eliminates frequency-dependent dispersion and radiation otherwise

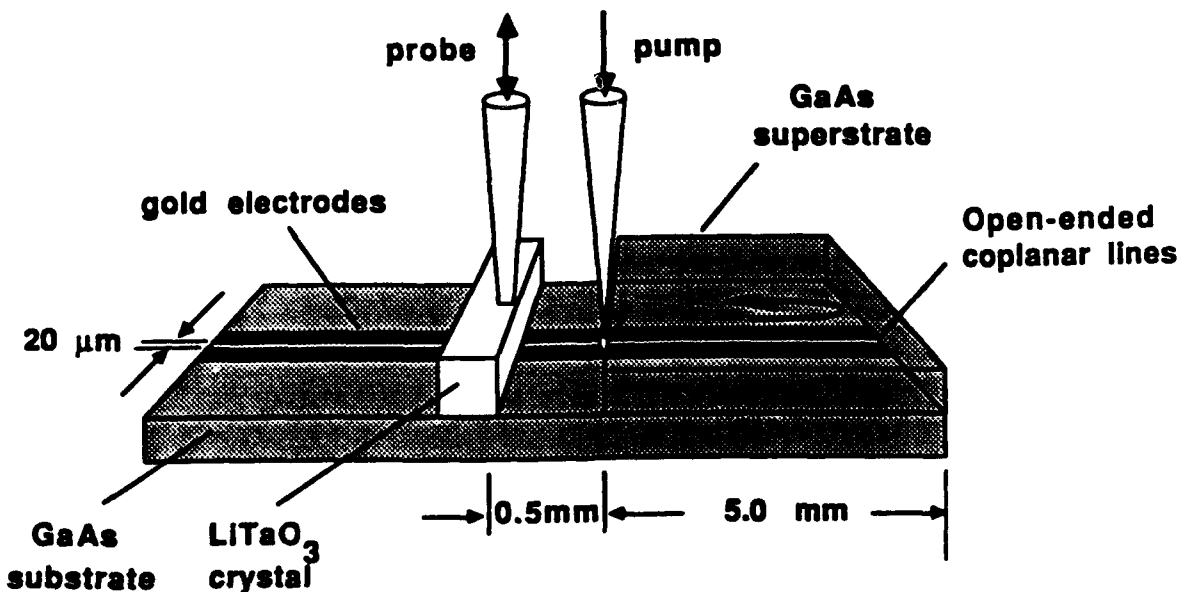


Figure 1. Experimental setup

present due to the dielectric mismatch. Losses associated with skin effect, and free-carrier absorption can be effectively eliminated by lowering the temperature.

Experiment

To test these principles we have constructed a coplanar transmission line fully encapsulated in unintentionally-doped [001] GaAs by first reactive ion etching 2800 Å-deep coplanar troughs into which 2800 Å of gold was deposited. The top surface of the electrodes is left flush with the surface of the substrate to within 200 Å. The pair of electrodes are 20 µm wide and separated by 20 µm. The dc resistance/millimeter for the electrodes is 4.9 Ω/mm at 293 K and 0.8 Ω/mm at 10 K. A second wafer of GaAs is then placed on top thereby fully enclosing the coplanar electrodes.

The transmission line structure was placed in a cryogenic environment. The technique of external electro-optic sampling [4] was used to characterize the device. A balanced, colliding-pulse, mode-locked dye laser [5] producing 150-fs pulses was used for both

switching and probing. Figure 1 depicts the experimental layout. The GaAs superstrate was placed at the end of the transmission line. The transmission line was left open-ended in order to reflect the electrical pulse.

The pump pulse excited an electrical signal on the transmission line at the entrance point of the superstrate. The signal propagated in both directions away from the point of excitation. The input pulse was measured from the electrical signal that directly propagated across the 0.5 mm air-superstrate region of the transmission line. The output pulse propagated twice the length of the superstrate and then across the air-superstrate region before being measured. This technique is preferred over single-pass transmission which requires the replacement of the probe crystal/beam at a second location, leading to errors in the measurement of both the propagation delays (hence effective dielectric constant) and waveforms. Reflection from an open end will nevertheless result in frequency-dependent loss by capacitively coupling energy to the adjacent line. The results that we observe, therefore, represent conservative values.

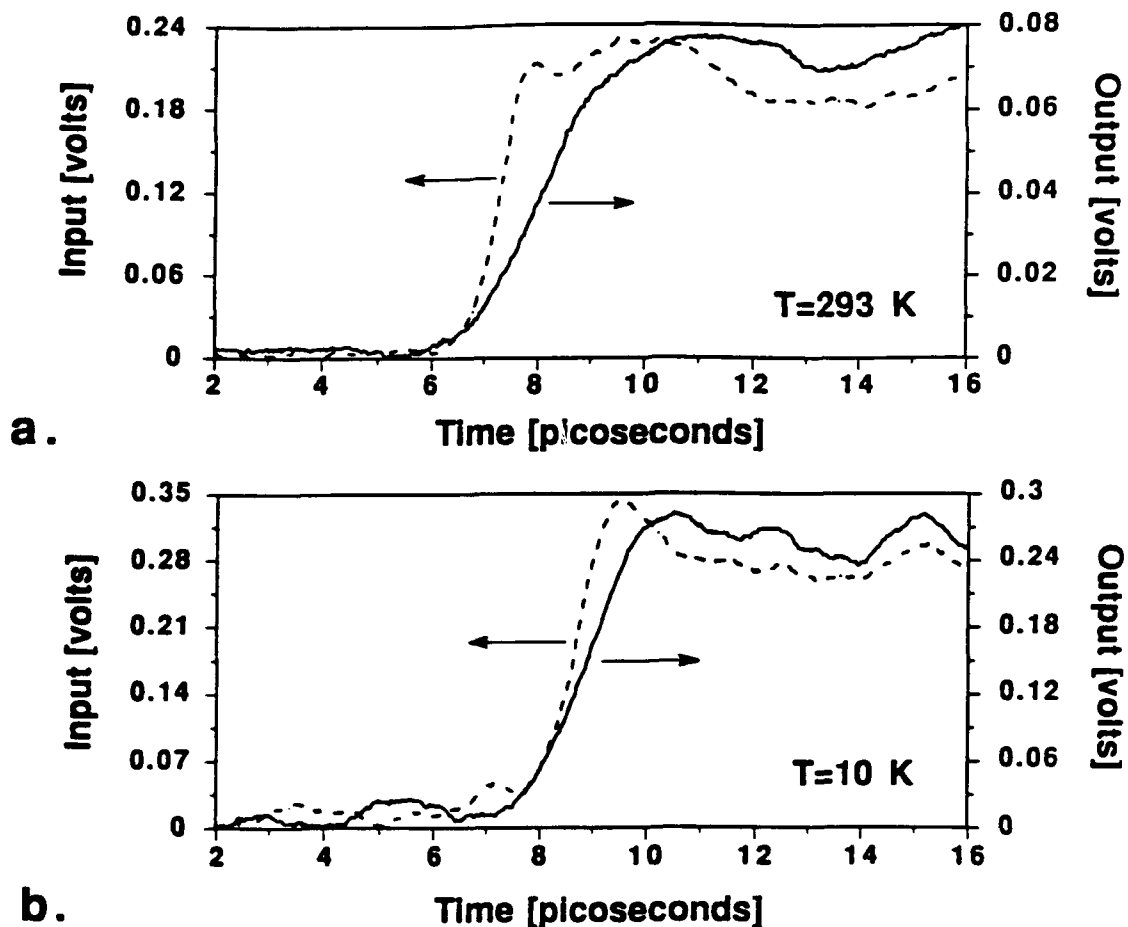


Figure 2. Pulse propagation on 20 µm GaAs-encapsulated transmission lines

Results

Figures 2a and 2b show the results at 293 K and 10 K respectively. The input for both temperatures is 1.3 ps. The output at 293 K is found to have been strongly attenuated and the risetime broadened to 3.0 ps. Both effects are primarily due to skin effect attenuation by the gold electrodes. At 10 K the amplitude of the propagated signal is preserved and the risetime of 2.0 ps more closely matches that of the input. The discrepancy in input/output risetimes is partially due to losses at the open-end of our transmission line and possibly residual modal dispersion remaining from a non-perfect interface. We note that this broadening takes place over a total propagation time of 120 ps.

A careful measurement of the propagation time was made by measuring the optical translational delay between the arrival of the input and output signals. Since the 0.5 mm air-superstrate region is traversed by both signals the optical delay directly relates to the propagation time of the electrical pulse within the superstrate. By knowing the propagation time and the length of the superstrate an accurate measurement of the effective dielectric constant can be determined. The effective dielectric constant was found to be 11.60 (+/- 0.02). This value agrees remarkably well with the bulk value of GaAs at 1.3 μ m, 11.62 [1]. The difference in arrival times between electrical and optical pulses propagating in this structure would amount to ~500 fs for a 10 mm interaction length.

This effective dielectric constant, however, deviates from the accepted value of 12.9 for bulk GaAs in the millimeter-wave regime.[6] Measurements were then made using structures having 50 μ m coplanar lines. The larger geometry should be less susceptible to an residual-air interface between the superstrate and substrate. The dielectric constant for this larger electrode geometry was found to be 12.85, suggesting that, indeed, a less-than-perfect interface exist.

Future work

The results thus far are qualitatively revealing. To fully assess the mechanisms responsible for dispersion and attenuation we will begin performing scattering parameter measurements.[7] Also, the use of a mechanically-applied GaAs superstrate has served to demonstrate the feasibility of velocity matching for ultrafast travelling-wave optoelectronic modulators. Practical use of this technique can be realized by

regrowing GaAs over the substrate forming a superstrate that is an integral part of the device. Regrowth techniques are now being investigated for compatibility with various electrode structures and compositions.

Acknowledgments: This work is supported by U. S. Army Research Office under the contract No. DAAL 03-89-K-0071, and the Air Force of Scientific Research under the URI Program, Contract No. AFSOR-90-0214.

References

1. S. K. Korothy, G. Eisenstein, R. S. Tucker, J. J. Veselka, and G. Raybon, 'Optical intensity modulation to 40 GHz using a waveguide electro-optic switch', *Appl. Phys. Lett.*, **50**, 1631, (1987).
2. J. Nees, S. Williamson, and G. Mourou, '100 GHz traveling-wave electro-optic phase modulator', *Appl. Phys. Lett.*, **54**, 1962, (1989).
3. E. D. Palik, 'Handbook of Optical Constants and Solids', Academic Press Inc. p433, 1985.
4. J. Valdmanis, '1 THz-bandwidth prober for high-speed devices and integrated circuits', *Electron. Lett.*, **23**, 1308, (1987).
5. J. A. Valdmanis and R. L. Fork, 'Design considerations for a femtosecond pulse laser balancing self phase modulation, group velocity dispersion, saturable absorption and saturable gain', *IEEE J. Quantum Electron.*, **QE-22**, 112, (1986).
6. M. N. Afsar, K. J. Button, 'Precise Millimeter-wave measurements of complex refractive index, complex dielectric permittivity and loss tangent of GaAs, Si, SiO₂, Al₂O₃, BeO, Macor, and Glass', *IEEE Trans. Microwave Theory Tech.*, **MTT-38**, 217, (1983).
7. M. Y. Frenkel, J. F. Whitaker, G. A. Mourou, J. A. Valdmanis, and P. M. Smith, '100-GHz electro-optic S-parameter characterization of high electron mobility transistors', submitted to *Picosecond Electronics and Optoelectronics Conference*, Salt Lake City, Utah, March 13-15, 1991.

Picosecond High-Voltage Photoconductive Switching

T. Motet, J. Nees, S. Williamson, and G. Mourou

Ultrafast Science Laboratory, University of Michigan, Ann Arbor, Michigan 48109-2099

Abstract

We report on the generation of 850 V electrical pulses with 1.4 ps rise time and 4 ps Full-Width-at-Half-Maximum using pulse biased Low-Temperature-grown GaAs photoconductive switch triggered by an amplified femtosecond dye laser. Dependence of the temporal pulse shape on both the electric field and the optical energy is observed and discussed.

I. Introduction

In recent years many applications have emerged for high-voltage, high-speed switching. Using photoconductive techniques both kilovolt switching and picosecond pulse generation have been achieved. High-voltage switching has been reported using high resistivity materials and high power lasers with large-dimension structures to achieve kilovolt switching. This resulted in pulses with duration down to 70 ps and rise time no less than 10 ps [1]. Conversely, high-speed switching has used short optical pulses with fast recovery time materials, small dimension structures and low power lasers to achieve generation of subpicosecond pulses with amplitude up to 6 V [2]. We successfully combined high-speed and high voltage by pulse biasing a Low-Temperature GaAs photoconductive switch triggered by submicrojoule level, 150 fs optical pulses. The following discussion reports on the generation of a 850 V pulse with 1.4 ps rise time and 4 ps full-width-at-half-maximum.

The maximum bias voltage that can be applied to a photoconductive switch is determined by the dimension across which the bias is applied and the breakdown of the semiconductor material. The breakdown voltage increases with material resistivity and separation of electrodes. Also, the material breakdown voltage may be increased by limiting the duration of the bias

voltage. The fraction of bias voltage effectively switched depends on the energy of the optical pulse. The rise time of the electrical signal is determined by the duration of the optical pulse and by the switch bandwidth, which is a function of the switch dimensions. The pulse duration is limited by the carrier lifetime. Ultimately the geometry of the switch determines the maximum possible bias and the minimum rise time.

With conventional high resistivity GaAs or Si, the electric field hold-off is around 10^4 V/cm. Therefore, the small dimensions necessary for picosecond signal generation would limit the applied voltage to few hundred volts. However, Low-Temperature MBE-grown GaAs (LT-GaAs) has recently demonstrated extremely high resistivity and breakdown threshold [2]. Furthermore, due to its subpicosecond carrier lifetime LT-GaAs satisfy the conditions for picosecond pulse generation. By using this material we have been able to apply a 1.3 kilovolt pulse bias to a 100 μ m switch making possible the generation of picosecond high-voltage pulses.

II. Experimental configuration

Efficient switching of kilovolt-level bias voltages requires an optical energy at the microjoule level, which necessitates the use of amplified laser pulses. Our laser (similar to that described in references 3 and 4) generates microjoule pulses at 620 nm at a 2-kHz repetition rate, using a two-stage dye amplifier pumped by a frequency doubled Nd:YAG regenerative amplifier. The laser pulse duration is 150 fs, ensuring that the picosecond electrical pulse generation and measurement are not limited by the optical pulse length.

A schematic diagram of the experimental configuration is shown in Figure 1. Pulse biasing is employed to prevent breakdown of the switch. Part of the frequency doubled Nd:YAG regenerative amplifier

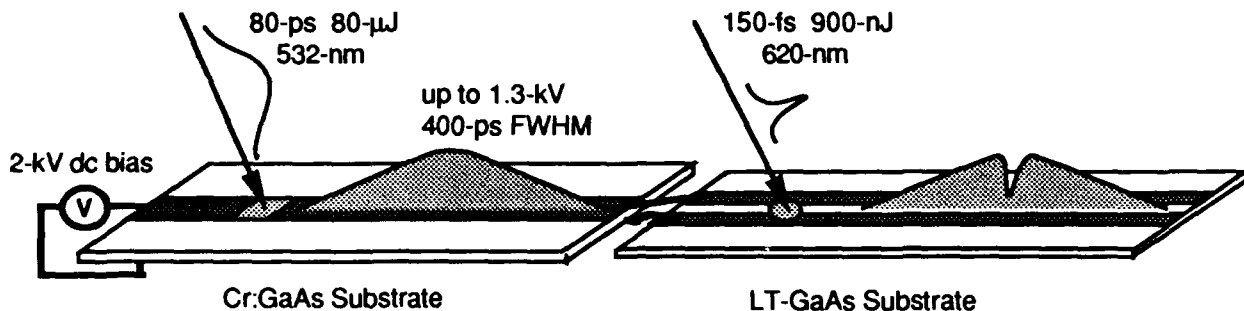


Figure 1. schematic of the experimental set up.

output is used to illuminate a dc-biased 4-mm-long semi-insulating-GaAs switch. A 80 μ J, 80 ps optical pulse at 532 nm generates an electrical pulse which has an amplitude equal to 70% of the dc bias voltage and a full-width-at-half-maximum of 400 ps. This pulse then biases a $90\ \Omega$ coplanar stripline (100 μ m wide gold conductors separated by 100 μ m) on a LT-GaAs substrate. As the bias pulse propagates along the transmission lines, a 150 fs optical pulse with energy up to 1 μ J illuminates the area between the conductors. This forms a plasma within the LT-GaAs which shorts the conductors together. This technique of switching, known as "sliding contact", in principle, allows total switching of the applied bias voltage [5]. The resulting electrical waveform is schematically shown in Figure 1. External electro-optic sampling [6] in a LiTaO₃ crystal with 150 fs, 100 pJ pulses is used to measure the signal 300 μ m from the switch site. Waveforms are recorded for different settings of bias voltage and illuminating energy. For convenience, the picosecond electrical waveforms are then extracted and displayed in a more conventional format.

II. Results

Figure 2 shows a 850 V pulse with duration of 4 ps and rise time of 1.4 ps. For incident optical energies

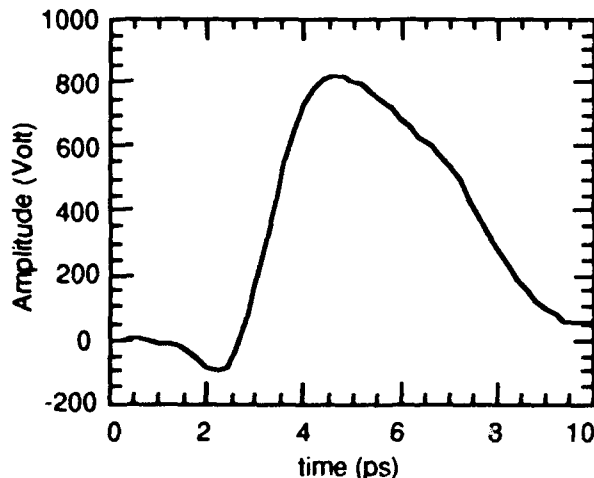


Figure 2. waveform showing an 850 V, 1.4 ps rise time and 4.0 ps duration pulse switched from a 1.3 kV bias with an optical energy of 900 nJ.

greater than 500 nJ we observe saturation of the switching efficiency, defined as the ratio of switched voltage to applied voltage as shown in Figure 3. While the maximum switching efficiency is ideally 100 %, the 70 % experimentally measured can be explained by a combination of factors including radiation, dispersion and contact resistance. The negative precursor to the pulse is attributed to the radiation from the dipole formed at the generation site. The rise time, ultimately limited by the 100 μ m transmission line dimensions, reveals a clear dependence on the carrier density. As illustrated in Figure 4, we observe a degradation from 1.1 ps to 1.5 ps over the range of optical energy from 100 to 900 nJ. This corresponds to the saturation of the slew rate. However, as shown in Figure 5, the rise time appears to be independent of the electric field. The relation of the rise time to the carrier density and the electric field is still not well understood. Explanations involving saturation of the current density and strong carrier scattering are presently under investigation.

While a subpicosecond fall time is expected from previous measurements of LT-GaAs carrier lifetime [7], this experiment reveals a much longer recovery time. This tail increases as we increase either the carrier density or the applied electric field (Fig 4 and 5). Significant local heating due to the extremely high current densities (up to $10^7\ A/cm^2$) drawn through the

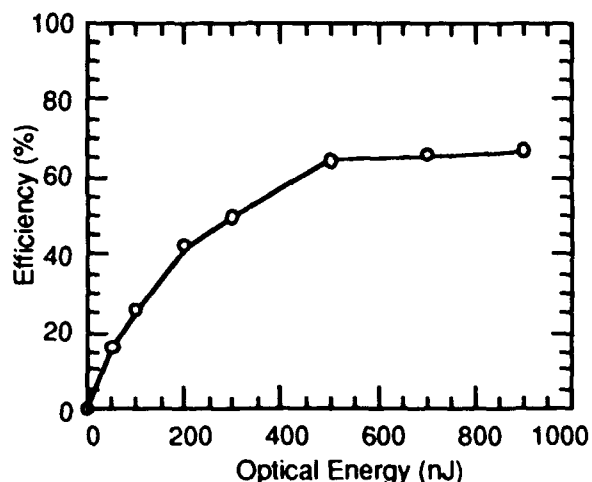


Figure 3. switching efficiency as a function of optical energy for an electric field of 100 kV/cm.

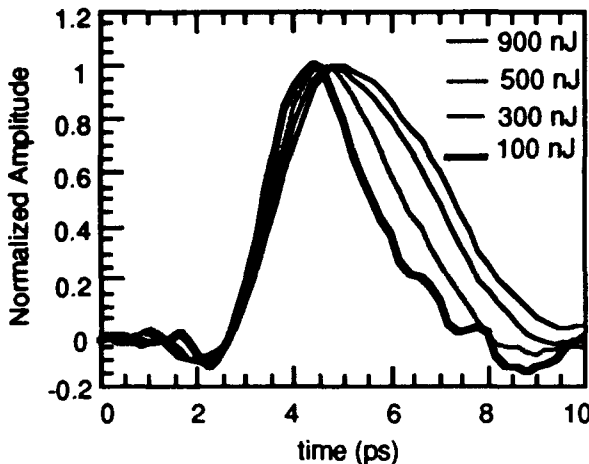


Figure 4. pulse shape as a function of optical energy for an electric field of 100 kV/cm.

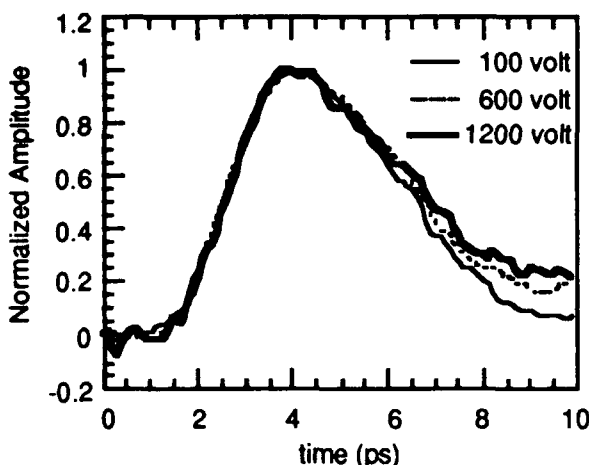


Figure 5. pulse shape as a function of applied bias for an optical energy of 900 nJ.

switch area results in generation of additional carriers and could explain this long recovery time, however it does not account for the rise time degradation. In the following, we present an other possible justification for the long recombination time, involving intervalley scattering which is known to be strongly dependent on both the electric field and the carrier density.

The switched electric pulse shape reflects the evolution of the current density which is proportional to the product of carrier density and average carrier velocity. A carrier's contribution to the switching process is then proportional to its velocity. In GaAs, a photogenerated hot electron under a strong electric field can scatter from the central valley to the high-effective-mass satellite X- and L-valleys greatly reducing its velocity and therefore its contribution to switching. The scattering probability increases with the electrical field and, under our experimental conditions, we estimate that more than 80 % of the carriers are in the satellite valleys after 100 fs [8]. The transfer of those electrons back into the central valley occurs on the

picosecond time scale [9]. As the pump energy increases the carrier density in the central valley rises. Consequently, the probability for an electron to scatter back into the central valley decreases. As the carriers still in the high mobility valley recombine within few hundred femtoseconds, the probability to transfer back from the satellite valleys increases with time. The satellite valleys can then be seen as sources reinjecting hot electrons into the central valley at a rate dependent on the electric field and the carrier density.

IV. Summary

In conclusion, we report on the application of LT-grown GaAs for photoconductive switching using a pulse bias technique leading to the generation of a 850 V pulse with 1.4 ps rise time and duration of 4 ps. This represents the highest voltage ever obtained in the single-picosecond time scale. This new capability to produce ultrashort high peak power pulses could be of interest for applications in fields such as millimeter-wave non linear spectroscopy, radar signal generation, source for linear accelerator of particles and ultrafast instrumentation. Future work will include spectroscopic studies to determine the carrier dynamics and populations during the switching process.

Acknowledgments

The authors wish to thank Frank Smith of MIT Lincoln Laboratory for providing high quality LT-grown GaAs samples. This work was carried out at the National Science Foundation Science and Technology center at University of Michigan. It was supported by the ARO-DAAL03-89-K-0071, AFOSR-90-0214 and by Thomson-CSF, France.

References

- [1] D.G.Stearns, "Electro-optic sampling of ultra short high voltage pulses", *J.Appl.Phys.* 65, February 1989
- [2] M.Y.Frankel, J.F.Whitaker, G.A.Mourou, F.W.Smith and A.R.Calawa, "High-Voltage Picosecond Photoconductor Switch Based on Low-Temperature-Grown GaAs", *IEEE Transactions on Electron Devices*. vol. 37. no. 12. December 1990
- [3] T.Norris, T.Sizer II, and G.Mourou, "Generation of 85-fsec pulses by synchronous pumping of a colliding-pulse mode-locked dye laser", *J. Opt. Soc. Am. B*, vol. 2, April 1985
- [4] I.N.Duling III, T.Norris, T.Sizer II, P.Bado, and G.A.Mourou, "Kilohertz synchronous amplification of 85 femtosecond optical pulses", *J. Opt. Soc. Am. B*, vol. 2, April 1985
- [5] D.R.Grischkowsky, M.B.Ketchen..., "Capacitance free generation and detection of subpicosecond electrical pulses on coplanar transmission lines", *IEEE J.Quantum Electron.*, vol.24, 1988
- [6] J.A.Valdmanis and G.A.Mourou, "Subpicosecond

electrooptic sampling: Principles and applications",
IEEE J. Quantum Electron., vol. QE-22, 1986

[7] S.Gupta, submitted for publication

[8] Dr.G.Iafrate, "High-Speed Transport in III-V
Compounds", in Gallium Arsenide Technology,
edited by D.K.Ferry, SAMS 1985

[9] M.C.Nuss and D.H.Auston, "Direct Subpicosecond
Measurement of Carrier Mobility of Photo Excited
Electrons in GaAs", in Picosecond Electronics and
Optoelectronics II, edited by F.J.Leonberger,
Springer-Verlag 1987

Electro-Optic Sampling

Two-Dimensional Field Mapping of GaAs Microstrip Circuit by Electro-Optic Sensing

Ming G. Li, Eve A. Chauchard, and Chi H. Lee

*Electrical Engineering Department, University of Maryland,
College Park, Maryland 20742*

Hing-Loi A. Hung

COMSAT Laboratories, Clarksburg, Maryland 20871

Abstract

A highly sensitive technique for 2-dimensional electric field detection in a GaAs microstrip circuit has been developed using electro-optic (E-O) sensing. With this method, the interference effect in the E-O sampling technique has been studied.

Introduction

Electro-optic sampling is a useful technique to measure the electric field in a GaAs microstrip circuit [1]. It has an extremely wide bandwidth capability and does not require physical or electrical contact to the device. Most of previous experiments sampled the electric field at one particular point or discrete location in the circuit. For some applications, it is desirable to map the field distribution in two dimensions (2-D). 2-D field distribution can be conveniently measured by electro-optic sampling because of its noncontact feature. W. Donaldson performed a time resolved 2-D measurement as follows[2]: after the polarized incoming light interacted with the electric field, the image of the reflected light which carried the field distribution information was focused onto a 2-D diode array. The data were then displayed on a monitor. This method has very good temporal resolution, but very low sensitivity. It requires a high power laser and can only measure strong electric field. In this paper, a highly sensitive technique to measure the 2 dimensional electric field distribution is presented. With this technique, the interference effect occurring when performing electro-optic sampling is studied.

In the previously reported polarization rotation modulation (PRM) techniques, which depend only on the E-O detection of signal from the back-side reflection, the interference between the mul-

tiple beam reflections from top (front) and bottom (back) surface of the GaAs substrate had not been accounted for. Since the index of refraction of GaAs is large, a substantial amount of light is reflected at the top surface, as well as at the bottom surface, therefore, the interference effect can not be neglected. This is especially important, when the laser pulse duration is longer than the optical pulse round-trip time in the GaAs substrate.

In this paper, the interference effect on the conventional electro-optic sampling technique, which requires the use of an analyzing polarizer, has been studied. It was observed that the interference effect is significant provided that the optical pulse duration used for electro-optic sampling is longer than or comparable to the optical round-trip transit-time through the substrate. Furthermore, the magnitude of the sampling signal depends critically on the local substrate thickness, causing difficulties in calibrating the amplitude of the electro-optic sampling signal in microwave circuit measurement.

It is interesting to note that when the interference effect is presented, the E-O signal can be detected even without analyzing polarizer. The microwave signal modulates the effective optical thickness of the GaAs substrate via electro-optic effect. This in turn gives rise to the modulation of the intensity of reflected optical probing beam.

Two-dimensional mapping

The 2-dimensional field mapping is achieved by scanning the probing laser beam with a galvanometer type beam scanner in one dimension and translating the sampled circuit in the other dimension. In order to obtain time resolved information, one would need to combine this setup with a

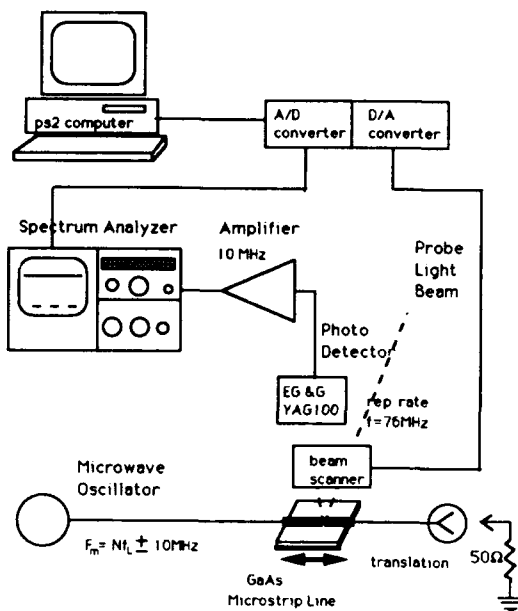


Figure 1. The schematic of 2-dimensional field mapping system.

technique to phase lock the microwave to the laser pulses [1]. We present at this meeting a new microwave phase locking technique which can phase lock an integrated voltage controlled oscillator [3]. The experimental setup for 2-D field mapping is shown in Fig. 1.

The frequency of the microwave signal applied to the GaAs circuit is set to fit the following formula:

$$f_m = N f_L \pm f_{IF}$$

where f_m and f_L are the microwave frequency and the laser repetition frequency respectively, and N is an integer. The microwave signal mixes with one of the harmonics of the laser repetition frequency and produces an intermediate frequency f_{IF} . In the present case, f_{IF} is 10 MHz, well above the laser intensity noise band which is below 1 MHz. This method is very simple, inexpensive and does not require the modulation of either the microwave or the light beam. The sensitivity in this system is basically limited by the shot noise and other noises associated with the photodetector. Thus, this system has very high sensitivity. For 1 mA photocurrent at the photodetector YAG 100, a sensitivity of $178 \mu V/\sqrt{Hz}$ has been measured. The spectrum analyzer is used to provide an adjustable narrow band amplifier (BW=10 KHz in this experiment) and an AC to DC converter. Its center frequency, bandwidth, gain and video filter can all be eas-

ily adjusted to optimize the system performance. The results are displayed by a computer through an analog to digital converter.

The laser used was a mode locked Nd:YLF laser with a pulse width of 50 picoseconds. The short laser pulses with duration of 3 to 5 picosecond were generated by using a fiber pulse compression technique.

Fig. 2 displays the details of the beam scanner. A light weight mirror attached to the needle axis of a galvanometer is located at focal length of the lens and scans the incoming beam. This lens arrangement keeps normal incidence on the surface of GaAs substrate, and also focuses the beam at the back surface of the substrate. The reflected beam follows the same trace but in opposite direction.

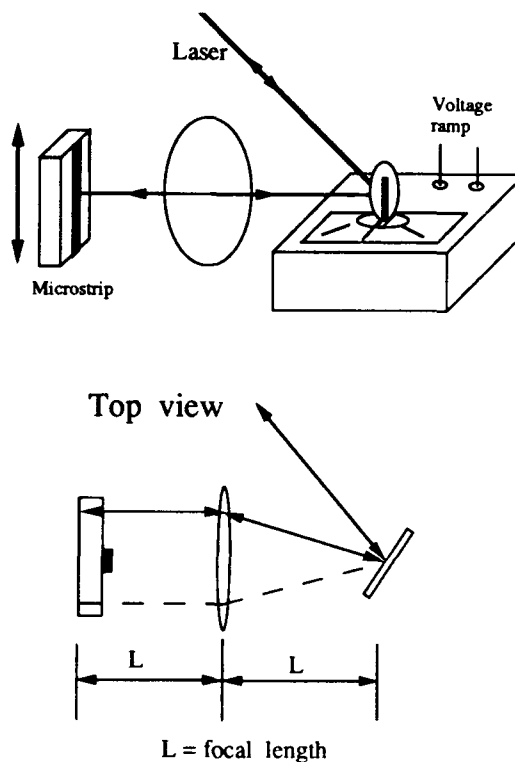


Figure 2. The detail of the beam scanner.

Interference effect

In a previous report, we presented the interference effect associated with the E-O sampling in GaAs microstrips [4]. Since the index of refraction of GaAs is high (3.5), a substantial amount of light (30 percent energy for normal incidence) is reflected at the top surface of GaAs and interferes with that reflected from the bottom surface. The interference effect is significant provided that the laser pulse duration used for E-O sampling is longer than or comparable to the light pulse

round-trip time in the GaAs substrate. Because of the interference effect, the magnitude of the E-O signal strongly depends on the local substrate thickness and the calibration of the sampled microwave amplitude is very difficult.

Fig. 3 shows the measurement of 2-D field distribution in a GaAs microstrip line with short laser pulse duration (3 to 5 picoseconds). The frequency of the RF signal applied to the microstrip line is 142 MHz and its amplitude is 1 V_{rms}. The measurement shown in Fig. 3 was completed in five minutes. Since the laser pulse width is shorter than the round trip time of light pulses through the substrate (7 pS, corresponding to 0.3 mm thickness), the interference effect does not occur. The measured result truly represents the electric field distribution in the device under test.

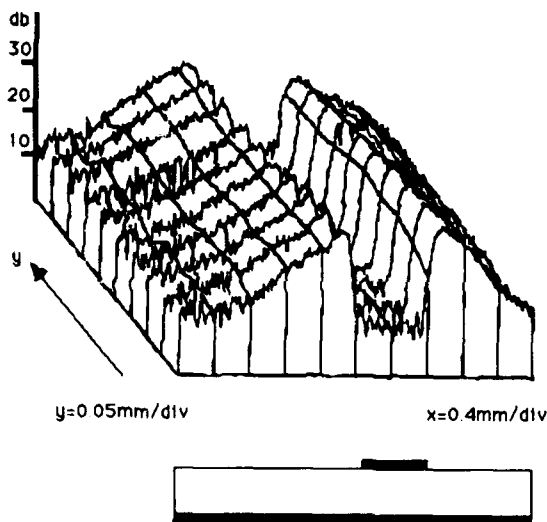


Figure 3. Field mapping of a microstrip line with short laser pulses (3-5 pS) showing no interference effect.

Fig. 4 displays a typical result of field mapping of the same sample with a laser pulse duration (50 ps) longer than the light pulse round trip time in the substrate (7 ps). The measured field distribution across the microstrip line should be similar to that in Fig. 3. Instead, Fig. 4 shows the additional drops (valleys) in the field distribution caused by the interference effect. This raises the issue of the difficulty to calibrate accurately the amplitude of the field distribution.

The interference effect can be explained by the following description.

Multireflection effect

The multiple-beam interference effect is shown in Fig. 5(a). The actual incident beam is almost normal to the surface of GaAs substrate, but for clarity of drawing, the angle has been exag-

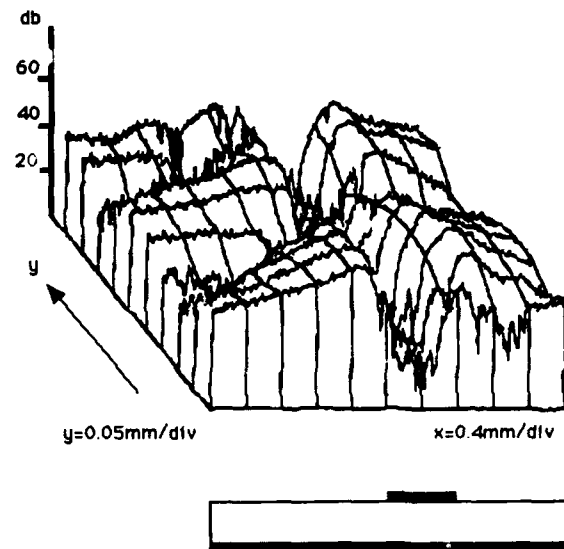


Figure 4. Field mapping of a microstrip line with long laser pulses (50 pS) showing strong interference effect.

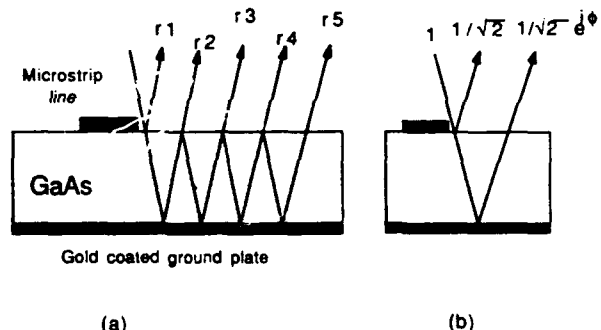


Figure 5. Multireflection in GaAs microstrip line substrate. (a) General case. r_i : electric field of the i th reflected beam. (b) Only the two first reflected beams are considered. ($\beta = 0.8$)

gerated. The calculation is carried out for normal incidence on the sample and assuming that all the light is collected by the photodetector.

The total reflection coefficient for the multiple beam interference in the GaAs is given by:

$$\begin{aligned}
 R_{total} &= r_1 + r_2 + r_3 + \dots + r_n + \dots \\
 &= R_1 - T_1 T_2 e^{i\phi} + R_2 T_1 T_2 e^{2i\phi} - R_2^2 T_1 T_2 e^{3i\phi} \\
 &\quad + \dots + (-1)^n R_{n-1} T_1 T_2 e^{ni\phi} \\
 &= R_1 - \frac{T_1 T_2 e^{i\phi}}{1 + R_2 e^{i\phi}}
 \end{aligned}$$

Where R_1 is the surface reflection coefficient, when the incident beam is directed from air towards the GaAs; and R_2 is the surface reflection coefficient, when the incident beam is directed from GaAs towards air. T_1, T_2 are the corresponding surface transmission coefficients.

It is very important to understand that the interference effect will result in a modulation of light intensity at the detector only if the back reflected beam suffers some loss. Calculation indicates that, for a lossless system, the amplitude of total reflection coefficient is a constant and there is no interference.(But the phase can be changed.)

For the lossy case, if $\beta = (1 - \alpha)$, where α is the loss factor (for lossless case $\beta = 1$), then

$$\begin{aligned} R_{total} &= R_1 - T_1 T_2 \beta e^{i\phi} + R_2 T_1 T_2 \beta^2 e^{2i\phi} - \dots \\ &= R_1 - \frac{T_1 T_2 \beta e^{i\phi}}{1 + R_2 \beta e^{i\phi}} \end{aligned}$$

The multiple-beam interference results for any incident polarization.

When $\beta = -R_2$, the case corresponds to the standard Febry-Perot interference.

The calculation of reflection coefficients shows that a very good approximation consists in considering only the two first reflections with equal amplitude ($E_o/\sqrt{2}$). One is reflected from the front (top) surface and the other is reflected from the back (bottom) surface as illustrated in Fig. 5(b).

In this case, the dependence of the measured E-O signal on the local substrate thickness appears in the following expression of the modulation of light intensity applied to the photodetector (ΔI) for conventional E-O sampling:

$$\Delta I = I_o \Delta \phi \cos(\phi/2) \sin(2(\theta' - \phi/4))$$

where I_o is the input laser intensity, θ' is the analyzing polarizer orientation relative to the GaAs crystal axis [011], $\Delta \phi = 2\pi V/V_\pi$ is phase modulation produced by the applied microwave voltage V . For GaAs, V_π is about 10 kV. ϕ is the round trip phase delay in GaAs substrate, which in turn is proportional to the local thickness of the substrate.

Fig. 6 is the schematic of the detection for conventional E-O sampling, and Fig. 7 displays the relation of E-O signal versus polarizer orientation θ' .

The effect of $\cos(\phi/2)$ can be observed in the measurement shown in Fig. 4. Calculation indicates that a small thickness change of 750 Å can cause the E-O signal to change from its maximum to zero.

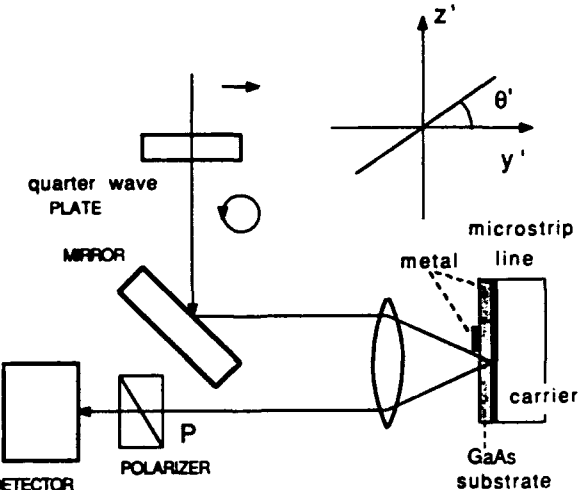


Figure 6. The conventional detection scheme using a polarizer and circularly polarized light beam.

In the same report [4], we also pointed out that E-O signal can be detected without using an analyzing polarizer. This is realized by utilizing the modulation of interference generated by multiple beam reflection in the GaAs substrate. It is also sensitive to the variation of substrate thickness. The calculated E-O signal is given by:

$$\Delta I = E_o^2 \Delta \phi \sin \phi \cos 2\theta$$

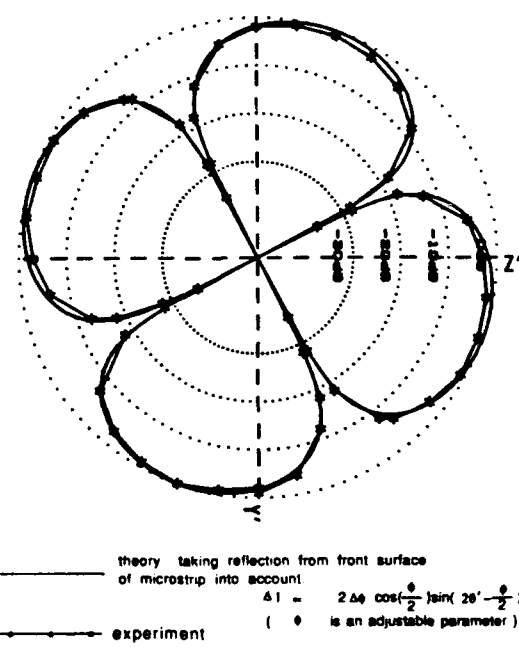


Figure 7. E-O signal versus polarizer orientation (detection with a polarizer, including interference effect).

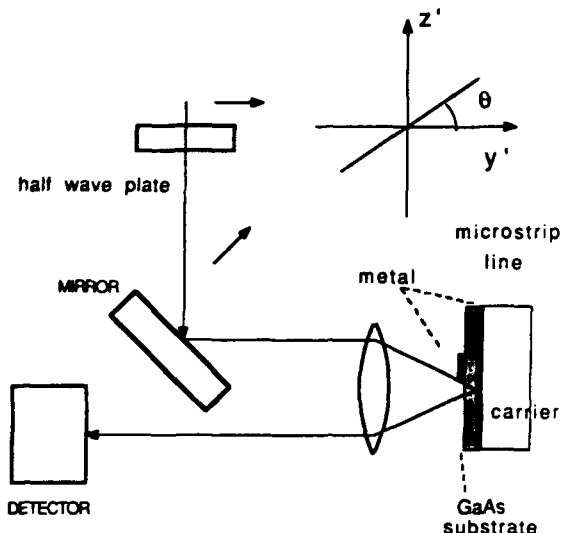


Figure 8. The new scheme using linearly light beam without using polarizer.

where θ is the incident polarization angle relative to the GaAs crystal axis [011], which can be varied by using a half-wave plate.

Fig. 8 is the detection scheme for this method, and Fig. 9 is relationship of E-O signal versus incident polarization angle.

Conclusion

In conclusion, a new scheme of 2-dimensional field mapping has been demonstrated on a GaAs microstrip line. This technique provides high detection sensitivity and can be extended to higher frequencies for the characterization of GaAs monolithic microwave integrated circuits without requiring physical or electrical contact to the device. The high sensitivity is achieved by intermixing technique, which does not require the modulation of the microwave or the light beam. A time resolved characterization could be obtained provided that the microwave is phase locked to the laser pulses. With this method, the interference effect, which occurs in E-O sampling when the laser pulse duration is longer than the optical round-trip time in the substrate, has also been studied. The calculation is carried out for normal incidence and in the good approximation of considering only the two first reflections. Thus, we show that the E-O output strongly depends on local substrate thickness. A variation of thickness of 750 Å is sufficient to change the signal from its maximum value to zero. An absolute amplitude calibration in the E-O sampling technique is very important for MMIC

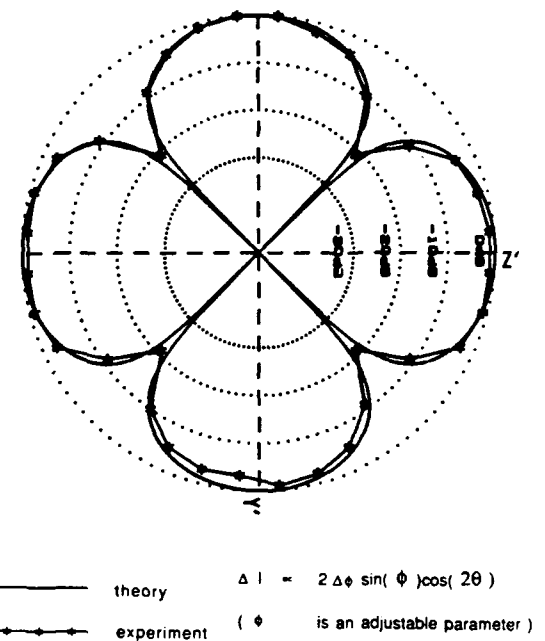


Figure 9. E-O signal versus polarization angle of incident light (detection without polarizer).

characterization and can only be obtained if one uses a laser pulse duration shorter than the optical round trip time (for $h = 200\mu m$, $\tau = 5ps$) of measured substrate.

Acknowledgment

This work was supported by the Maryland Industrial Partnership Program.

References

1. K. J. Weingarten, M. J. W. Rodwell and D. M. Bloom, "Picosecond Optical Sampling of GaAs Integrated Circuits", *IEEE J. of Quantum Electronics, QE-24*, pp. 198-220 (1988)- (and previous papers)
2. W. Donaldson "Photoconductive Switching and Break-down Investigated with Electro-optic Image", *Proceedings of "3rd SDIO /ONR Pulse Power Meeting '90"*, August 2-3, 1990, Norfolk, VA.
3. M. G. Li, S-L L. Huang, C.H. Lee and H-L.A. Hung, "Display of Microwave waveform via a Low Frequency Replica Using an Optical Phase-Locking and Sampling Technique" *Proceedings of Picosecond Electronics and Optoelectronics Conference*, March 13-15, 1991, Salt Lake City, Utah
4. M. G. Li, E. A. Chanchard, C.H. Lee and H-L.A. Hung, "Microwave Modulation of Optical signal by Electro-optic Effect in GaAs Microstrips", *IEEE MTT-S Int. Microwave Sym. Digest*, pp 945-948, May 1990.

Modeling of an Electro-Optically Probed Photoconductive Switching Experiment

K. M. Connolly, R. O. Grondin, S. M. El-Ghazaly, and
R. P. Joshi

*Center for Solid State Electronics Research, Arizona State University,
Tempe, Arizona 85287-6206*

Abstract

A modeling approach for optical probing of ultrafast switches is presented. The model couples a Monte-Carlo solution with Maxwell's equations to make as few assumptions as possible.

Introduction

Advances in photoconductive switching and electro-optic sampling make it possible to generate electrical waveforms with subpicosecond risetimes and detect submillivolt changes in the created line voltages [1-2]. A typical test circuit is shown in Fig. 1. The structure consists of a photoconductive switch and coplanar microstrip fabricated on a GaAs substrate. The switch is turned on by illuminating the gap with a laser pulse (called the pump beam) to generate electron-hole pairs. The electrons and holes then move according to the fields created by the bias voltage applied to one side of the switch, and induce a propagating wave on the microstrip structure.

Experimentally measuring the induced electrical waveforms can be achieved by using reflection-mode electro-optic sampling. This is done by placing an electro-optic sampling crystal, LiTaO₃, which has been coated on the side adjacent to the circuit with a high reflection dielectric coating over the photoconductive switch structure. A small hole has been etched in the LiTaO₃ to allow the pump beam to enter the gap. When the electric signal propagates along the microstrip some of the field lines above the microstrip penetrate into the sampling crystal and induce a small amount of transient birefringence. A probe beam is focussed a short distance from the gap. The probe beam passes through the region of induced birefringence and is reflected back out to a detector. The induced birefringence is detected as a polarization shift of the probe beam. The probe beam was optically biased to insure that the detected polarization change was a linear function of the electric field [3-4].

The output of these experiments is a polarization shift versus time. A calibration step is done before the transient experiment in order to relate a DC bias to a polarization shift of the probe beam. This is done by biasing one side of the switch with a known range of DC voltages and measuring the resulting polarization shifts. The transient experiment is conducted and the polarization shift data recorded. The data is then converted to a voltage, normalized to the bias voltage, and plotted versus time. This method assumes that the DC bias measurement of the polarization shift can be related to the transient measurement.

To properly model such an experiment the high frequencies and large switching fields must be considered. Circuit models have questionable accuracy due to the high frequencies involved in the switch. Semiconductor models cannot ignore the relatively large switching fields associated with the injection and motion of free carriers. Moreover, electromagnetic models are complicated by the higher order modes excited along the microstrips. In this paper, we shall describe how one can improve the modeling of such problems by embedding a bipolar ensemble Monte-Carlo (EMC) model of a photoconductive gap into a time-domain solution of Maxwell's equations for the field structures present on the line.

Theoretical Approach

To simulate the carrier transport in the semiconductor substrate, we use a bipolar EMC model. EMC simulations keep track of several thousand representative particles by following their trajectories through the system. The particles are accelerated by fields, and the various individual scattering mechanisms are statistically simulated in order to model energy flow. The model used is based upon a three valley electron and three band hole model for the GaAs substrate with all relevant carrier-phonon and carrier-carrier scattering mechanisms included. The electrodynamic forces influencing the carriers are considered through a complete model of Lorentz forces

which include the time evolving electric and magnetic fields. These fields, which depend upon the local charge imbalance and the related currents, are self-consistently calculated in each time step by the the electromagnetic model [5].

Creation of the electron-hole pairs is simulated by adding particles according to the line shape of the laser pulse, which can be approximated by a hyperbolic secant for several laser types of interest. Since the pump pulse is incident upon the surface of the GaAs in the microstrip gap, the carrier photogeneration monotonically decreases with depth. This inhomogeneity is introduced into the EMC by setting up an initial carrier profile, $N(x)$, as a decaying exponential. Carrier position x_n for the n^{th} carrier is assigned using the above weighted distribution, and picking random numbers r_n as :

$$x_n = -\frac{\ln \{ 1 - r_n [1 - e^{-\alpha d}] \}}{\alpha}$$

with α being the absorption coefficient, and d the depth of the simulation [5].

A time domain finite difference (TD-FD) solution of Maxwell's equations is used to model the electromagnetic fields in the switch. The TD-FD algorithm is implemented by filling the three dimensional space with a special arrangement of spatial nodes points called Yee's mesh. In Yee's mesh the components of \mathbf{E} and \mathbf{H} are arranged in such a way that each component of \mathbf{H} can be obtained by the loop integral of \mathbf{E} using the four surrounding \mathbf{E} nodal values according to Maxwell's curl equation for \mathbf{E} . Similarly, the components of \mathbf{E} can be obtained by the loop integral of \mathbf{H} over the four surrounding \mathbf{H} nodal values. In addition to offsetting the location of \mathbf{E} and \mathbf{H} in space, they are also offset in time by half a time step. This allows the values of \mathbf{E} to be calculated at time equal to $n\Delta t$, and then the values of \mathbf{H} to be calculated at time $(n+\frac{1}{2})\Delta t$. thus the solution progresses in a leapfrog manner [6].

Since computers have limited memory capabilities, the entire device cannot be simulated. To compensate for this, absorbing boundary conditions are used to truncate the simulation mesh. Ideally, absorbing boundary conditions allow waves to propagate through the mesh boundaries without reflection, thus giving the impression of simulating an infinitely large structure. Mur's first order approximation which completely absorbs waves at normal incidence, but reflects small portions of waves with incident at other angles, is used [7].

Coupling the EMC model with the solution to Maxwell's equations is accomplished through transformations of the information between the two models. This is necessary because the EMC is only simulated over a portion of the structure (the gap) while Maxwell's equations are solved over the entire device. The carriers appear in Maxwell's equations as sources of electromagnetic fields, and electromagnetic

fields appear in the EMC transport model as forcing functions. The EMC model therefore, takes an average value of the fields over a cell in its volume and uses that information to calculate carrier velocity and position, and also to trace the the carriers crossing the borders of each cell. The current density obtained is then transformed to properly interact with the electromagnetic model.

As was previously mentioned it is desirable to simulate the probe beam as it propagates through the electro-optic sampling crystal. The probe beam is stepped through the boxes of the TD-FD algorithm along its path. Thus at each time step of the simulation the magnitude of the fields seen by the probe beam is summed. When the probe beam leaves the crystal the fields summed after reflection from the high reflection dielectric coating are subtracted from the fields summed before the reflection due to the change in propagation direction. This provides us with data similar to the polarization versus time results obtained from experimental data. The data must also be transformed from a summation of the fields to a bias voltages. This can be accomplished by first changing the summation of the fields to a DC voltage and then normalizing by the bias voltage. A simpler method is to simply dividing the transient data by the DC field summation, since the field summation is linearly related to the bias voltage.

Results

This technique is used to simulate the photoconductive switch, shown in Fig. 1. The values used in our simulations are as follows. The thickness of the GaAs, D_x , is $10\mu\text{m}$. The width of each strip, W_s , is $10\mu\text{m}$ and the separation between them, W_g , is $10\mu\text{m}$. The microstrip gap length, L_g , is $10\mu\text{m}$ and the bias is 10 volts. The overall structure has dimensions $L_x = 15\mu\text{m}$, $L_y = 36\mu\text{m}$, and $L_z = 30\mu\text{m}$ and is discretized using a three dimensional mesh with a uniform grid spacing of $0.5\mu\text{m}$. A time step of $5\text{e-}17\text{s}$ is used to remain below the Courant stability limit [6].

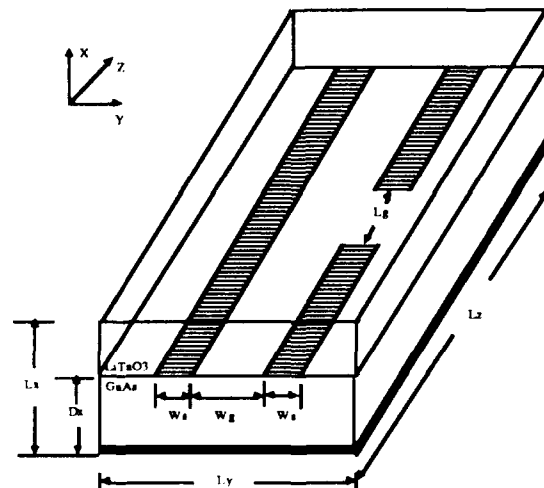


Figure 1. Dimensions of simulated structure.

A laser pulse of energy 1.55 eV and 30 fs (FWHM) duration is applied to the gap, generating a carrier concentration of $5 \times 10^{15} \text{ cm}^{-3}$.

Shown in Figs. 2 through 5 are normalized plots of the X and Z components of the total field located just below the GaAs/LiTaO₃ interface. Figs. 2 and 4 show the field components at time $t = 0.1 \text{ ps}$. These plots show the large bias fields, but the effect of the mobile carriers is not yet seen. This is because the carriers, which were introduced at time $t = 0$, have not had enough time to move and thus no noticeable AC field were created. On the other hand, Figs. 3 and 5 show the field components at $t = 2.0 \text{ ps}$. In these plots, the effects of the mobile carriers can be seen with the most noticeable changes occurring in the microstrip gap.

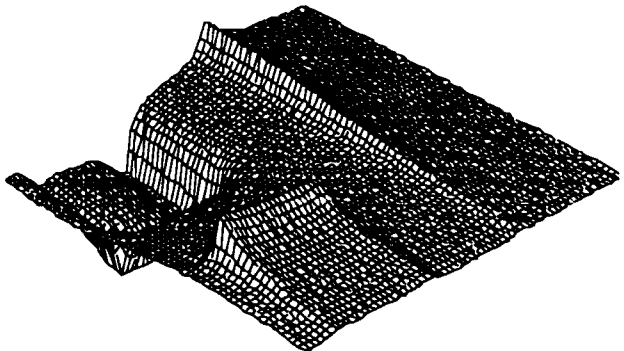


Figure 2. X component of the electric field at $t=0.1 \text{ ps}$.

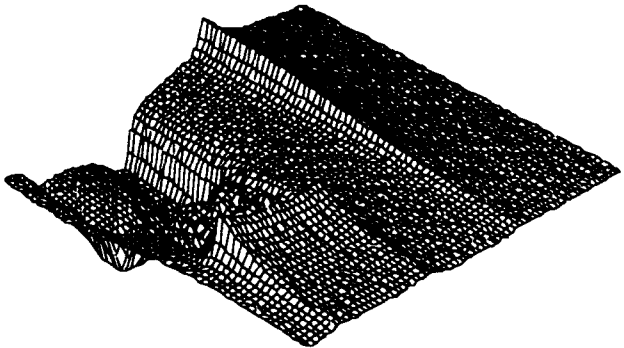


Figure 3. X component of the electric field at $t=2.0 \text{ ps}$.

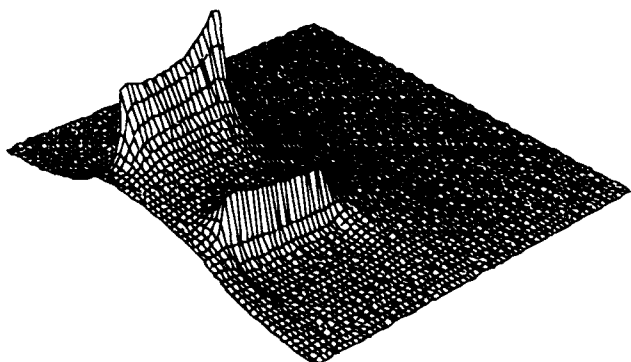


Figure 4. Z component of the electric field at $t=0.1 \text{ ps}$.

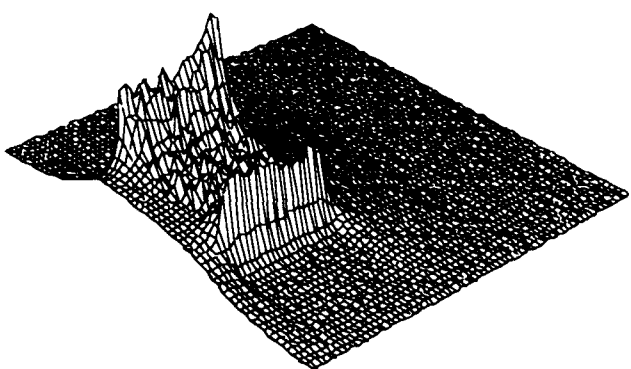


Figure 5. Z component of the electric field at $t=2.0 \text{ ps}$.

Next, the distribution of electrons and holes in the microstrip gap are shown in Figs. 6 through 9. These distributions represent the carriers in the GaAs just below the interface. The distributions at time $t=0.1 \text{ ps}$ are somewhat random, again this is expected due to the fact that the carriers lacked enough time to move. But by time $t=2.0 \text{ ps}$ some motion can be detected in the electron distribution with the electrons moving towards the positively biased electrode as expected. On the other hand, no noticeable change can be seen in the hole distribution due to the lower mobility of the holes.

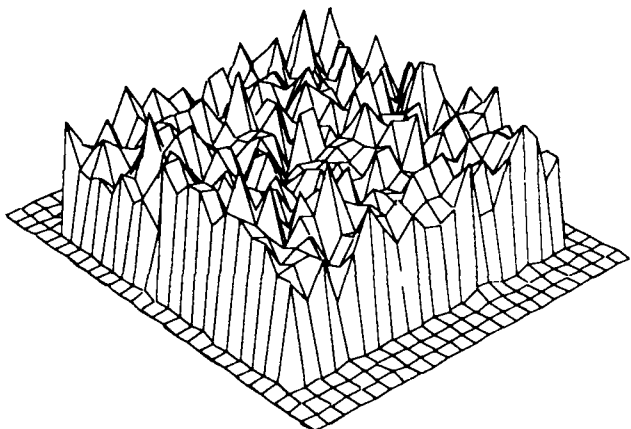


Figure 6. Electron distribution in the gap at $t=0.1 \text{ ps}$.

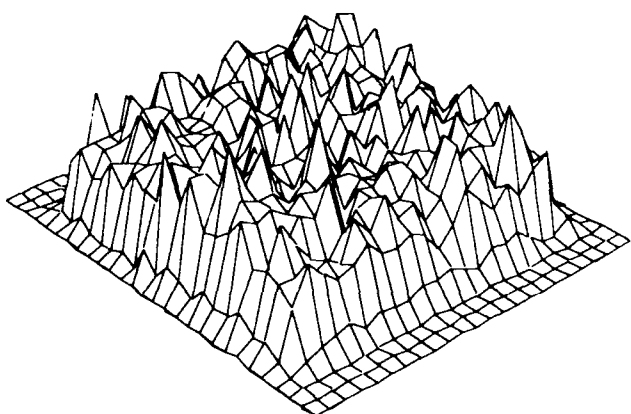


Figure 7. Electron distribution in the gap at $t=2.0 \text{ ps}$.

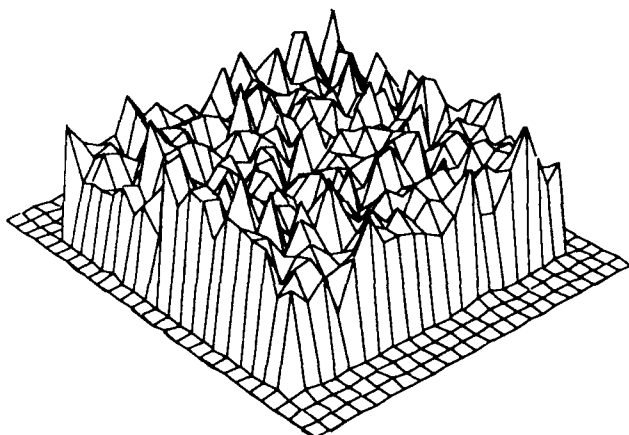


Fig. 8. Hole distribution in the gap at $t=0.1$ ps.

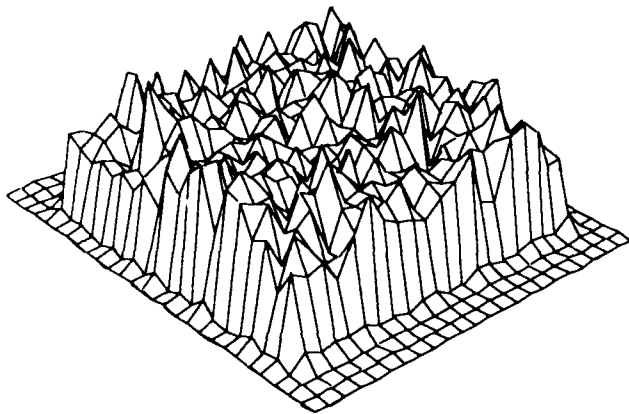


Figure 9. Hole distribution in the gap at $t=2.0$ ps.

The average electron velocity in the z direction is plotted in Fig. 10. The electron velocity plot shows the overshoot expected when carriers are introduced to high fields and then decay towards the steady state value.

The fields seen by the probe beam as it propagates through the LiTaO_3 are modelled and shown in Fig. 11.

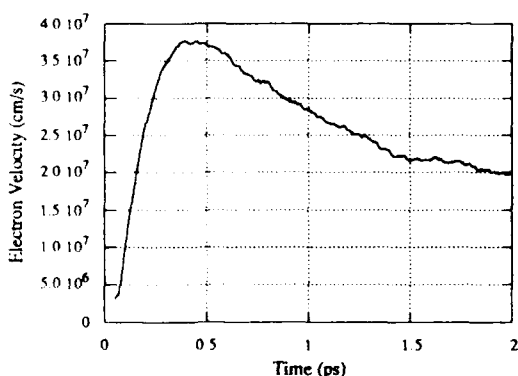


Figure 10. Average electron velocity in the z direction.

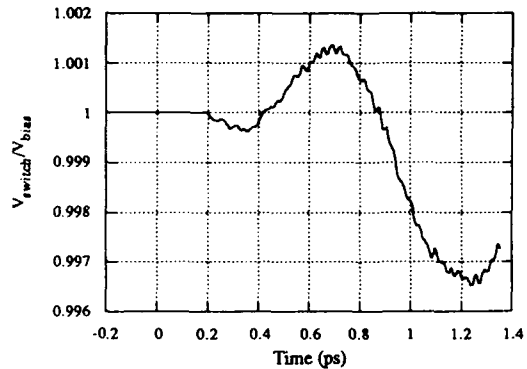


Figure 11. Normalized voltage versus time.

The probe beam travels at a 45° angle through the LiTaO_3 and is reflected at the probe point, which is centered between the two microstrips in the Y direction and next to the positively biased electrode in the Z direction. The probe point is then moved across the gap and positioned next to the grounded strip. The sampled voltage is depicted in Fig. 12.

The switching voltage patterns shown in Figs. 11 and 12 are analogous to the experimental results presented in [4-5].

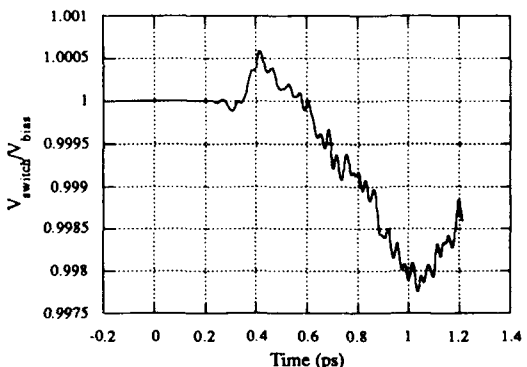


Figure 12. Normalized voltage versus time.

Conclusion

We have presented a new method for modeling photoconductive switches and directly comparing with experimental results. This model couples a three dimensional solution of Maxwell's equations in the time domain with a bipolar Ensemble Monte-Carlo model. This new model avoids oversimplifying assumptions, provides a method for obtaining the spatial and temporal evolution of carrier flow and electromagnetic wave propagation, and presents information on the probe pulse that can be used to verify experimental results.

*R. Joshi is at the Department of Electrical Engineering Old Dominion University, Norfolk, Virginia 23529.

References

1. D.H. Auston, "Impulse Response of Photoconductors in Transmission Lines," *IEEE J. Quantum Electronics* QE-19(4), 639-648 (1983).
2. S. N. Chamoun, R. Joshi, E.N. Arnold, R.O. Grondin, K.E. Meyer, M. Pessot, and G.A. Mourou, "Theoretical and experimental investigations of subpicosecond photoconductivity," *J. Appl. Phys.* 66, 236-246 (1989).
3. K.E. Meyer and G.A. Mourou, "Two Dimensional E-Field Mapping with Subpicosecond Resolution," in Picosecond Electronics and Optoelectronics, G.A. Mourou, D.M. Bloom and C.-H. Lee, eds. (Springer-Verlag, Berlin 1985).
4. K. Meyer, M. Pessot, G. Mourou, R. Grondin and S. Chamoun, "Subpicosecond Photoconductivity Overshoot in Gallium Arsenide Observed by Electro-optic Sampling," *Applied Physics Letters* 53(23), 2254-2256 (1988).
5. S. El-Ghazaly, R.P. Joshi and R.O. Grondin, "Electromagnetic and Transport Considerations in Subpicosecond Photoconductive Switch Modeling," *IEEE Trans. Microwave Theory Tech* 38(5), 629-637 (1989).
6. X. Zhang, and K.K. Mei, "Time-Domain Finite Difference Approach to the Calculation of the Frequency-Dependent Characteristics of Microstrip Discontinuities," *IEEE Trans. Microwave Theory Tech.* 36(12), 1775-1787 (1988).
7. G. Mur, "Absorbing Boundary Conditions for the Finite Difference Approximation of the Time-Domain Electro-magnetic Field Equations," *IEEE Trans. Electromagn. Compat.* 23(4), 377-382 (1989).

Improvement of the Minimum Detectability of Electro-Optic Sampling by Using a Structurally New Probe

Shinichiro Aoshima, Hironori Takahashi, Isuke Hirano, and Yutaka Tsuchiya

*Central Research Laboratory, Hamamatsu Photonics K. K. Research Park,
5000 Hirakuchi, Hamada 434, Japan*

The noise in Electro-Optic (E-O) sampling system is examined and is proved to be mainly due to wavelength dependence on the modulation. Then, we propose a structurally new E-O probe for noise reduction. Use of a new E-O probe having a spontaneous birefringence compensation crystal reduces the noise and resulted in a 6 fold improvement in minimum detectability. Finally, We have achieved a minimum detectable voltage of $7 \text{ mV}/\sqrt{\text{Hz}}$ with 32 ps time resolution at $d = 0$.

1. Introduction

E-O sampling is a useful technique for measuring high speed electrical waveforms at internal nodes in fast Integrated Circuits (ICs). For practical applications on the measurement mentioned above, we proposed, for the first time in 1989[1], E-O sampling using a longitudinal probe and laser diode (LD) pulses. This method has many advantages. For practical measurements, longitudinal probing is essential, because it measures electric fields just above the conductor. The laser diode pulser is more compact, convenient and reliable than dye lasers, and this makes the instrument much easier to handle. Moreover the strobe pulses can be easily synchronized with the clock signal of the Device Under Test (DUT), and its timing can also be easily changed electrically. This makes possible the measurement of electrical signals without their chopping.

In the present paper, firstly we make an overview of the system, including two advanced techniques developed making use of advantages of the proposed method. These

are monitoring of the measuring points[1,2], which makes measurement reliable, and measuring of non-chopped electric signals[2] by changing the timing of the strobe pulses, which is essential for practical use.

Next, we discuss improvements in the minimum detectability, including the analysis of noise sources in the E-O sampling system.

Then, we propose, for the first time, a structurally new probe which compensates for the output signal intensity fluctuation due to the temporal fluctuation of the spectra of the strobe pulses. We have improved the minimum detectability about 6 fold using the new probe.

2. Overview of The System

Operating Principle

The systematic diagram of the E-O sampling system using a longitudinal probe and an LD is shown in Fig.1. The LD generates highly

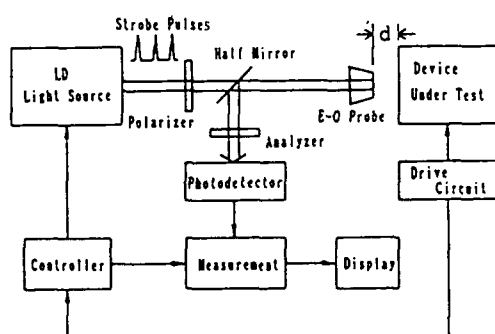


Figure1. Systematic diagram of the E-O sampling system using a longitudinal probe and a laser diode.

repetitive picosecond pulses synchronized with the electrical signal to be measured. These picosecond pulses are guided to the E-O probe and used as strobe pulses for E-O sampling, and reflected back at the end facet of the probe tip. The DUT is placed in front of the probe tip at the distance; d . The polarization of the strobe pulses are modulated in the E-O crystal of the probe due to the longitudinal electric field corresponding to the voltage to be measured.

The reflected strobe pulses are detected by the photodetector after passing through an analyzer. Then we can know the voltage to be measured. The entire voltage waveform is measured by changing the timing of the strobe pulses. The temporal resolution of the system almost corresponds to the duration of the strobe pulses. As we use the LD, the timing shift of the strobe pulses is easily performed electrically.

Monitoring of The Measuring Point[1,2]

It is essential to monitor the measuring point for practical use. Fig.2 shows the monitoring method. A microscope (Olympus; BHM) has been modified for this purpose. The DUT is illuminated by visible light reflected by a half mirror. A dichroic mirror is used as a reflection means for the

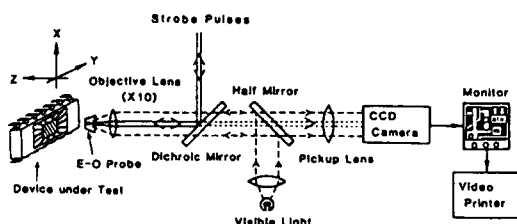


Figure2. Configuration to monitor the measuring point on the device under test.

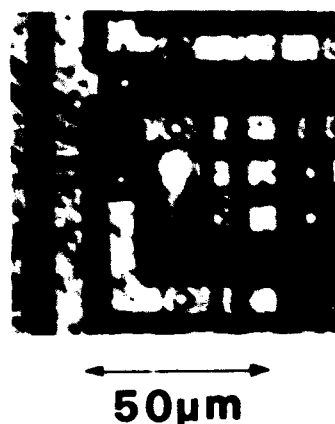


Figure3. Example of the monitor image of the measuring point on an IC.

strobe laser pulses. Incident laser pulses into the crystal are reflected back to the dichroic mirror by the dielectric coating on the crystal facet. Most of reflected laser pulses are reflected again by the dichroic mirror and are detected.

Small amounts of the laser pulses from the E-O crystal are passed through the dichroic mirror to a CCD camera (Hamamatsu; C3077). Then we can see the image of the measuring point which is superimposed on the structural image of the DUT on the monitor. This setup makes critical and fine adjustment of the measurement point easier. The image can be printed out by a video printer. Fig.3 shows an example of the monitor image, where the measuring point and the IC pattern can be seen clearly. The measuring point is indicated by a brighter spot in the figure. The brighter spot is already on which we want to make a measurement. This is a big merit of using the longitudinal E-O probe.

Measurement without Chopping The Electrical Signals[2]

To detect small changes of the strobe pulse intensity, the electric signal to be measured has until now been switched on and off (chopped), and the corresponding signal is lock-in detected. This presents, however, a serious problem for practical use. The chopping operation scheme is complicated and distortion of the signal to be measured may occur in the chopping device. To solve these problems, we have invented a new method.

The operating principle is schematically shown in Fig.4. The timings of the strobe pulses are switched at points a and b

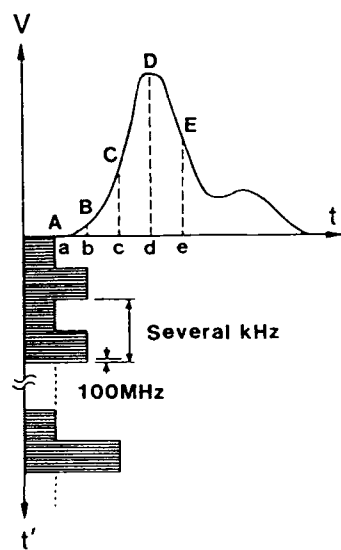


Figure4. Principle of the Strobe Pulse Timing Control Method (SPTCM).

alternately at several kHz. The signal component, at the switching frequency, in the output of the photodetector is pre-amplified and detected by a lock-in amplifier whose band width is very narrow. Using this scheme, we can detect the voltage B-A. If we choose the timing; a, at the neutral point in the waveform, and change the timing; b to c, d, ..., we can measure the entire waveform; B, C, D, ... We named this the Strobe Pulse Timing Control Method (SPTCM). As we use a laser diode pulser, we can easily change the strobe pulse timing and also synchronize its timing with the electrical signal to be measured.

3. Minimum Detectability

The minimum detectability of the E-O sampling system is mainly limited by halfwave voltage and noise of an E-O sampling system. We used an E-O probe made of LiNbO₃ (LN) whose halfwave voltage is the smallest of available crystals. Table.1 shows calculation results of halfwave voltages of several crystals for a longitudinal E-O modulator. In this calculation, we examined all degrees of θ , ϕ at 1 degree steps in the polar coordinate system.

The system noise is composed of (a) the noise of the photodetector and electronic circuit, (b) the noise or intensity fluctuation of the strobe pulses, and (c) the noise or fluctuation generated in the E-O probe. The noise in (a) was reduced to the shot noise level. The noise in (b) was reduced by opto-electric feedback. We have recently found that the noise in (c) was the largest of the system noise components.

Since the mechanism of generating the noise in (c) has not been well understood so

Table.1 Halfwave voltages of typical crystals for the longitudinal E-O modulator

Crystal Name	Halfwave Voltage (kV)
G a A S	6. 2
A D + P	2. 4
K D + P	3. 5
L i N b O ₃	2. 3
L i T a O ₃	3. 6
B S O	3. 9

far, we have studied it experimentally, and found out that the temporal fluctuation of the spectra of the strobe pulses originated intensity fluctuation of the output signal of the E-O sampling (which is the detected signal of light from the analyzer).

A pin photodiode and a low noise pre-amplifier were used as an optical receiver. The noise generated in the receiver was confirmed to be less than the shot noise of the input signal.

Then, we experimentally investigated the relationship between the noise and the driving circuit of the LD, and succeeded in reducing the noise down to near the shot noise level. The most effective means was by opto-electrical feedback of the laser light. One part of the laser pulse was detected and the corresponding electrical signal was fed back to the driver. By using this method, the laser noise was reduced to 1/3 ~ 1/4 of that without the feedback scheme.

Further, we experimentally investigated the origin of the remaining noise which

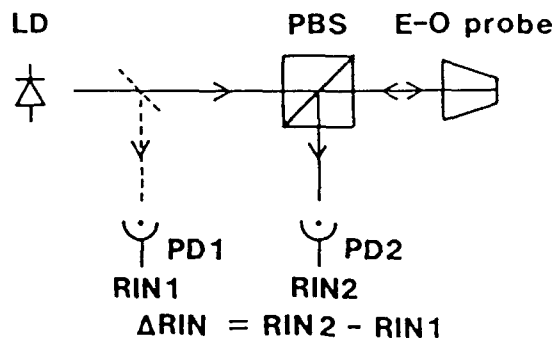


Figure 5. Experimental set-up for studying the origin of the noise (Babinet-Soleil compensator is not shown).

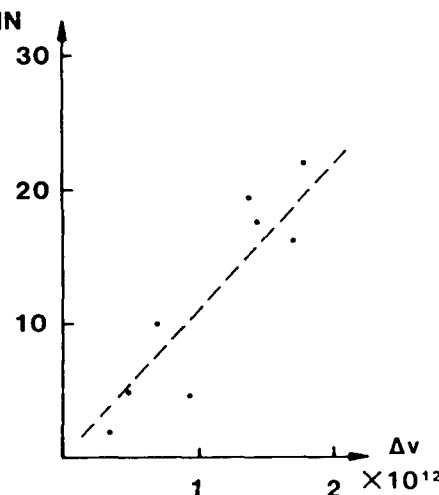


Figure 6. Relationship between ΔRIN and Δv for several separate LDs.

corresponds to the noise in (c) mentioned before. The experimental setup is shown in Fig.5. The relative intensity noise of light pulses, after passing through the Polarizing Beam Splitter (PBS) and the E-O probe; RIN₂ was found to be larger than relative intensity noise of the original laser pulses; RIN₁. To make this point clear, measurements were carried out for several separate types of laser diodes in the similar operation way. The measured $\Delta RIN = RIN_2 - RIN_1$ is plotted against the spectral width; $\Delta \nu$ in Fig.6. The ΔRIN means the noise added in the E-O probe. From Fig.6, we see the ΔRIN is in proportion to $\Delta \nu$.

Here, it is important to notice that the strobe pulses have multi-longitudinal-modes and spectral envelope has a FWHM of about 1 ~ 4 nm. Taking this point into account, the experimental results as shown in Fig.6 may be understood as that the spectra is fluctuating for each pulse, and results in fluctuation of the output signal due to the wavelength dependence on the parameters of modulation. Mode-hopping in the laser oscillation may be one of the spectral fluctuations.

Therefore, noise reduction is expected by the following three methods:

- (1) Use of LDs such as DFB-LD oscillating at single-longitudinal-mode.
- (2) Use of a crystal having a smaller spontaneous birefringence.
- (3) Compensation of wavelength dependence on modulation related to the spontaneous birefringence in the LN modulator.

Usage of DFB-LDs was experimentally proven effective to reduce noise. However, it is difficult to get 780 nm DFB-LDs at this time. Usage of a smaller birefringence crystal such as LiTaO₃ (LT) gives the disadvantage of a higher halfwave voltage as shown in Table.1. Consequently, we tried the method (3) mentioned above by adopting the compensation crystal to the E-O probe.

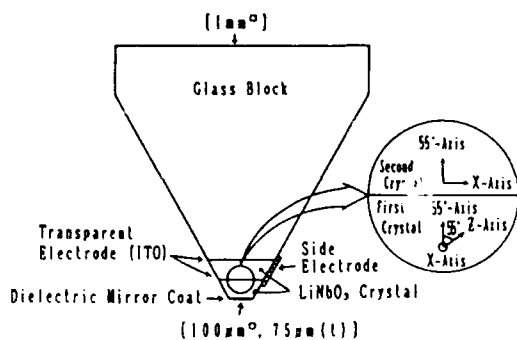


Figure7. Schematic diagram of the new E-O probe and its crystal axes.

4. Structurally New E-O Probe

The new probe is schematically shown in Fig.7, with axes of the crystal. The first crystal of LN is used as a longitudinal E-O modulator and second one is used as a compensator. The first crystal has dielectric mirror coat and is about 100 μ m(w) \times 100 μ m(l) \times 75 μ m(t) in size. The light incident axis makes an angle of 55° to the z-axis (optical axis of the crystal)[1]. The best sensitivity is obtained by this 55° cutting structure[3], in the case of the longitudinal modulator.

The second crystal is attached to the first crystal and supported by a glass block. There is no difference between the first and the second crystal except that the x-axis make a 90° angle with each other. Both end facets of the second crystal have transparent electrodes (backside electrodes) of ITO (Indium Tin Oxide) which are kept at the same electric potential by the side electrode.

The second crystal operates to compensate wavelength dependence on the modulation depth related to the spontaneous birefringence of the first crystal. By this new E-O probe, ΔRIN was reduced to about 2 dB for normal 780 nm laser diode pulses having a frequency width of 1.8×10^{-2} Hz.

5. Experimental Results

Fig.8 shows the waveform of the strobe pulses measured with a sampling optical oscilloscope (Hamamatsu; OOS-01). The FWHM of the optical strobe pulses is less than 30 ps. By using these strobe pulses in the SPTCM at a distance of $d \neq 0$ between the probe and the electrode, we have measured high speed electrical signals of 5 Vp-p which are generated by a comb generator. Observed waveforms using conventional and new E-O probe are shown in Fig.9 (a) and

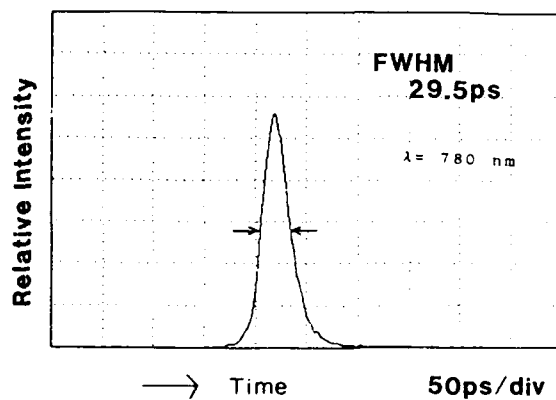


Figure8. Waveform of the optical strobe pulses measured with OOS-01.

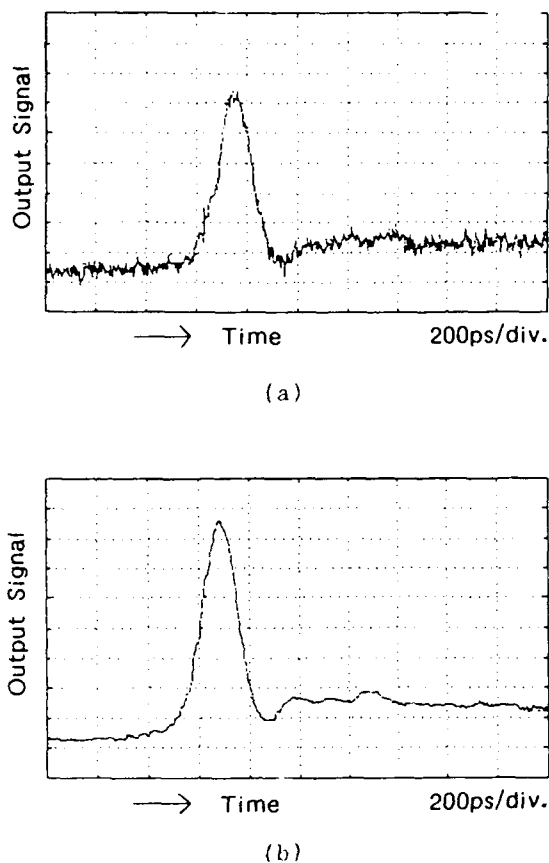


Figure 9. Measured electrical waveform using (a) a conventional E-O probe and (b) a new E-O probe.

(b), respectively. The DUT was microstrip electrode (Omni Spectra; Microstrip Test Fixture). In both cases, the measurement time was 14 s and the time constant of the lock-in amplifier was 10 ms. Using these values, scan speed for timing shift; 143 ps/s and the strobe pulse duration of 30 ps, the limiting time resolution of the system is calculated to be less than 32 ps, which is almost equal to the duration of the strobe pulses.

From these two figures, it is clearly seen that the noise is greatly reduced by the new E-O probe. The equivalent input noise were measured to be about $42 \text{ mV}/\sqrt{\text{Hz}}$ for (a) and $7 \text{ mV}/\sqrt{\text{Hz}}$ for (b), respectively. By adopting the second crystal as a compensator, the intensity fluctuation of the strobe pulses after passing through the analyzer was greatly reduced, improving the minimum detectability 6 fold.

The new E-O probe also has another advantage. its sensitivity is independent of temperature because the second crystal compensates automatically for the temperature drift of the optical parameters of the first crystal.

6. Conclusions

We made an overview of the E-O sampling system using a longitudinal probe and laser diode pulses including the monitoring system and a newly developed measuring method for non-chopped electric signals. Then we studied the main noise of the output signal, and we have proven that the main reason for this was the wavelength dependence on the modulation. We have developed a structurally new E-O probe, reduced the noise and improved the minimum detectability 6 fold.

We have achieved a minimum detectable voltage of $7 \text{ mV}/\sqrt{\text{Hz}}$ with 32 ps time resolution at $d = 0$. By adopting this technology to the system so far developed by us[1], the E-O sampling system gives the following performances:

- (a) Sensitivity; $V_{\min} = 7 \text{ mV}/\sqrt{\text{Hz}}$, at $d = 0$
- (b) Temporal resolution; 32 ps
- (c) Spatial resolution; $5 \mu\text{m}$
(Laser spot diameter at the probe tip)
- (d) Non-contact measurement
($0 \leq d \leq 20 \mu\text{m}$)
- (e) Absolute voltage measurement
(The possibility was proved[1,2,4])
- (f) Synchronization of the strobe pulses with the electric signal to be measured
- (g) A system without any mechanical delay means
- (h) Non-chopped electric signal measurement
- (i) Sensitivity free from the structural location of the device
- (j) Exact monitoring of the measuring point
- (k) Sensitivity is not a strong function of the distance; d
(Sensitivity Enhanced Method has been developed[1,2,4])

As of now, we are finishing the basic research. In the next stage, we will study the practical application field, e.g. where triggering of the laser pulses to the electric signal to be measured is very important.

7. Acknowledgment

The authors wish to thank Dr.G.A.Mourou, S.L.Williamson and J.A.Nees of the university of Michigan for collaboration at the beginning of the research and Dr.K.Kaufmann for useful discussion. We also thank T.Urakami and T.Nakamura for their technical supports, the members of fabrication group for making the E-O probe and Dr.Y.Suzuki, Director of Central Research Laboratory, for giving us the opportunity to do this research.

References

1. S.Aoshima, H.Takahashi, T.Nakamura and Y.Tsuchiya, "Non-contact picosecond electro-optic sampling utilizing semiconductor laser pulses", Proc. of SPIE, 1155, 499-510 (1989).
2. S.Aoshima, H.Takahashi and Y.Tsuchiya, "Non-Contact Picosecond Electro-Optic Sampling with Semiconductor Laser", Trans. of IEE Japan, 111-C, No.4 (1991) to be published.
3. Kenneth F.Hulme: "Oblique-Cut Longitudinal Electrooptic Modulators", IEEE J. Quantum Electron., QE-7, 236-239 (1971).
4. H.Takahashi, S.Aoshima and Y. Tsuchiya, "Improvement in Space-Dependent Sensitivity and Absolute Voltage Measurement in Non-contact Picosecond Electro-Optic sampling", in Technical Digest of Topical Meeting on Picosecond Electronics and Optoelectronics (Optical Society of America, Salt Lake City, 1991), paper FB5.

Improvement of Space-Dependent Sensitivity and Absolute Voltage Measurement in Noncontact Picosecond Electro-Optic Sampling

H. Takahashi, S. Aoshima, and Y. Tsuchiya

Central Research Laboratory, Hamamatsu Photonics K. K. Research Park,
5000 Hirakuchi, Hamakita 434, Japan

Non-contact picosecond electro-optic sampling utilizing semiconductor laser pulses is discussed in regard to improvement of space dependent sensitivity and absolute voltage measurement.

1. Introduction

While the need for measurement systems capable of characterizing ultrafast electrical signals has grown according to the increasing speed of electrical devices, Valdmanis et al. have, for the first time, achieved time-resolved ultrafast photodetection with accuracy of less than 1 ps by electro-optic sampling using a CPM dye laser (1-2). Nowadays the electro-optic sampling method has opened a new area as a measurement method of ultrafast electrical signals [3-7].

We proposed, for the first time, non-contact picosecond electro-optic sampling utilizing a longitudinal probe and semiconductor laser pulses for the purpose of practical use in 1989 [8]. The laser diode has the advantage of small size, easy handling, good reliability and the capability of synchronization with the clock signal for the device under test and measurement of non-chopped electric signals by changing the timing of the strobe pulse [9,10].

In the present paper we discuss new method for improving sensitivity, that is the capability to measure signals with small dependence on the distance between the E-O probe and the device under test, and a possibility to measure the absolute voltage.

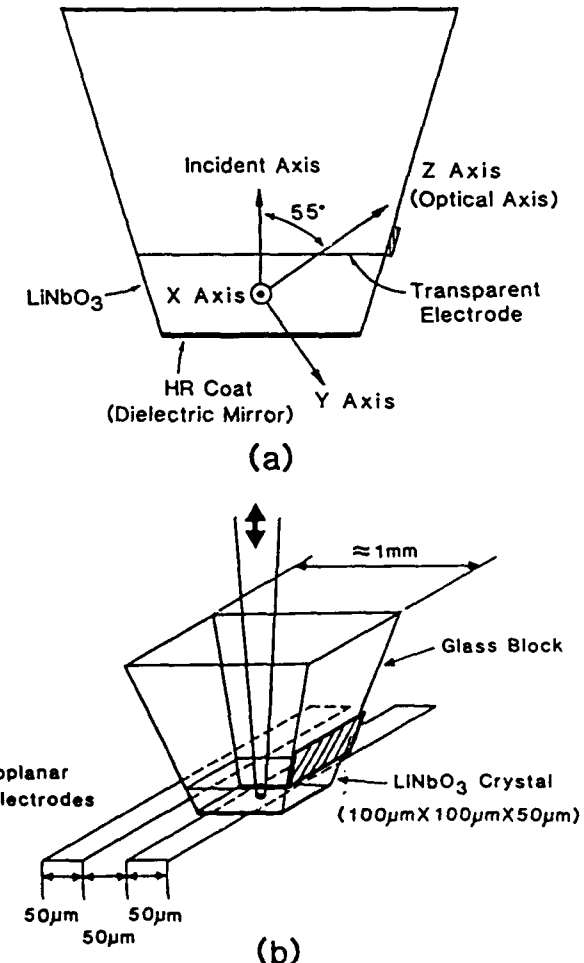


Figure 1. (a) Schematic diagram of the E-O probe and its axes. (b) Relationship among the incident light, an E-O probe and a coplanar electrodes.

2. Over View of the System

The longitudinal E-O probe has a backside electrode, and has the following advantages compared with traditional transverse E-O probes.

- 1) Sensitivity independent from the horizontal direction of the circuit.
- 2) Smaller cross talk results in higher spatial resolution.
- (3) Exact monitoring of the measurement point.

Fig.1(a) shows the structure of the longitudinal E-O probe made of LiNbO_3 . The light incident axis makes an angle of 55° to the Z-axis (optical axis of the crystal). The best sensitivity is obtained by 55° cutting structure, in case of longitudinal detection. The E-O probe is $100 \mu\text{m} \times 100 \mu\text{m} \times 50 \mu\text{m}$ in size and is supported by a glass block of about 1mm^3 . The bottom of the LiNbO_3 has a dielectric coating, and the upper side has a transparent electrode of ITO (Indium Tin Oxide). Fig.1(b) shows the schematic diagram of the E-O probe and the circuit under test; coplanar electrodes have a width of $50 \mu\text{m}$, and a separation of $50 \mu\text{m}$.

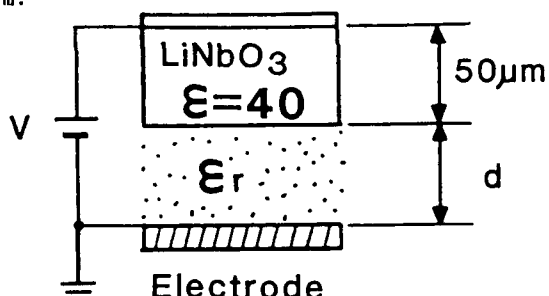


Figure.2 Explanatory schematic diagram of the principle improving the space dependency of the sensitivity.

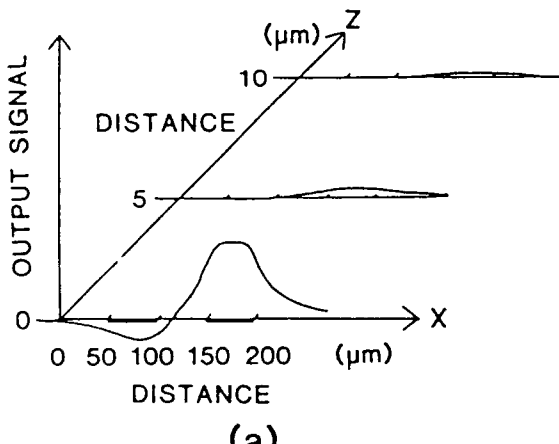


Figure.3. Output signal waveforms along the X-axis, against the distance Z; (a) traditional and (b) improved method.

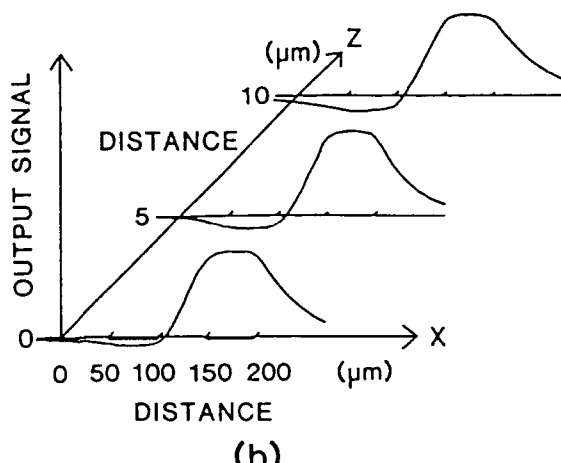
3. Improving Space Dependent Sensitivity

Recently we have greatly improved the space dependence of the sensitivity by a newly invented method. We were thinking about how to effectively gather the lines of electric force into the crystal in order to strengthen the induced birefringence. We dealt with the E-O probe and the electrode of the circuit as a capacitor consisting of parallel plates as shown in Fig.2. If the space between the crystal and the electrode is filled up with a material having a higher dielectric constant, stronger signals could be obtained than that without the material.

If the material is liquid, the E-O probe can be moved around smoothly. Hence, we decided to fill the space with alcohol as one of the possible materials. Alcohol is a safe material for the device. As the relative dielectric constant of alcohol is 25, we may expect 10 times stronger signal than usual.

We measured curves by changing the probe position along the Z axis, for both cases; air and alcohol in the space. Obtained curves are shown in Fig.3. Fig.3(a) is obtained under the usual method (air) and Fig.3(b) is obtained under the new method (alcohol).

We observed high speed electrical waveforms on the coplanar electrodes. As for comparison, measurements were carried out with (a) no material in the space and (b) alcohol in the space. Fig.4 shows the waveforms at a Z-distance of $20 \mu\text{m}$ ($d=20 \mu\text{m}$) and signal voltage of 5Vp-p . The difference is clearly seen. The peak to peak wave of the signal shown in Fig.4(b) is about half of that measured at $d=0$.



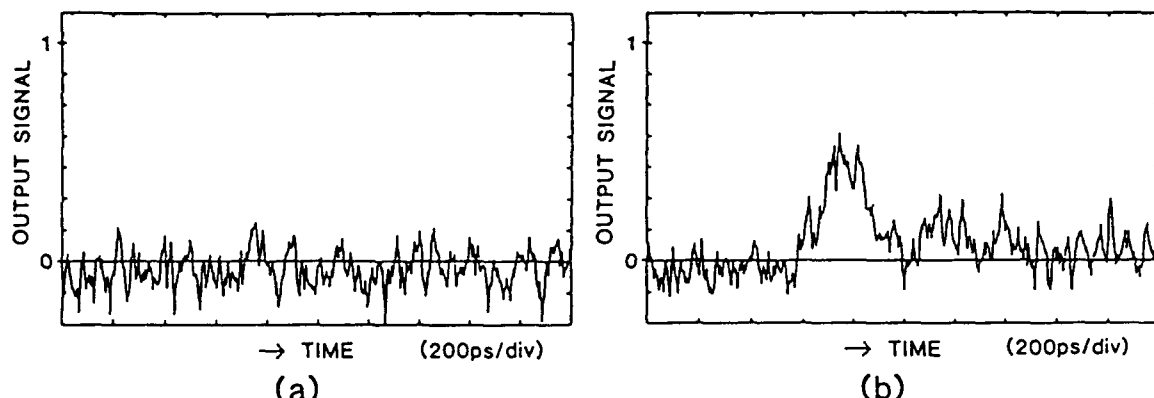


Figure 4. Output signal at the spacing $d=20 \mu\text{m}$; (a) without and (b) with alcohol.

The reduction of the signal amplitude along the space distance is faster than that in a static condition as shown in Fig.3. This is because the dielectric constant of alcohol in the high frequency range is not as large as that in the low frequency range. Further investigation for other materials is needed in order to obtain a better frequency response.

The equivalent input noise is calculated to be $125\text{mV}/\sqrt{\text{Hz}}$. This means sensitivity is improved 5 times than that without alcohol. The time constant of the lock-in amplifier is 10ms, and the timing shift rate of the system is 444ps/s. Therefore, 2ns real time scale corresponds to 4.5s on the record. Using these values and a laser pulse width of 40ps, the time resolution of the system is calculated to be less than 45ps.

The signal to noise ratio is improved by taking longer measurement time, without losing the time resolution.

4. Absolute Voltage Measurement

Next, we discuss the possibility of absolute voltage measurement. As said before, the probe has a backside electrode which can gather lines of electric force into the crystal effectively as shown in Fig.5(a) when the backside transparent electrode is grounded. In addition, the lines of electric force can be driven out by applying voltage to the backside electrode as shown in Fig.5(b).

We applied square waves at 2KHz to the transparent electrode in order to drive out the lines of electric power in the crystal. The square wave voltage should be synchronized with the chopping signal. At that time, the waveform shown in Fig.6(a), obtained by normal condition, changed its D.C. level as shown in Fig.6(b).

This data was measured at $d=20 \mu\text{m}$ with alcohol. We recorded the $\text{Acos}\theta$ component from the lock-in amplifier. If the signal A

of the lock-in amplifier is recorded, a reversed waveform at the ground level is observed. We applied 5Vp-p signal to be measured, and increased the applied voltage to the backside electrode from 0V, until the peak of measured waveform came down to the ground level as shown in Fig.6(b). In the case of Fig.6(b), a 0.88Vp-p square wave of 2KHz was applied to the backside electrode. This means we can measure the voltage of any point without changing the timing of the laser pulses. The voltage being applied to the transparent electrode is still a weak function of the distance between probe tip and circuit under test, and also the waveform to be measured. This may limit the application of the absolute voltage measurement. For example, we need to apply a 1.7Vp-p square wave at the distance $d=0$ with alcohol for the same signal. Also when the waveform to be measured is a sine wave having the same peak to peak voltage as before, we need to apply 1.2Vp-p at the distance of $d=20 \mu\text{m}$ with alcohol. We may be able to use this method to find the absolute voltage roughly by use of a lookup table or by other means.

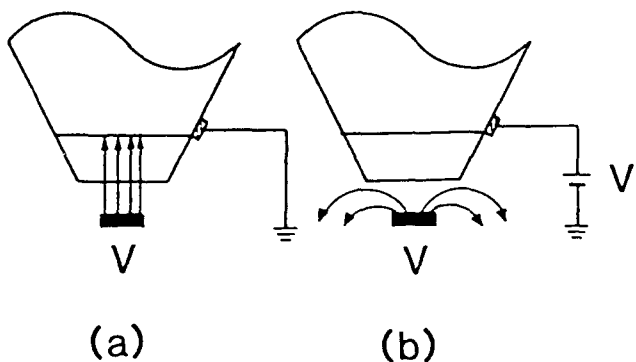


Figure 5. Schematic diagram showing the principle of the absolute voltage measurement; backside electrode is (a) grounded and (b) biased.

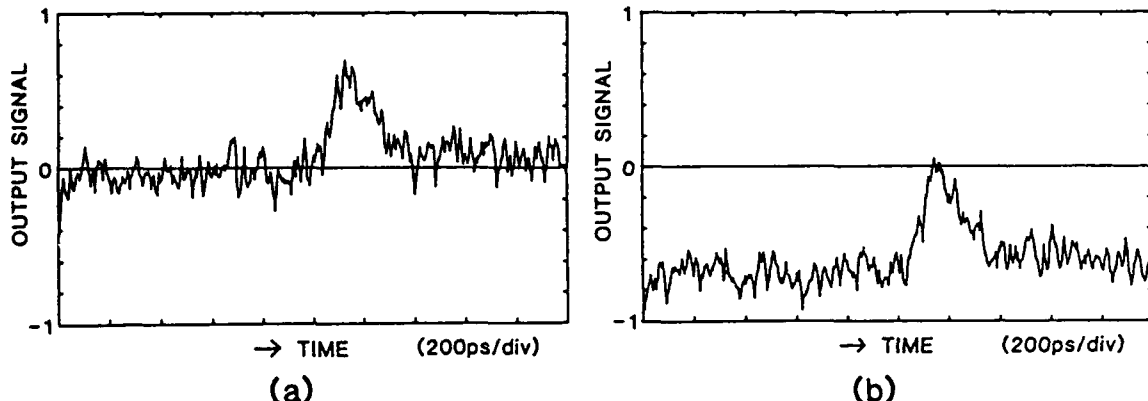


Figure 6. Example of the output signal showing the absolute voltage measurement. The signal obtained at normal condition (a) is shifted down by applying the bias voltage to the backside electrode. The absolute peak voltage of the signal to be measured can be known from the bias voltage when the peak of the output signal reaches the ground level (b).

5. Summary

For practical use of E-O sampling, such as high speed waveform measurement at internal nodes in integrated circuits, we have studied non-contact E-O sampling utilizing a longitudinal probe and a semiconductor laser. Progress is as follows: a) a new method for improving sensitivity, which doesn't depend strongly on the distance between the E-O probe and the device under test, b) possibility of absolute voltage measurement. As for a), we developed the idea of filling the space between the E-O probe and the device being tested with a high dielectric constant material. The sensitivity became 5 times better at a 20 μ m distance. Also we have demonstrated that b) can be solved by utilizing a longitudinal E-O probe with a backside electrode.

Finally, we achieved an equivalent input noise of 125 mV/ $\sqrt{\text{Hz}}$ with a 45ps time resolution at 20 μ m spacing. However, some system noise occurred. It is understood that the main cause of this is spectral broadening of the laser pulses. We expect the sensitivity to improve 10 times more by reducing this noise. Also the time resolution will be improved by using shorter, stabler, and stronger pulse lasers.

We feel that the basic research has been finished. At the next stage, we need to study the application field, e.g. where triggering of the laser pulses synchronized with the signal to be measured is very important.

6. Acknowledgment

We thank Mr.T.Nakamura and Mr.T.Urakami for their technical support and members of the

fabrication group for making the E-O probe and Dr.Y.Suzuki, Director of the Central Research Laboratory, for giving us the opportunity to do this research. We also would like to thank J.Nees, S.Williamson and G.A.Mourou of Univ. of Michigan.

7. References

- 1.J.A.Valdmanis, G.Mourou, and C.W.Gabel, "Picosecond electro-optic sampling system," *Appl. Phys. Lett.* 41, 211-212 (1982).
- 2.Janis A.Valdmanis, Gerard A.Mourou, and C.W.Gabel, "Subpicosecond electrical Sampling," *IEEE J. Quantum Electron.* QE-19, 664-667 (1983).
- 3.J.A.Valdmanis and S.S.Pei, *Picosecond Electronics and Optoelectronics II* (Springer-Verlag, New York, 1987), pp.4-9.
- 4.J.L.Freeman, D.M.Bloom, S.R.Jeffries and B.A.Auld, "Sensitivity of direct electro-optic sampling to adjacent signal lines," *Appl. Phys. Lett.* 54, 478-480 (1989).
- 5.U.Keller, S.K.Diamond, B.A.Auld, and D.M.Bloom, "Noninvasive optical probe of free charge and applied voltage in GaAs devices," *Appl. Phys. Lett.* 53, 388-390 (1988).
- 6.M.S.Heutmaker, Thomas B.Cook, Bruno Bosacchi, Jay M.Wiesenfeld, and Rodney S.Tucker, "Electrooptic Sampling of a Packaged High-Speed GaAs Integrated Circuit," *IEEE J. Quantum electron.* 24, 226-233 (1988).
- 7.J.Nees and G.Mourou, "Noncontact Electro-optic Sampling with a GaAs Injection Laser," *Electron. Lett.* 22, 918-919 (1986).

8.S.Aoshima, H.Takahashi, T.Nakamura and Y.Tsuchiya, "Non-contact picosecond electro-optic sampling utilizing semiconductor laser pulses," Proc. of SPIE, 1155, 449-510 (1989).

9.S.Aoshima, H.Takahashi and Y.Tsuchiya, "Non-Contact Picosecond Electro-Optic Sampling with Semiconductor Laser", Trans. of IEE Japan, 111-C, No.4 (1991) to be published.

10.S.Aoshima, H.Takahashi, I.Hirano and Y.Tsuchiya, "Improvement of Minimum Detectability of Electro-Optic Sampling by Using a Structurally New Probe", in Technical Digest of Topical Meeting on Picosecond Electronics and Optoelectronics (Optical Society of America, Salt Lake City, 1991), paper FB4.

New Scheme of Electro-Optic Sampling by Probe-Beam Polarization Modulation

Ryo Takahashi and Takeshi Kamiya

*Department of Electronic Engineering, University of Tokyo, 7-3-1 Hongo,
Bunkyo-ku, Tokyo 113, Japan*

ABSTRACT

A new scheme of noise suppression in electrooptic sampling system by the probe beam polarization modulation is proposed. Its operation principle is analyzed and the performance is demonstrated experimentally. The method has the advantages that narrow-band detection can be used instead of modulating the device under test with doubled sensitivity compared with the conventional methods.

1. INTRODUCTION

Electrooptic (EO) sampling is a potentially powerful technique to characterize very-high speed electrical waveforms in the time domain and to examine waveforms internal to integrated circuits, where external connections cannot be made[1-6]. Using mode-locked dye or Nd:YAG laser systems, temporal resolution less than 2ps, shot-noise limited voltage sensitivity in the microvolt/ $\sqrt{\text{Hz}}$ range have been reported[3,4]. However such laser systems are large and complex and may have limitations for practical use.

On the other hand, semiconductor laser system [5,6] have several significant advantages such as 1) compact size, 2) low timing jitter(<2ps) [7,8], and 3) arbitrary repetition rate for gain-switched operation (0.1-20GHz) which makes it possible to synchronize with the clock frequency of the device under test(DUT). Their disadvantages include the reduction of temporal resolution and the voltage sensitivity because of their broader pulse width and lower average power, although the former may be solved by the recent progress made in pulse compression techniques [9-11]. Therefore the most important point for improvement of the EO sampling system using a semiconductor laser is the sensitivity problem.

In this paper, we propose a novel scheme for noise suppression in EO sampling by probe beam polarization modulation.

2. BACKGROUND

To date, the method most frequently employed for the purpose of noise reduction is one where the DUT is electrically modulated at a modulation frequency, f_m , which is chosen to be beyond the 1/f noise band width[2] as shown in Fig.1., so called signal-amplitude modulation scheme. This method is, however, sometimes inapplicable to digital integrated circuits containing devices with threshold, where an addition of modulation voltage causes unwanted instabilities.

Under these circumstances an alternative non-modulation method has been attempted, choosing the offset frequency Δf to be higher than the 1/f noise band width [5] as shown in Fig.2., so called beat scheme. With this choice another noise penalty must be paid because of the wider spread of the signal harmonic components in frequency space, resulting in the need of wider band pass filter for 1/f noise elimination and shot noise reduction. For smoothing purposes, averaging procedures had to be iterated a number of times, hence longer measuring time. Furthermore the band pass filter for the 1/f noise elimination causes the additional inconvenience of having to eliminate a DC signal component.

These problems would be solved if a proper modulation scheme is devised applicable to the probe beam itself instead of modulating the DUT. We found that the present proposal as described below actually meets this requirement.

3. THEORY

A concept for a phase modulation scheme is schematically indicated in Fig.3, where we assumed a GaAs integrated circuits as the DUT which shows electrooptic effect. In a conventional scheme as shown in (a), the operating point is fixed at an optimal value given by a compensator which is usually equal to be $\pi/2$ rad, maximizing the signal amplitude. Therefore the probe beam power through an analyzer changes only in the presence of a signal field. In order to obtain a modulated probe

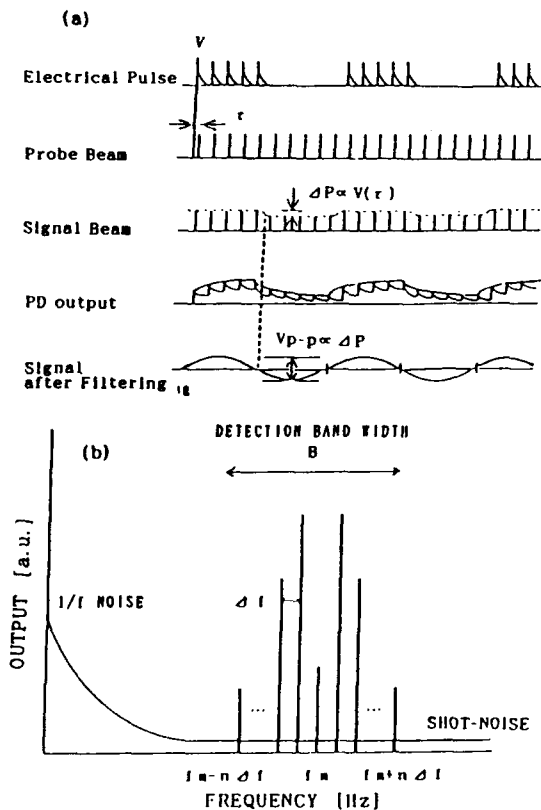


Fig.1 Signal amplitude modulation scheme:
(a) timing chart,(b)spectrum output signal

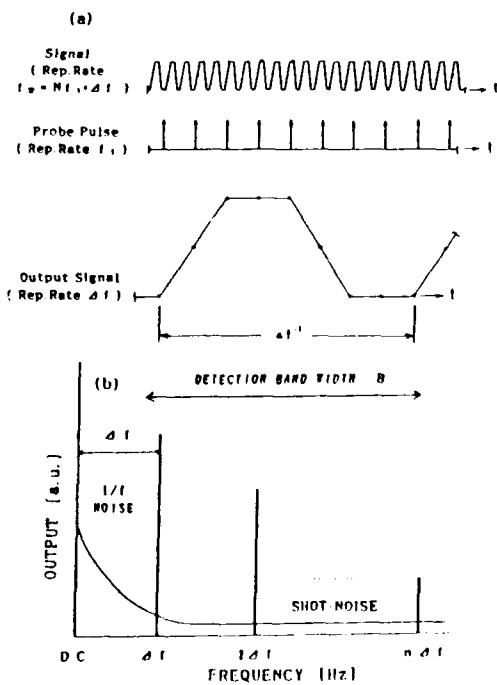


Fig.2 Beat scheme: (a)timing chart,(b)spectrum of output signal

beam, an EO modulator is introduced in place of the compensator as shown in Fig.3.(b). At an alternate operating point exchanged by the EO modulator, the probe beam changes inversely at the same frequency as the EO modulator, resulting in doubled sensitivity. However, the phase retardation induced by the signal voltage is so much smaller than that by the EO modulator as to be apt to be buried in retardation fluctuation caused by both an input voltage and temperature in the EO modulator. Therefore, such an additional noise may give a limitation to practical use, although this scheme can improve sensitivity theoretically. As will be shown below, we have found a novel configuration (polarization modulation scheme), which is capable of removing such noises, while retaining the advantages of this scheme.

Let us formulate the change of polarization states under the following geometrical configuration of optical components. Figure 4.(a) shows the general coaxial arrangement for the case of transmission probing configuration, where the GaAs substrate is assumed to act as the electrooptic sampling head. We also assume that the linearly polarized input probe beam, the principal dielectric axis of the EO modulator and GaAs sampling head are oriented at angles $\pi/4$, θ , and α , respectively to X axis in the X-Y plane. After propagation through the EO modulator and the GaAs sampling head, the optical field of probe beam is then written as

$$E_{out} = A(\alpha)B(\gamma)A(-\alpha)A(\theta)B(\Gamma)A(-\theta)E_{in} \quad (1)$$

$$A(\theta) = \begin{pmatrix} \cos\theta & -\sin\theta \\ \sin\theta & \cos\theta \end{pmatrix} \quad B(\Gamma) = \begin{pmatrix} \exp(j\Gamma) & 0 \\ 0 & 1 \end{pmatrix}$$

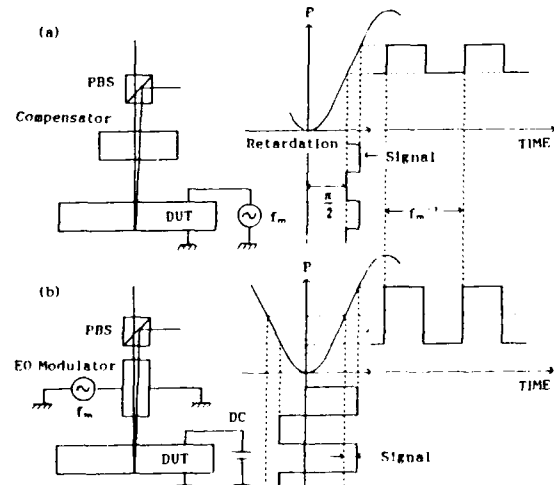


Fig.3 Configuration and Input vs output characteristics of (a) conventional signal modulation scheme and (b) phase modulation scheme

where $\Gamma(t)$ and $\gamma(\tau)$ are the retardations due to the EO modulator and the signal voltage in the sampling head, respectively. Here τ is the relative delay of the arrival time of the probe pulse with respect to the signal waveform. Therefore $\gamma(\tau)$ varies slowly with the offset repetition rate of [3]. Because the analyzer is assumed to be oriented at β to the X axis, the AC component of the output probe beam power can be approximated by

$$P_{out} = \frac{P_{in}}{2} \cos 2\theta \left[-\sin 2(\theta - \beta) \cos \Gamma(t) + \gamma(\tau) \sin 2(\alpha - \beta) \sin \Gamma(t) \right] \quad (2)$$

Generally the retardation $\Gamma(t)$ of the EO modulator is expressed as

$$\Gamma(t) = \Gamma_m \sin 2\pi f_m t + N(t) \quad (3)$$

where Γ_m and f_m are the amplitude and the frequency of the modulation of phase retardation, respectively, and the $N(t)$ represents the retardation perturbation by the fluctuations of temperature and input voltage applied to the EO modulator. Photodiode output, which is proportional to the optical power, eq.(2), is fed to a band pass filter centered at the frequency f_m , then the output photocurrent becomes

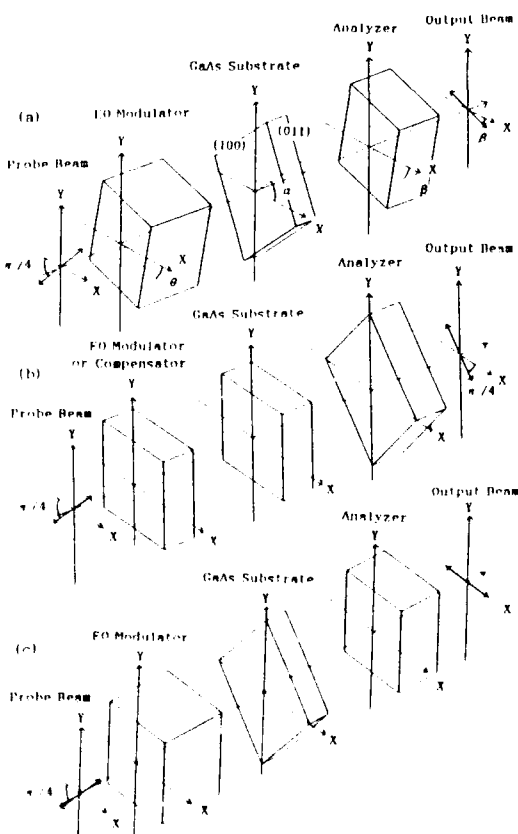


Fig.4 Coaxial arrangement for (a) definition of angles, (b) signal modulation or phase modulation scheme and (c) probe beam polarization modulation scheme

$$I_{out} = I_0 \cos 2\theta \left[\sin 2(\alpha - \beta) \gamma(\tau) + \sin 2(\theta - \beta) N(t) \right] J_1(\Gamma_m) \sin 2\pi f_m t \quad (4)$$

where I_0 is the maximum photocurrent for a given beam intensity P_{in} and J_1 is the first order Bessel function.

From eqs.(2) and (4), we can get the output equations of three cases of signal amplitude modulation scheme (Fig.1), phase modulation scheme (Fig.3) and polarization modulation scheme. In the conventional signal amplitude modulation scheme, as shown in Fig.4.(b), we have only to set $\gamma = (\gamma/2) \sin 2\pi f_m t$, $\Gamma = \pi/2$, $\theta = 0$, $\alpha = 0$ and $\beta = -\pi/4$ to eq.(2). Also in the phase modulation scheme, we obtain the equation by making $\theta = 0$, $\alpha = 0$ and $\beta \sim -\pi/4$ in eq.(4) (Fig.4.(b)). Specifically when such an operation as $\theta = 0$, $\alpha = \pi/4$ and $\beta \sim \theta$, shown in Fig.4.(c), is made, we get the final equation of polarization modulation scheme. In summary the output signals for the three cases are represented as follows:

$$I_{out} = \begin{cases} (I_0/4) \gamma(\tau) \sin 2\pi f_m t & (5.1) \\ I_0 \{ \gamma(\tau) + N(t) \} J_1(\Gamma_m) \sin 2\pi f_m t & (5.2) \\ I_0 \{ \gamma(\tau) + 2(\theta - \beta) N(t) \} J_1(\Gamma_m) \sin 2\pi f_m t & (5.3) \end{cases}$$

here eqs.(5.1), (5.2) and (5.3) indicate signal amplitude modulation scheme, phase modulation scheme and polarization modulation scheme respectively.

In the polarization modulation scheme it is clear that under the absence of the signal, the probe beam is not modulated at all, and with the signal it is modulated in proportion to γ . If β is set equal to θ , the advantages of the scheme derived from this equation are follows: 1) since the signal frequency components are shifted by f_m , the DC component can be detected without disturbance of the 1/f noise; 2) the offset frequency can be set to be arbitrarily low so that narrow-band detection is applicable in order to reduce the shot-noise; 3) when β is equal to θ , the effect of the noise $N(t)$ retardation can be suppressed; 4) because the optical change on both senses (± 1.84 rad) retardation adds up in the signal, we get 2.16 times sensitivity compared to the conventional methods ($2.16 = 4 \max J_1 = 4 J_1(1.84)$).

4. EXPERIMENT

The experimental set-up is indicated schematically in Fig.3. Here two synthesized signal generators are phase-locked and offset in frequency by 0.2Hz. One synthesizer drives a DUT which is here a comb generator, and the other drives a V-groove InGaAsP gain-switched laser diode which is biased well below threshold and pumped with a strong current pulse ($V_{p-p} = 12V$, pulse width = 130ps). The laser diode radiates probe photons at a wavelength $1.3 \mu m$, and its pulse width is less than 20 ps. The probe beam from the laser diode is modulated in polarization, as explained above, at 16kHz by an EO modulator which is made from KDP crystal with 650V half-wave voltage. By adjusting the compensator plate, the DC component of the retardation $\Gamma(t)$ was eliminated. The probe beam interacts with the fringing field produced by the signal voltage and is

reflected at the back surface of GaAs substrate, then is detected by a slow Ge photodetector through a Glan-Thompson polarizer, yielding the signal waveform proportional to V_{out} of eq.(5). This signal is then processed by a lock-in amplifier and an electrical spectrum analyzer with the resolution bandwidth of 100Hz with no use of accumulative signal averaging procedure.

The effect of the noise reduction is demonstrated as depicted in Fig.4.(a). Here the output waveform from a comb generator(HP33002A) is shown, operating at 100 MHz with peak-peak amplitude of 10

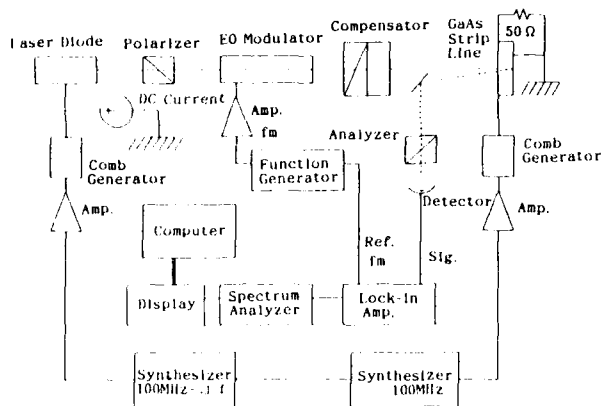


Fig.5 Experimental setup for EO sampling measurement

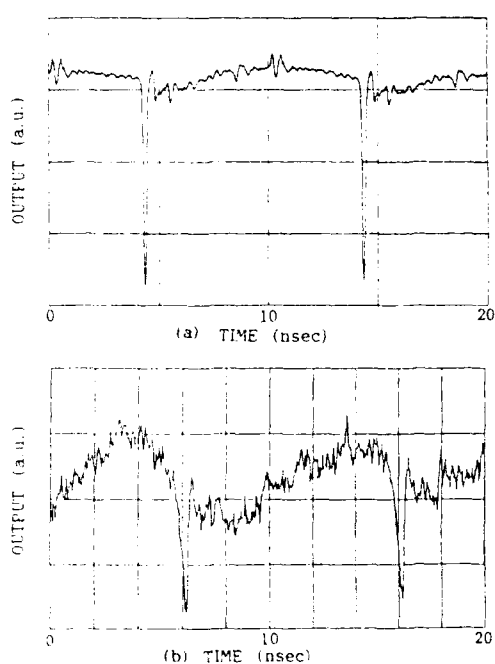


Fig.6 Comparison of the measurement results of a comb generator output waveform between (a) polarization modulation scheme and (b) conventional beat scheme.

V. Under the modulation frequency f_m of 16 kHz and the detection band width of 100 Hz, both the 1/f noise and the shot-noise were sufficiently suppressed. Here the measured waveform was reproduced with all the harmonic components of the signal. In comparison, the corresponding result based on the conventional non-modulation scheme[5] is shown in Fig.4.(b). The offset frequency Δf of 300Hz was chosen, the truncation of harmonic component at the 100 th order requires a filter bandwidth as large as 30 kHz, resulting in the poor noise elimination. Measured sensitivity in this scheme was $20 \text{ mV}/\sqrt{\text{Hz}}$, in contrast to the achievement of $1 \text{ mV}/\sqrt{\text{Hz}}$ using the novel scheme discussed in this paper.

5. CONCLUSION

In summary, a new scheme of noise suppression in electrooptic sampling system by the polarization modulation of the probe beam is proposed, its operation principle is analyzed and the performance is demonstrated experimentally. The method has the advantage of no need for electrically modulating the DUT. The probe beam is not modulated in intensity as far as the signal voltage is absent, meanwhile when the signal voltage is present, the beam is modulated with the amplitude in proportion to the signal voltage. Therefore it becomes possible to suppress the laser 1/f noise and detector originated shot-noise by making the detection bandwidth narrow. Using a gain-switched semiconductor laser as the probe beam source and a EO modulator, sensitivity of $1 \text{ mV}/\sqrt{\text{Hz}}$ was obtained.

6. ACKNOWLEDGMENTS

The authors would like to thank T.Nagatsuma, M.Shinagawa and A.Iwata of the NTT LSI Laboratories for their help through the study.

REFERENCES

- [1] J.A. Valdmanis and G.Mourou, in Picosecond Optoelectronic Devices, edited by C.H.Lee (ACADEMIC PRESS INC., London, 1984) Chap.8, p249
- [2] B.H.Kolner, and D.M.Bloom: IEEE J.Quantum Electron.,QE-22,79-93(1986)
- [3] K.J.Weingarten, M.J.W.Rodwell and D.M.Bloom :IEEE J.Quantum Electron. QE-24, 198-220 (1988)
- [4] J.A.Valdmanis, Electron.Lett.,23,1308-1310(1987)
- [5] J.M.Wiesenfeld, R.S.Tucker, A.Aantreasian, C.A. Burrus, A.J.Taylor, V.D.Mattera, and P.A. Garbinski, Appl.Phys.Lett.,50,1310-1312(1987)
- [6] M.S.Heutmaker, T.B.Cook, B.Bosacchi, J.A.Wiesenfeld, and R.S.Tucker: IEEE J.Quantum Electron., QE-24, 226-233 (1988)
- [7] A.J.Taylor, J.M.Wiesenfeld, G.Eisenstels, and R.S.Tucker, Appl.Phys.Lett.,49,681-683(1986)
- [8] E.Sano, M.Shinagawa and R.Takahashi,Appl.Phys. Lett.,55,522-524(1989)
- [9] A.Takada, T.Sugie, and M.Saruwatari: J.Lightwave Tech.,LT-5,1525(1987)
- [10] R.Takahashi, H.F.Liu, and T.Kamiya,Appl.Phys. Lett., 55,2377(1989)
- [11] H.F.Liu, Y.Ogawa, T.Kunii, and S.Oshiba, in post deadline papers of 12th IEEE International Semiconductor Laser Conference(Davos, Switzerland,1990), PD-8,p17

Electro-Optic Sampling for the Measurement of the Response of Fast Oscilloscopes

D. Henderson, A. G. Roddie, and A. J. A. Smith

National Physical Laboratory, Teddington, Middlesex TW11 0LW, UK

Abstract

A technique for measuring the impulse response and risetime of fast sampling oscilloscopes using picosecond electro-optic sampling is described. The results are compared with those obtained using a kick-out method and with measuring the spectral response in the frequency domain.

Introduction

Several new sampling oscilloscopes (CROs) have been introduced in recent years, the fastest claiming step risetimes of about 5 ps. Development of these CROs has been driven by rapid advances in areas such as optical fibre communications where they are often the limiting instrument in a measurement. Since these instruments are able to output waveforms to computers, knowledge of the impulse response can be used to increase the temporal resolution and accuracy of the CRO measurement. The purpose of this paper is to describe the techniques that we have applied to derive the impulse response of fast sampling CROs.

Various methods can be employed in measuring the response of a CRO to an impulse or a step^[1-3]. Electronic pulse generators have been used though the use of such step generators does not yield the risetime directly unless they are much faster than the CRO. This is difficult to achieve as the response time is governed largely by the same device technology.

Frequency domain measurements can give the power bandwidth response of the instrument and an estimate of the risetime can then be made from a model of the CRO temporal response.

Measurement of the kick-out pulse of a sampler by a

second, nominally identical sampler, has been demonstrated as a method of estimating the temporal response that is not limited by other measuring instruments.

Optoelectronic techniques offer considerable promise in measuring CRO response. Fast electrical pulses can be generated by photodiodes or photoconductive switches when illuminated by picosecond lasers. These pulses can be measured by photoconductive or electro-optic sampling techniques^[4].

We have used a modelocked dye laser and photodiode to generate very short electrical pulses and have measured the pulse waveform using electro-optic sampling (EOS). The impulse response of a CRO is derived by deconvolving the electro-optically measured waveform of the photodiode pulse from the waveform recorded by the CRO.

The results obtained by electro-optic sampling are presented here and compared with measurements obtained using a frequency sweeper and by analysing the CRO kick-out pulse.

Electro-optic sampling

A train of short optical pulses passes through a crystal which exhibits the Pockels' effect. Electrical pulses, phase-locked to the optical pulses, produce a transient electric field in the crystal, rotating the polarisation of each pulse in the same way. This can be detected using a polarisation analyzer, giving a change in intensity on a photodiode. By varying the delay between the optical and electrical pulses, the temporal shape of the electrical pulses can be obtained^[5].

A hybridly modelocked dye laser (Coherent 702-1), pumped by a Nd-YLF or Argon ion laser, produces pulses of 1 ps duration at 590 nm. The beam is focused

into a silica cone which has a lithium tantalate tip 100 μm thick, with a dielectric coating to reflect the beam. The polarisation of the beam is rotated when the tip of the cone is placed in an electric field. The system used is shown in Fig.1.

Since sampling CROs have coaxial input connectors, it is necessary to measure the electrical pulse at a reference plane in a coaxial transmission line. However, the electric field in coaxial geometry is not readily accessible to the sampler cone and so the pulse was launched onto a planar line. Both coplanar waveguide and microstrip were investigated for this purpose. We also probed a coaxial line directly through a hole in the outer skin of a K-connector.

The temporal resolution of the lithium tantalate cone is easily calculated for a uniform electric field. The main contributions are from the 1 ps optical pulse and the transit time of the optical pulse through the 100 μm Pockels' crystal. These two effects combine to limit the resolution to under 2 ps.

The resolution of the measurement of the pulse at the coaxial reference plane is less than this and is limited by the transmission line between this plane and the sampling plane. The effects of attenuation and dispersion by the line and changes in geometry have been measured by network analysis.

The electrical pulse generator (Fig.2) consisted of a photodiode illuminated by the picosecond dye laser. The diode was a GaAs Schottky barrier device [6] with 10 μm square active area, packaged with a K-connector. The pulse generator included a Wiltron K-250 bias tee and 6 dB Wiltron Gold-line attenuator. The attenuator was required to improve the source match to 50 Ω line. The measurement reference plane, at which the pulse shape was required, was the output side of the attenuator.

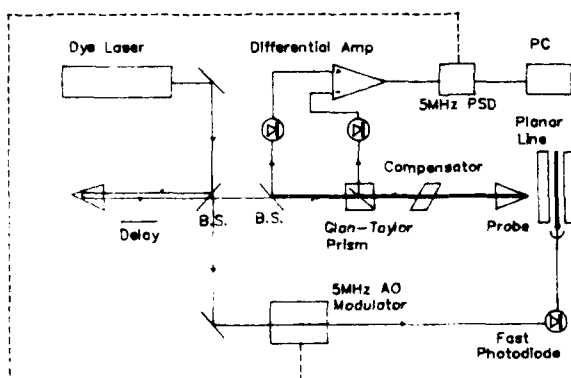


Figure 1. Diagram of the laser and electro-optic sampling system

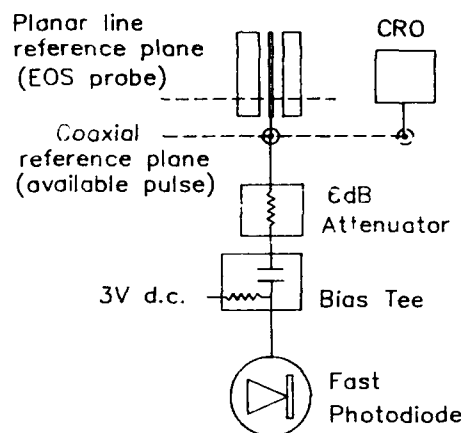


Figure 2. NPL pulse generator showing photodiode and associated circuitry.

Data acquisition and waveform processing

A number of processing steps are required to obtain the impulse response of a CRO using the waveform acquired by our electro-optic sampler (EOS). These are outlined below.

A PC was used to control the system, to acquire and process data from the CRO (HP 54121A) and EOS. The PC controlled the delay between the optical pulses on the photodiode pulse source and those probing the birefringence in the sampling cone and read a DVM connected to the phase sensitive detector. The resulting waveforms were averaged, filtered and modified as necessary.

The PC was also used to acquire the waveform from the CRO, controlling a shutter in the optical path to allow a record of the zero level to be subtracted. The time-base of the CRO was calibrated using a 10 GHz source.

The jitter in the triggering of the CRO was measured using the CRO's own software. The jitter was assumed to have a Gaussian distribution and was deconvolved from the results.

Waveforms of the photodiode signal recorded on the CRO and EOS are shown in Fig.3.

The impulse response of the CRO was obtained by deconvolving the EOS waveform from the measured CRO waveform, after correction for timebase and jitter. The difficulties encountered in the deconvolution have been treated in detail elsewhere [7], and in order to obtain a stable result, frequency domain filtering was used. The derived impulse is shown in Fig.4. The CRO risetime, the single parameter most widely used in defining a CRO's response was calculated by integrating the impulse response. This gave a risetime of 16.0 \pm 3.5 ps, with the uncertainty quoted for the 95% confidence level.

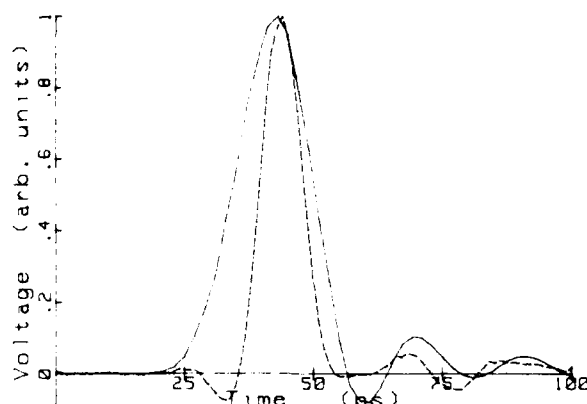


Figure 3. Photodiode waveforms recorded on the CRO (solid line, FWHM = 16.3 ps), and the EOS (dashed line, FWHM = 8.9 ps).

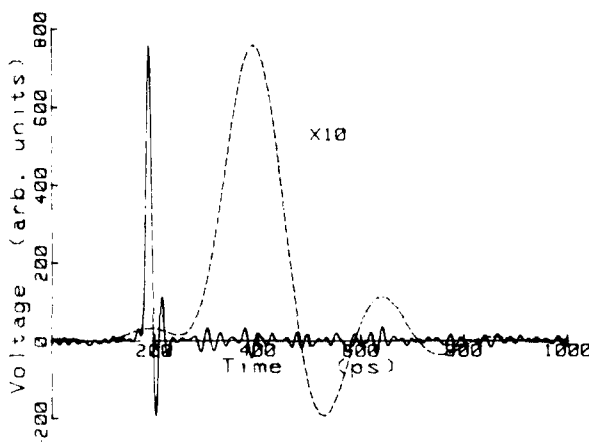


Figure 4. Derived impulse response of CRO showing FWHM = 11.7 ps.

De-embedding

The EOS measurement of the photodiode was made on the coplanar line whereas the electrical pulse should ideally be measured at the plane of the coaxial connector of the attenuator connected to the bias-tee.

Network analysis was used to attempt to quantify the distorting effect on the pulse of the line between the coaxial reference plane and the plane of the electro-optic probe. It is then, in principle, possible to de-embed the effect of the transition from the results. A two port K-connector test fixture was constructed, capable of holding lines of different lengths. A "through-reflect-line" calibration kit was constructed for our line (gold on fused silica). A resistive termination was included in the calibration kit, for low frequencies.

An Hewlett-Packard 8510 network analyser was used to find the S-parameters between the K-connector reference plane and the coplanar line. A 40 GHz test set

was used, but we had difficulty in obtaining physically realisable S parameters above about 32 GHz. Although the results obtained were not sufficiently accurate to allow de-embedding of the waveform data, they indicated the need for such an analysis.

Electro-optic sampling in coaxial line

As an alternative method of estimating the effect of the coaxial/coplanar transition, we measured pulses on coaxial line through a hole in the outer conductor of a line (Fig.5). The waveform was obtained by sampling through a 1.6 mm hole drilled in the outer of a male-to-male K-connector adaptor. Although there was a significant amount of ringing, believed to be due to the resonant cavity of the hole, shorter pulse widths were measured than on the line, indicating that the transition broadens the pulse by approximately 1.5 ps. The signal-to-noise ratio was poor when sampling in coaxial geometry with lithium tantalate. This is because the material exhibits a transverse electro-optic effect and the field in the coaxial cable is parallel to our probe beam.

Sampling CRO kick-out measurements

A novel method of measuring the impulse response of sampling CRO's, using a self-generated pulse, has been proposed^[8].

Impulses are generally present at the input connector of sampling CROs as a result of the sampling process, even when no input signal is applied. The waveform produced by an HP54121A CRO, set to its restricted bandwidth of 12.4 GHz is shown in (Fig.6). There are two independent contributions to these impulses, the sampling aperture current and the feedthrough of the sampling drive current. The sampling aperture current is due to current flowing through the finite resistance of the sampling gate during the very short time that it is turned on in the sampling process. This

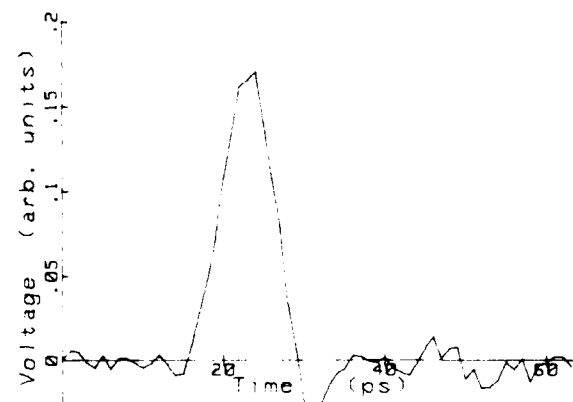


Figure 5. Photodiode pulse measured through hole in coaxial line. FWHM = 7.4 ps.

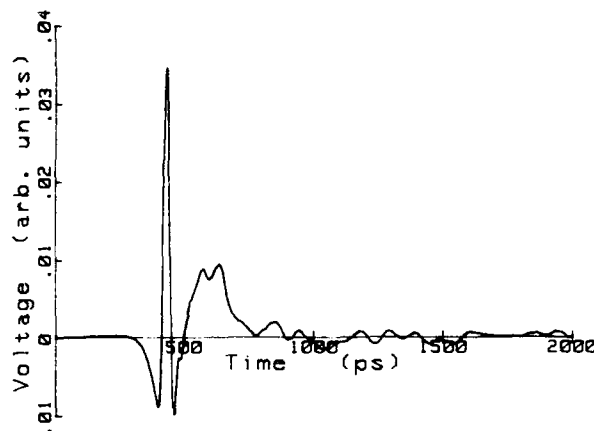


Figure 6. Kick-out signal measured at the input connector of an HP54121A CRO with bandwidth limit set to 12.4 GHz.

current is driven by a potential difference between the input line and the sampling gate hold capacitor, set by the sampling gate offset voltage, or vertical offset.

The sampling aperture current varies with the polarity and size of the sampling gate offset voltage, while the sampling gate drive current is independent of these. It has been shown that the contributions of the drive and the aperture current can be separated if the kickout pulses are recorded by an identical sampler for equal and opposite sampling gate offset voltages.

The CRO response can be considered as being composed of the combination of a filter response for the transmission line from the input connector to the sampling gate and the response of the sampling gate itself. The kick-out measurement technique assumes that the phase response of the sampling gate is ideal and that the gate used to measure the kick-out pulse is identical. The temporal response of the CRO is then obtained (Fig.7).

We have compared the frequency response of the

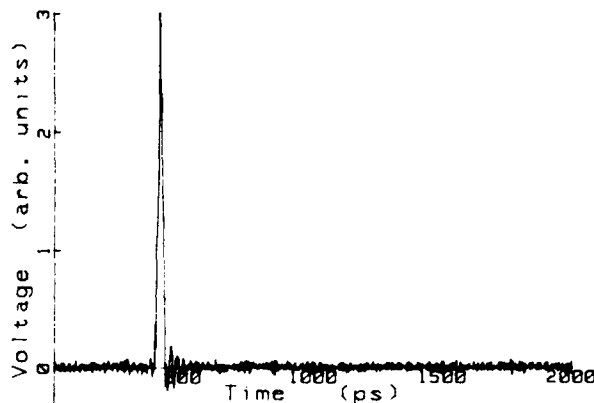


Figure 7. Impulse response of HP 54121A CRO (set at 12.4 GHz) derived from kick-out method. FWHM = 14.9 ps.

CRO, set to 12.4 GHz, derived by the kick-out method with that obtained by calculating the FFT of the EOS derived result (Fig.8).

The kick-out pulses of two other CROs, the Tektronix S4 sampling head and the Tektronix SD26, were also investigated. We found that, in these CROs, the kickout pulse did not vary detectably with vertical offset polarity^[9]. The sampling aperture function could not, therefore, be derived from it. It is important to note that, as the kick-out technique is not universally applicable, it cannot replace other measurement methods.

Frequency domain measurements

The risetime of fast sampling CROs is often estimated by measuring the magnitude of the frequency response. The phase response is required in order to calculate the temporal response. This is generally obtained from a model. In practice, the approximation of a single RC time constant is usually made.

We have made frequency response measurements using a Hewlett Packard 83597A sweeper (10 MHz-40 GHz) set to discrete frequencies. The sweeper power was levelled using a Hewlett Packard 8487 power sensor. The CRO was operated both triggered from the fundamental range of the oscillator and free running, using a statistical technique to determine the peak-to-peak value. Good agreement between the two methods was obtained.

The HP54121A CRO, set to its full 20 GHz bandwidth, was measured by the frequency domain method and compared to the FFT of the impulse response obtained by the electro-optic sampling method (Fig.9).

In order to determine whether the structure present in the CRO frequency domain measurements was caused

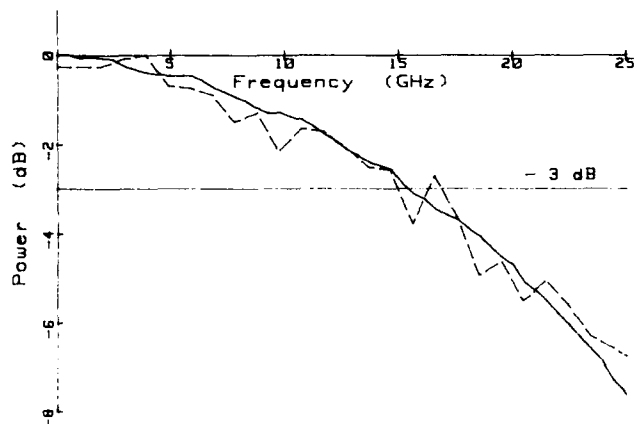


Figure 8. Frequency response of HP 54121A CRO (set at 12.4 GHz) measured using kick-out (solid line) and EOS (dashed line) methods.

by the photodiode or CRO, measurements of the photodiode were made using a spectrum analyzer (Hewlett Packard 7000 series). The response of the spectrum analyser was corrected using the sweeper, (levelled by the power sensor) at the same power level, the individual harmonics in the comb making up the photodiode pulse. This removes errors introduced by the I.F. gain accuracy and Log amplifier fidelity.

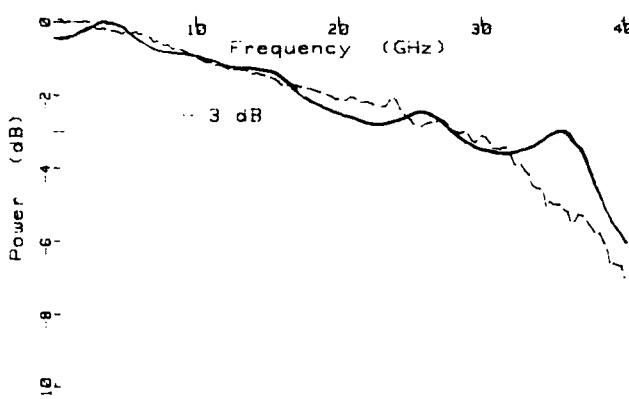


Figure 9. Frequency response of HP 54121A CRO (nominal bandwidth) measured using EOS (solid) and swept frequency (dashed) methods.

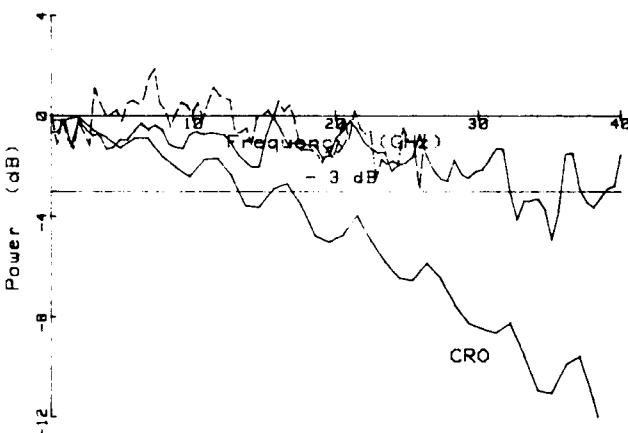


Figure 10. Photodiode measured using spectrum analyser (dashed) and EOS (solid). The FFT of the CRO is shown for comparison.

The spectrum analyser measurement of the pulse frequency spectrum to 26.5 GHz can be compared with the FFT of our electro-optic sampler waveform (Fig.10). The record of the pulse obtained by the HP 54121A is also shown after the FFT. We expect to see the CRO response falling off more rapidly because of the limited bandwidth. Any difference in structure is indicative of imperfections in the techniques.

Conclusion

We have investigated three methods for measuring the temporal response or bandwidth of fast sampling CROs. The results show very good agreement although some waveform features require further investigation.

The time domain approach using a photodiode pulse generator and electro-optic sampler show that the risetime of a 20 GHz CRO (nominally 17.5 ps risetime) can be measured with an uncertainty of ± 3.5 ps. Improvements in the uncertainties and extension to measuring faster CROs require the development of improved pulse generators and the use of de-embedding techniques.

References

1. W.L.Gans, IEEE Trans. Instrum. Meas., IM-25, 4 (1976).
2. J.R.Andrews, Topical Meeting on Picosecond Electron. & Optoelectron., Technical Digest, Incline Village, Nevada (1987)
3. D.Henderson, A.G.Roddie, Meas. Sci. Technol. 1, 8 (1990)
4. D.H.Austin,P.R.Smith, Appl.Phys.Lett.41,7,(1982).
5. J.A.Valdmanis, G.Mourou, IEEE J. Quant. Electron., QE-22, 1 (1986).
6. D.G.Parker, Electron. Lett., 22, 23 (1986).
7. N.S.Nahman, M.E.Guillaume, NBS Technical Note 1047 (1981).
8. K.Rush, J.Kerley, S.Drawing, IEEE Spectrum, September 1990.
9. J.Carlson, Tektronix Inc, Private communication (1990).

Ultrafast Photodetectors

Limitations of the Impulse Response of GaAs Metal-Semiconductor-Metal Photodetectors

J. Kuhl, M. Klingenstein, and M. Lambdorff

Max-Planck-Institut für Festkörperforschung, Heisenbergstrasse 1, 7000 Stuttgart 80, Federal Republic of Germany

C. Moglestone, J. Rosenzweig, A. Axmann, Jo. Schneider, and A. Hülsmann

Fraunhofer-Institut für Angewandte Festkörperforschung, Tullastrasse 72, 7800 Friburg, Federal Republic of Germany

Abstract

Photoconductive and electro-optic sampling of the photocurrent of GaAs metal-semiconductor-metal-photodiodes reveal the influence of field screening and optical phonon scattering on the frequency bandwidth of these detectors. The experimental results agree with theoretical predictions of a self-consistent two-dimensional Monte Carlo calculation.

Introduction

Interdigitated Metal-Semiconductor-Metal (MSM) Schottky diodes fabricated on GaAs and other III-V compounds are sensitive high speed photodetectors for multigigabit optical data processing systems. The compatibility of the fabrication process with the process technology of planar high speed electronic devices like FET's makes them extremely attractive for ultrafast integrated optoelectronic circuits. Narrow Schottky contact spacing permitting rapid carrier extraction after photo-excitation and a small active area in order to minimize the parasitic capacitance are the key design features of these diodes. First attempts to model the intrinsic transport of photoexcited carriers in MSM-diodes by a one-dimensional Monte Carlo simulation predict temporal separation of the electron and hole current [1,2] and durations of the electron and hole pulse of a few picoseconds and several ten picoseconds, respectively. Although frequency bandwidths in excess of several ten GHz for such detectors have been reported by several groups [3-5] a direct comparison of theoretical and experimental results and a definite identification of the performance-limiting factors is still missing, so far.

Here we present the first comprehensive experimental and theoretical analysis of the charge carrier transport in MSM-diodes. The diode output was directly analyzed in

the time domain by photoconductive and electro-optic sampling with 70 fs optical pulses for different diode geometries and in dependence on the excitation density and sample temperature. We measured signal rise times as fast as 1.7 ps and a decay with two different time constants of 4.5-10 ps and 10-50 ps, which can be attributed to the electron and hole current, respectively. Theoretical results obtained by a self-consistent two-dimensional Monte Carlo (MC) calculation yield a quantitative description of the measured diode response.

Our experiments and the MC simulations reveal the importance of low excitation densities in order to avoid field screening by space charge effects. The full-width at half-maximum (FWHM) of the diode pulses decreases continuously by almost a factor of two if the sample temperature is decreased from 300 K to about 80 K. This result confirms that the response speed is actually limited by phonon scattering rather than by the device capacitance.

Monte Carlo Simulation of the Transport

The response of the MSM-diode to a 70 fs laser pulse is calculated by two-dimensional Monte Carlo simulations of the carrier transport [6,7]. This method represents a self-consistent solution of Boltzmann's transport and Poisson's field equations, both in space and in time. The latter was iteratively solved every 40 fs over a rectangular uniform mesh of 10nm. An unintentional background doping density of $5 \times 10^{13} \text{ cm}^{-3}$ (n-type) was assumed. The scattering mechanisms taken into account to solve Boltzmann's equation are optical and acoustical phonon, intervalley, and impurity scattering. The model includes the Γ , X, and L minima of the conduction band and the heavy-hole, light-hole and split-off valence band. Carrier-carrier scattering and external parasitic effects (capacitance) have not been included in this simulation. During illumination lasting 70fs and terminating at

$t = 0$ ps electron-hole pairs were generated with a depth distribution

$$n(y) = N_0 \exp(-ay) \quad (1)$$

where N_0 represents the density at the surface and $a = 4.279 \times 10^4 \text{ cm}^{-1}$. The subsequent motion of these photogenerated electrons and holes to the anode and cathode, respectively, under the influence of the electric field and the stochastic scattering events is then calculated for successive 40 fs time intervals. The repetitive solution of Poisson's equation after every 40 fs effects that our analysis takes into account screening of the electric field caused by spatial separation of the photo-excited electrons and holes. The simulation results demonstrate the important impact of this screening on the carrier collection rate at high intensities or low bias. The output current is finally obtained by counting the net number of particles absorbed by the electrodes during each 40 fs time interval.

Owing to limitations in computer power and capacity, the simulation of the transport has to be confined to 10,000 individual particle pairs. Each simulated particle ("superparticle") is an artificial object. When solving Boltzmann's equation it is regarded as a single charge carrier. For the recalculation of the electric field by means of Poisson's equation and for estimation of the current, one superparticle is considered to consist of many real charged particles and the number depends on the light pulse intensity.

The upper part of Fig. 1 depicts the temporal evolution of the electron (o) current, the hole (x) current and the total (•) current predicted by this model for an MSM diode with a finger separation of 1.5 μm and a bias voltage of 2 V at a relatively modest excitation level of $5.1 \times 10^{15} \text{ cm}^{-3}$. The time dependence of the total current (•) exhibits a first rapid decay (1/e-time 8 ps) which can be attributed to the electron sweep-out and a second slow decay (1/e-time 30 ps) which results from the hole sweep-out. The signal rise time and the full-width at half-maximum amount to 4 ps and 11 ps, respectively. The curves in the lower part of Fig. 1 calculated for a carrier density of $5.1 \times 10^{16} \text{ cm}^{-3}$ reveal considerable changes of the carrier transport at higher intensity levels. The model predicts an initially faster decay of the photocurrent compared to the situation at lower excitation and a substantial slowing down of the transport after about 25 ps. At these later times the electron and hole population decays coincide. This behavior is explained by the formation of a field-free region near the anode originating from the initial spatial separation of electrons and holes which tends to screen the electric field between the anode and cathode. This field screening becomes important when either the electric field is small (small bias or large finger separation) or the excitation density is high.

At a further 10-fold increase of the excitation density (i.e. at 100 times the intensity applied in the upper part of Fig. 1) the transport properties are totally governed by screening effects which lead to an almost complete com-

pensation of the field across the entire space between anode and cathode after 2 ps. In this situation the collection rates of electrons and holes are almost the same. The output current decays to 30% of its peak value after 12 ps and then forms a long tail which extends over a few 100 ps.

Field screening becomes an even more severe problem in the case of low external bias. For a bias of only 0.5 V the weak internal field gets immediately screened even by

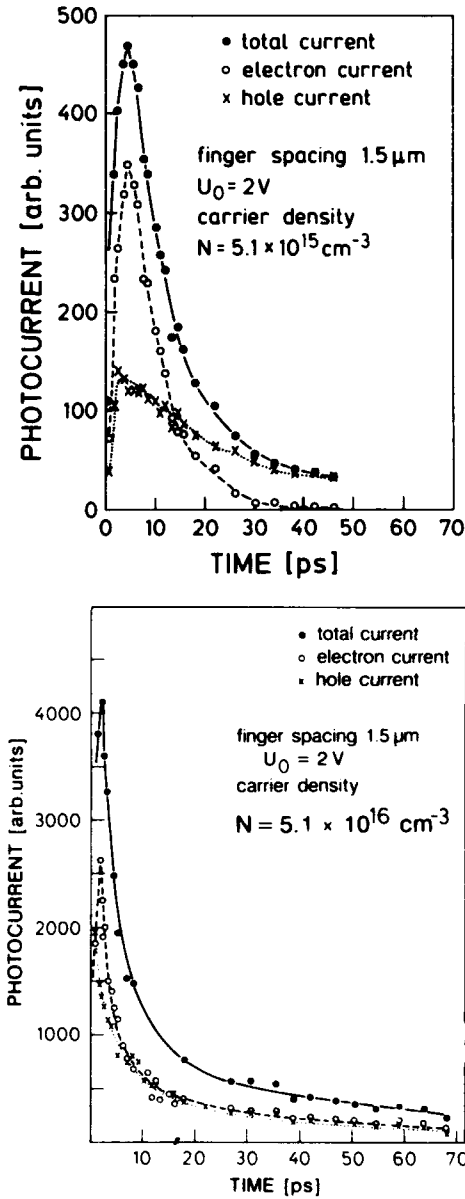


Fig. 1: Theoretical evolution of the electron (o), hole (x), and total current (•) in the MSM photodiode (finger separation 1.5 μm , bias voltage 2 V) for two different excitation densities of $N_0 = 5.1 \times 10^{15} \text{ cm}^{-3}$ (upper part) and $N_0 = 5.1 \times 10^{16} \text{ cm}^{-3}$ (lower part) as predicted by the Monte Carlo calculation.

the relatively low carrier density of $5.1 \times 10^{15} \text{ cm}^{-3}$. The current curve exhibits only a small peak sitting on top of a long pulse. Again no difference for the collection rates of electrons and holes is observed. In this case and in that of the very high excitation the screened plasma diffuses into the region under the anode so that a small amount of holes can escape through the anode via scattering.

The current pulse narrows noticeably if the finger separation is reduced to $0.5 \mu\text{m}$. For an excitation density of $N = 5.1 \times 10^{15} \text{ e-h pairs/cm}^3$ and a bias of only 0.5 V , the electron and hole parts of the current are temporally separated because of the higher field strength in the device. The pulse exhibits a rise time of 1.8 ps , a fast and slow decay time of 4.5 ps and 20 ps , respectively, and a FWHM of 6.3 ps . Thus, the computed speed of the detector is significantly higher than that of the $1.5 \mu\text{m}$ detector in spite of the 25% smaller average electric field between the anode and the cathode. The faster carrier collection is explained by the shorter transit times. The response, in particular the hole sweep-out becomes still faster if the bias is increased to 2 V .

If the excitation density is increased to $5.1 \times 10^{16} \text{ e-h pairs/cm}^3$ at the surface, the field screening reappears also in the $0.5 \mu\text{m}$ diodes (bias 2 V). Both the electron and hole current are slowed down but the reduction of the response speed is much less than in the $1.5 \mu\text{m}$ structures owing to the higher field in the device.

After another increase of the intensity by a factor of 10 (the excitation density now becomes $5.1 \times 10^{17} \text{ e-h pairs/cm}^3$) the screening is complete in the narrow structure, too. The electron and the hole current coincide. The decay of the current, however, is faster owing to the shorter transit time of the $0.5 \mu\text{m}$ diodes.

Experimental Results

The diodes have been fabricated by means of electron beam lithography on bulk LEC-GaAs using Ti/Pt/Au as the Schottky contacts. The diodes under investigation had an active area of $10 \times 10 \mu\text{m}^2$, and typically $0.5/1 \mu\text{m}$ wide fingers with $0.5/1.0 \mu\text{m}$ distance between them. The diode sensitivity is 0.2 A/W at 3 V and 825 nm wavelength with 40% of the area covered by the metal fingers.

For photoconductive sampling of the diode response, the photodiode was integrated with a photoconductive switch on the same GaAs chip which was locally ion damaged (see inset of Fig. 2) with a total dose of $4.11 \times 10^{14} \text{ H}^+ \text{ cm}^{-2}$. The GaAs carrier lifetime was thus reduced to 0.8 ps . The transmission line consists of two $5 \mu\text{m}$ wide strips with $10 \mu\text{m}$ spacing. The $5 \mu\text{m}$ wide sampling strip is located at 2.5 mm distance from the diode.

Besides photoconductive sampling, we applied also electro-optic sampling with a small LiTaO_3 tip [8] pressed against the transmission line at a distance of $100 \mu\text{m}$ from the diode. Excitation of the diode and photocurrent sampling were performed using the 70 fs optical pulses

derived from a dispersion-compensated colliding-pulse-mode-locked dye laser (wavelength 620 nm , repetition rate 116 MHz). The time resolution was determined to be 0.8 ps and 0.3 ps for photoconductive and electro-optic sampling, respectively.

The curves in Fig. 2 show the photocurrent signal versus time delay between exciting and sampling pulses as a result of photoconductive (lower curve) and electro-optic (upper curve) sampling for an MSM-diode with $0.5 \mu\text{m}$ finger separation (bias voltage 2 V). In the case of photoconductive sampling the slow rise of the photocurrent is caused by a tail in the photoconductivity of the damaged GaAs. If we neglect this part of the photocurrent curve the rise time amounts to 2.4 ps , which is longer than the 1.7 ps rise time measured in the case of electro-optic sampling (Fig. 2, upper curve). The deviation is attributed to pulse dispersion on the 2.5 mm propagation distance in the case of photoconductive sampling and to the better time resolution obtainable with electro-optic sampling (0.3 ps).

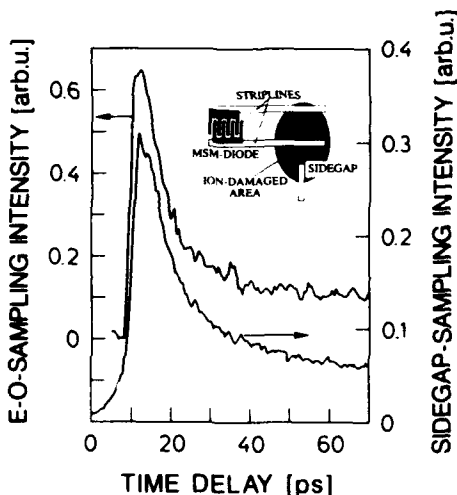


Fig. 2: Photocurrent vs. time delay for a GaAs-MSM-diode obtained by photoconductive (lower curve) and electro-optic (upper curve) sampling (bias voltage 2 V , finger distance $0.5 \mu\text{m}$). The inset shows a top view of the integrated GaAs chip.

Figure 3 depicts the response of a $0.5 \mu\text{m}$ diode (bias 2 V) to a time-averaged incident light power of $12 \mu\text{W}$ and $200 \mu\text{W}$ corresponding to electron-hole pair densities of 1.3×10^{16} and $2.2 \times 10^{17} \text{ per cm}^3$ at the surface, respectively. The photoconductive sampled signal has a rise time of 2.4 ps independent of the excitation level and a FWHM which grows continuously from 8.6 ps (for $N_0 = 1.3 \times 10^{16}/\text{cm}^3$) to 12.3 ps (for $N_0 = 2.2 \times 10^{17}/\text{cm}^3$) with increasing intensity. The fast initial decay times are 5.3 and 10.7 ps for the two intensities. Thus, the relevant time constants grow with light intensity in the studied interval whereas the Monte Carlo simulation predicts a decrease of the electron pulse duration when

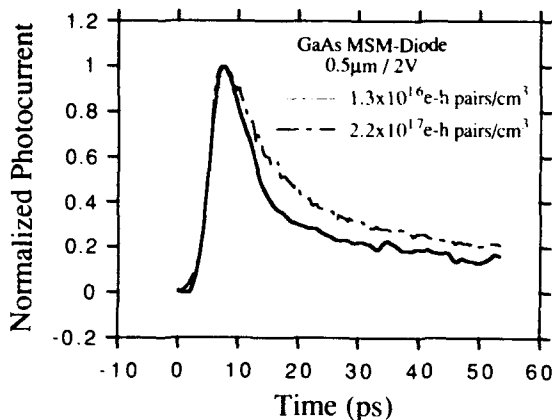


Fig. 3: Photocurrent response of a $0.5 \mu\text{m}$ diode (bias 2V) measured by photoconductive sampling for two different excitation densities.

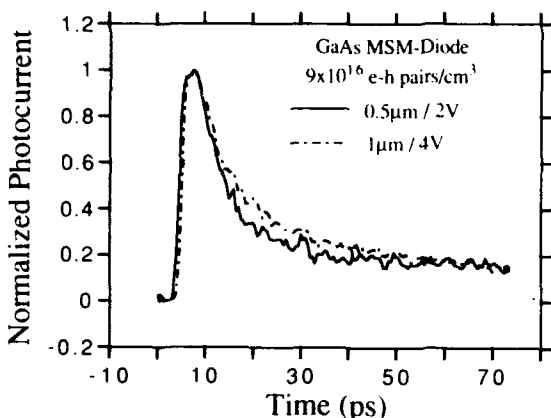


Fig. 4: Variation of the photocurrent pulse shape with finger separation for two diodes with the same ratio of bias voltage and finger distance.

the carrier density at the surface is increased from 5.1×10^{15} to 5.1×10^{16} e-h pairs/cm³. As we have explained above, such shortening of the first peak may be caused by field screening at the higher density. Obviously this effect is not observable in the experiments. The origin of the discrepancy is not fully understood at present. It may be probably due to increased carrier/carrier scattering at higher densities. The latter process is not considered in the MC-simulations.

The change of the shape of the collection current with an increase of the electrode separation d from 0.5-1 μm at "fixed" average electric field (fixed ratio of finger distance d and bias) and constant intensity (90 μW of average power) is displayed in Fig. 4. The increase of d by a factor of 2 leads to a broadening of the FWHM of the pulse from 9.8-11.2 ps, considerably less than the factor of 2 expected from the geometrical lengthening of the path. This may be partly due to the different sensitiv-

ity of the two structures to screening. This presumption is supported by results measured at ten times lower intensity (9 μW average power focused to the detector surface). Under the latter conditions the FWHM of the main current peak amounts to 7.8 and 10.5 ps for the $0.5 \mu\text{m}$ and the $1 \mu\text{m}$ structures, respectively. The residual lack of response speed of the $0.5 \mu\text{m}$ structure is most likely due to the much steeper decrease of the electric field with growing distance from the surface compared to the $1 \mu\text{m}$ diode. Thus, a larger fraction of the electrons is generated in low field regions. If the field strength in these regions falls below that required for transport at the saturation velocity the collection of the electrons takes much longer. This problem becomes even more severe if one takes into account the easily attainable screening of low fields.

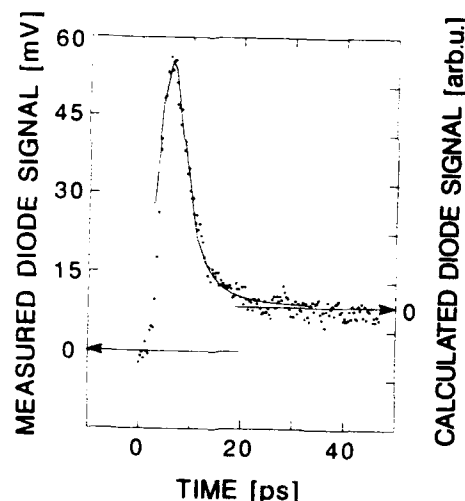


Fig. 5: Theoretical evolution of the total current (solid line) in the MSM photodiode (finger separation $0.5 \mu\text{m}$, bias 2V) and experimental photocurrent curve (•) measured by electro-optic sampling.

In Fig. 5 we depict a comparison of experimental data with theoretical predictions. The time dependence of the calculated photocurrent (solid line) is shown together with the experimental photocurrent curve measured by electro-optic sampling on an integrated GaAs sample (diode finger separation $0.5 \mu\text{m}$, bias 2V).

Excellent agreement between experiment and theory can be observed except for a long tail in the measured photocurrent which is not predicted by the theory and the origin of which is not yet understood. The measured rise time of the photocurrent amounts to 1.7 ps (10-90%), the first rapid decay to 4.5 ps and the second slow decay to 10 ps.

By changing the bias voltage or the carrier density, we investigated the influence of field screening on the photocurrent curves of diodes with $0.5 \mu\text{m}$ and $1.2 \mu\text{m}$ finger spacing. Dependent on the experimental conditions the photocurrent curves yielded first and second decay times in the order of 4.5-10 ps and 10-50 ps, respectively, and FWHM values of 6-14 ps.

Finally, we studied the variation of the photocurrent response as a function of temperature. For these experiments the diode (finger spacing: 0.75 μm , bias 4V, $N_0 = 3.5 \times 10^{16} \text{ cm}^{-3}$) was mounted in a He-cryostat and the photocurrent pulse shape was analyzed by photoconductive sampling.

Figure 6 shows the measured signal at 300 K, 100 K and 10 K. Screening of the electric field by the electron-hole plasma is expected to play a minor role at the chosen carrier density. The signal rise time (2-3ps) is almost constant for all measurements and corresponds to the time resolution limit of the photoconductive sampling. The FWHM decreases continuously from 10.8 ps at 300 K to 5.6 ps at 100 K. Between 100 K and 50 K the diode's signal shape remains almost unchanged. Further cooling increases the FWHM again from 5.6 ps at 50 K to 11.1 ps at 10 K.

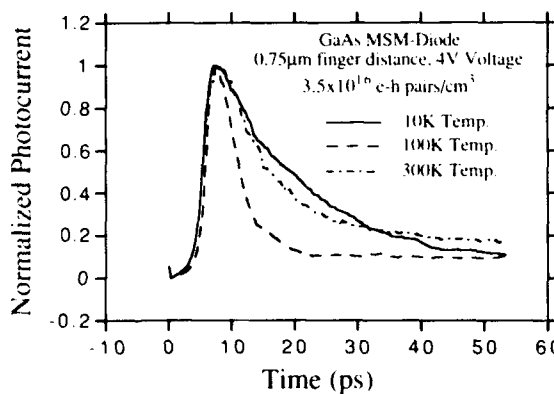


Fig. 6: Normalized photocurrent vs. time delay for a GaAs MSM diode (finger distance 0.75 μm) at a temperature of 300 K, 100 K and 10 K. Excitation density $3.5 \times 10^{16} \text{ e-h pairs/cm}^3$.

The high H^+ implantation dose of the photoconductive switch serves for a high concentration of deep defect states. Thus, a variation of the time resolution of the photoconductive sampling with temperature due to multiple trapping of carriers in shallow traps can be excluded [9] and the shortening of the signal between 300-100 K can be definitely attributed to an accelerated depletion of the diode after photoexcitation. This experimental finding can be explained by the increase of the electron drift velocity at lower temperatures because of a significant reduction of intra- and intervalley phonon scattering. The phonon scattering rates drop in accordance with the decreasing population of LO, LA and TA phonon modes with temperature. The model of intra- and intervalley phonon scattering predicts, however, an almost constant electron drift velocity for $T < 70$ K. The rapid increase of the response time observed for $T < 50$ K can be attributed to the dominating contribution of ionized impurity scattering at low temperatures [10].

This result confirms that the measured response at room temperature is limited by phonon scattering. The

time resolution is not influenced by the diode's intrinsic capacitance C , which was estimated to be 6fF [11], corresponding to an RC time constant of 600 fs (transmission line impedance $R \sim 100 \Omega$), about a factor of 3 below the shortest rise times. Consequently, the photocurrent rise and fall times are determined by carrier transit time effects.

Fourier transformation of the experimental photocurrent curves in Figs. 5 and 6 (100 K curve) yields a frequency bandwidth of 50 GHz (3dB point) and 75 GHz, respectively, if the long tail is neglected. These values are distinctly lower than the value of 105 GHz reported by van Zeghbroeck et al. [3]. The origin of this discrepancy is not clear. The Monte Carlo calculation predicts, however, a non-negligible influence of field screening on the response current for the values of the intensity and bias voltage given in Ref. [3].

Conclusion

In summary, we have studied the carrier transport in GaAs MSM-photodiodes after excitation with an ultra-short light pulse. We have demonstrated that the electron and hole contributions to the photocurrent are nearly separated in time. The response speed at low excitation densities is limited by optical phonon scattering. Field screening effects become important at higher intensities or low bias voltages.

In order to prevent space charge induced deterioration of the response the detector should be operated at high bias levels ($>2\text{V}$) and the optical pulse energy has to be limited to 100 fJ. Fortunately, these requirements which have been ignored in previous theoretical and experimental work concerning the characterization of MSM diodes will be surely achieved in future high bit rate optical communication systems. Ensemble Monte Carlo calculations support our experimental data.

References

1. W.C. Koscielniak, J.-L. Pelouard, and M.A. Littlejohn, "Intrinsic and Extrinsic Response of GaAs Metal-Semiconductor-Metal Photodetectors", *IEEE Photonics Technology Lett.* **2**, 125 (1990).
2. W.C. Koscielniak, J.-L. Pelouard, and M.A. Littlejohn, "Dynamic Behaviour of Photocarriers in GaAs Metal-Semiconductor-Metal Photodetector with Sub-Half-Micron Electrode Pattern", *Appl. Phys. Lett.* **54**, 567 (1989).
3. B.J. van Zeghbroeck, W. Patrick, J.-M. Halbout, and P. Vettiger, "105-GHz Bandwidth Metal-Semiconductor-Metal Photodiode", *IEEE Electron Device Lett.* **9**, 527 (1988).
4. W. Roth, H. Schumacher, J. Kluge, H.J. Geelen, H. Beneking, "DSI Diode - A Fast Large-Area Optoelectronic Detector", *IEEE Transactions on Electronic Devices* **32**, 1034 (1985).
5. M. Lambdorff, M. Klingenstein, J. Kuhl, C. Moglestue, J. Rosenzweig, A. Axmann, Jo. Schneider, J. Hülsmann, H. Leier, and A. Forchel, "Subpicosecond Characterization of Carrier

Transport in GaAs-Metal-Semiconductor-Metal Photodiodes", to be published in *Appl. Phys. Lett.*, April 1st, 1991.

6. C. Moglestue, "A Self-Consistent Monte Carlo Particle Model to Analyze Semiconductor Micro-components of Any Geometry", *IEEE CAD-5*, 326 (1986).

7. C. Moglestue, J. Rosenzweig, J. Kuhl, M. Klingenstein, M. Lambsdorff, A. Axmann, Jo. Schneider, and A. Hülsmann, "Picosecond Pulse Response Characteristics of GaAs Metal-Semiconductor-Metal Photodetectors", to be published in *Journ. of Appl. Phys.* (1991).

8. J.A. Valdmanis, "1 THz-Bandwidth Prober for High-Speed Devices and Integrated Circuits", *Electronics Letters* 23, 1308 (1987)

9. Th. Pfeiffer, J. Kuhl, E.O. Göbel, and L. Palmetshofer, "Temperature Dependence of the Picosecond Carrier Relaxation in Silicon-Irradiated Silicon-on-Sapphire films", *Journ. of Appl. Phys.* 62, 1850 (1987).

10. M. Klingenstein, J. Kuhl, J. Rosenzweig, C. Moglestue, and A. Axmann, "Transit Time Limited Response of GaAs Metal-Semiconductor-Metal Photodiodes", to be published in *Appl. Phys. Lett.* (1991).

11. G.D. Alley, "Interdigital Capacitors and Their Application to Lumped-Element Microwave Integrated Circuits", *IEEE Transactions on Microwave Theory and Techniques*, MTT-18, 1028 (1970).

Ultralast Graded Double-Heterostructure p-i-n Photodiode

D. L. Crawford, Y. G. Wey, K. Giboney, J. E. Bowers, and M. J. Rodwell

Department of Electrical and Computer Engineering, University of California at Santa Barbara, Santa Barbara, California 93106

P. M. Sylvestre, M. J. Hafich, and G. Y. Robinson

Center for Optoelectronic Computing Systems and Electrical Engineering, Colorado State University, Fort Collins, Colorado 80523

Abstract

A $5 \mu\text{m} \times 5 \mu\text{m}$ double heterostructure InGaAs/InP pin photodiode is reported with a measured response of 5 ps and a deconvolved device impulse response of 3.8 ps. The double heterostructure employed reduces carrier diffusion and the graded heterobarriers play a key role in optimizing the device response speed by minimizing charge storage and device series resistance.

Introduction

High speed photodiodes play a crucial role in many applications including optical communication systems and high speed optical measurement techniques. To date, the fastest impulse response for any photodiode was reported by Wang et al., (1), who observed an 8.5 ps FWHM response from a GaAs Schottky photodiode. In the InGaAs/InP material system the shortest measured response was demonstrated by this group, (2), in an InGaAs/InP single heterostructure pin photodiode. This paper describes an improved device design in which an InGaAs/InP

graded double heterostructure design is used leading to observation of state-of-the-art photodiode impulse responses.

In order to attain high speed operation from pin photodiodes, several issues must be addressed. The absorbing layer thickness of the device is designed to achieve the optimum impulse response by trading off transit time with device parasitic considerations. Essentially, the device capacitance must be minimized, therefore the device area must be scaled to small dimensions. However as the device area is scaled, the optimum absorbing layer thickness to achieve high speed operation reduces, therefore imposing detrimental consequences on the device quantum efficiency. Figure 1 demonstrates the combination of these

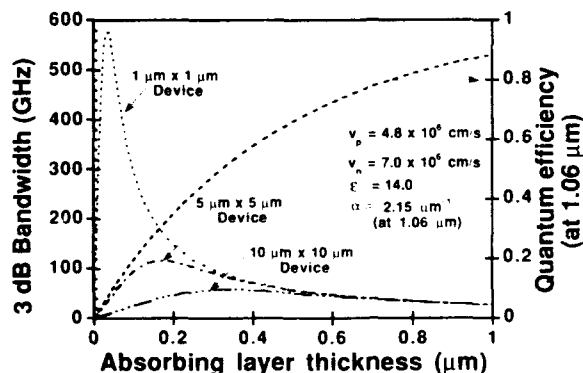


Figure 1 Pin photodiode design curves

effects and clearly, compromises must be made, these being primarily dependent upon the system application. Similarly, the device series resistance must also be minimized and so highly doped contact layers are necessary.

To minimize the photogenerated carrier transit time across the device absorbing region, the material structure is designed to ensure the nature of carrier transport is drift at the respective saturated carrier drift velocity and that the inherently slower diffusion transport mechanism is avoided. It is at this point that the conventional single heterostructure high speed pin photodiode design falls short. In these devices, the absorbing layer is typically thin to optimize high speed performance, and some carriers are optically generated within the highly doped InGaAs contact region in a diffusion length of the homojunction interface. These carriers then diffuse in a finite time into the vicinity of the electric field where they are swept across the absorbing region, thus slowing the device response speed. However in eliminating this effect by incorporating a double heterostructure design, careful attention must be paid to the resulting InGaAs/InP heterobarriers. Carriers may become trapped in the InGaAs absorbing region at the heterobarrier interfaces where they must tunnel or be thermionically emitted to escape, as shown in the band diagram of Figure 2. This is particularly a problem for holes in this material system since the valence band discontinuity is large and the hole effective mass is large. To address this problem, the devices reported here have a graded heterointerface.

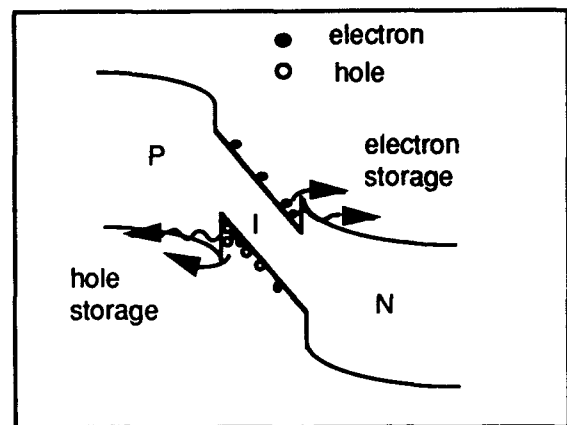


Figure 2. Band diagram demonstrating carrier storage in the ungraded double heterostructure pin diode

Material and Device Structure

The material structure, shown in Figure 3, was grown by Gas Source Molecular Beam Epitaxy on a (100) InP substrate at a growth temperature of 500 °C.

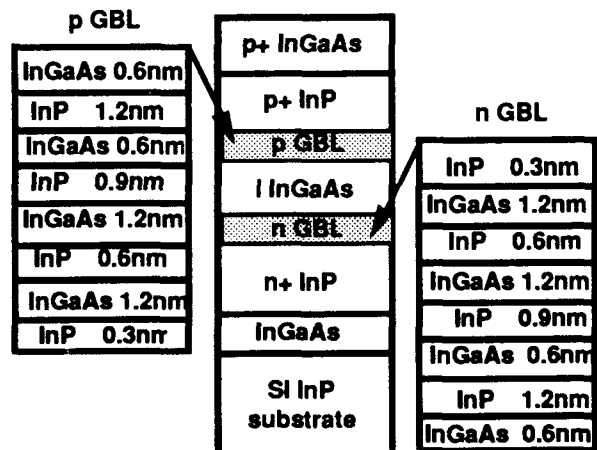


Figure 3. Material structure grown by GSMBE

The P_2 and As_2 beams were produced by thermal decomposition of arsine and phosphine gases and the dopants employed were Be and Si. The epitaxial layers are composed of a 5 nm InGaAs etch stop layer on which was grown a 370 nm $InP\ n+$ ($8 \times 10^{18} \text{ cm}^{-3}$) layer, and a 66 nm graded band gap layer (GBL) composed of four pairs of alternate (increasing in thickness) InGaAs and (decreasing in thickness) InP layers. An unintentionally doped 190 nm InGaAs absorbing layer was then grown, followed by four pairs of alternate (decreasing in thickness) InGaAs layers and (increasing in thickness) InP layers and a 280 nm $p+$ (graded in doping from 1 to $3 \times 10^{18} \text{ cm}^{-3}$) InP layer. Finally a 190 nm $p+$ ($5 \times 10^{19} \text{ cm}^{-3}$) InGaAs contact layer was grown. This layer structure was designed to achieve optimum device response for a $5 \mu\text{m} \times 5 \mu\text{m}$ device area.

Pin photodiodes were then fabricated into the structure shown in Figure 4.

This design permits device scaling to very small areas since the device is contacted via a 50Ω coplanar waveguide structure, which is therefore impedance matched to the load resistor.

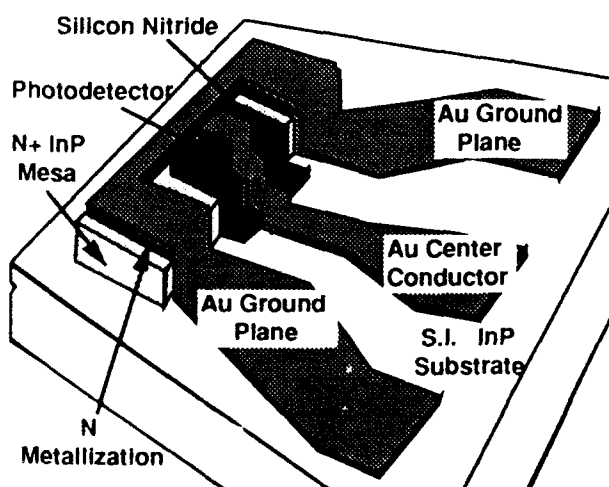


Figure 4. Photodetector Device Structure

Furthermore, this structure permits integration of a bias tee arrangement which may be used when operating the device under reverse bias conditions. This feature is important, since in high frequency operation, the bandwidth limitation of commercially available bias tees may ultimately limit the device performance.

The processing of these devices is achieved in five simple process steps. First of all, the device p -type metal contact is formed by evaporating a Ti/Pt/Au combination onto the $p+$ InGaAs layer. This metal is then topped with Ni which is used as the self-aligned etch mask to etch the devices into individual mesa structures using Cl_2 reactive ion etching. The InP n -type layers (common to a row of devices) are then patterned into mesa structures by wet-etching in $HCl:H_2O$, and the n -type contact metal AuGe/Ni/Au is e-beam evaporated onto these mesas. A 180 nm SiN_x film is then deposited by PECVD to passivate and isolate the device. Finally, a 250 nm Au layer is evaporated onto the sample to form the coplanar waveguide structures which are patterned by lift-off. The InP substrate is chemically and mechanically lapped to ensure optical smoothness, and the substrate is coated with an anti-reflecting coating of SiN_x which is sputter deposited.

Device Testing

The quantum efficiency of the devices is measured to be 31 %. The reverse breakdown voltage is 6 V and the leakage current is 40 nA at 1 V reverse bias.

The device response speed was characterized by electro-optic sampling, in which $1.06 \mu\text{m}$ 2 ps FWHM pulses from a mode-locked, pulse compressed Nd:YAG laser were used to excite the device under test. The electro-optic sampling system set-up is shown in Figure 5.

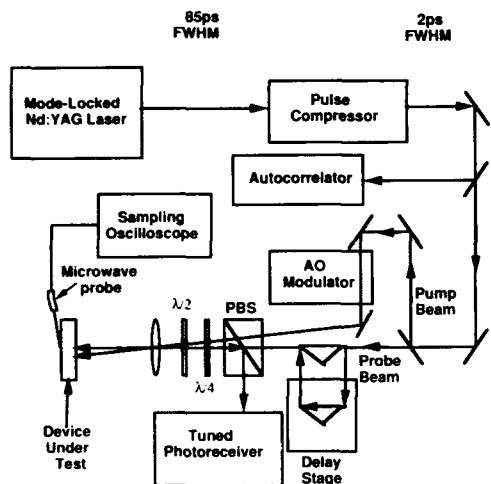


Figure 5. Electro-optic sampling system set-up

The measured response from a $5 \mu\text{m} \times 5 \mu\text{m}$ device at 2 V reverse bias is shown in Figure 6. This measured signal (solid line) is simply the correlation of the convolution of the detector impulse response with the excitation signal. Thus, the detector impulse response may be obtained by deconvolving the autocorrelation of the optical pulses from the measured response. The

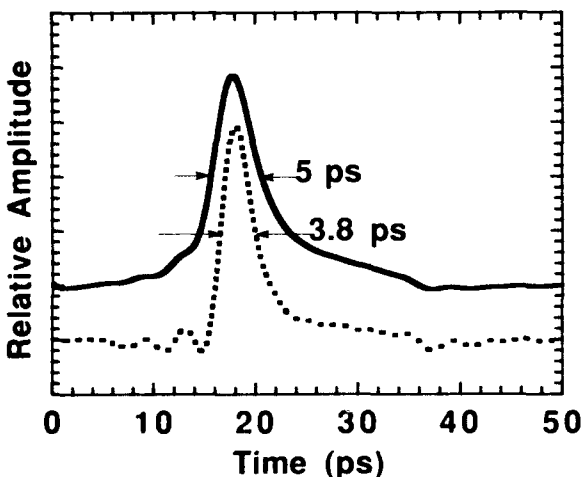


Figure 6. Measured (solid line) and deconvolved impulse response (dotted line) of a $5 \mu\text{m} \times 5 \mu\text{m}$ pin photodiode

resulting deconvolved device impulse response is shown in Figure 6 (dotted line), and is observed to be 3.8 ps FWHM.

From Figure 1 it is clear that devices of area greater than $5 \mu\text{m} \times 5 \mu\text{m}$ are limited by RC effects in the speed of operation, when the absorbing layer thickness is only 190 nm. This effect is demonstrated in Figure 7 where the impulse response of devices of different areas is compared. The experimentally derived impulse response is clearly in reasonable agreement with the theoretical curve.

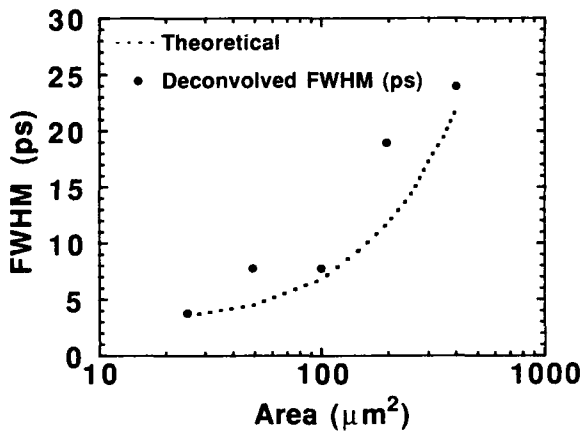


Figure 7. Device response speed as a function of device area

Summary

High speed graded double heterostructure pin photodiodes have been demonstrated to have state-of-the-art impulse responses. Further optimization of the device material design will result in increased operating speeds and will take high speed operation into the regime of 100's of GHz.

Acknowledgments

This work was sponsored by the DARPA, RADC and the Office of Naval Technology Block Program on Electro-Optics Technology.

References

1. S.Y. Wang and D.M. Bloom, "100 GHz Bandwidth Planar GaAs Schottky Photodiode", *Electron. Lett.*, **19**, 554-555, (1983).
2. D.L. Crawford, Y.G. Wey, A. Mar, J.E. Bowers, M.J. Hafich, and G.Y. Robinson, "High Speed InGaAs-InP p-i-n Photodiodes Fabricated on a Semi-Insulating Substrate", *Phot. Tech Lett.*, **2**, 647-649, (1990).

Picosecond Metal-Semiconductor-Metal Photodetectors with Sub-100-nm Finger Spacing and Finger Width in GaAs

Yue Liu, Paul B. Fischer, and Stephen Y. Chou

*Department of Electrical Engineering, University of Minnesota,
Minneapolis, Minnesota 55455*

Abstract

We have fabricated metal-semiconductor-metal photodetectors with sub-100-nm finger spacing and finger width on MBE-grown GaAs, which are, to our knowledge, the smallest ever reported. DC measurement shows that they have low dark current and high sensitivity. Monte-Carlo simulations demonstrate that the response time of the photodetectors for a 30 nm finger spacing can be as short as 0.4 ps, and the cut-off frequency can be over 1 THz.

Introduction

Metal-semiconductor-metal (MSM) photodetectors are very attractive for optical fiber communication systems and high-speed chip-to-chip connections^[1-4]. MSM photodetectors have several advantages over p-i-n photodiodes^[5], such as higher sensitivity-bandwidth product and compatibility with large scale FET integrated circuit technology. For high speed applications, it is very desirable to make spacing and width of interdigitated metal fingers small^[6-8]. In a GaAs crystal, the intrinsic response time of an MSM photodetector with finger spacing less than 200 μ m is determined by the electron transit time, since the carrier recombination time is longer than the transit time. The smaller the spacing, the faster the MSM photodetector. On the other hand, reduction of finger widths will speed up operation due to reduced capacitance^[11]. Previously, MSM photodetectors with finger spacing and width greater than 0.5 μ m have been reported.^[2,7-10]. The fastest GaAs MSM photodetector was fabricated by Van Zeghbroeck *et al* ^[10] which has a finger spacing of 0.5 μ m and a finger width of 0.75 μ m. The response time is 4.8 ps and an overall bandwidth is 105 GHz.

In this paper, we report the fabrication of GaAs MSM photodetectors with finger spacing and finger width smaller than 100 nm, which are, to our knowledge, the smallest ever reported. The DC characteristics show that the devices have a low dark current (< 40 nA) and a high sensitivity (0.2 A/W). A theoretical analysis and Monte-Carlo simulation results are also presented, which indicate a sub-picosecond operation.

Fabrication

The MSM photodetectors were fabricated on a 0.4 μ m thick undoped GaAs layer grown, using MBE, on a semi-insulating GaAs substrate with an AlGaAs/GaAs superlattice in between. The metal (Ti/Au) Schottky barrier contacts were fabricated on GaAs by using electron beam lithography and a lift-off technique. Two layers of polymethylmethacrylate (PMMA) were spun on the GaAs layer with high molecular weight (950K) layer on top and low molecular weight (100K) layer at the bottom. After spinning, each layer was baked at 160°C for about 12 hours. The double layer resist is used for achieving a good undercut profile suitable for the lift-off technique. Interdigitated line patterns were exposed in the resist using a high resolution electron beam lithography system at a beam energy of 35 KeV and at various doses, and developed in cellosolve:methanol (3:7) developer at 20°C for 7 seconds. Details of the electron beam system and lithography process have been described elsewhere^[12]. After exposure and development, metals (Ti/Au) were evaporated onto the samples and were lifted-off in acetone. The basic processing sequence is illustrated in Fig. 1.

Fig. 2 shows scanning electron micrographs of MSM photodiodes with different active areas and finger structures. The smallest line spacing is 30 nm, which is shown in Fig. 2(b).

DC characteristics

The dc characteristics of a GaAs MSM photodetector is shown in Fig. 3. The dark current of photodetector is typically 40 nA for a device area of $15 \mu\text{m} \times 15 \mu\text{m}$, and is determined by the properties of GaAs layer. The

Fabrication steps

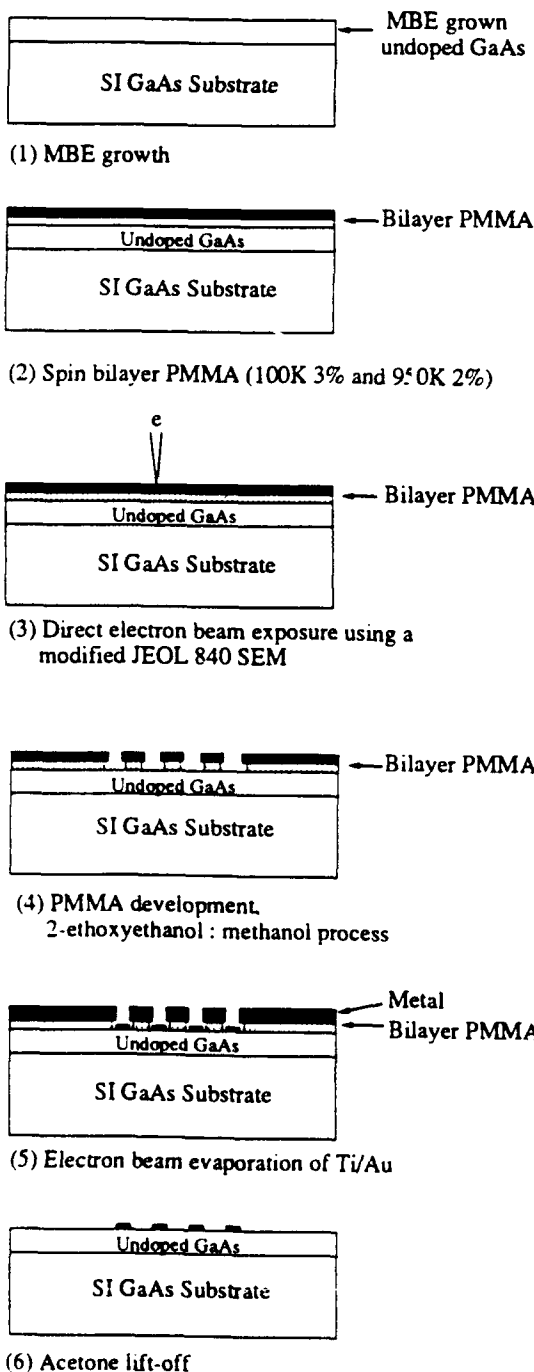


Figure 1. Basic steps for fabricating sub-100-nm finger spacing and width MSM photodetectors

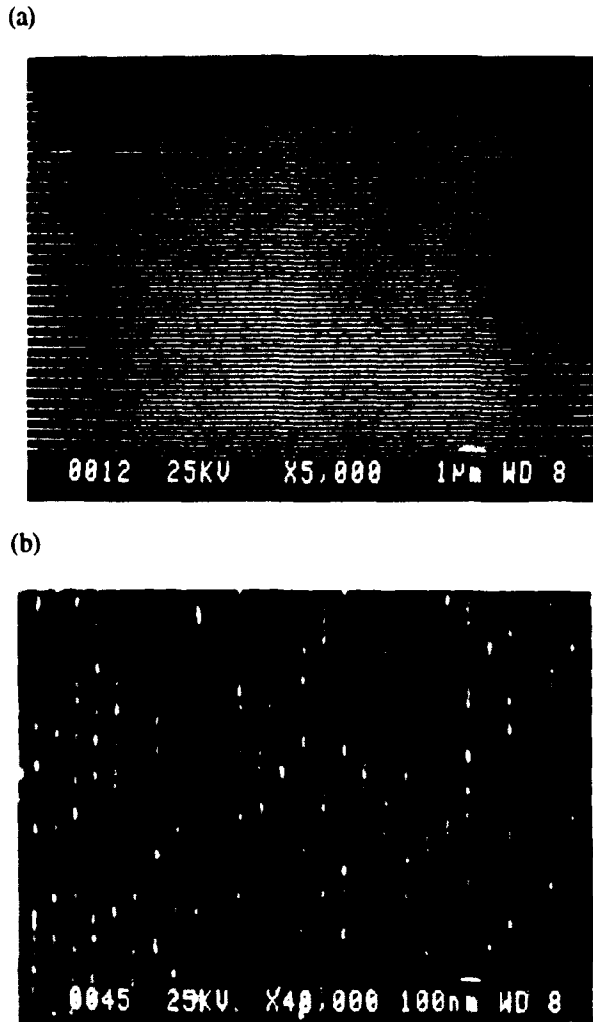


Figure 2. Scanning electron micrographs of GaAs MSM photodetectors of (a) finger spacing and width 160 nm and 40 nm, total detection area $14.5 \mu\text{m} \times 15 \mu\text{m}$, and (b) 70 nm wide Ti/Au lines with 30 nm spacing on GaAs.

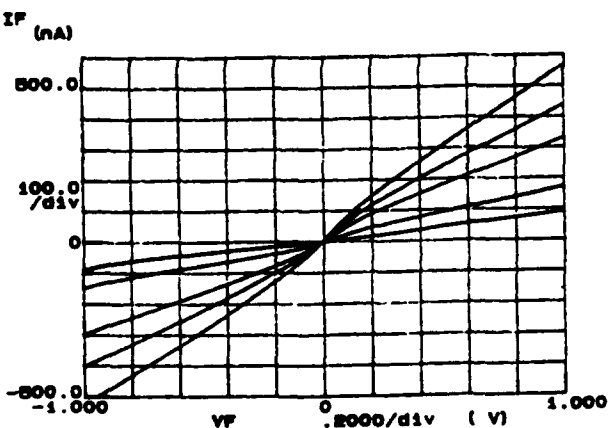


Figure 3. Current - voltage characteristics of an MSM photodetector for different light intensities. Current is 100 nA/div and voltage 0.2 V/div.

sensitivity of the devices is about 0.2 A/W. A passivation layer can be coated onto the devices to prevent surface oxidation and minimize the light reflection, therefore improving the dark current and sensitivity. The I-V characteristics do not show saturation because of the surface recombination centers.

Theoretical analysis

A Monte-Carlo simulation program has been developed for calculation of electron transit time. Several assumptions were made in the simulation: (1) The optical pulse waveform is assumed to be a δ -function, and the illumination is spatially uniform over the whole device. (2) Electric field is one-dimensional and uniform in the semiconductor, which becomes inaccurate for the case that finger spacing smaller than the thickness of semiconductor layer and can be improved by introducing a two-dimensional analysis^[13]. (3) Electrons are not injected from metal into the semiconductor over the Schottky barrier. (4) Scatterings from phonons, electrons, and impurities are

characterized by a single scattering time constant, which is so chosen that it is self-consistent with the measured parameters (electron and hole mobilities) of GaAs sample.

Figure 4 shows the Monte-Carlo simulation of (a) the intrinsic current of photodetector and (b) the external current after introducing the parasitic capacitance. The parasitic capacitance of our devices was calculated using conformal mappings^[11], and the capacitance per finger length is $0.08 \text{ fF}/\mu\text{m}$ for an MSM photodetector with equal finger width and spacing. The slopes in the intrinsic current profile are due to the assumption that light is spatially uniformly illuminated over the whole devices, instead of only in the middle of two fingers as assumed by W.C. Koscielniak *et al* [6]. For a 30 nm finger-spacing MSM photodetector, the intrinsic response time is 0.3 ps, the external response time is 0.4 ps, and the cut-off frequency can be over 1 THz.

By reducing the finger spacing, the intrinsic response time decreases as shown in Fig. 5(a). But reducing finger spacing does not always lead to decreasing external response time, because of increasing of the parasitic capacitance which is determined by the ratio of finger width to finger spacing. If this ratio is reduced, so is the parasitic capacitance per finger length, leading to

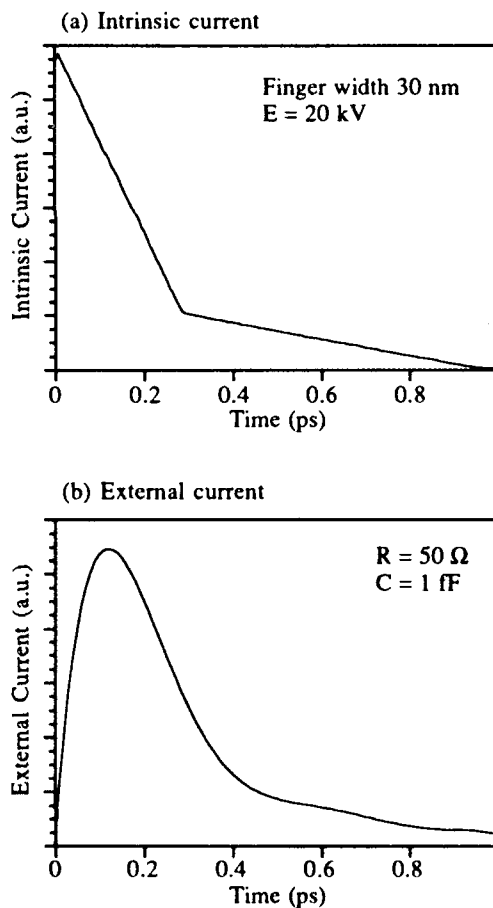


Figure 4. Monte-Carlo simulation results of the intrinsic and external current response for 30 nm finger spacing MSM photodetector, the electric field in GaAs is 20 kV/cm. The parasitic capacitance of 1 fF and the load resistance of 50Ω were used to calculate the external current.

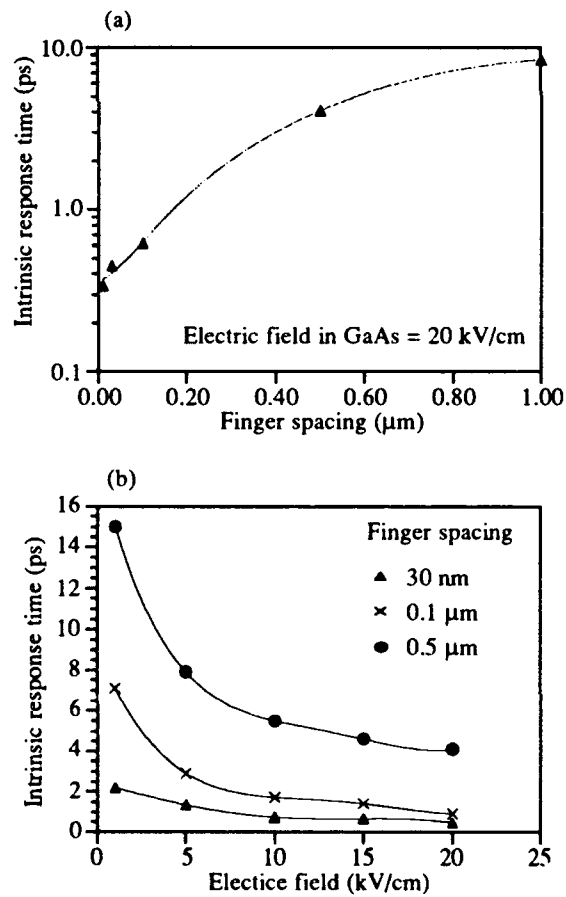


Figure 5. Intrinsic response time vs. (a) finger spacing and (b) average electric field.

a faster external response time. Therefore, a proper scaling of MSM photodetectors requires shrinking the finger spacing and the ratio of width to spacing at the same time.

The response time is strongly affected by biasing voltage as shown in Fig. 5(b). At low bias, photon-generated carriers will move at a small drift velocity and give rise to a long transit time. During simulation, the drift velocity is assumed to saturate at 2×10^7 cm/s. However, in sub-100-nm MSM photodetectors, electron velocity overshoot can occur which will lead to much shorter response time[15,16]. This unique feature of sub-100-nm finger spacing MSM photodetectors is not included in the simulation.

Conclusion

By using high resolution electron beam lithography, we fabricated MSM photodetectors with sub-100-nm finger spacing and width, which are, to our knowledge, the smallest ever reported. DC measurement showed low dark current and high sensitivity. An autocorrelation technique[14] is being used to study the high-speed performance. The Monte-Carlo simulation showed that the sub-picosecond response time can be achieved as the finger spacing shrinks below 100 nm. The parasitic elements will become very important to high speed operation. By optimizing the device structure, however, one can minimize the effects caused by parasitic elements to achieve the sub-picosecond response time. For the 30 nm finger spacing and finger width MSM photo-detector, the simulated intrinsic response time is 0.3 ps, but the actual time can be even shorter, because of velocity overshoot. The external response time of the 30 nm spacing device is 0.4 ps, and the cut-off frequency is over 1 THz.

Acknowledgment

We thank Y. Wang and J.P. Hu for assistance in processing, and J.S. Harris, Jr. for MBE wafers. The work is partly supported by Army Research Office under Contract No. DAAL03-90-0058, and a Packard Fellowship.

References

1. M. Ito and O. Wada, "Low dark current GaAs metal-semiconductor-metal (MSM) photodiodes using WSi_x contacts," *IEEE J. Quantum Electronics*, QE-22, 1073-1077(1986)
2. G.K. Chang, H. Schumacher, R.F. Leheny, "On-chip characteristics of fully integrated photo-receivers using high-yield ion-implanted GaAs IC technology," in *GaAs IC Symposium*(1987), p.57-60
3. Ch.S. Harder, B. van Zeghbroeck, H. Meier, W. Patrick and P. Vettiger, "5.2-GHz bandwidth monolithic GaAs optoelectronic receiver," *IEEE Electron Device Lett.*, EDL-9, 171-173(1988)
4. N. Yamanaka and T. Takada, "A 1.5 Gbit/s GaAs four-channel selector LSI with monolithically integrated newly structured GaAs ohmic contact MSM photodetector and laser driver," *IEEE Photonics Technology Lett.*, Vol.1, 310-312(1989)
5. Ch.S. Harder, B.J. van Zeghbroeck, M.P. Kesler, H.P. Meier, P. Vettiger, D.J. Webb and P. Wolf, "High-speed GaAs/AlGaAs optoelectronic devices for computer application," *IBM J. Res. Develop.*, Vol.34, 568-583(1990)
6. W.C. Koscielniak, J.L. Pelouard, M.A. Littlejohn, "Dynamic behavior of photocarriers in a GaAs metal-semiconductor-metal photodetector with sub-half micron electrode pattern," *Appl. Phys. Lett.*, 54, 567-569(1989)
7. M. Lambstroff, J. Kuhl, M. Klingenstein, C. Moglesteue, J. Rosenzweig, A. Axmann, J. Schneider, H. Leier and A. Forchel, "Direct observation of the electron and hole contributions in the impulse response of a metal-semiconductor-metal Schottky diode," in *Ultrafast Phenomena VII* (Monterey, CA, 1990), p.291-293
8. K. Nakajima, T. Iida, K.-I. Sugimoto, H. Kan and Y. Mizushima, "Properties and design theory of ultrafast GaAs metal-semiconductor-metal photodetector with symmetrical Schottky contacts," *IEEE Trans. Electron Devices*, ED-37, 31-35(1990)
9. W.C. Koscielniak, R.M. Kolbas, M.A. Littlejohn, "Performance of a near-infrared GaAs metal-semiconductor-metal (MSM) photodetector with islands," *IEEE Electron Device Lett.*, EDL-9, 485-487(1988)
10. B.J. van Zeghbroeck, W. Patrick, J.M. Halbout and P. Vettiger, "105-GHz bandwidth metal-semiconductor-metal photodiode," *IEEE Electron Device Lett.*, EDL-9, 527-529(1988)
11. Y.C. Kim and R.A. Moore, "Properties of alternately charged coplanar parallel strips by conformal mappings," *IEEE Trans. Electron Devices*, ED-15, 173-180(1968)
12. S.Y. Chou and P.B. Fischer, "Double 15-nm-wide metal gates 10 nm apart and 70 nm thick on GaAs," *J. Vac. Sci. Technol. B8*, 1919-1922(1990)
13. R.L. Peterson, "Numerical study of currents and fields in a photoconductive detector," *IEEE J. Quantum Electronics*, QE-23, 1185-1192(1987)
14. D.H. Auston, A.M. Johnson, P.R. Smith, J.C. Bean, "Picosecond optoelectronic detection, sampling and correlation measurements in amorphous semiconductors," *Appl. Phys. Lett.*, 37, 371-373 (1980)
15. J.G. Ruth, "Electron dynamics in short channel field-effect transistors," *IEEE Trans. Electron Devices*, ED-19, 652-654(1972)
16. S.Y. Chou, D.A. Antoniadis and H.I. Smith, "Observation of electron velocity overshoot in sub-100-nm-channel MOSFET's in Silicon," *IEEE Electron Device Lett.*, EDL-6, 665-667(1985)

2.0 ps GaAs Monolithic Photodiode and All-Electronic Sampler

E. Ozbay, K. D. Li, and D. M. Bloom

E. L. Ginzton Laboratory, Stanford University, Stanford, California 94305

Abstract

An ultrafast GaAs Schottky photodiode is monolithically integrated with an all-electronic sampler. The high-speed photodiode/electronic-sampling circuit has a temporal response of 2.0 psec corresponding to a 3-dB bandwidth of 150 GHz. The photodiode has an external quantum efficiency of 33%. This is the highest speed photodiode ever reported.

Introduction

High-speed photodetectors play an important role in optical communication and measurement systems. Photodetectors are made from many different materials, but only GaAs and InGaAs devices have been used as high-speed detectors. GaAs devices are sensitive only for wavelengths shorter than 890 nm. For longer wavelength high-speed applications, InGaAs photodetectors are used. S.Y. Wang and D.M. Bloom [1] were the first to demonstrate a GaAs photodiode with a 3-dB bandwidth exceeding 100 GHz and a temporal response of 5.4 psec. Later, Parker et al. [2] succeeded in achieving up to 110 GHz performance. For InGaAs photodetectors, Wey et al. reported a 3.8 psec FWHM corresponding to a bandwidth of 70 GHz [3]. All these results have been limited by their measurement techniques. The speed of the actual device had to be indirectly determined by a deconvolution of the system response from the measured data.

In order to overcome these measurement problems, we have pursued a monolithic approach. A GaAs based all-electronic sampler is monolithically fabricated with a high-speed Schottky photodiode. Without deconvolution, we are able to measure a temporal response of 2.0 psec FWHM, corresponding to a 3-dB bandwidth of 150 GHz.

Photodiode and Sampler Design

Because the fabrication technologies for 290 GHz bandwidth GaAs samplers [4] and 100 GHz Schottky photodiodes are very similar, it is a simple step to combine the two devices. Using the same process technology, we designed our device to incorporate the photodiode, sampler and strobe nonlinear transmission line (NLTL) on the same chip. Our samplers were fabricated on MBE-grown GaAs with a $0.3 \mu\text{m}$ thick N^- active layer ($1.2 \times 10^{17} \text{ cm}^{-3}$ doping) on top of a $0.8 \mu\text{m}$ N^+ highly conductive layer ($3 \times 10^{18} \text{ cm}^{-3}$ doping).

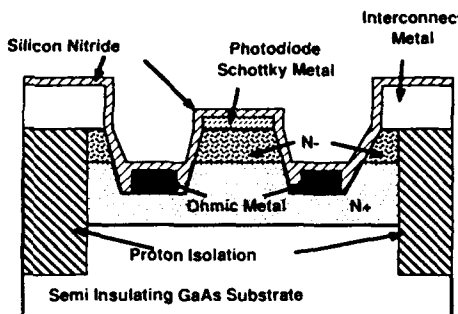


Figure 1. Diagram showing the cross section of the $5 \times 5 \mu\text{m}^2$ semi-transparent Schottky photodiode.

Photodiodes were then fabricated by using the top N⁻ layer as the depletion region. The relatively heavy-doping of this layer results in a punch-through voltage of 6.7 V. This large punch-through voltage enables us to vary the thickness of the photoactive region by simply changing the bias voltage.

A cross section of our Schottky photodiode is shown in Fig. 1. First, ohmic contacts to the N⁺ layer are formed by a recess etch through the 0.3 μm N⁻ layer followed by a self-aligned Au/Ge/Ti liftoff and a rapid thermal anneal. Next, proton implantation is used to define our active regions as well as to convert the rest of the epilayers to semi-insulating material. 100 Angstroms of gold are then deposited over the photoactive region to make the semi-transparent Schottky contact. This last step is the only additional photolithography step that is needed for monolithic integration of the sampler and photodiode. Finally, interconnect metal and silicon nitride are deposited. We chose the thickness of the silicon nitride layer to act as an anti-reflection coating for the Schottky photodiode.

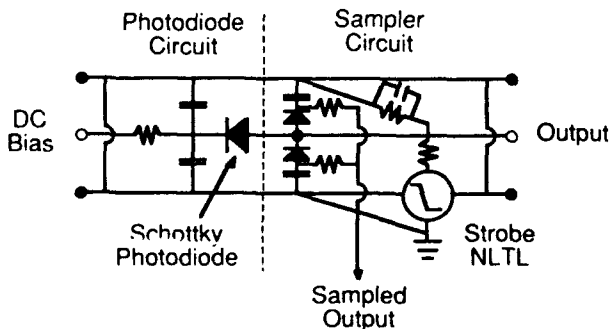


Figure 2. Circuit schematic of the photodiode, sampler and nonlinear transmission line (NLTL) strobe.

The circuit schematic of the monolithic photodiode/sampler is shown in Fig. 2. The output of the photodiode is connected to the sampler through a coplanar transmission line. The step-like waveform produced by the NLTL strobe is differentiated by the shorted transmission lines, resulting in a voltage pulse across the sampler diodes. This turns on the sampling diodes for the duration of this electrical pulse and enables the sampling capacitors to sample the photodiode signal on the transmission line. The sampled signal is then filtered out by using resistors. The photodiode signal which propagates further on the transmission line can be either terminated by a 50 ohm resistor or extracted through bond wires or microwave probes.

High Frequency Measurements

Pulses from a Spectra-Physics Nd: YAG modelocked laser were compressed in a fiber-grating compressor and frequency-doubled in a KTP crystal before they were used to excite our photodiode/sampler circuit. The laser was modelocked at 82.16 MHz and produced 50 psec FWHM pulses. After compression, the pulse duration was 1.6 psec, producing 1.1 psec durations at 532 nm. The optical pulses then were focused on the photodiode. Sampling of the photodiode was done at the 50th harmonic of the modelocker frequency with a 10 Hz offset. This oversampling reduced the sampler output by a factor of 50. A buffer amplifier was used at the output of the sampler to increase its IF bandwidth. The resulting equivalent time waveform had a period of 100 msec which corresponded to 242 psec in real time.

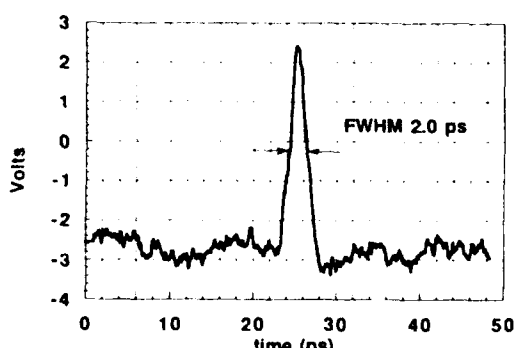


Figure 3. Electronically sampled photodiode output.

The sampled output of the photodiode signal is shown in Fig. 3. By changing the reverse-bias voltage, we found the minimum device response, or for our photodiode layout, its optimum depletion width, at 4.5 V. This corresponds to a $0.25 \mu\text{m}$ depletion region. At this bias voltage, we measured 2.0 psec FWHM pulses. This is a direct measurement from the sampler. It corresponds to a total system response which includes contributions from the photodiode impulse response, the sampler aperture time, the laser pulse duration, the laser timing jitter (< 600 fs), and the microwave synthesizer jitter.

The Fourier transform of the measured output is shown in Fig. 4. The overall system response has a 3-dB bandwidth of 150 GHz. We measured a responsivity of 0.15 A/W which corresponds to an external quantum efficiency of 33% at 532 nm (Fig. 5). Such high

efficiency indicates an effective AR coating. The typical operating average photocurrent while using the sampler was kept below $2 \mu\text{A}$ which corresponds to a peak current density of $4.8 \times 10^4 \text{ A/cm}^2$ or a peak voltage of 0.6 V into a 50 ohm load.

Conclusion

We have fabricated a monolithic photodiode/sampler. The total response of the system was measured to have a FWHM of 2.0 psec and a 3-dB bandwidth of 150 GHz. The external quantum efficiency is found to be 33%. To our knowledge, this device is the fastest photodetector.

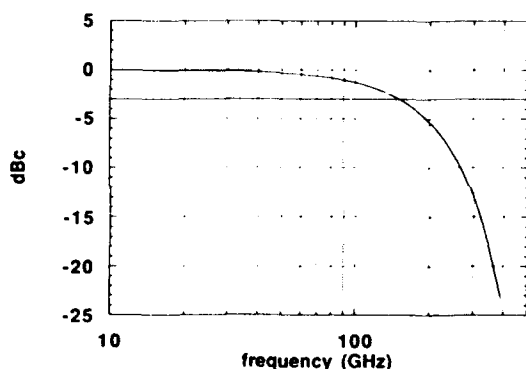


Figure 4. Fourier transform of the data shown in Fig. 3.

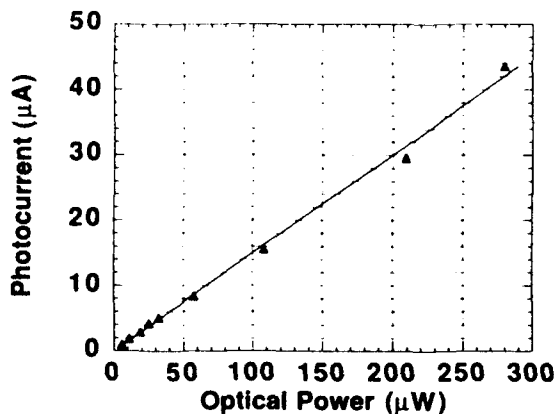


Figure 5. Measured responsivity of the photodiode.

Acknowledgments

The authors would like to thank Julie Sheridan for experimental help, and Pauline Prather for her packaging expertise. K.D. Li would like to acknowledge an AT&T Bell Laboratories GRPW grant and a Hertz fellowship.

References

1. S.Y. Wang, D.M. Bloom, "100 GHz Bandwidth Planar GaAs Schottky Photodiode," *Electron. Lett.* **19**, 554-555 (1983).
2. D.G. Parker, P.G. Say, A.M. Hanson, and W. Sibbett, "110 GHz High-Efficiency Photodiodes Fabricated from Indium Tin Oxide/GaAs," *Electron. Lett.* **22**, 1266-1267 (1989).
3. Y.G. Wey, M. Kamegawa, A. Mar, K.J. Williams, K. Giboney, D.L. Crawford, J.E. Bowers, and M.J. Rodwell, "Hybrid Integration of an InGaAs/InP PIN Photodiode with an Ultrafast Sampling Circuit," PD12-1 - PD12-4 (Optical Fiber Conference, 1991).
4. R.A. Marsland, C.J. Madden, D.W. Van Der Weide, M.S. Shakouri, and D.M. Bloom, "Monolithic Integrated Circuits for MM-Wave Instrumentation," in *Technical Digest of the GaAs IC Symposium* (1990).

Picosecond GaAs Photodetector Monolithically Integrated with a High-Speed Sampling Circuit

Masayuki Kamegawa,* K. Giboney, J. Karin, S. Allen, M. Case, R. Yu, M. J. W. Rodwell, and J. E. Bowers

*Department of Electrical and Computer Engineering,
University of California at Santa Barbara, Santa Barbara, California 93106*

Abstract

We have fabricated an optoelectronic sampling circuit for direct measurement of picosecond optical waveforms. The monolithic device incorporates a GaAs Schottky photodetector and a high-speed sampling circuit gated by a nonlinear transmission line strobe pulse generator. Excited by an 850 nm modellocked dye laser, a 5.6 ps FWHM impulse response is measured; we estimate a deconvolved impulse response of approximately 4.5 ps FWHM.

Introduction

Photodetectors are fundamental components for wideband optical instrumentation. In conjunction with sampling oscilloscopes, high speed photodetectors provide measurements of optical waveforms occurring in multi-GigaBaud optical transmission systems, picosecond mode-locked lasers, and picosecond optical and optoelectronic devices. The measurement bandwidth is limited by the 50 GHz bandwidth of commercially-available oscilloscopes, and by the parasitic responses of the photodetector package and connectors. Because of this limited bandwidth, the pulse durations of picosecond mode-locked lasers are instead determined through measurements of the laser second-harmonic intensity autocorrelation; but pulse shapes cannot be determined from autocorrelations, and more general optical signals (e.g. multiple pulses, sinusoidal or pulse-code modulation) cannot be measured.

The fabrication processes and device geometries required for 100 GHz Schottky-barrier GaAs photo-

todetectors [1,2,3] and recently-reported \approx 275 GHz-bandwidth diode sampling circuits [4,5] are similar. Adding to the 3-mask sampling circuit fabrication sequence [4] a single process step for semitransparent Schottky contacts, we have fabricated an optoelectronic sampling circuit consisting of a GaAs Schottky photodetector integrated with a high speed sampling bridge. With a measured 5.6 ps full-width-at-half-maximum (FWHM) impulse response, the device permits direct measurement of picosecond optical waveforms.

Circuit Description

The optoelectronic sampling circuit (Fig. 1) combines a photodetector (D_3) and a diode sampling circuit similar to that reported by Yu. et. al. [4]. A nonlinear transmission line (NLTL) [6] compresses an input strobe signal to \approx 1.5 ps falltime step-function. The strobe signal is then passed through a differentiating network, generating both positive and negative impulses which gate sampling diodes (D_1) and (D_2). The photodetector (D_3) is connected to the sampling circuit input through a section of 40Ω coplanar waveguide (CPW). This CPW is terminated at the sampling circuit input by 80Ω resistors (R_3) and (R_4); CPW source termination resistors (R_1) and (R_2), also 80Ω , provide a near-zero photodetector source reflection coefficient, suppressing secondary reflection of any small pulse reflection from the sampling circuit. The low (20Ω design value) photodetector load resistance increases the system bandwidth. During the sampling aperture time, the complementary strobe impulses drive the sampling diodes into forward bias, and the photocurrent signal partially charges the coupling capacitors,

*On leave from Shimadzu corporation, Kyoto, Japan.

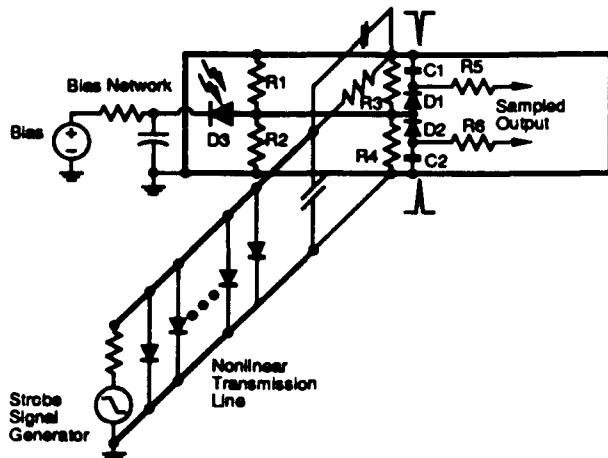


Figure 1: Schematic diagram of sampling circuit with photodiode.

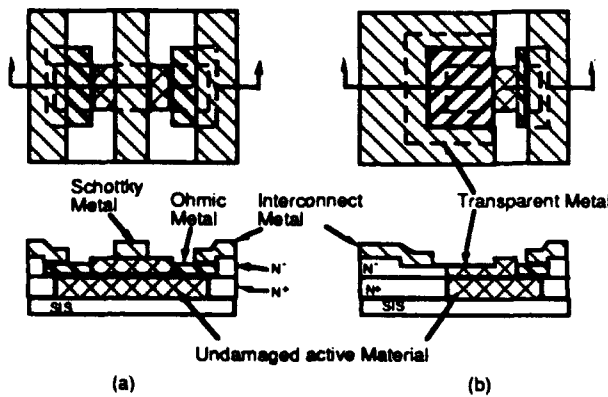


Figure 2: Structural diagrams of the hyperabrupt Schottky diodes used in the sampling circuit and NLTL, (a), and of the semitransparent Schottky photodetector, (b).

(C_1) and (C_2). The resulting voltage change is coupled to the sampled (IF) output through the isolation resistors, (R_5) and (R_6). A photodiode bias network is also integrated on the wafer. To simplify processing, instead of using thin-film dielectric capacitors, all capacitors are implemented using reverse-biased Schottky diodes.

Device Fabrication

Circuit fabrication requires hyperabrupt Schottky contacts (Fig. 2a) for the sampling circuit (D_1 , D_2) and NLTL, and semitransparent Schottky contacts with thinner N^- active layers for the top-illuminated photodetector (Fig. 2b). Starting with a semi-insulating GaAs substrate, a heavily doped

($6 \times 10^{18} \text{ cm}^{-3}$, $1\mu\text{m}$ thick) N^+ layer is grown by molecular beam epitaxy. This serves as the diode cathode connection. A surface N^- active layer (425 nm thick), with an exponentially-graded hyper-abrupt doping profile ($6 \times 10^{18} \text{ cm}^{-3}$ surface doping, 225 nm grading constant), is then grown. Ohmic contacts to the N^+ layer are formed by a $0.5\mu\text{m}$ recess etch through the N^- layer, a self-aligned AuGe/Ni/Au liftoff, and a subsequent rapid thermal anneal. Measured contact resistance and N^+ layer sheet resistance are $30\Omega\cdot\mu\text{m}$ and 9Ω per square, both larger than design values ($20\Omega\cdot\mu\text{m}$ and 7.5Ω per square) based upon previous process data [4]. Proton implantation converts the N^+ and N^- layers to semi-insulating material, determining diode junction areas and defining resistors in the N^+ layer. A dual-energy implant, at 180 keV ($1.7 \times 10^{15} \text{ cm}^{-2}$) and 110 keV ($4 \times 10^{14} \text{ cm}^{-2}$), is used to penetrate the combined N^+ and N^- layers. During implantation, the diode regions and resistors are protected by a $1.6\mu\text{m}$ Au on polyimide mask.

In the photodetector, reducing the depleted N^- layer thickness decreases the carrier transit times but increases the detector capacitance. For a given detector junction area and given parasitic and load resistances, there is an optimum N^- layer thickness (approximately 150 nm for a $5\mu\text{m} \times 5\mu\text{m}$ junction) which optimizes the detector bandwidth. In a single self-aligned step, the photodiode region is therefore recess etched to leave a 150 nm thick N^- layer before deposition and liftoff of a 10 nm Ti/Pt semi-transparent Schottky contact. The Ti/Pt contact has 20% optical transmissivity and 49Ω per square sheet resistivity. The active photodiode region is the $5\mu\text{m} \times 5\mu\text{m}$ area where the semitransparent metal overlaps the unimplanted N^- material; the semi-transparent metal and ohmic contact are separated by $3\mu\text{m}$. Completing the process, interconnections and Schottky contacts for the sampling circuit and NLTL diodes are formed with a $1.1\mu\text{m}$ Ti/Pt/Au liftoff.

Results

The devices were tested on a microwave wafer probe station. An 80 MHz pulse train from a mode-locked $\lambda = 850$ nm dye laser is focused on the photodetector through the objective lens of the probe station microscope. The strobe signal input, the photodiode bias terminal, and the two IF outputs are connected with CPW wafer probes.

A complete sampling oscilloscope consists of a sampling circuit, a low-noise and high-input-impedance IF preamplifier, a display system, and a triggered timebase which provides the sampling cir-

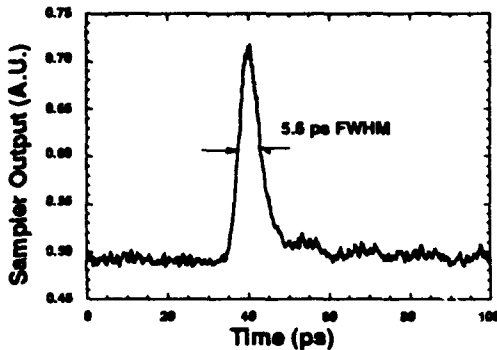


Figure 3: Measured impulse response of a GaAs Schottky photodiode with sampler to a 1 ps laser pulse at a wavelength of 850 nm.

cuit with a strobe pulse synchronized to the signal under test. The falltime of the strobe signal generated by the timebase must be less than the NLTL maximum falltime compression [6], 47 ps in this implementation.

To test the optoelectronic sampling circuits without construction of the timebase and IF preamplifier, the strobe NLTL is instead driven directly with a microwave synthesizer, and the IF output is amplified by a lock-in amplifier. Because the NLTL requires a strobe input with falltime significantly less than 47 ps, the synthesizer frequency must be above 7 GHz. The strobe frequency was set at 9,039,999,998 Hz, a frequency 2 Hz below the 113th harmonic of the 80 MHz laser pulse repetition rate, which results in a 2 Hz sampled (IF) output. The sampling rate is 113 times the 80 MHz laser pulse repetition rate, corresponding to 113 : 1 oversampling, and resulting in a 41 dB reduction in the sampled amplitude. The lock-in amplifier serves to recover the resulting low-amplitude sampled signal levels and requires mechanical chopping of the laser beam. With 120 μ W average laser power and 0 V detector bias, we measure a clean 5.6 ps FWHM impulse response (Fig. 3) without significant ringing. Of six optoelectronic sampling circuits fabricated on the wafer, all function and all show similar impulse responses, indicating good process controllability and high yield. The measured detector quantum efficiency is 1%, close to the predicted 0.9%.

Analysis

The measured 5.6 ps FWHM impulse response is limited by five mechanisms; the sampling circuit aperture time, the photodiode RC time constant and carrier transit time, and the dye laser pulse

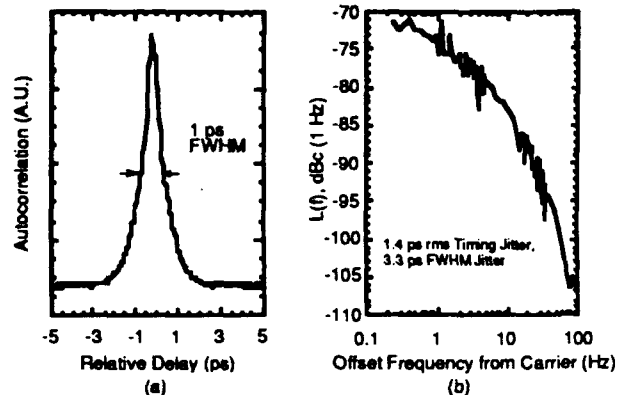


Figure 4: (a) Dye laser autocorrelation function, (b) Dye laser phase noise.

width and timing jitter. An estimated 2 ps sampling circuit aperture time was determined through measurement by the sampling circuit of the risetime of an on-wafer NLTL test pulse generator. This is substantially greater than that measured on earlier devices [4] processed on wafers with lower N^+ sheet and ohmic contact resistivities.

From measured sheet and contact resistivities and measured capacitances of large-area test structures, we calculate a 23 Ω photodiode series resistance and a 21 fF photodiode depletion capacitance. The measured external termination resistance ($R_1||R_2||R_3||R_4$) is 32 Ω , 60% greater than the design value, and is shunted by an estimated 33 fF parasitic layout capacitance. The combined network of photodetector resistance, photodetector capacitance, termination resistance, and layout capacitance contributes a predicted impulse response of 2.1 ps FWHM. Photodetector carrier transit time [8], as calculated from the 150 nm depletion layer thickness and a 6×10^6 cm/s saturation hole velocity [9], contributes 1.25 ps FWHM to the impulse response. Since the N^- layer is almost fully depleted at zero bias, no significant improvement in pulse response is observed when the photodiode reverse bias is increased.

Dye laser performance is shown in Fig. 4. The laser intensity autocorrelation (Fig. 4,a) is 1 ps FWHM, corresponding to a ≈ 0.7 ps FWHM uncorrelated pulse width, while phase noise measurements (Fig. 4,b) [7] indicate the presence of $\sigma_J = 1.4$ ps r.m.s timing jitter. With the assumption of a Gaussian probability distribution for this jitter, the peak-peak laser timing deviations at the 50% probability points will be $\Delta T_{FWHM} = 2.36$ ps, $\sigma_J = 3.3$ ps, and contribute 3.3 ps FWHM to the measured impulse response. In confirmation of the phase noise

measurements, successive scans of the sampled signal are observed to fluctuate in timing by 3 – 4 ps.

Using a rudimentary sum-of-squares convolution, and based upon the measured sampling circuit aperture time and calculated photodetector transit time and photodetector RC charging time, a 3.1 ps FWHM impulse response is predicted for the optoelectronic sampling circuit. Based upon the measured 5.6 ps FWHM response and the measured laser pulse width and phase noise, the measured impulse response of the optoelectronic sampling circuit after deconvolution is approximately 4.5 ps FWHM.

Feedback stabilization of the laser timing [7] will permit more accurate determination of the device's impulse response. With reduced photodetector geometries, improved circuit layouts eliminating parasitic layout capacitances, and with reduction in ohmic contact and N^+ sheet resistances (to previously-attained values), a 1.5 ps FWHM impulse response is attainable. Improved photodetector efficiency can also be attained through use of Indium Tin Oxide transparent Schottky contacts [2].

Conclusions

In summary, we have developed a monolithic GaAs optoelectronic sampling circuit for direct measurements of picosecond optical waveforms. Modulation waveforms in multi- GHz fiber-optic analog and PCM transmission systems can be directly measured. With attainable improvements in detector and circuit speed, the device can supplant autocorrelation and cross-correlation techniques for measurements of picosecond optical phenomena.

Acknowledgments: This work was supported by the DARPA Optoelectronics Technology Center (program number 8-442530-59106).

References

- [1] S.Y. Wang, D.M. Bloom, "100 GHz Bandwidth Planar GaAs Schottky Photodiode", Electronics Letters, Vol. 19, No. 14, 7 July 1983, pp. 554-555.
- [2] D.G. Parker, P.G. Say, A.M. Hanson and W. Sibbett, "110 GHz High- Efficiency Photodiodes Fabricated from Indium Tin Oxide/GaAs", Electronics Letters, 22 November 1989, pp. s66-s67.
- [3] B.J. VanZeghbroeck, W. Patrick, J.-M. Halbout, and P. Vettiger, "105-GHz bandwidth metal-semiconductor-metal photodiode", IEEE Electron Device Letters, Vol. 9, No. 10, Oct. 1988, pp. 527-529.
- [4] R. Yu, M. Case, M. Kamegawa, M. Sandram, M.J.W. Rodwell and A. Gossard, "275 GHz 3 mask Integrated Sampling Circuit". Electronics Letters, Vol. 26, No. 13, 21 June 1990, pp. 949-951.
- [5] R.A. Marsland, C.J. Madden, D.W. Van Der Weide, M.S. Shakouri, and D.M. Bloom, "Monolithic Integrated Circuits for MM-Wave Instrumentation", in Technical Digest, 1990 GaAs IC Symposium, Oct. 7-10, New Orleans, La.
- [6] C.J. Madden, M.J.W. Rodwell, R.A. Marsland, Y.C. Pao, and D.M. Bloom, "Generation of 3.5 ps Falltime Shock-waves on a Monolithic GaAs Nonlinear Transmission Line," IEEE Electron Device Letters, Vol. 9, No. 6, pp. 303-305, June, 1988.
- [7] M.J.W. Rodwell, D. M. Bloom, K.J. Weingarten "Subpicosecond Laser Timing Stabilization". IEEE J. Quantum Electron., vol. QE-25, pp. 817-827, 1989.
- [8] G. Lucovsky, R.F. Schwarz, and R.B. Emmons, "Transit-Time Considerations in p-i-n Diodes", Journal of Applied Physics, Vol. 35, No. 3, March 1964, pp. 622-628.
- [9] V. L. Dalal, "Hole Velocity in p-GaAs", Applied Physics Letters, Vol. 16, No. 12, 15 June 1970, pp. 489-491.

High-Speed Transistors and Electronics

75-GHz SiGe Heterojunction Bipolar Transistors: GaAs Performance in Si Technology?

J. M. C. Stork, J. H. Comfort, G. L. Patton, E. F. Crabbé, and B. S. Meyerson

IBM T. J. Watson Research Center, P.O. Box 218, Yorktown Heights, New York 10598

Abstract

SiGe HBTs have demonstrated new device and circuit records, extending the speed of silicon bipolar devices closer to a regime dominated by GaAs and other compound semiconductor technologies. This paper gives a review of recent results and describes our present understanding in order to address the potential merits of SiGe HBTs as an extension to Si bipolar technology.

Device Performance

The record breaking cut-off frequency results of SiGe and Si epitaxial base transistors (cf. Figs. 1 and 2) demonstrates the performance potential of Si profile and SiGe bandgap engineering (1). As can be seen in Fig. 3, the combination of a thin epitaxial base and shallow polysilicon emitter technology allows sub 50 nm base widths with low base resistance and acceptable breakdown voltages. The base doping at the emitter-base and base-collector junctions is reduced to lower the electric field at the junction, and thus succeeds in improving the leakage and breakdown characteristics. The retrograded base profile at the emitter-base transition would degrade performance in Si-only devices, due to the reverse built-in field, retarding the electron flow. However, the Ge is used to overcome this profile induced field by grading the bandgap across the neutral base. The field induced by the bandgap grading of the Ge (see Fig. 4) increases the velocity of electrons through the base, reducing the base transit time component of the intrinsic profile delay according to (2)

$$\frac{\tau_b(\text{SiGe})}{\tau_b(\text{Si})} \simeq \frac{2kT}{\Delta E_{gG}} \left(1 - \frac{kT}{\Delta E_{gG}} \right) \quad (1)$$

where ΔE_{gG} is the bandgap grading across the heavily-doped portion of the neutral base profile. Figure 5 shows the calculated transit time components for a retrograde base profile, with and without SiGe. As a result of the simultaneous reduction in both base transit time and base-emitter junction capacitance, very high frequency response is obtained even at moderate current densities (see also the data in Fig. 1).

The Lightly Doped Collector has been shown (3) to improve the impact ionization breakdown of the base-collector junction without penalty on current density capability and cut-off frequency. As the electric field is more uniformly distributed across the junction region, the average velocity remains high, but the energy the carriers acquire from the field is reduced. An adequate description of the average energy can be obtained from the energy balance equation directly using the following simplifying assumptions (4): heat flow is neglected and kinetic energy is assumed to be negligible compared to the thermal energy. If it is further assumed that the energy relaxation length λ_w is constant, the second-order moment of the Boltzmann equation can be solved explicitly for the average energy as a convolution of the electric field and the exponential decay length λ_w as

$$W(x) - W_o = \frac{3}{5} q \int_0^x F(\xi) \exp \left\{ -\frac{(\xi - x)}{\lambda_w} \right\} dx \quad (2)$$

where F is the electric field and $W_o = (3/2)kT_o$ the energy at thermal equilibrium. Although the average energy is not a perfect representation of the energy of the hottest electrons responsible for impact

ionization, it gives an adequate prediction of the breakdown voltage as shown in Fig. 6. Because the maximum carrier energy is located deep inside the base-collector junction, the multiplication factor of Si and SiGe-base devices is essentially equal (cf. Fig. 7). Any difference in breakdown voltage is only due

Table 1

	Si	SiGe
$A_E(\mu\text{m}^2)$	0.6x4.3	0.6x4.3
$f_T(\text{GHz})$	29	50
$R_{bl}(\text{k}\Omega/\text{d})$	3.8	8
$R_{bx}(\Omega)$	60	60
$R_E(\Omega)$	16	8
$BV_{CEO}(\text{V})$	2.4	3.2
$BV_{CBO}(\text{V})$	11	11
$C_{CB,int}(\text{fF}/\mu\text{m}^2)$	1.7	1.6
$C_{CB,ext}(\text{fF}/\mu\text{m}^2)$	0.9	0.9
$C_{EB}(\text{fF}/\mu\text{m}^2)$	7.8	6.3

Table 1 (ref 5)
Summary of device parameters of circuit transistors

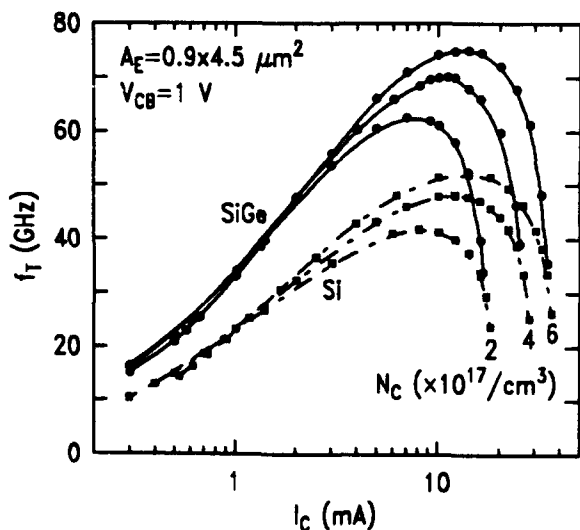


Figure 1 (ref 1)
Measured cut-off frequency versus collector current, for Si and SiGe devices, showing the dependence on collector doping level.

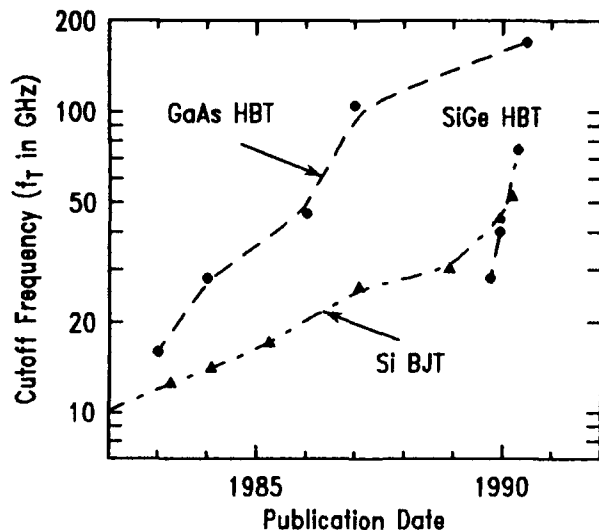


Figure 2
Reported cut-off frequency records in the past decade (at RT). A rapid increase in Si and SiGe performance is apparent.

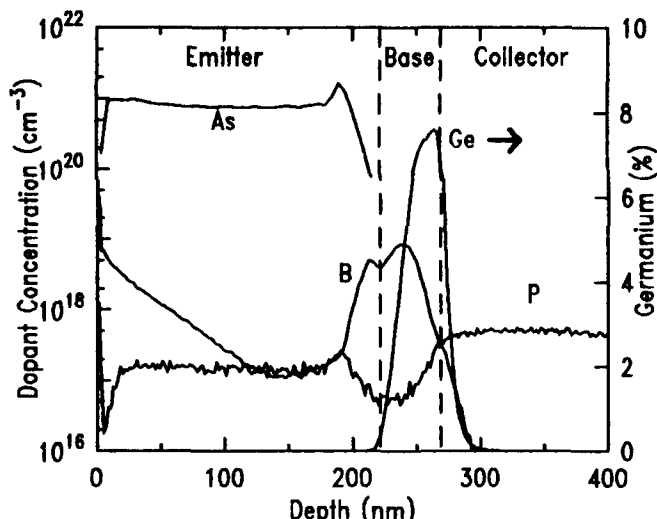


Figure 3 (ref 1)
SIMS profile for the SiGe-base transistors of Fig. 1. The Ge grading is positioned precisely in the most heavily doped region of the base to enhance the base transit time.

to the usually higher gain of the SiGe transistors. The net effect of reduced base transit time, nearly equal (BV_{cbo}) or better (BV_{ebo}) breakdown characteristics compared to Si-only devices, presents a significant paradigm shift of conventional breakdown-speed trade-off as shown in Fig 7.

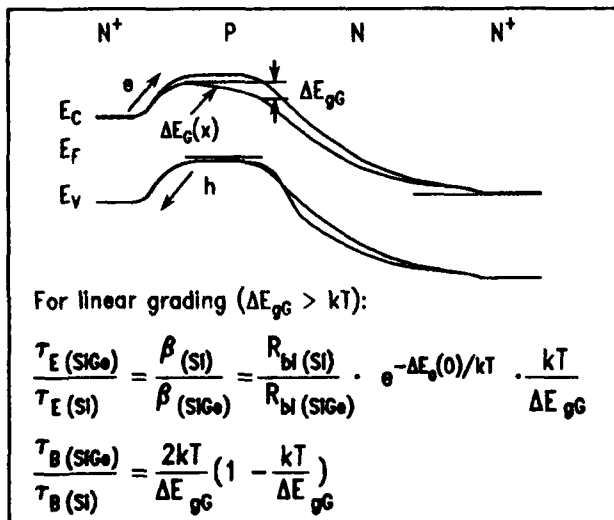


Figure 4 (ref 2)

Energy band diagram illustrating first-order design equations for graded-SiGe-base enhancements in gain and transit times.

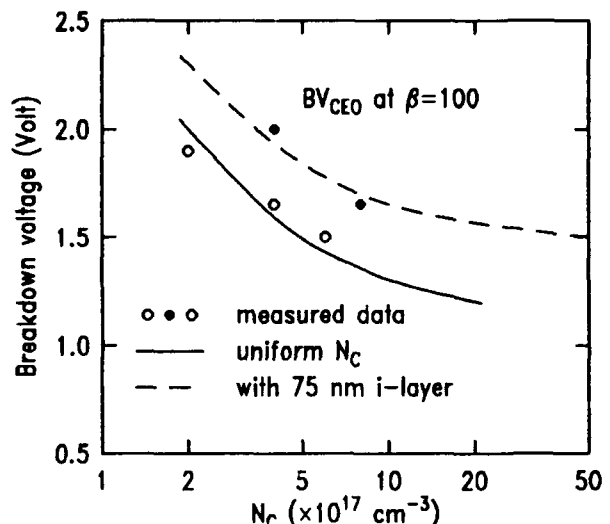


Figure 6 (ref 4)

Base-collector voltage at which the base current reverses as a function of collector doping. The insertion of an I-layer increases the breakdown voltage by 0.3-0.5 Volt.

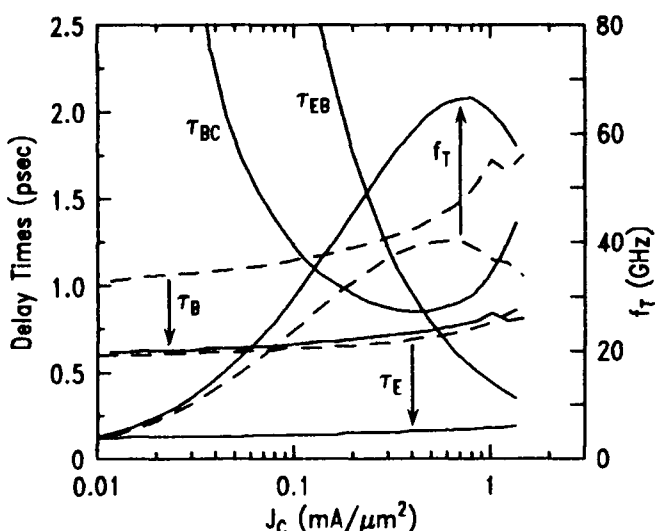


Figure 5 (ref 9)

Calculated transit time components for Si (dashed) and SiGe (solid) profiles showing reduction in both τ_e and τ_b due to the graded Ge profile.

Digital Circuit Performance

Recently, the first circuit results using self-aligned SiGe-base transistors (5 and 6) established new

world records (cf. Fig. 9) and demonstrated a 13% circuit speed improvement in a direct comparison with Si-base devices (cf. Fig. 10). The SiGe profile was designed to produce transistors with $f_T = 50$ GHz (50 % higher than the 30 GHz for Si) and keep the collector capacitance low for better circuit performance (see Table 1 for a summary of the Si and SiGe device characteristics). The following general relationship for the delay of a current switch (7) can be used to understand the device optimization trade-off's for circuit performance:

$$\tau_d \propto \sqrt{\frac{(2 \times R_b + R_L)(2 \times C_{bc} + C_L)}{2\pi f_T}} \quad (3)$$

where f_T , R_b , and C_{bc} are the cut-off frequency, base resistance, and collector-base capacitance respectively. For an ECL gate with emitter follower, $C_L = C_{bc} + C_{cs}$, and $R_L = V_s/I_s$, inversely proportional to the switching current.

At very high currents, $\tau_d \propto F_{max}$, which reaches from an estimated maximum of 33 GHz for Si to 45 GHz for SiGe devices (cf. Fig. 11). Improvements in F_{max} are achieved with self-alignment schemes to reduce C_{bc} and C_{cs} , and can be further reduced by designing the device layout for minimum base resistance, i.e. long, narrow emitter stripes. The corresponding required current does not allow for high levels of integration however.

Instead, much better efficiency is obtained when the capacitive term $R_L \times (C_L + 2 \times C_{bc})$ is approximately equal to the profile contribution $(1 + R_b \times I_s/V_s)/2\pi f_T$. It can easily be seen that higher f_T at the expense of high base resistance and/or collector capacitance has minimal impact on circuit performance. The measurements on unloaded ring oscillators support this conclusion as shown in Fig. 12.

Minimum parasitic capacitances are even more important to reduce the power-delay product at low current. In this regime the performance of the vertical doping profile is no longer dominated by the base and collector transit times, but rather the specific junction capacitance is key to reduce power and delay. As discussed above, for the same basewidth delay, lower base-emitter junction capacitance can be obtained, to further improve the speed of ECL digital circuits.

Other Applications

For analog or other applications not limited by power, the designer can use the additional degree of freedom of the Ge profile more liberally to match the circuit performance to the intrinsic transistor profile capabilities. As expected from Equation (1), the f_T cut-off frequency has been shown (8) to increase from 75 GHz at room temperature to 94 GHz at liquid nitrogen temperature (cf. Fig. 13). Note that the speed of the Si devices also increased at low temperature, albeit only at extremely high current density. This trade-off between speed and current density is a fundamental difference between the various material systems for device operation. As can be seen in Figs. 1 and 14, SiGe achieves higher speed than Si (but less than InGaAs based HBTs for example) for a given current density, while higher profile speed through conventional scaling always requires higher current density. Due to the fact that a thinner base demands higher base doping, the base-emitter capacitance per unit area is increased. Thus a higher current density is required before the capacitive junction charging time equals the shorter base transit time (cf. Fig. 5). Since the collector doping should be designed to support this current density, it too has to be raised. This in turn increases the base-collector capacitance, which hinders circuit speed (see Equation (3)). Another important factor for analog applications, namely current gain, can be controlled independent of the base doping:

$$\frac{\beta(Si)}{\beta(SiGe)} \simeq \frac{\rho_{bi}(Si)}{\rho_{bi}(SiGe)} e^{-\Delta E_{g(BE)}/kT} \frac{kT}{\Delta E_{gG}} \quad (4)$$

where $\Delta E_{g(BE)}$ is the bandgap reduction due to the Ge at the base-emitter depletion edge. This profile design flexibility allows for lower noise and higher Early voltage designs.

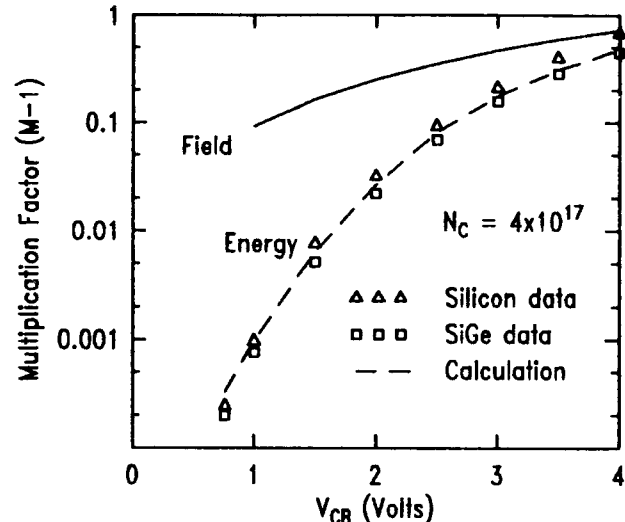


Figure 7 (ref 4)
Measured and calculated multiplication factors for Si and SiGe-base profiles using $\lambda = 80$ nm for the energy calculation.

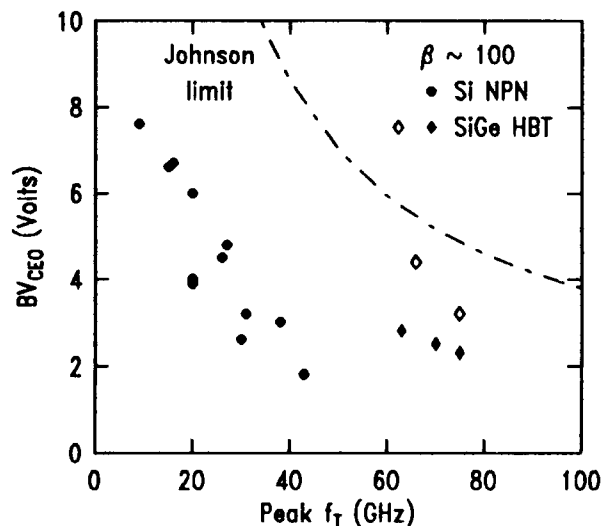


Figure 8 (ref 5)
Measured f_T and BV_{CEO} values illustrating the speed-breakdown trade-off for implanted and epitaxial Si base and SiGe base devices.

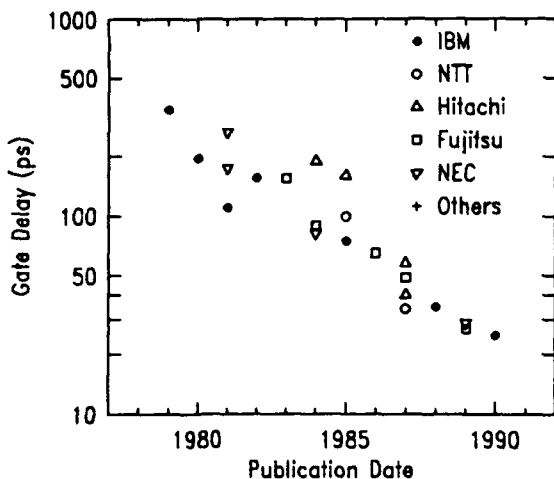


Figure 9
Reported unloaded ECL ring-oscillator speed records versus year, showing a doubling about every three years.

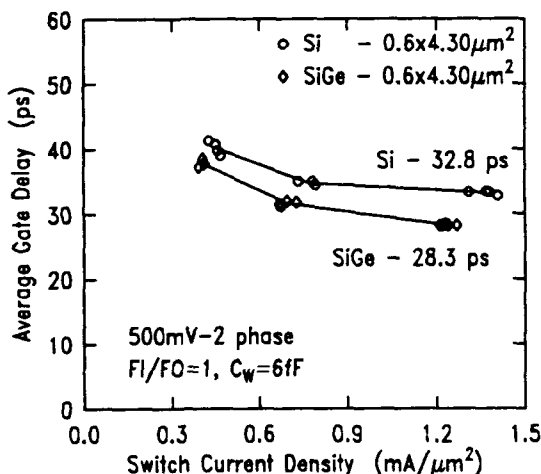


Figure 10 (ref 5)
Comparison of ECL delay of Si and SiGe transistors detailed in Table 1.

Discussion

The advantage of SiGe for profile design is that it provides an extra degree of freedom to work within the design constraints of base resistance, cut-off frequency, and breakdown/leakage (9), since the base transport time can be reduced without changing the doping profile. The additional flexibility of device optimization using Ge depends on the application. Digital ECL logic has probably the least leverage, but push-pull circuits are expected to benefit much more from high f_T transistors. On the other hand, it is clear that the even the intrinsic device potential of SiGe HBTs is not as great as that of, for example, AlGaAs-InGaAs HBTs, primarily because of the

Si-like electronic properties of low percentage SiGe alloys. On the other hand, it is indeed the compatibility with Si technology that makes SiGe technology so exciting: an extra degree of freedom is available to Si technology, allowing better device design optimization and making inroads in applications which are out of reach for pure Si, while capitalizing on the vast technology base of Si technology. However, the technology challenge of integrating strained epitaxial-base devices into exist-

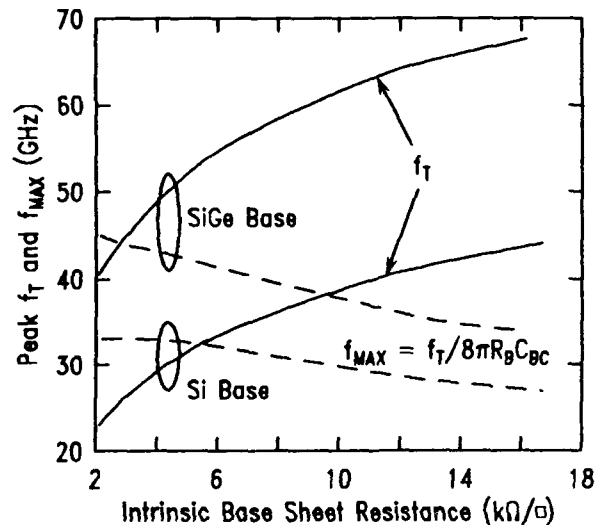


Figure 11 (ref 9)
Simulation showing f_T (solid lines) and f_{MAX} (dashed lines) dependence on zero bias intrinsic base resistance. The structure of the devices detailed in Table 1 was assumed.

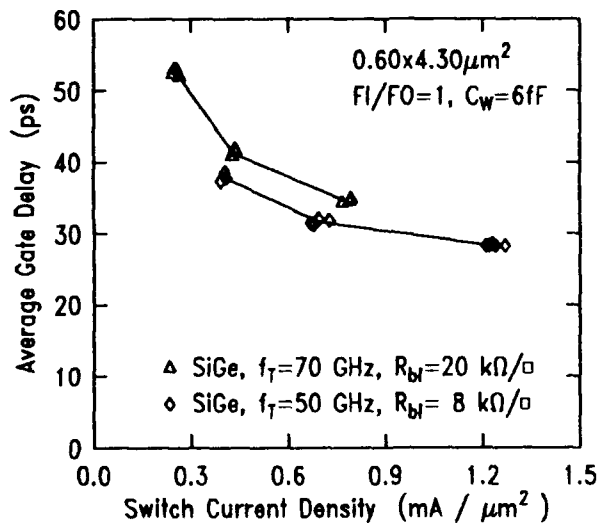


Figure 12
Comparison of ECL delay of "high" f_T - R_{bi} - C_{bc} and "low" f_T - R_{bi} - C_{bc} SiGe devices. The circuit performance with the higher f_T device is actually the slower of the two.

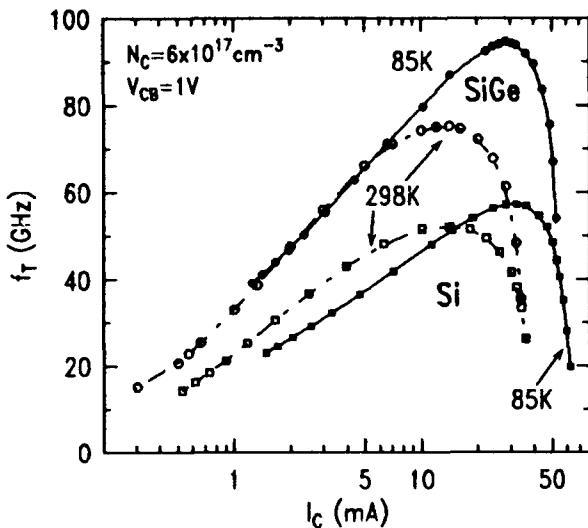


Figure 13 (ref 8)

Collector current dependence of f_T at 298K and 85K for Si and SiGe devices. In both cases, peak f_T and maximum current density increase with lower temperatures.

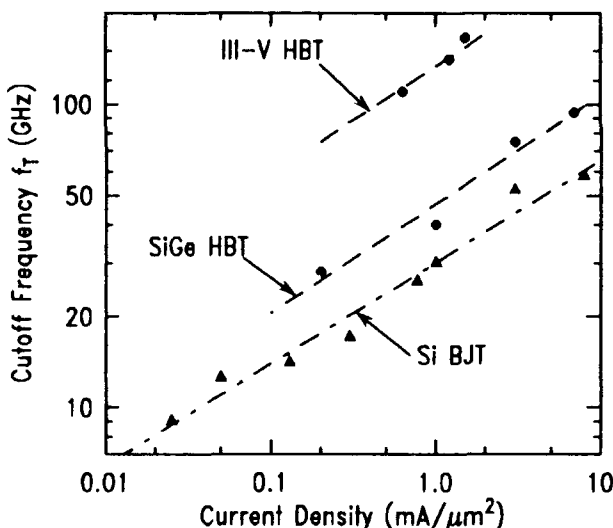


Figure 14

Reported record f_T versus current density comparing the intrinsic potential of III-V and SiGe HBTs with Si homojunction transistors.

ing processing techniques and achieving adequate control of all the critical parameters is an enormous engineering challenge.

References

1. G.L. Patton, J.H. Comfort, B.S. Meyerson, E.F. Crabbe, G.J. Scilla, E. deFresart, J.M.C.

Stork, J.Y.-C. Sun, D.L. Harame, and J.N. Burghartz, "63-75 GHz f_T SiGe-Base Heterojunction Bipolar Technology," in Technical Digest of 1990 VLSI Symposium, pp. 49-50.

2. J.M.C. Stork, G.L. Patton, E.F. Crabbe, D.L. Harame, B.S. Meyerson, S.S. Iyer, and E. Ganin, "Design Issues for SiGe Heterojunction Bipolar Transistors" in Proceedings of the 1989 BCTM, Sept 1989, pp. 57-64.
3. J.H. Comfort, E.F. Crabbe, G.L. Patton, J.M.C. Stork, J.Y.-C. Sun, and B.S. Meyerson, "Avalanche Multiplication Reduction in SiGe HBTs," 1990 Device Research Conference, June 1990, paper VI-A-3.
4. E.F. Crabbe, J.M.C. Stork, G. Baccarani, M.V. Fischetti, and S.E. Laux, "The Impact of Non-Equilibrium Transport on Breakdown and Transit Time in Bipolar Transistors," in IEDM Technical Digest., Dec 1990, pp. 463-466.
5. J.H. Comfort, G.L. Patton, J.D. Cressler, W. Lee, E.F. Crabbe, B.S. Meyerson, J.Y.-C. Sun, J.M.C. Stork, P.F. Lu, J.N. Burghartz, J. Warnock, K.A. Jenkins, K-Y. Toh, M.M. D'Agostino, and G.J. Scilla, "Profile Leverage in a Self-Aligned Epitaxial Si or SiGe Base Bipolar Technology," in IEDM Technical Digest, Dec 1990, pp. 21-24.
6. J.N. Burghartz, J.H. Comfort, G.L. Patton, J.D. Cressler, B.S. Meyerson, J.M.C. Stork, J.Y.-C. Sun, G.J. Scilla, J. Warnock, B.J. Ginsberg, K.A. Jenkins, K-Y. Toh, D.L. Harame, and S. Mader, "Sub-30ps ECL Circuits Using High- f_T Si and SiGe Epitaxial Base SEEW Transistors," in IEDM Technical Digest, Dec 1990, pp. 297-300.
7. J.M.C. Stork, "Bipolar Transistor Scaling for Minimum Switching Delay and Energy Dissipation," in IEDM Technical Digest, Dec 1988, pp. 550-553.
8. E.F. Crabbe, G.L. Patton, J.M.C. Stork, J.H. Comfort, B.S. Meyerson, and J.Y.-C. Sun, "Low Temperature Operation of Si and SiGe Bipolar Transistors," in IEDM Technical Digest, Dec 1990, pp. 17-20.
9. G.L. Patton, J.M.C. Stork, J.H. Comfort, E.F. Crabbe, B.S. Meyerson, D.L. Harame, and J.Y.-C. Sun, "SiGe-Base Heterojunction Bipolar Transistors: Physics and Design Issues," in IEDM Technical Digest, Dec 1990, pp. 13-16.

Recent Advances in Ultrafast High-Electron-Mobility Transistor Technology

Loi D. Nguyen

Hughes Research Laboratories, 3011 Malibu Canyon Road, Malibu, California 90265

INTRODUCTION

Recent advances in material growth and fabrication process have made possible the realization of a new class of ultra-fast High Electron Mobility Transistors (HEMTs) in the AlInAs/GaInAs material system (lattice-matched to InP). In the last three (3) years alone, through improvements in materials and shrinking of gate length, the speed of state-of-the-art AlInAs/GaInAs HEMTs has been increased at an astounding rate: from 80 GHz in 1987 to 250 GHz as of today [1-4].

Such a pace of progress, however, cannot be maintained indefinitely. As the gate length approaches the 0.1 μm regime, it becomes increasingly more difficult to improve the device speed by simply reducing the gate length. In this gate length regime, parasitic delays, such as drain delay (due to the extension of the drain depletion region) and capacitance charging time (gate pad and fringe), represent a large portion of the total delay and will ultimately limit the device extrinsic speed [5-7]. Evidences that support this claim are plenty and can be readily observed by plotting the f_T as a function of gate width [6] or gate length [8]. Due to parasitic delays, the f_T decreases with reducing gate width; and its rate of increase with reducing gate length diminishes as the gate length approaches 0 (see Fig. 1).

In order to further advance this technology, significant breakthroughs must be made in the following areas: (1) modeling of sub-0.1 μm (or nanometer) gate length HEMTs, (2) growth and characterization of pseudomorphic AlInAs/Ga_{1-x}In_xAs materials, and (3) nanofabrication. In the following, the present author will present a brief discussion on a number of key advances in each of these areas, as well as a projection for their pace of progress in the near future.

SCALING MODELS

In order to significantly improve the speed of state-of-the-art HEMTs, one must develop a thorough understanding and an accurate model for the scaling of gate length devices. As a minimum, such a model must take into account the effects of the gate pad and fringe capacitances, extension of the drain depletion region, and parasitic resistances (ideally, it should also be able to model the effects of the output conductance and feedback capacitance as well).

Although significant progress in this area has been made in the last two (2) years or so, we still do not have a complete model that can be used with a high degree of confidence. Presently, we only have partial models which can take into account some, but not all, of the parasitics. These models are capable of predicting the f_T with reasonable accuracy, at least down to the 0.1 μm regime [7, 9]. Such models are being evaluated at the author's

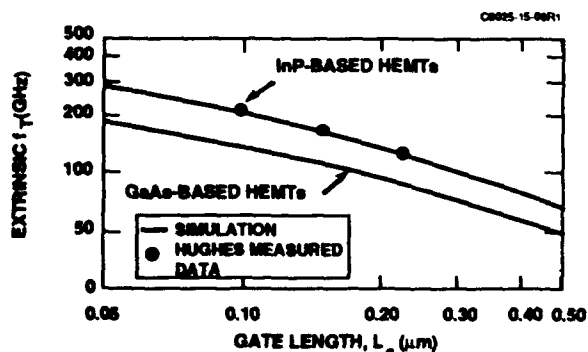


Fig. 1. Scaling of AlInAs/GaInAs HEMTs with gate length. The effects of parasitics on f_T are evident at $L_G < 0.1 \mu\text{m}$.

laboratories for use in the design and optimization of nanometer gate length AlInAs/GaInAs HEMTs and the results will be reported at the time of the conference.

MATERIALS

The key to realize ultra-fast HEMTs with nanometer gate length lies in the optimization of materials and device structures to reduce their parasitics. For a given gate length, one must maximize the device transconductance (g_m), minimize the parasitic resistances, and suppress the extension of the drain depletion region. Therefore, ideally, one must utilize a material system with the following characteristics:

- (1) A low Schottky barrier height and high achievable doping density to allow an extremely close gate-to-channel separation,
- (2) A high two-dimensional electron gas (2DEG) sheet density and high mobility to maximize the modulation efficiency [10] as well as minimize the parasitic resistances, and
- (3) A high peak velocity.

Among all existing material systems, the AlInAs/GaInAs system, grown on an InP substrate, is the only one that possesses all of the above characteristics and therefore is the system of choice for ultra-fast nanometer gate length HEMTs. Its low Schottky barrier height (~ 0.4 eV), high achievable doping density ($\sim 10^{19}$ cm $^{-3}$), high 2DEG sheet density ($> 3.5 \times 10^{12}$ cm $^{-2}$), high mobility (10,000 to 13,000 cm 2 /V-s), and high peak velocity ($> 2.6 \times 10^7$ cm/s) have resulted in devices with the highest f_T yet reported.

Currently, state-of-the-art AlInAs/Ga $_{1-x}$ In $_x$ As HEMTs have been successfully fabricated in materials with $0.53 < x < 0.65$. However, the improvements in electron mobility and peak velocity with increasing indium composition are very modest in this regime and are not expected to result in significant performance improvements for nanometer gate-length HEMTs. Recently, there has been mounting evidence that the electron mobility and peak velocity in strained (or pseudomorphic) AlInAs/Ga $_{1-x}$ In $_x$ As quantum well are rapidly improved for $x > 0.65$ [11, 12]. A record room temperature mobility of 15,200 cm 2 /V-s with a 2DEG sheet density of 1.8×10^{12} cm $^{-2}$ has been reported for such a quantum well with $x = 0.8$ [11]. At the author's laboratories, we have grown similar strained AlInAs/Ga $_{1-x}$ In $_x$ As layers and have obtained a room-temperature mobility of 12,600 cm 2 /V-s with a 2DEG sheet density as high as 3.6×10^{12} cm $^{-2}$ [13]. These layers are currently being evaluated and the results will be reported at a later time.

FABRICATION

The gate lithography is without question the most critical step in the fabrication of ultra-fast HEMTs. At the present time, electron beam lithography is still the dominant exposure method for sub-micrometer geometries (0.1 to 0.3 μ m), as well as part of the nanometer regime (50 to 100 nm), although other exposure methods, such as focus ion beam (FIB) lithography, may eventually be required for finer resolution and repeatability.

Until recently, most state-of-the-art HEMTs with gate length of 0.1 μ m or longer employ a T-, or mushroom-gate to reduce the gate metal resistance whereas those with gate length shorter than 0.1 μ m, due to processing complexity, often employ the conventional high-resistance triangular gate. Within the last year, however, two (2) significant processes have been successfully developed at the author's laboratories that have altered this conventional approach. The first was the demonstration of a new self-aligned gate process in which the sub-micrometer T-gate is used as a shadow mask during ohmic deposition, allowing the ohmic contacts to be self-aligned with the gate [4]. The second was the successful fabrication of a 80 nm T-gate using a 50 kV electron beam [14]. By combining the two processes, we have fabricated a 80 nm self-aligned T-gate HEMT with a f_T as high as 250 GHz.

At the present time, a significant amount of effort is being devoted at the author's laboratories in order to reduce the gate length to 50 nm and optimize the materials for that particular gate length. This author predicts that, with proper scaling, an extrinsic f_T as high as 400 GHz will be obtained in the near future for 50 nm gate length HEMTs (see Fig. 2).

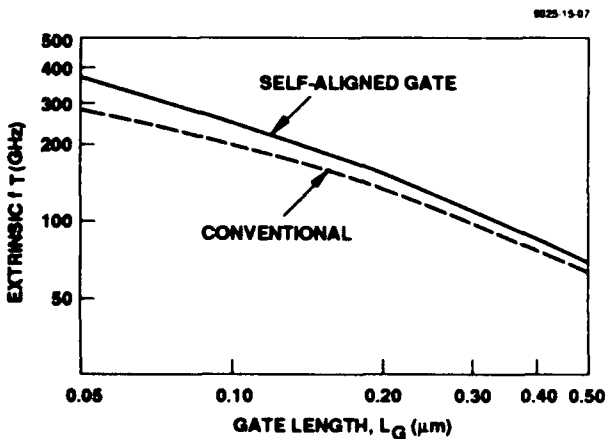


Fig. 2. Projected performance of a self-aligned gate AlInAs/GaInAs HEMTs in the early 1990s.

POTENTIAL LIMITATIONS

Although the scaling of HEMTs appears to be straight forward in terms of f_T , we do not yet have a complete scaling model that can predict the scaling of the power gain cutoff frequency (f_{max}). At the present time, the modeling and scaling of two of the device parasitics, namely the gate-to-drain capacitance and output conductance, are poorly understood and, thus, it is not yet possible to predict the fundamental limit for f_{max} . However, from the preliminary work of the present author (and co-workers) [14], it appears that these parasitics may present serious potential limitations for nanometer gate length HEMTs and must be further reduced.

CONCLUSIONS

Significant progress has been made in ultra-fast HEMT technology in the last few years, resulting in a factor-of-three improvement in f_T for state-of-the-art HEMTs. The present author believes that this fascinating pace of progress can still be maintained in the early 1990s, with further reductions of gate length and device parasitics, as well as

substantial improvements in electron mobility and peak velocity.

REFERENCES

1. Mishra et al., presented at 1987 DRC, Jun. 1987
2. Mishra et al., presented at 1988 DRC, Jun. 1988
3. Mishra et al., in 1988 IEDM Tech. Dig., Dec. 1988
4. Mishra et al., in 1989 IEDM Tech. Dig., Dec. 1989
5. Moll et al., IEEE Trans. Electron Dev., vol. 35, No. 7, Jul. 1988
6. Nguyen et al., IEEE Trans. Electron Dev., vol. 36, No. 10, Oct. 1989
7. Tasker et al., IEEE Electron Dev. Lett., vol. 10, No. 7, Jul. 1989
8. Tasker et al., SPIE vol. 1288, High-Speed Electronics and Device Scaling, 1990
9. Nguyen et al., SPIE vol. 1288, High-Speed Electronics and Device Scaling, 1990
10. Foisy et al., IEEE Trans. Electron Dev., vol. 35, No. 7, Jul. 1988
11. Chin et al., J. Vac. Sci. Tech., B8(2), Mar/Apr 1990
12. Thobel et al., Appl. Phys. Lett., 56(4), 22 Jan. 1990
13. Brown et al. (private communication)
14. Nguyen et al., in 1990 IEDM Tech. Dig., Dec. 1990

Picosecond Radiation-Induced Current Transients in Digital GaAs MESFETs

Dale McMorrow, Arthur B. Campbell, and Alvin R. Knudson

U.S. Naval Research Laboratory, Washington, DC 20375

Todd R. Weatherford

Sachs/Freeman Associates, Landover, Maryland 20785

Abstract

Picosecond-resolution measurements of the current transients produced when energetic ions (alpha particles) interact with high-speed digital GaAs MESFETs are presented. Measurements as a function of device bias and temperature reveal the presence of several different contributions to the charge-collection transients, ranging in time scale from picoseconds to microseconds. The effects of permanent radiation damage are found to degrade device performance to the extent that reliable measurement of the ion-induced transients is difficult and, in many cases, impossible. The use of above-band-gap picosecond laser excitation is revealed to be a viable alternative to the use of heavy ions for characterization of the charge-collection dynamics in semiconductor devices.

Introduction

Single event upsets (SEUs) are transient errors (changes in state) in digital circuit elements induced by energetic ions. SEUs have been observed both on Earth and in space in a variety of integrated circuits, including random-access memories (RAMs) and microprocessors [1], with both GaAs and silicon based technologies being susceptible. On Earth, SEUs can be caused by components of cosmic rays (the intensity of which varies with altitude), and by alpha particles produced by the decay of naturally occurring radioactive impurities in packaging and fabrication materials [2]. Space-based electronics are particularly susceptible to single-event phenomena, with SEUs posing a serious reliability problem for space-based digital systems because of the large flux of energetic ions in

cosmic rays and the Earth's radiation (proton) belts.

In this paper we describe a study of ion-induced transient phenomena in a digital GaAs MESFET that is typical of those found in today's high-speed memories and logic. GaAs is desirable for applications in space systems because of its high-speed and low power consumption characteristics, but GaAs devices have exhibited a low threshold for single-event upset phenomena. With the current state of GaAs technology, significant problems must be overcome before a widespread utilization of GaAs technology in space is possible.

Energetic ions interact with semiconductor devices to produce ionization tracks that consist of dense plasmas of free carriers. These thermalize with the lattice on a time scale of a few picoseconds and, under the influence of drift and diffusion, are collected at the various circuit nodes. A large amount of work has been devoted to measurement of the time-integrated charge produced by the interaction of energetic ions with semiconductor devices (such measurements are commonly referred to as charge collection [3-12]). Numerous phenomena of general significance in the understanding of ion/semiconductor interactions (many with practical implications with regard to SEU) including the charge-funneling effect [5,6], the ion-shunt effect [8], and the gate-edge effect [7,11] have been discovered in this manner. It has long been recognized, however, that time-resolved measurements of charge-collection transients are essential for a complete understanding of the charge-collection process, as well as its relationship to single-event phenomena. Early measurements utilized transient digitizers and sampling oscilloscopes to measure the

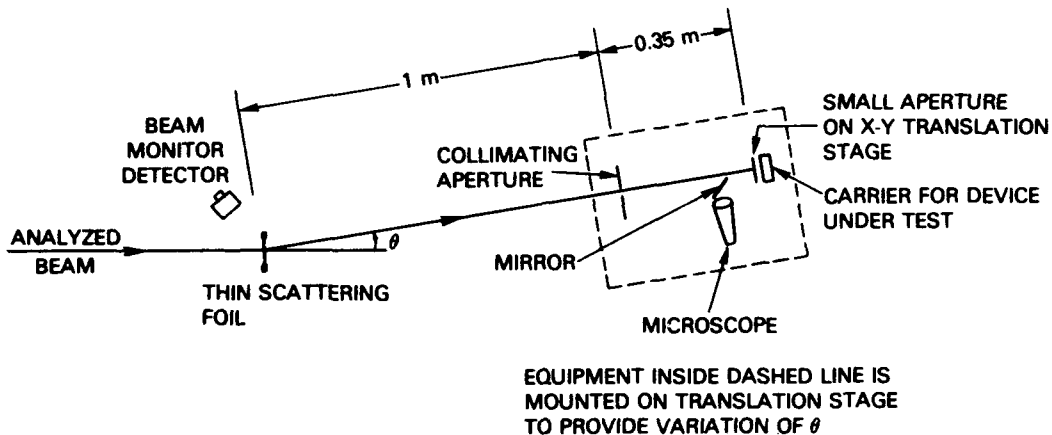


Figure 1. Schematic diagram of the NRL ion microbeam apparatus.

charge-collection transients [4-6, 8-10]. In general, the measured transients were observed to consist of faster and slower contributions, which commonly were attributed to charge collection by drift (including funneling) and diffusion mechanisms, respectively. These measurements, however, were plagued by poor temporal resolution, making any detailed interpretations difficult.

Recently it has become possible to resolve the dynamical evolution of charge-collection transients with picosecond resolution [11-13]. In this paper we describe some of the first picosecond-resolution measurements of the current transients produced when energetic ions interact with GaAs MESFETs. These results reveal details of the charge collection process that could not be deduced from measurements performed with lower temporal resolution. Additionally, we illustrate the utility of picosecond laser excitation to simulate the effects of heavy ions in these devices. In particular, it is demonstrated that measurements with above band-gap picosecond laser irradiation reproduce both the qualitative and quantitative features of excitation by ionizing radiation. This result is particularly significant because the optical experiments can be performed without the cumulative effects of permanent radiation damage, which are quite severe for the small area GaAs devices of this study. It also permits us to draw on the body of work already performed on optical excitation of GaAs devices [14-17].

Experimental

The energetic ions used in these experiments were produced by a 3-MV tandem Van de Graff accelerator. Figure 1 shows a schematic of the NRL ion

microbeam facility [18], with the ion beam entering from the left. All components shown in this figure (except the microscope) are under vacuum. The ion beam, which is typically ~ 1 mm in diameter, is diffused by the thin (Ni) scattering foil. Those ions scattered at the angle θ will pass through the collimating aperture and a $2.5 \mu\text{m}$ pinhole (labeled "small aperture" in fig. 1) that is located directly in front of the device under test. The pinhole is suspended from an x-y translation stage, permitting precise control over the position of ion strikes on the surface of the device. The beam flux at the device is controlled through variation in θ .

The device under test is mounted in a high-frequency (50 GHz) microwave package, with the source grounded and the gate and drain wirebonded to microstrip transmission lines. The transient signals are launched from the microstrip lines onto 50 GHz, 2.4 mm coaxial connectors, fed through the vacuum wall with a semi-rigid cable, and passed through a bias tee into the input of a HYPRES PSP-750 70 GHz superconducting sampling oscilloscope. In these experiments, each ion striking a sensitive region of the device produces a current pulse. A fundamental difficulty associated with measurement of these high-frequency transients is the random time interval between ion strikes, coupled to the difficulty in obtaining a jitter-free trigger signal. The HYPRES system currently is the best instrument available for the measurement of such transients. In addition to its 70 GHz bandwidth, the HYPRES contains a built in, effectively dispersion free (to 70 GHz), superconducting delay line that permits the sampling of randomly arriving transients while maintaining its full instrumental bandwidth.

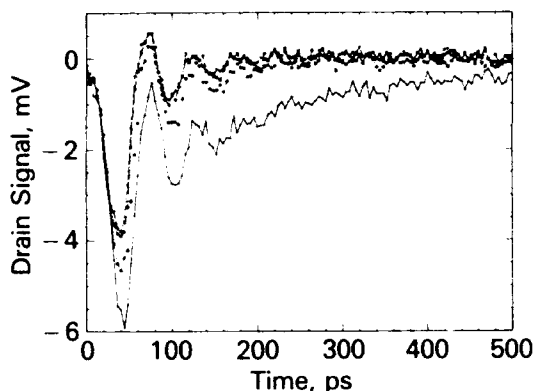


Figure 2. Current transients detected at the drain of a $1.2 \mu\text{m} \times 50 \mu\text{m}$ depletion-mode GaAs MESFET as a function of exposure (lower to upper) to a $2.9 \text{ MeV} {}^4\text{He}$ ion beam. $V_G = -1.0 \text{ V}$, $V_D = 4.0 \text{ V}$, with the source grounded.

For the optical experiments, laser pulses of $\sim 10 \text{ ps}$ duration were produced with a cavity-dumped dye laser synchronously pumped by the second harmonic of a continuous-wave modelocked Nd:YAG laser. Because of the slow ($\sim 1 \mu\text{s}$) relaxations observed in this study, cavity-dumped operation is essential to eliminate device charging effects from successive laser pulses; pulse repetition rates of 400-800 KHz were used. For the experiments reported here, an excitation wavelength of 800 nm was used. We have performed experiments with excitation wavelengths as long as 875 nm , on the low-energy side of the GaAs bandgap. The longer-wavelength excitation will penetrate deeper into the substrate, and is expected to better approximate the charge distribution created by an ion strike. Experiments were also performed with 10 ps , 527 nm excitation generated with a modelocked Nd:Glass laser system [19]. The wavelength-dependent results provide additional insights into the charge-collection mechanisms. The conclusions of those studies are consistent with those presented here, and will be described elsewhere.

Results and Discussion

In Figure 2 we show representative current transients produced on the drain of a $1.2 \mu\text{m} \times 50 \mu\text{m}$ depletion mode GaAs MESFET by 2.9 MeV α -particle (${}^4\text{He}$) irradiation. This device was operated in a pinched-off condition with the gate and drain biased at -1.0 V and 4.0 V , respectively, with the source grounded. This figure shows a series of four successive runs (lower to upper), with the lower curve representing a nominally undamaged device

(each run spans five to ten minutes and involves approximately 100,000 ion strikes). The ion strikes were centered on the high-field region between the gate and drain. The rapid evolution of the measured transients as a function of beam exposure is indicative of permanent radiation damage effects (displacement damage). The effects of radiation damage are obviously quite significant, and it is only possible to perform a limited number of experiments on a given device before the transients are no longer representative of an undamaged device. For ions heavier than ${}^4\text{He}$ the effects are even more severe. Our experience indicates that displacement damage effects are more severe in GaAs than in Si. This has also been reported by Brown and Williams for somewhat different excitation conditions [20].

Evident in the undamaged transient of figure 2 is a rapid rise followed by an exponentially relaxing tail exhibiting a time constant of $\sim 150 \text{ ps}$. Also evident is a finite signal amplitude at 500 ps . This amplitude is characteristic of an underlying slow component to the charge-collection transient. This slow component exhibits a relaxation time on the order of $1 \mu\text{s}$ [12], and is believed to arise from deep-level traps known to be prevalent in GaAs. The "ringing" evident in each curve is due to the bond wire inductance interacting with the intrinsic capacitance of the device. Calculations representing the device and its bond wires by a series resistance, inductance, and capacitance have reproduced the observed oscillations. Measurements performed on a device in which the bond wire lengths are minimized show significantly reduced ringing (cf., figure 5). Devices are currently being fabricated with co-planar transmission lines on chip to eliminate entirely the problem of bond-wire inductances.

The evolution in the shape of the charge collection transient as a function of radiation exposure shown in figure 2 is consistent with an increased concentration of recombination sites, resulting in a reduced carrier lifetime. The data reveal that the amplitudes for both the $\sim 150 \text{ ps}$ and the $\sim 1 \mu\text{s}$ components are reduced significantly with increasing radiation exposure. Time-integrated charge-collection measurements should correspond to the area under the transients of figure 2. As is evident, the time-integrated charge collection efficiency also is decreased significantly with increasing radiation exposure.

The radiation-damage effects discussed in the previous paragraphs represent an intrinsic liability of ion-induced charge-collection measurements performed with sampling techniques. Such effects typically become more severe as device feature size

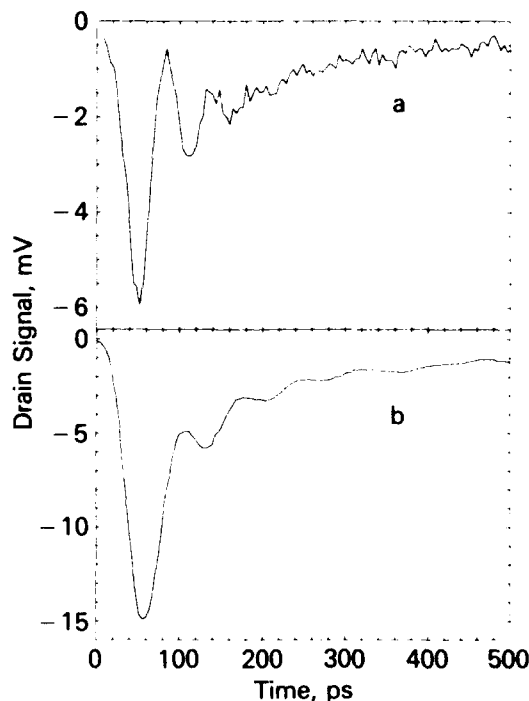


Figure 3. Drain current transients for $1.2 \mu\text{m} \times 50 \mu\text{m}$ depletion-mode GaAs MESFETs with excitation by (a) ^4He ion beam and (b) 800 nm, 10 ps laser pulse. The bias conditions for (a) are as in figure 2; in (b) the device was biased with $V_G = -1.5 \text{ V}$, $V_D = 5.0 \text{ V}$, with the source grounded.

is reduced. To gain added insight into the dynamics of the charge-collection process, without the complications introduced by radiation-damage effects, we have investigated the transients produced by above-band-gap picosecond laser excitation. Figure 3 shows a comparison of the nominally undamaged ion-induced transient (figure 3a) with a transient produced with $\sim 10 \text{ ps}$, 800 nm laser excitation (figure 3b). The data of figure 3 reveal that, for the devices of this study, the essential features of the ion-induced charge-collection transients are also present in the transients produced by picosecond laser excitation. Evident in the transient of figure 3b are the rapid rise, the $\sim 150 \text{ ps}$ relaxation, the finite amplitude at long times associated with a slower signal contribution, as well as the ringing associated with the bond wire inductances. Therefore, it may be concluded from this result that a significant amount of information can be determined through the use of optical techniques without inflicting damage to the device.

In figure 4 we show the drain bias dependence of the laser-induced (800 nm) current transients for

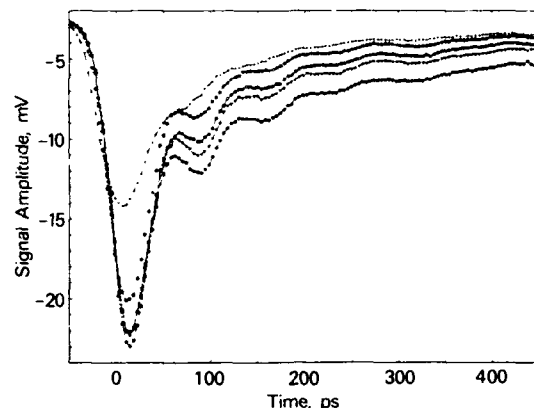


Figure 4. Drain bias dependence of the laser-excited drain current transients for the same device as in figure 3b: $V_D = 5.0 \text{ V}$; 3.0 V; 2.0 V; 1.0 V; and 0.5 V (lower to upper); $V_G = -1.5 \text{ V}$; $V_S = 0.0 \text{ V}$.

the same device used to generate figure 3b. While this data set contains significant information on the mechanisms of charge collection in this device, we wish to focus initially on the fact that this experiment, which is trivial when using optical techniques, is effectively impossible for ionic excitation because of the degradation associated with radiation-damage effects. A limited number of bias-dependent heavy ion measurements have been performed on different devices, producing results that are consistent with those of figure 4.

The bias-dependent transients of figure 4 show four general trends: *i*) the signal amplitude at short times increases initially with increasing source to drain bias, and then tends to saturate; *ii*) the area under the transient increases with increasing bias; *iii*) the amplitude at long times increases with increasing bias; and *iv*) at very low drain bias ($< 1 \text{ V}$) the dynamics are somewhat slower than at the higher biases. We note that these transients were measured on the HYPERES system using the internal trigger mode; therefore, the relative position (along the time axis) is dependent on the trigger level and is not of physical significance. It is expected that if the time axis were absolute, the 0.5 V and 1.0 V curves showing the slower dynamics would be shifted to the right. Observation (*i*), the amplitude saturation, may be due to velocity saturation during the initial drift collection process. This is consistent with the observation of slower dynamics at lower bias conditions (point *iv*). Observations (*ii*) and (*iii*) are closely related, with most of the increased charge at higher biases being associated with an increased amplitude for the slower ($\sim 1 \mu\text{s}$) signal contribution. This conclusion

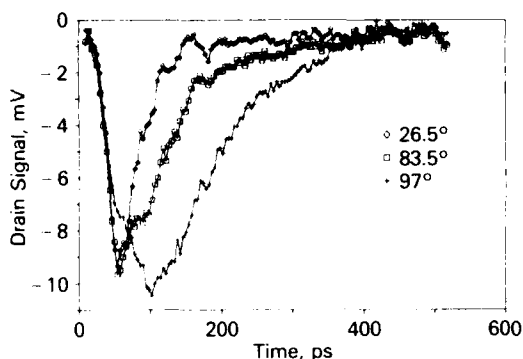


Figure 5. Drain current transients for a $1.2 \mu\text{m} \times 50 \mu\text{m}$ depletion-mode GaAs MESFET as a function of temperature (given in degrees Celsius) for excitation by 2.9 MeV ${}^4\text{He}$ ions. The device was biased with the gate at -1.5 V , the drain at 2.0 V , with the source grounded.

is consistent with wavelength-dependent studies in which the $\sim 1 \mu\text{s}$ component is observed to increase in amplitude with excitation at longer wavelengths, decreasing significantly for 527 nm excitation.

There are several reasons for using optical methods to investigate charge-collection dynamics. We have already mentioned the significant problem of radiation damage. In addition, optical methods are desirable because: they are significantly less expensive to set up, and more convenient in practice than accelerator testing; all-optical techniques possess inherently higher temporal resolutions than those utilizing electronic detection methods; and because the laser technique readily provides spatial information that is difficult to extract from ion experiments. The data of figures 3 and 4 illustrate the fundamental utility of picosecond laser techniques for investigating the charge-collection process. There are, however, fundamental differences in both the mechanisms of charge production, and the initial distribution of carriers produced by optical pulses and energetic ions that should be noted. For the ${}^4\text{He}$ ions of this study, the initial radial distribution of carriers is significantly smaller than that produced by a laser pulse ($\sim 0.1 \mu\text{m}$ compared to $\sim 2 \mu\text{m}$ diameter [21]), and the charge column created by the ion penetrates deep ($\sim 5 \mu\text{m}$) into the substrate [21]. Therefore, subtle (and possibly some not-so-subtle) differences between the ion- and laser-induced charge collection transients are expected. It is evident that the optical- and ion-excited transients of figure 3 are not identical. We note first that the two transients were obtained for different devices under slightly different bias conditions. The most evident difference between the two, the "ringing" frequen-

cy, therefore, is not expected to be identical. Since this ringing tends to dominate the transients, the observation of the more subtle differences associated with the initial carrier distribution will require more work.

In figure 5 we show some preliminary measurements of the ion-induced ($2.0 \text{ MeV} {}^4\text{He}$) drain transients as a function of temperature. These measurements were performed on a $1.2 \times 50 \mu\text{m}$ depletion mode device packaged in the same manner as the previous results but, in this case, care was taken to minimize bond wire lengths. While some ringing is still evident in this data set, its amplitude is significantly reduced over that in the previous figures. As in the previous figures, the device was operated in a pinched-off condition with the gate and drain biased at -1.45 V and 2.0 V , respectively; temperatures are in degrees Celsius.

Measurements of the charge-collection transient as a function of temperature were initiated for three reasons. First, it was anticipated that temperature-dependent changes in the detailed shape of the transients would provide insight into the mechanisms of charge collection. In addition, since microelectronic circuits must operate in a wide variety of environments, it is of fundamental importance to determine the effects of temperature on the charge collection transients. And finally, a recent observation [20] that radiation damage in GaAs is significantly reduced in the temperature range of $80\text{--}100 \text{ }^\circ\text{C}$ suggests that it might be possible to perform more detailed measurements on a single device at higher temperatures.

The data of figure 5 show that dramatic changes in the charge-collection waveform occur for rather modest temperature changes. The most obvious observation is that the charge-collection pulse width increases significantly with increasing temperature. This observation can be accounted for, at least qualitatively, in terms of the decreased carrier mobility [22] associated with the increased cross section for phonon scattering mechanisms at elevated temperatures. A closer inspection of the data of figure 5 reveals that the detailed shape of the charge-collection transient is a complex function of temperature, suggesting the possibility that several different and competing phenomena are of significance. A detailed investigation of these results is currently in progress; at this time we will limit our comments to some preliminary observations.

Each of the transients of figure 5 exhibits a contribution with an instrument-limited rise. This fast contribution dominates the short-time charge-collection dynamics for the two lower temperatures,

and shows up as a shoulder on the leading edge of the 97°C trace. At higher temperatures a slower charge-collection mechanism becomes prevalent, with a finite risetime of ~75 ps being clearly evident in the 97°C data. This slower rise is consistent with a slower drift velocity arising from the decreased carrier mobility noted above.

Also evident in the data of figure 5 is a significant increase in the time-integrated charge collection efficiency for times shorter than 500 ps. At 97°C the charge collected within the 500 ps temporal window shown accounts for approximately two-thirds of the total charge produced by the 2.0 MeV He ion. This observation may indicate that charge trapped in the semi-insulating substrate is collected more efficiently at the elevated temperatures, and can have a significant influence on the SEU sensitivity of circuits utilizing GaAs MESFETs similar to those of this study.

As a final point we note that displacement damage effects are significantly reduced at the elevated temperatures, consistent with the earlier study noted above [20]. This result is expected to be of significance in future investigations.

Conclusions

We have presented some of the first measurements with picosecond time resolution of the current transients produced in GaAs MESFETs by energetic ions. The transients produced by ^4He irradiation reveal complex temporal waveforms that are indicative of charge collection involving several different phenomena. This is especially evident in the temperature-dependent measurements which reveal an instrument-limited contribution that appears to be independent of temperature, followed by a slower component whose dynamics and relative amplitude vary significantly with temperature.

We have observed rather significant effects of permanent radiation damage on the picosecond charge-collection dynamics. The effect of radiation exposure is to increase the decay rates of the various dynamical contributions, consistent with the production of recombination centers that reduce carrier lifetimes. Radiation-damage effects greatly complicate, and in some cases render impossible, the measurement of ion-induced transients in these devices.

Charge-collection measurements performed with above-band-gap picosecond laser irradiation are shown to reproduce the essential characteristics of the ion induced transients for these devices, thus providing a viable alternative to the use of heavy ions for characterization of the charge-collection

dynamics in semiconductor devices. Future measurements utilizing optical techniques will permit a more detailed investigation of charge-collection dynamics in these devices than would be possible with heavy ion irradiation.

Acknowledgments

The optical experiments of this study were performed in the laboratories of Prof. Chi H. Lee at the University of Maryland, College Park, and Professor Ray Chen of the University of Maryland, Baltimore County. The authors thank the various individuals in these two laboratories for their assistance.

References

1. E.L. Peterson and P.W. Marshall, *J. Rad. Effects: Research and Engineering* **6**, 1 (1988).
2. T.C. May and M.H. Woods, *IEEE Trans. Elect. Dev.* **ED-26**, 2 (1979).
3. A.B. Campbell and A.R. Knudson, *IEEE Trans. Nuc. Sci.* **NS-29**, 2067 (1982).
4. A.B. Campbell, A.R. Knudson, P. Shapiro, D.O. Patterson and S.E. Seiberling, *IEEE Trans. Nuc. Sci.* **NS-30**, 4486 (1983).
5. F.B. McLean and T.R. Oldham, *IEEE Trans. Nuc. Sci.* **NS-29**, 2018 (1982); *IEEE Trans. Nuc. Sci.* **NS-30**, 4493 (1983).
6. C.M. Hsieh, P.C. Murley and R.R. O'Brien, *IEEE Trans. Elect. Dev.* **ED-30**, 686 (1983).
7. P.J. McNulty, W. Abdel-Kader, A.B. Campbell, A.R. Knudson, P. Shapiro, F. Eisen and S. Roosild, *IEEE Trans. Nuc. Sci.* **NS-31**, 1128 (1984).
8. A.R. Knudson, A.B. Campbell, P. Shapiro, W.J. Stapor, E.A. Wolicki, E.L. Peterson, S.E. Diehl-Nagle, J. Hauser and P.V. Dressendorfer, *IEEE Trans. Nuc. Sci.* **NS-31**, 1149 (1984); J.R. Hauser, S.E. Diehl-Nagle, A.R. Knudson and A.B. Campbell, *IEEE Trans. Nuc. Sci.* **NS-32**, 4115 (1985).
9. M.A. Hopkins and J.R. Srour, *IEEE Trans. Nuc. Sci.* **NS-31**, 1116 (1984).
10. Z. Shanfield, M.M. Moriwaki, W.M. Digby, J.R. Srour and D.E. Campbell, *IEEE Trans. Nuc. Sci.* **NS-32**, 4104 (1985).
11. A.B. Campbell, A.R. Knudson, D. McMorrow, W. Anderson, J. Roussos, S. Espy, S. Buchner, K. Kang, D. Kerns and S. Kerns, *IEEE Trans. Nuc. Sci.* **NS-36**, 2292 (1989).
12. D. McMorrow, A.R. Knudson and A.B. Campbell, *IEEE Trans. Nuc. Sci.* **NS-37**, 1092 (1990).

13. R. Wagner, N. Bordes, J. Bradley, C. Maggiore, A. Knudson, and A. Campbell, IEEE Trans. Nuc. Sci. NS-35, 1578 (1988).
14. T. Sugeta and Y. Mizushima, Jpn. J. Appl. Phys. 19, L27 (1980).
15. J.C. Gammel and J.M. Ballantyne, IEDM Technial Digest, 120 (1978).
16. C. Baack, G. Elze and G. Walf, Electron. Lett. 13, 193 (1977).
17. T. Carruthers, W.T. Anderson, and J.F. Weller, IEEE Elect. Dev. Lett. EDL-6, 580 (1985).
18. A.R. Knudson and A.B. Campbell, IEEE Trans. Nuc. Sci., NS-28, 4017 (1981).
19. L. Yan, P.T. Ho, C.H. Lee and G.L. Burdge, Appl. Phys. Lett. 54, 690 (1989).
20. R.A. Brown and J.S. Williams, in *Proceedings of the 6th Australian Conference on Nuclear Techniques of Analysis*, Lucas Heights, N.S. Wales, November 1989, p. 80.
21. D. McMorrow, A.R. Knudson and A.B. Campbell, in *Ultrafast Phenomena VII*, C.B. Harris, E.P. Ippen, G.A. Mourou and A.H. Zewail, eds. (Springer, Berlin, 1990) p. 300.
22. J.S. Blakemore, J. Appl. Phys. 53, R123 (1982).

Transient Simulation of Ultrasmall GaAs MESFET Using Quantum Moment Equations

J.-R. Zhou, A. M. Kriman,^{*} and D. K. Ferry

*Center for Solid State Electronics Research, Arizona State University,
Tempe, Arizona 85287-6206*

Abstract

We present transient simulations of small GaAs MESFETs. Transient switching oscillation exhibit a strong peak in the frequency domain which is modified by quantum effects.

Introduction

Since the advent of the integrated circuits in the late 1950's, the number of devices contained on a single chip has approximately doubled every three years and this process has caused semiconductor devices to be made smaller and smaller. However, little is understood about the physical limitations that will determine whether or not these devices are practical. These questions have opened a new field for semiconductor research and technology in which a great opportunity is provided to study many new physical phenomena, some of which have been described in [1-4], and exploring a new generation of device structures and system architectures for the potential application of Ultra Large Scale Integrated (ULSI) system in the near future.

The physical effects inherent in the operation of the ultra-small devices (which have been observed and which have the promise to be observed) are based on the fact that the critical length (e.g. the gate length or the depletion length) becomes so small that it approaches the coherence length of the electrons that provide the operation, which suggests that such small devices must be treated as quantum mechanical objects. The coherence length, or the inelastic mean free path, can be more than 1 μm at low temperature and as much as 0.1 μm at room temperature in high quality heterojunction device structures. This is much larger than the gate length ($\sim 20\text{nm}$) of the smallest transistor that can be made [5,6]. Due to the quantum interference within the devices as well as between the devices, these physical effects may greatly modify the operation of a single device as well as an integrated circuit. It is very

important to fully understand these effects on the device and circuit operations.

The classical semiconductor transport theory is based on Boltzmann transport equation (BTE). Numerous analytical and numerical methods have been developed for solving this equation on various semiconductor problems. Among which, Monte Carlo method provides most accurate and detailed solution but is hardly used in practical engineering applications for its computational expenses. As a practical alternative, a reduced description of the BTE, the moment equations, especially the drift-diffusion model, has played a significant role in the evolution of IC technology, providing critical insight into device scaling, leading to the VLSI. Simulators continue to be applied in the analysis of new device concepts and have become an essential component of the technology design process. As device feature sizes reduce to submicron regime, device simulation faces new challenge. Simple drift-diffusion model is no longer adequate, instead a full hydrodynamic model must be used to investigate non-stationary and hot electron dynamics, which allows the distinction of the momentum and energy relaxation times. As scaling continues to ultra-submicron realm ($< 0.1 \mu\text{m}$), quantum transport method becomes necessary.

We have performed a simulation of an ultra-small GaAs MESFET device, using a set of quantum moment equations developed from density matrix (Wigner function) prototype [7]. In this paper, we examine the transient (picosecond) response of such devices to ascertain the effect that the non-local quantum potential has on the switching behavior. Interesting time-dependent current oscillation behavior has been observed when a step voltage is applied to an initial steady state.

Quantum moment equations

The detailed treatment of the quantum moment equation is described in elsewhere. Here we only give a short summary. In principle, large-scale devices can be

modeled classically, with an accurate description given by the Boltzmann transport equation (BTE). This equation time-evolves a complete single-particle phase space distribution. However, the accurate simulation of ultra-small devices requires quantum effects such as tunneling and quantum repulsion (complementary to barrier penetration) to be included. A full quantum description, at the single particle level, can be based on the Wigner distribution function, a transformation of the density matrix which is a natural generalization of the classical phase space distribution function. Its time evolution equation derived from Schrödinger equation or Liouville equation has similar form as that of the BTE, but with quantum corrections built in by including static potential into the equation non-locally. The Wigner distribution function has been successfully used in simulation of resonant tunneling diode in one dimension [8,9], but it is not expected to be directly used for multi-dimensional device simulation for its expenses in memory storage and computation time. For a device simulation with a higher dimensional description, the practical alternative is the reduced description of the Wigner distribution function, i.e., its moments, which are very useful because the lowest several moments represent the basic physical quantities such as density, momentum and energy of a physical system. The equations of motion of the distribution functions then results in the moment equations, following the same procedure as that for the classical BTE. However, the lowest three moment equations are formally identical to their classical analogue under the relaxation time approximation and do not contain explicit quantum corrections, as they are expected. The key step to preserve quantum corrections in the lowest three moment equations relies on the method in decoupling these equations from higher order moment equations. In order to get explicit quantum corrections into the moment equations, several different methods have been proposed [10]. Based on the quantum representation of the second moments $\langle p^2 \rangle$ [11], we explicitly incorporate the quantum corrections through the energy representation

$$w = \frac{1}{2}mv^2 + \frac{3}{2}k_B T + U_q, \quad (1)$$

where

$$U_q = -\frac{\hbar^2}{8m} \nabla^2 \ln(n). \quad (2)$$

and developed a set of quantum moment equations with temperature representation

$$\frac{\partial n}{\partial t} + \nabla \cdot (nv) = 0, \quad (3)$$

$$\frac{\partial v}{\partial t} + v \cdot \nabla v = -\frac{qE}{m} - \frac{1}{nm} \nabla(nk_B T_q) - \frac{v}{\tau_m}, \quad (4)$$

$$\begin{aligned} \frac{\partial T}{\partial t} + \frac{1}{3}v \cdot \nabla(T_q) &= -\frac{2}{3} \nabla \cdot (v T_q) + \\ \frac{mv^2}{3k_B} \left(\frac{2}{\tau_m} - \frac{1}{\tau_w} \right) - \frac{T - T_0}{\tau_w}, \end{aligned} \quad (5)$$

using a convenient notation

$$T_q = T + \frac{2}{3k_B} U_q. \quad (6)$$

This set of equations preserves all classical features except the heat flow property (it may be added in), and gives explicit quantum corrections.

Transient simulation of ultra-small MESFET

All the results we present here are for a MESFET device with 24 nm gatelength. The typical doping in the channel is $1.5 \times 10^{18} \text{ cm}^{-3}$, and a semi-insulating substrate is included. The lattice temperature is taken to be 300 K. The transient simulation starts from an initial steady state. The simulation time step of 0.5 fsec is found to be suitable. Figure 1 plots the switching currents for an initial increase and then decrease in the magnitude of the drain potential. Both source and drain currents are shown, with the difference corresponding to the substrate current. In the initial steady state, the gate voltage V_g is -0.5 V and the drain voltage V_d is 0.5 V. The simulation begins with the applied voltages stepped to $V_g = 0$ V and $V_d = 2.5$ V. The time interval between the first voltage step to the second voltage step ($V_d = 2.0$ V) is 17.5 psec, and the other time intervals between the applied step voltages are 7.5 psec. Extensive ringing in the response is obvious, which promotes the further investigation of the oscillation property. The stability of the simulation has been carefully checked to identify whether the current oscillations are numerical or physical. This includes the change of mesh sizes, time step, doping density and

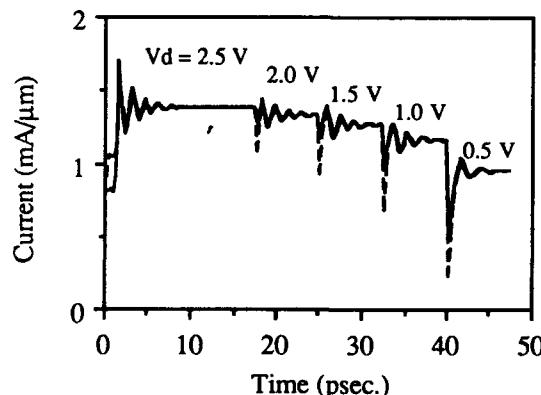


Figure 1. Plot of transient current of source (dashed line) and drain (solid line).

total simulation area of the device (e.g., to increase the simulation area by extending the source and drain contacts). Fig. 2 shows that simulations with different mesh sizes [3 nm (120x35 grids) and 1.5 nm (240x70 grids)] are found to match very well, both during the oscillations and in the steady-state. Change of time step give the same results. Furthermore, simulation of larger area devices didn't show down-shift of the oscillation frequency peak, which excludes the possibility of numerical boundary reflection.

The oscillations do, however, depend upon the density in the device. Figure 3 shows the Fourier transform of the current for different doping levels, the three frequency peaks correspond to $3 \times 10^{18} \text{ cm}^{-3}$, $1.5 \times 10^{18} \text{ cm}^{-3}$ and $5 \times 10^{17} \text{ cm}^{-3}$ dopings from higher frequency to lower frequency. For comparison, the amplitudes are multiplied by 100 and 3 for dopings $5 \times 10^{17} \text{ cm}^{-3}$ and $1.5 \times 10^{18} \text{ cm}^{-3}$ respectively. The

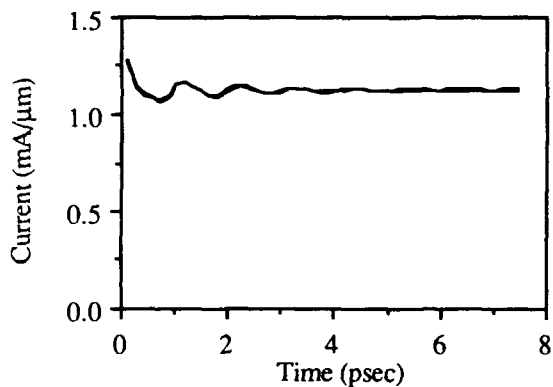


Figure 2. Switch current vs time plot for simulations with 120x35 grids (solid line) and 240x70 grids (dashed line). The two curves match very well.

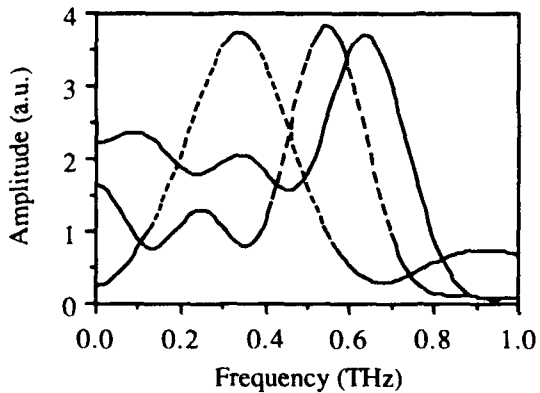


Figure 3. Fourier transform of the currents for different doping levels. The three frequency peaks correspond to $3 \times 10^{18} \text{ cm}^{-3}$, $1.5 \times 10^{18} \text{ cm}^{-3}$ and $5 \times 10^{17} \text{ cm}^{-3}$ dopings from higher frequency to lower frequency, clearly showing the density dependence of the oscillation.

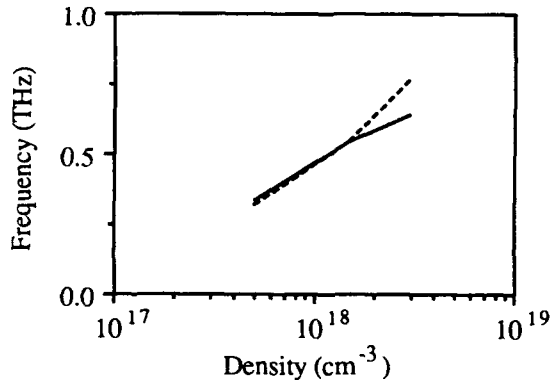


Figure 4. Oscillation frequency vs electron density plot, the solid line represents the peak frequencies from the simulation, while the dashed line describe a simple square-root law.

oscillation amplitude increases as the doping increase according to the simulation. Strong frequency peaks occur around 500 GHz. The results clearly show that the frequency peaks largely depend on the electron density in the device and, as the density decreases, the peak shifts to lower frequency. These results suggest that the current oscillation are physical. The density dependence of the peak frequency implies that the oscillation response is related to the quasi-ballistic and plasma response of the free carriers in the channel. While the peak frequencies in the curves of Fig. 3 change with the density, this does not follow a simple square-root law. In Fig.4, we plot the oscillation frequency against the log density, the solid line is the results of the simulation and the dashed line is the simple square-root law. It turns out that the oscillation is closer to the square-root law at lower densities but far from the square-root law at high densities. This implies that the response is not simply a plasma oscillation, but that the ballistic response and inhomogeneity and dimensional modifications of the plasma response are involved.

Furthermore, with the doping of the device fixed, the change of the gate potential will actually modulate the electron density in the conduction channel of the device. We would then expect the same behavior on the shifts of the frequency peaks as we switch the gate voltage corresponding to the increase or decrease of the electron density in the channel. Fig. 5 illustrates two switching processes of the gate voltage, the solid curve results from the switching process $V_g = -0.0 \text{ V} \rightarrow -0.5 \text{ V} \rightarrow -1.0 \rightarrow -1.5 \text{ V}$, and the dashed curve is with a reverse process $V_g = -1.5 \text{ V} \rightarrow -1.0 \text{ V} \rightarrow -0.5 \rightarrow -0.0 \text{ V}$. Both processes give higher oscillation frequency with smaller gate voltages, which correspond to higher electron density in the conduction channel of the device. It is also clear that the steady-state currents agree very well as gate voltage is switched to the same bias from opposite directions. And it needs a longer time to reach steady state for smaller gate voltage. This means a larger oscillation amplitude, a property also similar to that found for higher doping level. Fig. 6 plots the

Fourier transform of the currents of the switch responses in the process represented by the solid curve in Fig. 5. As gate voltage increases, the frequency peak shifts downwards and the amplitude is also reduced, as one expected. A comparison of the difference between switch conditions for the same final bias state is made in Fig. 7, where the final gate voltage is -1.0 V, the solid curve is for the switching from $V_g = -1.5$ V to -1.0 V, and the dashed curve is for the switching from $V_g = -0.5$ V to -1.0 V. The oscillation properties for the two cases are essentially the same, except the difference between the amplitudes that accounts for the effect of the different switching process on the response at the beginning.

In the simulation, it is very convenient to investigate the quantum effect on the oscillation, as one can 'turn off' the quantum corrections. In Fig. 8, the difference with, and without, the quantum potential terms is

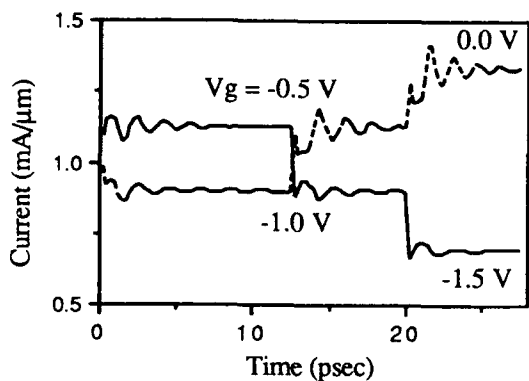


Figure 5. Current response for different gate voltages with drain voltage fixed to 2.0 V. Here, the solid curve describes the process of increase of the gate voltage, while the dashed curve is for the process of decreasing gate voltage.

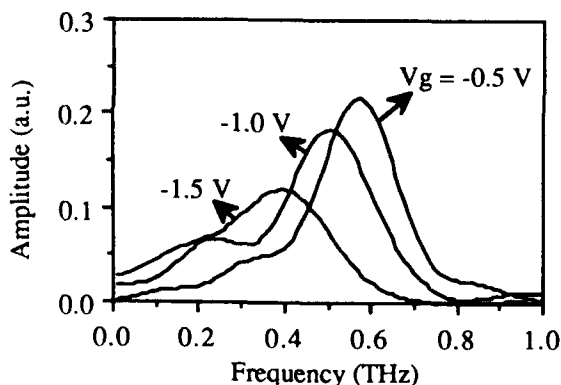


Figure 6. Fourier spectra of the current response for different gate voltages for a single doping level ($1.5 \times 10^{18} \text{ cm}^{-3}$) as the switching $V_g = -0.0 \text{ V} \rightarrow -0.5 \text{ V} \rightarrow -1.0 \text{ V} \rightarrow -1.5 \text{ V}$ is taken.

shown for the Fourier spectrum at $V_d = 2.5 \text{ V}$ (V_g is switched from -0.5 to 0 as V_d is switched on). The presence of the quantum correction reduces the peak of the spectrum, which is indicative of softening of the potential steps in time and space, an expected quantum result. The lower microwave response is thought to be due to the effect of quantum potential smoothing the general potential variation and therefore lowering the effect of gate charge control.

Conclusion

We have performed a simulation of an ultra-small GaAs MESFET device, using a set of quantum moment equations. Interesting time-dependent current oscillation behavior has been observed when a step voltage is applied to an initial steady state. Detailed investigation of the current oscillation in the time domain reveals a density dependence of the oscillation frequency, which suggests that the oscillations are

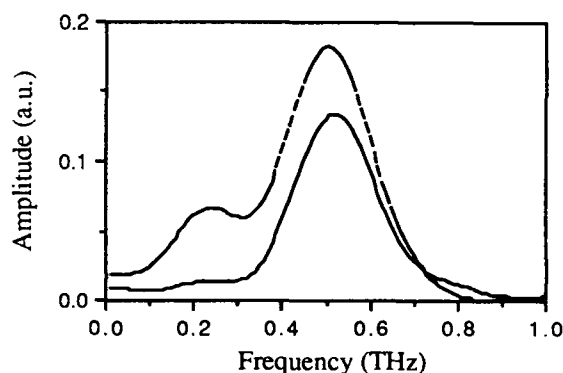


Figure 7. Fourier spectrum of current for opposite switching directions for the same final gate voltage $V_g = -1.0 \text{ V}$. The switches are from $V_g = -1.5 \text{ V}$ to -1.0 V for the solid line and from $V_g = -0.5 \text{ V}$ to -1.0 V for the dashed line.

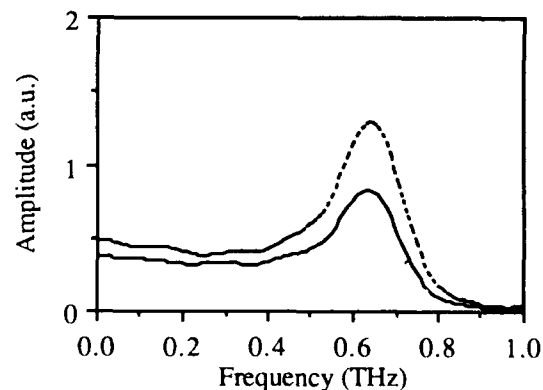


Figure 8. Comparison of the response with (solid curve) and without (dashed curve) the quantum correction terms in the simulation.

related to the quasi-ballistic and plasma response of the free carriers in the channel. The effect of the non-local quantum potential on the switching behavior implies the softening of the potential barriers in time and space and lowering the effect of the gate in charge control.

Acknowledgments

This work was supported in part by the Army Research Office.

*A. M. Kriman is currently at the Department of Electrical Engineering, SUNY, Buffalo, N.Y..

References

1. D. K. Ferry, "Lateral surface superlattice and the future of ULSI microelectronics," in *Granular Nanoelectronics*, Ed. by D. K. Ferry, J. R. Barker, and C. Jacoboni (Plenum, New York, 1991).
2. G. Baccarani, M. R. Wordeman, and R. H. Dennard, "Generalized scaling theory and its application to a 1/4 micrometer MOSFET design," *IEEE Trans. Electron Dev.* **31**, 452 (1984).
3. J. R. Barker, and D. K. Ferry, "On the physics and modeling of small semiconductor devices-I," *Solid-State Electron.* **23**, 519 (1980).
4. J. R. Barker, and D. K. Ferry, "On the physics and modeling of small semiconductor devices-II," *Solid-State Electron.* **23**, 531 (1980).
5. J. Han, D. K. Ferry, and P. Newman, "Ultra-submicron gate AlGaAs/GaAs HEMTs," *IEEE Electron Dev. Lett.* **11**, 209 (1990).
6. A. Ishibash, K. Funato, and Y. Mori, "Heterointerface field effect transistor with 200 Å-long gate," *Jpn. J. Appl. Physics* **27**, 2382 (1988).
7. G. J. Iafrate, H. L. Grubin, and D. K. Ferry, "Utilization of quantum distribution functions for ultra-submicron device transport," *J. Physique (Colloq. C-10)* **42**, 307 (1981).
8. N. C. Kluksdahl, A. M. Kriman, D. K. Ferry, and C. Ringhofer, "Self-consistent study of the resonant-tunneling diode," *Phys. Rev. B* **39**, 7720 (1989).
9. W. R. Frensley, "Wigner-function model of a resonant-tunneling semiconductor device," *Phys. Rev. B* **38**, 1570 (1987).
10. J. Zhou, A. M. Kriman and D. K. Ferry, "The conditions of device simulation using full hydrodynamic equations," in *Computational Electronics*, Ed. by K. Hess, J. P. Leburton, and U. Ravaioli (Kluwer Academic Publishers, Boston, 1991).
11. H. L. Grubin, and J. P. Kreskovsky, "Quantum moment balance equations and resonant tunneling structures," *Sol.-State Electron.* **32**, 1071 (1989).

Theoretical Model of the Photon Transport Transistor

A. K. Chu, Y. Gigase, and B. Van Zeghbroeck

Electrical and Computer Engineering Department, and the Optoelectronic Computing Systems Center, University of Colorado, Boulder, Colorado 80309-0425

Abstract

A theoretical model for the photon transport transistor (P.T.T.) is developed, based on a set of rate equations. With this model the small signal differential current gain β ($\beta = dI_C/dI_B$) is calculated and compared with measurement results. Our model confirms that the differential current gain is dominated at low carrier densities by the spontaneous emission. It then decreases once stimulated emission becomes dominant and finally collapses to a small value at the lasing threshold carrier density. We were able to quantify the non-radiative carrier recombination lifetime, which for our experimental results was found to be 300 ns, and the scattering loss in the waveguide, which amounts to 2.7cm^{-1} for an assumed total waveguide loss of 5cm^{-1} .

Introduction

Nowadays the optical telecommunication systems and high-speed optical data transmission between digital computers have become increasingly important. Interfacing optical and electrical signals made the study of optoelectronic devices important. Recent activities focus on improving the existing optoelectronic devices and circuits as well as developing new optoelectronic structures. However, the technological difficulties in optoelectronic integration have not been overcome completely, although successful demonstrations were reported [1], [2]. Recently a novel optoelectronic device was presented, namely the photon transport transistor [3].

This paper describes a theoretical model for this device, which consists of a GaAs/AlGaAs GRINSCH single quantum well ridge laser diode integrated on top of an N-i-p photodiode (figure 1(a)). This structure results in a tight optical coupling between the light emitter and the photodiode.

The device was named a 'transistor' since it has both current and voltage gain, it has isolation between the input and the output electrodes, and it is capable of inverting an electrical signal. In this device, photons rather than minority carriers transit the base region. The device does not exhibit the Early effect and the thickness of the base region does not affect the performances. Experimental devices show a current gain of 4 and a voltage gain of 10,000.

By forward biasing the photodiode, this device acts as a solar cell and converts the spontaneous emitted photons of the laser diode into electrical power. This photon recycling results in a 42% reduction of the threshold pump power of the laser diode [4].

An analysis of the PTT must focus on the behavior of the carriers in the light emitting region, on the generation of the photons and on the absorption or scattering of those photons last ones as they propagate to the photodiode.

As a starting point for our calculation we propose a set of rate equations. The steady-state solutions of this set is then used to calculate the terminal currents (I_E, I_C and I_B), and the current gain β . Some important parameters such as the scattering loss of the waveguide α_s and the non-radiative carrier recombination lifetime τ_{nr} can be extracted from the model by comparison with experimental results.

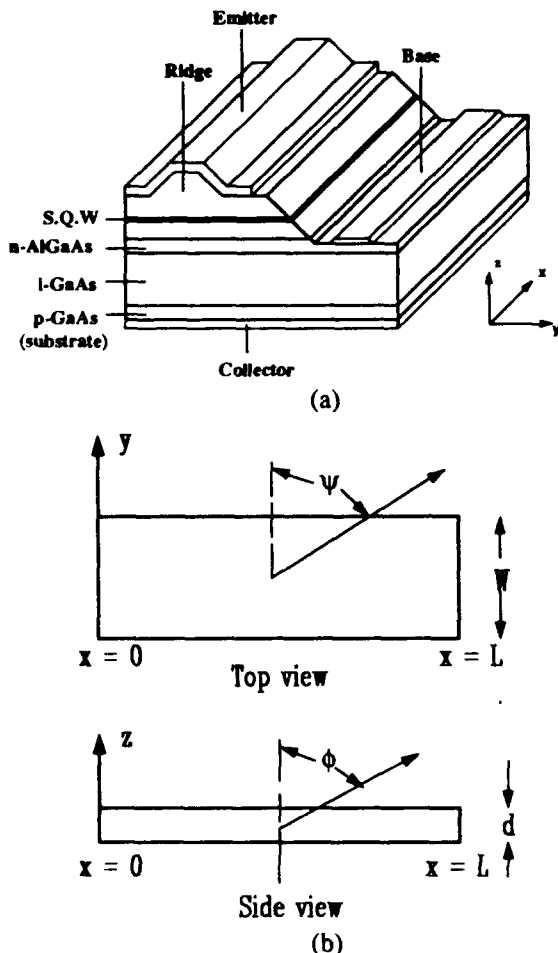


Figure 1(a). Physical structure of the photon transport transistor. (b). Definition of the angle coordinates.

Rate Equation Model of the PTT

According to their direction of emission, the photons will have a different effect on the device. If the photons propagate away from the plane of the active layer they will end up in the photodiode, eventually after being reflected at the top metal. Some of these photons are absorbed at the metal or in the different layers. Those are lost for the transistor. If the photons propagate within the confining layer structure but away from the active region, they will induce some stimulated emission. Due to the presence of the absorbing QW-layer we assume that all these photons are eventually absorbed and thus, also lost for the transistor. If the photons propagate in the waveguide they will induce stimulated emission and eventually lasing action. Normally all these photons are also lost for the transistor action but we assume that a fraction

of these photons scatter out of the waveguide region and are then detected by the photodiode.

In the analysis we consider three independent variables: the carrier density in the active region (i.e. the Q.W.), the carrier density in the photodiode and the photon density in the lasing mode.

Below lasing threshold, spontaneously emitted photons are assumed to be propagating in random directions. The fraction of those photons, which are confined within the laser cavity, is characterized by β_x :

$$\beta_x \equiv \frac{\Gamma \lambda^4}{4\pi^2 n^3 V_{act} \Delta \lambda_{sp}} \quad (1)$$

where Γ , V_{act} and $\Delta \lambda_{sp}$ are the optical confinement factor, the active layer volume and FWHM of the spontaneous emission spectrum, respectively. The optical confinement factor Γ is equal to the overlap integral of the optical mode profile with the carrier density in the Q.W. and is typically $\Gamma \approx 0.02-0.04$. The fraction of photons leaving the laser cavity are characterized by β_z and β_y and are determined from the Brewster angles ϕ_B and ψ_B , in the vertical and lateral directions. The angles ϕ and ψ are defined in Figure 1(b). The photon fraction β_y is amplified through stimulated emission while leaving the active region. The average optical gain of these photons is given by:

$$\langle g \rangle = \frac{1}{2\psi_B} \int_{-\psi_B}^{\psi_B} e^{(\Gamma G \frac{W}{2\cos\psi})} d\psi \quad (2)$$

where G is the optical gain per unit length and ψ_B is Brewster angle in the lateral direction.

The waveguide losses are split up into the absorption of photons within the waveguide and the scattering of photons from the waveguide into the underlying photodiode as follows:

$$\alpha_t = \alpha_a + \alpha_s, \quad (3)$$

where α_a and α_s are the absorption and scattering factors per unit length.

The operation of the photon transport transistor can be described by a following set of rate equations [5].

$$\frac{dN_L}{dt} = \frac{J_e}{e} \cdot (\beta_x + \langle g \rangle \beta_y + \beta_z) R(N_L) - V_{gr} \Gamma G(N_L, S_L) S_L \quad (4a)$$

$$\frac{dS_L}{dt} = \frac{-S_L}{\tau_{ph}} + \beta_x B N_L^2 \cdot V_{gr} \Gamma G(N_L, S_L) S_L \quad (4b)$$

$$\frac{dN_D}{dt} = -\frac{J_c}{e} + \beta_z B N_L^2 + \eta V_{gr} \alpha_s S_L \quad (4c)$$

$$V_L = \frac{E_g}{e} + V_T \ln[(e^{N_L/N_C} - 1)(e^{N_L/N_V} - 1)] + J_c \cdot L \cdot W \cdot R_{es} \quad (4d)$$

The symbols used in these equations and typical values of the device parameters and material constants are listed in Table 1, Table 2 and Table 3. Equations (4a) and (4b) describe the rate of change of the carrier density $N_L(\text{cm}^{-2})$ and photon density $S_L(\text{cm}^{-2})$ in the laser diode. We included spectral hole burning (SHB) which reduces the optical gain by a factor $(1-\epsilon S_L)$ where ϵ characterizes the SHB [6]. The optical gain of the laser diode is given by [7],

$$G(N_L, S_L) = A(N_L - N_{tr} \cdot \delta_{sat} \cdot N_L^2) \cdot (1 - \epsilon S_L) \quad (5a)$$

N_{tr} is the transparency carrier density and δ_{sat} is the second order gain saturation constant. In our model we assume that the carrier recombination rate equals:

$$R(N_L) = \frac{N_L}{\tau_{nr}} + B N_L^2 \quad (5b)$$

where τ_{nr} is the non-radiative time constant and B is the bimolecular recombination constant. The photon lifetime inside the cavity is determined by the reflectivity (R) of the facets, the total waveguide loss (α_t) and the length of the cavity (L) in the following way:

$$\frac{1}{\tau_{ph}} = V_{gr} \cdot (\alpha_t + \frac{1}{L} \cdot \ln(\frac{1}{R})) \quad (5c)$$

Equation (4c) states that the carriers (N_D) generated or removed in the photodiode come from three sources. The last two terms in equation (4c) are due to the absorption of spontaneously emitted photons in the z direction and scattering loss from the laser diode. Owing to the reflection at the top surface metal, most of the spontaneously emitted and scattered photons will be absorbed in the photodiode. The first term in equation (4c) is due to the photodiode current. The

Table 1. Material Constants

Effective density of states in the conduction band :	$N_C = 0.72 \cdot 10^{12} \text{cm}^{-2}$
in the valence band :	$N_V = 4.86 \cdot 10^{12} \text{cm}^{-2}$
Bandgap of quantum well :	$E_g = 1.46 \text{eV}$
Non-radiative time constant :	$\tau_{nr} = 300 \text{ns}$
Bimolecular recombination constant :	$B = 5 \cdot 10^{-5} \text{cm}^2 \text{s}^{-1}$
Transparency carrier density :	$N_{tr} = 1.6 \cdot 10^{12} \text{cm}^{-2}$
Second order gain saturation :	$\delta_{sat} = 6.5 \cdot 10^{-14} \text{cm}^2$
Optical gain saturation :	$\epsilon = 1 \cdot 10^{-12} \text{cm}^2$
Group velocity :	$V_{gr} = 0.75 \cdot 10^{10} \text{cm s}^{-1}$
Thermal voltage at 300° K:	$V_T = 25.9 \cdot 10^{-3} \text{V}$

Table 2. Device variables

Current :	$I (\text{A})$
Current density :	$J (\text{Acm}^{-2})$
Carrier density in laser diode :	$N_L (\text{cm}^{-2})$
Carrier density in photodiode :	$N_D (\text{cm}^{-2})$
Photon density :	$S_L (\text{cm}^{-2})$
Voltage across laser diode :	$V_L (\text{V})$
Spontaneous recombination rate :	$R(N_L) (\text{cm}^{-2} \text{s}^{-1})$
Optical gain :	$G(N_L, S_L) (\text{cm}^{-1})$
Waveguide loss :	$\alpha_t (\text{cm}^{-1})$
Spontaneous emission coupling constant in the x direction :	$\beta_x \approx 10^{-4}$
in the y direction :	$\beta_y \approx 0.17$
in the z direction :	$\beta_z \approx 0.83$

Table 3. Device parameters

Brewster angle in z direction :	$\phi_B \approx 80.4^\circ$
Brewster angle in y direction :	$\psi_B \approx 89.5^\circ$
Photon lifetime :	$\tau_{ph} = 7.2 \cdot 10^{-12} \text{s}$
Optical confinement factor :	$\Gamma \approx 0.03$
Width of the laser diode :	$W = 10^{-3} \text{cm}$
Length of the laser diode :	$L = 7.5 \cdot 10^{-2} \text{cm}$
Reflectivity of laser facets :	$R = 0.31$
Effective absorption efficiency:	$\eta \approx 0.91$

effective quantum efficiency η in equation (4c) includes the effects of both the reflection at the top surface metal and the absorption in the photodiode. Equation (4d) relates the voltage (V_L) across the laser diode to the carrier density (N_L) in the quantum well (Q.W.) and the emitter current density (J_e). R_{ES} is the series resistor of the laser diode. The lateral diffusion of the carriers is also included in our model by changing the effective width (W) of the laser diode. Finally we apply Kirchoff's law:

$$J_e = J_c + J_b \quad (5d)$$

By setting the left hand side of the equations (4) to zero, together with equations (5), we can find a set of steady-state solutions. The resulting D.C. differential current gain β above lasing is:

$$\beta \equiv \frac{\eta \alpha_s}{[(1-\eta)\alpha_s + \alpha_a + \frac{1}{L} \ln(\frac{1}{R})]} \quad (6)$$

A numeric solution of equations (1-4) resulted in figure 2, which shows the emitter, base and collector current together with the carrier density as a function of the base-to-emitter voltage. The onset of lasing can easily be recognized as the point at which the carrier concentration and the collector current become almost independent of the applied voltage.

Comparison with experimental results

Figure 3a. compares the calculated and measured current gain below and above the lasing threshold. At low current density, the current gain depends primarily on the ratio between the spontaneous emission and the non-radiative recombination. Knowing the bimolecular recombination rate and measuring the collector current at which $\beta = 1$, one can obtain the non-radiative time constant from:

$$\tau_{nr} = \sqrt{\frac{e\eta\beta_z}{BJ_c}} \frac{1}{2(2\eta\beta_z - 1)} \quad (7)$$

The experimental value obtained is $\tau_{nr} = 300$ ns. Figure 3b. shows the calculated gain curve for different non-radiative time constants. The figure illustrates the sensitivity of the gain curve to the non-radiative time constant. (Note that the horizontal scale is logarithmic). Therefore we can use the gain measurement to accurately determine the non-

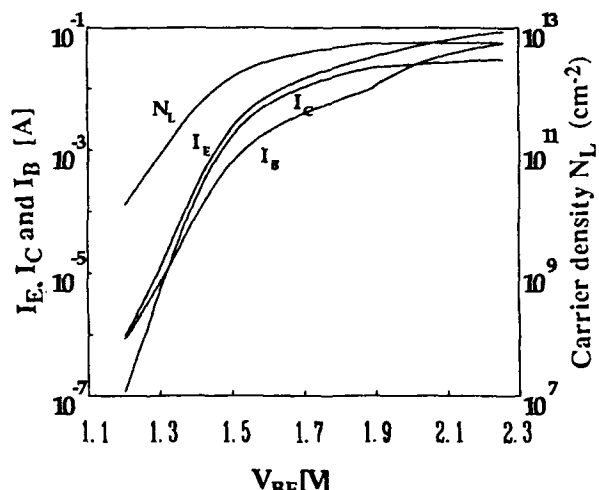


Figure 2 Calculated Gummel plot showing the emitter, base and collector current as well as the carrier density per unit area versus the base-to-emitter voltage.

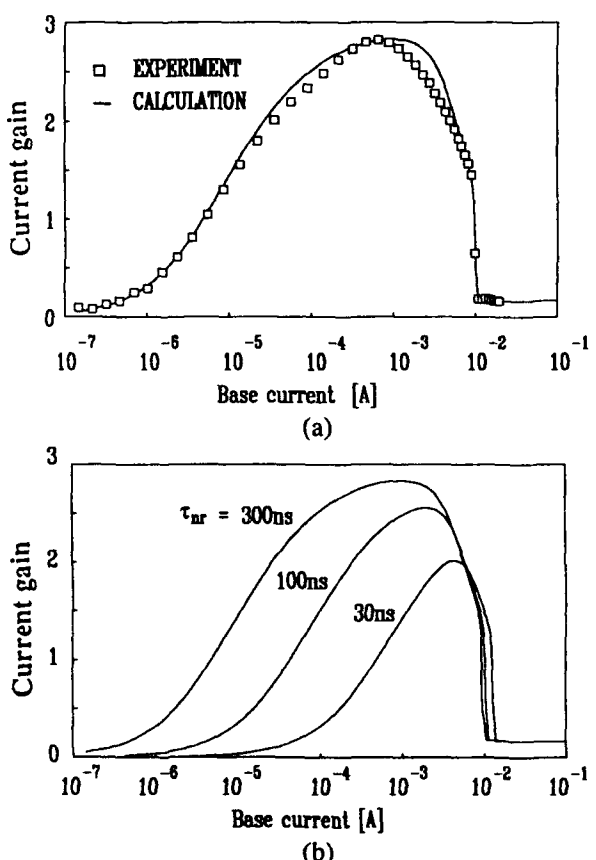


Figure 3(a). Comparison between the calculated current gain with the experimental results, 3(b). Current gain versus base current for different values of the non-radiative lifetime.

radiative time constant of the laser. No other method can provide τ_{nr} of a laser diode with the same ease and accuracy.

For intermediate current densities we observe the gain to decrease with increasing pumping current. This is caused by increased stimulated emission of photons which remain confined within the guiding layers of the laser structure and are not coupled into the photodiode. Since these photons are caused by an increased emitter current, but do not contribute to the collector current this effect reduces the observed current gain. The fraction of photons lost in the lateral direction is determined in our model by the Brewster angle ψ_B . Assuming a step index waveguide one obtains a Brewster angle of 85°. The actual value we used to fit the experimental data was 89.5°. Part of this discrepancy can be explained by the inaccuracy of the step-index waveguide assumption and by the neglection of carrier induced index changes in the active region. The correspondence between simulation and experiments does confirm that stimulated emission causes the current gain reduction with increasing current at intermediate current densities.

At and above the lasing threshold current, the carrier density becomes almost constant so that the coupling of spontaneously emitted photons into the photodiode does not contribute to the current gain. The residual gain (≥ 0.16) above threshold is due to the absorption of the scattered photons in the photodiode. By matching the calculated residual gain with the measured value, we can determine the scattering loss ($\alpha_s \geq 2.7 \text{ cm}^{-1}$) of the laser waveguide using an effective absorption efficiency η , as used in Eq.(6), of 91%. Measurements reveal that the residual gain does not change significantly with increasing photon density. Therefore optical gain saturation is negligible in our device.

Conclusions

In conclusion, a computer model has been constructed to understand the detailed operation of the photon transport transistor. We obtained good agreement between the calculated and the measured results. From the first region of the gain curve, a non-radiative time constant of 300 ns is extracted. In the second region, we found that the lateral loss in our device reduces the

current gain. By increasing the lateral confinement, one could reduce this lateral loss of photons yielding an increased current gain of the photon transistor and a reduced threshold of the laser diode. The current gain collapses at the lasing threshold. The residual gain is due to the scattering loss of the laser cavity. A comparison with our model yields a value of 2.7 cm^{-1} . And finally, since the residual gain does not change significantly with increasing photon density, optical gain saturation is negligible in our device.

Acknowledgment

The authors like to thank Dr. Ch. Harder of the IBM Zurich Research Laboratory for providing the photon transport transistors.

References

1. U.Koren, T.L.Koch, B.I.Miller, G.Eisenstein and R.H.Bsworth, "Wavelength division multiplexing light source with integrated quantum well tunable lasers and optical amplifiers" *Appl.Phys.Lett* 54, (21), 22 May 1989, 2056-2058.
2. O. Wada, T. Sakurai, and T. Nakagami, "Recent progress in optoelectronic integrated circuits (OEIC's), *IEEE J. Quant. Electr.*, Vol. QE-22, No.6, 805-821(1987).
3. B.J. Van Zeghbroeck, Ch. Harder, H.P. Meier and W.Walter, "Photon transport transistor", *Proc. of IEEE Int'l Electron Devices Meeting*, Washington DC, 543-546(1989).
4. Y.B. Gigase, Ch. Harder, M.P. Kesler, and B.J. Van Zeghbroeck, "Threshold reduction through photon recycling in semiconductor lasers", *Appl. Phys. Lett.*, 57(13), 1310-1312(1990).
5. Ch. Harder, B.J. Van Zeghbroeck, M.P. Kesler, H.P. Meier, P. Vettiger, D.J. Webb and P. Wolf, "High speed GaAs /AlGaAs optoelectronic devices for computer Applications", *IBM J. Res. Develop.* Vol. 34, No.4, 568-584(1990).
6. T.L. Koch and R.A. Linke, "Effect of nonlinear gain reduction on semiconductor laser wavelength chirping", *Appl. Phys. Lett.* 48(10), 613-615(1986).
7. Y. Arakawa and A. Yariv, "Theory of gain, modulation response, and linewidth in AlGaAs quantum well lasers", *IEEE J. Quantum Electron.*, Vol. QE-21, No.10, 1666-1674 (1985).

Subpicosecond Jitter Triggering Using Resonant Tunneling Diodes

Ekmel Özbay and David M. Bloom

Edward L. Ginzton Laboratory, Stanford University, Stanford, California 94305 4085

Abstract

Resonant tunneling diodes (RTD's) have been monolithically integrated with resistors to form trigger circuits. These circuits have been used to trigger signals at frequencies as high as 110 GHz.

Introduction

Resonant tunneling diodes (RTD's) with their superior high frequency characteristics are attractive for high speed applications. As RTD's have terminal characteristics very similar to the Esaki Tunnel Diode, current high speed applications of Esaki Tunnel Diode are good targets for this new tunneling device. One such application is high frequency trigger circuits.

The principles of a trigger circuit have been explained in a paper by Arpad Barna [1]. A device used as a threshold detector must have two threshold levels and hysteresis. The hysteresis, which differentiates this circuit from a limiter in which the output is continuous, eliminates output fluctuations due to noise when the input reaches the threshold level. This type of circuit has already been realized by using Esaki tunnel diodes. But, the frequency performance has been limited to a maximum of 20 GHz due to the speed limitations of Esaki tunnel diode.

RTD's have many advantages over Esaki tunnel diodes. One such advantage is speed. RTD pulser-circuits that we have recently fabricated and tested have been shown to have

switching times as low as 6 psec, whereas Esaki tunnel diodes have switching times of only 20 psec [2,3]. Second, Esaki tunnel diode pulse generators have a voltage swing that is limited by the bandgap of the material. The voltage swing of the RTD pulse generators can be easily changed by proper device design. In addition, Esaki tunnel diode circuits must be built from discrete parts. We have developed a fabrication process for monolithic RTD integrated circuits. Therefore, by replacing Esaki tunnel diodes with RTD's, we can achieve both faster and simpler circuits.

Experiment

We first investigated the triggering performance of a circuit that contained a single RTD. The circuit consisted of a resonant tunneling diode shunted to ground in the middle of a coplanar transmission line. A DC bias and the sum of two different signals were applied to the transmission line. One signal was a high frequency (HF) sinusoid with a relatively small amplitude. The other signal was a relatively slow sinusoid with a larger amplitude. The resulting sum resembled an HF signal superimposed on a slowly rising ramp function. For such an input voltage, switching occurred near the maximum of the HF signal. The train of switching pulses generated on the transmission line is then synchronous with the HF signal and can be used for triggering in other experiments.

To demonstrate useful triggering, the

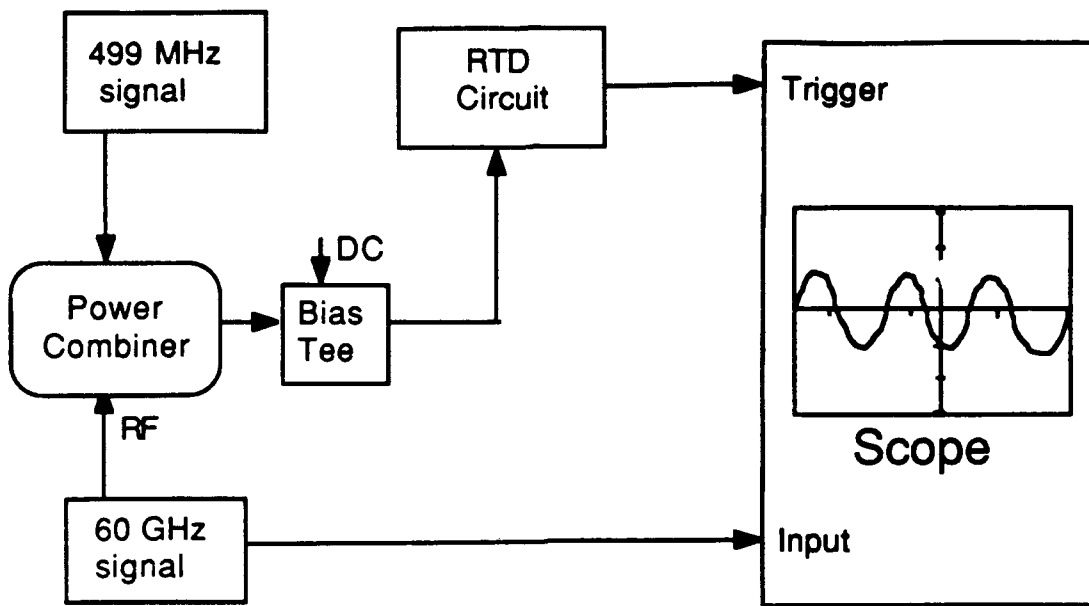


Figure 1. Experimental set-up for using the RTD circuit for triggering 60 GHz.

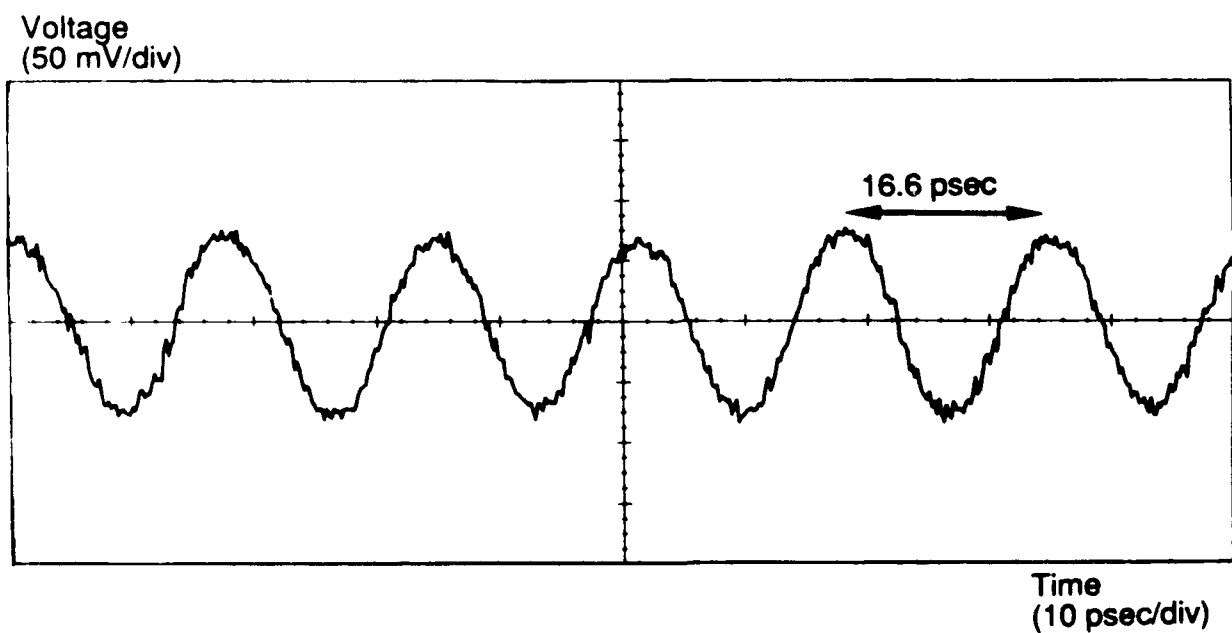


Figure 2. Oscilloscope trace of a 60 GHz signal triggered by the RTD circuit

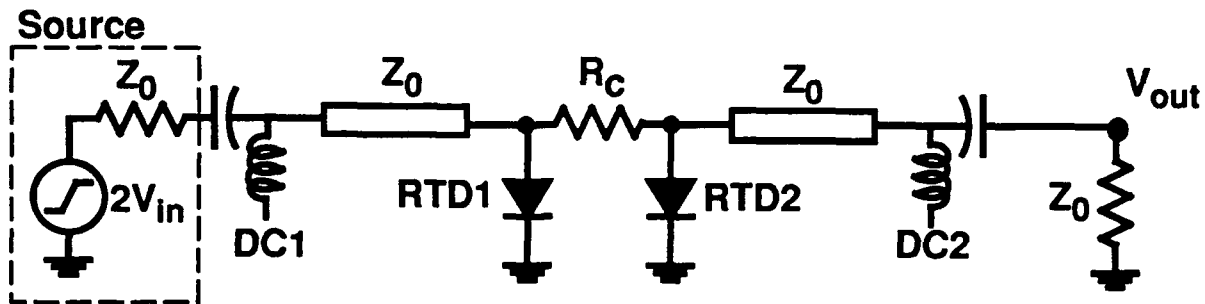


Figure 3. Circuit schematics of the new RTD trigger circuit

output of the RTD circuit was applied to the trigger input of a digitizing oscilloscope (Fig.1). To ensure that the triggering was not due to the synchronization of the slow signal with the fast 60 GHz signal, a 499 MHz (which is not a subharmonic of 60 GHz signal) slow signal was chosen. Observation of the 60 GHz signal which is triggered by the RTD circuit is shown in Fig. 2. This was at a frequency three times higher than what can be obtained with conventional trigger circuits using Esaki tunnel diodes.

Although triggering performance up to 60 GHz was achieved, jitter was a limitation. In this circuit, the switching of the RTD occurred around one of the maxima of the HF sine waveform at a point where the slope is a minimum. This translates as a maximum timing uncertainty in the switching event and a resulting voltage pulse with maximum timing jitter. Such a timing jitter severely limits higher frequency operations.

In order to overcome this jitter problem we have pursued a two diode approach. Previously, a similar approach using hybrid connections of Esaki tunnel diodes, was shown to have operating frequencies up to 18 GHz [4]. Using our fabrication process we monolithically integrated a circuit consisting of two RTD's and a resistor. The circuit was connected through coplanar transmission lines (Figure 3). Microwave probes were used to apply the input signal and to extract the output signal.

High frequency experiments were carried out by applying the sum of a ramp and a high frequency (HF) sine waveform as the input

signal. As explained before, such an input forces the first diode (RTD1 in Figure 3) to switch around one of the maxima of the HF signal. This switching then results in an instant bias level change for the second RTD (RTD2 in the figure). If the DC bias level of the second diode is chosen appropriately, the switching of the second diode occurs around the maximum slope of the HF signal. This translates as less timing uncertainty for the switching step when compared to switching around the maximum of the HF signal. The voltage step produced by RTD2 is now synchronous with the HF signal and as it had lower jitter, it can be used at higher operating frequencies.

We have tested this principle in our circuits using HF signals at W-band frequencies (75-110 GHz). Signals at this frequency range were obtained by using microwave synthesizers and W-band waveguide multipliers. We used a W-band to V-band adapter and a microwave probe with a V-band input to apply the signal to the circuit. A ramp signal at 60 MHz with a DC bias was applied through the bias input of the microwave probe. This DC bias was used for biasing the RTD1. RTD2 was biased from the other end of the circuit by another microwave probe which was also used to get the switching step as the output signal. The output signal was then applied to the trigger input of a Tektronix CSA803 waveform analyzer with a SR-32 sampling head. The input of the sampling head was fed with the output of another W-band multiplier which shares the same microwave synthesizer with the first W-band multiplier. We then observed the HF signal on the

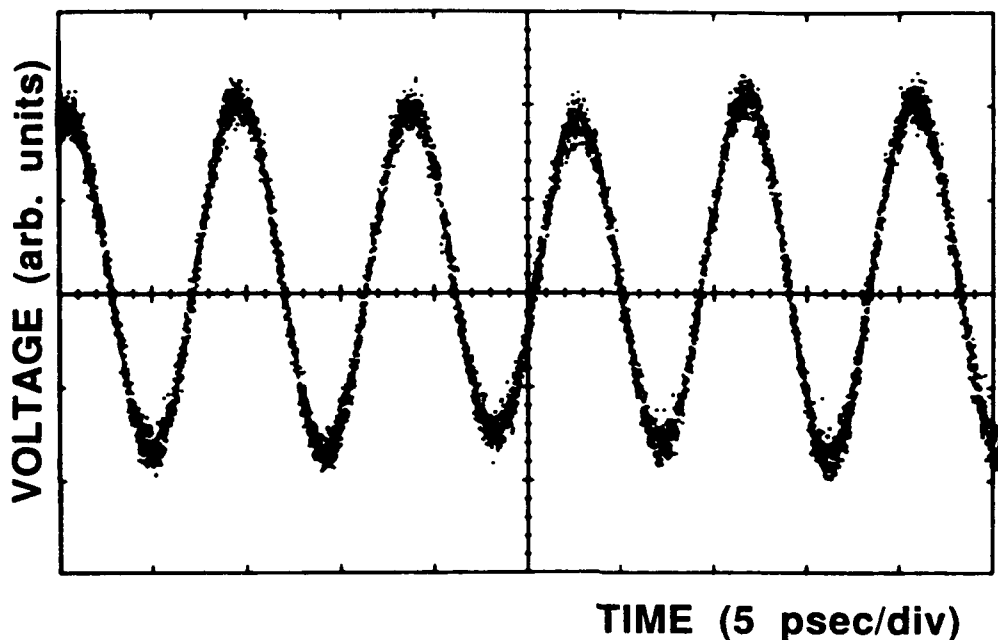


Figure 4. 2-diode RTD trigger circuit has been used to trigger off a 110 GHz signal

oscilloscope. A typical measurement at 110 GHz is shown in Figure 4. This is at a frequency six times higher than that obtained with trigger circuits using Esaki tunnel diodes. Furthermore, we have done jitter measurements of the observed signal using the waveform analyzer. Jitter measurements were made by taking 1000 samples recorded in a total of 60 seconds. We were able to measure as little as 0.75 psec timing jitter. Most of this timing jitter was introduced by the waveform analyzer and the high frequency synthesizers. This shows that our circuits indeed have timing jitter in hundreds of femtoseconds range.

Conclusion

Currently, the largest commercial application of tunnel diodes is trigger recognition in high-speed oscilloscopes. We expect that it is here that the RTD will also find its greatest utility. As has already been demonstrated, RTD's fabricated with the planar process that we have developed can be used to trigger off signals up to 110 GHz, a factor of 5 faster than the Esaki tunnel diode. Furthermore, the speed of the RTD could allow it to serve an even broader role in high-speed instrumentation. RTD's also have fast risetimes, less than 10 ps, making them well

suited to time base measurement systems. Our work has shown the possibility of broad system applications of the device as a timing element.

Acknowledgments

The authors are grateful to M. Shakouri for the valuable help in the high frequency measurements, Y. C. Pao for the material growth and B. A. Auld for useful discussions.

References

1. Arpad Barna "Nanosecond Trigger Circuits," IEEE transactions on Nuclear Science, p. 17-21, 5 Oct 1973.
2. S. K. Diamond, E. Özbay, M. J. W. Rodwell, Y. C. Pao, E. Wolak, J. S. Harris and D. M. Bloom, "Fabrication of Resonant Tunneling Diodes for switching applications," Electron Device Letters, EDL-10, p.104-106 (1989).
3. E. Özbay, S. K. Diamond and D. M. Bloom, "Pulse Forming and Triggering using Resonant Tunneling Diode Structures," Electronics Letters, Vol. 26, No.14, p.1046-1048 (1990).
4. HP 54118A Trigger, operating and service manual.

Impulse Generation and Frequency Multiplication Using Soliton Effects in Monolithic GaAs Circuits

Michael Case, Eric Carman, Masayuki Kamegawa,^{*} Kirk Giboney, Ruai Yu, Kathryn Abe, M. J. W. Rodwell,[†] and Jeff Franklin[‡]

Department of Electrical and Computer Engineering,
University of California at Santa Barbara, Santa Barbara, California 93106

Abstract

Using soliton propagation effects in GaAs nonlinear transmission lines, we have demonstrated picosecond impulse generation and broadband frequency multiplication.

Introduction

Picosecond duration, large-amplitude electrical impulses have broad applications: as strobe generators for sampling and switching circuits, as high-order harmonic generators, and as stimulus signals in high speed electrical measurements. Broadband harmonic multipliers are also very useful as medium-power sources in millimeter-wave systems.

Picosecond shock waves have been generated on GaAs nonlinear transmission lines (NLTLs) [1,2,3]. In circuits requiring a pulse waveform, the NLTL output must be differentiated. Here, we discuss methods for frequency multiplication and direct impulse generation using NLTLs similar to those used in shock-wave formation. This method of impulse generation results in significant pulse amplitude increase in the absence of skin-effect losses, and has the potential for generation of picosecond pulses with amplitudes in the tens of volts.

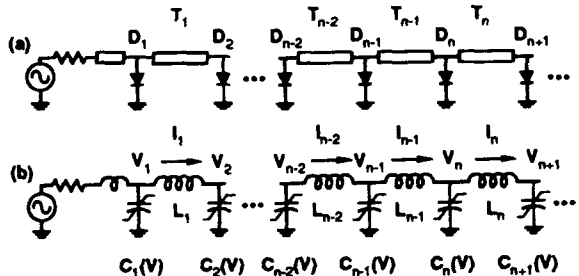


Figure 1: Nonlinear transmission line consisting of (a) a high-impedance line periodically loaded with diodes, and (b) its *LC* equivalent circuit.

Solitons on NLTLs

A solitary wave is a traveling wave having a localized transition, such as a voltage pulse, and propagating without distortion in a nonlinear, dispersive medium. Solitons have the further property that they preserve their shape and velocity after collision with other solitons [4]. The soliton can be qualitatively understood as a pulse waveform for which the effects of nonlinearity and dispersion are balanced.

NLTLs provide a nonlinear, dispersive medium for soliton propagation [4,5,6]. An NLTL (Fig. 1a) is a ladder network of high-impedance transmission line sections (T_n) periodically loaded with reverse-biased diodes (D_n) serving as voltage-variable capacitors. If the diodes D_n have capacitance $C_{n,d}(V)$ and the line sections T_n have characteristic impedance Z_L and electrical delay τ_n , then the approximate equivalent circuit (Fig. 1b) is an *LC* ladder network with $L_n = Z_L \tau_n$ and $C_n(V) = C_{n,d}(V) + (\tau_{n-1} + \tau_n)/2Z_L$. The NLTL is then a synthetic transmission line with nonlinearity arising from the diodes, and dispersion

^{*}On leave from Shimadzu corporation, Kyoto, Japan.

[†]This work was support by the Air Force Office of Scientific Research under grant number AFOSR-89-0394.

[‡]Varian Associates III-V Device Center, Santa Clara, CA 95054.

arising from its periodicity. Above the Bragg cutoff frequency $f_b = \omega_b/2\pi = 1/\pi\sqrt{LC_n(V)}$, waves do not propagate.

If the capacitance at node n has the form $C_n(V) = C_0/(1 + V/V_0)$ and $L_n = L$ for all n (i.e., if the line is homogeneous), the LC ladder network supports propagation of solitons [5] of the form

$$V_n(t) = V_{max} \operatorname{sech}^2(1.212(t - nT_D)/T_{FWHM}), \quad (1)$$

where

$$T_D = \sqrt{LC_0V_0/V_{max}} \sinh^{-1}(\sqrt{V_{max}/V_0}) \quad (2)$$

and

$$T_{FWHM} = 1.212\sqrt{LC_0V_0/V_{max}}. \quad (3)$$

For given transmission line and diode characteristics (L , C_0 , and V_0), the soliton amplitude V_{max} has a unique corresponding full-width at half-maximum (FWHM) width T_{FWHM} and propagation delay per section T_D .

On the NLTL, impulses of amplitude V_{max} having duration $T_{FWHM} > 1.212\sqrt{LC_0V_0/V_{max}}$ correspond to a nonlinear superposition of a set of solitons having differing amplitudes (i.e., different V_{max} 's) and hence differing per-section propagation delays T_D ; applied to the NLTL, the impulse will decompose into this set of two or more solitons [5] during propagation. Figure 2 shows a circuit simulation of a $V_{max} = 6$ volt, $T_{FWHM} = 62.5$ ps FWHM raised-cosine input impulse splitting during propagation into a pair of solitons by the 26th diode. The larger soliton has $V_{max} = 8.9$ volts and $T_{FWHM} = 27$ ps. In this and subsequent simulations, we modeled the NLTL structure as a high impedance (90Ω) transmission line loaded by diodes whose model parameters matched those of our process. By fitting our $C(V)$ characteristics to the $C(V)$ assumed in the above solutions, we estimate the characteristic parameters of this simulated soliton line as $L \approx 1$ nH, $C_0 \approx 740$ fF, and $V_0 \approx 3.6$ volts. The f_b of this network is 16 GHz with the diodes biased at -3 volts (i.e. the average of the input pulse voltage).

With a broader input pulse, a larger number of solitons is produced. Figure 3 shows a simulation of a $V_{max} = 6$ volt, $T_{FWHM} = 94$ ps FWHM raised-cosine input impulse decomposing into three solitons by the 42nd diode on the same NLTL as used in the first example. The largest of the three solitons has $V_{max} = 7.9$ volts and $T_{FWHM} = 31$ ps.

Harmonic Generation

We use the splitting of input pulses into pairs of solitons as a method of second-harmonic generation.

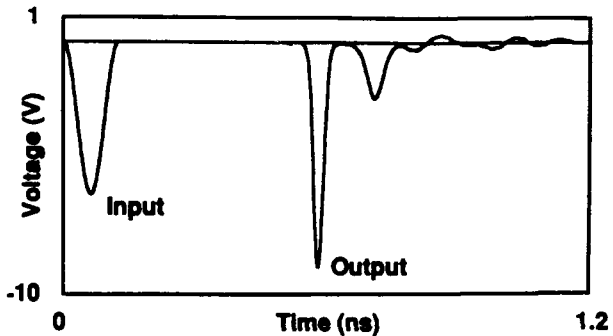


Figure 2: Simulation of a raised-cosine pulse decomposing into two solitons on a homogeneous line.

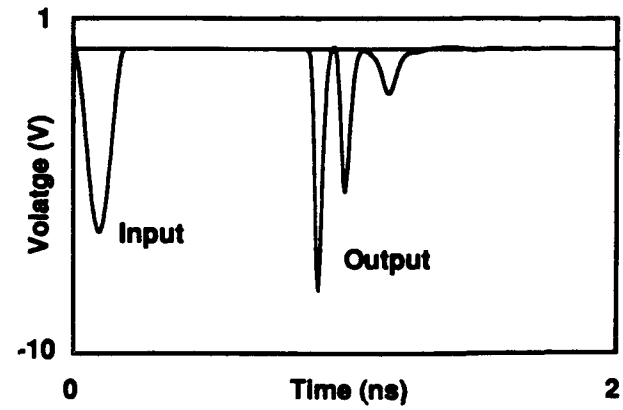


Figure 3: Simulation of a broad pulse decomposing into three solitons on a homogeneous soliton line.

A sinusoidal input at frequency ω_1 corresponds to a repetitive train of negative-going input impulses of duration $T_{FWHM} = \pi/\omega_1$. On the NLTL, each of these pulses corresponds to a superposition of a set of solitons which subsequently separate during propagation. Applying a 15 GHz, 20 dBm input to a 20-diode monolithic NLTL with $f_b = 44$ GHz, each negative cycle of a 15 GHz, 20 dBm input decomposes into a pair of negative-going pulses which progressively separate during propagation (Fig. 4), as measured using electrooptic sampling [7]. A strong second harmonic component is generated in the output.

With further propagation on a longer NLTL, the lower-amplitude soliton of a given input cycle merges with the larger-amplitude soliton of the subsequent input cycle, and the input waveform is recreated, decreasing the second-harmonic power to zero. This recurrence phenomenon forces a limit to the length of the NLTL for efficient harmonic conversion [8]. Pulses much longer than $2\pi/\omega_b$ separate into progressively larger numbers of solitons; a 10 GHz input (Fig. 4) decomposes into sets of 3 solitons per

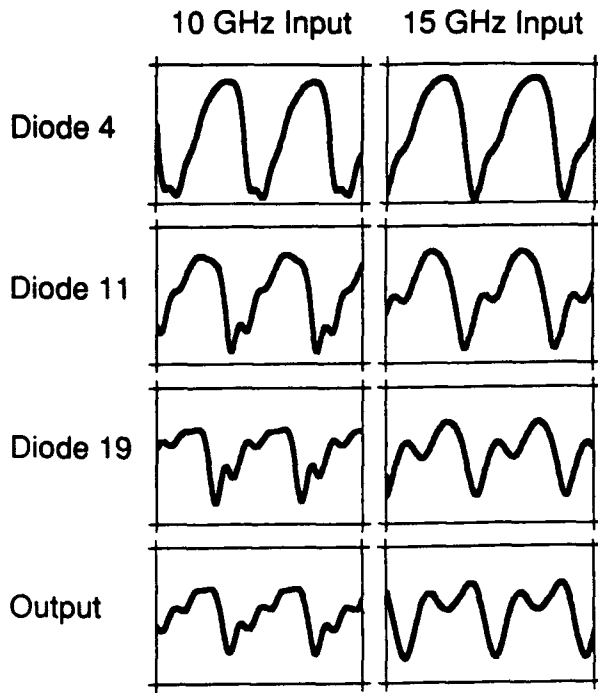


Figure 4: Experimentally observed waveforms illustrating soliton decomposition on a 20-diode NTL.

cycle, and a strong output third harmonic is generated. Efficient 2nd harmonic generation thus occurs for $\omega_b/3 < \omega_1 < \omega_b/2$.

A 20-diode NTL distributed harmonic generator was fabricated, having $Z_L = 90\Omega$, $\tau = 4$ ps, and $f_b = 44$ GHz. The NTL's characteristics fit to the soliton line model are $L \approx 0.36$ nH, $C_0 \approx 274$ fF, and $V_0 \approx 3.2$ V. Neglecting skin-effect losses, circuit simulations using a harmonic-balance algorithm predict 3 dB conversion loss at peak efficiency, and < 6 dB loss from 13.2 to 18.1 GHz input frequency.

Conversion efficiency was measured on-wafer using wafer probes, microwave synthesizer, and spectrum analyzer. With 20 dBm input power, the NTL attains 9.3 dB insertion loss at peak efficiency and 13.5-18 GHz bandwidth at < 12 dB loss (Fig. 5). The lower-than-predicted conversion loss arises from skin-effect losses on the 90Ω line sections (1.4 μm thick gold with 10 μm line width), which have relatively low Q . When skin losses are modelled, measured conversion loss is ~ 2 dB greater than simulation. Circuit implementation with less lossy inductors will permit conversion efficiency approaching 3 dB.

Impulse Generation

A pulse with $T_{FWHM} > 1.212\sqrt{LC_0V_0/V_{max}}$ input to an NTL will decompose into its characteristic set

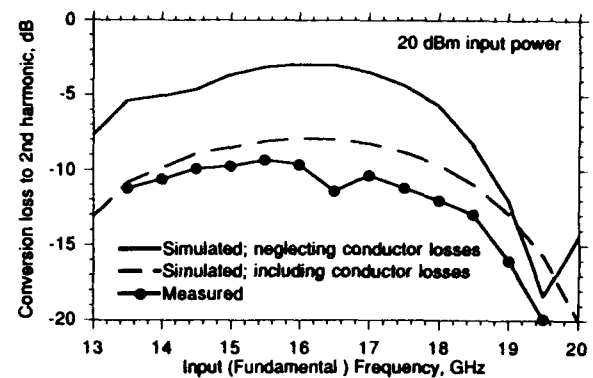


Figure 5: Simulated and measured conversion loss in second harmonic generation.

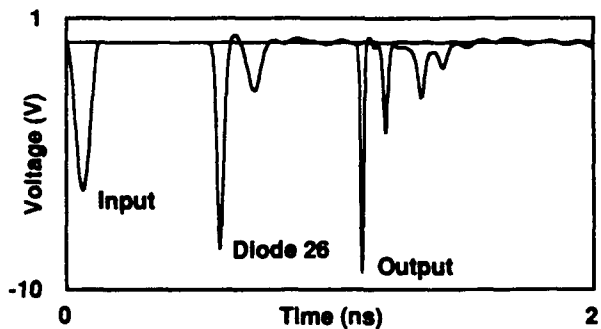


Figure 6: Simulation of soliton impulse compression on a two-stage step-tapered NTL.

of solitons. Longer input pulses decompose into progressively larger numbers of solitons [5]. To attain larger impulse compression ratios while maintaining predominantly a single impulse, a step-tapered network consisting of cascaded sections of NTLs with progressively decreasing diode spacings and sizes, or equivalently progressively decreasing characteristic time constant $\sqrt{LC_0}$, can be used. Figure 6 shows a simulation of a cascaded impulse compression line with 80 diodes and two compression sections. For the first compression section of 26 diodes ($n = 1$ to 26) the ladder network parameters are $L_n \approx 1$ nH and $C_{0,n} \approx 740$ fF as in the previous simulation, while the second, cascaded compression section of 54 diodes ($n = 27$ to 80) has $L_n \approx 500$ pH, $C_{0,n} \approx 370$ fF; $V_0 \approx 3.6$ volts in both sections. Within each compression section, the line is homogeneous. In the first compression section, the input impulse splits into a pair of solitons, each having impulse width related to impulse amplitude by Eq. 2, where $L \approx 1$ nH and $C_0 \approx 740$ fF. Applied to the second compression section, each of the two impulses from the first section have T_{FWHM} longer than the soliton duration in the second line section, because of the

impulse compression ratio. The second compression section then splits each of the two impulses into two smaller pulses, and so on. The final output is a sequence of increasingly smaller pulses, representing the compressed impulse.

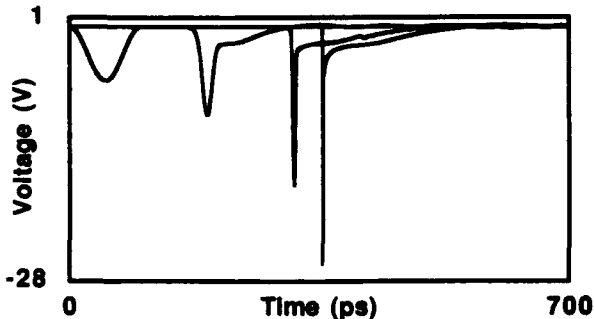


Figure 7: Simulation of soliton impulse compression on a continuously tapered NLTL. Voltages are shown at the input, after 8.9 mm and 17 mm propagation, and at the output.

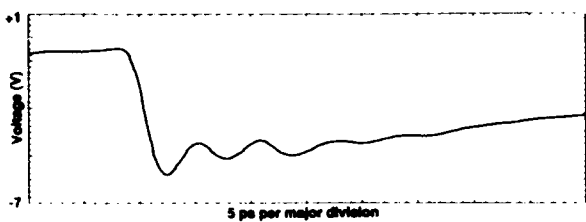


Figure 8: Measured step response of the on-wafer sampling circuit. The sampling circuit has a risetime of ~ 1.26 ps and 275 GHz bandwidth.

2 : 1 decrease in $\sqrt{LC_0}$. Each of the two impulses is thus again split during propagation into a pair of solitons. The line output, at diode 80, then consists of 4 impulses, the first of which at $V_{max} = 9.31$ volts and $T_{FWHM} = 13.8$ ps, has 4.5 : 1 shorter duration than the input. More homogeneous compression sections, with progressively smaller $\sqrt{LC_0}$ time constants, could be added. In each successive section, the leading impulse is compressed further, providing a very large compression ratio, but also generating a large number of parasitic (undesired) impulses extending over a long period of time.

Impulses can also be compressed [6] in inhomogeneous NLTLs where the diode spacings and diode capacitances are continuously tapered. We let the transmission line lengths $\tau_n = k^n \tau_0$, and diode capacitances $C_{n,d} = k^n C_{0,d}$ decrease ($k < 1$) in an exponential progression along the NLTL structure. The inhomogeneous NLTL is a limiting case of a step-tapered network having a large number of cascaded homogeneous compression sections, with each section having only one diode. For the exponentially tapered network (Fig. 7), circuit simulations predict formation of a highly compressed impulse accompanied by a pedestal. In the simulation, $k = 0.94$, $\tau_0 = 11$ ps, $Z_L = 90 \Omega$, $C_{0,0} \approx 740$ fF, $V_0 \approx 3.6$

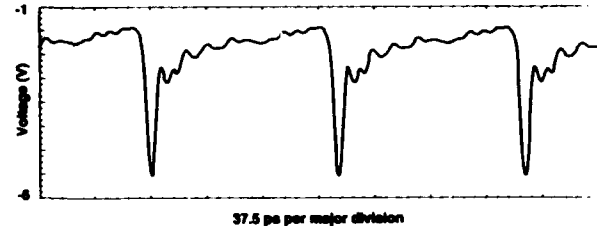


Figure 9: Measured 5.5 ps FWHM impulse train generated by the continuously tapered NLTL. 8 GHz, 20 dBm sinusoidal input.

volts, and the line has 66 sections. The SPICE simulation includes diode series resistances r_n consistent with an 865 GHz diode zero-bias cutoff frequency, but skin-effect losses cannot be modelled. Harmonic-balance simulators allow skin-loss modelling, but do not converge when simulating tapered impulse compressors. The SPICE simulation shows a 50 ps FWHM, 6 volt raised-cosine impulse at the input compressed to a 0.5 ps, 26 volt impulse at the output.

Using the circuit parameters of the simulation above, continuously tapered impulse compression lines were fabricated on GaAs semi-insulating substrates. In the monolithic structures, we again use $V_0 = 3.6$ volts and $C_{0,0} = 740$ fF (for a $508 \mu\text{m}^2$ diode) to provide an approximate fit of the soliton model capacitance [5] $C_n(V) = C_{0,n}/(1 + V/V_0)$ to the combined hyperabrupt diode and transmission-line capacitance. The characteristic $\sqrt{L_n C_{0,n}}$ time constant grades from 27 ps at the line input ($n = 0$) to 0.46 ps at the output ($n = 66$). An on-wafer 275 GHz bandwidth sampling circuit [3] measures the impulse generator's output. The step response of this sampler is shown in Figure 8. In testing, an 8 GHz, 20.7 dBm sinusoidal input superimposed on a 2.75 volt negative bias generated (Fig. 9) an output $3.9 V_{p-p}$, 5.5 ps FWHM impulse train with 30% pedestal amplitude.

The low (3.9 V measured, Fig. 9, vs. 26 V simulated, Fig. 7) output amplitude arises from high skin-effect losses on the ~ 2 cm long structure, not modelled in the simulation. This loss in amplitude greatly inhibits impulse width compression, since the diodes provide less nonlinearity for a smaller voltage swing. Sinusoidal drive also degrades compression efficiency. As with the harmonic generators, skin loss can be reduced by using less lossy interconnecting structures. More abrupt diode doping profiles will reduce V_0 , reducing the propagation distance necessary to separate solitons, and hence reduce the overall device length.

Summary

Using soliton nonlinear transmission lines, we have directly generated picosecond pulses without differentiation and have generated second harmonic with moderate efficiency over a 33% fractional bandwidth. Both structures suffered greatly from skin-effect losses, and their performance will be greatly enhanced by using lower impedance interconnecting transmission lines (on the order of 75Ω) or planar spiral inductors, both of which have higher Q than the 90Ω lines in the current structure. Once these metallic losses have been reduced, ~ 20 volt, ~ 1 ps impulse generators and ~ 3 dB conversion loss second harmonic broadband multipliers will be realizable.

Acknowledgments: We acknowledge John Bowers for the use of his laser facilities.

References

- [1] C. J. Madden, R. A. Marsland, M. J. W. Rodwell, D. M. Bloom, Y. C. Pao, "Hyperabrupt-doped GaAs Nonlinear Transmission Line for Picosecond Shock-wave Generation," *Applied Physics Letters*, **54** (11), 1019 (1989)
- [2] R. A. Marsland, V. Valdivia, C. J. Madden, M. J. W. Rodwell, D. M. Bloom, "130 GHz GaAs
- [3] R. Y. Yu, M. Case, M. Kamegawa, M. Sundaram, M. J. W. Rodwell, A. W. Gossard, "275 GHz 3-Mask Integrated GaAs Sampling Circuit," *Electronics Letters*, **26** (13), 949 (1990)
- [4] A. C. Scott, F. Y. F. Chu, D. W. McLaughlin, "The Soliton: a New Concept in Applied Science," *Proc. IEEE* **61** (10), 1443 (1973)
- [5] R. Hirota and K. Suzuki, "Theoretical and Experimental Studies of Lattice Solitons in Nonlinear Lumped Networks," *Proceedings of the IEEE* **61** (10), 1483 (1973)
- [6] M. Tan, C. Y. Su, and W. J. Anklam, "7X Electrical Pulse Compression on an Inhomogeneous Nonlinear Transmission Line," *Electronics Letters* **24** (4), 213 (1988)
- [7] K.J. Weingarten, M.J.W. Rodwell, and D.M. Bloom, "Picosecond Optical Sampling of GaAs Integrated Circuits," *IEEE Journal of Quantum Electronics*, **24** (2), 198 (1988)
- [8] K. S. Champlin, D. R. Singh, "Small-Signal Second Harmonic Generation by a Nonlinear Transmission Line," *IEEE Transactions on Microwave Theory and Techniques*, **34** (3), 351 (1986)

Millimeter-Wave Circuits

100-GHz Electro-Optic S-Parameter Characterization of High-Electron-Mobility Transistors

M. Y. Frankel, J. F. Whitaker, G. A. Mourou, and J. A. Valdmanis

Ultrafast Science Laboratory, University of Michigan, Ann Arbor, Michigan 48109-2099

P. M. Smith

GE Electronics Laboratory, Syracuse, New York 13221

I. Introduction

Progress in the research of modern semiconductor devices has advanced their response frequencies above 400 GHz.[1] Such performance exceeds the conventional, purely electronic test instrumentation bandwidth, with the major limitations being imposed by the connectors and waveguides that are required for signal coupling to the device under test (DUT). This lack of convenient and accurate high-bandwidth device characterization methods imposes a serious obstacle to progress in semiconductor device development and utilization.

Ultrafast optoelectronic techniques provide a viable alternative to electronic ones. In particular, photoconductive switching is used for multi-hundred-gigahertz-bandwidth electrical-stimulus generation, and photoconductive or electro-optic sampling are used for similar bandwidth measurements.[2-5] Their advantage lies primarily in both the stimulus-generation site and response-measurement planes being physically close to the DUT. This has the potential to completely eliminate any discontinuities, although the previously reported measurements have been bandwidth limited by two other factors -- the choice of microstrip lines as transmission media, and photoconductive sampling as measurement technique.

We now report the first application of the external electro-optic sampling (EEOS) technique combined with high-bandwidth coplanar strip transmission lines (CPS) [6] for the extraction of small-signal S-parameters of an active device. This technique enables one to determine device characteristics to a frequency of 100 GHz without extrapolation. In Section II, we discuss the parameters and the results affecting the selection of electro-optic sampling as the measurement technique of choice. The

motivation for selecting the CPS geometry as transmission media is presented, also. In Section III, we address the issues of designing a complete small-signal device characterization fixture.

II. Stimulus Measurement, Generation and Propagation.

We have used a balanced colliding-pulse mode-locked laser providing 100-fs pulses at 100 MHz [7], along with a two-stage lock-in detection technique in all of the following experiments.[8] The electro-optic measurements were performed with an external electro-optic transducer.[6] The substrates used were ion-implant damaged silicon-on-sapphire (SOS) to allow for photoconductive generation of sub-picosecond pulses.[9]

We have selected the external electro-optic sampling technique for its excellent bandwidth and the fact that it may be used with any circuit substrate material. The accuracy and invasiveness of such a measurement have been investigated.[10] Figure 1 shows the possible sources of error that affect the accuracy of EEOS: i) the reflection of electrical signals from the vertical interfaces of bulk LiTaO₃; ii) the switch-emitted radiation reflecting from the substrate boundary up to the measurement sight; iii) the transmission line impedance change induced by the LiTaO₃ material appearing as a superstrate.

Our investigations have shown that the primary source of error can be attributed to the LiTaO₃ bulk electrical resonance.[10] Figure 2 shows the response signals of a picosecond photoconductor switch embedded in a CPS measured with external electro-optic probes (EEP) of various thickness. We can readily identify the resonances directly related to the EEP thickness in the top three traces. However, the thinnest (20 μm) EEP is small enough to behave as a

lumped element and suppress the bulk resonance. The response measured with this probe is the same as that expected for the photoconductor switch. The small amplitude bulge appearing on the tail of this signal is due to switch radiation detection by the EEP [(iii) in Fig.1]. This phenomenon is common to all optoelectronic technique, but can be easily handled by increasing the substrate thickness. The small shoulder on the falling edge of the pulse is due to the reflection of the electrical signal from the output facet of the EEP. We note, however, that we are typically interested in the relative difference between two measurements. Thus, this linear response perturbation is cancelled out in the frequency domain and high measurement accuracy is maintained.

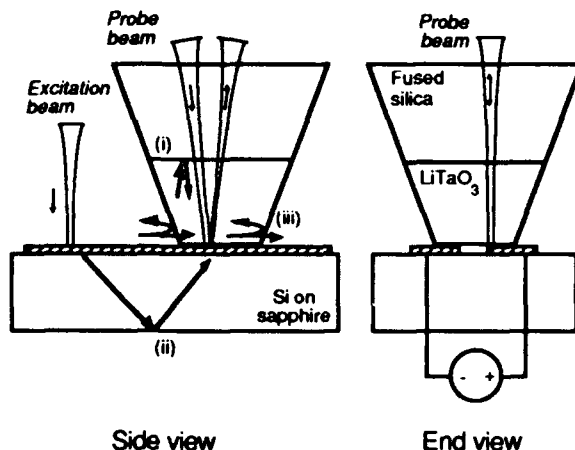


Figure 1. External electro-optic probe, with reflection sources that may create error.

The invasiveness of the EEP was determined by measuring the additional phase delay introduced by the EEP material. The effective superstrate permittivity computed from these measurements was ~5, which is substantially below the LiTaO_3 permittivity of 41. The reason for this discrepancy can be seen from Fig. 3, where the equipotential lines for a CPS on a sapphire substrate are plotted. The dielectric screening of the LiTaO_3 material, combined with the air gap due to finite CPS metallization thickness and mechanical imperfections, expels the electric field out of the high-dielectric-constant EEP. The result is an only slightly reduced impedance of the CPS over the length where the EEP is positioned.

The selection of microstrip or coplanar strip transmission line is dictated by the considerations of high bandwidth electrical signal generation and propagation properties. The microstrip bandwidth is primarily determined by the thickness of the dielectric substrate, and mechanical constraints impose an upper limit on its bandwidth. However, the CPS is photolithographically defined and can be scaled to much higher bandwidths. Figure 4 shows the responses of $50\text{-}\Omega$ microstrip and CPS transmission

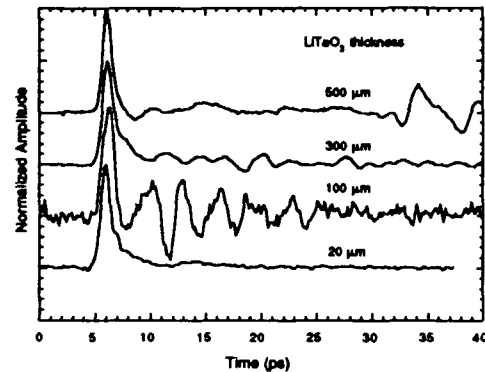


Figure 2. EEP measured signals.

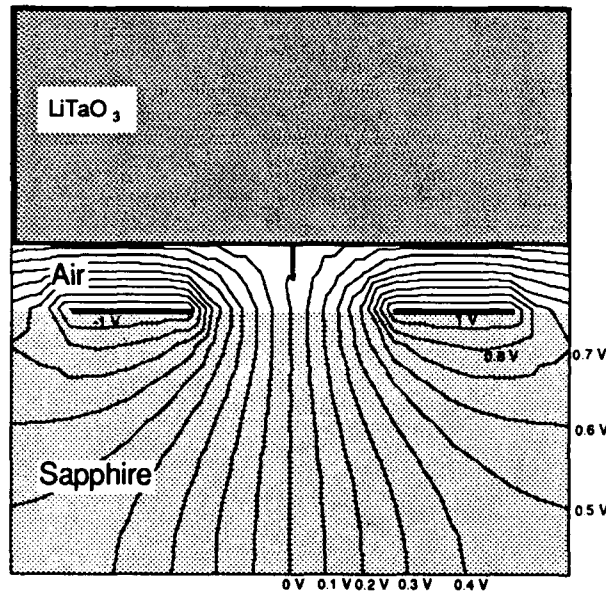


Figure 3. Equipotential lines around CPS with EEP.

lines. The microstrip response is longer in time indicating lower bandwidth. The electrical signal round-trip time between top electrode and ground plane is greater than the photoconductor-switch response time, resulting in substantial ringing in the microstrip response. Thus, the CPS is a better choice for high-bandwidth stimulus generation. Additionally, the planar nature of the CPS potentially allows for a parasitic-less integration with the planar devices under test (i.e., connections through via holes to microstrip ground plane are not necessary).

The propagation properties of the CPS have been investigated to determine the most suitable geometry. The dispersion and the attenuation characteristics can be obtained from the ratios of the Fourier transforms of electrical signals measured at spatially separated points along the CPS. For example, Figure 5(a,b) shows such data obtained from

a CPS with 30- μm electrodes spaced by 20 μm . The calculated results are from semi-empirical analytic formulas.[11] We should note the good agreement between the measurements and calculations over a tremendous bandwidth of near-dc to near-THz frequencies.

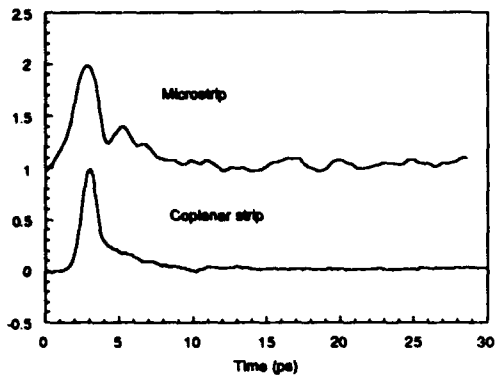


Figure 4. Photoconductor switch responses.

III. Device Characterization.

The results from the previous section were combined into a device S-parameter characterization fixture shown in Fig. 6. The device is wirebonded into a symmetric CPS holder allowing for two-port network analysis. The CPS had 50- μm -wide conductors separated by 5 μm , and it was fabricated on an ion-damaged, silicon-on-sapphire substrate. Photoconductor switches are embedded into the CPS and the dc biases are brought to the DUT on the same lines as the broadband stimulus pulses. Two measurement points on the input CPS were used to characterize its dispersion and attenuation characteristics. A measurement point on the input CPS was used to obtain the incident and reflected signals. It was separated by 1.2 mm from the DUT to allow for time-windowing of these signals. The input CPS is sufficiently long so that one can separate in time the reflected DUT signal from signals arising at other discontinuities. A measurement 200 μm from the output of the DUT was used to obtain the forward transmission signal. Again, the CPS was long enough to time-window the transmitted DUT signal from those due to other discontinuities. Following a similar procedure at the output side, two-port time-domain characteristics can be measured.

The DUT was a 0.15- μm -gate-length pseudomorphic heterojunction FET supplied by General Electric. Its design, shown in Fig. 7, is different from conventional high-electron-mobility transistors. An AlGaAs/GaAs superlattice is used below the channel to improve carrier confinement. An additional planar doped layer in the strained channel

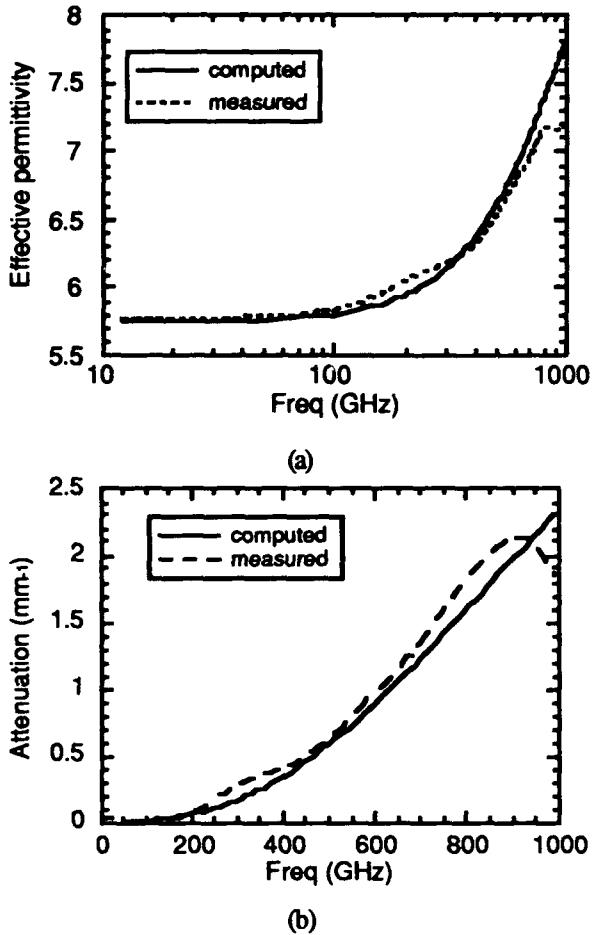


Figure 5. CPS dispersion and attenuation.

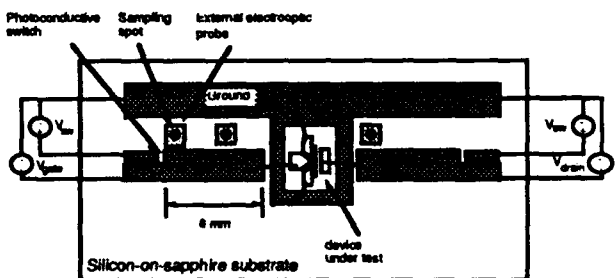


Figure 6. S-parameter characterization fixture.

improves charge density, which more than compensates for somewhat lower mobility.[12]

Figure 8 shows the signals measured on the gate input and drain output of the DUT. The measurement plane is removed from the DUT, allowing us to time-window the incident and reflected signals. We see that the input signal recovers to zero baseline before the reflected signal arrives. The long input CPS assures that the DUT reflected response

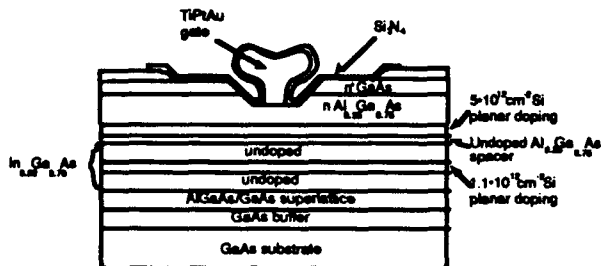


Figure 7. Heterojunction Field-Effect Transistor.

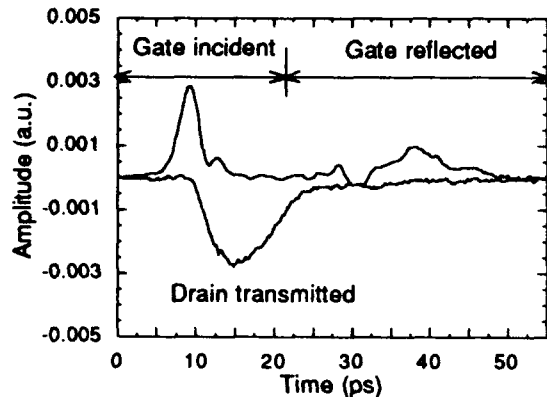


Figure 8. Time-domain signals measured via EEOs for network analysis.

recovers to zero before any other reflections arrive to the measurement plane. Similarly, the drain output is seen to recover to zero completely within the measurement time-window.

The reflection (S_{11} , S_{22}) and transmission (S_{21} , S_{12}) S-parameters were obtained from the ratios of the Fourier transforms of the reflected, transmitted and input waveforms from both the gate and drain sides of the device. The effective measurement planes were shifted up to the DUT wirebonds by taking into account the phase delay and attenuation introduced by the lengths of CPS separating the physical measurement planes. Figure 9 shows the S-parameters extracted from these measurements up to 100 GHz. For comparison, S-parameters obtained from conventional HP8510 measurements up to 40 GHz for a similar device are shown, too. It can be seen that the agreement is quite good in the range where conventional measurements have been made. The discrepancy in the S_{22} measurements is currently under investigation, although it might be attributed to the differences in the DUT or in the wirebond parasitics.

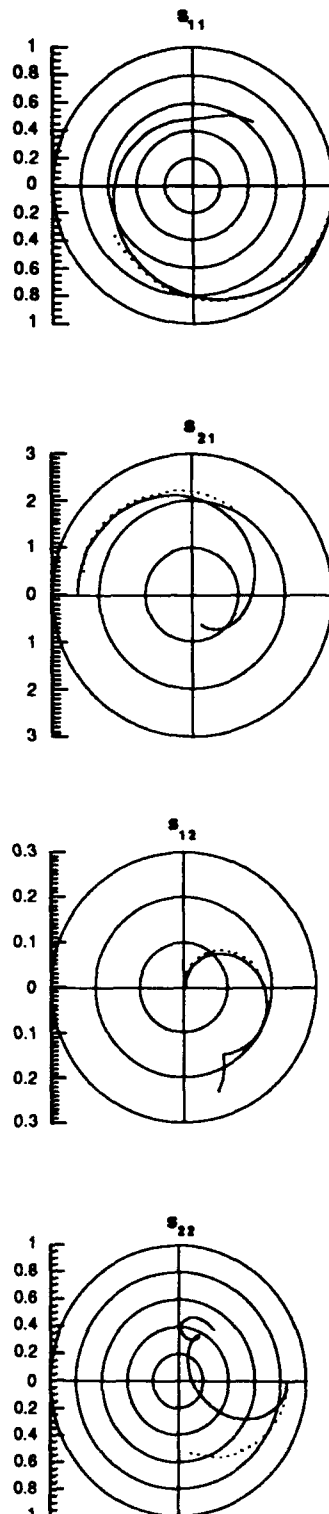


Figure 9. Measured S-parameters.
 (—) E/O up to 100 GHz;
 (---) HP8510 up to 40 GHz.

Conventional figures of merit, such as the unity current gain frequency and the maximum frequency of oscillation (f_{max}) can be determined from the measured S-parameters *without need for extrapolation*. Figure 10 shows the maximum available gain curve computed from both the electro-optic (—) and HP8510 (---) measured S-parameters. The directly measured f_{max} is seen to be ~92 GHz. This is slightly lower than that extrapolated from the HP8510 measurement, although this could be due to the sources of error previously mentioned.

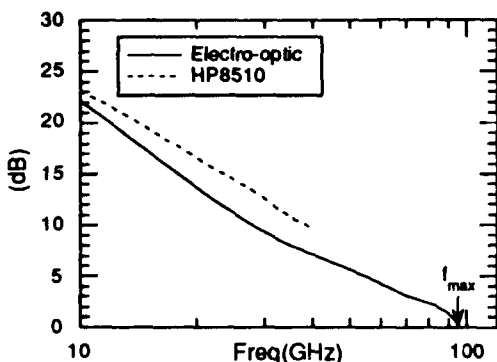


Figure 10. Maximum unilateral gain.

Work is in progress to apply this technique to the characterization of much faster devices.

IV. Conclusion

We have demonstrated the application of external electro-optic sampling and coplanar strip transmission lines to the S-parameter characterization of modern ultrafast devices. A measurement bandwidth of 100 GHz has been experimentally demonstrated (i.e., without need for extrapolation). Work is in progress to extend this bandwidth by several times, while characterizing devices with cutoff frequencies greater than those reported here.

Acknowledgments

M.Y. Frankel would like to thank Siemens, Munich for financial support. This work was supported by NASA under contract number NCC3-130 and the Air Force Office of Scientific Research, University Research Initiative under contract number AFOSR-90-0214.

References

1. A.J. Tessner, P.C. Chao, K.H.G. Duh, P. Ho, M.Y. Kao, S.M.J. Liu, P.M. Smith, J.M. Ballingall, A.A. Jabra, and T.H. Yu, "Very high performance $0.15 \mu m$ gate-length InAlAs/InGaAs/InP lattice matched HEMTs," 12th Biennial IEEE/Cornell University Conf. on Advanced Concepts in High Speed Semiconductor Devices and Circuits.
2. D.E. Cooper and S.C. Moss, "Picosecond optoelectronic measurement of the high-frequency scattering parameters of a GaAs FET," IEEE J. Quantum. Electron., vol. QE-22, pp. 94-100, Jan. 1986.
3. M. Matloubian, H. Fetterman, M. Kim, A. Oki, J. Camou, S. Moss, and D. Smith, "Picosecond optoelectronic measurement of S-parameters and optical response of an AlGaAs/GaAs HBT," IEEE Trans. on Microwave Theory Tech., vol. 38, pp. 683-686, May 1990.
4. C.H. Lee, "Picosecond optics and microwave technology," IEEE Trans. on Microwave Theory Tech., vol. 38, pp. 596-607, May 1990.
5. C. Rauscher, "Photoconductor-based 10-110 GHz on-chip device characterization technique," 1990 IEEE Microwave Theory and Techniques Symposium Digest, pp. 607-610.
6. J.A. Valdmanis, "1 THz-bandwidth prober for high-speed devices and integrated circuits," Electronics Letters, vol. 23, pp. 1308-1310, 19 Nov. 1987.
7. J.A. Valdmanis and R.L. Fork, "Design considerations for a femtosecond pulse laser balancing self phase modulation, group velocity dispersion, saturable absorption and saturable gain," IEEE J. Quantum Electron., vol. QE-22, pp. 112-118, Jan. 1986.
8. J.M. Chwalek and D.R. Dykaar, "A mixer based electro-optic sampling system for submillivolt signal detection," Review of Scientific Instr., vol. 61, pp. 1273-1276, Apr. 1990.
9. F.E. Doany, D. Grischkowsky, and C.-C. Chi, "Carrier lifetime versus ion-implantation dose in silicon on sapphire," Appl. Phys. Lett., vol. 50, pp. 460-462, 1987.
10. M.Y. Frankel, J.F. Whitaker, G.A. Mourou, J.A. Valdmanis, "Experimental characterization of external electrooptic probes," IEEE Microwave and Guided Wave Letters, vol. 1, pp. 60-62, March 1991.
11. M.Y. Frankel, S. Gupta, J.A. Valdmanis, G.A. Mourou, "Terahertz attenuation and dispersion characteristics of coplanar transmission lines," IEEE Trans. on Microwave Theory Tech., vol. 39, June 1991.
12. P.M. Smith, L.F. Lester, P.-C. Chao, P. Ho, R.P. Smith, J.M. Ballingali, and M.-Y Kao, "A $0.25-\mu m$ gate-length pseudomorphic HFET with 32-mW output power at 94 GHz," IEEE Electron Dev. Letters, vol. 10, pp. 437-439, Oct. 1989.

Display of Microwave Waveform Through a Low-Frequency Replica Using an Optical Phase-Locking and Sampling Technique

Ming G. Li, Sheng-lung L. Huang, and Chi H. Lee

*Electrical Engineering Department, University of Maryland,
College Park, Maryland 20742*

Hing-Loi A. Hung

COMSAT Laboratories, Clarksburg, Maryland 20871

Abstract

A new microwave waveform sampling system, which employs a combined optical phase-locking and photoconductive sampling techniques, has been demonstrated. This system can directly display a replica of microwave waveform on a conventional oscilloscope.

Introduction

Waveform measurement and display are very important for characterizing oscillator, amplifier or other device output performance. At frequencies below 400 MHz, conventional real time oscilloscope is the usual means to study this kind of waveform, while above 400 MHz, sampling scope takes this place. At present, conventional RF/microwave sampling scope has a maximum bandwidth of 20 GHz. A superconductive sampling scope, (by Hypres, PSP-1000) has extended the bandwidth up to 70 GHz, but this instrument is designed to operate at cryogenic temperature, cooled with liquid helium during normal operation.

Unlike electrical sampling, optical sampling technique can easily detect waveform of frequencies above 100 GHz, since picosecond or subpicosecond laser is presently readily available. The most commonly used techniques for optic sampling are electro-optic sampling and photoconductive sampling. Electro-optic sampling is only applicable to GaAs, InP substrate materials, which have electric induced birefringence; but this technique can be used to sample waveforms at any arbitrary point in a digital or microwave circuit

fabricated on such substrates. In contrast, photoconductive sampling can be applied to other substrates, such as Si, but it can only be used to sample waveform at particular point in a circuit where additional electrode must be incorporated. In this paper, both techniques will be described for the waveform measurements, and either technique can be used in the experiment.

Sampling principle

Sampling technique is a well known method to scale down high frequency repetitive waveform to a low frequency waveform. Fig.1 shows the sampling principle in time domain.

The narrow optic pulse train gates the input microwave signal, produces the output proportional to the input value at the particular time

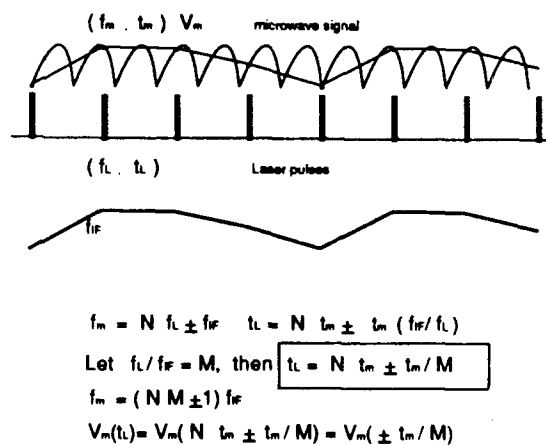


Figure 1. *Sampling principle (for N=2, M=4, "-").*

moment. If the microwave signal satisfies the follow conditions:

$$f_m = Nf_L \pm f_{IF}$$

or

$$t_L = Nt_m \pm \Delta t_m$$

where N is integer, $f_{IF} \ll f_L$, $\Delta t_m = t_m/M$, $M = f_L/f_{IF}$, M represents the number of sampling points per period, which may not an be integer. Then

$$V_m(t_L) = V_m(Nt_m \pm \Delta t_m) = V_m(\pm \Delta t_m)$$

Thus, the equivalent time enlarge factor is:

$$\frac{t_L}{\pm \Delta t_m} = \frac{(Nt_m \pm \Delta t_m)}{\pm \Delta t_m} = \pm(NM \pm 1)$$

where the minus sign represents reverse time sequence. With sufficient sampling point M , the IF waveform should be similar to the microwave waveform but with $\pm(NM \pm 1)$ time enlargement.

Phase synchronization

Since time synchronization between microwave signal and laser pulses is essential for applying sampling technique to reproduce a high quality waveform, any time jittering between the two signals can result in inaccuracy in waveform measurement. The synchronization can be established by using a sophisticated frequency synthesizer as the microwave source and synchronizing it with the laser acoustooptic (AO) modulator driver (another frequency synthesizer) [1]. This type of system is very complex and expensive, especially when applied to the millimeter wave frequency range. Moreover, the usage of this technique is limited and can not be applied to measure waveform of oscillator signals. Other methods to maintain the coherence between microwave oscillation and laser pulses are indirect optical locking of a free running millimeter wave IMPATT oscillator[2] and optical mixing of injection-locked laser diode[3].

Recently, we reported a new technique of phase locking a microwave oscillation with picosecond laser pulses by electro-optic (E-O) sampling[4]. Fig.2 shows the schematic of phase locked loop (PLL).

The laser used in this experiment is a mode locked Nd:YLF laser with repetition rate of 76 MHz. The output of this laser is then compressed

by a fiber pulse compressor. The compressed pulse with width of 3 picosecond and wavelength of $1.06 \mu m$ is partially applied to the E-O sampler in the PLL. The most of energy is used in the frequency doubler. Through an optical delay line, the produced $0.53 \mu m$ light is employed to activate the photoconductive sampler.

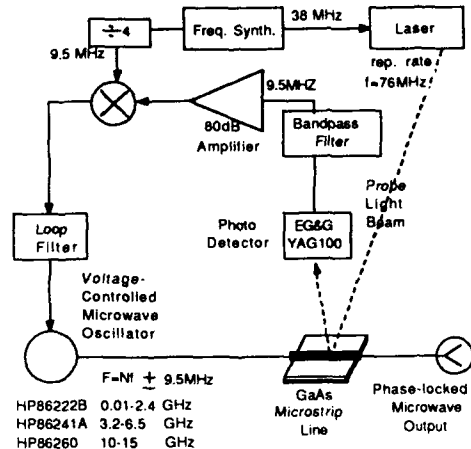


Figure 2. Phase locked loop.

Optical-microwave intermixing scheme consists of a GaAs microstrip line, a polarizer and a photodetector. The microwave signal modulates the reflected laser beam in the GaAs substrate via the E-O effect. The demodulation can be achieved by using the polarizer and photodetector. The output signal from the detector is amplified by a 9.5 MHz amplifier with a gain of 80 db, and then mixed with a 9.5 MHz reference signal derived from the driver of the same AO modulator that mode-lock the laser. The resultant error signal is applied to the controlled terminal of the microwave generator through a loop filter. The microwave signal source used in the PLL is a voltage-controlled oscillator (VCO), currently represented by signal generators: HP86222B (0.01-2.4 GHz), or HP86241A (3.2-6.5 GHz) or HP86260 (10-15 GHz). The locked frequencies are: $f_m = Nf_L \pm f_{IF}$, where $f_L = 76 \text{ MHz}$, $f_{IF} = 9.5 \text{ MHz}$.

Using the described synchronization scheme, it is possible to measure the output performance of an oscillator with capability of varying the frequency through a voltage control. Since E-O sampling can be accomplished without requiring high frequency electrical contacts, this technique can potentially phase lock any monolithic oscillator circuits to frequencies up to 100 GHz at the wafer level before the wafer is diced and device is packaged.

Experiment

The phase locked microwave signal is sent to the device under test (in the first experiment, this was only a cable or the oscillator itself) and then applied to the photoconductive sampler (O^+ implanted GaAs photoconductive switch) (Fig.3).

The desired output is f_{IF} and its harmonic, which can be picked up by a low pass filter. The output of the low pass filter is amplified and sent to the regular oscilloscope. The resultant waveform for a sinusoidal microwave signal is shown on Fig.4.

For an optimal replication of the waveform, the value of $M = f_L/f_{IF}$ should be as large as possible, as long as f_{IF} is above the laser intensity noise band. For $f_{IF} = 9.5\text{MHz}$ and $f_L = 76\text{MHz}$,

the number of the sampling points per cycle, M , is 8. If we externally trigger the scope by the 9.5 MHz reference signal from the divider in the phase locked loop, and optically delay the $0.53\mu\text{m}$ sampling beam, the displayed waveform on the scope will horizontally shift. Thus, we can accurately determine the wavelength of measured microwave signal.

In the other experiment, in order to display the capability of replicating a distorted waveform, an over driven amplifier was used as DUT. To double the sampling points M , f_{IF} was reduced to 4.75 MHz in the phase locked loop and in the photoconductive sampling system. The output waveform of 536 MHz from a saturated amplifier was measured simultaneously by a regular sampling scope (Fig.5(a)) and by the photoconductive sampler (Fig.5(b)). Evidently, these two waveforms are very alike.

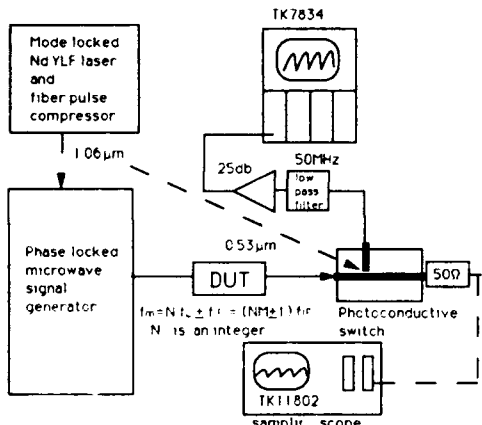


Figure 3. Schematic of optic sampling system.

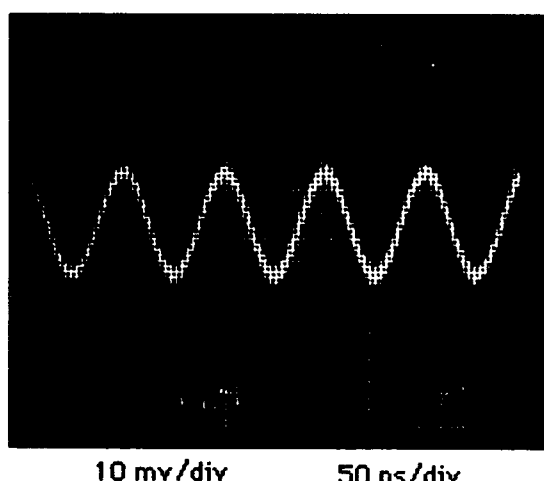


Figure 4. The displayed output waveform of a 2.4 GHz microwave signal.

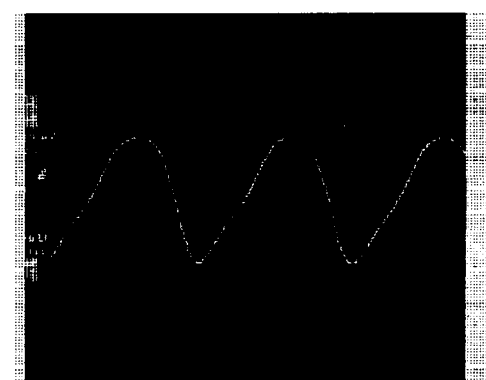


Figure 5(a). The output waveform from an over driven amplifier was displayed by a regular sampling scope.

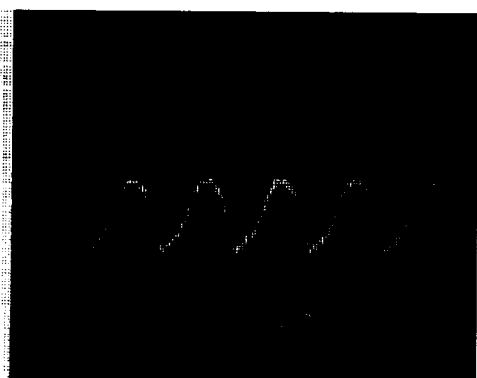


Figure 5(b). The output waveform from an over driven amplifier was displayed by the optical sampling system.

The intermixing performance of the above O^+ implanted GaAs photoconductive sampler was also examined. By scanning the applied microwave frequency and monitoring the output f_{IF} signal, the frequency response of the sampler can be obtained as shown in Fig.6(a),(b),(c).

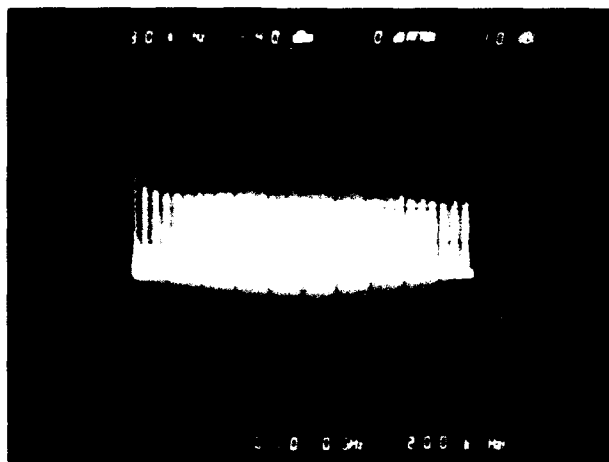


Figure 6(a). The intermixing response of the photoconductive sampler as function of frequency (in frequency range of 0-2.4 GHz).

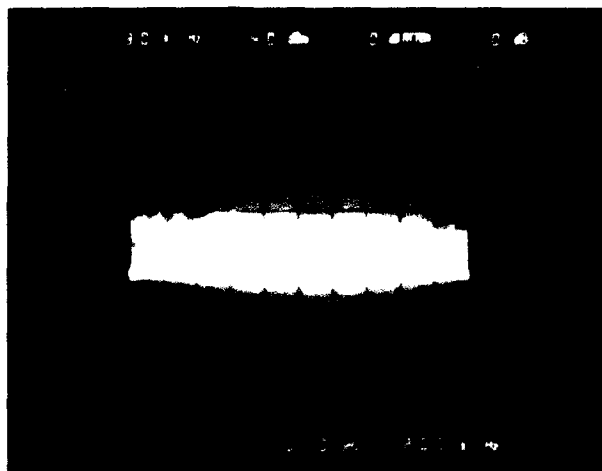


Figure 6(b). The intermixing response of the photoconductive sampler as function of frequency (in frequency range of 3.2-6.5 GHz).

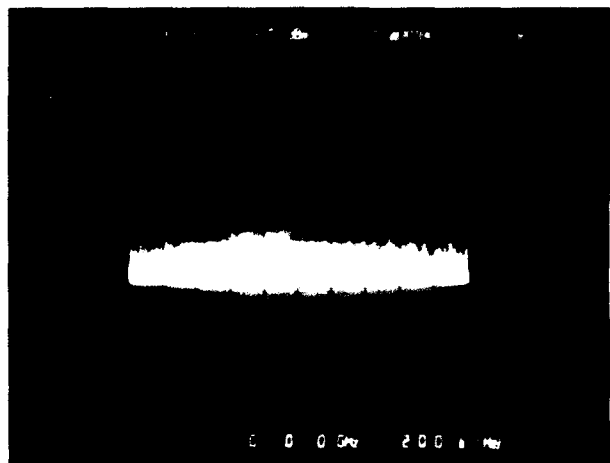


Figure 6(c). The intermixing response of the photoconductive sampler as function of frequency (in frequency range of 10-15 GHz).

Illuminated by 20 mw laser pulses with 3ps pulse width and $0.53\mu m$ wavelength, the photoconductive sampler exhibits the conversion loss of -79 db at low frequency and -94db at frequency of 15 GHz. The noise associated with this sampler is so small that it is below the noise level of the testing equipment and hence can not be measured in this experiment. This indicates that photoconductive sampler could offer higher sensitivity than E-O sampler does.

Conclusion

In conclusion, an optical sampling system, which can potentially be applied to measure the microwave waveform beyond 100 GHz, has been developed. In this system, both electro-optic sampler and photoconductive sampler have been used, both samplers have exhibited excellent performance. This experiment also proves that the phase-lock/sampling arrangement is simple, economical and feasible.

Acknowledgment

This work was supported by the Maryland Industrial Partnership Program.

References

1. M. Rodwell, M. Riazat, K. Weingarten, B. Auld, D. Bloom "Internal Microwave Propagation and Distortion Characteristics of Travelling -Wave Amplifiers Studied by Electro-

optic Sampling ", IEEE Trans. on Microwave Theory Tech. Vol. MTT-34, No.12, December 1986, pp. 1356-1362.

2. A. S. Daryoush, P. R. Herczfeld, A. Rossen, A. K. Sharma and V.M.Contarino "Indirect Subharmonic Optical Injection Locking of Millimeter-wave IMPATT Oscillator ", IEEE MTT-S Int. Microwave Symp. Dig. pp. 109-112, 1986.

3. T. Berceli, A. Daryoush, P. Herczfeld, W. Jemison, A. Paoella " A MMIC-Based Injection-Locked Oscillator for Optically-Fed Phased-Array Antennas" IEEE MTT-S Int. Microwave Symp. Dig. pp. 131-134, June 1989.

4. M. G. Li, Eve A. Chauchard,C.H.Lee, H.-L. A.Hung "Microwave Phase Locking Using Electro-optic Harmonic Mixer" Ultrafast Phenomena Symp. Digest. pp. 266-267, 1990

All-Optical Microwave Gain Measurements on MMIC Amplifiers

Kurt J. Weingarten

*Lightwave Electronics, 1161 San Antonio Road,
Mountain View, California 94043*

Majid Riaziat

Varian Research Center, Palo Alto, California 94303

Abstract

All-optical swept-frequency measurement of the gain of two types of microwave integrated circuits, a feedback amplifier and a distributed amplifier, is demonstrated. A diode laser excites an on-chip photodetector and the circuit response is measured with electro-optic sampling. The only physical contact probes are DC bias probes for the circuit and the on-chip MSM photodetector. The optically measured gains compare favorably to independent network analyzer measurements using contact probing. The integrated photodetector needed for signal generation is process compatible with MMIC technology, occupies a small space on the wafer, and requires no additional processing steps. Since the yield of the photodetector is very high compared to the MMICs, the all optical test is potentially a practical and low cost approach for RF monitoring of circuits.

Introduction

Electro-optic (EO) sampling for high speed measurements of electrical signals on integrated circuits has been in experimental use for a number of years [1-3]. It utilizes the electro-optic effect in compound semiconductors to sample fast electrical signals in circuits built on such materials. Some advantages of this technique over contact probing are: 1) The electro-optic sampler can probe in areas of the circuit that are inaccessible to contacting probes. This is an important advantage in testing complex circuits. 2) Contacting probes wear out and need to be replaced. The optical sampler is free from that operating cost. 3) Electro-optic sampling has been demonstrated with a frequency bandwidth exceeding 100 GHz. This limit far exceeds that of high frequency probes.

This work extends a swept-frequency EO sampling system by replacing microwave, sinusoidal excitation typically supplied by a synthesizer and contact probes with an optically generated sinusoidal excitation delivered to an on-chip photodetector.

EO Sampling Station

Figure 1 shows a block diagram of the optical test system used in this project. The laser produces <10 psec pulse width at a rate of 250 MHz, wavelength of 1047 nm, and an output power greater than 100 mW [4,5]. The pulses are jitter stabilized and phase locked to a microwave synthesized source by an electronic feedback loop, reducing the jitter between the laser and the synthesizer to less than 1 psec. A bandwidth of 30 GHz can be achieved with this system. This compact laser substitutes for a combination of a conventional flashlamp-pumped mode-locked laser and a pulse compressor used previously [1]. This substitution simplifies the system and reduces its size considerably. The trade-off is the bandwidth, which is reduced from >100 GHz to 30 GHz.

The optical beam is focused into the GaAs substrate where it senses the microwave line voltage through the electro-optic effect. Since the testing was to be made on MMICs with microstrip transmission lines, frontside probing was used, where the probe beam first passes through the substrate then is returned to the detector by reflection from the backside ground plane. One problem with frontside probing using pulses longer than the optical transit time through the GaAs substrate is variations in the reflected intensity due to étalon effects. This effect makes signal calibration difficult.

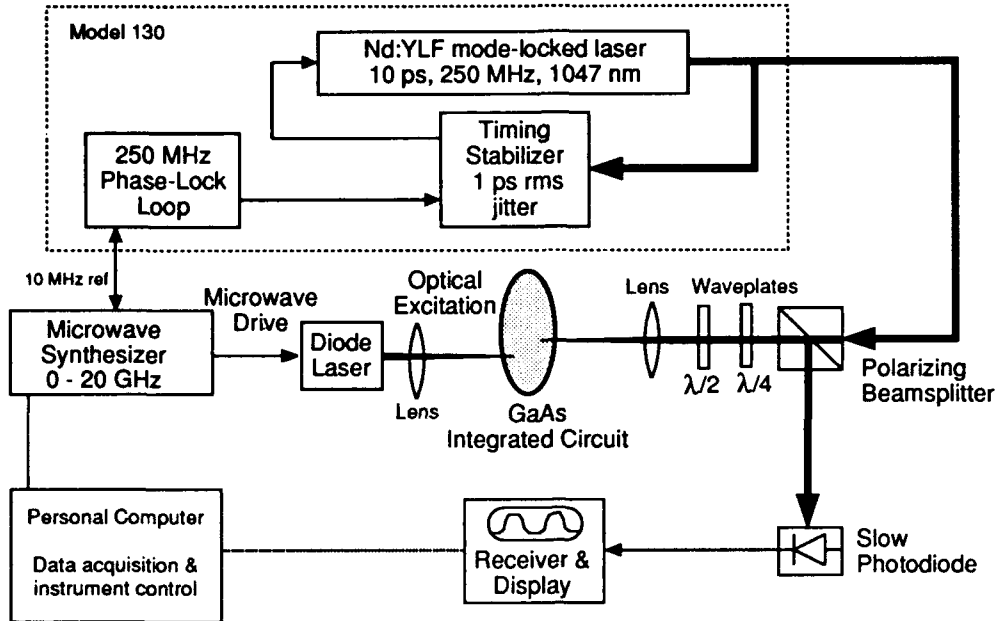


Figure 1. Block diagram of the electro-optic sampling system with optical excitation. The diode laser excitation beam is delivered near the IR probe beam by using a dichroic beamsplitter, which is omitted for clarity.

The excitation beam is delivered through a system consisting of an XYZ stage with turning mirrors to allow for horizontal positioning of the beam on the circuit. The collimated light passes through a focusing lens (50 mm focal length) then is turned 90° by a dichroic beamsplitter. The beamsplitter reflects the shorter wavelength excitation beam but has high transmission of the 1047 nm infrared probe beam, allowing the two beams to be independently positioned on the circuit. One disadvantage of this approach is that the beamsplitter introduces astigmatism in the IR probe beam focused through it. This limits the IR spot size on the test device. For our experiments, we had a spot size diameter of approximately 25 μm , and consequently the astigmatism introduced by the beamsplitter was acceptably small.

Optical Sources of Microwave Signals

Several possibilities exist for delivering microwave excitation on an optical beam. For our measurements, we chose a commercially available laser diode that allowed for modulation up to 12 GHz [6]. The diode laser is driven directly by a microwave synthesizer, and delivers an average output power of approximately 5 mW at a wavelength of 850 nm through a pigtailed multimode fiber. The output from the multimode fiber was collimated with a fiber optic positioner assembly and delivered to the EO station. The DC drive current for the device was 50 mA typically, and to produce the microwave modulation the device was driven with approximately 13 dBm from a microwave synthesizer.

The direct modulation diode laser sufficiently meets

our key considerations. Its weaknesses are its limited modulation rates and its limited output power. Its strengths are its simplicity and its ability to be driven with a microwave synthesizer, allowing for vector measurements. To allow for improved modulation rates and average power, we investigated a second approach using two single frequency lasers mixed together to generate a microwave beat note in the optical detector. The source lasers are diode laser pumped, monolithic ring cavity lasers [7]. They produce single wavelength light at 1.064 μm with a linewidth of less than 10 kHz. The laser is frequency tuned slowly (over seconds), with a range greater than 20 GHz by adjusting the temperature of the laser crystal. To quickly adjust (over microseconds) the laser frequency over a more limited range, <100 MHz, a piezoelectric element attached directly to the laser crystal applies stress to slightly change the cavity length. By overlapping two laser beams on a photodetector, a microwave signal at the lasers' difference frequency (a beat note) is generated. By changing the crystal temperature, the beat note can be swept from DC to 20 GHz. Phase locking has also been demonstrated using the piezo element to control the laser frequency in a phase lock loop [8].

To stimulate the GaAs photodetector, the wavelength must be less than 850 nm, and the output of the diode pumped lasers can not be used directly. To generate a short enough wavelength, an external resonant cavity frequency doubling crystal is used [9]. This is a way to efficiently generate light at 532 nm from the 1.06 μm lasers. Then the two frequency-doubled single fre-

quency lasers are combined on the GaAs photodetector to generate the difference frequency. Note that the range of the beat note is effectively doubled, so that a laser system capable of 20 GHz modulation at 1.06 μm would be capable of up to 40 GHz modulation at 532 nm.

MSM Detectors

In the past few years very fast and efficient detectors that are process compatible with MMICs have been reported using the MSM structure, which consists of two Schottky contacts with a depleted light gathering gap on undoped GaAs. Electrical pulses faster than 5 psec have been obtained [10], and sensitivities as high as 0.25 A/W have been reported [11].

The active material for the photodetector is undoped GaAs normally used as a buffer layer in MMICs. The peak spectral response for this material occurs at about 800 nm. An interdigitated layout was chosen (Fig. 2) in order to simultaneously allow for a small gap and a large light gathering area. The active area of the MSM detector is a circular region 100 μm in diameter. One disadvantage of the interdigitated structure is that roughly one-half the light is blocked by the metallization. A 2 μm gap was found to be sufficiently small for the required speed without putting stringent requirements on the lithography. Optical reflection from the air-GaAs interface also causes a loss of signal in the detector. To reduce this reflection, a process-compatible anti-reflection (AR) coating was implemented, consisting of a single layer quarter-wave coating of SiO_2 . This reduces the level of reflections from 31% to less than 6%.

In order to avoid multiple reflections on the input line and assure the stability of the circuit, the MSM detector is placed in a module matched to the 50 Ω transmission line. The matching is done by a shunt 50 Ω resistor which also consumes half of the output current. The bias voltage of the MSM is decoupled from the output through an isolation capacitor. The capacitor dielectric extends over the detector area and serves as the AR coating. Varian's MMIC process normally uses 2000 \AA of SiO_2 . This thickness had to be reduced to 1400 \AA for a quarter-wave AR coating. This was the only design rule modification that the addition of the source module required.

Also, the output of the circuit under test is terminated in a 50 Ω load. Both the photodiode module and the load are connected to the circuit by airbridges which can be scribed away upon completion of testing.

Limitations on the frequency response of photodetectors come from either internal charge transfer transit time or from the response of the external electrical circuit. The extrinsic circuit was modeled (Fig. 3) and its bandwidth calculated to be 39 GHz. Based on a saturated

velocity of GaAs of $2 \cdot 10^7$ cm/s, the charge transfer time constant is predicted to be 10 psec, corresponding to a frequency bandwidth of 16 GHz. This MSM should therefore operate in the transit time limited regime.

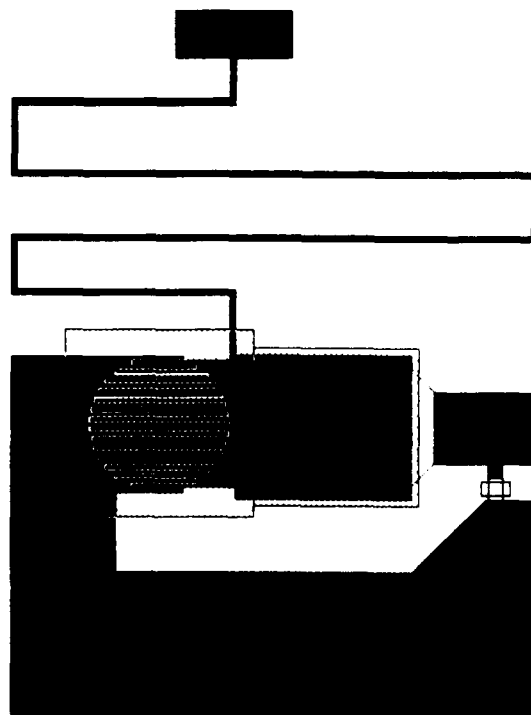


Figure 2. Matched MSM source module for integration with the MMIC. Active area is 100 μm in diameter. Connections to the circuit are made by airbridges. The top pad is for DC bias. The dielectric used for the isolation capacitor also serves as the AR coating. This module is then integrated with the amplifier and placed in a scribe lane so that it can be removed during packaging.

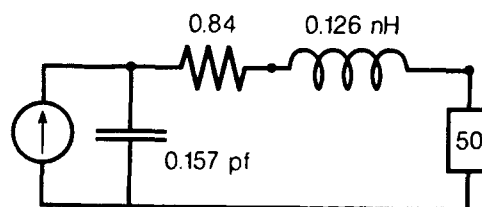


Figure 3. Equivalent extrinsic circuit model for the MSM photodetector. The element values were optimized to fit measured S parameter data. The calculated 3 dB bandwidth of the extrinsic circuit is 39 GHz for a 2 μm gap.

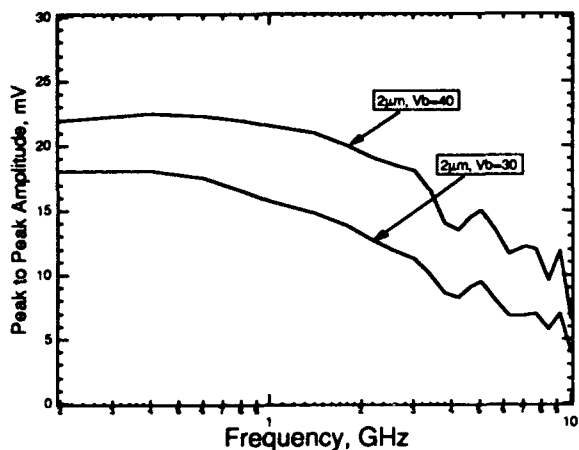


Figure 4. Typical measured frequency response of MSM detector module at two bias voltages, 30V & 40V.

The minimum required photodetector responsivity depends on the sensitivity of the sampling system. The EO sampling system has a typical sensitivity of $100 \mu\text{V}$ per root Hz. If an averaging time of roughly one second is used, a signal level of 1.0 mV , corresponding to a current of $20 \mu\text{A}$ in a 50 ohm system, is required for a 20 dB signal to noise ratio. The photodetector should be capable of generating this current when driven by the diode laser. With a diode laser output of 5 mW , with one-half of the photodetector's output current consumed for matching, and assuming one-half the output power of the laser is delivered to the detector, the required responsivity of the photodetector is 16 mA/W at the measurement frequency. For these detectors, we measured a typical responsivities of $10\text{--}100 \text{ mA/W}$ at microwave frequencies. Figure 4 shows as typical measured frequency response.

Measurements on MMICs

Two different microstrip circuits were tested using the all optical approach. One is a 2-20 GHz distributed amplifier with 7-8 dB of gain [12]. The other is a 2-8 GHz feedback amplifier with 15-20 dB of gain [13].

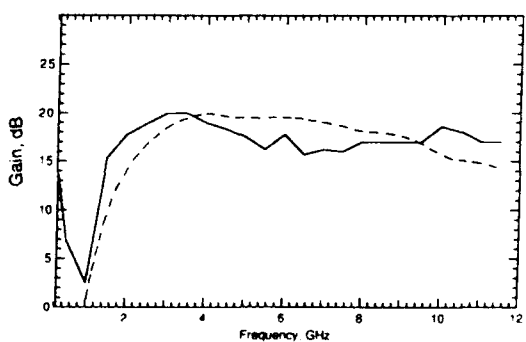


Figure 5. All optical measurement of the gain of the feedback amplifier compared with measurements made by contacting probes.

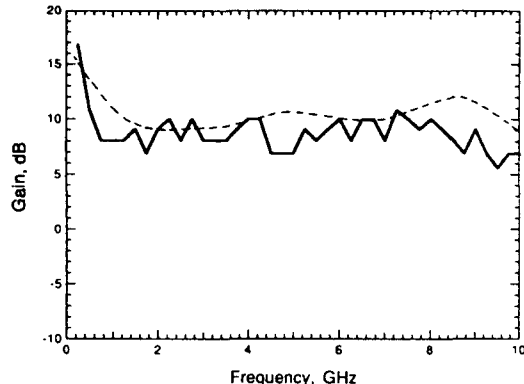


Figure 6. All optical measurement of the gain of the distributed amplifier compared with measurements made by contacting probes.

Figures 5 and 6 show the measured voltage gain as a function of frequency for these two circuits using the all optical system. This data was taken by measuring the relative signal level at the amplifier output versus its input. These measurements are made on wafer using the monolithic integrated source module and a 50Ω output termination with the circuit under test. Both figures also show the response of the circuit measured with contacting probes (dotted lines). The contact probe measurements were made on similar amplifiers which were processed on the same wafer without the source and detector modules.

These results can be scaled to higher frequencies. First, the MSM detectors can be readily scaled for faster response. Simulations show a $16 \mu\text{m}$ diameter device with $0.25 \mu\text{m}$ finger spacing should have a 100 GHz bandwidth. Secondly, optical modulation to 100 GHz can potentially be generated using two single-frequency lasers to generate a microwave difference frequency [12]. Finally, the system response can be improved by reducing the 10 psec pulse width of the diode-pumped laser to less than one picosecond using a fiber-grating pulse compressor.

Acknowledgments

This work was supported by DARPA MIMIC Phase III contract no. F30602-89-C-0040. The equipment used in the EO sampler was partially supported by RADC SBIR contract no. F30602-86-C-0228. Development of the diode-pumped mode-locked laser was partially supported by the Department on Energy SBIR contract no. DE-AC03-88ER80653. The authors would also like to thank Dr. C. Yuen whose circuit designs were used in this project.

References

1. K. Weingarten, M. Rodwell, and D. Bloom, "Picosecond Optical Sampling of GaAs Integrated

Circuits." *IEEE J. of Quantum Electronics*, Vol. 24, No. 2, pp. 198-220, 1988.

2. M. Rodwell, M. Riaziat, K. Weingarten, and D. Bloom, "Internal Microwave Propagation and Distortion Characteristics of Travelling Wave Amplifiers Studied by Electro-Optic Sampling," *IEEE Trans. MTT*, Vol. MTT-34, No. 12, pp. 1356-1362, 1986.
3. J.A. Valdmanis, "1 THz-bandwidth prober for high-speed devices and integrated circuits," *Electron. Lett.*, Vol. 23, pp. 1308-1310, 1987.
4. Lightwave Electronics Model 130 mode-locked laser
5. U. Keller, et. al., "High Frequency Acousto-Optic Mode Locker for Picosecond Pulse Generation." *Optics Letters*, Vol. 15, No. 1, pp. 45-47, 1990.
6. Model 1210C, Ortel Corporation, 2015 W. Chestnut Street, Alhambra, CA 91803.
7. Lightwave Electronics Model 120 single frequency ring laser
8. T.J. Kane and E.A.P Cheng, "Fast frequency tuning and phase locking of diode-pumped Nd:YAG ring lasers," *Opt. Lett.*, Vol. 13, pp. 970-972, 1988.
9. W.J. Kozlovsky, C.D. Nabors, and R.L. Byer, "Efficient second harmonic generation of a diode-laser pumped cw Nd:YAG laser using monolithic MgO:LiNbO₃ external resonant cavities," *IEEE J. Quantum Electron.*, Vol. 24, pp. 913-919, 1988
10. B.J. Van Zeghbroeck, "Analysis of Picosecond and Subpicosecond MSM Photodiodes with Very Low Bias Voltage," in *Proc. DRC Conf.*, P. IIB-1, June 1988.
11. O. Wada, et. al., "Monolithic Four-Channel Photodiode/Amplifier Receiver Array Integrated on GaAs Substrate." *J. Lightwave Tech.*, Vol. LT-4, No. 11, pp. 1694-1702, 1986.
12. S. Bandy, et. al., "A 2-20 GHz High Gain Monolithic HEMT Distributed Amplifier," *IEEE Trans. MTT*, Vol. MTT-35, No. 12, 1987.
13. C. Yuen et. al., "A Monolithic Three Stage 2-8 GHz Feedback Amplifier." *IEEE Electron Device Letters*, Vol. EDL-7, No. 3, 1986.

Propagation of 100-GHz Bandwidth Electrical Pulses on a Silicon-Based Microstrip Line with Buried CoSi₂ Groundplane

Hartmut Roskos, Martin C. Nuss, Keith W. Goossen, David W. Kisker,* and Ben Tell

AT&T Bell Laboratories, Crawfords Corner Road, Holmdel, New Jersey 07733

Alice E. White, Ken T. Short, Dale C. Jacobson, and John M. Poate

AT&T Bell Laboratories, 600 Mountain Avenue, Murray Hill, New Jersey 07974

ABSTRACT

We present a microstrip line that uses a highly conducting cobalt silicide layer buried 7 μm below the surface of single-crystalline silicon as groundplane. This novel transmission line shows significantly reduced dispersion for electrical pulses of 100 GHz bandwidth compared to a conventional microstrip line with the groundplane on the back of the substrate. The 2.5 ps risetime (10%-90%) of electrical pulses propagating on the line increases to only 3.7 ps after a distance of 5 mm compared to an increase from 2.7 ps to 11.3 ps on a conventional microstrip line.

INTRODUCTION

Microstrip transmission lines consisting of a narrow center conductor and an extended groundplane are the most commonly used device interconnections in millimeter-wave integrated circuits. Usually, the groundplane of a microstrip line is located on the backside of the typically 500 μm thick semiconductor wafer that carries the circuit elements. For frequencies of several GHz and above, this simple scheme can lead to a limitation of the useful bandwidth of ultra-high-speed electronic circuits because dispersion can significantly distort the electrical pulses propagating on the microstrip interconnects [1,2].

The dispersion is a consequence of a change of the effective refractive index of the microstrip when the wavelength of the electrical pulse becomes comparable to the separation h of the center conductor and the groundplane. This implies, however, that the onset of dispersion can be shifted to higher frequencies by

reducing the conductor spacing. An illustration of this basic idea is given in Fig. 1 showing the frequency dependence of the effective refractive index of a 5 μm wide microstrip line on a silicon substrate for different values of h . For a spacing of 500 μm the microstrip is dispersive in the frequency range from 5 GHz up to 1 THz. Reducing h to 10 μm shifts the onset of dispersion above 100 GHz and beyond the current range of interest. The actual implementation of a microstrip with small conductor spacing is difficult. Thinning of the substrate

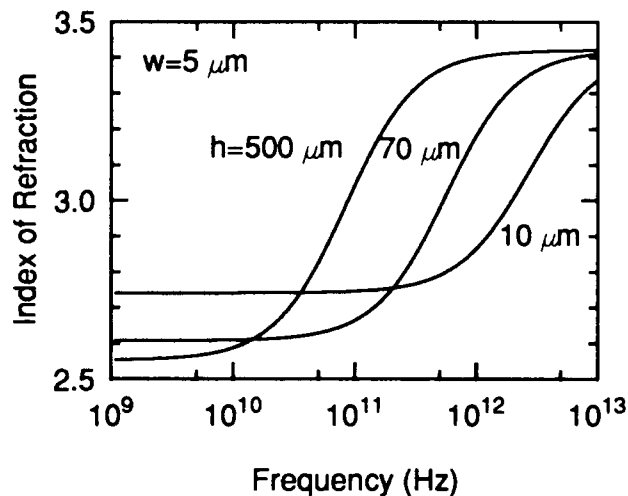


Fig. 1 Frequency dependence of the effective index of refraction of a microstrip line for a line width of 5 μm . As the spacing of the conductors is reduced, the dispersion is shifted to higher frequencies.

is not desirable because it renders the wafer more fragile and reduces the heat-sinking capability. A better choice is to fabricate microstrip lines with both the center conductor and the groundplane on top of the wafer. Recently, we proposed to use a highly conducting silicide layer, buried a few microns under the surface of the silicon wafer, as groundplane for microstrip lines [3]. This approach offers several advantages: (i) Both the silicide layer as well as the silicon dielectric on top are crystalline and can be used for the definition and integration of devices [4], (ii) the silicide layer has a room temperature conductivity comparable to that of evaporated aluminum [10], and (iii) contacting of the buried silicide is easily accomplished through via-holes from the top that are opened by reactive ion etching with CF_4 or SF_6 without problems because the buried CoSi_2 acts as a stop-etch layer. The microstrip line presented here also compares favorably with coplanar lines [5] because of the absence of radiation losses [6] and a reduced crosstalk resulting from the stronger confinement of the modes in microstrips.

Here, we test this novel transmission line concept experimentally by measuring the propagation characteristics of picosecond electrical pulses on microstrip lines with buried groundplane and comparing them with the characteristics of conventional microstrip lines.

SAMPLE FABRICATION

A highly conducting buried silicide layer is created by mesotaxy [7-10] in (100)-oriented high purity (1000 Ωcm) silicon wafers as well as in lightly doped (4-10 Ωcm) and highly doped (0.01 Ωcm) wafers. The silicon is first implanted with cobalt ions (energy 1.5 MeV) at a dose of $8.5 \times 10^{17} \text{ cm}^{-2}$. Then the samples are annealed at 600 °C for 1 h, at 1000 °C for 45 min and finally at 1100 °C for 1.5 h which causes the cobalt atoms to coalesce into a single-crystalline CoSi_2 layer, lattice-matched and with sharp interfaces to the silicon. The silicide layer is 3000 Å thick and located 9000 Å below the silicon surface. Its room temperature resistivity is about 10 $\mu\Omega\text{cm}$ [10]. In the case of the highly doped substrate all but 1800 Å of the silicon on top of the silicide layer is then etched away. On all three samples a 6 - 7 μm thick epilayer of nominally undoped silicon (resistivity roughly 10 Ωcm) is grown on top of the wafer by chemical vapor deposition (CVD). This silicon regrowth allows us to raise the impedance of the microstrip line to approximately 50 Ω . The epilayer is followed by a 3000 Å thick CVD-grown SiO_2 -film that electrically isolates

the buried silicide from the center conductor of the microstrip line. The center conductor consists of a 5 μm wide, 2700 Å thick strip of aluminum ending in contact pads for the bonding of wires.

Fig. 2 displays a cross-sectional view of the microstrip line with buried groundplane. Unlike a conventional microstrip line, the width of the center conductor in this configuration is comparable to the separation of the center conductor and the groundplane.

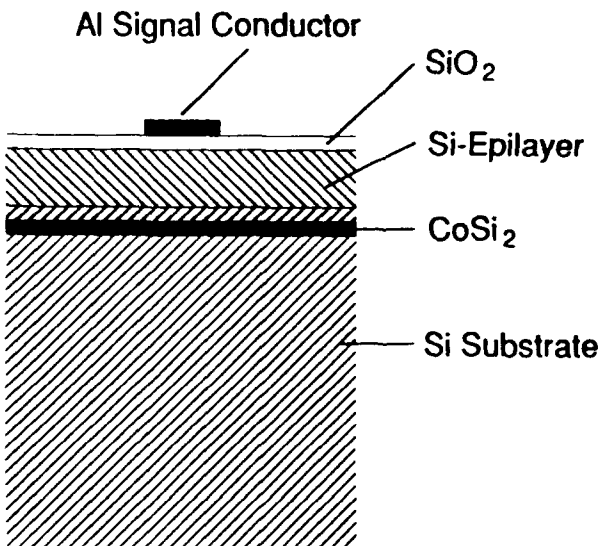


Fig. 2 Cross-section through the microstrip line with buried groundplane

For comparison of the pulse propagation characteristics, we also fabricate microstrip lines of conventional design - i. e. with the groundplane on the backside of the wafer - on 500 μm thick highly resistive ($\rho = 500 \Omega\text{cm}$) silicon wafers. The dimensions of the center conductor are the same as those of the microstrip lines with buried groundplane.

MEASUREMENT TECHNIQUE

Electrical pulses with a bandwidth in the 100 GHz range are generated and detected photoconductively with side-sampling gates [11] using 100 fs optical pulses from a colliding-pulse-modelocked Rhodamine 6G dye laser. The gates consist of 5 μm wide gaps between the center

line and 10 μm wide side contacts. A 4000 \AA thick film of polycrystalline CdTe, deposited at 250 $^{\circ}\text{C}$ by UV-enhanced MOCVD on top of the finished electrical circuit, is used as photoconductive material with subpicosecond photocurrent decay time [12,13].

RESULTS AND DISCUSSION

Fig. 3 displays the detected waveform of an electrical pulse propagating on a conventional microstrip line for distances of 100 μm , 2 mm and 5 mm. The time delay zero of each curve is chosen to obtain coincidence in time of the pulse maxima. The data are plotted normalized in height; the ratio of the peak amplitudes of the original data is 1 : 0.32 : 0.085. The full width at half maximum (FWHM) of the pulse detected after a propagation distance of 100 μm is 3.7 ps. The width and the strongly asymmetric shape of the pulse are determined by the microstrip impedance Z_0 (for our structure: $Z_0 = 314 \Omega$) and the capacitance C_s of the side-sampling gaps rather than by the intrinsic speed of the photoconductor [11]. For distances longer than 500 μm , dispersion manifests itself as an increase of the risetime and a ringing in the trailing part of the pulse, both resulting from the higher speed of the low-frequency components of the pulse. The 10%-90%-risetime of the pulse increases with the propagation distance L from 2.7 ps for $L = 100 \mu\text{m}$, to 5.6 ps for $L = 2 \text{ mm}$, to 11.3 ps for $L = 5 \text{ mm}$.

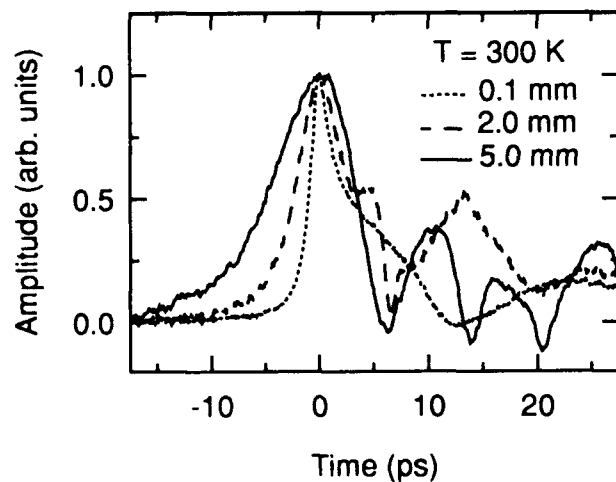


Fig. 3 Time dependence of the detected electrical field of a pulse on a microstrip line of conventional design (groundplane on substrate backside) for propagation distances from 0.1 mm to 5.0 mm.

In Fig. 4, the detected waveform of a pulse launched on the buried groundplane microstrip line (sample with 4-10 Ωcm substrate resistivity) is shown for propagation distances of 100 μm , 2 mm and 5 mm at room temperature. The data are plotted normalized in height, the peak amplitude ratio of the unnormalized data is 1 : 0.31 : 0.062. For a propagation distance of 100 μm , the pulses generated on this microstrip line are shorter (FWHM: 2.0 ps) and less asymmetric than those generated on the conventional microstrip which we attribute to the smaller characteristic impedance $Z_0 = 52 \Omega$. We cannot detect any ringing in the trailing end of the pulses at any propagation distance. However, the losses at room temperature are quite large and affect the high-frequency peak of the pulse more than the low-frequency trailing pedestal which makes the pedestal appear to increase with distance after normalizing the data. This pedestal presumably originates from a residual hopping conductivity in the photoresponse of the CdTe-film. The 10%-90%-risetime of the pulse detected after a distance of 100 μm is 2.5 ps and increases only slightly to 3.7 ps after 5 mm propagation.

To determine whether the losses occur predominantly in the conductors or in the silicon, we repeat our

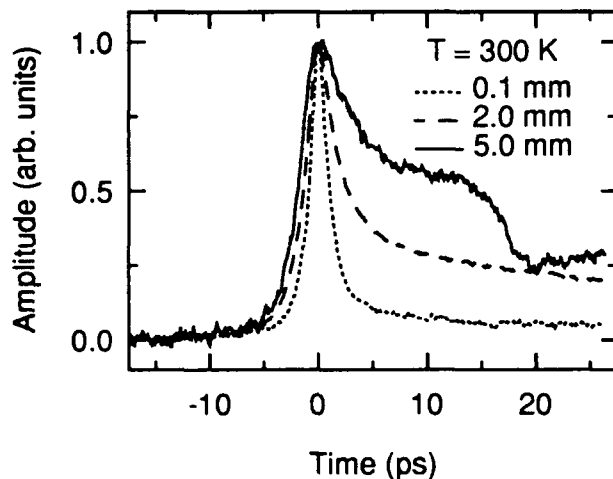


Fig. 4 Time dependence of the detected electrical pulse propagating on a microstrip line with buried silicide groundplane. Propagation distances are 0.1 mm, 0.2 mm and 5.0 mm. The reflection of the pulse on the contact pad produces the dip in the curve for 5 mm distance 18 ps after time delay zero.

measurements on the buried groundplane microstrip line at reduced sample temperatures. Fig. 5 displays the waveforms detected after propagation distances of 100 μm and 5 mm for a temperature of 10 K. The risetime of the pulse detected after a propagation distance of 100 μm is 2.5 ps and its full width at half maximum 1.6 ps. To our knowledge, this represents the shortest electrical pulse generated on a microstrip line. No pedestal is observed in the trailing part of the pulse supporting the interpretation of the room temperature data that this pedestal results from the thermally activated hopping conductivity in the CdTe photoconductor.

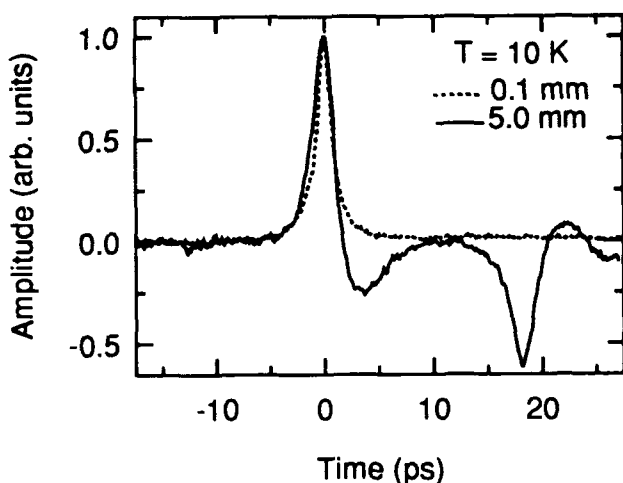


Fig. 5 Pulse propagation on the silicide groundplane microstrip at low temperature ($T = 10 \text{ K}$). Propagation distances are 0.1 mm and 5.0 mm. The inverted signal 18 ps after time delay zero in the data for 5 mm distance is a reflection from the contact pad.

After propagating 5 mm, the pulse develops a negative lobe at the trailing end that extends to about 10 ps after time delay zero. The inverted signal 18 ps after the main pulse is a reflection from the contact pad of the microstrip line that is 1 mm away from the sampling gate. We can also observe this reflected pulse in the room temperature data for a propagation distance of 5 mm in Fig. 4 and - not so obviously - in the corresponding data of Fig. 3. The bipolar shape of the pulses can be explained qualitatively by residual dispersion, although calculations with a standard model [2] do not yield quantitative agreement with the experiment. The peak amplitude of the pulse has decreased after 5 mm propagation distance

to 0.35 relative to the height of the pulse after propagating 100 μm . This value is more than five times higher than the corresponding relative amplitude of 0.062 obtained at room temperature, indicating strongly reduced propagation losses at low temperatures. The risetime of the pulse has not changed during propagation while its full width at half maximum has slightly increased to 2.1 ps. Meaningful for a bipolar pulse is also the width measured from the 10%-point in the leading part of the pulse to the -10%-point at the end of the negative lobe; this 10%(-10%)-width is 8.8 ps. The only slight increase in risetime and full width at half maximum as well as the observation that the 10%(-10%)-width is even smaller than the risetime of 11.3 ps of a pulse after propagating 5 mm on a conventional microstrip, indicate the strongly reduced dispersion on a buried groundplane microstrip line. The reduction of pulse broadening is even more significant taking into account that the pulses generated on the buried groundplane microstrip line are shorter and have about twice the bandwidth (200 GHz) of those generated on the conventional microstrip and therefore should be more strongly affected by dispersion.

The reflection of the pulse on the contact pad allows us to determine the attenuation of the electrical signal per unit propagation distance by comparing the relative heights of the original and the reflected pulse. The ratio of the peak heights has to be corrected for the reflection

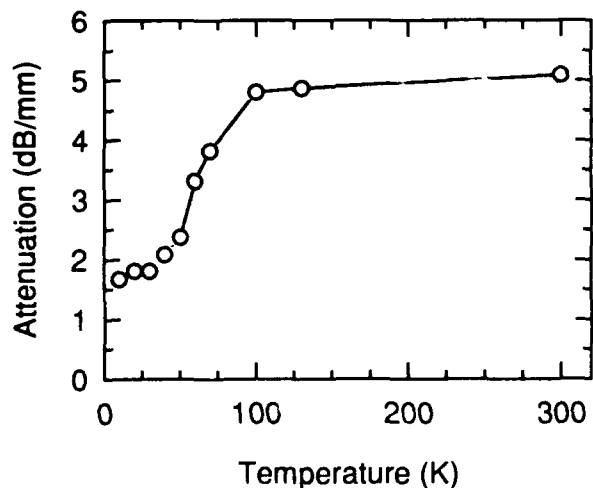


Fig. 6 Temperature dependence of the power attenuation of a picosecond pulse propagating on the microstrip line with buried groundplane.

coefficient, r_{cp} , of the boundary between the center conductor and the contact pad. r_{cp} is given by the impedance ratio $(Z_{pad}-Z_0)/(Z_{pad}+Z_0)$ which in our case is calculated to be -0.94. Fig. 6 displays the attenuation constant determined from the peak height ratio as a function of the sample temperature. The attenuation constant at 10 K is about 3.5 dB/mm smaller than at room temperature. It increases rapidly with temperature around 60 K, but hardly changes from 100 K to room temperature. This suggests that the losses at room temperature are predominantly dielectric losses due to the conductivity of the silicon which decreases dramatically at low temperatures because of freeze-out of the carriers. The observation that the attenuation changes only slightly from 100 K to 300 K, whereas the conductivity of CoSi_2 decreases by nearly a factor of five over this temperature range [10], further supports the conclusion that losses in the groundplane contribute little to the total losses.

To further narrow down the origin of the losses we repeat the room temperature measurements on the sample with a substrate resistivity of 1000 Ωcm . The detected waveforms and the losses are very similar to those obtained for the lightly doped substrate which leads us to the conclusion that the unintentional doping of the epilayer of regrown silicon is the principal source for the losses.

Measurements on the sample fabricated on a highly doped (0.01 Ωcm) substrate reveal strongly increased room temperature losses that do not allow us to detect a pulse after propagation distances of more than 3 mm. The additional losses occur in part in the 1800 \AA thick layer of highly doped silicon that was left on top of the silicide layer after the etch-back procedure. The pulse also suffers further attenuation in the substrate below the silicide because the electrical field penetrates to some extent through the silicide layer.

SUMMARY

Concluding, we have shown that a microstrip line with a buried silicide groundplane has significantly lower dispersion than conventional microstrips for electrical pulses of roughly 100 GHz bandwidth. The measured losses of the buried groundplane line are dominated at room temperature by the residual doping in the silicon epilayer, as indicated by experiments on samples of different doping density and by low temperature measurements, where dopant carriers are frozen out and a significant decrease in attenuation is observed. The silicide layer does not seem to contribute greatly to the loss.

Therefore we have demonstrated that the use of a buried silicide groundplane lowers dispersion significantly without incurring an additional loss penalty. The buried groundplane microstrip line can be readily integrated in high-speed circuits if a silicon epilayer is either not needed or can be grown with high purity.

ACKNOWLEDGMENT

We are pleased to acknowledge technical help from J. Centanni, J. Osenbach, H. Praefcke, K. Tokuda, and J. Walker. During this work, H. Roskos was partially supported by the Deutsche Forschungsgemeinschaft.

*now with IBM Thomas Watson Research Center, Yorktown Heights, NY 10598

REFERENCES

1. E. Yamashita, K. Atsuki, and T. Ueda, "An approximate dispersion formula of microstrip lines for computer-aided design of microwave integrated circuits", *IEEE Trans. Microwave Theory Tech.* MTT-27, 1036-1038 (1979).
2. K. W. Goossen, and R. B. Hammond, "Modeling of picosecond pulse propagation in microstrip interconnections on integrated circuits", *IEEE Trans. Microwave Theory Tech.* MTT-37, 469-478 (1989).
3. K. W. Goossen, A. E. White, and K. T. Short, "Proposed ultrahigh frequency microstrip utilising a buried silicide groundplane", *Electron. Lett.* 26, 49-50 (1990).
4. A. E. White, K. T. Short, K. Maex, R. Hull, Y.-F. Hsieh, S. A. Audet, K. W. Goossen, D. C. Jacobson, and J. M. Poate, accepted for publication in *Nucl. Instr. and Meth. B*.
5. M. B. Ketchen, D. Grischkowsky, T. C. Chen, C.-C. Cui, I. N. Duling III, N. J. Halas, J.-M. Halbout, J. A. Kash, and G. P. Li, "Generation of subpicosecond electrical pulses on coplanar transmission lines", *Appl. Phys. Lett.* 48, 751-753 (1986).
6. D. B. Rutledge, D. P. Neikirk, and D. P. Kasilingam, "Integrated-circuit antennas", in *Infrared and millimeter waves*, Vol. 10, K. J. Button, ed. (Academic Press, New York, 1983) part II, 1-90.

7. A. E. White, K. T. Short, R. C. Dynes, J. P. Garno, J. M. Gibson, "Mesotaxy: single-crystal growth of buried CoSi₂ layers", *Appl. Phys. Lett.* 50, 95-97 (1987).
8. A. E. White, K. T. Short, D. J. Eaglesham, R. Hull, R. C. Dynes, S. D. Berger, H. A. Huggins, and D. Loretto, "Mesotaxy: formation of buried silicides by implantation", *Proceedings of ECS Symposium on Ion Implantation and Dielectrics for Elemental and Compound Semiconductors* (1990), paper 90-13, p. 224.
9. R. Hull, A. E. White, K. T. Short, and J. M. Bonar, "Formation of continuous CoSi₂ layers by high Co dose implantation into Si(100)", *J. Appl. Phys.* 68, 1629-1634 (1990).
10. J. M. Vandenberg, A. E. White, R. Hull, K. T. Short, and S. M. Yalisove, "Anisotropic strain relaxation in buried CoSi₂ layers formed by mesotaxy", *J. Appl. Phys.* 67, 787-791 (1990).
11. D. H. Auston, "Picosecond photoconductors: physical properties and applications", in *Picosecond Optoelectronic Devices*, C. H. Lee, ed. (Academic Press, Orlando, 1984) 73-117.
12. A. M. Johnson, D. W. Kisker, W. M. Simpson, and R. D. Feldman, "Picosecond Photoconductivity in polycrystalline CdTe films prepared by UV-enhanced OMCVD", in *Picosecond Electronics and Optoelectronics*, G. A. Mourou, D. M. Bloom, and C. H. Lee, eds. (Springer, Berlin, 1985), 188-192.
13. M. C. Nuss, D. W. Kisker, P. R. Smith, and T. E. Harvey, "Efficient generation of 480 fs electrical pulses on transmission lines by photoconductive switching in metalorganic chemical vapor deposited CdTe", *Appl. Phys. Lett.* 54, 57-59 (1989).

High-Frequency Analog Signal Processing with High-Temperature Superconductors

W. G. Lyons, R. S. Withers, J. M. Hamm, R. H. Mathews, and
B. J. Clifton

*Lincoln Laboratory, Massachusetts Institute of Technology,
Lexington, Massachusetts 02173-9108*

P. M. Mankiewich and M. L. O'Malley

AT&T Bell Laboratories, Holmdel, New Jersey 07733

N. Newman

Conductus Inc., Sunnyvale, California 94086

ABSTRACT

Several classes of superconductive, passive microwave devices have been demonstrated at temperatures as high as 77 K using thin films of the high- T_c superconductor $\text{YBa}_2\text{Cu}_3\text{O}_{7-x}$. The devices include long delay lines, tapped-delay-line transversal filters with multigigahertz bandwidths and time-bandwidth products as large as 30, and narrowband (from one to three-percent bandwidth) microstrip filters. A GaAs sample-and-hold circuit was also operated at 77 K along with a $\text{YBa}_2\text{Cu}_3\text{O}_{7-x}$ microstrip delay line to simulate a pre-trigger function and demonstrate the compatibility of semiconductors and high-temperature superconductors at moderate cryogenic temperatures. The successful operation of these superconductive devices demonstrate that thin films of high-temperature superconductors can be patterned into useful devices and the devices illustrate the potential performance advantages superconductive thin films offer to the designer of a high-frequency, wide-bandwidth analog signal processing system.

INTRODUCTION

The low conductor loss of superconducting materials makes it possible to build passive microwave devices that cannot be built with normal conductors. These devices are particularly suited to high-frequency, wide-bandwidth analog signal processing applications [1]. The very low, but still finite surface resistance of superconductors can be understood by considering a simple two-fluid model for a bulk superconductor [2]. The two-fluid model separates the conduction band carriers (electrons for low- T_c materials, holes for high- T_c materials) into two fluids. One fluid contains the paired carriers that have condensed into the superconducting state and a second fluid contains the rest of the carriers remaining in the normal state. It requires a finite amount of energy to break a superconducting pair up into two normal particles. This pair binding energy acts as a superconducting energy gap for the formation of unpaired, normal carriers. Thus, the number of normal carriers is temperature dependent and only at $T = 0$ are all of the

carriers in an ideal superconductor condensed into the superconducting state. The two fluids, normal and superconductive pairs, flow in parallel in response to an applied electric field. The paired superconducting carriers are dissipationless because they cannot be scattered without breaking pairs, but have a finite mass and therefore are modeled as an inductance. The normal carriers are subject to dissipation and therefore represent a resistance in parallel with the inductance of the superconducting pairs. For dc applied currents the superconductor is clearly lossless since the superconducting pairs carry all of the current. However, at ac frequencies a voltage develops across the inductance that is out of phase with the applied current. This voltage drives an in-phase current through the fluid in the normal state, dissipating energy. The presence of the superconducting pairs and the small number of normal carriers produces a conductor with very little loss at microwave frequencies. In an ideal superconductor, the loss can always be reduced by lowering the temperature since the number of normal carriers is thermally activated.

Recent advances in thin-film deposition techniques for high-temperature, copper-oxide superconductors have made possible the demonstration of surface resistances well below that of cooled copper at 77 K. Figure 1 diagrams the current state of the art in thin films of the high-temperature superconductor $\text{YBa}_2\text{Cu}_3\text{O}_{7-x}$ (YBCO) by plotting the surface resistance as a function of frequency for thin films of YBCO as well as several benchmark curves (copper at 77 K, superconducting niobium at 4.2 K, and superconducting Nb_3Sn at 4.2 K). Because YBCO films typically are chemically sensitive and the YBCO can degrade during patterning, especially at the edges of a transmission line where the currents peak, measured surface resistance is shown for both patterned and unpatterned films. The cross-hatched region represents the surface resistance obtained on patterned films used in this work. The "LL, 77 K" curve represents the latest results on a patterned stripline resonator [3]. To illustrate the potential performance of YBCO, theoretical curves obtained using the standard two-fluid model for the surface

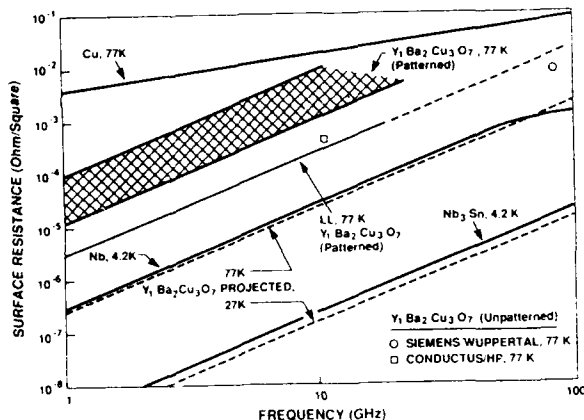


Figure 1. Measured surface resistance versus frequency for cooled copper and for superconducting niobium, Nb_3Sn , and YBCO. Values for both patterned and unpatterned YBCO films are shown. Theory curves for YBCO were generated using the two-fluid model. The latest results on a patterned YBCO stripline resonator ($1.3 \times 1.3 \text{ cm}$ LaAlO_3 substrate) are also shown for comparison [3].

resistance of YBCO [2] are also plotted. The parameters used were $\lambda_0 = 150 \text{ nm}$, $T_c = 93 \text{ K}$, and $\sigma_n = 2 \times 10^6 \Omega^{-1} \text{ m}^{-1}$. It should be noted that the Siemens/Wuppertal data point at 77 K is within a factor of two of the prediction of the two-fluid model if the actual T_c of that film is used in the model.

Figure 2 shows the propagation losses for a collection of transmission media at microwave frequencies [2]. The copper and YBCO stripline geometry is a 175- μm -wide signal line with 1000 μm of ground plane spacing using a substrate with $\epsilon_r = 10$. For a given surface impedance and transmission line impedance, the propagation losses caused by the conductor increase as dielectric thickness is decreased. Dielectric loss is neglected in Figure 2. For comparison, losses are calculated using typical values of surface resistance measured for patterned YBCO devices (shaded region). Theoretical values of loss for YBCO are based on the two-fluid model.

The low conductor loss of a superconductor can be used quite readily in two general classes of passive microwave devices. Long delay lines take advantage of the low propagation loss and dispersionless nature of a thin film superconductor, and resonator-based filters take advantage of the large conductor quality factor (Q) that can be obtained using thin-film superconductors.

THIN FILMS AND DEVICE FABRICATION

Two types of growth techniques were used to deposit thin films of YBCO. The first technique is an *ex-situ*-growth process in which amorphous YBCO is deposited on a substrate by co-evaporation of BaF_2 , Y, and Cu followed by a post-deposition annealing, typically at 850°C in flowing O_2 containing water vapor to remove the fluorine [4]. The second technique is an *in-situ*-growth process using off-axis single-target sputtering [5], with substrate temperatures typically between 600 - 700°C . The postannealed process [6] and the *in-situ* sputtering process [7] have been applied successfully to produce large-area films

with good uniformity over 50-mm-diameter areas [6,7]. Uniformity is crucial in obtaining low values of surface resistance and correspondingly good microwave performance. The postannealing process can also be used to produce films on both sides of a substrate by annealing both sides simultaneously, while the current *in-situ*-sputtering process is limited to single-sided film production because silver paste is used to mount the back side of the substrate to the substrate heater block. However, the postannealing process is apparently incapable of growing fully c-axis-oriented films of YBCO at film thicknesses of greater than 300 nm, and multilayer film deposition is also precluded. Thus, optimized *in-situ*-growth processes should ultimately provide the best YBCO thin films.

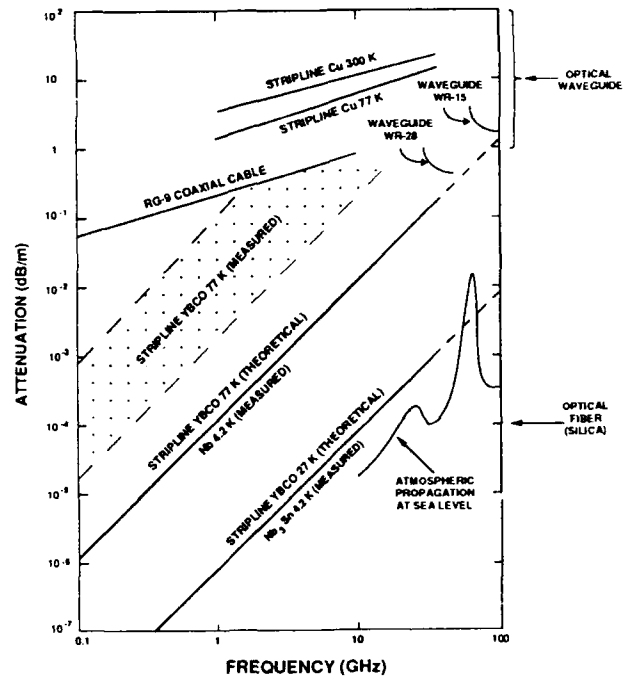


Figure 2. Propagation loss per meter as a function of frequency for various transmission media. Theoretical values for YBCO stripline are based on the two-fluid model.

Typical YBCO film thicknesses used in this work are 200-300 nm. Patterning of the YBCO signal line was accomplished with standard AZ1470 photoresist and a spray etch of 0.25-percent H_2PO_4 , which successfully prevented the formation of a residual film typically found with other wet-etching methods. Undercutting of 1-2 μm is typical for this etch and these YBCO film thicknesses. Figure 3 illustrates the excellent pattern definition obtained with this etch technique. The twin boundaries visible in the LaAlO_3 substrate result from the structural phase transition that occurs in this material. The twin boundaries clearly create a local variation in the index of refraction at optical wavelengths and they also produce a rough surface since the twin boundaries polish preferentially. A trilayer resist (PMMA/Ti/AZ1470) and liftoff process were used to pattern 1.5- μm -thick silver contacts on the signal line. The trilayer resist was used so that the chemically sensitive YBCO was not exposed to AZ photoresist developer. Low-resistance ohmic contacts

were produced by annealing the structure at 400 °C in flowing O₂. Final packaging is performed using ultrasonic wedge bonding of aluminum ribbon directly to the annealed silver ohmic contacts on the signal line to form highly reliable contacts. A 4-μm-thick, e-beam-evaporated silver film was used to form the device ground planes.

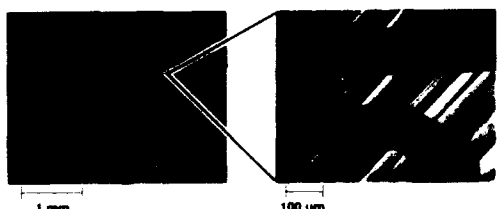


Figure 3. Photograph taken with an optical microscope (in transmitted light) of patterned YBCO lines on LaAlO₃ substrate. Pattern definition of the YBCO is excellent. Twin boundaries in the LaAlO₃ are clearly visible.

TAPPED-DELAY-LINE CHIRP FILTERS

Most analog signal processing structures are variations of the transversal filter. A tapped delay line can be used to implement matched filtering, correlation, and Fourier transformation. Compact transversal filters in the form of tapped delay lines have previously been fabricated from superconducting niobium to operate with multigigahertz signal processing bandwidths [8,9]. One example of a fixed-tap-weight transversal filter is a linearly frequency modulated delay line or chirp filter. Figure 4 shows the architecture of a chirp filter made using superconducting striplines with a cascaded series of backward-wave couplers, in this case forming a down-chirp. Each coupler has a peak response at the frequency for which it is 1/4 wavelength long. By making the length of the couplers inversely proportional to the distance down the line, the filter has a local resonant frequency which is a linear function of delay. Design of the stripline chirp filters is based on coupling of modes theory [8].

Figure 5 diagrams the enhancement of the signal/noise ratio through the use of a matched filter. The impulse response of the filter is equal to the time-reverse of the signal to be processed. The noise entering the filter will suffer the insertion loss of the filter, but the matched signal will have its energy compressed coherently into a quasi-impulse (compressed pulse). The filter effectively forms the autocorrelation of the signal. The width of the center lobe of the autocorrelation is inversely proportional to the bandwidth (B) of the waveform. In the case of

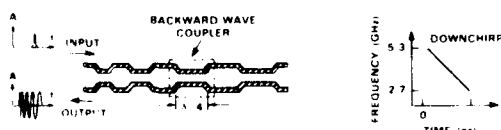


Figure 4. Chirp filter architecture and instantaneous frequency of the impulse response of a down-chirp filter. A typical superconducting niobium-on-silicon chirp filter can contain hundreds of backward-wave couplers.

comparable signal and noise powers, the correlation peak rises well above the level of the noise at the filter output. This improvement in signal/noise ratio is referred to as processing gain and is given by the time-bandwidth (TB) product in an ideal filter. The TB product represents the number of information cycles of the waveform gathered coherently in the filter. The TB is typically in the range of 100 to 1000 (20-30 dB). To realize the full processing gain, the dynamic range of the filter must significantly exceed the TB product.

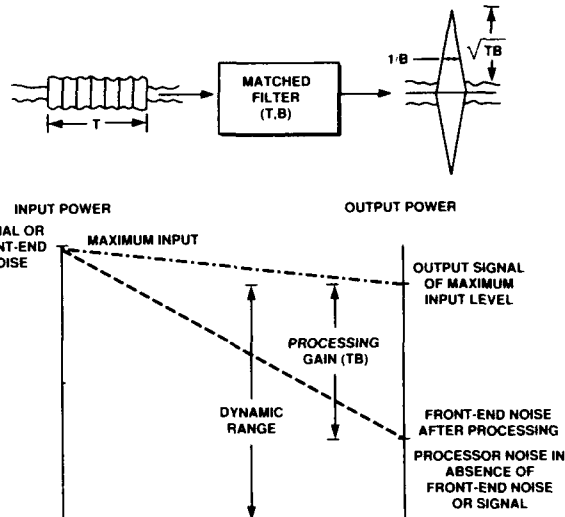


Figure 5. Signal/noise ratio enhancement illustrating the signal processing gain of a matched filter.

Near-term projections for the signal processing gain available from various technologies are shown in Figure 6 [2]. A model [10] for the digital implementation of continuous signal filtering was used to determine the analog signal processing possible with a Cray-2 computer with 2 Giga-operations-per-second (GOPS) and a dedicated parallel processor operating at 10 GOPS. Recent advances in charge coupled devices (CCD), acoustic charge transport (ACT) devices, surface acoustic wave (SAW) devices, and acousto-optic (AO) devices are included for comparison. Projections for superconducting Nb tapped delay lines are made by imposing the physical constraints that the lines be 50-Ω lines on 50-mm-diameter substrates with a dielectric constant of 10. A maximum of five substrates can be stacked to form one continuous delay line. Ground plane spacing is allowed to vary from 10 μm to several hundred microns. Line-to-line isolation is typically 55 dB and this determines the maximum amount of delay that can be obtained on five, 50-mm-diameter substrates. The maximum operating frequency, assuming 3 dB of loss can be tolerated, is then calculated using known values of surface resistance, neglecting dielectric loss, and using a 67-percent fractional bandwidth. Eventually a limit of one-fourth of the dielectric wavelength must be placed on the ground plane spacing, limiting the bandwidth at the highest frequencies. Projections for YBCO devices were made using surface resistances calculated from the theoretical two-fluid model, as plotted in Figure 1. The signal processing capability of a Cray-2 computer (GOPS) falls more than an order of magnitude short of the signal processing capability of the most recent YBCO chirp device (shown as the triangular data point in Figure 6).

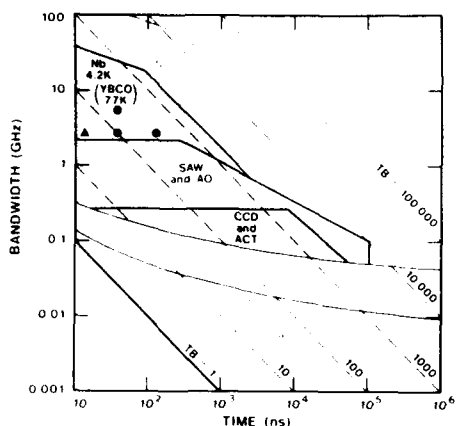


Figure 6. Near-term projections of signal processing capabilities for various technologies [see Ref. 2]. Represented are digital signal processing (DSP), charge-coupled device (CCD), acoustic charge transport (ACT), surface acoustic wave (SAW), acousto-optic (AO), and superconducting delay lines using Nb and YBCO. Projections for YBCO are based on the theoretical values of surface resistance shown in Fig. 1. The triangular data point represents the time-bandwidth product of 30 for the most recently demonstrated YBCO tapped-delay-line chirp filter operated at 77 K (see Fig. 7). The closed circles represent previous demonstrations of superconducting chirp filters using niobium-on-silicon substrates (see Ref. 9).

Figure 7 shows the most recent YBCO chirp filter ready for final packaging. This device was fabricated using an in-situ sputtered YBCO film grown at Conductus on a 50-mm-diameter LaAlO_3 . The film had a uniform transition temperature of approximately 90 K. This device has 11.5 ns of dispersive delay with 48 backward-wave couplers and 14 ns of total delay. The device has a bandwidth of 2.7 GHz and a time-bandwidth product of 30. The chirp-filter design incorporates a tapered-line impedance transformer so that the tapped portion of the filter could be implemented with $40\text{-}\Omega$, 120- μm -wide lines on a 50-mm-diameter, 500- μm -thick LaAlO_3 substrate. The use of 20- μm -wide line was crucial to the success of this design based on previous work with YBCO delay lines [11]. The fabrication of narrow YBCO signal lines is very difficult due to film nonuniformities and defects introduced during photolithography and patterning.

Figure 8 shows the frequency-domain response of the chirp filter shown in Figure 7. The agreement with design is quite good. Recall that the output of this filter is produced by backward-wave coupling a signal to a second line. The 5 dB of insertion loss actually represents fairly strong coupling between the lines. Propagation loss is immeasurable. Figure 9 is a plot of the group delay (derivative of the phase versus frequency) of the down-chirp response for this chirp filter. No attempt was made to smooth this data. Time-domain-reflectometry data also indicates excellent performance from this filter [12]. The filter produced a chirp waveform at temperatures as high as 89 K.



Figure 7. Flat-weighted YBCO chirp filter fabricated on 50-mm-diameter LaAlO_3 with 11.5 ns of dispersive delay and 14 ns of total delay. Klopfenstein-taper impedance transformers make the transition between the narrow $50\text{-}\Omega$ input lines and the wider $40\text{-}\Omega$ tapped delay lines.

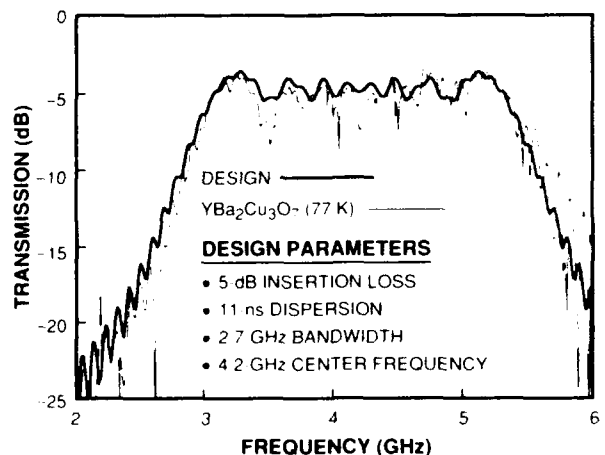


Figure 8. Designed and measured performance at 77 K of the YBCO chirp filter shown in Fig. 7.

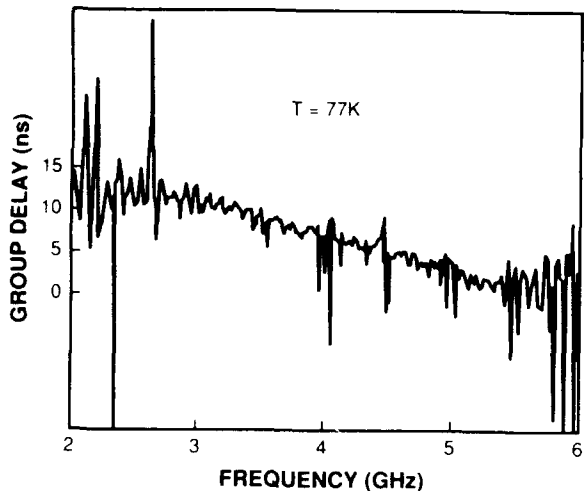


Figure 9. Group delay in the down-chirp mode as a function of frequency at 77 K for the YBCO chirp filter shown in Fig. 7.

DELAY/SAMPLER CIRCUIT USING GaAs AND YBCO AT 77 K

The possibility of combining high-temperature superconductors and semiconductor components at cryogenic temperatures is very exciting from a high-performance systems standpoint. A very simple demonstration of combined semiconductor and superconductor performance at 77 K was made using postannealed YBCO microstrip delay lines and a track-and-hold circuit fabricated with GaAs permeable base transistors (PBT). The combined operation simulated an oscilloscope pretrigger function. The YBCO microstrip delay line device is shown in Figure 10. The device contains two $50\text{-}\Omega$ microstrip delay lines, 1.5 and 7 ns in length, with 160- μm -wide linewidths. This device was designed as a YBCO delay line test vehicle [13]. Successful operation of this device preceded the design and fabrication of the YBCO chirp filters and made clear the importance of wide linewidths in fabricating long YBCO delay lines.

A simplified circuit schematic of the track-and-hold circuit is shown in Figure 11. The simplified circuit schematic does not show the input PBT source-follower that functioned as an input buffer. The delay line device and the track-and-hold device were packaged separately but were operated side-by-side immersed in liquid nitrogen. Figure 12 is a photograph of the GaAs hybrid track-and-hold circuit. Measurements indicated a tracking bandwidth of 2.6 GHz. A dynamic range of 45 dB was obtained from spectrum analyzer and noise-floor measurements. SPICE simulations predicted a tracking bandwidth of 3 GHz with a 2-pF hold capacitor.

Figure 13 shows a step-function signal, time reversed by the measurement apparatus, sampled by the track-and-hold with (left edge) and without (right edge) the insertion of the two YBCO delay lines at 77 K. Note that the step edge is faithfully reproduced consistent with the 2.6 GHz tracking bandwidth. Note

also that there is some insertion loss (-1.5 dB) measurable in the 7 ns delay line. The insertion loss of the 7 ns delay line resulted from the patterned YBCO line crossing several narrow scratches that existed on a small area of the substrate before thin film growth.

The YBCO that grew over the scratches apparently had either a degraded transition temperature or a very broadened resistive transition. In an attempt to repair the damaged region, a silver patch was applied to this small area in the same manner as ohmic contacts were placed at the inputs to the lines. This ohmic patch completely eliminated the 1.5 dB insertion loss. Subsequent time-domain-reflectometry (TDR) measurements indicated that the patch completely repaired the line since no abrupt change in the TDR signal was observed at the position of the scratches after the patch had been put in place and annealed.

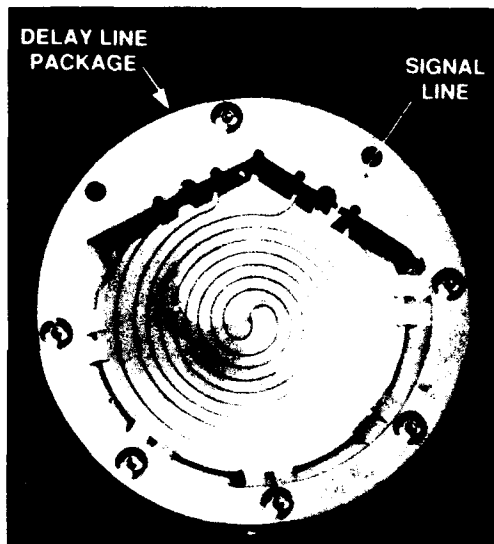


Figure 10. Microstrip delay lines (1.5 ns and 7 ns) fabricated from postannealed YBCO on 50-mm-diameter LaAlO_3 .

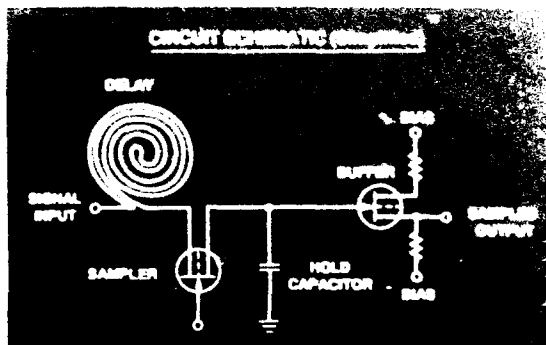


Figure 11. Simplified schematic of the combination of a YBCO delay line and GaAs track-and-hold circuit.

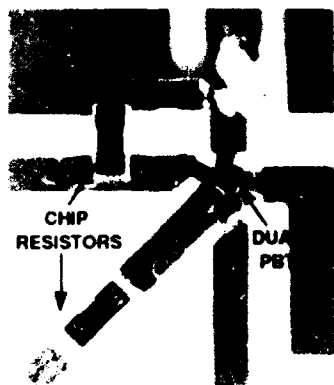


Figure 12. Photograph of hybrid track-and-hold circuit implemented with GaAs permeable base transistors.

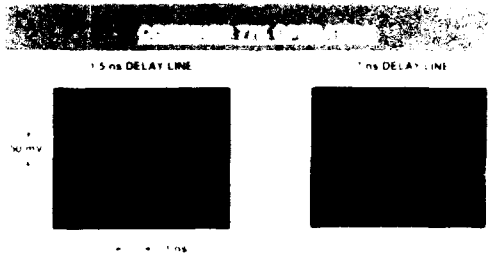


Figure 13. Pulse response of the track-and-hold circuit shown in Figs. 11 and 12 operated at 77 K with and without a YBCO microstrip delay line (shown in Fig. 10).

RESONATOR-BASED BANDPASS FILTERS

The Q of normal-metal microstrip lines is too low to support the low insertion loss and sharp filter skirts needed for channelizing microwave communication bands on communication satellites, where nearly lossless filters with bandwidths less than 3 percent are required. Superconducting microstrip filters could eventually replace the dielectrically loaded cavity filters currently in use with a significant reduction in weight of a multiplexing filter bank requiring dozens of filters. In addition, the potential exists to produce superconducting filters with much sharper filter skirts so that communication bands can be utilized more efficiently. Figure 14 shows a four-pole YBCO filter that operates at 4.8 GHz with a 1.3% bandwidth. This filter was redesigned from an original four-pole, 3% bandwidth filter [14] to reduce the sensitivity of the filter to variations in linewidth and substrate dielectric constant. Due to inaccuracies in microwave CAD packages for large dielectric constants ($\epsilon_r \sim 24$ for LaAlO_3), design of the bandpass filters was accomplished in a semi-empirical fashion [14]. A first iteration was designed using an existing CAD package. Two line couplings were then measured on this design and used to adjust the CAD design to more closely match the actual filter parameters. Figure 15 shows the measured filter response for this design using several different conductors at temperatures of 300 and 77 K. The filter was fabricated on 20-mil-thick LaAlO_3 using gold, silver, and postannealed YBCO [4]. The YBCO filter had 1.0 dB of insertion loss at 77 K compared with 5.9 dB for the silver filter at 77 K and 10.6 dB of

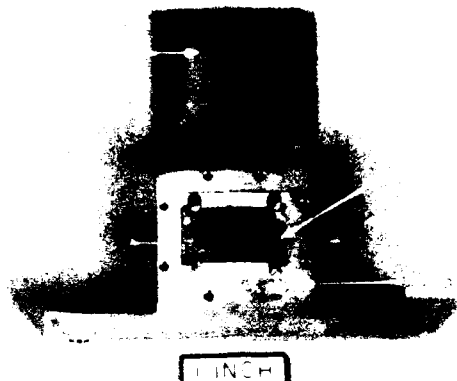


Figure 14. Four-pole microstrip filter fabricated from postannealed YBCO on LaAlO_3 substrate shown prior to final hermetic sealing in a microwave package. The filter operates at 4.8 GHz with a 1.3% bandwidth.

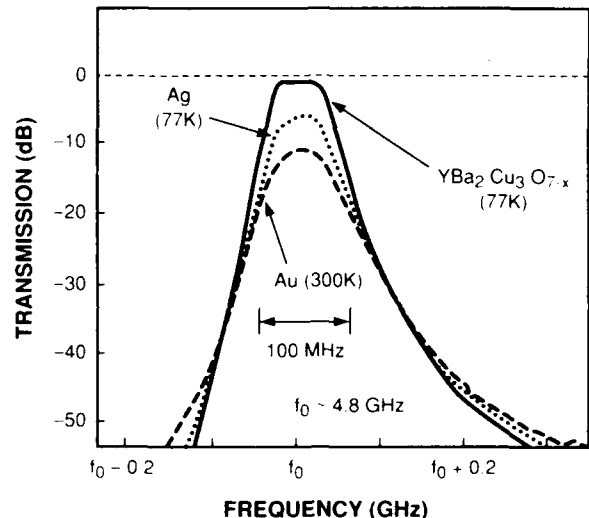


Figure 15. Measured response of the filter shown in Fig. 14 fabricated from gold (measured at 300 K), silver (measured at 77 K), and postannealed YBCO (measured at 77 K).

insertion loss for the gold filter at 300 K. Filters fabricated from YBCO using the previous 4.2 GHz, 3% bandwidth design had exhibited, at 77 K, a passband insertion loss as low as 0.3 dB compared to the 2.8-dB loss of similar gold metallic filters at the same temperature [15].

FUTURE RESEARCH

The design and fabrication of YBCO devices is challenging because of the wide linewidths required by current patterning techniques, the chemical sensitivity of YBCO, the difficulty in depositing uniform YBCO over large areas (up to 50-mm-diameter), the high dielectric constant of LaAlO_3 substrate material, and the thickness of the available LaAlO_3 substrates (which necessitates large line-to-line spacings). Resonator-based filters are very sensitive to linewidth variations, their design for high dielectric constant or anisotropic substrate materials is difficult because of the current deficiencies of CAD routines, and shifts in resonator

frequencies due to variations in the substrate dielectric constant or large kinetic inductance effects cannot be tolerated. In general, YBCO deposition techniques will continue to improve and new dielectric materials or combinations of dielectrics will be examined. Finally, the availability of thinner, large-area substrates and multilayer dielectrics will eventually allow much more complex circuits to be designed.

CONCLUSIONS

Two distinct classes of superconductive, passive microwave devices were demonstrated, both with a significant performance advantage over normal-metal versions of the same devices: long delay lines and resonator-based bandpass filters. A stripline chirp filter was fabricated and operated at 77 K with a 2.7-GHz bandwidth, a 4.2-GHz center frequency, and 11.5 ns of dispersive delay giving a time-bandwidth product of 30. The total transmission-line length of the chirp filter represents 14 ns of delay. A 7-ns and a 1.5-ns microstrip delay line were fabricated and operated in conjunction with a GaAs sampling circuit at 77 K, demonstrating the compatibility of semiconductor and superconductive devices at cryogenic temperatures. Microstrip narrowband bandpass filters were also fabricated and operated at 77 K with bandwidths ranging from 1 - 3% at 4.8 GHz. These devices were four-pole Chebyshev filters. Both of these classes of microwave devices illustrate that the low conductor loss of superconducting materials makes it possible to build passive microwave devices that cannot be built with normal metal conductors. Operation of these superconducting devices is now possible at temperatures up to 77 K, opening up new opportunities for high-frequency, wide-bandwidth analog signal processing systems.

ACKNOWLEDGMENTS

The authors wish to thank Andy Denneno for mask making, Roger Tompkins for device packaging, George Fitch for computer programming, Rick Slattery for assistance with the microwave package fabrication, and Earle Macedo for conventional thin-film depositions. We would also like to acknowledge the technical guidance of Richard Ralston, very useful technical exchanges with Alfredo Anderson and Dan Oates, and the secretarial assistance of Jane Clark and Anne LaRose. This work is supported, in part, by the US Department of the Navy and, under the auspices of the Consortium for Superconducting Electronics, the Defense Advanced Research Projects Agency.

REFERENCES

1. R. S. Withers and R. W. Ralston, "Superconductive Analog Signal Processing Devices," *Proc. IEEE* 77, 1247-1262 (1989).
2. W. G. Lyons and R. S. Withers, "Passive Microwave Device Applications of High- T_c Superconducting Thin Films," *Microwave Journal* 33, 85-102 (1990); and references therein.
3. D. E. Oates and A. C. Anderson (personal communication).
4. P. M. Mankiewich, J. H. Scofield, W. J. Skocpol, R. E. Howard, A. H. Dayem, and E. Good, "Reproducible Technique for Fabrication of Thin Films of High Transition Temperature Superconductors," *Appl. Phys. Lett.* 51, 1753-1755 (1987).
5. R. L. Sandstrom, W. J. Gallagher, T. R. Dinger, R. H. Koch, R. B. Laibowitz, A. W. Kleinsasser, R. J. Gambino, B. Bumble, and M. F. Chisholm, "Reliable Single-Target Sputtering Process for High-Temperature Superconducting Films and Devices," *Appl. Phys. Lett.* 53, 444-446 (1988); C. B. Eom, J. Z. Sun, K. Yamamoto, A. F. Marshall, K. E. Luther, T. H. Geballe, and S. S. Laderman, "In Situ Grown $YBa_2Cu_3O_{7-x}$ Thin Films from Single-Target Magnetron Sputtering," *Appl. Phys. Lett.* 55, 595-597 (1989).
6. P. M. Mankiewich (personal communication).
7. N. Newman, B. F. Cole, S. M. Garrison, K. Char, and R. C. Taber, "Double Gun Off-Axis Sputtering of Large Area $YBa_2Cu_3O_{7-x}$ Superconducting Films for Microwave Applications," *IEEE Trans. Magn.* 27, 1276-1279 (1991).
8. R. S. Withers, A. C. Anderson, J. B. Green, and S. A. Reible, "Superconductive Delay-Line Technology and Applications," *IEEE Trans. Magn.* MAG-21, 186-192 (1985).
9. M. S. Dillorio, R. S. Withers, and A. C. Anderson, "Wide-Band Superconductive Chirp Filters," *IEEE Trans. Microwave Theory Tech.* 37, 706-710 (1989).
10. J. H. Cafarella, "Wideband Signal Processing for Communication and Radar," *IEEE National Telesystems Conference*, pp. 55-58, November 1983.
11. W. G. Lyons, R. S. Withers, J. M. Hamm, A. C. Anderson, P. M. Mankiewich, M. L. O'Malley, and R. E. Howard, "High- T_c Superconductive Delay Line Structures and Signal Conditioning Networks," *IEEE Trans. Magn.* 27, 2932-2935 (1991).
12. W. G. Lyons, R. S. Withers, J. M. Hamm, A. C. Anderson, P. M. Mankiewich, M. L. O'Malley, R. E. Howard, R. R. Bonetti, A. E. Williams, and N. Newman, "High-Temperature Superconductive Passive Microwave Devices," *MTT-S Digest*, to be published (1991).
13. W. G. Lyons, R. S. Withers, A. C. Anderson, R. R. Bonetti, A. E. Williams, P. M. Mankiewich, M. L. O'Malley, and R. E. Howard, "High-Temperature Superconductive Passive Microwave Devices," *IEEE Device Research Conference*, Santa Barbara, CA, June 1990.
14. R. R. Bonetti and A. E. Williams, "Preliminary Design Steps for Thin-Film Superconducting Filters," *MTT-S Digest*, 273-276 (1990).
15. W. G. Lyons, R. R. Bonetti, A. E. Williams, P. M. Mankiewich, M. L. O'Malley, J. M. Hamm, A. C. Anderson, R. S. Withers, A. Meulenbergh, and R. E. Howard, "High- T_c Superconductive Microwave Filters," *IEEE Trans. Magn.* 27, 2537-2539 (1991).

Ultrafast Lasers

Femtosecond Monolithic Colliding-Pulse Mode-Locked Quantum-Well Lasers

M. C. Wu, Y. K. Chen, T. Tanbun-Ek, and R. A. Logan

AT&T Bell Laboratories, Murray Hill, New Jersey 07974

Abstract

Monolithic colliding pulse mode-locked (CPM) multiple quantum well lasers generating optical pulses as short as 600 femtoseconds are reported. The CPM laser is built on a single chip of InGaAs/InGaAsP multiple quantum well lasers. The pulse repetition rates are synchronized with an rf synthesizer up to 40 GHz in hybrid mode-locking. In passive mode-locking, a record high repetition rate of 350 GHz has been achieved. All the sub-picosecond pulses obtained have pulse shapes of sech^2 and transform-limited time-bandwidth products between 0.30 to 0.34.

Monolithic mode-locked semiconductor lasers [1-7] are compact and stable sources of ultrashort optical pulses. Their applications include multi-hundred Gbit/sec time-division multiplexed optical communication systems, ultra-high speed electro-optic sampling systems, optical soliton sources for ultra-long distance transmission in optical fibers, and generation of millimeter and sub-millimeter waves. The fully integrated optical cavities not only eliminate the tedious optical alignment processes in mode-locked semiconductor lasers using external cavities and bulk optics [8], they also suppress the undesired multiple pulse output generated by residue intra-cavity reflections [9]. Picosecond pulses have been generated in semiconductor lasers with integrated passive cavities [2], tandem-contact semiconductor lasers [3,5], and hybrid mode-locked semiconductor lasers with active waveguides [4]. The monolithic colliding pulse mode-locked (CPM) multiple quantum well lasers [6,7] are the first monolithic mode-locked semiconductor lasers that generate optical pulses in the femtosecond regime.

The monolithic CPM laser consists of a saturable

absorber in the center of the cavity, two modulators near the facets for synchronization with external electrical clocks, and two active waveguides (gain sections) linking the modulators and the saturable absorbers, as shown in Fig. 1. Though ring cavity is preferred in the first CPM dye laser [10], the linear-cavity configuration is used in our experiments for two reasons: (1) the linear-cavity laser with cleaved facets is compatible with standard semiconductor laser technology; and (2) the problem of critical positioning of the absorber dye jets in linear-cavity CPM dye lasers [10] is solved by microfabrication technology used in the monolithic CPM lasers. The saturable absorber is placed exactly in the center of the cavity by photolithography and cleaving processes.

The monolithic CPM laser can be synchronized with external electrical clocks (hybrid mode-locking) by sending an rf signal to the two modulators. The rf signal is distributed through integrated microstrip transmission lines to guarantee the exact timing between the two counter-propagating pulses. The length of center saturable is designed to be smaller than the spatial duration of the optical pulses and ranges from $10\mu\text{m}$ to $50\mu\text{m}$, depending on the cavity lengths.

Figure 2 shows the schematic layer structure of the step-graded index separate confinement heterostructure (GRINSCH) multiple quantum well lasers used here. The active region consists of five InGaAs quantum wells and six InGaAsP (bandgap wavelength $\lambda_g = 1.25\mu\text{m}$) barriers. The GRIN regions are synthesized by four quaternary layers with monotonically varying λ_g . Iron-doped semi-insulating InP is then regrown around the active stripe to form a buried heterostructure. The lasing wavelength is $1.55\mu\text{m}$. The dc characteristics of the quantum well lasers has been reported elsewhere

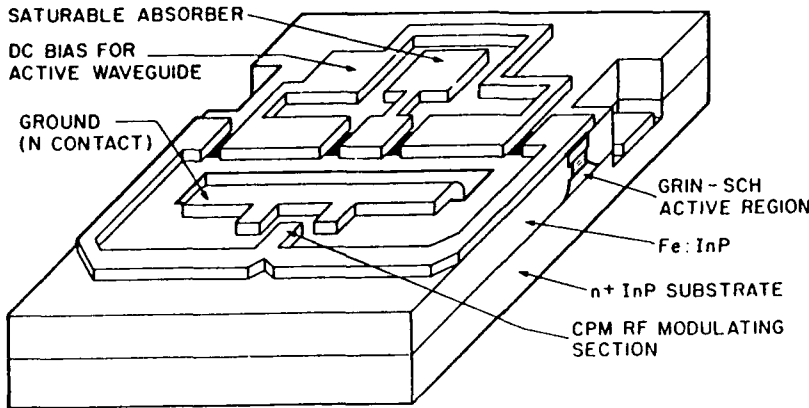


Figure 1. The schematic diagram of the monolithic CPM laser.

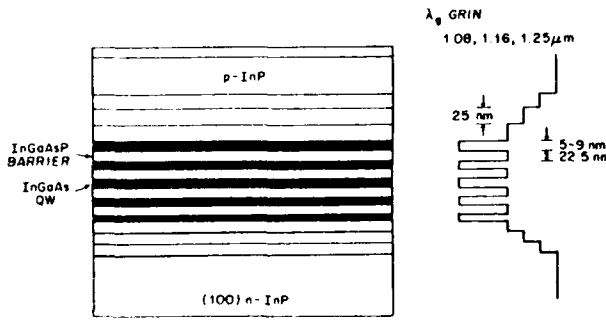


Figure 2. The schematic layer structure of the InGaAs/InGaAsP MQW laser.

[11]. The same quantum-well material can be used as either the gain medium or the saturable absorber, depending on the bias conditions. Forward-biased quantum wells provide saturable gain, while reverse-biased quantum wells function as saturable absorbers. Because of the step-like density-of-states in quantum wells, the saturable absorber cross section is larger than the gain cross section. The condition for mode-locking [12] can thus be satisfied in separately biased semiconductor lasers with continuous active quantum wells. The various sections of the CPM laser are defined by separate top electrodes.

Background-free second-harmonic generation (SHG) autocorrelator is used to measure the widths of the mode-locked pulses, and an optical spectrum analyzer is employed to simultaneously monitor the time-averaged optical spectrum. Figure 3 shows the SHG autocorrelation trace of the output pulses from a hybrid mode-locked CPM laser. The SHG trace agrees very well with that of a sech^2 pulse shape, and the corresponding full-width-at-half-maximum (FWHM) pulse width is 0.95 ps. Simultaneous measurement of

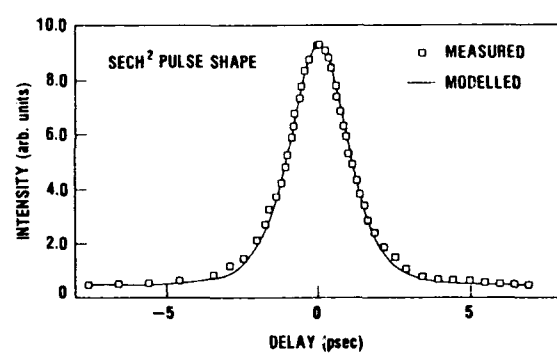


Figure 3. The measured and modeled SHG autocorrelation traces of the pulses generated by a 2.1mm-long hybrid mode-locked monolithic CPM laser.

the optical spectral bandwidth shows a time-bandwidth product of 0.32, which is very close to the transform-limit value of 0.31. The effect of saturable absorber is illustrated in Fig. 4. With increasing reverse bias on the saturable absorber, the dc level gradually decreases and the pulse width becomes shorter. As the reverse bias reaches -0.4 V, the dc level reduced to almost zero and the pulse shape becomes that of a sech^2 .

The repetition rate of 38.5 GHz corresponds to twice of the round-trip frequency of the 2.1-mm-long cavity. Because of the CPM configuration, there are two pulses traveling in the cavity. In hybrid mode-locking, the two modulators force the pulses to collide in the central saturable absorber. However, the "forced collision" is not necessary for this monolithic laser to operate in the CPM regime. In fact, the laser prefers to operate in CPM regime even in the absence of the rf signal, as will be shown later in the passive CPM case. Here the rf signal simply serves to synchronize the

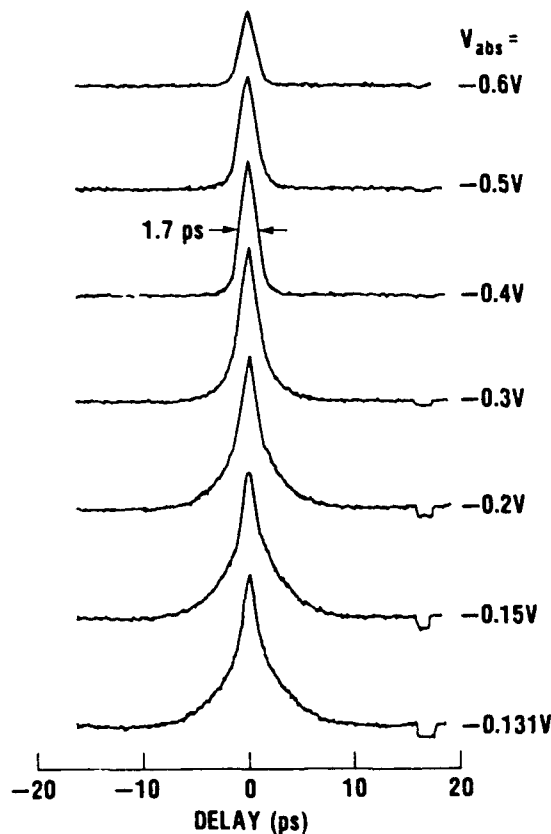


Figure 4. The SHG autocorrelation traces for various saturable absorber bias.

pulse repetition rate with the external clocks. Therefore, very little rf power (15dBm) is needed to achieve hybrid mode-locking.

The repetition rate of the hybrid CPM pulses can be detuned by varying the frequency of the rf signals. Figure 5 shows the FWHM width of the SHG autocorrelation traces versus the rf driving frequency. The repetition rate can be detuned by about 5% of the center frequency without significantly increasing the pulse width. The wide frequency tuning range results from the use of active waveguides, where the refractive index adapts itself so that the cavity round-trip frequency matches the external rf frequency. This feature is very important for most applications which require the optical pulses be synchronized with some standard electrical clocks (e.g., data rate) or another CPM laser (e.g., in optical time division multiplexing).

In passive CPM operation, the modulators are shorted with the active waveguides. The two counter-propagating pulses time themselves to collide in the center saturable absorber because minimum energy is lost to the absorber. Figure 6(a) and (b) shows the SHG autocorrelation trace and the optical spectrum of

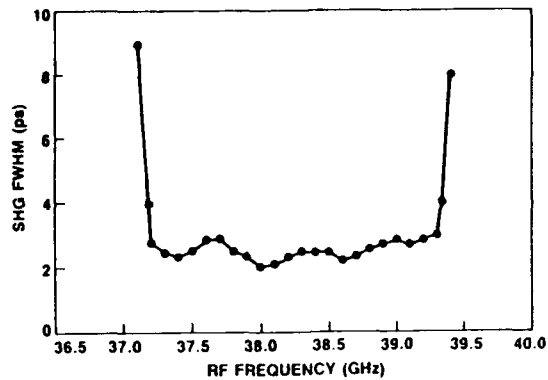


Figure 5. The FWHM width of the autocorrelation traces versus the rf frequency.

the same CPM laser without applying rf signal. Transform-limited pulses with sech^2 pulse shape is obtained with slightly longer pulse width (1.15 ps). Since no rf source is needed in passive mode-locking, the repetition rate is not limited by the rf synthesizer. Passive mode-locking of the CPM lasers with repetition rates of 40 GHz, 80 GHz, 160 GHz, and 350 GHz have been demonstrated [7]. The record high repetition rate of 350 GHz is obtained with a 250 μ m-long CPM laser.

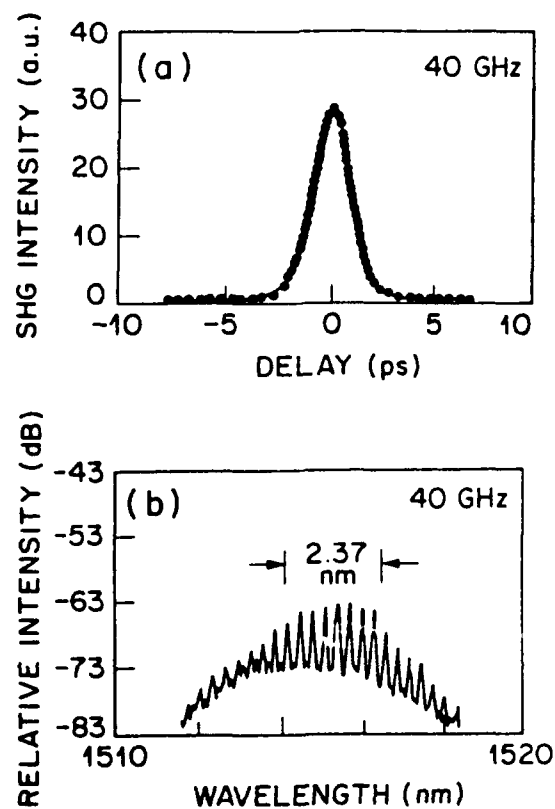


Figure 6. The autocorrelation trace and the optical spectrum of the passive CPM laser.

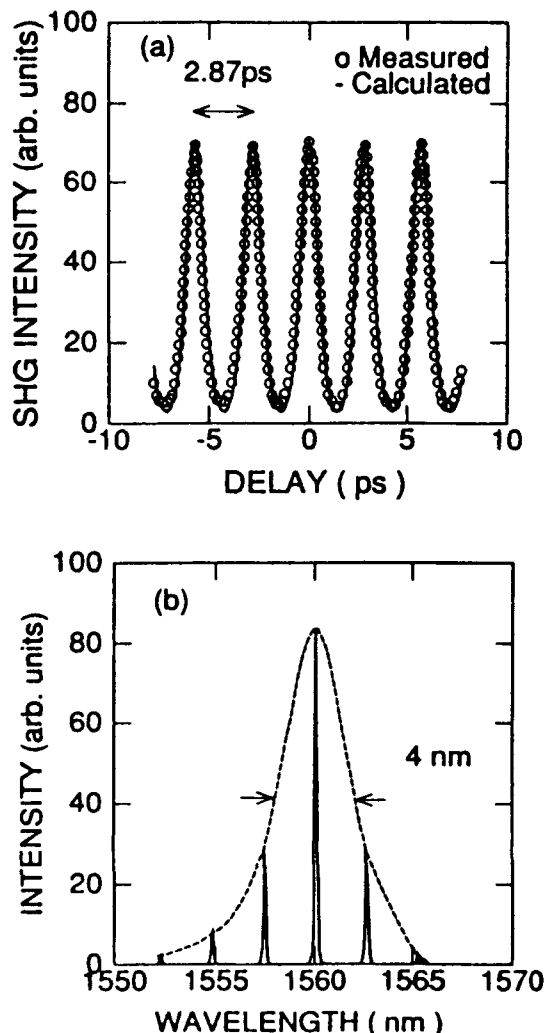


Figure 7. The autocorrelation trace and the optical spectrum of the optical pulses from the passive CPM laser with a repetition rate of 350 GHz.

The SHG autocorrelation trace and the optical spectrum are shown in Fig. 7(a) and (b), respectively. Even at such high repetition rate (period = 2.87 ps), the pulse shape still agrees very well with that of sech^2 . The transform-limited pulse width of 640 femtosecond (FWHM) is the shortest ever reported for monolithic mode-locked semiconductor lasers. Though the optical spectrum in Fig. 7(b) shows only three major modes, the same spectrum with logarithmic scale indicates that more than nine modes are mode-locked.

A wide range of dc biases can be used to generate the nearly transform-limited short optical pulses in both the active- and the passive-monolithic CPM lasers. For example, Fig. 8 shows the optimum saturable absorber bias voltage versus the gain-section current for the 350-GHz passive CPM laser. Two curves are shown for saturable absorber lengths of (a) 25 μm and (b) 15

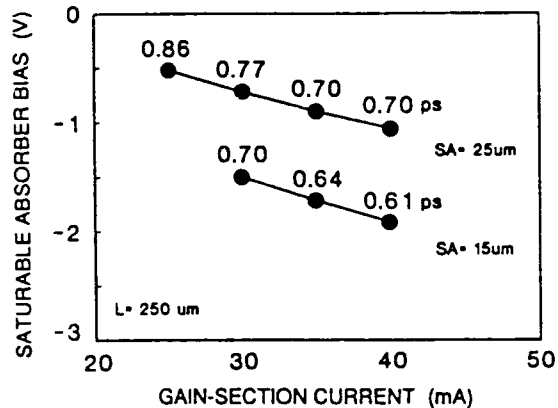


Figure 8. The optimum saturable absorber bias versus the current of the gain section for two CPM lasers with saturable absorber lengths of 25 μm and 15 μm , respectively. The pulse widths at the corresponding bias conditions are also shown.

μm . Sub-picosecond pulses are generated for gain current from 20 mA to 40 mA. Shorter pulses are generated when the gain sections are more forward-biased and the saturable absorber are more reverse-biased. The CPM laser with shorter saturable absorber (15 μm) needs more reverse bias for the absorber and produces shorter pulses. The shortest pulse width of 610 fs is generated with saturable absorber bias of -2 V and gain current of 40 mA in the CPM laser with 15 μm -long absorber.

In summary, we have successfully generated transform-limited sub-picosecond optical pulses using novel monolithic colliding pulse mode-locked quantum well lasers. The pulse width of 600 fs is the shortest ever reported for monolithic semiconductor lasers. The optical pulses are synchronized with external rf signals up to 40 GHz using hybrid mode-locking. A record high repetition of 350 GHz is also achieved in passive mode-locking. All the pulses generated have pulse shapes of sech^2 , time-bandwidth products of 0.30 ~ 0.34, and near 100% intensity modulation depth.

REFERENCES

1. K.Y.Lau, *Appl. Phys. Lett.*, **52**, 2214 (1988).
2. R.S.Tucker, U.Koren, G.Raybon, C.A.Burrus, B.I.Miller, T.L.Koch, G.Eisenstein, and A.Shahar, *Electron. Lett.*, **25**, 622 (1989).
3. P.P.Vasil'ev and A.B.Sergeev, *Electron. Lett.*, **25**, 1050 (1989).
4. P.A.Morton, J.E.Bowers, L.A.Koszi, M.Soler, J.Lopata, and D.P.Wilt, *Appl. Phys. Lett.*, **56**, 111 (1990).

5. S.Sanders, L.Eng, J.Paslaski, and A.Yariv, *Appl. Phys. Lett.* **56**, 310 (1990).
6. M.C.Wu, Y.K.Chen, T.Tanbun-Ek, R.A.Logan, M.A.Chin, and G.Raybon, *Appl. Phys. Lett.*, **57**, 759 (1990)
7. Y.K.Chen, M.C.Wu, T.Tanbun-Ek, R.A.Logan, and M.A.Chin, to be published in *Appl. Phys. Lett.*, (1991).
8. For a review, J.P. van der Ziel, in *Semiconductors and Semimetals*, Vol. 22, Part B, edited by W.T. Tsang, Academic Press (1985)
9. S.W.Corzine, J.E.Bowers, G.Przybylek, U.Koren, B.I.Miller, and C.E.Soccolich, *Appl. Phys. Lett.*, **52**, 348 (1988)
10. R.L.Fork, B.I.Greene, and C.V.Shank, *Appl. Phys. Lett.*, **38**, 671 (1981).
11. T.Tanbun-Ek, R.A.Logan, H.Temkin, K.Berthold, A.F.J.Levi, and S.N.G.Chiu, *Appl. Phys. Lett.*, **55**, 2283 (1989).
12. H.A.Haus, *IEEE J. Quantum Electron.* **QE-11**, 736 (1975)

Optimization of Packaged, Actively Mode-locked 1.5- μ m InGaAsP Diode Laser for >10 Gb/s OTDM Transmission Systems

I. W. Marshall, A. J. Lowery, * P. D. Constantine, D. J. Cooper, and D. Elton

British Telecom Research Laboratories, Martlesham Heath, Ipswich, Suffolk IPS 7RE, UK

**Department of Electrical and Electronic Engineering, University of Melbourne, Melbourne, Victoria 3052, Australia*

Abstract

A packaged, mode-locked semiconductor laser is described, which emits 4 ps wide transform limited pulses at 10 GHz, and is optimised using only bias current (± 1 mA) and cavity detuning (± 50 MHz).

Introduction

Work on transatlantic communications systems has already shown [1] that the maximum bit-rate/distance product for any system length is always obtained by transmitting well spaced transform limited pulses (solitons), e.g. 20 ps pulses for 10 Gbit/s transmission over 5000 km [2]. In a 40 Gbit/s network similar techniques would allow transmission over 1-2000 km using 3-5 ps pulses [3]. The principal barrier to development of such systems has always been the lack of a suitable pulse transmitter, which must produce high power, transform limited ps pulses at GHz rates, and must also be portable and stable for long periods (years). Recently it has been shown that suitable pulses can be generated by optically amplified semiconductor laser sources [4-6], similar to those used in current lightwave transmission systems. Two techniques have been used; gain switching and filtering [4], which is simple to implement but produces substantial pulse to pulse jitter, and mode-locking [5,6], which produces better pulses but is subject to stability problems. In this paper we show for the first time that the mechanical problems associated with external cavity mode-locked lasers can be overcome, without compromising on output pulse quality, by building a packaged cavity, and that the important operating parameters are amenable to external control for long term stability.

Package

The packaged laser is shown in Fig. 1. The fixed parameters (e.g. laser chip design, cavity dimensions) were chosen, after extensive experimentation and modelling using a well known accurate model [7], to be close to the optimum. The laser consisted of a 250 mm long trenched buried heterostructure laser [8] with a broadband anti-reflection coating [9] (reflectivity = 5×10^{-4}) on one facet which faced an external cavity. The external cavity consisted of a 2 mm diam. anti-reflection coated sphere lens (fixed in place using u.v. curing epoxy) which collimated the laser output, and a gold coated 1200 line/mm grating blazed for 1.5mm. The total cavity length was 3 cm (corresponding to a round trip frequency of 5 GHz) and the feedback efficiency was estimated (from the cw threshold of the laser) to be 30%. The grating mount was similar to that used in the external cavity laser which was successfully demonstrated in recent field trials [10]. The output from the laser (at the uncoated chip facet) was coupled into a single mode fibre (with a loss of 3 dB) using an anti-reflection coated tapered lensed fibre. The entire laser was mounted on a Peltier cooler which enabled temperature control to within $\pm 0.1^\circ\text{C}$. This assembly was then placed in a sealable box to eliminate thermo-acoustic variations of the cavity.



Fig. 1 Packaged Mode-locked laser

The cavity was found to be stable for several days without placing the laser on a vibration isolation system. The R.F. modulation was supplied via a bias tee (0.05 -26 GHz) and a 50Ω strip line, which was epoxied directly onto the laser chip to avoid introducing stray inductance in any bond wires. 0.5 W R.F. were supplied to the laser from an ultra low phase noise oscillator. Successful mode-locking was achieved at 5,10 and 20 GHz using this arrangement.

Performance

The best output pulses were obtained when the grating was adjusted so that the laser emitted at 1.56 mm, 10 nm shorter than the peak gain wavelength, to take advantage of the greater dg/dn , and with modulation at 5 GHz. The pulses showed residual A.M. of less than 1% (measured on a lightwave analyser) and less than 250 fs of jitter (estimated from phase noise build up in R.F. spectrum). Harmonic mode-locking at the higher frequencies was found to be less stable (pulse to pulse A.M. increased) so for optimum operation at 10 or 20 GHz the cavity had to be shortened to allow fundamental mode locking. The laser output was optimised by tuning the cavity length for minimum pulselength (generally at the point when secondary pulses due to gain relaxation become apparent), and then reducing the D.C.bias till the secondary pulse disappeared again. The dependence of the output pulse width on D.C. bias is shown in Fig. 2.

Three curves are shown, a measured curve with no cavity retuning (length changes), a predicted curve from the model with no cavity retuning, and a measured curve with cavity retuning to restore optimised operation. The modelled curve was obtained using the parameters given in [11], suitably modified to match the cavity described above, and shows a close agreement with the measured results. The measurements show that if no cavity retuning is allowed the operating current range for near optimum output is

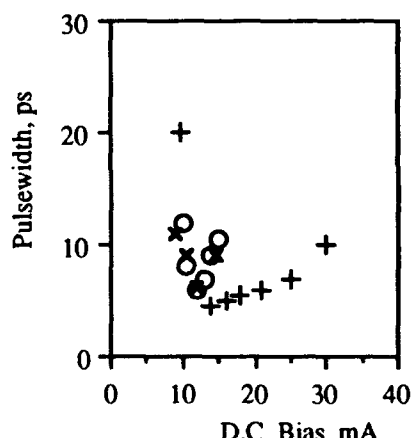


Fig. 2 Pulsewidth vs D.C. Bias, X = modelled results, + = Observations with cavity retuning, O = Observations without cavity retuning

very small, but if the cavity is retuned a remarkably large range of stable operating points is obtained with a broad pulselength minimum around 90% of the cw threshold of the laser and pulselengths increasing with bias above threshold. Interestingly the range of pulselengths available from a single cavity configuration can be varied by almost an order of magnitude thus the laser output can be compatible with a large range of bit rates from 10-100 Gbit/s. The pulses are narrowest near threshold because the gain bandwidth is greater (more bias = more gain = stronger residual F-P chip modes = less bandwidth). The pulse obtained at the cw lasing threshold current is shown in Fig. 3a, together with the pulse predicted by the model. The pulselength (measured on a streak camera with a time resolution of 2-3 ps) was 7 ps and the time bandwidth product was 0.35. The optimum single peak pulse (Fig. 3b) had a pulselength of 4 ps and a time bandwidth product of 0.32. Numerically transforming a digitised version of the measurement yields a predicted time bandwidth product of 0.29. The lower chirp is the result of a reduction in the dynamic gain saturation effects at the lower bias current (pulses obtained at the highest stable bias currents have time bandwidth products of approx. 0.44, confirming this observation). Further reduction of the bias resulted in narrower pulses (2 ps) with substructure (Fig. 3c) within a broader envelope. The secondary peaks are the result of the output bandwidth exceeding the bandwidth of the residual Fabry-Perot modes of the laser and correspond to secondary peaks in the laser spectrum.

It should be noted that the modelled pulses are very similar to the observed pulses thus indicating the predictability of the source and confirming that the observations are the result of the gain dynamics and not an artefact of experimental conditions. The optimum measured pulses are both shorter and less chirped than comparable pulses obtained by other authors [12,13].

Detuning and long term stability

The accuracy and range of the cavity retuning needed to access the stable range of bias currents are illustrated in

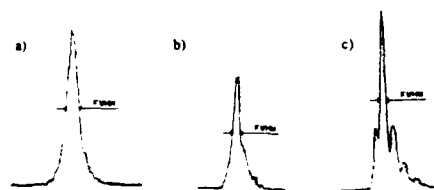


Fig.3 Pulsewidths ----- = experiment, ... = theory
a) 17 mA bias, FWHM = 7 ps, b) 14 mA bias, FWHM = 4 ps, c) 12 mA bias, FWHM = 2 ps

Fig. 4, which shows the dependence of cavity detuning on bias current.

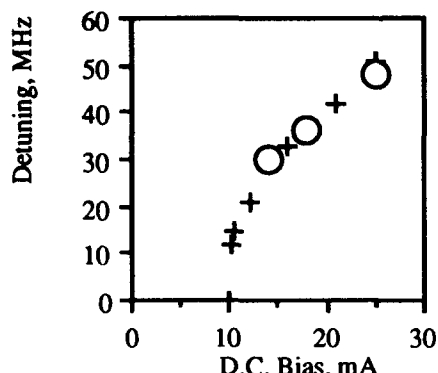


Fig. 4 Cavity detuning vs D.C. Bias, + = measurements, O = Theory predictions

Again a measured curve and a model prediction are shown and close agreement is clear. Cavity detuning is defined as the difference in the length of the laser cavity when the output is maximised for small signal modulation (sine wave output) and the length of the cavity for optimum pulse output. This difference arises from the dynamic effects of gain saturation in the laser chip [14] which lead to the pulse peak advancing in time on each transit and thus a reduction in the effective cavity length, requiring a corresponding lengthening of the actual cavity to restore equilibrium. Under normal conditions the delay is approx 3 ps. This is entirely consistent with the prediction obtained for a single pass amplifier when the following equation [14], is solved for t

$$\frac{dh}{dt} \frac{2t}{\tau_0^2} = 0 \quad (1)$$

where $h(t)$ is the phase variation across the pulse (obtained from the numerical laser model), t is the time normalised to the pulse peak and τ_0 is $1.665\tau_p$ (where τ_p is the pulsewidth). The detuning increases as the bias current increases because the effects of gain saturation increase at higher gains (or bias currents since gain μ bias). It can be seen in Fig. 3 that for stable operation the cavity length needs to be stable over ± 10 MHz or 0.1 mm, which is readily achieved, and the range necessary to maintain stable operation over a large range of currents is 3 mm (i.e. small enough to be accessible via piezo-electric control). This means that it would be possible to construct a control loop, which optimises D.C. bias and cavity detuning according to a simple algorithm, which would maintain stable operation even if increases in threshold (due to laser ageing or cavity drift) were to occur. Stability could thus be achieved on the timescales necessary for use in telecommunication networks.

Conclusion

An optimised packaged mode-locked laser has been constructed. The optimised laser design produces 4 ps wide near transform limited pulses at GHz rates and is ideal for use in linear and non-linear OTDM lightwave transmission systems at bit rates of 10 to 100 Gbit/s. Short term stability of the source is excellent and long term stabilisation is possible. The laser is well understood and can be modelled accurately.

References

1. L.F.Mollenauer and K.Smith, "Demonstration of soliton transmission over more than 4000 km fibre with loss periodically compensated by Raman gain," Opt. Lett. **13**, 675-7 (1988)
2. L.F.Mollenauer et.al., "Experimental demonstration of soliton transmission over more than 10000 km," in Technical Digest of Conference on Lasers and Electro-Optics (Optical Society of America, Washington DC, 1990), Paper PDP17
3. I.W.Marshall, G.N.Brown and D.M.Spirit, "Non-linear transmission with practical semiconductor source," in IEE Digest no. 1990/159 (Institution of Electrical Engineers, London, 1990) paper no. 11
4. M.Nakazawa, K.Suzuki and Y.Kimura, "Generation of optical solitons in the Gigahertz region using a directly modulated distributed feedback laser diode," Opt. Lett. **15**, 588-90 (1990)
5. I.W.Marshall, D.M.Spirit, G.N.Brown and L.C.Blank, in Technical Digest of Optical Fibre Communication (Optical Society of America, Washington DC, 1990), Paper PD6
6. N.A.Olsson et. al., "4 Gbit/s soliton data transmission experiment," in Technical Digest of Optical Fibre Communication (Optical Society of America, Washington DC, 1990), Paper PD4
7. A.J.Lowery, "New time domain model for active mode locking based on the transmission line laser model," IEE Proc. J, **136**, 264-72 (1989)
8. D.M.Cooper et. al., "High performance, high reliability buried heterostructure lasers by MOVPE," Electron. Lett., **24**, 519-21 (1988)
9. W.J.Devlin, D.J.Elton et.al., "Polarisation insensitive high output power 1.3 and 1.5 μ m optical amplifiers made by MOVPE," Proc IOOC, Kobe, **3**, pp148-9 (1989)
10. M.J.Creaner et. al., "Field demonstration of 565 Mbit/s DPSK coherent transmission system over 176 km of installed fibre," Electron. Lett., **24**, 1354 (1988)
11. A.J.Lowery and I.W.Marshall, "Stabilisation of

mode-locked pulses using a travelling-wave semiconductor laser amplifier," *Electron. Lett.*, **26**, 104-5 (1990)

12. G.Eisenstein, R.S.Tucker, U.Koren and S.K.Korotky, "Active mode-locking characteristics of InGaAsP single mode fibre composite cavity lasers,"., *IEEE J. Quantum Electron.*, **QE-22**, 142-8 (1986)

13. M.Serenyi, J.Kuhl and E.O.Göbel, "Pulse shortening of actively mode-locked diode lasers by wavelength tuning," *App. Phys. Lett.*, **50**, 1213 (1986)

14. G.P.Agrawal and N.A.Olsson, "Self-phase modulation and spectral broadening of optical pulses in semiconductor laser amplifiers," *IEEE J. Quantum Electron.*, **QE-25**, 2297-305 (1989)

Generation of High-Power Femtosecond Optical Pulses from a Semiconductor Diode Laser System

P. J. Delfyett, L. Florez, N. Stoffel, T. Gmitter, and N. Andreadakis

Bell Communications Research, 331 Newman Springs Road, Red Bank, New Jersey 07701

G. A. Alphonse

David Sarnoff Research Center, Princeton, New Jersey 08543

Abstract

Optical pulses less than 207 fsec with over 150 watts of peak power have been generated from an all semiconductor laser diode system.

Introduction

Compact and efficient sources of high repetition rate, high peak power ultrashort optical pulses are needed to replace the standard ultrashort optical pulse generation schemes due to their relatively large size and poor wall plug efficiency. It has been previously demonstrated that an external cavity hybrid mode locked semiconductor laser system has been able to produce optical pulses as short as 460 fsec in duration with over 70 watts of peak power {1}. In this paper, a modification of this system which incorporates a four prism sequence to compensate for intracavity group velocity dispersion is described. This system produces optical pulses that are 207 fsec in duration with over 150 watt of peak power. These optical pulses are both the shortest and most intense optical pulses ever generated from an all semiconductor laser diode system.

Experiment

The experimental setup employed is shown in Fig. 1. The ultrashort optical pulses were generated from an external cavity hybrid mode locked laser. The advantage of utilizing a hybrid mode locking scheme is that it takes advantage of the stability which is offered by the actively mode locked system, and also takes advantage of the additional pulse shortening mechanisms provided by the saturable absorber. The device structure is

an angled stripe semiconductor traveling wave amplifier {2}. The key feature of utilizing this type of structure is that the residual facet reflectivity of the diode is sufficiently low so that single mode locked optical pulses can be obtained, without the usual multiple coherent spike or multipulse output. In addition, the thin active region (~ 80 nm) associated with these devices allows them to have a large saturation energy, thus enabling the amplified pulses to contain a large amount of energy, typically 100 pJ.

The mode locked laser was formed by placing the traveling wave amplifier inside of an external cavity. The transverse mode profile of the laser is controlled by an adjustable slit S. The rear reflector is a multiple quantum well structure which has been epitaxially lifted off and attached

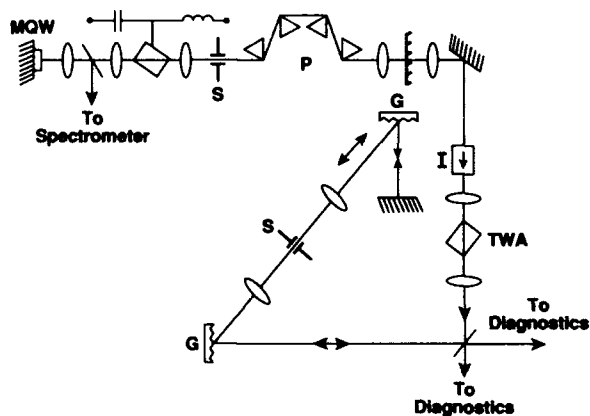
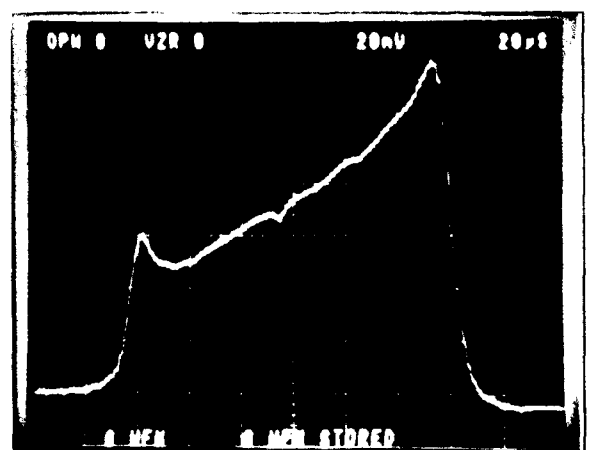


Fig. {1}: Schematic of the experimental setup. Legend: MQW-multiple quantum well saturable absorber; TWA-traveling wave amplifier; S-slit; I-isolator; G-grating; P-prism set.

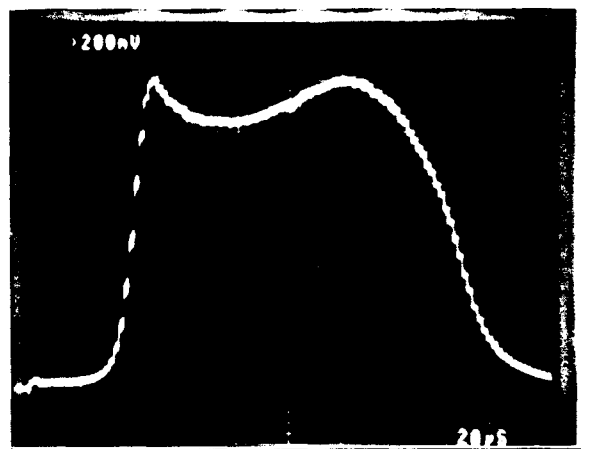
to a silver mirror reflector (3). The purpose of the multiple quantum well structure is that it serves as a saturable absorber which initiates passive mode-locking. The intracavity dispersion compensating prisms were included to compensate for any intra-cavity group velocity dispersion and the chirp which is impressed upon the optical pulse during the mode locking process.

Passive mode-locking could be achieved by utilizing the chromatic dispersion of the focussing lenses, thus forcing the laser to operate in the excitonic absorption region. By monitoring the spectrum which was reflected from the MQW-mirror reflector, a substantial broadening of the lasing spectrum would occur when the laser was tuned to operate in the excitonic absorption region. By applying ~ 0.5 watts of RF to the oscillator where the RF frequency was matched to the third harmonic of the longitudinal mode frequency, the lasing spectrum was broadened to 8.4 nm, with a prism separation of 33 cm. The typical d.c. bias threshold current in this case was 209 mA. Under these conditions the laser would emit pulses of approximately 2.5 psec in duration at 830 nm, with a repetition frequency equal to the third harmonic of the longitudinal mode spacing of the external cavity, i.e., 355 MHz. The difficulty in obtaining passive mode locked pulse trains at the fundamental longitudinal mode frequency is due to the the short gain recovery time associated with diode lasers and the large cavity length required in order to contain the four prism sequence.

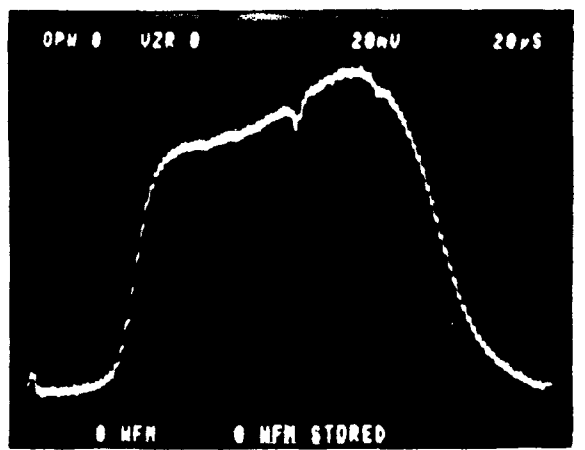
The inclusion of the four prism sequence only partially compensates for the group velocity dispersion, while simultaneously increasing the lasing bandwidth. The effects of the large nonlinearities experienced by the optical pulse as it oscillates within a round trip greatly effects the pulse shaping mechanisms and prevents the production of transform limited optical pulses directly from the laser oscillator. These effects can be observed by examining the optical pulse spectra at three important locations inside of the laser cavity. These features can be seen in Fig. 2(a,b,c). In Fig 2(a), the optical pulse spectra is shown as the pulse exits the TWA after the pulse has gone through a double pass through the prism sequence. The shape of the spectrum is reminiscent of the classical self phase modulated spectrum which is obtained for ultrashort optical pulses after traversing a nonlinear medium. In Fig. 2(b), the optical pulse spectrum is shown after the pulse exits the MQW saturable absorber. The enhancement of the high energy side of the spectrum is due to the creation of real



(a)



(b)



827 833 (c)
Wavelength nm

Fig.(2): Optical pulse spectrum (a) before MQW absorber; (b) after MQW absorber; (c) output spectrum

carriers and the resultant reduction in the refractive index. In Fig. 2(c), the optical pulse spectrum is shown after the output coupler. The energy distribution in this spectrum has been shifted towards the lower energy side, due to gain depletion which results in an increase in the refractive index.

The large time-bandwidth product (typically ~ 8) of the hybrid mode locked laser pulse suggests that there possibly exists a large frequency sweep, or chirp, impressed on the mode-locked pulse. In order to take advantage of this frequency sweep, a standard dual grating pulse compressor was constructed and employed to compress the mode-locked pulse.

The pulse compressor utilized two gold coated blazed gratings with 1800 grooves/mm, with two 16 cm focal length lenses. An adjustable slit was located at the Fourier plane of the telescope inside of the compressor, thus acting as a spectral filter (4). The compressor was constructed in the double pass geometry. The position of the second grating in the pulse compressor was varied in both the positive and negative dispersion regimes to achieve the maximum compression ratio. From our experiments, the maximum pulse compression occurs by having the grating in the negative dispersion regime, approximately 7 cm away from the zero dispersion position.

In order to obtain the shortest pulses, the alignment of the mode locked oscillator was initially adjusted so that the oscillator operated with

the widest possible bandwidth. The bandwidth in this case could be as much as 8.4 nm. Under these conditions, optical pulses could be compressed down to 207 fsec, with 11 mW of amplified signal power directly after the compressor. The spectral window in the compressor filters out the spontaneous emission giving only 100 μ W of additional spontaneous emission power. In Fig. 3 is the autocorrelation trace of the optical pulse for this experimental configuration. The pulse after the compressor, with 11 mW of amplified average signal power imply a peak power of 150 watts. These results represent both the shortest and most intense optical pulses ever obtained from an all semiconductor laser diode system.

In summary, hybrid mode locking with optical pulse compression and spectral windowing techniques has yielded optical pulses of 207 fsec in duration with peak powers over 150 watts. The pulses obtained from this system are both the shortest and most intense ever generated from an all semiconductor diode laser system. The peak powers obtained from this type of system may make photonic switching and other applied nonlinear optical applications possible with a compact laser source.

Acknowledgments

The authors wish to thank J. P. Heritage, Y. Silberberg and A. M. Weiner for their helpful comments and suggestions.

References

- (1) P. J. Delfyett, C.-H. Lee, I. Florez, N. Stoffel, T. Gmitter, and N. Andreadakis, "Generation of subpicosecond high power optical pulses from a hybrid mode-locked semiconductor laser", *Optics Lett.*, Vol. 15, No. 23, 1371, (1990).
- (2) G. A. Alphonse, D. B. Gilbert, M. G. Harvey and M. Ettenberg, "High power superluminescent diodes", *I.E.E.E. J. Quant. Electr.*, QE-24, 2454, (1988).
- (3) E. Yablonovich, T. Gmitter, J. Harbison, and R. Bhat, "Extreme selectivity in the lift-off of epitaxial GaAs films", *Appl. Phys. Lett.*, 51, 2222, (1987).
- (4) A. M. Weiner, J. P. Heritage, E. M. Kirschner, "High resolution femtosecond pulse shaping", *J. Opt. Soc. Am. B5*, 1563, (1988).

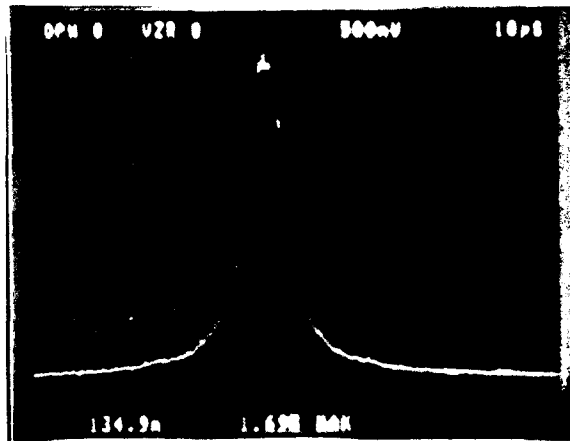


Fig.(3): Autocorrelation trace of the compressed pulse showing a pulselength of 207 fsec assuming a hyperbolic secant squared pulse shape.

Scale: 320 fsec/div

Numerical Simulations of an Actively Q-Switched Semiconductor Laser

Björn Jonsson and Sverre T. Eng

Department of Optoelectronics and Electrical Measurements,
Chalmers University of Technology, S-412 96 Göteborg, Sweden

Abstract

In this work, the travelling-wave rate-equations have been used to numerically simulate the performance of an actively Q-switched GaAs/AlGaAs twin-electrode laser. For modulation frequencies from 1.0 to 3.0 GHz optical output pulses of 20–23 ps were obtained. The calculated results of this model have been compared with experimental results and good agreement was found. The computer model is versatile, easy to implement on a small PC-type computer, and it can, without any modifications, be used to simulate the dynamic behavior of a large variety of optoelectronic devices. Hence, we believe that the travelling-wave rate-equations can be an important tool for simulating ultrafast pulse generation in optoelectronic devices.

Introduction

The direct modulation of semiconductor lasers and optical amplifiers is of considerable interest for applications in high speed fiber-optic communication systems [1–2]. As the structures of new devices become more and more complicated, detailed understanding of the operating characteristics of new devices can only be obtained by computer simulation. In such a computer model not only the temporal and spatial variations but also the interaction between the optical field and the carriers must be treated consistently [3]. Assuming a longitudinally uniform distribution of

photons and carriers, it is possible to obtain computer models for the lateral variations [4–6]. This assumption may be justified in devices with longitudinally uniform geometries, but not in optoelectronic devices with explicit longitudinal variations [7–8]. Examples of new devices with explicit nonuniform longitudinal variations are multisegment lasers [9], lasers for active Q-switching [10], and semiconductor lasers with asymmetric mirror reflectivities [11].

The objective for this work is to develop a computer model which is applicable to a large variety of longitudinally nonuniform optoelectronic devices with general cross-sectional geometries. Furthermore, the model should be able to handle longitudinal variations in both the injection current and absorption, as well as variations in the reflectivities of the end-facets. Although an inclusion of lateral effects into our model would be straightforward, it would require an excessive amount of computer resources, and we therefore focus this work on the longitudinal and temporal behavior of the device. This work follows the same lines as Shore [7] and Wong and Carroll [8] but there are three main differences:

- We include an explicit longitudinal and temporal variation of the absorption.
- We allow for an explicit longitudinal and temporal variation of the injected current.
- We make a rigorous multimode calculation, whereas [7] and [8] restricted their calculations to only one longitudinal mode.

$$\frac{\partial S_m^+}{\partial t} = \frac{c_0}{n_{\text{eff}}} \cdot [G_m - \alpha_{\text{eff}}] \cdot S_m^+ + \Gamma \cdot \frac{\beta}{2} \cdot \frac{N}{\tau_s} - \frac{c_0}{n_{\text{eff}}} \cdot \frac{\partial S_m^+}{\partial z} \quad (1)$$

$$\frac{\partial S_m^-}{\partial t} = \frac{c_0}{n_{\text{eff}}} \cdot [G_m - \alpha_{\text{eff}}] \cdot S_m^- + \Gamma \cdot \frac{\beta}{2} \cdot \frac{N}{\tau_s} + \frac{c_0}{n_{\text{eff}}} \cdot \frac{\partial S_m^-}{\partial z} \quad (2)$$

$$\frac{\partial N}{\partial t} = \frac{J}{e \cdot d} - \frac{c_0}{n_{\text{eff}}} \cdot \sum_m g_m \cdot (S_m^+ + S_m^-) - \frac{N}{\tau_s} \quad (3)$$

Theory

In this section a short derivation of the rate-equations is given and some important aspects of the numerical method is delineated. A more elaborate treatment of the implementation can be found in [12]. Inside an optical device the optical field is assumed to propagate back and forth in the longitudinal direction between the two end-facets with reflectivities R_1 at $z = 0$ and R_2 at $z = L$. Our model is based on the multimode travelling-wave rate-equations for semiconductor lasers (Eqs. (1), (2), and (3)) [13]. (For convenience all the variables used in the text are collected and explained in Table 1.)

Assuming a finite number of longitudinal modes, the photon density is divided into counter-propagating waves. We have used the notation S^+ for photons travelling in the $+z$ -direction and S^- for the $-z$ -direction. Thus, the total photon density at a given point along the z -axis is given by:

$$S_{\text{tot}}(z) = \sum_{m=-M}^{+M} S_m^+(z) + S_m^-(z) \quad (4)$$

The confinement factor Γ is defined as the proportion of the optical field that is located inside the active region. Furthermore, we have assumed that the spontaneous recombination rate R_{sp} can be linearised to a single time constant τ_s representing the average carrier lifetime: $R_{\text{sp}}(N) = N / \tau_s$ inside the active region. Outside the active region R_{sp} is set to zero. It would be a straightforward matter in this model to incorporate a more complicated carrier dependence of the spontaneous recombination rate, such as a carrier dependent lifetime, $\tau_s(N)$. Moreover, the modal gain inside the active region G_m is expressed as; $G_m(N) = \Gamma \cdot g_m(N, \lambda)$, where g_m is the material gain for mode m . Outside the active region, G_m is set to zero. The material gain, g_m , is taken to have a linear dependence in carrier concentration and a parabolic dependence in wavelength:

$$g_m = a_m \cdot (N - N_0) - b_m \cdot (\lambda_m - \lambda_0)^2 \quad (5)$$

where a_m and b_m are gain-constants and N_0 is the carrier concentration at thermal equilibrium. The effective losses in the cavity, denoted α_{eff} , are calculated as

$$\alpha_{\text{eff}} = \Gamma \cdot \alpha_1 + (1 - \Gamma) \cdot \alpha_2 \quad (6)$$

where α_1 and α_2 represent the material absorption inside and outside the active region, respectively. Finally, it should also be noted that the surface current density J in Eq (3) is related to the total current I by the simple expression:

$$J = \frac{I}{w \cdot L_I} \quad (7)$$

where L_I is the length of the biased region ($L_I \leq L$).

Table 1. Notation used in the text.

Symbol	Unit	Description
α_1	[m ⁻¹]	Material absorption in active region.
α_2	[m ⁻¹]	Material absorption outside act. reg.
α_{eff}	[m ⁻¹]	Effective modal absorption.
β		Spontaneous emission factor.
Γ		Optical confinement factor.
λ_0	[m]	Wavelength for gain-max (m = 0).
λ_m	[m]	Wavelength for longitudinal mode m.
$\eta_{d,j}$	[m ⁻¹]	Mirror loss factor.
τ_p	[s]	Absorption time for photons.
τ_s	[s]	Recombination time for carriers.
a_m	[m ²]	Gain-constant for mode m.
b_m	[m ⁻³]	Gain-constant for mode m.
c_0	[m/s]	Speed of light in vacuum.
d	[m]	Thickness of active region.
e	[As]	Elementary charge.
G_m	[m ⁻¹]	Modal gain per unit length.
g_m	[m ⁻¹]	Material gain.
h	[Js]	Planck's constant.
I	[A]	Injected current.
I_{th}	[A]	Threshold current.
J	[A/m ²]	Current surface density.
L	[m]	Device length.
L_I	[m]	Length of biased region.
M		Maximum number of modes.
m		Mode-index.
N	[m ⁻³]	Density of electrons in active region.
n_{eff}		Effective refractive index.
P	[W]	Optical output power.
Q		Number of grid points.
R_1		Reflectivity of end-facet at $z = 0$.
R_2		Reflectivity of end-facet at $z = L$.
R_{sp}	[s ⁻¹]	Rate of spontaneous recombination.
S_m	[m ⁻³]	Density of photons in mode m.
w	[m]	Width of active region.

Numerical method

Finite differences were used to discretise the longitudinal dependence of the optical field. In our model the device is divided into $Q + 1$ grid-points with uniform spacing, Δz , between them. By using a first order discretisation scheme the time-dependent rate-equations are transformed into a set of ordinary differential equations in time which are easily solved according to the second order Runge-Kutta method. The boundary conditions (at $z = 0$ and $z = L$) for the photon waves are written:

$$S_m^+(0, t) = R_1 \cdot S_m^-(0, t) \quad (8)$$

$$S_m^-(L, t) = R_2 \cdot S_m^+(L, t) \quad (9)$$

Furthermore, the optical output power from one end-facet is related to the total photon density adjacent to the facet according to the following expression;

$$P_1(t) = \frac{h \cdot c_0^2 \cdot w \cdot d}{\Gamma \cdot \lambda \cdot n_{\text{eff}}} \cdot (1 - R_1) \cdot \sum_{m=-M}^M S_m^-(0, t) \quad (10)$$

$$P_2(t) = \frac{h \cdot c_0^2 \cdot w \cdot d}{\Gamma \cdot \lambda \cdot n_{\text{eff}}} \cdot (1 - R_2) \cdot \sum_{m=-M}^M S_m^+(L, t) \quad (11)$$

A note should also be made here about the definition of the cavity losses. The average losses in the cavity are usually expressed as an inverted photon lifetime:

$$\frac{1}{\tau_p} = \frac{c_0}{n_{\text{eff}}} \cdot [\alpha_{\text{eff}} + \eta_{d, 1} + \eta_{d, 2}] \quad (12)$$

where the mirror loss factor, $\eta_{d, i}$, is defined as

$$\eta_{d, i} = \frac{1}{2L} \cdot \ln[1/R_i] \quad (13)$$

Equation (12), however, is not applicable when a longitudinally variable loss term, $\alpha(z)$ is considered. Therefore in our model the mirror losses (Eq. (13)) are accounted for by the boundary conditions (Eqs. (8) and (9)) and are not included in the loss terms.

Results

An actively Q-switched laser may be constructed by monolithically integrating a 50 μm long modulator section with a 250 μm long multiple quantum well laser section as described in Fig. 1 [10]. The laser section is operated by a bias current above threshold and the Q-switching is achieved by varying the voltage across the modulator section and thus also varying the absorption inside the active region. Typical values of the material absorption in the experiment described by Arakawa et al. [10] were $\alpha_1 = 3000 \text{ cm}^{-1}$ for a modulator bias voltage of +1 V to $\alpha_1 = 12000 \text{ cm}^{-1}$ for a modulator bias of -1 V.

In our computer model we allow for the possibility of simulating this variation of the absorption inside the laser cavity. Thus, the absorption profile in the 300 μm long device is described by

$$\alpha_{\text{eff}}(z) = \begin{cases} \alpha_{\text{laser}} & (0 \leq z \leq 250 \mu\text{m}) \\ \alpha_{\text{mod}} & (250 < z \leq 300 \mu\text{m}) \end{cases} \quad (14)$$

where

$$\alpha_{\text{mod}} = \Gamma \cdot \alpha_1 + (1 - \Gamma) \cdot \alpha_2 + \alpha_m \cdot \sin(\omega_{\alpha} \cdot t) \quad (15)$$

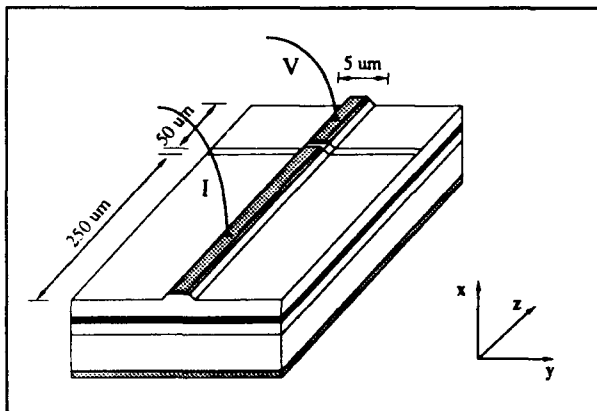


Figure 1. Schematic diagram of a Q-switched GaAs/AlGaAs MQW laser. The device consists of a 50 μm long modulator section adjacent to a 250 μm long laser section.

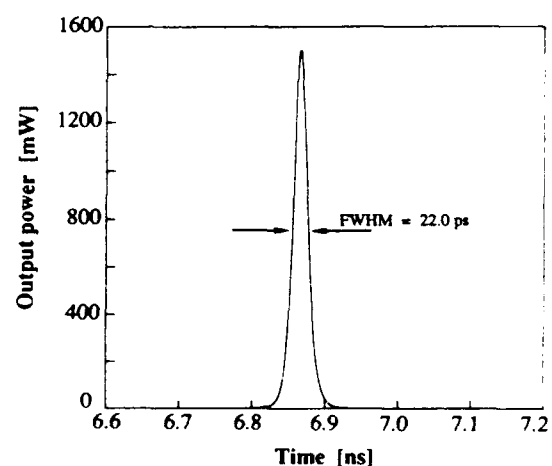


Figure 2. Calculated optical output pulse 6 ns after a dc bias current of 170 mA is applied. The modulation frequency of the absorption was 1.5 GHz.

For our calculations we have used the figures $\alpha_1 = 5000 \text{ cm}^{-1}$, $\alpha_2 = 100 \text{ cm}^{-1}$, and $\alpha_m = 3000 \text{ cm}^{-1}$ in the modulator section (i.e. z -values between $250 \mu\text{m}$ and $300 \mu\text{m}$). In the laser section ($0 < z < 250 \mu\text{m}$) the losses were taken to be $\alpha_{\text{laser}} = 100 \text{ cm}^{-1}$. For all the following numerical calculations we have used these values of the absorption profile together with the device parameters presented in Table 2.

Table 2. Parameter values used in the calculations.

L	=	300	[μm]
w	=	5	[μm]
d	=	0.1	[μm]
τ_s	=	2.0	[ns]
β	=	0.0001	
N_0	=	$1.0 \cdot 10^{24}$	[m^{-3}]
R_1	=	30	%
R_2	=	30	%
n_{eff}	=	3.5	
λ_0	=	0.85	[μm]
Γ	=	0.13	
a_m	=	$1.5 \cdot 10^{-20}$	[m^2]
b_m	=	$2.0 \cdot 10^{22}$	[m^{-3}]
α_{eff} *)	=		
Q	=	30	
M	=	2	

*) Value changed in the calculations.

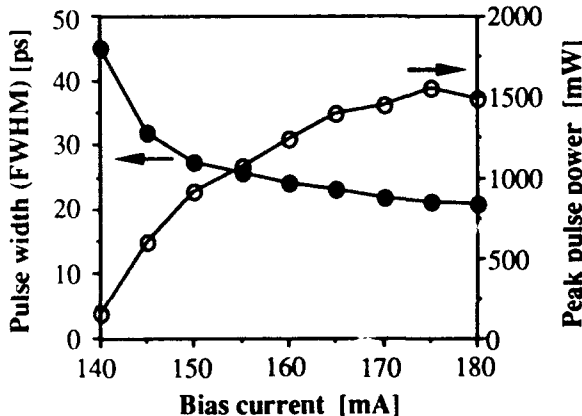


Figure 3. Pulse width as a function of the dc bias current applied in the laser section. The modulation frequency of the absorption in the modulator section was set to 1.5 GHz.

With $\alpha_m = 0$ the threshold current was estimated to $120 - 130 \text{ mA}$, which should be compared with the value $I_{\text{th}} = 115 \text{ mA}$, measured by Arakawa et al. [10].

Applying a dc bias current in the laser section at time $t = 0$, together with a modulation of the absorption profile, as described above in Eqs. (14) and (15), produced distinct Q-switched optical output pulses. For an input bias current of $I = 170 \text{ mA}$ and a modulation frequency of 1.5 GHz optical pulses of $\Delta\tau_{1/2} = 22.0 \text{ ps}$ (FWHM) was observed after the system had stabilized, Fig. 2. The calculated value of the pulse width is in good agreement with the 18.6 ps measured by Arakawa et al. [10], using second harmonic generation (SHG). Maintaining the modulation of the absorption in the modulator section at a constant frequency of 1.5 GHz and varying the dc bias current in the laser section resulted in the dependence of both the pulse width and the peak power of the optical output pulses, shown in Fig. 3.

Arakawa et al. also reported the measured pulse widths to be nearly independent of the modulation frequency. In the range 500 MHz to 3.2 GHz pulse widths from 19 ps to 22 ps were measured at a bias current of $I = 150 \text{ mA}$. In our calculations we have obtained pulse widths between 20 and 23 ps for modulation frequencies from 1.0 to 3.0 GHz at a bias current of 165 mA (Fig. 4). In Fig. 4 we show both the variation of the calculated pulse widths as well as the peak pulse power as a function of the modulation frequency of the absorption. The results shown in Fig. 3 and 4 are plotted approximately 6 ns after the bias current is applied.

In Fig. 5 on the next page we show a three-dimensional view of the calculated electron density (Fig. 5a) and photon density (Fig. 5b) for an actively Q-switched laser biased with $I = 165 \text{ mA}$ and with a modulation frequency of 1.5 GHz. It can be seen that the abrupt change in the absorption inside the cavity (at $z = 250 \mu\text{m}$) results in a dramatic change in the electron and photon density.

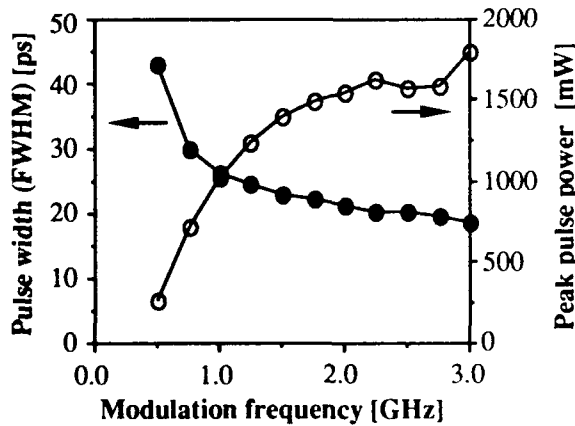


Figure 4. Pulse width as a function of the modulation frequency at a bias current in the laser section of $I = 165 \text{ mA}$. Parameters used for the calculations are given in Table 2.

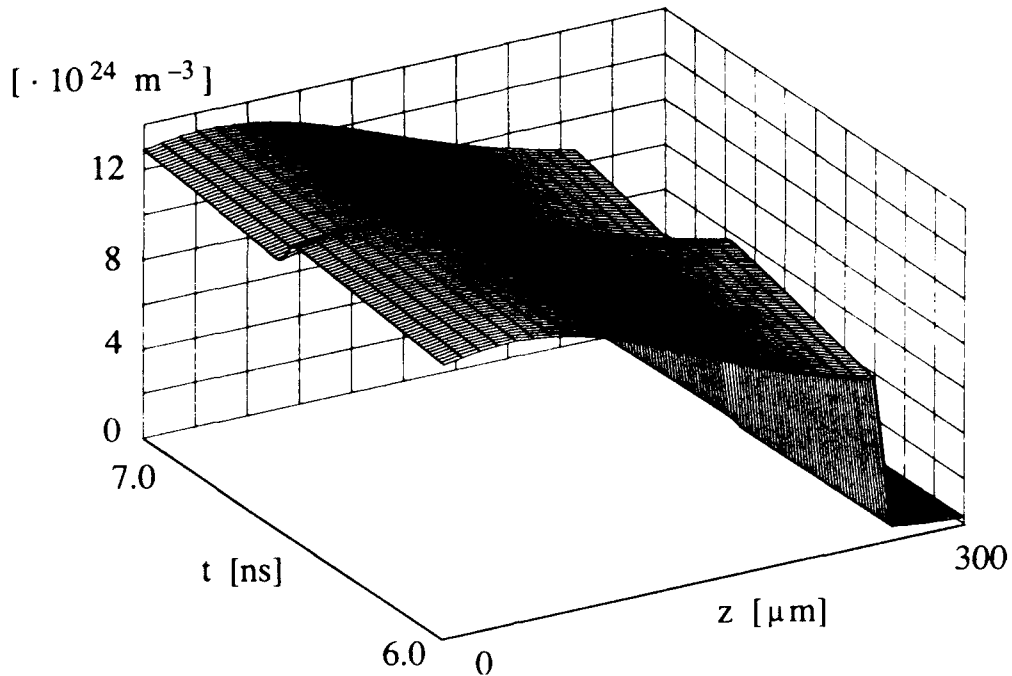


Figure 5a. A three dimensional view of the electron density as a function of time t and longitudinal coordinate z . For this calculation the device was biased with a dc current $I = 165 \text{ mA}$ in the laser section ($0 < z < 250 \mu\text{m}$) and the absorption was modulated with a frequency of 1.5 GHz in the modulator section ($250 \mu\text{m} < z < 300 \mu\text{m}$).

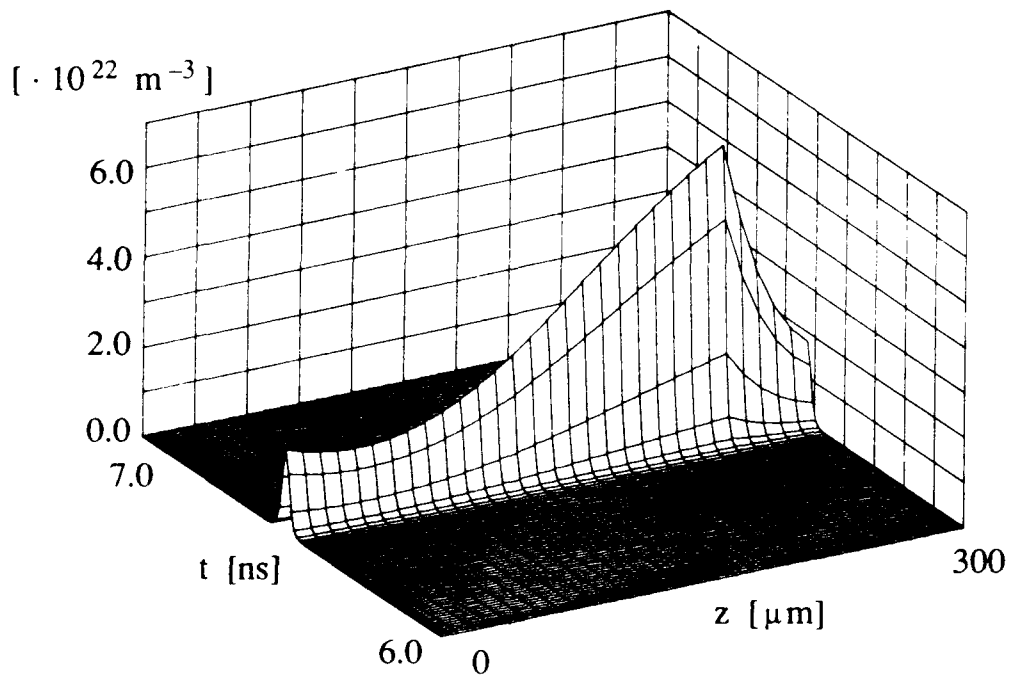


Figure 5b. A three dimensional view of the photon density in the Q-switched laser. Parameters used for the calculations are the same as in Fig. 5a.

Conclusions

We have presented a computer model based on the multimode travelling-wave rate-equations. The model has been used to simulate the dynamic behavior of an actively Q-switched semiconductor laser and we have found good agreement between our calculations and experimental results. While most computer models are especially designed for some specific type of problem, the key feature of our model is its ability to simulate longitudinally nonuniform semiconductor structures over a wide span of applications. Furthermore, our model can easily be implemented on a small PC-type computer, even though the theory incorporates advanced topics such as explicit multimode behavior and longitudinal variations of the injected current and absorption profile. An extension of the model, to incorporate, for example, nonlinear terms in the recombination rate and a longitudinal dependence of the refractive index, is straightforward and does not entail numerical difficulties. Hence, we believe that the relatively simple travelling-wave rate-equations can be a valuable tool for scientists working in the field of optoelectronics, and especially those who are interested in simulating ultrafast pulse generation in optoelectronic devices.

Acknowledgments

This work was sponsored by the National Swedish Board for Technical Development (STU).

References

1. G. Arnold, P. Russer, and K. Petermann, "Modulation of laser diodes," in Semiconductor devices for optical communication, pp 213 – 242, H. Kressel, ed. (Springer-Verlag, New York, 1980).
2. M. J. Adams, J. V. Collins, and I. D. Henning, "Analysis of semiconductor laser optical amplifiers," IEE Proc. Pt. J 132, 58 – 63 (1985).
3. H. S. Sommers, "Threshold and oscillation of injection lasers: A critical review of laser theory," Solid-State Electron. 25, 25 – 44 (1982).
4. J. Buus, "Principles of semiconductor laser modelling," IEE Proc. Pt. J 132, 42 – 51 (1985).
5. T. Ohtoshi, K. Yamaguchi, C. Nagaoka, T. Uda, Y. Murayama, and N. Chinone, "A two-dimensional device simulator of semiconductor lasers," Solid-State Electron. 30, 627 – 638 (1987).
6. T. K. Yee and D. Welford, "A multimode rate-equation analysis for semiconductor lasers applied to the direct intensity modulation of individual longitudinal modes," IEEE J. Quantum Electron. QE-22, 2116 – 2122 (1986).
7. K. A. Shore, "Model for semiconductor laser structures incorporating longitudinal and transverse variations," IEE Proc. Pt. J 132, 52 – 57 (1985).
8. Y. L. Wong and J. E. Carroll, "A travelling-wave rate equation analysis for semiconductor lasers," Solid-State Electron. 30, 13 – 19 (1987).
9. R. J. S. Pedersen, U. Gliese, B. Broberg, and S. Nilsson, "Characterization of a 1.5 μm three-electrode DFB laser," in Proceedings from the 16th European Conference on Optical Communication, ECOC-90, Amsterdam, Sept. 16 – 20, 1990, Vol. 1, pp. 279 – 282.
10. Y. Arakawa, A. Larsson, J. Paslaski, and A. Yariv, "Active Q switching in a GaAs/AlGaAs multiquantum well laser with an intracavity monolithic loss modulator," Appl. Phys. Lett. 48, 561 – 563 (1986).
11. M. Hagberg, A. Larsson, and S. T. Eng, "Single-ended output GaAs/AlGaAs single quantum well laser with a dry-etched corner reflector," Appl. Phys. Lett. 56, 1934 – 1936 (1990).
12. B. Jonsson and S. T. Eng, "A Travelling-wave rate-equation model for semiconductor lasers," Technical Report No. 90240, Dept. of Optoelectronics and Electrical Measurements, Chalmers University of Technology, 1990.
13. K. Y. Lau and A. Yariv, "High-frequency current modulation of semiconductor injection lasers," in Semiconductors and Semimetals, W. T. Tsang, ed. (Academic Press, 1985), Vol. 22, Part B.

Injection Seeding of a Gain-Switched Semiconductor Laser with a Mode-Locked Master Oscillator

E. A. Chauchard, L. G. Joneckis, J. S. Wey, and Chi H. Lee

University of Maryland, College Park, Maryland 20742

G. Burdge

*Laboratory for Physical Sciences, 4928 College Avenue,
College Park, Maryland 20740*

Abstract

Pulsed injection seeding, where the master laser is mode-locked and the slave laser gain switched, presents several advantages over CW injection seeding and yields stable, higher power, coherent, short pulses.

Introduction

High speed logic (>10 Gbit rates) requires a synchronously distributed clock, which preserves coherence. Because of clock fanout, the clock source must generate high average power pulses. With this motivation, we have developed techniques, which use actively mode-locked semiconductor lasers. Active mode-locking of a semiconductor laser in an external cavity can generate a train of nearly transform limited short pulses (0.5-30 pS) with a narrow spectrum consisting of only one cluster of locked longitudinal modes [1,2]. However, when the DC bias current is raised well above threshold in an attempt to generate higher power, the spectrum of the emission becomes multi-mode clusters. Therefore, it is difficult to achieve high power output with desirable spectral and temporal characteristics from the laser oscillator alone. One way to achieve these goals is by injection seeding

a slave laser. In this work we report the successful demonstration of this concept. Good temporal (30 pS) and spectral control (single mode cluster) have been achieved with a power gain of up to 17 dB in a gain switched slave laser. These results indicate that coherent power combining should be possible for the generation of high average power picosecond pulses by this injection seeding and amplifying technique, when locking together a large number of the gain-switched slave lasers with a single master laser.

Recently, we demonstrated that the emission spectral width of a mode-locked slave laser high above threshold can be reduced to one cluster by injection seeding with a CW laser, while introducing only a small pulse broadening [1,2]. However, in this work we report a significantly new approach, whereby we can generate higher power, more stable pulses by mode-locking the master laser and by gain switching the slave laser (without external cavity) instead of synchronously mode-locking the slave laser. The resultant output retains the best features in the master-slave combination (spectral purity of the master and high power, short pulse duration of the slave) while eliminating the undesirable ones. In addition, we compare pulsed injection seeding to the previously reported CW injection seeding [1,2] by using a mode-locked master laser

close to threshold. It was found that pulsed injection seeding has two advantages over CW seeding. First, the stability of the system is greatly improved with a pulsed master laser. Second, a lower injected average optical power is needed to obtain the same level of sidemode suppression and the same pulse duration as in the CW case. Pulsed injection did not result in a broader spectrum than CW injection. With this technique, short pulses (less than 40 pS) can be generated even when the slave laser is operated high above threshold, emitting higher power.

Experimental setup

The master and slave lasers were a pair of wavelength-matched Hitachi HLP 1400 lasers emitting close to 830 nm. The master laser was mounted in a 7 cm long external cavity, and both lasers were driven by a dc bias current and a sinusoidal modulation at a frequency around 1.9 GHz (Fig. 1). The master laser was isolated from the slave laser by a Faraday isolator, and its emission was injected into the slave laser by a 50% reflection beam splitter. The output

average power of the gain switched slave laser was 2 to 7 mW. The output was characterized with a monochromator and a Hamamatsu optical sampling oscilloscope (OOS-1) with a rise time of 10 pS. The coherence of the output was measured by a Mach-Zehnder interferometer where one pulse interfered with the second successive pulse. The interference fringes were recorded by a BeamScan (Photon, Inc.), which scans the spatial profile of the beam with a rotating slit.

Optimization of the injection was obtained by careful alignment of the master laser beam into the slave laser, by adjustment of the microwave modulation timing using the phase shifter, and by temperature tuning the slave laser to match the master's wavelength.

Results and discussion

A typical result of pulsed injection seeding is shown on Fig. 2. The gain switched slave laser was emitting short pulses (32 pS FWHM measured) and a broad spectrum of many clusters (Fig. 2, middle). After injection by the master laser with narrow spectrum (Fig. 2, top), the output spectrum of the slave laser contains only one cluster, the frequency side mode suppression ratio is better than 22 dB, and the pulse duration has increased only slightly to about 37 pS (Fig. 2, bottom). The same results could be achieved with CW injection only if the injected power was doubled. Moreover, the pulsed injection scheme produces a much more stable output. The recorded interference fringe pattern demonstrates the coherence of the injected slave output. The output power was 6.1 mW while the injected power was 0.4 mW, resulting in a "gain" of 15. When the injected power was lowered to 0.13 mW--increasing the "gain" to 46--the side mode suppression ratio decreased to 17 dB. It should be noted that the set-up could be improved by injecting the master laser light through the back facet of the slave. If the power were raised above 8 mW by raising the DC current to the slave

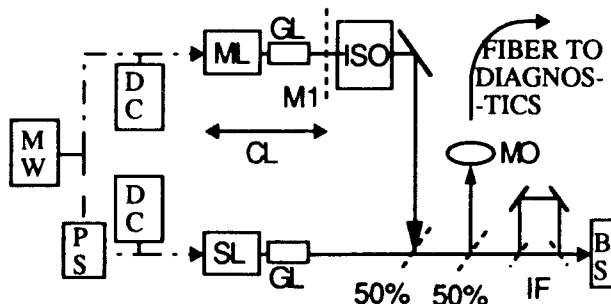


Fig. 1: Experimental setup. MW: microwave synthesizer; DC: dc bias current; PS: phase shifter; ML, SL: master and slave lasers (Hitachi HLP 1400); GL: GRIN lens; M1: mirror (50%); CL: cavity length (7 cm); ISO: optical isolator; MO: microscope objective; IF: Mach-Zehnder interferometer; BS: Beam Scan (Photon Inc.).

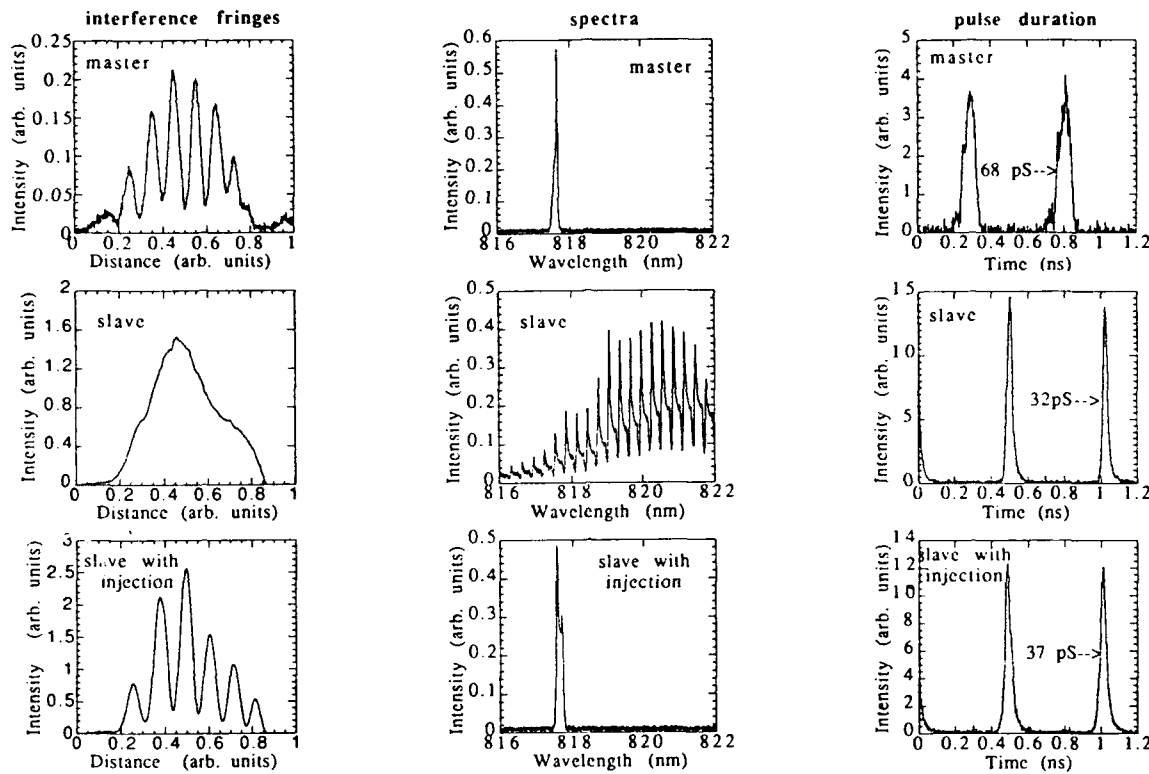


Fig. 2: Example of pulsed injection seeding result: interference fringes (first column), spectra (second column) and temporal pulse shapes (third column). Top: master laser alone, center: slave laser alone, bottom: slave laser with injection.

laser, a shoulder appeared in the temporal pulse shape of the output, due to the formation of a second pulse. This phenomena limits the output power attainable with this type of lasers.

The word "gain" was left in quotes to stress the fact that this injection seeding technique differs from a simple amplification approach, as explained in the following two arguments. First, the slave laser is lasing high above threshold when the injection is performed. Second, with this technique, the pulses from the master laser are not only amplified in the slave laser but also shortened in duration. The output spectrum is also wider than the master laser spectrum alone.

The large chirp of the output light may be used in a pulse compression scheme to shorten the output pulse duration. If this is successful, this source would be suitable for electro-optic sampling of ultrafast circuits.

All of our experimental results were obtained with simple, inexpensive commercial lasers. However, the technique

should be applicable to many other types of lasers, commercial or experimental, for instance, with a larger power output capability.

Because only a small amount of master laser power is required for one slave laser, it should be possible to lock together a large number of slave lasers with one master laser. This will be an effective coherent power combining scheme to obtain stable, high power, coherent, short pulses.

References

1. L. G. Joneckis, PhD Thesis "Dynamics of mode-locked AlGaAs semiconductor lasers.", University of Maryland, 1990. Submitted for publication.
2. L. G. Joneckis, P. T. Ho and G. Burdge, "High power and injection-seeded mode-locking of semiconductor lasers", Conference on Lasers and Electro-optics, May 21-25, 1990, Anaheim, CA.

Tunneling

Electron Transport in Double-Barrier Diodes Studied by Differential Absorption Spectroscopy

T. K. Woodward,^{*} D. S. Chemla,[†] I. Bar-Joseph,[‡] D. L. Sivco,^{**} and A. Y. Cho^{**}

^{*}AT&T Bell Laboratories, Holmdel, New Jersey 07733

[†]University of California, Lawrence Berkeley Laboratories, Berkeley, California 94720

[‡]Physics Department, Weizmann Institute of Science, Rehovot 76100, Israel

^{**}AT&T Bell Laboratories, Murray Hill, New Jersey 07974

1 Abstract

Charge transport in several double barrier diodes has been studied with optical transmission-based methods. The quantum-well stored charge is quantified, and accumulation and depletion regions are observed. Evidence for both inter- and intra-subband scattering is found.

2 Introduction

Double-barrier tunneling heterostructures are part of an emerging class of devices that rely on quantum-mechanical effects for their operation. A deeper understanding of these devices is possible when diagnostic methods that augment electrical measurements are employed. In our project, we have used differential absorption spectroscopy (DAS) to investigate the operation of the resonant-tunneling double-barrier diode (DBD).

This technique, whose experimental realization is detailed in Fig. 1, relies on measurements of normalized changes in optical transmission, $\Delta T/T = [T(V) - T(V_0)]/T(V_0)$ where $T(x)$ is the transmission at voltage x , arising from electrical modulation imposed upon the device.^[1,2] For small signals $\Delta T/T \simeq -l\Delta\alpha$, where $\Delta\alpha = \alpha(V) - \alpha(V_0)$ is the change in absorption and l is the length over which the change occurs. Lock-in signal extraction allows the observation of $\Delta T/T$ signals as small as $\sim 10^{-4}$, permitting observation of events on length

scales $\sim 10\text{\AA}$ with low probe intensities (we use an incandescent lamp). DBD depletion and accumulation regions can be seen, as can signals originating in the QW. This signal can be calibrated to obtain the QW stored charge Q . These methods have previously been applied to modulation-doped field-effect transistors.^[2]

Other workers have studied the charge accumulation in a DBD using photoluminescence,^[3] excitation spectroscopy in conjunction with photoluminescence,^[4] as well as methods involving magnetic fields.^[5] Since we can use low light intensities and rely on optical absorption—a technique allowing *absolute calibration*—we believe DAS to be both a significantly more accurate^[3], and a much

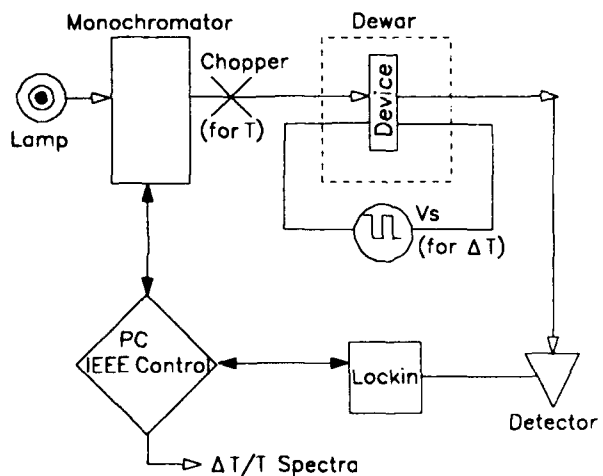


Fig. 1 Schematic Experimental geometry.

less invasive method of determining Q . In addition, we can determine the energy distribution of the electrons stored inside the QW, without the confusion caused by creating large numbers of highly excited electron-hole pairs in the measurement process.

All samples were grown by molecular beam epitaxy on conducting InP substrate and show profound negative differential resistance (NDR). Electrode doping in single resonance samples was $5 \times 10^{17} \text{ cm}^{-3}$, and the QW thickness was 45 \AA . Barrier thickness varied between 55 and 95 \AA , with intended geometries indicated in the legend of Fig. 4. [1] The barrier material is $\text{In}_{0.52}\text{Al}_{0.48}\text{As}$, with QW and electrodes being $\text{In}_{0.53}\text{Ga}_{0.47}\text{As}$. Measurements were performed on $150 \mu\text{m}^2$ mesas at 10K .

3 Results

Representative 10 K DAS data are shown in Fig. 2. The three $\Delta T/T = [T(V) - T(0)]/T(0)$ spectra were obtained for modulation between zero and points indicated on the I - V curve: low voltage prior to the onset of tunneling (smallest curve), at the peak of the NDR, and at the valley of the NDR (dotted curve). The major features of the data are a negative going signal peaked at $\sim 0.83 \text{ eV}$ due to the formation of a depletion layer, a positive feature at $\sim 0.9 \text{ eV}$ due to the formation of an accumulation region, and a set of signals near 1 eV coming from the QW. In the accumulation layer, increases in carrier density relative to zero bias increase the number of occupied states at $E > E_g + E_f$ (E_g is the bandgap and E_f is the zero bias Fermi energy), preventing absorption from taking place and making the sample slightly more transparent in this energy range. This causes a positive $\Delta T/T$ signal. Similarly, depletion of carriers from beyond the collector barrier enhances absorption for $E_g < E < E_g + E_f$ and causes a negative peak.

QW signals have two distinct lineshapes, which is helpful in identifying device activity. Differential (two-signed) signals are due to field induced shifts of the exciton resonance, and arise from the quantum confined stark effect. These signals are indicative of a mainly empty QW. As electrons populate the QW, the dominant effect becomes a bleaching of the excitonic absorption via the Pauli exclusion principle, and a strictly positive spectral feature results. Thus, we can see the filling and emptying of the QW during transport. At low voltages, prior to the onset of tunneling, the QW signal is small and differential, consistent with the empty state of the QW resonance. At the peak of the NDR, the signal is strong and positive, indicating charge ac-

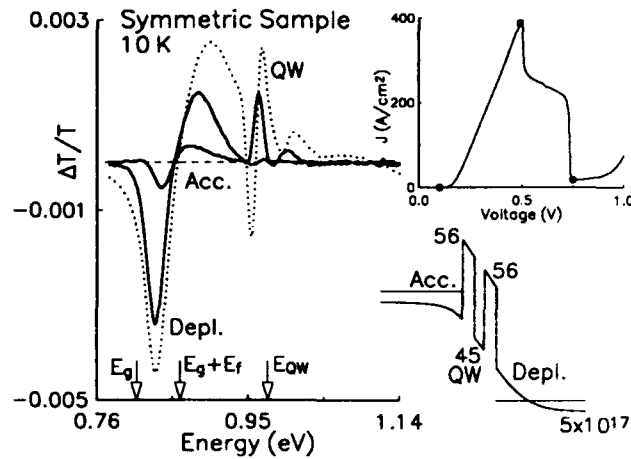


Fig. 2 Representative DAS data, band diagram, and I - V curve, with modulation voltages indicated.

cumulation. At the valley of the NDR, the signal becomes abruptly differential in nature, consistent with a mostly empty QW.

Focusing on the QW signals in more detail, Fig. 3 presents I - V curves along with the QW signals obtained from two samples. Modulation was between zero and various voltages ranging between the onset of tunneling and the peak of the NDR. $\Delta T/T$ signal strength steadily increases with bias. These spectra provide information about the accumulation of charge in the QW. In Fig. 3(a), spectra for the structure having barrier/well/barrier dimensions of $55/45/80 \text{ \AA}$ are presented, for the bias direction in which the emitter barrier (denoted by l with transmission T_l) is 55 \AA thick. In Fig. 3(b), we present similar data for a corresponding symmetric sample, having a $56/45/56 \text{ \AA}$ geometry. The peak current densities for both samples are similar. However, the $\Delta T/T$ signals from the asymmetric sample are much larger than those from the comparable symmetric sample. This is due to enhanced charge accumulation in the QW of the asymmetric sample, and can be attributed directly to changes in transmission of the collector barrier (denoted by r and T_r). The absorption bleaching in the asymmetric sample is approximately equal to the total exciton absorption strength, as measured on a 45 \AA multiple quantum well (MQW) calibration sample, while the signals in Fig. 3(b) are less than 17 percent of this value. This, coupled with the increasing asymmetry of the DAS lineshape-indicative of the onset of continuum band filling-tell us that the exciton has been completely bleached in the asymmetric sample. Conversely, when biased such that the emitter barrier is 80 \AA thick, QW charge accumulation is not observable.

Bleaching signals obtained for current densities ranging from the onset of tunneling to the peak of the NDR can be calibrated to obtain the QW stored charge to an accuracy of better than 50 percent. Calibration is achieved by knowing the amount of exciton bleaching induced by a known population of electrons. We get this information from measurements of a 50 period MQW sample having 45 Å $\text{In}_{0.53}\text{Ga}_{0.47}\text{As}$ wells and 70 Å $\text{In}_{0.52}\text{Al}_{0.48}\text{As}$ barriers. In this sample we can measure the absolute exciton absorption strength, binding energy, and saturation density. Knowing the absolute absorption strength of the QW, coupled with its saturation behavior, provides a 'ruler' against which the absorption bleaching in our DBD samples can be compared. We can thus obtain a calibrated measure of the stored QW charge. It should be emphasized that DAS is unique among techniques used to measure Q in providing such an absolute external calibration. Specifically, we use relations between carrier population and absorption bleaching to allow us to obtain the QW stored charge.[1,2,6,7] The most basic of these relationships, valid in the small signal regime, is $\Delta\alpha/\alpha = -N/N_s^e$, where $\Delta\alpha$ is obtained from $\Delta T/T$ data, α is the unperturbed exciton absorption (obtained from the calibration sample and taken here to be 20000 cm^{-1} and N_s^e is the exciton saturation density for electrons.[8] In Fig. 4 we summarize the results of these studies with tabulation of Q and Q/J as a function of J for various samples.

Analysis of QW charge density in the asymmetric sample presents a special problem, because of the large exciton bleaching involved. For low levels of bleaching, we can use $\Delta\alpha/\alpha = -N/N_s^e$ to find N . In the large signal regime, we take advantage of the lineshape of the DAS, which tells us that we have just reached the point of complete exciton bleaching. This will occur when all the states that contribute to the exciton wavefunction are occupied. In energy space, this corresponds to $0 < E \leq E_b$, where E_b is the exciton binding energy. From the absorption spectra of the same 50 period MQW on which N_s^e was measured, we find $E_b = 9.5 \text{ meV}$, and thus a density of $1.63 \times 10^{11} \text{ cm}^{-2}$ for complete exciton bleaching. We thus have confidence in our charge density values at low and high levels of exciton bleaching, and linearly interpolate between them to obtain the data for the asymmetric sample shown in Fig. 4.

4 Interpretation

Observe that the NDR peak bleaching signal in Fig. 3(b) is that of a carrier population localized near

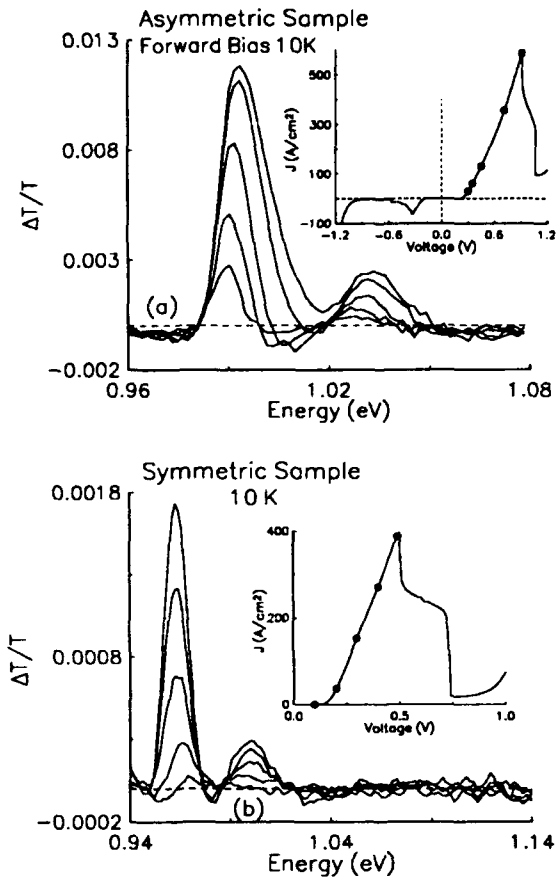


Fig. 3 QW DAS signals and I - V curves for (a) a 55/45/80 Å geometry asymmetric sample, biased so that the emitter barrier is 55 Å, and (b) a 56/45/56 Å symmetric barrier sample. The greatly increased bleaching signal in the asymmetric sample corresponds to increased QW charge accumulation as compared to the symmetric sample.

the bottom of the band, in that no evidence of absorption bleaching is observed at higher energies. If carriers were present at higher energies, continuum absorption bleaching would result in positive DAS signals at higher energies. The sensitivity level to such bleaching is estimated to be $5 \times 10^8 \text{ cm}^{-2}$ in a 2 meV bandwidth typical for these measurements.

This observation implies that parallel momentum relaxation has taken place. At the peak of the NDR, the resonance level aligns with the conduction band edge of the injecting electrode. Therefore, tunneling electrons have essentially zero momentum directed perpendicular to the barriers and a wide range of energies $E_{\parallel} = (\hbar k_{\parallel})^2/(2m)$ associated with k_{\parallel} , the momentum directed parallel to the barriers: $0 < E_{\parallel} < E_f$.[9] In our samples $E_f \geq 55 \text{ meV}$. We conclude that almost all the carriers have relaxed

via intra-subband scattering from an initial distribution of $0 < E_{\parallel} < E_f$ to one of $0 < E_{\parallel} < E_b$, where $E_b \simeq 9$ meV is the exciton binding energy in this sample. Such relaxation clearly requires *inelastic* scattering events to occur. This relaxation is observed in all our samples and demonstrates the inelastic nature of the resonant tunneling process in them. This result is not particularly surprising when the time scales over which carriers reside in the QW are considered and compared to typical (< 1 ps) phonon emission. Q/J provides such a time scale and is plotted in Fig. 4(b).

Of particular interest is the behavior of Q/J in the asymmetric sample (the open squares in Fig. 4). The strong decrease in Q/J with bias in the asymmetric sample is consistent with the theoretical form for Q/J that derives from the classical period in the well and the transmission probability T_r of the collector barrier. We find that

$$\frac{Q}{J} = \frac{2L}{vT_r} = \frac{\hbar\pi}{T_r\sqrt{E_1 E_r}}, \quad (1)$$

where E_r is the energy of the quasibound QW resonance and $E_1 = \hbar^2\pi^2/(2mL^2)$ (m is the effective mass, L is the well width, and v is the carrier velocity perpendicular to the barriers). However, it is inconsistent with the bias dependence of the coherent state lifetime $\hbar/\Delta E$, where ΔE is the full width at half maximum of the overall transmission resonance. This transmission function is very similar to that of a Fabry-Perot cavity[10]. Without scattering, we find

$$\frac{\hbar}{\Delta E} \simeq \frac{\hbar\pi}{(T_r + T_l)\sqrt{E_1 E_r}}, \quad (2)$$

and the two theoretical forms are not equal.[11]

Since bias causes T_l to *decrease* while T_r *increases*, the differences between Q/J and $\hbar/\Delta E$ are clearly illuminated via the bias dependence of Q/J in a sample in which T_l exceeds T_r . In symmetric samples placed under bias, T_r rapidly dominates T_l and Eqs. (1) and (2) become similar. In the asymmetric sample, however, the two forms predict opposite trends, with Eq. (1) indicating a strong decrease with bias while Eq. (2) shows an increase. Experimentally, we observe a decrease, confirming that Q/J and $\hbar/\Delta E$ are not equal.

It is interesting to note that while our experimental results demonstrate that inelastic scattering

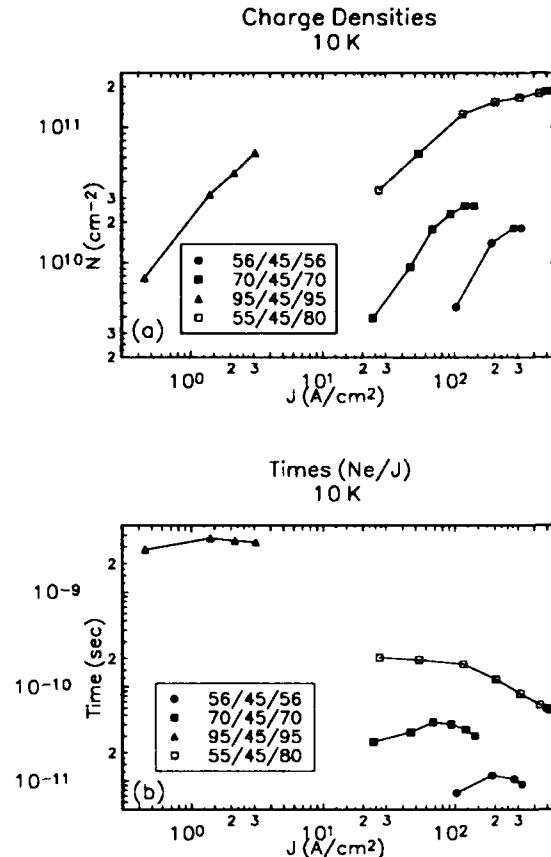


Fig. 4. (a) Q vs J for all samples, (b) Q/J vs J for all samples

does occur during the transport through our samples, simple scattering-free calculations of Q/J using Eq. (1) and transfer matrix calculations of T_r agree reasonably well (within a factor of 2) with our experimental results for Q/J ranging from 10 ps to over 2 ns. There are several possible explanations for this interesting observation. Initially, we note that parallel momentum relaxation in the QW does not affect Eq. (1), since it depends only on the velocity of carriers perpendicular to the barriers. Further, Stone and Lee[12] have argued (in one dimension) that scattering preserves the area under the transmission peak. That is, scattering tends to broaden the transmission resonance while decreasing its height such that the area under the transmission is conserved. Since the three-dimensional carrier distribution in the emitter electrode is much wider in energy than the resonance, tunneling injection occurs across the *entire* width of the resonance. Quantities such as Q and J must then be relatively insensitive to scattering, because they integrate across the transmission peak.

Corrections to this model that take into account k_{\parallel} distribution effects, such as coupling to k_{\parallel} and variation in barrier height with k_{\parallel} , have not been considered.

Fig. 4 permits several observations to be made about the accumulated charge in symmetric barrier structures. First, we observe that the largest charge accumulations in a given device occur at the peak of the NDR, where the current is maximum. This is the case because the number of carriers capable of tunneling into the resonant state steadily increases as the resonance level is brought into alignment with the emitter electrode band edge, and despite the fact that the finesse of the DBD, when viewed as a Fabry-Perot cavity, degrades with bias. The finesse (F) can be defined for a cavity with transmissions $T_l, T_r \ll 1$ as

$$F = \frac{2\pi}{T_l + T_r}. \quad (3)$$

The current through the device at the NDR peak is related to the overall maximum resonant transmission. In the absence of scattering and for $T_l, T_r \ll 1$ this is [10,13]

$$T_{max} = \frac{4T_l T_r}{(T_l + T_r)^2}. \quad (4)$$

From this and Eq. (1) it follows that Q depends not just on F , but also on T_l as

$$Q \propto \frac{T_l}{(T_l + T_r)^2} \propto T_l F^2, \quad (5)$$

where these equations assume carrier transport from l to r . We stress that this equation does not consider *all* the factors on which Q can depend, just the barrier transmissions. Eq. (5) shows that it is possible for an asymmetric structure to have charge accumulation exceeding that of a symmetric structure having much higher finesse, provided T_l exceeds T_r .

Finally, we note that the electric field due to the Q values we have measured is small compared to the externally applied field. At the peak of the NDR, the electric field imposed on the structure is in the $1 - 2 \times 10^5$ V/cm range, while the maximum electric field arising from the *largest* Q values is roughly 1.3×10^4 V/cm. Therefore, these levels of charge accumulation should not have a significant screening effect on the external field. Larger charge accumulations could be expected for more heavily doped electrodes, since Q depends on the number of electrons capable of tunneling at a given voltage.

5 Two-resonance samples

Evidence for inter-subband scattering can be found by studying a sample containing two confined states and having two NDR regions.[5] This sample has 70 Å barriers and a 100 Å QW and is doped in the electrodes to 1.5×10^{17} cm $^{-3}$. Biasing to voltages approaching the second NDR region injects carriers into the second QW level. In Fig. 5, we present data for the two-resonance sample, specifically the DAS signals arising from the second QW level, obtained at various modulation voltages. The I - V curve is also shown, with intersections denoting the electrical state of the device. The DAS signal from the second QW level is differential in shape at all voltages, indicating *no significant accumulation of charge in the second QW level*. This establishes the tunneling process here as being sequential in nature, in that electrons relax from the second level to the first before tunneling out of the structure. Although it can be qualitatively observed, we have not been able to quantify the resulting charge accumulation in the first resonant state, because the QW signal from this state now overlaps with that of the accumulation layer.

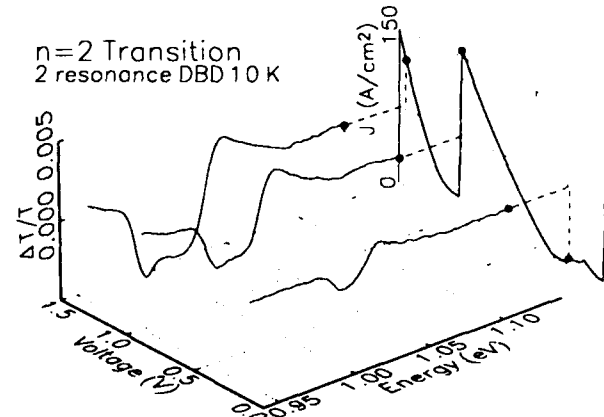


Fig. 5. DAS data for a two-resonance sample. Modulation was between zero and the points indicated on the I - V curve.

6 Conclusions

We have been able to reach several conclusions about DBD transport from our DAS studies. We can observe the formation of depletion and accumulation regions as well as the character of the QW behavior. We can quantify Q , the QW stored charge,

and through our studies obtain information about the energy distribution of tunneling carriers that presents direct evidence of both inter- and intra-subband scattering. Studies of an asymmetric sample are particularly interesting, showing enhanced charge accumulation in one bias direction, and providing experimental demonstration that Q/J is *not* equal to the coherent state lifetime $\hbar/\Delta E$. Finally, our experiments demonstrate the value of DAS as a diagnostic tool for study of quantum-well devices.

We would like to acknowledge the contributions of H. U. Baranger, H. A. Fertig, Y. Gedalyahu, D. A. B. Miller, G. Sucha, M. Wegener, S. Weiss, and A. Yacoby.

References

- [1] I. Bar-Joseph, T. K. Woodward, D. S. Chemla, D. Sivco, A. Y. Cho, *Phys. Rev. B* **41**, 3264 (1990).
- [2] D. S. Chemla, I. Bar-Joseph, J. M. Kuo, T. Y. Chang, C. Klingshirn, G. Livescu, and D. A. B. Miller, *IEEE J. Quant. Electron.* **24**, 1664 (1988).
- [3] Jeff F. Young, B. M. Wood, G. C. Aers, R. L. S. Devine, H. C. Liu, D. Landheer, B. Buchanan, A. J. SpringThorpe, P. Madeville, *Phys. Rev. Lett.* **60**, 2085 (1988). and a comment about this work, W. R. Frensley, M. A. Reed, J. H. Luscombe, *Phys. Rev. Lett.* **62**, 1207 (1989).
- [4] Hisao Yoshimura, Joel N. Schulman, Hiroyuki Sakaki, *Phys. Rev. Lett.* **64**, 2422 (1990).
- [5] M. S. Skolnick, D. G. Hayes, P. E. Simmonds, A. W. Higgs, G. W. Smith, H. J. Hutchinson, C. R. Whitehouse, L. Eaves, M. Henini, O. H. Hughes, M. L. Leadbeater, D. L. Halliday, *Phys. Rev. B* **41**, 10754, (1990).
- [6] S. Schmitt-Rink, D. S. Chemla, and D. A. B. Miller, *Phys. Rev. B* **32**, 6601 (1985).
- [7] S. Schmitt-Rink, C. Ell, *Jnl. of Luminescence* **30**, 585 (1985) and H. Haug, S. Schmitt-Rink, *Progress in Quantum Mechanics* **9**, 3 (1984).
- [8] Measurements of the saturation density in the calibration multiple QW sample yield N_s^{eh} , the saturation density for electron hole pairs. For $N < 2 \times 10^{11} \text{ cm}^{-2}$ we find $N_s^e = 1.6N_s^{eh} = 1.16 \times 10^{11} \text{ cm}^{-2}$. This differs from that published previously in [1] of $2.7 \times 10^{11} \text{ cm}^{-2}$. Charge densities appearing there should be *reduced* by the ratio of 1.16/2.7 to reflect this new information.
- [9] Serge Luryi, *Appl. Phys. Lett.* **47**, 490 (1985).
- [10] M. Buttiker, *IBM Jnl. Res. and Develop.* **32**, 63 (1988).
- [11] L. Gu, B. Y. Gu, *Solid State Communications* **72**, 1215 (1989).
- [12] A. D. Stone, P. A. Lee, *Phys. Rev. Lett.* **54**, 1196 (1985).
- [13] R. Ricco and M. Ya. Azbel, *Phys. Rev. B* **29**, 1970 (1984). and P. J. Price, *Phys. Rev. B* **36**, 1314 (1987). and E. E. Mendez, in *NATO ASI Series, Series B: Physics, Vol 170*, E. E. Mendez and K. von Klitzing, editors, Plenum Press, NY pp. 159-188 (1987).

Coherent Oscillations of a Wave Packet in a Semiconductor Double Quantum-Well Structure

Karl Leo,^(a) Jagdeep Shah, Ernst O. Göbel,^(b) and T. C. Damen

AT&T Bell Laboratories, Room 4D-417, Holmdel, New Jersey 07733

Stefan Schmitt-Rink and Wilfried Schäfer^(c)

AT&T Bell Laboratories, Murray Hill, New Jersey 07974

Klaus Köhler

Fraunhofer-IAF, D-7800 Freiburg, Federal Republic of Germany

Abstract

We present the first observation of the spatial dynamics of a wavepacket in a solid. Using an ultrashort laser pulse, we create an excitonic wavepacket in one well of an asymmetric double quantum well structure. The oscillation of this wavepacket from one well to another and back is traced by time-resolved pump-probe spectroscopy as well as time-resolved degenerate four-wave-mixing. We present results for two GaAs/AlGaAs double quantum wells with oscillation periods of about 1.3ps and 800fs, respectively. The experimental observations are compared with a theory that shows that the two experimental techniques give complementary information about the relaxation dynamics of the coupled system. The analysis of the experiment explains the strong damping of the oscillations by the fast thermalization between the delocalized states.

Introduction

Coupled double well systems are important in many different areas of physics. The theoretical aspects of such systems in the presence of dissipation have been studied in detail and were recently reviewed by Leggett et al. [1]. Advances in the fabrication of ultrathin layered semiconductor heterostructures in the last two decades made it possible to design quantum well structures with high crystal quality artificially. The anticrossing of the electronic levels in a semiconductor double well structure was first observed by Dingle et al. [2]. One advantage of coupled wells that are realized in semiconductor heterostructures is the possibility of tuning the relative energy of the various levels by

embedding the heterostructures in the intrinsic region of a p-i-n-diode. The anticrossing of the levels in coupled well structures due to application of an electric field has been reported in several publications (see, for example, [3-5]).

Another interesting feature of semiconductor heterostructures is the possibility of observing tunneling transport through the barrier layers. Double barrier structures (DBS) [6] have shown promising properties as microwave generators with operating frequencies up to several hundred Ghz [7]. Such structures also have been investigated with optical techniques [8-11]. Recent investigations with time-resolved optical techniques have been concentrated on asymmetric double barrier structures (a-DQW). The main advantage of an asymmetric structure is the ability to discriminate transitions in the two wells by their spectral position. Resonant tunneling of electrons [12-14] and holes [15-17] have been observed in a-DQW's in several experiments. However, already the first experiments [12] have shown that the tunneling times observed in such experiments are considerably longer than expected for a coherent tunneling process. It was recently shown [15] that a unified picture of tunneling and relaxation can qualitatively explain the observation of longer tunneling times. It turns out that the tunneling time in the limit of strong scattering and relaxation (i.e., the scattering and relaxation are faster than the coherent tunneling time) becomes inversely proportional to the relaxation time. Results of hole tunneling [15] were in close agreement with theoretical expectations. Additionally, extrinsic effects like sample imperfections might play a role, as discussed recently [14].

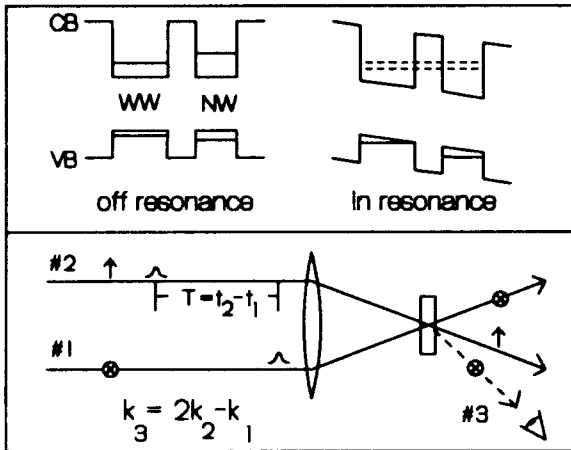


Figure 1: Upper part: asymmetric double quantum well out of (left) and in (right) resonance. Bottom: Schematical set-up of the pump-probe and four-wave-mixing experiment.

Figure 1 shows a schematic picture of an asymmetric double quantum well structure. The wide well (WW) and narrow well (NW) consist in our case of GaAs, the barrier between the wells and the cladding layers of $\text{Al}_x\text{Ga}_{1-x}\text{As}$ with a larger bandgap. The electronic levels of the wide and the narrow well are localized in the wells when no electric field is applied (left side). Application of a reversed bias (right side) causes a resonance and a subsequent delocalization of the wavefunctions. (Note that the hole levels are out of

resonance). The upper part of Fig.2 shows the wavefunction of the lower delocalized level ($\psi_{\text{symmetric}}$) and of the upper delocalized level ($\psi_{\text{antisymmetric}}$). Resonant excitation of, e.g., the WW with a short laser pulse (vertical arrow) with a bandwidth covering the two delocalized levels will create a wavepacket in the WW consisting of a linear superposition of the two wavefunctions [18,19]. This wavepacket will then oscillate between the wells (as schematically shown in the lower part of Fig.2) with a time period T_{osc} given by

$$T_{\text{osc}} = \frac{\hbar}{\Delta E} \quad (1)$$

where ΔE is the splitting between the delocalized states. Such oscillations are a pure quantum-mechanical process without classical analog [1]. Half the oscillation time can be considered as the tunneling time of an ideal coherent tunneling process. The idealized picture as given in Fig.2 is modified in a real system due to collisions and relaxation, which will lead to a damping of the oscillation. Wavepacket oscillations have recently been observed in atoms [20], which offer favorable conditions for coherent experiments due to the long dephasing times involved. However, these systems are much more complicated than the simple double well system discussed here, and they are not tunable.

We report here the first observation of coherent wavepacket oscillations in a solid [21]. The oscillations are traced in the time domain by pump-and-probe (PP) as well as degenerate four-wave mixing (DFWM) spectroscopy. The oscillation time constants agree with the coherent tunneling model (Eq.1). By varying the alignment of the levels, the properties of the wavepacket and its dynamics can be strongly influenced. We develop a theoretical model based on the optical Bloch equations of a three-level system. The theoretical results are in qualitative agreement with the experiment. They show that pump-probe and four-wave-mixing experiments give complementary information about the relaxation dynamics of the system.

Experimental Results

We present results for two sample structures: Both structures contain ten periods of an a-DQW system and were grown by molecular beam epitaxy. Sample A consists of a 170 Å GaAs wide well, followed by a 17 Å $\text{Al}_{0.35}\text{Ga}_{0.65}\text{As}$ barrier, and a 120 Å GaAs narrow well; Sample B of a 150 Å GaAs wide well, followed by a 25 Å $\text{Al}_{0.20}\text{Ga}_{0.80}\text{As}$ barrier, and a 120 Å GaAs narrow well (all parameters given are nominal values; optical characterization indicates that the values are precise

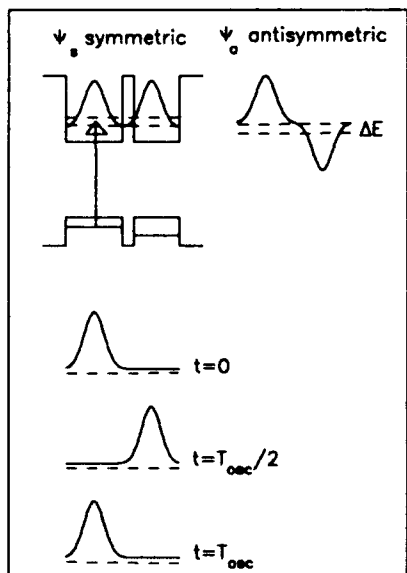


Figure 2: Upper part: coupled wells with symmetric (left) and antisymmetric (right) delocalized state. Bottom: oscillation of a wavepacket created by a superposition of the delocalized states.

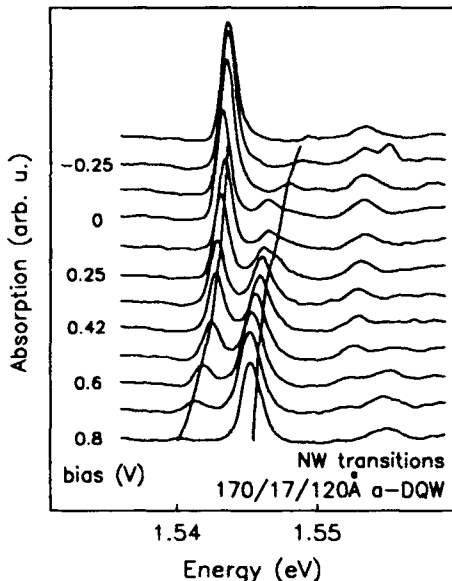


Figure 3: Absorption spectra of sample A, taken in the vicinity of the NW heavy-hole transition.

within 10%). Figure 3 shows as an example absorption spectra of sample A in the vicinity of the first heavy-hole (hh) and light-hole (lh) transition of the NW, taken at low density with a cw laser. For low electric field (+0.8V), the spectrum shows the first hh and lh exciton transitions of the NW. As the field is increased, a new peak appears below the hh exciton peak (+0.6V). This peak gains strength and the original hh exciton peak

loses strength until both have about equal intensity at resonance (+0.3V). The splitting between the peaks is about 3meV. With further increase in field, the upper energy peak rapidly moves to higher energy and loses strength, while the lower energy peak moves slowly and acquires the strength of the original hh exciton peak. The spectra reflect the eigenstate probability distribution in the wells: At electronic resonance, both states are delocalized and have nearly equal probability in both wells; out of resonance, the delocalization gradually disappears, and only the transitions within a well are important. The observation of the anticrossing in both hh and lh transition clearly shows that the anticrossing is taking place between electron states, not between hole states. Figure 4 shows corresponding spectra of the first hh and lh transition of the WW: The anticrossing of the electronic levels is similarly observed as in the NW transition shown in Fig.3. Note that the resonance of the electronic levels is obtained at higher fields in the WW transition than in the NW transition: This effect is caused by the different binding energies of direct and indirect excitons and has been experimentally observed before [22,23]. It is very pronounced in our case due to the similar width of both wells. The observation of the different fields for the resonances is also a reminder that one has to deal with *excitonic* rather than *electronic* wavepackets. Absorption spectra of sample B (not shown) show similar anticrossings with a larger splitting of about 5meV.

Up to now, most studies of tunneling in DQW have used time-resolved luminescence to trace the dynamics of the carriers. All those experiments were performed with excitation high up in the bands, e.g., the carriers first have to relax to the bandgap. In an earlier

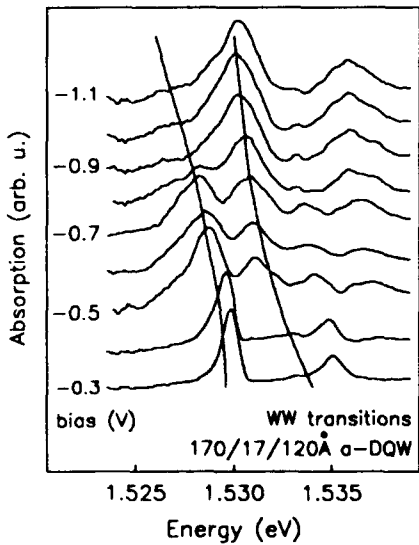


Figure 4: Absorption spectra of sample A, taken in the vicinity of the WW heavy-hole transition. Note that the electronic resonance is at higher voltage, compared to the NW (Fig.3).

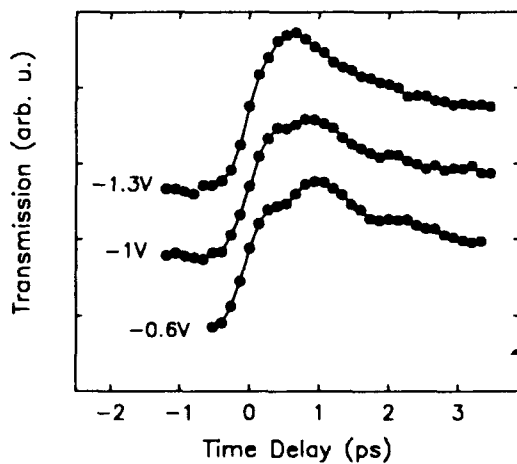


Figure 5: Pump-probe signal for sample A, with excitation of the WW. The electronic resonance is at about -0.6V.

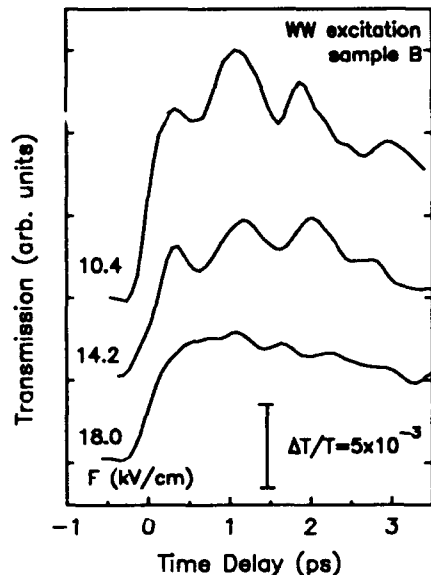


Figure 6: Pump-probe signals for sample B. The electronic resonance is at about 11kV/cm.

publication [24], we have already shown that experimental techniques using resonant creation are better suited to study *coherent* tunneling transport. In the present study, we trace the oscillation of the wavepacket in a pump-probe (PP) experiment as well as in FWM. The lower part of Fig.1 shows a schematic drawing of both experiments: In the case of PP, the "pump" pulse (direction k_1) with a duration of about 50fs creates the wavepacket; the sample transmission is probed with a weak "probe" pulse (k_2) as a function of delay time T . Figure 5 shows the change in transmitted probe intensity versus delay time. The excitation is chosen resonantly to the WW transition, thereby creating an excitonic wavepacket in this well. Temperature (about 5K) and density (about $5 \times 10^8 \text{ cm}^{-2}$) are kept low to avoid fast dephasing of the transition due to carrier-phonon or carrier-carrier scattering. The trace for a bias of -1.3V represents the case of nonresonant conduction electron levels: The signal has a step-like onset due to the bleaching of the absorption by the carriers and decays subsequently. The trace for electronic resonance of the wells (-0.6V) clearly shows an oscillatory modulation, with a period of about 1.3 ps. The oscillation period agrees reasonably with that expected from the measured splitting $\Delta E \approx 3 \text{ meV}$ in the linear absorption spectrum at resonance (Figs. 3 and 4). In this sample, we observe only one pronounced peak and a weak second oscillation. If the conduction electron levels are detuned (-1V), the modulation becomes weaker and the period shorter, as expected due to the increased splitting between the levels and an increased localization of the wavefunctions. The spatial oscillation of the wavepacket

can also be described as quantum beats of the delocalized levels. The data shown here are the first observation of absorption quantum beats in a solid [21].

Figure 6 shows the results of a pump-probe experiment in sample B with larger splitting ($\Delta E \approx 5 \text{ meV}$). At electric fields [25] close (10.4kV/cm) or slightly above the resonance (14.2kV/cm), the transmitted signal shows a strong modulation that reflects the oscillation of the wavepacket. The oscillation period is about 800fs, as expected from Eq. (1) for a splitting of about 5meV. Further away from the resonance (18.0kV/cm), the modulation becomes weaker and the oscillation period smaller. This shows very clearly the increasing localization of the wavefunctions in the wells and the increase of the splitting between the levels. Pump-probe experiments at the NW transition also show the oscillations with approximately the same period.

These results are fully confirmed by time-resolved self-diffracted DFWM experiments. Here, two incoming

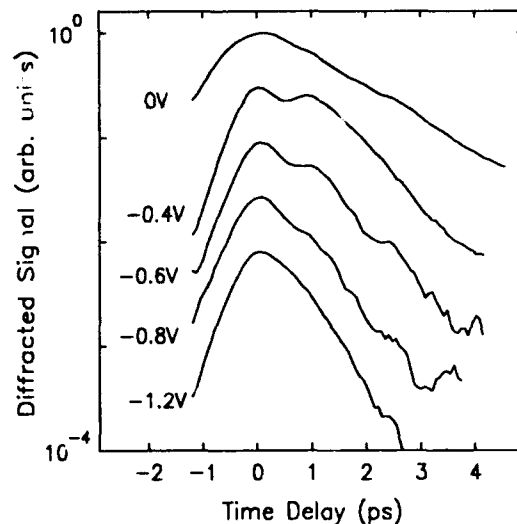


Figure 7: DFWM-signals for sample A with excitation of the WW transition. The electronic resonance is at about -0.6V.

beams with the directions k_1 and k_2 form an excitonic grating, and a probe signal is diffracted from this grating into the background-free direction $k_3 = 2k_2 - k_1$ (Fig.1, bottom). This time-integrated diffracted signal is measured as a function of the delay time T between the incoming pulses and gives information about the exciton dynamics. The DFWM signal versus the delay time for sample A is shown in Fig.7 for various applied voltages.

If the electric field is below (0V) or above (-1.2V) the field where the electronic levels are in resonance, the signal is exponential and reflects the free decay of the polarization, i.e., the loss of phase coherence of the excitons due to scattering processes [26]. The decay shows a periodic modulation, if the conduction electron levels are tuned in resonance (-0.6V). The modulation of the DFWM signal reflects the oscillatory behavior of the wavepacket, which was photoexcited in the WW. The modulation period agrees with the period observed in the PP experiment. If we tune the conduction electron levels slightly out of resonance (-0.4V and -0.8V), the modulation becomes weaker due to the increasing localization of the eigenstates in the wells.

Figure 8 shows the FWM results for sample B with larger splitting. Around the resonance of the levels (at about 11kV/cm), the FWM signal clearly shows an oscillatory modulation, which becomes weaker further away from resonance. The general picture is similar to sample A, however, the oscillation is again less damped than for sample A. Similar signals are observed when we tune the laser in the resonance of the NW. In this case, however, the oscillation is more strongly damped. This can be explained by the scattering by free carriers, which are simultaneously created in the WW when the excitation is resonant to the NW transition [25]. For higher temperatures and densities, the oscillations also become more strongly damped.

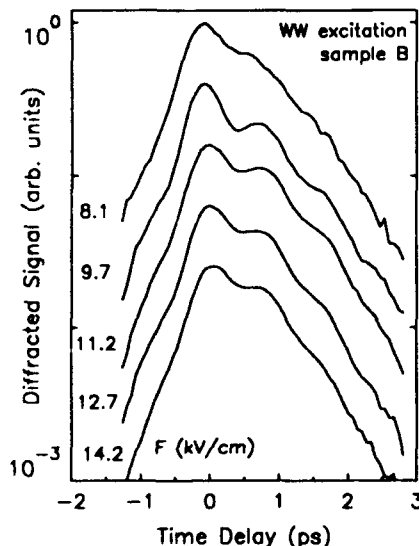


Figure 8: DFWM-signals for sample B and excitation of the WW. The electronic resonance is at about 11kV/cm.

Theoretical results

We analyze the experimental results with a theoretical model describing the coupled wells as a three-level-like system. The hole state is defined as level $|0\rangle$, the two delocalized states are $|1\rangle$ and $|2\rangle$. We define relaxation rates γ_1 and γ_2 , which describe the dephasing of the two upper levels to the ground state (i.e., the decay of the density matrix elements n_{01} and n_{02}), and a relaxation rate γ_3 , which describes the dephasing due to relaxation between the two upper states (i.e., the decay of n_{12}). The signals for the PP and the FWM experiments are calculated using a density matrix theory in a perturbation ansatz. The signal for pump-probe I_{PP} and four-wave-mixing I_{FWM} signal are then proportional to the third-order polarization in direction \mathbf{k}_1 and \mathbf{k}_3 , respectively. For δ -shaped pulses and purely homogeneous broadening, we obtain the following relations: ($\hbar=1$)

$$I_{PP} \propto w_1^2 + w_2^2 + w_1 w_2 [1 + \cos(\Delta ET) \exp(-\gamma_3 T)] \quad (2)$$

and for the FWM signal

$$I_{FWM} \propto \left[\frac{w_1^2}{2\gamma_1} + \frac{w_2^2}{2\gamma_2} + \frac{2w_1 w_2 (\gamma_1 + \gamma_2)}{(\gamma_1 + \gamma_2)^2 + \Delta E^2} \right] \times \\ (w_1^2 e^{-2\gamma_1 T} + w_2^2 e^{-2\gamma_2 T} + 2w_1 w_2 \cos(\Delta ET) \exp[-(\gamma_1 + \gamma_2)T]) \quad (3)$$

where w_1 and w_2 are the spectral weights of the transitions. Note that the phase relaxation between the delocalized levels γ_3 is responsible for the damping of the oscillation in the PP experiment, in contrast to the FWM experiment, where the relaxation to the ground states γ_1 and γ_2 leads to the damping. The present theory does not allow a quantitative analysis due to the approximations of δ -shaped pulses and homogeneous broadening. However, a preliminary analysis of the data [21] shows that the thermalization time between the extended levels is short (about 1ps), which leads to a strongly damped wavepacket motion. This explains why sample B with a faster oscillation frequency shows more oscillations. The scattering rate between such delocalized levels has been calculated by Liu et al. [27]. The main scattering mechanisms they considered were scattering at impurities and interfaces. Scattering times were in the ps range for the a-DQW structures they modeled in their calculation.

Another interesting aspect of our experiment is that coherent oscillations in a DQW can be considered as the most simple case of Bloch oscillations: A recent theoretical study [28] of the dynamics of a wavepacket in a Wannier-Stark ladder corresponds for the case of a "superlattice" consisting of two wells exactly to our experiment. The Bloch oscillation frequency ω_B is then identical to the coherent oscillations frequency described by Eq. 1.

Acknowledgments

We are indebted to J. Gordon for his contribution to this work. We thank M. Fox, S. Luryi, and D.A.B. Miller for useful discussions, and P. Ganser for assistance in the MBE growth. The work of K.L. was partially supported by the Max-Planck-Gesellschaft zur Förderung der Wissenschaften e.V.

- (a) now: Institute for Semiconductor Electronics, Univ. Aachen, Sommerfeldstraße 24, D-5100 Aachen, Germany
- (b) permanent address: Philipps-Universität, D-3550 Marburg, Germany
- (c) permanent address: Forschungszentrum Jülich, HLRZ, D-5170 Jülich, Germany

References and Notes

1. A. J. Leggett, S. Chakravarty, A.T. Dorsey, P.A. Fisher, A. Garg, and W. Zwerger, *Rev. Mod. Phys. (USA)* **59**, 1 (1987).
2. R. Dingle, W. Wiegmann, and C. H. Henry, *Phys. Rev. Lett.* **33**, 827 (1974).
3. T. Furuta, K. Hirakawa, J. Yoshino, and H. Sakaki, *Jap. J. Appl. Phys.* **25**, L151 (1986).
4. J.W. Little and R.P. Leavitt, *Phys. Rev. B* **39**, 1365 (1989).
5. J. E. Golub, P. F. Liao, D. J. Eilenberger, J. P. Harbison, L. T. Florez, and Y. Prior, *Appl. Phys. Lett.* **53**, 2584 (1988).
6. F. Capasso, K. Mohammed, and A. Y. Cho, *IEEE J. of Quantum Electronics* **QE-22**, 1853 (1986).
7. T. C. L. G. Sollner, W. D. Goodhue, P. E. Tannenwald, C. D. Parker, and D. D. Peck, *Appl. Phys. Lett.* **43**, 588 (1983).
8. M. Tsuchiya, T. Matsusue, and H. Sakaki, *Phys. Rev. Lett.* **59**, 2356 (1987).
9. J. F. Young, B. M. Wood, G. C. Aers, R. L. S. Devine, H. C. Liu, D. Landheer, M. Buchannan, A. J. SpringThorpe, and P. Mandeville, *Phys. Rev. Lett.* **60**, 2085 (1988).
10. I. Bar-Joseph, T. K. Woodward, D. S. Chemla, D. Sivco, and A. Y. Cho, *Phys. Rev. B* **41**, 3264 (1990).
11. H. Yoshimura, J.N. Schulman, and H. Sakaki, *Phys. Rev. Lett.* **64**, 2422 (1990).
12. D. Y. Oberli, J. Shah, T. C. Damen, T. Y. Chang, C. W. Tu, D. A. B. Miller, J. E. Henry, R. F. Kopf, N. Sauer, and A. E. DiGiovanni, *Phys. Rev. B* **40**, 3028 (1989).
13. B. Deveaud, F. Clerot, A. Chomette, A. Regreny, R. Ferreira, and G. Bastard, *Europhys. Lett.* **11**, 367 (1990).
14. M. G. W. Alexander, M. Nido, W.W. Rühle, and K. Köhler, *Phys. Rev. B* **41**, 12295 (1990).
15. K. Leo, J. Shah, J. P. Gordon, T. C. Damen, D. A. B. Miller, C. W. Tu, and J. E. Cunningham, *Phys. Rev. B* **42**, 7065 (1990).
16. M. Nido, M.G.W. Alexander, and W.W. Rühle, *Phys. Rev. B* **43**, 1839 (1991).
17. T.B. Norris, N. Vodjdani, B. Vinter, E. Costard, and E. Böckenhoff, *Phys. Rev. B* **43**, 1867 (1991).
18. S. Luryi, *Sol. St. Commun.* **65**, 787 (1988).
19. C.L. Foden and K.W.H. Stevens, *J. Phys.: Condens. Matter* **2**, 5179 (1990).
20. J.A. Yeazell and C.R. Stroud, Jr., *Phys. Rev. Lett.* **60**, 1494 (1988); A. ten Wolde, L.D. Noordam, A. Lagendijk, and H.B. van Linden van den Heuvell, *Phys. Rev. Lett.* **61**, 2099 (1988).
21. K. Leo, J. Shah, E.O. Göbel, T.C. Damen, S. Schmitt-Rink, W. Schäfer, and K. Köhler, *Phys. Rev. Lett.* **66**, 201 (1991).
22. G. Bastard, C. Delalande, R. Ferreira, and H.W. Liu, *J. Lumin.* **44**, 247 (1989).
23. A. M. Fox, D. A. B. Miller, G. Livescu, J. E. Cunningham, J. E. Henry, and W. Y. Jan, *Phys. Rev. B* **42**, 1841 (1990).
24. K. Leo, J. Shah, E. O. Göbel, T. C. Damen, and K. Köhler, *Appl. Phys. Lett.* **56**, 2031 (1990).
25. The electric field in sample B was calibrated using the shift of the QW transitions due to the Quantum-Confinement Stark Effect.
26. L. Schultheis, A. Honold, J. Kuhl, K. Köhler, and C.W. Tu, *Phys. Rev. B* **34**, 9027 (1986).
27. H. W. Liu, R. Ferreira, G. Bastard, C. Delalande, J. F. Palmier, and B. Etienne, *Appl. Phys. Lett.* **54**, 2082 (1989).
28. G. Bastard and R. Ferreira, in *Spectroscopy of Semiconductor Microstructures*, NATO ASI Series Vol. 206 (Plenum Press, New York 1989), p.333.

Carrier Sweep-Out from Quantum Wells in an Electric Field

A. M. Fox,[†] D. A. B. Miller, G. Livescu,[‡] J. E. Cunningham, and
W. Y. Jan

*AT&T Bell Laboratories, Crawfords Corner Road,
Holmdel, New Jersey 07733*

Abstract

We show that the carrier sweep-out from GaAs/Al_xGa_{1-x}As quantum wells with $x \leq 0.3$ is thermally assisted at low fields, and dominated by tunneling at high fields.

Introduction

The physics of carrier escape from quantum wells in an electric field is important for improving the quantum well electroabsorptive devices such as the Self Electrooptic Effect Device (SEED) [1]. The carrier lifetime is important not only because it puts a lower limit on the switching time [2], but also because it affects other properties such as the electroabsorption and the exciton saturation intensity [3]. This latter point in fact proves to be very significant for SEED systems, because these systems tend to run at intensity levels much greater than that required to switch a single device. (Sufficient energy must be passed to the next device in the system to switch it after allowing for the system losses.) At these high power levels, the exciton absorption saturates, which puts an upper limit on the intensity which can be used. We have recently shown how the saturation intensity is strongly affected by the design of the quantum well structure, most likely because of the changes in carrier sweep-out times which accompanied the change in design [3].

In this paper we report measurements of the field- and temperature-dependent sweep-out

times in three carefully designed GaAs/Al_xGa_{1-x}As quantum well p-i-n structures. The principal variable between the samples is the height and thickness of the AlGaAs barriers: the reference sample had $x = 0.3$ and a barrier thickness L_b of ~ 60 Å; the second sample had the same x -value, but L_b was reduced to 35 Å, and the third sample had approximately the same L_b as the reference, but had x reduced to 0.2. Since the barrier height is determined by the x -value, these samples allow us to study the variation of the sweep-out time against the barrier height at constant barrier thickness, and vice versa.

Carrier Sweep-out Measurements

We measured the sweep-out times by the technique of time-resolved electroabsorption [4]. In Fig. 1 we show our results for the three samples. (The sample details are given in the figure caption.) Measurements were performed between 10K and room temperature.

On comparing the results for the three samples, we note that:

- The sweep-out times tend to decrease as the field is increased.
- All three samples show a minimum in the escape time at the voltage for resonant tunneling of electrons. The position of the minima agree well with the resonant voltage found from careful spectroscopic studies [5].
- Escape times decrease on reducing x or L_b .
- Below the resonant voltage the escape time decreases strongly with temperature, but above resonance, the sweep-out time is practically

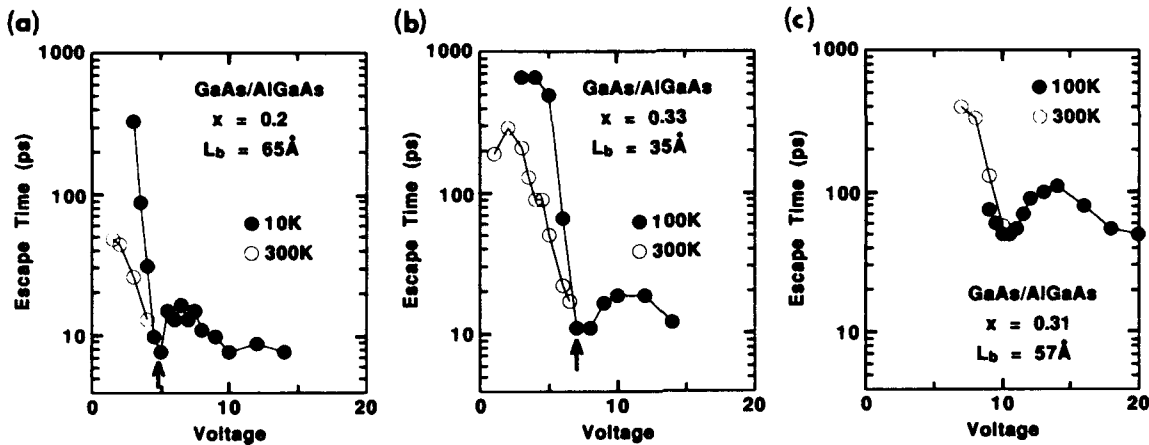


Figure 1. Measured sweep-out times for our GaAs/Al_xGa_{1-x}As p-i-n quantum well structures against reverse bias and temperature. The sample details are as follows: (a) 65 periods with L_w = 95 Å, L_b = 65 Å, x = 0.20 ; (b) 80 periods with L_w = 95 Å, L_b = 35 Å, x = 0.33 ; (c) 75 periods with L_w = 65 Å, L_b = 57 Å, x = 0.31. The arrows in (a) and (b) indicate the resonant tunneling voltage determined from photocurrent spectroscopy.

independent of temperature. (The absence of 100K data points in Fig. 1(c) for voltages below 9V indicates a very long lifetime).

The results clearly show the importance of the barrier design in determining the sweep-out time.

Discussion

The carrier lifetime in a quantum well in an electric field F can be written as:

$$\frac{1}{\tau} = \frac{1}{\tau_R} + \frac{1}{\tau_E} + \frac{1}{\tau_T} \quad (1)$$

The three terms refer to recombination, thermionic emission and tunneling respectively. In the conditions we are considering, the recombination rate is usually negligible compared to the thermal emission and tunneling rates, and thus we will discuss only the second and third terms on the right of Eq. (1). If we assume that the thermal current in the direction contrary to the field is negligible, the thermal emission time τ_E is given approximately by [6]:

$$\frac{1}{(\tau_E)_i} = \left(\frac{k_B T}{2\pi m_i L_w^2} \right)^{\frac{1}{2}} \exp - \left[\frac{H_i(F)}{k_B T} \right] \quad (2)$$

Since the sweep-out rate of the electrons and holes may differ, we have added a subscript i in Eq. (2) to indicate the particle type. T is the temperature, m_i is the effective mass in the well, and L_w is the well width. H_i(F) is the effective barrier height for thermal emission, and may be written approximately as:

$$H_i(F) = Q_i \Delta E_g - E^{(n)}_i - |e| F L_w / 2 \quad (3)$$

where Q_e/Q_h is the ratio of conduction to valence band discontinuities, (Q_e + Q_h = 1), ΔE_g is the difference in band gaps between the well and barrier material, and E⁽ⁿ⁾_i is the confinement energy of the nth subband relative to the center of the well. Usually we will be restricted to the case of n = 1 .

Following the analysis of Larsson *et al* [7], we write the tunneling rate as the product of an attempt frequency and a tunneling probability. The time for tunneling through a *single* potential barrier is then given approximately by:

$$\frac{1}{(\tau_T)_i} = \frac{n \hbar \pi}{2 L_w^2 m_i} \exp - \left[\frac{2 L_b \sqrt{2 m_{bi} H'_i(F)}}{\hbar} \right] \quad (4)$$

where L_b is the barrier width, m_{bi} is the effective

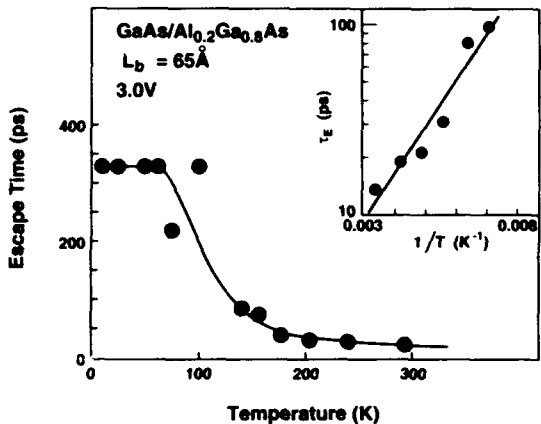


Figure 2. Sweep-out time for sample (a) of Fig. 1 at 3.0V between 10K and 300K. The inset is an Arrhenius plot of the thermal emission time deduced from the data by assuming a temperature independent tunneling time of 330ps. The fits to the sweep-out and thermal emission times assume the same activation energy of 49meV.

mass in the barrier, and n is the quantization number of the sub-level into which the particles are excited. $H'_i(F)$ is the effective barrier height for tunneling, and would be given by a similar expression to Eq. (3), but $L_w/2$ replaced by the position of the weighted mean potential of the tilted barrier.

Our experimental results compare favorably with the predictions of Eqs. (1)-(4). The changes in τ brought about by varying F , x and L_b are well explained by the variation of the thermionic emission and tunneling times. The fact that τ is insensitive to temperature at high fields indicates that the dominant high field escape mechanism is tunneling. The sensitivity of τ to T at low fields clearly points to the importance of thermal emission.

To examine the thermal emission process in more detail, we show in Fig. 2 the measured sweep-out time for the sample with $x=0.2$ and $L_b = 65\text{ \AA}$ (sample (a) from Fig. 1) as a function of temperature at 3.0V reverse bias. We find two different types of behavior. Up to 100K, the sweep-out time is independent of temperature. Above 100K, the sweep-out time decreases strongly with temperature until it approaches the experimental resolution of $\sim 10\text{ ps}$. The results can be readily explained in terms of Eqs. (1) - (4). At low temperatures, the thermal emission process is frozen out, and we simply measure the tunneling time ($\sim 330\text{ ps}$ in this case). As the

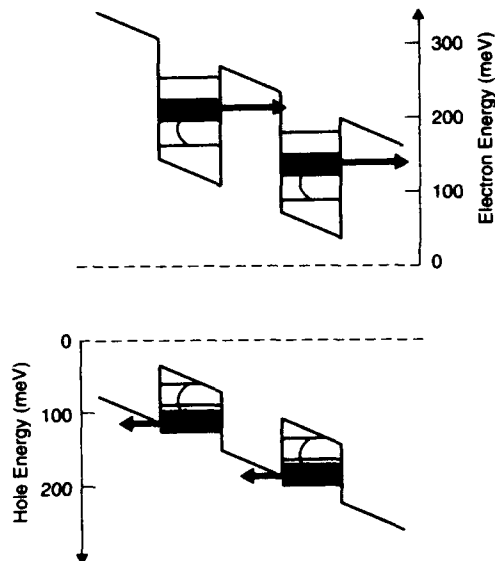


Figure 3. Electron and heavy hole energy level diagram corresponding to Fig. 2. The shaded bands indicate the range of possible energy states which participate in the thermally-activated escape mechanism.

temperature is increased, thermal emission becomes increasingly *more important*, and we can use Eq. (1) to deduce τ_E . The values of τ_E deduced in this way are plotted against T^{-1} between 140K and room temperature in the inset of Fig. 2. This Arrhenius plot allows us to determine the thermal activation energy to be $49 \pm 15\text{ meV}$. The uncertainty allows for the estimated accuracy of the deduced thermal emission times, and also for the relative insensitivity of the straight line fit to small changes in the activation energy. The curve fitted to the sweep-out time in Fig. 2 was obtained using a temperature independent tunneling time of 330ps and the 49meV activation energy. We repeated this analysis at 3.5V reverse bias and found a tunneling time of 100ps and an activation energy of 47meV.

We can obtain a clearer understanding of the measured activation energies by referring to Fig. 3, which shows the electron and hole energy levels of the sample at a field strength of 45 kVcm^{-1} . This field strength corresponds to about 3.0V reverse bias after allowing for the built-in voltage of the diode. The energy levels were calculated by the tunneling resonance technique [8] using a band offset ratio $Q_e:Q_v$ of 67:33, and checked for consistency with the low temperature absorption spectra. The shaded

bands indicate the energies which correspond to the experimentally determined limits of the activation energy. This energy level diagram suggests two possible escape mechanisms:

- (a) Thermal emission of holes from the $n = 1$ heavy hole sub-level over the top of the AlGaAs confining barrier.
- (b) Thermal activation of electrons to the minimum energy at which they only have to tunnel through just a single barrier in order to couple to the continuum states.

Our results do not seem to be consistent with pure thermal emission of electrons over the top of their confining barrier, nor with the proposed escape mechanism of thermal population of higher sublevels followed by rapid tunneling [7]. There is however a third escape mechanism which is consistent with the results:

- (c) Phonon-assisted tunneling of electrons or holes [9,10].

Since the low field escape time is also very sensitive to barrier thickness, it seems likely that the dominant mechanism is in fact a thermally-assisted tunneling process such as (b) or (c).

Conclusions

We have demonstrated the importance of thermal emission of carriers as an escape mechanism at low fields, and of tunneling at high fields. The precise mechanism of the thermal emission is still not fully resolved, and is worthy of further study. An improved understanding of the sweep-out physics should lead to further technological advances such as the recently demonstrated 33ps SEED switch [2].

Acknowledgments

We would like to acknowledge the work of J.E. Henry and M.M. Becker in processing the samples.

† Present address: Clarendon Laboratory, Parks Road, Oxford OX1 3PU, UK

‡ Present address: AT&T Bell Laboratories, Solid State Technology Center, Breinigsville, PA 18031

References

1. For a recent review see D.A.B. Miller, Optical and Quantum Electronics **22**, S61 (1990)
2. G.D. Boyd, A.M. Fox, D.A.B. Miller, L.M.F. Chirovsky, L.A.D'Asaro, J.M. Kuo, R.F. Kopf and A.L.Lentine, Appl. Phys. Lett. **57**, 1843 (1990)
3. A.M. Fox, D.A.B. Miller, G. Livescu, J.E. Cunningham, J.E. Henry and W.Y. Jan, Appl. Phys. Lett. **57**, 2315 (1990)
4. G. Livescu, A.M. Fox, D.A.B. Miller, T. Sizer, W.H. Knox, J.E. Cunningham, A.C. Gossard and J.H. English, Semicond. Sci. and Technol. **5**, 549 (1990)
5. A.M. Fox, D.A.B. Miller, G. Livescu, J.E. Cunningham, J.E. Henry and W.Y. Jan, Phys. Rev. B **42**, 1841 (1990); *Quantum-Well and Superlattice Physics III*, G.H. Dohler, E.S. Koteles and J.N. Schulman, Eds., Proc. SPIE 1283, 164 (1990)
6. H. Schneider and K. v. Klitzing, Phys. Rev. B **38**, 6160 (1988)
7. A. Larsson, P.A. Andrekson, S.T. Eng and A. Yariv, IEEE J. Quantum Electron. **QE-24**, 787 (1988)
8. D.A.B. Miller, D.S. Chemla, T.C. Damen, A.C. Gossard, W. Wiegmann, T.H. Wood and C.A. Burrus, Phys. Rev. B **32**, 1043 (1985); D.A.B. Miller, J.S. Weiner and D.S. Chemla, IEEE J. Quantum Electron. **QE-22**, 1816 (1986)
9. D.Y. Oberli, J. Shah, T.C. Damen, J.M. Kuo, J.E. Henry, J. Lary and S.M. Goodnick, Appl. Phys. Lett. **56**, 1239 (1990)
10. M.G. Shorthose, J.F. Ryan and A. Moseley, Solid State Electron. **32**, 1449 (1989)

Temperature Dependence of the Resonant Tunneling Process

I. Bar-Joseph, Y. Gedalyahu, and A. Yacoby

Department of Physics, Weizmann Institute of Science, Rehovot, Israel

T. K. Woodward, D. S. Chemla, D. L. Sivco, and A. Y. Cho

AT&T Bell Laboratories, Holmdel, New Jersey 07733

Abstract

We use differential absorption spectroscopy to investigate the temperature dependence of the accumulated charge in a resonant tunneling diode. We find that the charge density is approximately constant between 10-300K, and that the electrons are thermalized with the lattice at all temperatures.

The nature of a resonant tunneling process that involves inelastic scattering events is of a wide interest lately[1 – 3]. In this paper, we investigate the influence of inelastic scattering by measuring the tunneling characteristics at various temperatures. We show that the stored charge and the transit time are not sensitive to a large temperature change.

We used a symmetric double barrier diode under electric bias to study the electrons tunneling process. Our sample was composed of two 70Å InAlAs barriers and a 45Å InGaAs well between them. The zero bias Fermi energy in the emitter and collector was 55 meV. A more detailed description of the sample is given at ref(4). The experimental method we used is differ-

ential absorption spectroscopy (DAS): We modulated the charge density in the well by modulating the voltage applied to the diode. This in turn caused a modulation of the absorption coefficient α of the well material. The absorption coefficient is related to the electrons density N , primarily due to Pauli exclusion principle, which inhibits transitions into states filled by electrons. This mechanism, often referred as phase-space-filling, affects both the excitonic and the continuum band-to-band spectra. At low densities, $\alpha_c(\hbar\omega) = \alpha_c^0(\hbar\omega)[1 - f_e]$ where α_c and α_c^0 are the continuum contribution to the absorption coefficients when the QW is filled (α_c) or empty (α_c^0), and f_e is the electrons normalized distribution function. For the excitonic case it is common to de-

fine a characteristic saturation density N_s , such that $\Delta\alpha/\alpha = N/N_s$. Low carrier densities produce small changes in the absorption coefficient, and then $\Delta T/T = -\Delta\alpha l$, where T is the transmitted light through the sample and l is the well thickness. Hence, by modulating the voltage on the diode between $V = 0$ and V , and measuring ΔT using a lock-in technique, one can calculate the change in the electrons density in the quantum well, if N_s and α are known. In our measurements V is the voltage that corresponds to maximal current, and is denoted V_{peak} .

Figure 1 shows 4 DAS measurements taken at $T=10K$, $90K$, $170K$ and $290K$.

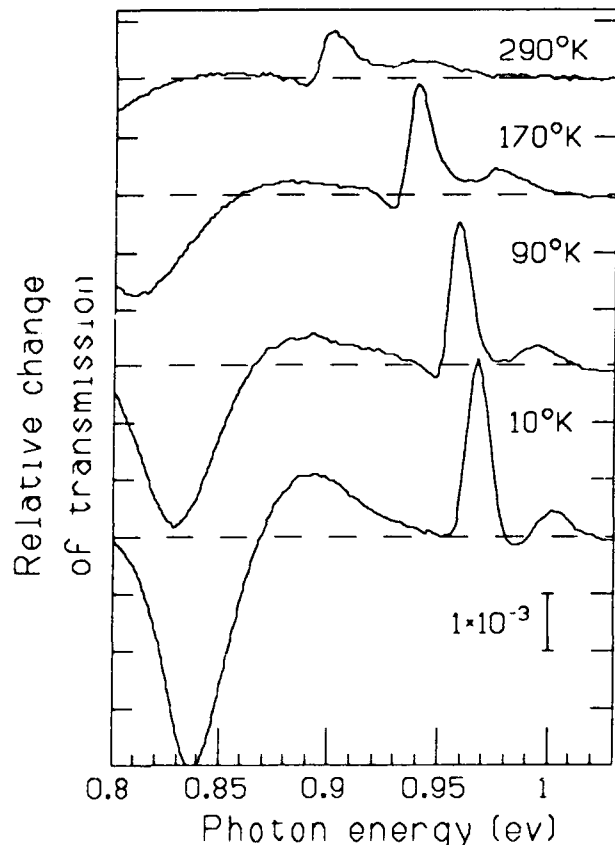


Figure 1. Differential absorption spectra at 4 different temperatures measured at V_{peak} .

The largest positive peak is due to bleaching of the heavy-hole (hh) exciton, and it is accompanied by a small positive peak (higher in energy), which is due to bleaching of the light-hole (lh) exciton. The lower energy features originate from the contact layers, and will not be discussed here.[4] The absorption bleaching at all temperatures is concentrated at the bottom of the band, although hot electrons are also injected to the well from the emitter, where the Fermi energy is about 55meV. This is an evidence to electrons thermalization through phonons emission. At high temperatures, when the typical time between collisions is much smaller than the transit time, phonon absorption becomes the dominant process, and a tail toward the high energies appears in the DAS.

To analyze the measurements, we performed a careful fit of the DAS at each temperature, to a curve which is a sum of differential signals from the hh and lh excitons and the continuum. The excitons were assumed to have a gaussian line shape and the continuum was described by a temperature broadened step function multiplied by the Sommerfeld enhancement. We included both the bleaching due to phase space filling and the small contribution due to a Stark shift of the QW energy level. Figure 2 shows the *relative integrated change* of the area under the hh exciton, Δ_{hh}/A_{hh} , as a function of temperature, where $\Delta_{hh} = \int \Delta\alpha_{hh}(\hbar\omega)d(\hbar\omega)$ and

$A_{hh} = \int \alpha_{hh}(\hbar\omega) d(\hbar\omega)$. $A_{hh}(T)$ was obtained by measuring the absorption spectra of a 50 QW's calibration sample with identical well and barriers width. Measurements were done at various temperatures, although A_{hh} is essentially temperature independent.

As mentioned above, one has to know the saturation density N_s at each temperature, in order to find the electrons density N . We derived the temperature dependence of $N_s^e(T)$ and $N_s^{e-h}(T)$, the exciton saturation density in the presence of electrons and in the presence of electron-hole pairs, respectively[5]. This allowed us to determine $N_s^e(T)$ from optical measurements[4] of N_s^{e-h} at 10K. The solid line in Fig. 2 shows N/N_s^e as a function of temperature for the calculated $N_s^e(T)$ and for a constant N . It can

be seen that the decrease in Δ_{hh} is consistent with the expected increase of the saturation density N_s^e over that temperature range. We can thus conclude that the temperature dependence of Δ_{hh} is due to that of N_s^e and that the electron density in the QW is essentially independent of the temperature. The resulting value for the constant electrons density, which is obtained by a best fit procedure, is $2.5 \times 10^{10} \text{ cm}^{-2}$. An analysis similar to that we performed at ref. 4, which is based on the peak values for $\Delta\alpha_{hh}$ and α_{hh} gives a higher value for N , $3.8 \times 10^{10} \text{ cm}^{-2}$.

The current density J was also measured at each temperature, and found to be almost constant over the entire temperature range: $J_{peak} \approx 60 \text{ A/cm}^{-2}$. Dividing the accumulated charge Q by the current density J we can get the transit time through the

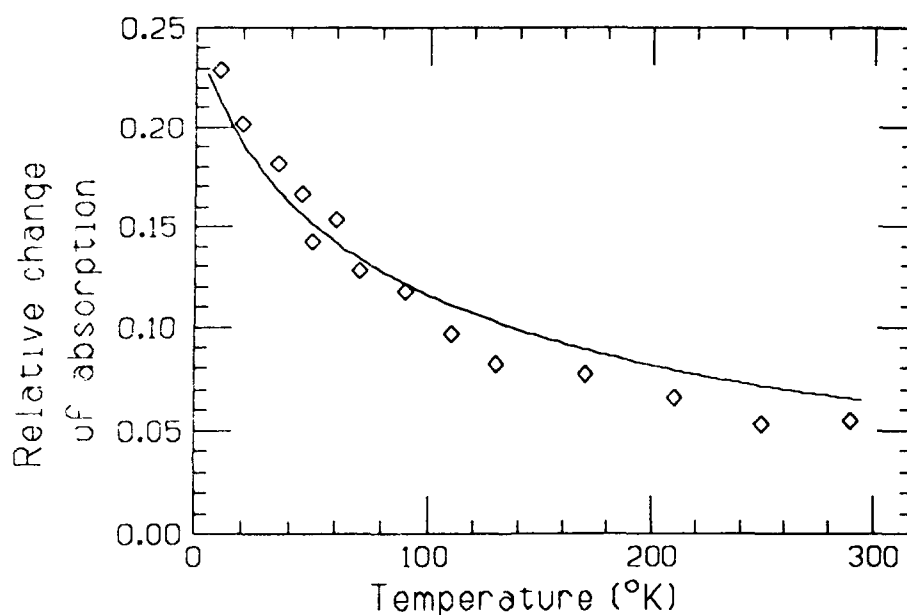


Figure 2. The relative change of the heavy hole exciton absorption area as a function of temperature. The solid line is the calculated $N/N_s^e(T)$ for $N = 2.5 \times 10^{10} \text{ cm}^{-2}$.

structure $\tau = Q/J \approx 75\text{ps}$, in a reasonable agreement with a transfer matrix calculation. Since J and τ are temperature independent, so are the total transmission probability and the escape rate from the well. This is in agreement with the quantum mechanical description of the tunneling process given in Ref(3).

We also note, that the intrinsic (elastic) width of the resonance, Γ_{el} , depends only on the decay rates through the barriers, which are temperature independent. When temperature is increased, the *inelastic* width Γ_{in} increases. At room temperature, although $\Gamma_{in} \gg \Gamma_{el}$, the process characteristics changes only slightly due to conservation of the *integrated* transmission probability.

To summarize, inelastic scattering processes involving the tunneling electrons were shown to occur in the well, such that the electrons distribution is thermalized with the lattice at all temperatures. Nevertheless, the three major physical quantities

which characterize the tunneling process, the current density, the stored charge and the transit time, are insensitive to a large temperature change. We demonstrated that resonant tunneling *can* be observed even when its inelastic width is grater than the elastic one, and that the electron transmission probability through the structure is modified by inelastic scattering in such a way that the integrated probability remains constant.

References:

1. M. Buttiker. IBM J. Res. and Develop. **32**, 63 (1988)
2. A.D. Stone and P.A. Lee, Phys. Rev. Lett. **54**, 1196 (1985).
3. N.S. Wingreen, K.W. Jacobsen, and J.W. Wilkins Phys. Rev. **B40**, 11834 (1989), and Phys. Rev. Lett. **61**, 1396 (1988).
4. I. Bar-Joseph, T.K. Woodward, D.S. Chemla, D. Sivco, and A.Y. Cho, Phys. Rev. **B41**, 3264 (1990).
5. S. Schmitt-Rink, D.S. Chemla, and D.A.B. Miller, Phys. Rev. **B32**, 6601 (1985).

Tunneling and Relaxation in Coupled Quantum Wells

B. Deveaud, A. Chomette, F. Clérot, and A. Regreny

CNET (LAB/OCM), 22301 Lannion, France

S. Gurvitz and I. Bar-Joseph

Weizmann Institute, Rehovot, Israel

In a double barrier resonant tunnelling diode, the lifetime of the electrons in the well is governed by the coupling of the confined states to the continuum of states outside the barriers. The well states are broadened by the interaction with the continuum on each side of the structure and are thus metastable, even without any relaxation mechanism such as phonon emission. If an electron is injected into the structure as in the experiment of Tsuchiya et al [1], it will leak out with a time constant given only by the barrier thickness.

In a system of coupled quantum wells (CQW) on the contrary, we are dealing with eigenstates of the system. Even at resonance, when one level of the narrow well (NW) is at the energy of a level of the wide well (WW), finite lifetimes are only observed because of additional perturbations to the system. In the absence of such perturbations, electrons would stay forever on the coupled levels (we are dealing here with a system prepared in a "classical mixture" i.e. with electrons equally distributed in the two wells, we refer the reader to Leo et al. [2] for the case where a wavepacket is created in one of the wells). The strongest perturbation, in the case where the coupled levels are separated from the ground state by more than one optical phonon, is the coupling to LO phonons [3]. If the coupled levels are the ground states of the system, the lifetime of electrons will be mainly radiative [2].

We now consider the case where resonance occurs between the first level of the NW and the second level of the WW. In the simple picture of perfect alignment of the levels in the two wells, coupling by a thin barrier gives rise to the well-known bonding and anti-bonding states split by an energy δ which is exponentially varying with the barrier thickness. The eigenfunctions $|\Phi_{\pm}\rangle$ would then read:

$$|\Phi_{\pm}\rangle = 1/\sqrt{2} (|\phi_{1n}\rangle \pm |\phi_{2w}\rangle) \quad (1)$$

where $|\phi_{1n}\rangle$ and $|\phi_{2w}\rangle$ are the wavefunctions of the first and second levels of the isolated NW and WW respectively. In this very simple picture, where perfect resonance is achieved and where phonon emission is treated as a small perturbation to the system, the coupling to phonons leads to a scattering time equal to exactly twice the time in one isolated quantum well, independently of the barrier thickness. More precise calculations only show a change in time for very narrow barrier when the splitting between the coupled levels cannot be neglected and results in a difference in the q vector of the emitted LO phonon [4].

CQWs have been studied by time resolved luminescence in order to get information on the dynamics of the system : the parameter of importance is the time constant of the NW luminescence decay. Resonance has been obtained by applying an electric field [5,6]. This has the great advantage of tunability: it allows to go through the resonance with only one sample.

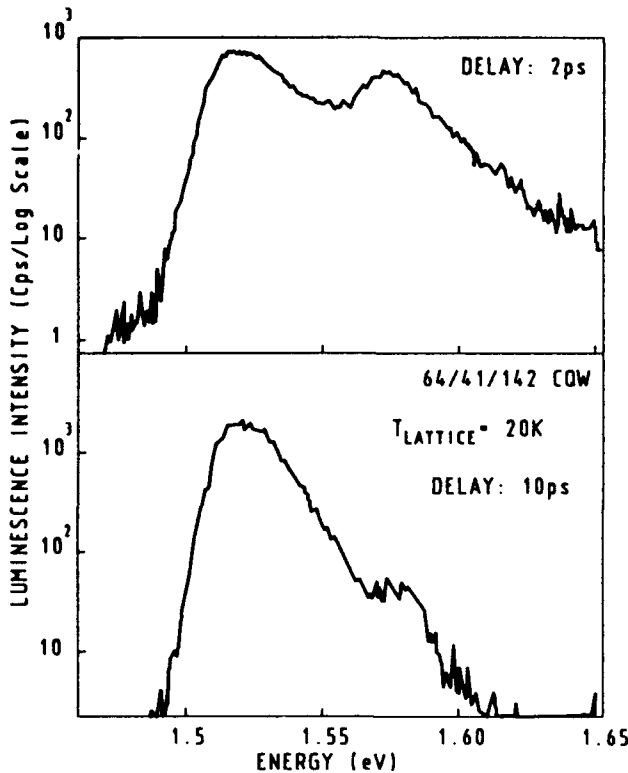


Fig.1: Luminescence of a 64/41/142 CQW at two different time delays after the excitation pulse : 2 ps and 10 ps. Note the strong decrease of the narrow well luminescence.

resolution by upconversion of the luminescence signal [8]. Resolution of our system is basically limited by the width of the laser pulses which can be as short as 120 fs. The measurements are carried out with 600 to 800 fs pedestal free pulses with an energy of 2.04 eV.

We show on Fig.1 the spectrum of one of our samples, measured to be a 64/41/142 i.e. a sample designed to be as close as possible to the resonance condition. The spectrum is plotted on a Log scale which explains the rather broad shape of the luminescence peaks. We observe two different transitions, one at 1.51 eV due to the recombination in the large well and one at 1.57 eV corresponding to the narrow well. As in all experiments of that kind, we measure the time decay of the narrow well luminescence. The time behaviour of the narrow well luminescence intensity is reported on Fig.2. It shows a rather short risetime and a decay time of 2 ps. The resolution of our system is checked at the same energy by measuring the luminescence of a GaAs sample implanted with oxygen and not annealed. In such a case, the lifetime of the carriers is known to be very short [9] and the luminescence decay is given by the time resolution of the system. The decay of this

We have chosen to study the resonance by a proper adjustment of the growth parameters [7] : resonance is achieved by growing a series of samples, only changing one parameter (in our case the width of the WW or of the tunneling barrier). This method necessitates of course the growth of more samples, but it has a number of advantages. First it allows to work on several CQW periods without any problem with the field inhomogeneity. Second our samples have been p-doped in order to:

-Increase the cooling rate of the electrons, which interact with the background holes,

-Increase the luminescence efficiency (proportional to the number of holes),

-Select electron effects as the possible movement of photocreated holes has a negligible effect on the observed dynamics in the low density regime.

The first two effects are of great importance as we want to study very short transients. Our samples are grown in the GaAs/AlGaAs system by molecular beam epitaxy. The width and Al content (around 26 %) of the different layers are carefully checked by using x-ray diffraction together with a simulation program of the different diffracted intensities [4]. After measurements the samples are labelled as $L_N/L_b/L_w$, where L_N is the width of the narrow well, L_b the tunnel barrier thickness, L_w the width of the large well.

We study the dynamics of the different luminescence transitions with subpicosecond

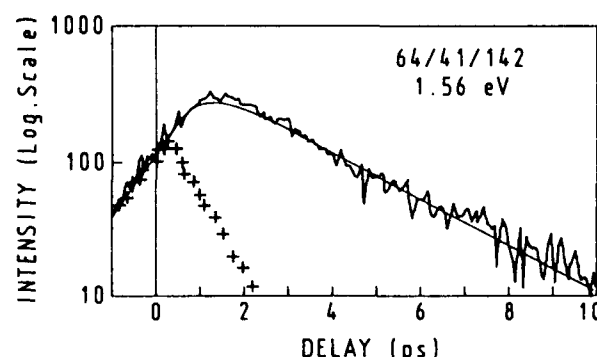


Fig.2: Time behaviour of the narrow well luminescence. The crosses indicate the resolution of the system, and the solid line is a fit (see text).

luminescence is shown by crosses on Fig.2, it demonstrates : first that we have generated pedestal free pulses, second that the resolution of our experiment in the energy region where we perform our measurements is better than 1 ps. The luminescence data of Fig.2 can be fitted by using three level model and assuming exponential transfer between the different states. It also takes into account the width of the excitation pulses which is responsible for the signal at negative delays. The pulsedwidth is obtained as a gaussian of 600 fs full width half maximum, and the decay time of the last level is 2.2 ps.

Fig.3 evidences the resonance effect for a series of samples with the same barrier thickness. As the width of the wide well is changed from 120 Å to 190 Å, the two wells go through resonance. A clear minimum in the decay time is observed for thicknesses around 150 Å. Also shown on the figure is the expected decay time dependence. Clearly the resonance is roughly at the correct position, but is much broader and less deep than expected. The same is true for the experiments of Oberli et al [5] as well as Alexander et al. [6].

We show on Fig.4 the results obtained on two

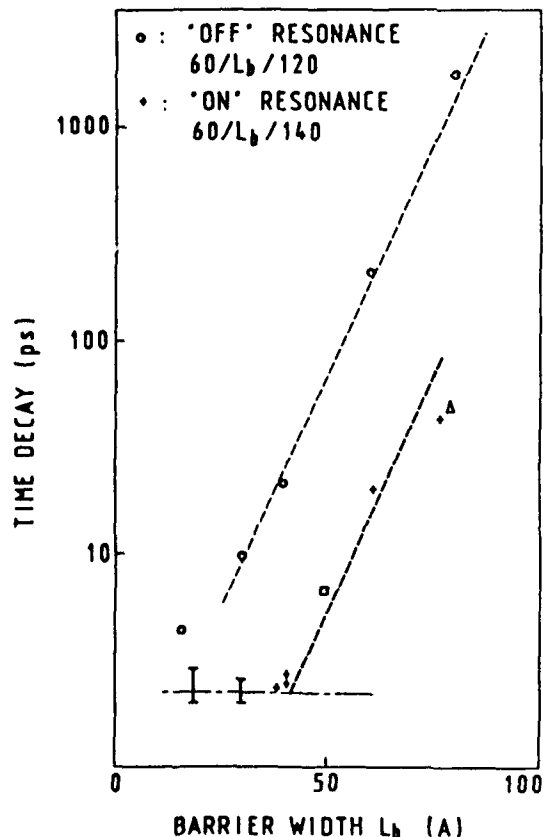


Fig.4: Decay time of the NW luminescence as a function of the barrier thickness for two series of samples: (o) "off resonance", and (+) "on resonance". On resonance times observed by Oberli et al [4] (□) and by Alexander et al [5] (▲) are also plotted.

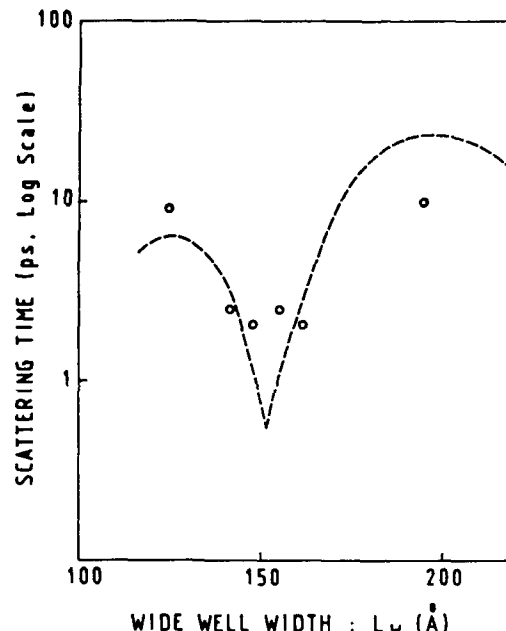


Fig.3: Decay time of the narrow well, as a function of the wide well width for a series of samples with 40 Å barriers.

series of samples: one grown to be "on resonance", and the other to be "off resonance". On this figure, we have plotted the NW luminescence decay time as a function of L_b , the thickness of the tunnelling barrier. On the same figure, we have also reported the results of the studies by Oberli et al [5] and Alexander et al [6]. For these 3 studies the samples are in fact quite similar as made out of GaAs/AlGaAs with comparable Al content in the barriers. Note that all "on resonance" experimental results follow the same trend.

The decay times for the "on resonance" samples show two well defined regions : one corresponding to barrier thicknesses larger than 40 Å where the variation of the decay time with the barrier thickness is exponential (note that the slope in that case is exactly the same as for the "off resonance" samples). In the second region, below 40 Å, the decay time stays approximately constant (between 1.7 and 2.5 ps, taking into account the uncertainties in the measurement) for the seven different samples studied (whose barrier thicknesses range from 42 Å to 22 Å).

One possible interpretation of this behaviour is the following. For barrier thicknesses below 40 Å, it is indeed possible to grow samples where $|\phi_{1n}\rangle$ and $|\phi_{2w}\rangle$ are resonantly coupled. By "resonantly coupled" we mean that the wavefunctions of the bonding and antibonding states $|\Phi_+\rangle$ and $|\Phi_-\rangle$ both extend over the two wells, with approximately equal probabilities. The situation of resonant coupling is rather easy to obtain for very narrow barriers, even if the resonance condition is not

perfect. On the contrary, when the barrier becomes large, the resonance condition is much more stringent. In a simplified picture, the wavefunctions of the two coupled levels would read:

$$|\Phi_+\rangle = (1-\epsilon/2\delta) |\phi_{1n}\rangle + \epsilon/2\delta |\phi_{2w}\rangle \quad (2)$$

$$|\Phi_-\rangle = \epsilon/2\delta |\phi_{1n}\rangle + (1-\epsilon/2\delta) |\phi_{2w}\rangle \quad (3)$$

where ϵ is the energy mismatch between the two levels and δ the strength of the coupling. It is easy to see that for small coupling, $|\Phi_+\rangle$ is localized in the NW and $|\Phi_-\rangle$ in the WW.

Since the ground state of the system is almost entirely localized in the WW, relaxation of $|\Phi_+\rangle$ to the ground state is governed by the small lobe of the wavefunction still extending into the large well [4,7]. Due to the exponential variation of δ with the barrier thickness, the relaxation of $|\Phi_+\rangle$ to the ground state will also vary exponentially, as experimentally observed. The same interpretation exactly holds for the case of purposely "off resonance" samples: the small part of the wavefunction ($\epsilon/2\delta$) $|\phi_{2w}\rangle$ extending in the WW still governs the relaxation of the NW.

Thus the observed behaviour in the different experiments is quite well reproduced by the very simple calculations exposed here. More detailed calculations using the envelope function formalism are exposed in ref. 4 (see also [10,11]), they lead to the same qualitative tendencies, the quantitative agreement is also quite satisfactory. The results of such calculations are reported on Fig.5. It shows that an error of 1 Å only is enough to localize the wavefunctions if the barrier thickness is larger than 50 Å. The main limitation of this description is not in the region of narrow barriers but in the case of large barriers where our way of treating the coupling to phonons as a small perturbation to the energy levels of the system is not adequate anymore close to the resonance. This is then especially true for the experiments of Oberli et al [4], and Alexander et al [5] where it may be though that they come closer to resonance than in our adjustment of the growth parameters.

In order to improve over these calculations, it is necessary to perform a calculation treating on an equal footing the coupling between the two wells and the phonon scattering. This can be performed in the framework proposed in [12]. The result of such a calculation will only be briefly exposed here. The decay time T of the population in the coupled levels can be written as:

$$T = 2/\Gamma_0 + (1+n_3)(4\epsilon^2+\delta^2)/(2\Gamma_0\delta^2) + \delta(2\epsilon n_1 + \Gamma_0 n_2)/(\Gamma_0\delta^2) \quad (4)$$

where Γ_0 is the strength of the phonon scattering, and $n_{1,2,3}$ describe the initial carrier distribution. In our experiments, it is reasonable to assume that we start with a classical mixture: the initial distribution is equally distributed over the two wells. Then, $n_3=n_1=n_2=0$ and the above equation reduces to:

$$T = 2/\Gamma_0 + (4\epsilon^2+\Gamma_0^2)/(2\Gamma_0\delta^2) \quad (5)$$

This equation describes the main features of the observed phenomena. It seems similar to the equation derived by Leo et al. [13] but improves the description as it allows to consider all limiting cases (strong

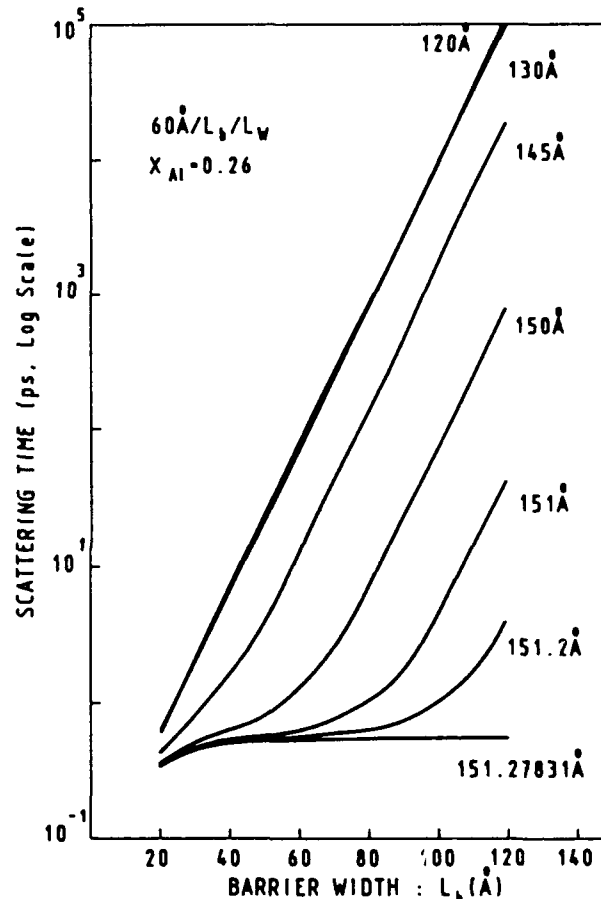


Fig.5: Calculated scattering time from the wavefunction mainly localized in the narrow well for different values of the large well width, i.e. for different detunings.

mismatch, strong coupling and strong scattering), our description also allows to describe the different initial carrier distributions : classical mixture as well as wavepacket in one of the wells (then $n_3=1$, $n_1=n_2=0$).

Let us consider now a few limiting cases of interest, the system being prepared in a classical mixture as in the experiments that we just described.

For a strong mismatch ($\epsilon > \delta$), it gives :

$$T = 2\epsilon^2 / \Gamma_0 \delta^2 \quad (6)$$

Owing to δ^2 , T varies exponentially with the barrier thickness, which explains the exponential variation of the observed times, for both the "off resonance" samples and the "on resonance" ones with large barriers, in a way exactly similar to the simple description of eq. 2 and 3.

If on the contrary we assume a negligible detuning, then we have two main regimes : the first where the electronic coupling δ is strong enough ($\delta \gg \Gamma_0$, i.e. narrow enough barriers), then :

$$T = 2/\Gamma_0 \quad (7)$$

and we find the same result than in the preceding description : the decay time should be twice the scattering time in an equivalent isolated quantum well.

If now the coupling is small (compared to Γ_0) the time should follow :

$$T = 2/\Gamma_0 + \Gamma_0/\delta^2 \quad (8)$$

T should show a non monotonic behaviour as a function of Γ_0 , a conclusion different from that proposed by Leo et al. [13]. A possible configuration to check this non monotonic behaviour is proposed in ref.12. Numerical estimates for the case of refs. 4 and 5 improve the quantitative agreement, but do not explain totally the observed times. The largest change would be observed for the experiment of Alexander et al [5], where the barrier is quite large (80 Å). Eq.8 would predict a decay time between 5 and 12 ps at resonance (depending on the precise value of the scattering strength) significantly longer than the 2 ps calculated in the previous model, but still shorter than the experimental time of 50 ps. The rest of the discrepancy at resonance (50 ps versus 10ps) must be due to residual interface roughness effects which have been neglected up to now.

Acknowledgments

We would like to acknowledge numerous discussions with M.G.W. Alexander, G. Bastard, R. Ferreira, W.W. Rühle. We are grateful to P. Auvray for his determination of the sample parameters.

References:

- [1] M. Tsuchiya, T. Matsutsue, H. Sakaki, *Phys. Rev. Lett.*, **59**, 2359 (1987)
- [2] K. Leo, J. Shah, E.O. Göbel, T.C. Damen, S. Schmitt-Rink, W. Schäfer, K. Köhler, *Phys. Rev. Lett.*, **66**, 201 (1991)
- [3] R. Ferreira, G. Bastard, *Phys. Rev.*, **B40**, 1074 (1989)
- [4] B. Deveaud, A. Chomette, F. Clérot, P. Auvray, A. Regreny, R. Ferreira, G. Bastard, *Phys. Rev.*, **B42**, 7021 (1990)
- [5] D.Y. Oberli, J. Shah, T.C. Damen, C.W. Tu, D.A.B. Miller, J.E. Miller, R.F. Kopf, N. Sauer, A. di Giovanni, *Phys. Rev.*, **B40**, 3028 (1989)
- [6] M.G.W. Alexander, Nido, W.W. Rühle, K. Köhler, *Phys. Rev.*, **B41**, 12295 (1990) to be published
- [7] B. Deveaud, F. Clérot, A. Chomette A. Regreny, R. Ferreira, G. Bastard, *Europhys. Lett.*, **11**, 367 (1990)
- [8] J. Shah, T.C. Damen, B. Deveaud, D. Block, *Appl. Phys. Lett.*, **50**, 1307 (1987)
- [9] R. Höpfel, in *Spectroscopy of quantum wells and superlattices*, NATO ARW, Eds. G. Fasol, A. Fasolino; P. Lugli, p.201 (1989)
- [10] T. Weil, B. Vinter, *J. Appl. Phys.*, **60**, 3227 (1986)
- [11] R. Ferreira, G. Bastard, *Phys. Rev.*, **B40**, 1074 (1989)
- [12] S. Gurvitz, I. Bar Joseph, B. Deveaud, to appear in *Phys. Rev. B*
- [13] K. Leo, J. Shah, J.P. Gordon, T.C. Damen, D.A.B. Miller, C.W. Tu, J.E. Cunningham, *Phys. Rev.*, **B42**, 7065 (1990)

Competition Between Tunneling and Exciton Formation for Photoexcited Carriers in Asymmetric Double Quantum Wells

J. Kuhl, R. Strobel, and R. Eccleston

Max-Planck-Institut für Festkörperforschung, Heisenbergstrasse 1, Postfach 80 06 65, D-7000 Stuttgart 80, Federal Republic of Germany

K. Köhler

Fraunhofer-Institut für Angewandte Festkörperphysik, D-7800 Freiburg, Federal Republic of Germany

Abstract

The formation of excitons from photoexcited free carriers in a GaAs asymmetric double quantum well tunneling structure is shown to occur by a bimolecular process. Using the non-linear luminescence cross-correlation technique, a bi-molecular formation coefficient of $6 \times 10^{-12} \text{ cm}^2/\text{ps}$ is determined. The electron and hole tunneling times are also simultaneously obtained.

Introduction

Asymmetric double quantum well (ADQW) structures consist of a wide and narrow quantum well separated by a thin barrier through which tunneling may occur. ADQW's (and very similar double barrier tunneling structures) have been studied using time-resolved photoluminescence (TRPL) to investigate non-resonant electron tunneling times as a function of barrier thickness and the transition to resonant tunneling by means of an electric field applied perpendicular to the plane of the well. Resonant and non-resonant hole tunneling times have been measured, also using a perpendicular electric field [1]. A limitation of the TRPL method is that it is not possible to measure the electron and hole tunneling times simultaneously, or to determine hole tunneling times directly in the absence of an electric field, because in both cases the TRPL decay

time only gives the tunneling time of the carrier type (the electrons) which tunnels faster. In this work, the non-linear photoluminescence cross-correlation technique [2] is used to simultaneously measure the electron and hole tunneling times in two ADQW's under the same sample conditions. We show that the non-linear signal originates from competition between tunneling and bimolecular exciton formation and can be used to determine an important additional quantity, the time required to form excitons from photo-excited free carriers.

Experimental

The samples under investigation were 3 GaAs- $\text{Al}_x\text{Ga}_{1-x}\text{As}$ ADQW's grown on a Si doped n^+ GaAs (100) substrate. The sample structures consisted of a buffer layer (600nm GaAs, 20nm $\text{Al}_{0.35}\text{Ga}_{0.65}\text{As}$, 1nm GaAs, 10nm $\text{Al}_{0.35}\text{Ga}_{0.65}\text{As}$, five periods of a 2nm GaAs/3nm $\text{Al}_{0.35}\text{Ga}_{0.65}\text{As}$ superlattice), 100nm $\text{Al}_{0.35}\text{Ga}_{0.65}\text{As}$, a 10nm wide quantum well (QW_w), a $\text{Al}_{0.35}\text{Ga}_{0.65}\text{As}$ tunneling barrier of various thicknesses, a 5nm narrow GaAs quantum well (QW_n), 100nm $\text{Al}_{0.35}\text{Ga}_{0.65}\text{As}$ and a 4nm GaAs cap. The barrier thicknesses were 3nm in sample 3, 4nm in sample 4, and 20nm in sample 20. Sample 20 was used as a reference structure since tunneling is negligible for a barrier of this width. The experimental arrangement for the non-linear cross-correlation measurement is shown schematically in Figure 1. A hybrid mode-locked

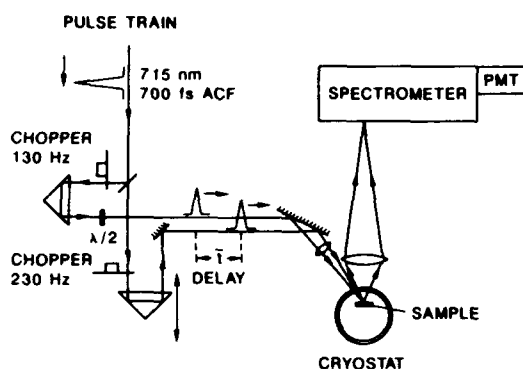


Figure 1. The non-linear PL cross-correlation measurement.(ACF - autocorrelation function, PMT - photomultiplier tube).

Pyridine 1 dye laser is used to generate pulses of around 700fs (FWHM autocorrelation function) at 715nm. The laser output is divided into two beams which are then overlapped on the sample which is maintained at 8K in a helium cryostat. The photoluminescence is dispersed by a 1/2m spectrometer and detected using a cooled GaAs photomultiplier. Beam 1 is chopped at 230Hz and beam 2 at 130Hz and the photoluminescence signal is detected at the sum frequency, 360Hz. The beams are perpendicularly polarized by a $\lambda/2$ plate to suppress any coherence artifact in the detected signal [2].

A signal is only generated at the sum frequency when the PL emission is a non-linear function of the excitation density. By varying the delay between the two pulses, the decay of the non-linear change in PL output generated by the two pulses may be measured.

Theoretical Model

The origin of the PL non-linearity in these measurements is the bimolecular nature of the exciton formation process, i.e. the exciton formation rate is proportional to the product of the free electron and free hole densities. In an isolated single quantum well, this bimolecular formation process does not affect the quantity of excitonic PL finally emitted from the sample, all carriers eventually form exci-

tons which then recombine radiatively, and a linear dependence of PL output on n_{ex} is obtained. However, for free carriers photoexcited in the narrow well of an ADQW structure, strong competition exists between exciton formation in the narrow well (and thus excitonic photoluminescence from the narrow well) and tunneling from the narrow well to the wide well. The generation of a non-linear change in the PL output as a function of n_{ex} can be seen as follows. At low n_{ex} , such that the free electron and/or hole tunneling rate is much larger than the exciton formation rate, the probability of exciton formation, and consequently of excitonic luminescence, is relatively low. As n_{ex} is increased, the exciton formation rate increases but the tunneling rate (independent of n_{ex}) remains constant. The probability of a photo-created carrier contributing to excitonic luminescence therefore is increased, giving a non-linear change in the excitonic luminescence from the narrow well as n_{ex} is varied.

The cross-correlation signal can be modeled using a system of rate equations:

$$\frac{dn}{dt} = -Cnp - \frac{n}{\tau_e} + \frac{N}{\tau_h} + G(t) + G(t - \bar{t}) \quad (1)$$

$$\frac{dp}{dt} = -Cnp - \frac{p}{\tau_h} + \frac{N}{\tau_e} + G(t) + G(t - \bar{t}) \quad (2)$$

$$\frac{dN}{dt} = Cnp - \frac{N}{\tau_e} - \frac{N}{\tau_h} - \frac{N}{\tau_{LT}} \quad (3)$$

where n , p , and N are the density of free electrons, free holes, and excitons, respectively; τ_e and τ_h are the tunneling times for electrons and holes; τ_{LT} is the exciton radiative lifetime; $G(t)$ and $G(t - \bar{t})$ are carrier generation terms given by two Gaussian pulses of appropriate FWHM; \bar{t} is the delay between the two pulses. The bimolecular generation rate of excitons is given by the term Cnp , where C is the bimolecular exciton formation coefficient; n/τ_e , p/τ_h are the tunneling rates for free electrons and holes. Tunneling of an electron or hole bound in an exciton ('excitonic' electrons or holes) is given by the rates N/τ_e and N/τ_h . We assume throughout that there is no difference between the tunneling rates for excitonic electrons and free electrons and between excitonic holes and free holes. It should be noted that the excitonic tunneling terms N/τ_e and N/τ_h not only decrease the density of excitons but also give a positive contribution to the free hole and

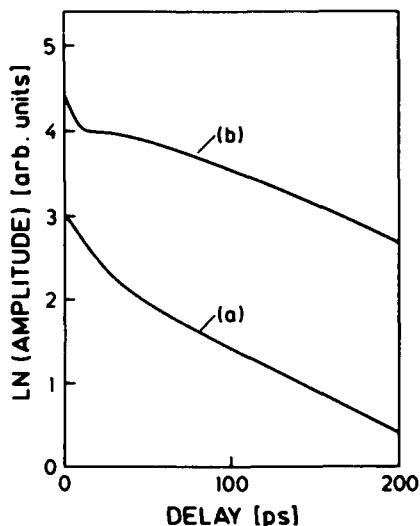


Figure 2. The modeled non-linear PL cross-correlation signal (arb. units) vs. delay (ps) for the two categories of solutions described in the text (LN denotes natural logarithm). Curve (a) $\tau_e < \tau_{ex}$. Curve (b) $\tau_e > \tau_{ex}$. For both curves $\tau_e = 15\text{ps}$, $\tau_h = 150\text{ps}$ and $n_{ex} = 10^{10}\text{cm}^{-2}$ were used. In (a), $C=3 \times 10^{-13}\text{cm}^2/\text{ps}$ giving $\tau_{ex}=570\text{ps}$. In (b), $C=3 \times 10^{-11}\text{cm}^2/\text{ps}$ giving $\tau_{ex}=5.7\text{ps}$.

free electron densities, respectively. Finally, the radiative recombination term, N/τ_{LT} , determines the photoluminescence intensity emitted from the sample.

Solving the (1)(2)(3) numerically, $n(t, \bar{t})$, $p(t, \bar{t})$, and $N(t, \bar{t})$ can be obtained and the time integration of $N(t, \bar{t})/\tau_{LT}$ gives the total time-integrated photoluminescence as a function of the delay between the two pulses. The non-linear part of the luminescence is then calculated by subtracting twice the luminescence calculated for one pulse from the total luminescence. Since the non-linearity in the photoluminescence output originates from a bimolecular process, we assume that terms in the excitation density dependence of the PL intensity higher than n_{ex}^2 are small. This assumption is supported by spectrally and temporally integrated PL measurements described later. In this case, the sum frequency signal in the PL cross-correlation measurement is proportional to the calculated non-linearity.

Because exciton formation is a bimolecular process, the growth of the exciton population is non-exponential and has no single characteristic time. However, we can define a density dependent forma-

tion time, τ_{ex} , equal to the $1/e$ time for a photoexcited population of electrons and holes to form excitons in the absence of tunneling. Setting all tunneling rates to zero in (1)(2)(3), this $1/e$ time is given by $\tau_{ex} = (e-1)/Cn_{ex}$. Assuming that $\tau_e \ll \tau_h$, two categories of solutions may be obtained depending whether $\tau_e < \tau_{ex}$ or $\tau_e > \tau_{ex}$, as illustrated in Figure 2. For $\tau_e < \tau_{ex}$ (curve a), the modeled signal closely approximates to two exponential decays with time constants given by τ_e and τ_h . For $\tau_e > \tau_{ex}$ (curve b), the fast decay becomes first faster than τ_e but then exhibits a non-exponential 'shoulder'. Finally, a slow decay in the signal is obtained which tends to an exponential decay with a time constant given by τ_h . The initial fast decay followed by a non-exponential shoulder corresponds to the case where the non-linearity is first strongly reduced by very fast exciton formation and then recovers slightly as excitonic electrons tunnel and free holes are released which may contribute again to further exciton formation.

Note that an exact solution to (1)(2)(3) exists for excitation by a single delta-like pulse if the tunneling times are short compared to the exciton formation time. For this approximation the total luminescence intensity is proportional to n_{ex}^2 . Since τ_{ex} increases with decreasing n_{ex} , below a certain excitation intensity which is low enough to make $\tau_{ex} \gg \tau_e, \tau_h$ a square law dependence of the photoluminescence on n_{ex} is expected.

The value of the radiative lifetime has negligible influence on the temporal decay of the non-linearity as long as the radiative lifetime is much longer than the fastest tunneling time. The value of τ_{LT} in the narrow well is taken to be the same as the TRPL decay time of the narrow well of sample 20 (230ps) so this condition is easily satisfied in the samples studied here.

Finally, it should be noted that only excitons with centre of mass momentum, K , near $K=0$ may recombine radiatively [3]. The increase of the number of excitons near $K=0$ due to hot exciton cooling to the lattice temperature causes a finite rise-time of the excitonic PL as measured in conventional TRPL measurements performed below 60K [4]. We emphasise that because the time-integrated PL is measured in our experiments, hot exciton cooling has no influence on the measured non-linear PL signal as a function of delay, but only introduces a constant amplitude pre-factor. This is a particular

advantage of this technique compared to conventional TRPL, where the strong influence of exciton cooling on the PL risetime makes accurate measurement of exciton formation rather difficult.

Results

Figure 3 shows the spectrally and temporally integrated exciton PL (arbitrary units) as a function of n_{ex} for QW_n and QW_w of sample 4 and QW_n of sample 20. Photoluminescence excitation spectroscopy measurements verified that the luminescence originated from the heavy-hole exciton line.

For QW_n of sample 4, where the tunneling out of the well is efficient, the expected strong non-linear variation of the integrated luminescence signal is observed. The gradient of 2 on the log-log scale indicates a square law dependence at low excitation as predicted for the model when $\tau_e < \tau_{ex}$. By contrast, the PL from QW_w of sample 4 and QW_n of sample 20, where tunneling out of the well is absent, exhibits no measurable non-linearity over almost four orders of magnitude variation in the excitation density. This is consistent with the bimolecular exciton formation model since competition with tunneling is required for the non-linear dependence of the PL on n_{ex} to be revealed. Figure 4 shows non-linear PL curves from sample 4 (4nm barrier) at two different excitation densities, the best fit to the data using

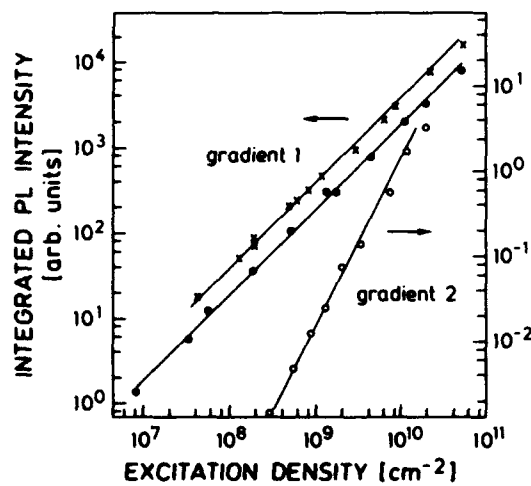


Figure 3. Integrated PL (arb. units) vs. n_{ex} at 8K for: QW_n of sample 4 (circles), QW_w of sample 4 (dots) and QW_n of sample 20 (crosses).

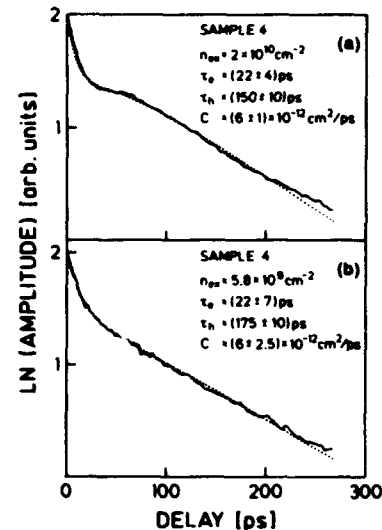


Figure 4. PL cross-correlation signal vs. delay for QW_n of Sample 4 at (a) $n_{ex}=2 \times 10^{10} \text{ cm}^{-2}$ and (b) $n_{ex}=5.8 \times 10^9 \text{ cm}^{-2}$. Also shown is the theoretical fit.

the model described above, and the fit parameters used. The same values of C ($6 \times 10^{-12} \text{ cm}^2/\text{ps}$) and τ_e (22ps) are used in both cases but a smaller hole time is required in the higher density case. However, the difference between the hole times only slightly exceeds the maximum error in the fitting procedure.

The higher excitation curve (Fig. 4a) shows the non-exponential shoulder region predicted by the model for the $\tau_e > \tau_{ex}$ case (see Fig. 2). The value of C is determined most accurately in this regime because the fast decay is then given mainly by the exciton formation process.

Figure 5 shows the results of the higher excitation measurement on sample 3. The initial rapid decay in the full delay range measurement (Fig. 5a) is time resolution limited by the large electronic time constant required on this extremely weak luminescence line. Fig. 5b shows a repeated measurement over a shorter delay range which is not resolution limited. The fit is the same as in Fig. 5a, showing good agreement using these fit parameters. Shorter tunneling times ($\tau_e = 7 \text{ ps}$ and $\tau_h = 66 \text{ ps}$) are obtained, as expected for a thinner barrier, but the same C value as for sample 4 has been used. The non-exponential shoulder near 60ps observed for sample 4 is now absent because τ_e is now less than τ_{ex} . A similar ratio of the electron and hole tunneling times is obtained for samples 3 and 4.

The good agreement between experiment and

model as a function of barrier thickness and n_{ex} confirms that the non-linear PL originates from the competition between exciton formation and tunneling, and demonstrates the bimolecular nature of exciton formation. It should be stressed that although the quantitative values are obtained from a three parameter fit, the accuracy of the values remains quite high since τ_h is relatively independent of the other parameters, and C and τ_e may be distinguished by varying n_{ex} .

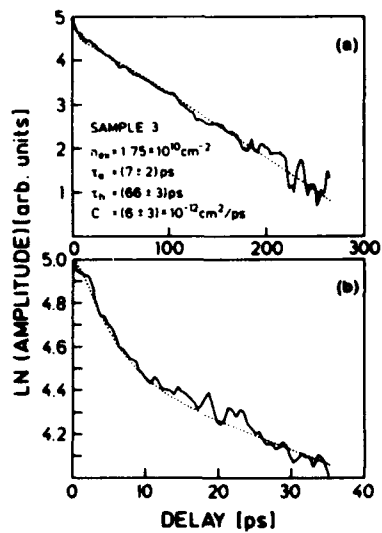


Figure 5. PL cross-correlation signal vs. delay for QW₃ of sample 3 at $n_{ex}=1.75 \times 10^{10} \text{ cm}^{-2}$. Also shown is the theoretical fit to the data.

Discussion

We have obtained a value for the bimolecular exciton formation coefficient, C, in the range $n_{ex}=6 \times 10^9 \text{ cm}^{-2}$ to $2 \times 10^{10} \text{ cm}^{-2}$ for excitation at 715nm. The exciton formation time, τ_{ex} , is $(14.4 \pm 2.0) \text{ ps}$ at $2 \times 10^{10} \text{ cm}^{-2}$. This value of C is strictly only determined in the time between photo-excitation and electron tunneling, raising the question whether, in the absence of tunneling, the value of C would change at later times. For example, as the carriers cool the probability of exciton formation could be altered. Note however that an exponential decay of the non-linearity due to free hole tunneling is observed in both sample 3 and 4 as predicted by a model that assumes C is constant and independent of carrier temperature. This suggests

that at least the cooling of free holes (which remain from the first pulse) on a 50ps to 250ps timescale does not strongly affect the probability of exciton formation.

Next, we comment on another possible mechanism for exciton formation: that exciton formation could occur mainly geminately, i.e. between electrons and holes created by the same excitation photon. We might expect this possibility if the Coulomb correlation in the band between the photo-created free electron-hole pair dominates over any scattering processes which allow the electron and hole to move apart. In the limit of only geminate exciton formation, no non-linear signal would be generated in our samples because geminate formation is effectively a monomolecular process with a single characteristic time which is independent of excitation density. We therefore discount this possibility. We can also exclude the possibility of a small geminate contribution to the exciton formation rate because the square law variation obtained in Figure 3 is in agreement with that predicted for pure bimolecular exciton formation in a tunneling sample (geminate formation would generate a linear dependence). Such a geminate contribution should also become more significant as the excitation density is lowered since the bimolecular rate becomes weaker, but no deviation from a gradient of two is observed over the entire range. We therefore conclude that in our experiment, for excitation densities above 10^8 cm^{-2} , excitons are formed purely non-geminately. This is perhaps not surprising since the carriers in this experiment are photoexcited with large excess energy. Several LO-phonons are immediately emitted and separation of the geminate pair is likely to be a very efficient process. Similar arguments can also be used to justify the extension of our conclusions to samples without tunneling. Geminate formation should in principle be more favoured at early times before scattering allows the geminate pair to move apart. Therefore the observation of a bimolecular mechanism at early times (20ps or less) strongly suggests that the same mechanism also applies at later times in isolated quantum wells, at least where the excess photon energy is sufficient to allow LO phonon emission.

Finally, we consider briefly the relative magnitude of the electron and hole tunneling times. The values of τ_e and τ_h differ by factors of 7.3 and 9.7 in samples 4 and 3, respectively. Such factors are

in clear disagreement with the factor of the order of 3000 predicted from the simple semi-classical model for electron and heavy-hole tunneling, and has also been observed elsewhere [1]. It should be noted that these experiments are performed at low excitation so that the small hole tunneling time is not due to the motion of the electron and hole populations being coupled by space charge induced field effects [5]. The explanation may be a reduction in the hole tunneling times due to valence band mixing effects [6], or may be more fundamental to the non-resonant tunneling process, the details of which, in particular the role of momentum conservation in the inter-well transfer process, are not yet well understood.

Conclusion

We have shown that the PL output of the narrow well of ADQW structures varies non-linearly with excitation density due to the competition between tunneling and bimolecular exciton formation. Using PL cross-correlation measurements we determine a value of $6 \times 10^{-12} \text{ cm}^2/\text{ps}$ for the bimolecular exciton formation coefficient. Values for the non-resonant electron and hole tunneling times are also obtained simultaneously under the same sample conditions. The hole tunneling times are much shorter than predicted by the simple semi-classical tunneling theory. We would like to thank W.W.Rühle and M.G.W.

Alexander for helpful discussions, and A.Schulz, H. Stützler, and S.Wöhrl for technical assistance.

References

1. For details of these experiments see for example : M. Nido, M.G.W. Alexander, W.W. Rühle, T. Schweizer, and K. Köhler, "Nonresonant electron and hole tunneling times in GaAs/Al_{0.35}Ga_{0.65}As in asymmetric double quantum well structures", *Appl. Phys. Lett.* **56**, 355 (1990), and the references therein.
2. D. von der Linde, J. Kuhl, and E. Rosengart, "Picosecond correlation effects in the hot luminescence of GaAs", *J. Luminescence* **24/25**, 675 (1981).
3. T.C. Damen, J. Shah, D.Y. Oberli, D.S. Chemla, J.E. Cunningham, and J.M. Kuo, "Exciton dynamics in GaAs quantum wells", *J. Luminescence* **45**, 181 (1990).
4. J. Feldmann, G. Peter, E.O. Göbel, P. Dawson, K. Moore, C. Foxon, and R.J. Elliot, "Linewidth dependence of radiative exciton lifetimes in quantum wells", *Phys. Rev. Lett.* **59**, 2337 (1987).
5. R. Sauer, K. Thonke, and W.T. Tsang, "Photo-induced space charge field build-up by asymmetric electron and hole tunneling in coupled quantum wells", *Phys. Rev. Lett.* **61**, 609 (1988).
6. E.T. Yu, M.K. Jackson, and T.C. McGill, "Hole tunneling times in GaAs/AlAs double barrier structures", *Appl. Phys. Lett.* **55**, 744 (1989).

Quantum Transport of an Electron Wave Packet Across a Heterostructure Discontinuity: Applications in the GaAs/Al_xGa_{1-x}As Heterosystem

Vasu Sankaran and Jasprit Singh

*Department of Electrical Engineering and Computer Science, 2234 EECS
Building, University of Michigan, Ann Arbor, Michigan 48109-2122*

Abstract

A formalism is presented to study quantum transport properties of electrons in semiconductor heterostructures. The time evolution of multiband electronic states is determined by numerically solving the time dependent Schrödinger equation in the tight-binding representation. We have studied the transport of an electron wavepacket injected from Al_xGa_{1-x}As across $\Gamma - \Gamma$ and $\Gamma - X$ discontinuities into GaAs. The gross transport properties of the transmitted wavepacket are altered within a time scale of the order of 100 fs. We have also studied tunneling through direct and indirect Al_xGa_{1-x}As barriers, and find it reasonable to use WKB-type expressions to describe tunneling through direct barriers. But the problem is more complicated for indirect barriers, where the character of the bandedge states in the barrier is drastically different from that in the well, and there is a strong suppression of tunneling.

I Introduction

Ia Tunneling

Tunneling of electrons and holes through barriers has been an area of intense research for decades, and there is renewed interest in the subject due to recent advances in heterostructure technology. A particular feature of tunneling which has drawn much attention recently is the role of the symmetry of the basis states underlying the representation of elec-

tronic states in the tunneling process. For example, in direct bandgap structures made from GaAs, Al_xGa_{1-x}As with $x \leq 0.3$, tunneling is adequately described by simplistic formalisms such as the WKB method based on single band effective mass theory. The conduction band minimum is at the Γ point in both well and barrier materials, where the cell periodic part of the electron wavefunction is primarily *s*-type. But this is not true for indirect barriers (Al_xGa_{1-x}As with $x \geq 0.4$), since electrons in the Γ minimum of the well region are primarily *s*-type, while the barrier states have strong *s-p* character. Tunneling prefactors have been observed to drop by orders of magnitude when the barrier changes from direct to indirect [1].

Tunneling properties are often deduced from the asymptotic behaviour of stationary scattering states, by examining the transmitted and reflected components of an incident plane wave. For instance, in the scalar case, we would seek solutions to the time independent Schrödinger equation with the asymptotic boundary conditions:

$$\psi(x) = \begin{cases} e^{ikx} + Re^{-ikx}, & x \rightarrow -\infty \\ Te^{-ikx}, & x \rightarrow +\infty \end{cases}$$

This method can be extended to multiband wavefunctions [2, 3, 4]. Analytic solutions, however, can be obtained only for heterostructures with simple potential profiles. For arbitrary potential profiles, or even with simple profiles under an applied electric field, one has to resort to numerical means of solving for the stationary solutions. This difficulty is circumvented to some extent by the WKB approximation. But this approach is valid only for smoothly

varying potentials, and introduces significant error when applied to heterostructures of narrow dimensions. Moreover, there is no straightforward way of extending the WKB expressions to multiband wavefunctions.

An alternative dynamic formulation of the tunneling problem that we have chosen for our work involves direct time domain study of the time evolution of localized wavepackets, an approach that is more suitable for studying tunneling and transport in localized heterostructure potentials in the presence of applied electric fields. To study the dynamic problem of the time evolution of a wavepacket $\psi(x, 0)$ in a time independent potential, we can consider the formal solution in terms of the stationary states of the system [5]:

$$\begin{aligned}\psi(x, t) &= \exp(-iHt/\hbar) \psi(x, 0) \\ &= \int dk a(k) e^{-iE(k)t/\hbar} u_k(x)\end{aligned}$$

where

$$a(k) = \langle u_k(x), \psi(x, 0) \rangle$$

However, we again face the problem of having to solve for a large number of stationary states first, and subsequently evaluate the integrals involved in the above expression. For arbitrary potentials, this is a cumbersome procedure. A different method, which has been applied to the scalar Schrödinger equation [6], is to expand the time evolution operator $\exp(-iHt/\hbar)$ as a power series in t , and to truncate the series by proceeding in infinitesimal time steps. In this work we have extended this method to study the time evolution of multiband wavepackets in heterostructures.

Ib Quantum Transport

Theoretical techniques to study time dependent electron transport in heterostructures use several approximations. In Monte Carlo methods the electron is described as a point particle whose transport properties (such as effective mass, scattering rates, etc.) change abruptly when it moves across a heterointerface. As the electron moves across a boundary, the role of central cell symmetries (i.e., Γ , X , L character) is suppressed. This description is valid in heterostructures where electrons travel ≈ 1000 Å in each region and where the character of the band extrema is unaltered across different regions. In quantum transport models based on effective mass theory the electron wavepacket is assumed to abruptly see different material properties

across a discontinuity. Usually a one band effective mass equation is employed, with the implicitly assumption that the character of the Bloch function is not significantly altered across different regions. This description is satisfactory in heterostructures of ≈ 100 Å dimension where effects of quantum confinement are important, but where the character of the band extrema are again unaltered. Such approximations do not hold in a number of ultrasmall electronic devices such as hot electron transistors and tunneling transistors, and cannot describe transport from direct to indirect materials across a heterointerface. To address quantum transport problems in such structures we have employed the numerical solution of the time dependent Schrödinger equation in the tight-binding representation to study the transport of an electron wavepacket launched from $\text{Al}_x\text{Ga}_{1-x}\text{As}$ into GaAs.

II Representation of Electronic States

The envelope function approximation based on the multiband effective mass theory of Luttinger and Kohn [7] has been applied extensively to study static and dynamic properties of charge carriers in heterojunctions and superlattices. In this description, the electronic state is described by "envelope functions" obeying Schrödinger-like equations which explicitly contain only the external perturbing potentials and not the underlying lattice potential. But this formalism is useful only if the materials comprising the heterostructure are chemically similar. To derive feasible boundary conditions for the envelope functions at an interface between two materials, the assumption is made that the zone center Bloch functions do not vary appreciably between them [8, 9]. This assumption will breakdown, for example, if the band extrema in the different materials lie at different points in the Brillouin zone. This situation arises in the $\text{GaAs}/\text{Al}_x\text{Ga}_{1-x}\text{As}$ heterosystem with an indirect AlGaAs barrier (X point minimum).

In this work, we choose to describe electron states in the conduction band in the tight-binding representation. The empirical tight-binding method [10] has proved useful in studying the electronic properties of solids and has been applied to study the real and complex band structure of bulk materials, energy levels in superlattices, and electronic states and transport properties at interfaces. These properties are derived implicitly through matrix elements dependent on the tight-binding pa-

rameters of materials comprising the heterostructure. Choosing the latter to yield the correct band gaps and band curvatures at points of high symmetry in the bulk bandstructures of these materials ensures an accurate description of the electronic state in the heterostructure. This implicit treatment is particularly well suited to study electronic properties in the GaAs/Al_xGa_{1-x}As system, since the tight-binding parameters of Al_xGa_{1-x}As for varying Al content may be obtained from those of GaAs and AlAs using the virtual crystal approximation, and experimentally measured band discontinuities built in by a right choice of the self-energy parameters. Moreover, since the complete bandstructure is contained in the tight-binding description, one need not be concerned specifically with the appearance of multiple band extrema or explicit boundary conditions for the components of the electronic wavefunction.

The bulk tight-binding state may be expressed in the familiar form:

$$\psi_n(\mathbf{k}, \mathbf{r}) = \sum_{\nu} \sum_l c_{n,\nu}(\mathbf{k}) e^{i\mathbf{k} \cdot (\mathbf{R}_l + \mathbf{r}_{\nu})} \times \xi_{\nu}(\mathbf{r} - [\mathbf{R}_l + \mathbf{r}_{\nu}]) \quad (1)$$

where:

- $\psi_n(\mathbf{k}, \mathbf{r})$ is the n^{th} eigenstate of crystal at wavevector \mathbf{k}
- l indexes Bravais lattice sites of the crystal
- ν runs over the different orbitals in the LCAO basis, (indexing multiple ions as well as multiple orbitals of the same ion in the primitive cell)
- \mathbf{r}_{ν} is the relative position of center of orbital ν within the primitive cell
- $\xi_{\nu}(\mathbf{r} - \mathbf{r}_{\nu})$ are atomic-like orbitals
- $c_{n,\nu}(\mathbf{k})$ are the bulk expansion coefficients.

We have employed an 8-band, sp^3 basis set (4 cation and 4 anion orbitals) for the GaAs/Al_xGa_{1-x}As system, retaining up to second nearest neighbour interactions, although our approach can be extended to any multiband Hamiltonian.

Since we are interested in studying dynamical effects in heterostructures, we generalise the bulk tight-binding representation to construct time dependent states:

$$\psi(\mathbf{r}, t) = \sum_{\nu} \sum_l c_{\nu}(\mathbf{R}_l + \mathbf{r}_{\nu}, t) \xi_{\nu}(\mathbf{r} - [\mathbf{R}_l + \mathbf{r}_{\nu}]) \quad (2)$$

We thus define a separate envelope function c_{ν} for each distinct orbital in LCAO basis [11]. The atomic orbitals constituting our basis may be assumed to satisfy the orthonormality condition:

$$\int d\mathbf{r} \xi_{\nu}^*(\mathbf{r} - [\mathbf{R}_l + \mathbf{r}_{\nu}]) \xi_{\nu'}(\mathbf{r} - [\mathbf{R}_{l'} + \mathbf{r}_{\nu'}]) = \delta_{\nu,\nu'} \delta_{l,l'} \quad (3)$$

With the aid of this condition the probability of finding an electron within a region much larger than the dimension of the primitive cell is taken to be

$$P_e(t) = \sum_{\nu} \sum_l |c_{\nu}(\mathbf{R}_l + \mathbf{r}_{\nu}, t)|^2 \quad (4)$$

where the summation is over those lattice sites contained in the said region.

The in-plane periodicity of the heterostructure ensures that coherent tunneling conserves the in-plane wavevector, and we need only construct states which are eigenstates of the in-plane translation operators:

$$\psi(\mathbf{r}, t) = \sum_m \sum_{\nu} c_{\nu}(m, t) \sum_n e^{i\mathbf{k}_{\parallel} \cdot \mathbf{R}_n} \xi_{\nu}(\mathbf{r} - [\mathbf{R}_n + \mathbf{r}_m]) \quad (5)$$

where:

- m is an index over lattice planes, \mathbf{r}_m being an arbitrarily chosen origin in each plane
- n is an index over *in-plane* lattice translations \mathbf{R}_n

All the ions in a given lattice plane are identical, and ν identifies the different orbitals associated with these ions, as before. We are thus left with one-dimensional envelope functions $c_{\nu}(m, t)$, one for each distinct orbital in the basis.

In order to model the escape of electrons from a quantum well through a barrier of finite width, the initial electron wavepacket is constructed as a bound state in the well. Using the form (5) for ψ , we solve the Schroedinger equation:

$$H\psi(\mathbf{r}, 0) = E\psi(\mathbf{r}, 0) \quad (6)$$

This may be readily converted to a matrix equation by taking the scalar product of either side successively with distinct orbitals on each plane. For the right hand side we obtain:

$$\int d\mathbf{r} \xi_{\mu}^*(\mathbf{r} - [\mathbf{R}_p + \mathbf{r}_p]) \psi(\mathbf{r}, 0) = c_{\mu}(p, 0) e^{i\mathbf{k}_{\parallel} \cdot \mathbf{R}_p} \quad (7)$$

where \mathbf{R}_k is an in-plane lattice translation in plane p . On the left hand side we have:

$$\int d\mathbf{r} \xi_\mu^*(\mathbf{r} - [\mathbf{R}_k + \mathbf{r}_p]) H \psi(\mathbf{r}, 0) = \sum_m \sum_\nu c_\nu(m, 0) \sum_n e^{i\mathbf{k}_\nu \cdot \mathbf{R}_n} \times \int d\mathbf{r} \xi_\mu^*(\mathbf{r} - [\mathbf{R}_k + \mathbf{r}_p]) H \xi_\nu(\mathbf{r} - [\mathbf{R}_n + \mathbf{r}_m]) \quad (8)$$

The summation on the right is over those neighbouring orbitals with which the orbital centered at $[\mathbf{R}_k + \mathbf{r}_p]$ has nonzero matrix elements. The latter are, in fact, exactly the known tight-binding parameters of the bulk material. For parameters describing interactions at an interface, we have used the average value of the corresponding bulk parameters of the two materials on either side of the interface. The infinite set of equations obtained in this manner may be truncated using the boundary condition that the envelope functions vanish at sufficient distances into barriers on either side.

We model electron transport across an interface by studying the time evolution of the wavepacket

$$\psi(\mathbf{r}, 0) = \int dk_z A(k_z) \psi_n(\mathbf{k}, \mathbf{r}) \quad (9)$$

where $A(k_z)$ is an envelope function in \mathbf{k} -space, peaked at wavevector \mathbf{k}_0 . Such a wavepacket moves in the bulk material with the group velocity at \mathbf{k}_0 :

$$v_g = \frac{1}{\hbar} \frac{\partial E_n(\mathbf{k}_0)}{\partial k_z} \quad (10)$$

Thus tight-binding form of the above wavepacket is:

$$\psi(\mathbf{r}, 0) = \sum_m \sum_\nu c'_\nu(m, 0) \sum_n e^{i\mathbf{k}_\nu \cdot \mathbf{R}_n} \xi_\nu(\mathbf{r} - [\mathbf{R}_n + \mathbf{r}_m]) \quad (11)$$

where

$$c'_\nu(m, 0) = \int dk_z A(k_z) c_{n,\nu}(\mathbf{k}) e^{i\mathbf{k}_z z_m} \quad (12)$$

The transport properties of electrons across the interface is determined by studying the time evolution of this wavepacket.

III Time Evolution of Multi-band Wavepackets

For a scalar Schrödinger equation, the time evolution of a wavepacket in a time-independent potential is known to be:

$$\psi(\mathbf{r}, t) = e^{-iHt/\hbar} \psi(\mathbf{r}, 0) \quad (13)$$

The details of solving this equation by discretising the time interval of interest into infinitesimal steps δt are given in Ref. [6]. For δt sufficiently small, we can approximate

$$\exp(-iH\delta t/\hbar) \approx 1 - iH\delta t/\hbar \quad (14)$$

However, this approximation is not unitary, and probability is not conserved. A better approximation which is unitary and also second order accurate in δt , is the Cayley form:

$$\exp(-iH\delta t/\hbar) \approx \frac{1 - iH\delta t/2\hbar}{1 + iH\delta t/2\hbar} \quad (15)$$

A numerically stable implicit form of the above equation is:

$$(1 + iH\delta t/2\hbar)\psi(\mathbf{r}, t + \delta t) = (1 - iH\delta t/2\hbar)\psi(\mathbf{r}, t) \quad (16)$$

We have extended this procedure to the multi-band tight-binding Hamiltonian. Using the tight-binding wavefunction, and taking scalar product on both sides of above equation with $\xi_\nu(\mathbf{r} - [\mathbf{R}_i + \mathbf{r}_p])$, we obtain simultaneous equations at each time step for the coefficients $c_\nu(p, t + \delta t)$, in terms of $c_\nu(p, t)$, and the bulk tight-binding parameters. To reduce the resulting infinite set of equations to a finite number, it is necessary to maintain the boundary condition of the wavefunction vanishing at the edges of the simulation region. It is therefore necessary to choose a simulation region that is long enough not to introduce spurious wave reflections during the initial time evolution.

Assuming that the tunneling escape of carriers can be described by an exponential decay law, tunneling times τ are obtained from the initial decay rate of probability in the starting well:

$$\tau = \frac{P(0)}{(\Delta P/\Delta t)} \quad (17)$$

IV Results and Conclusion

We examine the escape of the quasibound, ground state electron wavepacket from an 56 Å (30 monolayer) GaAs well through direct and indirect Al-GaAs barriers (Al_{0.3}Ga_{0.7}As barrier for the direct case, and Al_{0.6}Ga_{0.4}As barrier for the indirect case). The on-site tight-binding parameters adjusted to give a Γ - Γ conduction band discontinuity of 0.25 eV for the direct barrier, and 0.5 eV for the indirect barrier, yielding 0.23 eV Γ - X separation in the indirect barrier. The character of the cell periodic

part of the Bloch function is found to be critical in the tunneling process. The wavepacket emerges rapidly through the direct barrier, but much more slowly through an indirect barrier of the same width even though the X barrier height of 0.23 eV is nearly equal to the direct barrier height. The process considered here is quite similar to nuclear alpha decay, and we can obtain an estimate for τ based on single-band effective mass theory and the WKB approximation [5], as $\tau = (\nu T)^{-1}$, where ν is the frequency of electron collisions with the barrier, and T the transmission coefficient through the barrier. We use the expressions

$$\nu = \frac{1}{L_w} \sqrt{\frac{E_l}{2m_{wl}}} \quad (18)$$

and

$$T = \exp \left[-\frac{2}{\hbar} \int_0^{L_b} dz \sqrt{2m_{bl}(V_b - E_l - Fz)} \right] \quad (19)$$

where $m_{wl}(m_{bl})$ is the longitudinal effective mass in the well (barrier), $L_w(L_b)$ is the width of the well (barrier), V_b the barrier height and E_l the energy of longitudinal motion in the well,

$$E_l = \frac{\hbar^2}{2m_{wt}} (k_x^2 + k_y^2) \quad (20)$$

with E being the energy of the quasibound state measured with respect to the bottom of the conduction band in bulk GaAs, and m_{wt} the transverse effective mass.

The tunneling time obtained from our model is compared with the WKB estimate based on the Γ barrier minimum, for varying electric field strengths and barrier thicknesses in Fig. 1 and Fig. 2, respectively. We see good agreement between the WKB estimate and our more complete model for direct barriers. Single band effective mass theory works well for this case since the conduction band minimum is at Γ in both well and barrier, and nature of Bloch functions in the two regions are compatible. But neither the Γ nor the X barrier heights provides an acceptable WKB fit for the indirect barrier. Tunneling in indirect barrier is also strongly suppressed as compared to an identical direct barrier. The dependence of indirect barrier tunneling on electric field and barrier thickness suggests that it is primarily the Γ -point states in the barrier contributing to the tunneling process.

Figure 3 depicts the transient velocity of a Γ -electron wavepacket as it is launched from $\text{Al}_{0.3}\text{Ga}_{0.7}\text{As}$ into GaAs. The velocity of the transmitted wavepacket (velocity of its peak) attains a

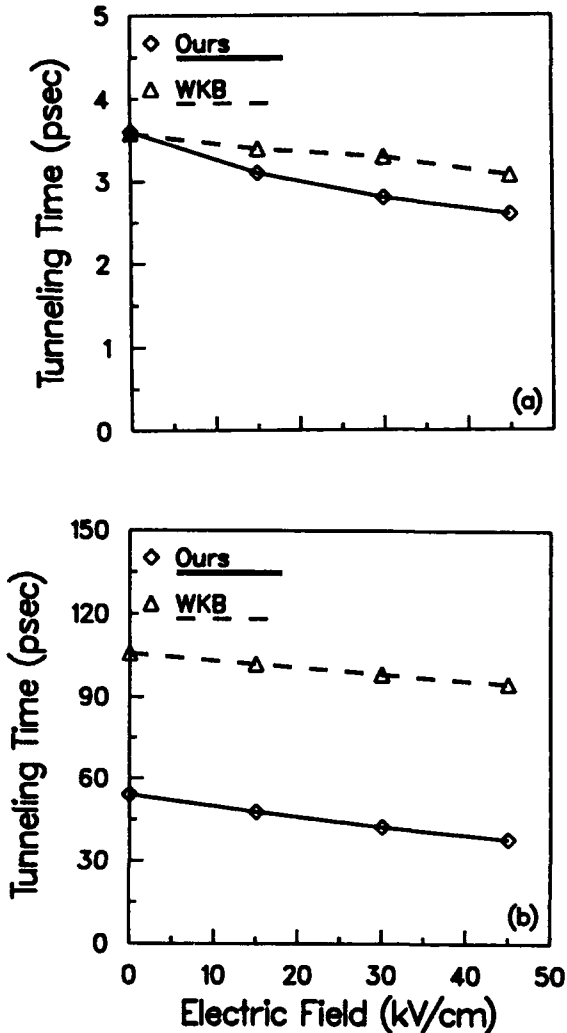


Figure 1: Tunneling time dependence on electric field for tunneling from a ≈ 100 meV quasibound ground state of a 56 Å GaAs well through 42 Å barriers of (a) $\text{Al}_{0.3}\text{Ga}_{0.7}\text{As}$, and (b) $\text{Al}_{0.6}\text{Ga}_{0.4}\text{As}$.

steady value after 60 fsec. This steady value is exactly the group velocity in GaAs as obtained from the bandstructure using Eqn. (10), at a value of k_z at which the bulk conduction band energy is equal to the mean energy of the incident wavepacket, both measured with respect to a common reference. The mean energy of the incident wavepacket was 103 meV from the Γ -point in $\text{Al}_{0.3}\text{Ga}_{0.7}\text{As}$. Similarly, Fig. 4 depicts the transient velocity of an X -valley electron launched from $\text{Al}_{0.6}\text{Ga}_{0.4}\text{As}$ into GaAs. The mean energy of the initial wavepacket was 105 meV with respect to the X -minimum of $\text{Al}_{0.6}\text{Ga}_{0.4}\text{As}$. The transient time is found to be 150 fsec in this case. Thus electron transport becomes bulk-like in ≈ 100 fsec for both cases.

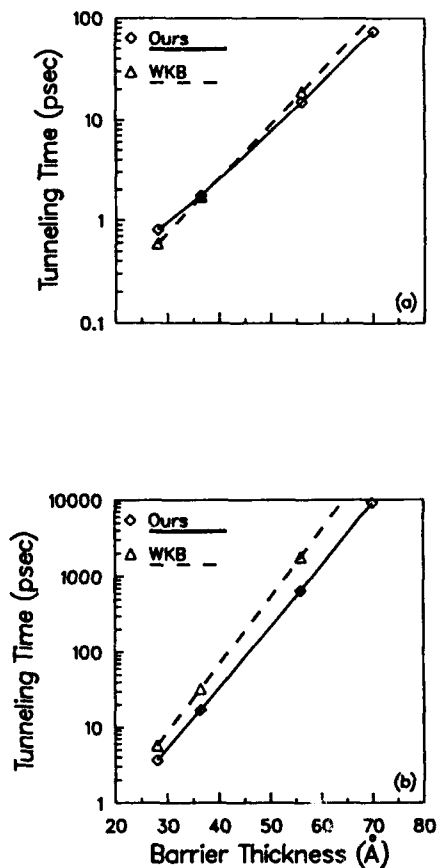


Figure 2: Tunneling time dependence on barrier thickness for tunneling from a ≈ 100 meV quasibound ground state of a 56 Å GaAs well at 15.0 kV/cm through (a) $\text{Al}_{0.3}\text{Ga}_{0.7}\text{As}$, and (b) $\text{Al}_{0.6}\text{Ga}_{0.4}\text{As}$ barriers.

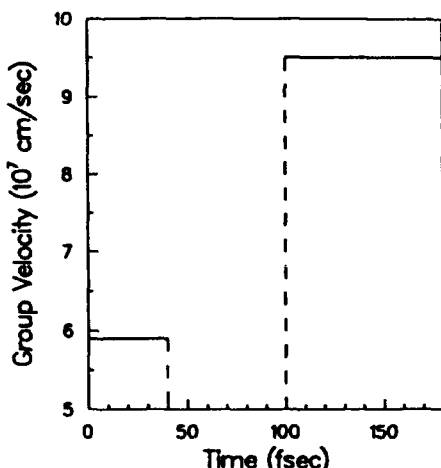


Figure 3: Transient group velocity of a Γ -electron wavepacket launched from $\text{Al}_{0.3}\text{Ga}_{0.7}\text{As}$ into GaAs.

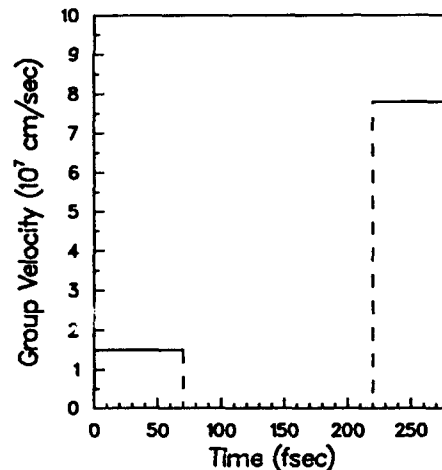


Figure 4: Transient group velocity of an X -electron wavepacket launched from $\text{Al}_{0.6}\text{Ga}_{0.4}\text{As}$ into GaAs.

Acknowledgement

This work was funded by the U.S. Army Research Office (URI Program) under Grant DAAL03-87-K-0007. Part of this work was also supported by the Air Force URI program.

References

- [1] P. M. Solomon, S. L. Wright, and C. Lanza, *Superlattices and Microstructures* **2**(6), 521 (1986).
- [2] R. Wessel, and M. Altarelli, *Phys. Rev. B*, **39**(17), 12802 (1989).
- [3] R. Wessel, M. Altarelli, *Phys. Rev. B*, **39**(14), 10246 (1989).
- [4] S.-L. Chuang, *Phys. Rev. B*, **40**(15), 10379 (1989).
- [5] L. I. Schiff, *Quantum Mechanics*, McGraw-Hill, New York (1949).
- [6] A. Goldberg, H. M. Schey, and J. L. Schwartz, *Amer. J. Phys.*, **35**(3), 177 (1967).
- [7] J. M. Luttinger, and W. Kohn, *Phys. Rev.* **97**(4), 869 (1955).
- [8] G. Bastard, and J. A. Brum, *IEEE J. Quant. Elec.* **QE-22**(9), 1625 (1986).
- [9] M. Altarelli, in *Heterojunctions and Semiconductor Superlattices*, Proc. of Les Houches Winterschool, ed. G. Allan, G. Bastard, et al, Springer (1986).
- [10] J. C. Slater, and G. F. Koster, *Phys. Rev.* **94**(6), 1498 (1954).
- [11] J. M. Ziman, *Principles of the Theory of Solids*, II edn., Cambridge Univ. Press, Cambridge (1979).

Materials

Strained-Layers for Electronics and Optoelectronics

David R. Myers

Division 1141, Sandia National Laboratories,
Albuquerque, New Mexico 87185-5800

Abstract

The strain associated with intentionally lattice-mismatched (strained-layer) heteroepitaxy provides a novel method for tailoring material band structure to enhance device performance through optimization of material structure. The applications of strained-layer epitaxy to heterojunction transistors and semiconductor lasers are presented.

Introduction

Progress in heterojunction lasers transistors began in the (essentially) lattice-matched (Al,Ga)As/ GaAs compound semiconductor system -- that is, in a system in which the materials in their bulk crystalline form have lattice constants that are identical to $\approx 0.3\%$. Unfortunately, nature provides relatively few lattice-matched compound-semiconductor systems: (Al,Ga)As/GaAs, (In,Ga)As/InP, (In,Al)As/InP, (In,Ga)AsP/InP, and HgTe/CdTe. To expand the number of heterojunction systems that can be exploited to fabricate advanced electronic and optoelectronic devices, substantial effort has recently been devoted to understanding the heteroepitaxy of materials which differ in the lattice spacings of their bulk crystals. As a result, this field of lattice-mismatched, or *strained-layer*, heteroepitaxy has produced a dramatic increase in our understanding of the mechanisms for the accommodation of lattice mismatch, strain-tailoring of material band structures, and the stability of strained-layer structures.

Five major mechanisms that allow the accommodation of lattice mismatch have been experimentally observed.

In Fig. 1 we illustrate these mechanisms: dislocation generation at the heteroepitaxial interface [1, 2]; coherent epitaxy [3] (accommodation of the lattice mismatch by distortion of the epitaxial layer); metastable epitaxy [4] (distortion of the epitaxial layer with only a fraction of the strain energy in excess of that allowed by equilibrium thermodynamics being relieved by dislocations); bending of the epitaxial layer [5]; and tilt of the lattices with respect to each other [6]. However, not all of these mechanisms are compatible with device optimization. It was the critical insight of Obsourn [7] in 1983 that the strain associated with strained-layer, coherent epitaxy could be exploited to tailor material band structures, and thus provide an extra degree of freedom to optimize device performance in dislocation-free structures.

Strained-Layer Stability Limits

The stability of lattice-mismatched epitaxial layers is determined by the competition between the energy required to distort epitaxial layers vs. the energy required to nucleate the dislocations that would relieve the lattice strain. This simple concept still causes considerable confusion, mainly because strained-layer growth occurs under non-equilibrium (kinetically controlled) conditions. Thus, the material that emerges from the growth system can exceed the limits set by equilibrium thermodynamics by as much as an order of magnitude. As has been described in recent reviews [1,8], the ultimate stability of a lattice-mismatched epitaxial layer can best be determined by a post-growth treatment (implantation and/or annealing at elevated temperatures) that provides sufficient energy to the materials to drive a potentially metastable system over any kinetic barriers that separate its equilibrium configuration from its metastable configuration.

FIVE WAYS TO ACCOMODATE LATTICE MISMATCH

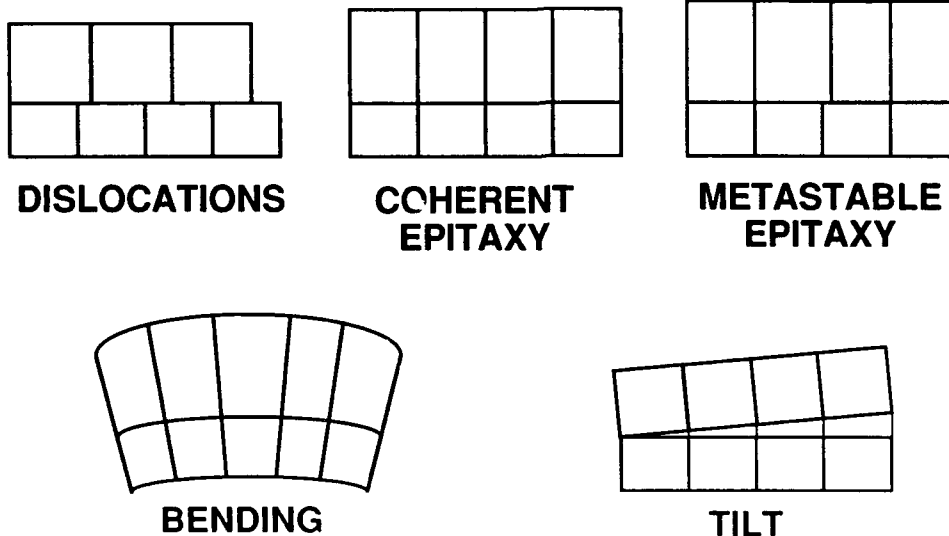


Figure 1. Schematic illustration of the five major ways to accommodate lattice mismatch in heteroepitaxy. These mechanisms have been experimentally observed (refer to text).

Confusion also arises regarding the appropriate equations to apply in calculating the critical thicknesses (thermodynamic stability limit). Matthews and Blakeslee, in their pioneering early work [9], determined equations appropriate for two limiting cases: either a single, strained, surface epitaxial layer (single-kink strain relief [8]), or a strained layer in an infinitely repeating superlattice (the double-kink strain relief [8]). Although well described, these limiting conditions are rarely seen in device applications. Instead, most devices contain strained layers of finite thickness usually capped with unstrained surface layers, also of finite thicknesses. These more commonly encountered structures were examined by Tsao and Dodson [10], who discovered that the stability of such strained heteroepitaxial layers against the single-kink strain-relief mechanism could be accurately predicted by evaluating an equivalent average surface strain to use with the Matthews and Blakeslee equation for a surface strained layer. The equivalent average surface strain is obtained by summing the strain-thickness product for each of the surface layers and dividing by the total epitaxial layer thickness. This Tsao-Dodson procedure determines the stability limits for most device structures, as long as the

strained-layers themselves satisfied the typically less demanding double-kink strain-relief stability criterion. For structures with multiple strained layers, this process needs to be repeated to examine the stability of each of the strained layers independently [8]. It is only the limiting case of the double-kink stability criteria that determines thermodynamic stability through only two parameters: the lattice mismatch and layer thickness. The more commonly encountered single-kink stability limit requires knowledge of three parameters: the lattice mismatch, the strained-layer thickness, and the thickness of the unstrained surface overlayer.

As an example, strained epitaxial layers used in most device applications exploit lattice mismatch of $\approx 1\%$. Such mismatch would be found for an epitaxial layer of $\text{In}_{0.14}\text{Ga}_{0.86}\text{As}$ strained to match the in-plane lattice spacing of a GaAs substrate, or for an epitaxial layer of $\text{Si}_{0.76}\text{Ge}_{0.24}$ strained to match the in-plane lattice spacing of a Si substrate. The maximum thickness of such strained layers, as set by the double-kink stability limit is 23 nm. If such layers are at the free surface of the device structure, their maximum thicknesses for

thermodynamic stability is approximately 12 nm. As unstrained surface material is grown above our example strained layer of 1% mismatch, the critical thickness as set by the more-demanding single-kink limit increases monotonically from the 12 nm limit to the 23 nm limit.

Thermodynamic stability limits become important **only** when device fabrication or device operation exposes the structure to sufficient energy to drive the material from its metastable configuration. For example, many devices, such as heterojunction field-effect transistors [11], can be fabricated from strained layers that exceed thermodynamic stability limits (i.e., metastable materials) without degrading material quality or device performance. The materials properties of these metastable devices are **not** degraded during fabrication precisely because they require only low-temperature processing, such as etching and alloying of ohmic contacts. The kinetic barrier that separates metastable materials from their strain-relieved state are substantial. To nucleate strain-relieving dislocations, one must break atomic bonds, at the cost of eV/atom. Such energies are not encountered during normal device operation, and thus allow metastable devices to remain in their metastable, as-grown configurations indefinitely. In contrast, processes that require thermal annealing at temperatures above the epitaxial growth temperature, such as implant activation anneals, intentional compositional disordering of quantum-well structures, or thermal oxidation of SiGe surface layers, provide sufficient amounts of external energy to the strained-layer system to drive metastable materials into their equilibrium (dislocated) configuration. If processes requiring elevated-temperature annealing and/or high-fluence ion bombardment are required, materials that satisfy the thermodynamic stability limits must be used in the device structure.

Strain Effects on III-V Semiconductor Band structures

As previously described, mismatch of $\approx 1\%$ can be tolerated by layers whose thicknesses are on the order of 10 to 30 nm - the range over which quantum size effects become important in determining energy levels of the strained layers. Quantum size effects for strained structures have been demonstrated to have important device advantages for direct-bandgap III-V semiconductors, and thus will form the basis for the following discussion.

Good successes in predicting the electronic structure and optical properties of strained quantum wells has been obtained by applying a two-band envelope-function model, as has been recently demonstrated by Fritz, et al. [12]. This model includes the effects of strain through deformation-potential and elasticity theory, including coupling to the split-off valence band. This model is an extension of Obsourn's original theory

[7], and includes empirically derived materials parameters. Similar treatments have already been described by other workers [13-15].

The direct bandgap III-V semiconductors of interest have the valence-band maxima and the conduction-band minimum at the center of the Brillouin (the Γ point). These bands consist of a conduction band of symmetry Γ_6 with a two-fold degeneracy, a four-fold degenerate valence band of symmetry Γ_8 , and a two-fold degenerate valence band (the split-off band) of symmetry Γ_7 , which is separated in energy from the Γ_8 valence bands due to the spin-orbit interaction. As summarized by Bastard [16], it is most convenient to use a basis in which the total angular momentum $J = L + \sigma$ and its projection along the z axis are diagonal, due to the non-zero spin-orbit interaction. This results in the Γ_6 conduction band having $|J, m_J\rangle$ components $|1/2, 1/2\rangle$; the degenerate Γ_8 valence band being characterized by one $|3/2, 3/2\rangle$ band and one $|3/2, 1/2\rangle$ band, and the split-off band Γ_7 being characterized by $|1/2, 1/2\rangle$.

The effects of biaxial compression on $<001>$ -oriented strained layers can be readily understood by following the process schematically illustrated in Fig. 2. A biaxial strain is identically equal to a hydrostatic compression plus an opposing uniaxial strain. The hydrostatic component does **not** alter the symmetry of the original crystal; thus, its effect is to change the relative positions of the conduction and valence bands. The hydrostatic component does not split degenerate energy levels. Unfortunately, empirical deformation potentials can only be obtained for the shift of the band gap with pressure, and not for the conduction bands and valence bands individually. Good fit to experiments have been obtained [12] in the absence of direct results by applying the theory of van de Walle [17] to estimate the pressure-induced shift of each of the conduction or valence bands. In contrast to the hydrostatic component, the uniaxial strain component lowers the symmetry of the crystal from that of unstrained bulk material; thus, it splits degenerate energy levels and further repositions the energy bands of the strained material.

Correct treatment of the bandgap for biaxially strained material requires consideration of the coupling between the $|3/2, 1/2\rangle$ valence band and the $|1/2, 1/2\rangle$ split-off band. Convenient formulas that include the coupling to the split-off band are provided by Ji, et al. [14]. Inclusion of this coupling is particularly important for material under biaxial tension and/or with type II (spatially indirect) offsets.

The Effect of Biaxial Compression on III-V Semiconductor Band Structures

Since:

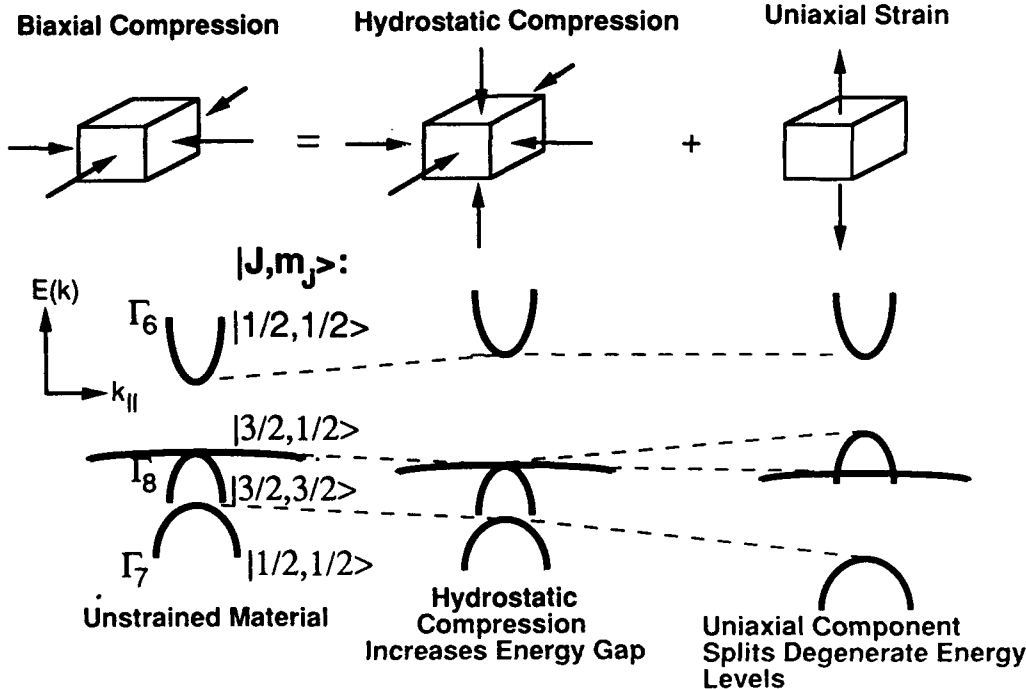


Fig. 2. Illustration of the effects of biaxial compression on the band structure of direct-gap III-V semiconductors. Because the biaxial compression is identically equivalent to a hydrostatic compression with an opposing uniaxial strain, one can intuitively understand the shifts in the band positions. The bands are labeled both by their symmetry representation and also by their total spin components $|J, m_J\rangle$. Shifts produced by biaxial tension would be opposite those produced by biaxial compression.

The correct band states form the basis for the calculation of the quantum-confined states using the envelope-function method (e.g., [12,13,16]). Remarkably, this approach has proven effective even for the calculation of quantum-well states that are perturbed by a single strained monolayer [18]. To conclude our discussion, the identical equations apply to the calculation of shifts produced by biaxial tension; however, since the sign of the strain is changed, the shifts from biaxial tension are opposite those produced by biaxial compression.

Experimental results demonstrate that a direct benefit for a strained layer under biaxial compression is that the strain-split $|3/2, 1/2\rangle$ valence band features a reduced density of states in the plane normal to the growth direction (although the same deformations lead to a greater density of states for the $|3/2, 1/2\rangle$ along the growth direction). Because the effective mass is related to the density of states per unit energy, the strained layer under biaxial compression sees a lower transport

effective mass along directions parallel to the quantum well [19]. This reduced hole mass is of interest for improving p-channel heterojunction transistors and semiconductor lasers, as is described below. In contrast, the effect of the strain on electron masses is substantially smaller [19].

When strained layers are grown on surfaces that differ from the $<001>$ orientation, an additional effect arises because the III-V semiconductors are piezoelectric. The strain distortion of the layers induces electric fields in these materials; from crystalline symmetry, these piezoelectric fields cancel only for $<001>$ -oriented strains. For other crystalline orientations the piezoelectric contribution is nonzero, and is maximized for $<111>$ -oriented layers. The piezoelectrically induced fields for alternative (non- $<001>$) crystallographic orientations lead to interesting possibilities for optical modulators, etc. [20]

Device Applications

The major benefits for heterojunction device performance from strained-layer epitaxy are the flexibility in composition made possible by the use of lattice-mismatched alloys, splitting of degenerate valence bands, and the use of strain as well as composition to tailor bandgaps. These advantages of strained-layer epitaxy are demonstrated by heterojunction-field-effect transistors (FETs) and semiconductor lasers.

The initial application of strained-layer epitaxy to heterojunction transistors was motivated by a desire to replace the GaAs channel in n-channel, MODulation-Doped Field-Effect Transistors (MODFETs) with a strained-layer (In,Ga)As channel [21]. In these devices, the compositional flexibility of strained layer epitaxy allowed the use of a deeper quantum well of (In,Ga)As to replace the wider bandgap GaAs channels. Thus, the same degree of quantum confinement in these MODFETs could be obtained by an (In,Ga)As channel with barrier layers of lower Al mole fractions in modulation doping region than was possible with GaAs-channel MODFETs with higher Al mole fractions in the modulation-doping region. The use of lower Al mole-fraction material in the modulation doping region eliminated problems with DX centers that occur in higher-Al-mole-fraction, (Al,Ga)As/GaAs devices. These DX centers are responsible for persistent photoconductivity and degraded transconductances in the unstrained devices. The same desire to obtain deeper quantum wells for heterojunction FETs motivates the use of intentionally lattice-mismatched (In,Ga)As ternary layers to improve n-channel transistors grown over InP substrates [22]. Most of these heterojunction FETs maximize gate control over channel current by minimizing the thickness of unstrained surface material between the gate and the quantum-well channel, and thus are metastable against the single-kink mechanism [11]. Since these devices are manufactured using mesa isolation and alloyed contacts, they survive the fabrication process, and as described earlier, do not degrade during operation.

The deeper quantum well and reduced hole mass found in strained (Al,Ga)As/(In,Ga)As quantum wells can also improve the performance of p-channel, field-effect transistors. Transconductances as high as 117 mS/mm have been demonstrated in self-aligned p-channel (Al,Ga)As/(In,Ga)As field-effect transistors with 1- μ m gate lengths [23]. By combining self-aligned n-channel and p-channel strained-layer transistors, complementary logic circuits have been demonstrated that substantially outperform their silicon-based counterparts [24].

By far the most dramatic impact of the reduced hole density for strained-layer materials is observed in its effect on the threshold and modulation characteristics of semiconductor lasers. In those devices, the reduction in the valence-band density of states that characterizes biaxially compressed layers has led to reductions in laser threshold currents [25, 26, 27] by approximately

50% compared to those of unstrained alternatives in similar geometries. The reduced valence-band density of states also improves modulation performance [28]. Preliminary studies also suggest that strained-quantum well lasers are less prone to catastrophic degradation from dark line defects, perhaps related to strain effects on dislocation propagation.

Summary

This paper has considered the limits over which lattice-mismatched (strained-layer) heteroepitaxy can be applied to fabricate electronic and optoelectronic devices, and has described the conditions under which such concerns matter. Improvements in device performance brought about by strained-layer epitaxy have been presented in terms of the effects of strain on III-V compound-semiconductor bandstructure.

Acknowledgments

The author wishes to gratefully acknowledge his many coworkers who have participated in numerous studies of strained-layer semiconductors. Particular thanks are due to G. A. Vawter, I. J. Fritz, and E. D. Jones, B. W. Dodson, and J. Y. Tsao for valuable discussions during the preparation of this manuscript. This work was performed at Sandia National Laboratory and was sponsored by the U. S. Department of Energy under contract DE-AC04-DP00789.

References

1. D. R. Myers, "Ion Implantation of III-V Compound Semiconductor Strained-Layer Superlattices," in Compound Semiconductor Strained-Layer Superlattices, R. M. Biefeld, ed. (Trans Tech, Zurich, 1989), pp. 165-198.
2. G. H. Olsen, M. S. Abrahams, C. J. Buiocchi, and T. J. Zamerowski, *J. Appl. Phys.* **46**, 1643 (1975).
3. J. W. Matthews and A. E. Blakeslee, *J. Crys. Growth* **27**, "Defects in Epitaxial Multilayers, I. Misfit Dislocations" **118** (1974).
4. P. S. Peercy, B. W. Dodson, J. Y. Tsao, E. D. Jones, D. R. Myers, T. E. Zipperian, L. R. Dawson, R. M. Biefeld, J. F. Klem, and C. R. Hills, "Stability of Strained Quantum-Well Field-Effect Transistor Structures," *IEEE El. Dev. Lett.* **2**, 621-3 (1988).
5. D. R. Myers, G. W. Arnold, C. R. Hills, L. R. Dawson, and B. I. Doyle, "High-Fluence Ion Damage Effects in Ar-Implanted (InGa)As/GaAs Strained-Layer Superlattices," *Appl. Phys. Lett.* **51**, 820-2, (1987).
6. B. W. Dodson, D. R. Myers, A. K. Datye, V. S. Kaushik, D. L. Kendall, and B. Martinez-Tovar, "Asymmetric Tilt Boundaries and Generalized Heteroepitaxy," *Phys. Rev. Lett.* **61**, 2681-4 (1988).

7. G. C. Osbourn, "Strained-Layer Superlattices from Lattice-Mismatched Materials," *J. Appl. Phys.* **53**, 1586 (1982).
8. G. A. Vawter and D. R. Myers, "Useful Design Relationships for the Engineering of Thermodynamically Stable Strained-Layer Structures," *J. Appl. Phys.* **65**, 4769-73 (1989).
9. J. W. Matthews and A. E. Blakeslee, "Defects in Epitaxial Multilayers, III. Preparation of Almost Perfect Multilayers," *J. Cryst. Growth* **32**, 265 (1976), and references therein.
10. J. Y. Tsao and B. W. Dodson, "Excess Stress and the Stability of Strained Heterostructures," *Appl. Phys. Lett.* **53**, 848-50 (1988).
11. P. S. Peercy, B. W. Dodson, J. Y. Tsao, E. D. Jones, D. R. Myers, T. E. Zipperian, L. R. Dawson, R. M. Biefeld, J. F. Klem, and C. R. Hills, *IEEE El. Dev. Lett.* **EDL-9**, 621 (1988).
12. I. J. Fritz, T. M. Brennan, and D. S. Ginley, "Electroreflectance Spectra of InGaAs/AlGaAs Multiple Strained Quantum-Well Structures," *Sol. State. Comm.* **75**, 289-92 (1990).
13. J. Y. Marzin, "Strained Superlattices," in *Heterojunctions and Semiconductor Superlattices*, edited by G. Allen, G. Bastard, N. Boccara, M. Lannoo, and M. Voss, (Springer, Berlin, 1986), p.161-176.
14. G. Ji, D. Huang, U. K. Reddy, T. S. Henderson, R. Houdre, and H. Morkoc, "Optical Investigations of Highly Strained InGaAs-GaAs Multiple Quantum Wells," *J. Appl. Phys.* **62**, 3366-73 (1987).
15. D. J. Arendt, K. Denefle, C. Van Hoof, J. De Boeck, and G. Borghs, "(InGa)As/GaAs Quantum Wells and Band Offsets," *J. Appl. Phys.* **66**, 1739 (1989).
16. G. Bastard, *Wave Mechanics Applied to Semiconductor Heterostructures* (les editions de physique, Les Ulis, 1990).
17. C. G. van de Walle, "Band Offsets at Strained-Layer Interfaces," *Mat. Res. Soc. Symp. Proc.* **102**, 565-70 (1988).
18. M. Sato and Y. Horikoshi, "Modulation of Quantized Energy Levels of GaAs/AlGaAs Quantum Wells by InAs Monomolecular Plane Insertion," *Appl. Phys. Lett.* **56**, 1555-7 (1990).
19. E. D. Jones, S. K. Lyo, J. F. Klem, J. E. Schirber, and C. P. Tigges, "Simultaneous Measurements of the Conduction and Valence-Band Masses in Strained-Layer Structures," *Inst. Phys. Conf. Series* **96**, 243-7 (1988).
20. D. L. Smith and C. Mailhot, "Nonlinear Optical Response of [111] Growth-Axis, Strained-Layer Quantum Structures," *J. Vac. Sci. Technol. A*, **5**, 2060-4 (1987).
21. H. Morkoç, T. Henderson, W. Kopp, and C. K. Peng, "High-Frequency Noise of $In_xGa_{1-x}As/Al_xGa_{1-x}As$ MODFETs and Comparison to $GaAs/Al_xGa_{1-x}As$ MODFETs," *Electron. Lett.* **22**, 578-80 (1986).
22. U. K. Mishra, A. S. Brown, and S. E. Rosenbaum, "DC and RF Performance of 0.1- μm Gate Length $Al_{0.48}In_{0.52}As - Ga_{0.38}In_{0.62}As$ Pseudomorphic HEMTs," in *Technical Digest of the 1988 International Electron Devices Meeting* (IEEE, NY, 1989), pp. 180-3.
23. R. R. Daniels, P. P. Ruden, M. S. Shur, D. Grider, T. E. Hohava, and D. K. Arch, "Quantum-Well, p-Channel AlGaAs/InGaAs/GaAs Heterostructure Insulated-Gate Field-Effect Transistors with Very High Transconductance," *IEEE El. Dev. Lett.*, **9**, 355-7 (1988).
24. P. Ruden, A. Akinwande, D. Narum, D. Grider, and J. Nohava, "High-Performance Complementary Logic Based on GaAs/InGaAs/AlGaAs HIGFETs," in *Technical Digest of the 1990 International Electron Devices Meeting* (IEEE, NY, 1989), pp. 117-20.
25. A. Adams, "Band Structure Engineering for Low-Threshold, High-Efficiency Lasers," *Electron. Lett.* **22**, 249-50 (1986).
26. D. F. Welch, W. Streifer, C. F. Schaus, S. Sun, and P. L. Gourley, "Gain Characteristics of Strained Quantum-Well Lasers," *Appl. Phys. Lett.* **56**, 10 (1990).
27. J.-I. Hashimoto, T. Katsuyama, J. Shinkai, I. Yoshida, and H. Hayashi, "Effects of Strained-Layer Structures on the Threshold Current Density of AlGaInP/GaInP Visible Lasers," *Appl. Phys. Lett.* **58**, 879-880 (1991).
28. I. Suemune, L. A. Coldren, M. Yamanishi, and Y. Kan, "Extremely Wide Modulation Bandwidth in a Low-Threshold-Current Strained Quantum-Well Laser," *Appl. Phys. Lett.* **53**, 1378-80 (1989).

Characterization of Terahertz Optoelectronic Behavior of GaAs Epilayers Containing Arsenic Precipitates

A. C. Warren, N. Katzenellenbogen, D. Grischkowsky, and
J. M. Woodall

*IBM Research Division, Thomas J. Watson Research Center, P.O. Box 218,
Yorktown Heights, New York 10598*

M. R. Melloch and N. Otsuka

*Schools of Electrical Engineering and Materials Engineering,
Purdue University, West Lafayette, Indiana 47907*

Abstract

Using GaAs epilayers with arsenic precipitates (GaAs:As) as the photoconductive material in a broad-band optoelectronic terahertz beam system, we have generated and detected freely-propagating, subpsec electromagnetic pulses. The As precipitates occur as a result of epi-growth at 250°C followed by a 600°C anneal, yielding a high-quality, epitaxial matrix essentially free of point defects.

Using GaAs epilayers with arsenic precipitates (GaAs:As) [1] as the photoconductive material in a complete, broad-band optoelectronic terahertz beam system [2], we have generated and detected freely-propagating, subpsec electromagnetic pulses. Our results indicate that the photoconductive response of the GaAs:As consists of an ultrafast, subpsec turn on time followed by a turn off time of several picoseconds. Both the transmitter's and receiver's performances are dominated by the leading edge (turn on time), with the receiver working effectively in an "integrating mode." The ultrafast turn on is indistinguishable from that of epi-GaAs and indicates a GaAs matrix that is essentially free of point defects. The short "effective" carrier lifetime of several psec is consistent with capture by the embedded, closely-spaced (about 20 nm) arsenic precipitates. This behavior is contrasted with that of materials containing a uniform distribution of recombination centers, such as implanted silicon-on-sapphire or unannealed, low-temperature GaAs.

The prototypical subpicosecond material, namely implanted silicon-on-sapphire (SOS), achieves short carrier lifetimes via high defect densities, with the best results indicating a full photoconductive response pulse of about 0.6 psec full-width-half-maximum (FWHM). GaAs grown by MBE at 200-250°C (LT GaAs) is characteristically arsenic rich and also contains a high density of point defects. When used as the photoconductive material in a transmission line, electrical pulse "launcher" [3], it produced an electrical pulse width of 1.6 ps and a large improvement in signal amplitude over SOS-based structures. From these early results, a carrier mobility of 200 cm²/volt-sec was inferred for this type of GaAs. More recently, electrical pulses as short as 0.6 psec have been generated on coplanar transmission lines with this material [4].

Under proper growth and annealing conditions, we have found that the excess arsenic in LT GaAs will coalesce into arsenic precipitates (GaAs:As) about 6 nm in diameter with an average spacing of about 20 nm [1]. Since there is some debate as to the microscopic nature of GaAs grown at low temperatures, especially regarding the distribution of excess As in the films, we will describe the preparation of samples used in this work. The epilayers used here were grown in a Varian GEN II MBE system on two-inch diameter, liquid-encapsulated-Czochralski (100) GaAs substrate. The epitaxial layers consisted of 0.75 μm of normal GaAs buffer (grown at 600°C) followed by a temperature ramp down to 250°C over the next 0.25 μm of growth, and 1.0 μm of LT GaAs grown at 250°C. The substrate temperature was then ramped back to 600°C during the growth of the next 500 Å of GaAs, and the structure was capped with an additional 100 Å of undoped GaAs. This growth was followed by an in-situ anneal for one hour at 600°C. The arsenic source used throughout the epi-growth and post-annealing steps was the dymer As₂, although we have found that using an As₄ source will also produce arsenic precipitates. Transmission electron microscopy has confirmed the existence of these precipitates (roughly 6 nm average diameter) in samples grown by this procedure.

In this study, we compare the photoconductive responses of GaAs:As, SOS and normal GaAs by pairing various combinations of devices made with each material as transmitter and receiver in a complete measurement system. The photoconductive response of SOS is known to be a pulse with FWHM of 0.6 psec, and having a fast rise time of roughly 200 fsec and an exponential decay with a time constant of 600 fsec. Normal GaAs also has an extremely fast rise time of approximately 200 fsec, but followed by a long fall time of the order of 100 psec - this permits its use as a transmitter where the resulting electromagnetic pulse is generated by the leading edge (derivative), but precludes its use as a receiver material. The noise in the full receiver circuit is proportional to the "ON" time of the photoconductive switch, and for GaAs' on time extended response, the signal-to-noise ratio is prohibitive. The devices used in this work are identical to those in Ref. 2, with the substitution of GaAs:As (with Au:Ge:Ni contacts and antennae) for the implanted SOS. The patterned photoconductive gaps and transmission lines had spacings of

5 and 30 microns, respectively. The transmitter is biased at 9 volts and driven with 70 fsec optical pulses with a 100 MHz repetition rate and coming from a colliding-pulse, mode-locked dye laser to generate the terahertz pulse radiation. This radiation is then focused on the receiver antenna which is being gated by identical, but time-delayed, photoexcitation pulses.

We find that the GaAs:As photoconductive response is intermediate to these two, namely an ultrafast subpicosecond followed by a relatively slow decay of several psec. When operated as a transmitter, the leading edge gives rise to a strong electromagnetic pulse. Used as a receiver, the temporal overlap between the incident terahertz pulse which biases the gap of the receiver antenna and the step-function photoconductive response of the receiver results in a transfer of charge (current) across the photoconductive gap proportional to the negative integral of the electric field of the incoming subpicosecond electromagnetic pulse. A measured pulse using GaAs:As as both the transmitter and receiver material, is shown in Fig. 1a, while its amplitude spectrum is given in Fig. 1b. The FWHM of the integral pulse is found to be 0.71 psec, which can be compared to 0.54 psec for sampling mode measurements using ion-implanted SOS in the same THz beam system [2]. An important difference, however, is that the measured peak signal (current) in Fig. 1 is more than 5 times larger than that obtained from the all-SOS system. The comparison of different photoconductive materials leads to the following interesting results. First, it is found that the substitution of intrinsic GaAs for the GaAs:As transmitter produces essentially no differences in the measured signal with either the SOS or GaAs:As receiver. This confirms that the

leading edge of the GaAs:As response is indistinguishable from that of GaAs. The fact that the GaAs and GaAs:As transmitters gave the same signals is indicative of the high quality of the GaAs matrix in the low temperature material and lack of mobility degradation. Second, while exact numbers are unclear, it is certain that the signal strength for the GaAs:As is several times larger than for SOS for both the transmitter and receiver sides, resulting in the above factor of 5 between the all-GaAs:As and all-SOS transceiver configurations. Third, an indirect pulsedwidth comparison was made by using a GaAs:As transmitter with both receivers (GaAs:As and SOS), and differentiating the GaAs:As receiver results. The resultant pulseshapes yielded minimum-maximum differences of 0.58 psec for the GaAs:As receiver and 0.65 psec for the SOS. Lastly, by comparing noise levels in the GaAs:As and SOS receivers, we estimate that the photoexcitation decay in the GaAs:As is on the order of 2 psec. This is long enough to enable an integrating mode of operation, but short enough that signal-to-noise ratio is not an adverse factor. In addition, this time constant is consistent with mediation by sparse As clusters rather than a high density of bulk defects (as in SOS).

Due to system configuration differences, it is difficult to make a direct comparison with other LT GaAs work. Our pulse measurements and corroborating DLTS measurements indicate that the quality of the GaAs matrix in GaAs:As approaches that of intrinsic GaAs. And while the amplitude spectrum of the measured pulse is less than that for the SOS sampling detection using either an SOS transmitter or a GaAs transmitter [5], this is expected for an integral measurement mode. When a numerical derivative is performed on the measured integral pulse of Fig. 1a, the spectral extent of the derivative is comparable to these previous systems.

We would like to acknowledge the excellent mask and wafer fabrication by Hoi Chan and the assistance of David McInturff. Some of the earlier measurements using this material were performed by Soren Keiding. The work done at Purdue University was partially supported by the Office of Naval Research under grant #N00014-89-J-1864.

References

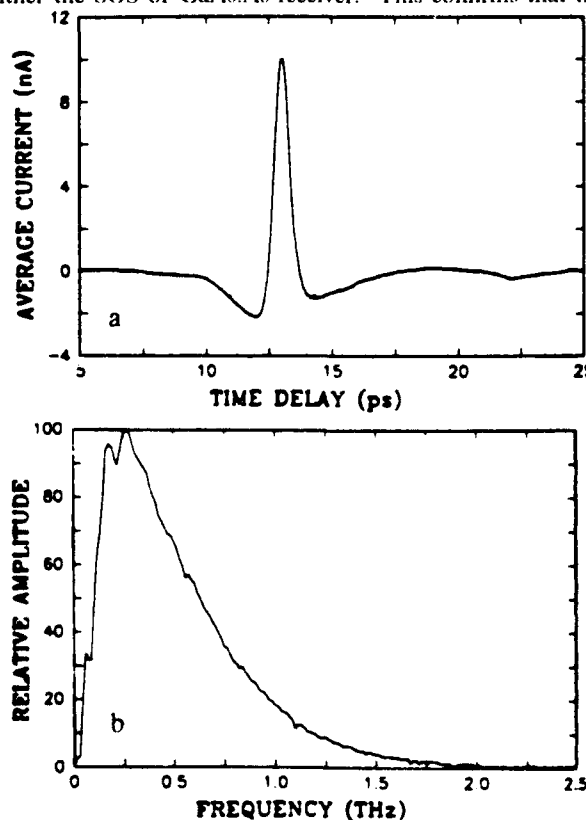


Figure 1. Measured response using GaAs:As as both transmitter and receiver. 1a shows the negative integral of the THz pulse incident on the detector, while 1b shows its amplitude spectrum.

1. M.R. Melloch, N. Otsuka, J.M. Woodall, A.C. Warren and J.L. Freeouf "Formation of arsenic precipitates in GaAs buffer layers grown by MBE at low substrate temperatures", *Appl. Phys. Lett.*, **57**, (15), 1531 (1990).
2. M. van Exter and D. Grischkowsky, "Characterization of an optoelectronic terahertz beam system", *IEEE Trans on Microwave Theory and Tech.*, **38**, (11), 1684 (1990).
3. F.W. Smith, H.W. Lee, V. Diadiuk, M.A. Hollis, A.R. Calawa, S. Gupta, M. Frankel, D.R. Dykaar, G.A. Mourou and T.Y. Hsiang, "Picosecond GaAs-based photoconductive optoelectronic detectors", *Appl. Phys. Lett.*, **54**, 890 (1989).
4. S. Gupta, J. Pamulapati, J. Chwalek, P. Battacharya, J. Whitaker and G. Mourou, "Subpicosecond photoconductivity in III-V compound semiconductors using low temperature MBE growth techniques", *Intl. Conf. on Quantum Elec., Tech. Digest 1990*, V8 (Opt. Soc. of America), Washington, DC (1990), p. 132; *Tech Digest on Ultrafast Phen. 1990*, Washington, DC (1990), p. 297, **57**, 1331 (1990).
5. D. Grischkowsky, S. Keiding, M. van Exter and Ch. Fattinger, "Far-infrared time-domain spectroscopy with terahertz beams of dielectrics and semiconductors", *J. of Opt. Soc. of Amer. B*, **Vol. 7**, 2006 (1990).

Transient Absorption of Low-Temperature Molecular-Beam Epitaxy Grown GaAs

T. B. Norris and W. Sha

*Ultrafast Science Laboratory, University of Michigan, 2200 Bonisteel,
Ann Arbor, Michigan 48109-2099*

W. J. Schaff and X. J. Song

The School of Electrical Engineering, Cornell University, Ithaca, New York 14850

Z. Liliental-Weber and E. R. Weber

*Department of Materials Science, Lawrence Berkeley Laboratory, University of California,
Berkeley, California 94720*

Abstract

We have applied time-resolved absorption spectroscopy to study the near-band-edge carrier dynamics of low-temperature-MBE-grown GaAs, in order to directly observe the carrier relaxation and lifetime for this material.

Introduction

MBE growth of GaAs is normally performed at a substrate temperature around 600 °C. It has recently become apparent, however, that GaAs grown at lower temperatures (LT GaAs) has some very interesting and useful properties. The material was first grown as a buffer layer to eliminate backgating in GaAs MESFET's, taking advantage of the high resistivity of this material [1]. Subsequently the LT GaAs was investigated as a photoconductive detector, where a response recovery of as short as 600 fs was observed [2]. The high breakdown field of this material makes it extremely promising for high-speed photoconductive switching of high fields [3]. The promise of this material for fast photoconductive devices has motivated a study of the carrier dynamics in LT GaAs. Gupta *et al.* [4] have investigated the time-resolved reflectivity of LT GaAs in an attempt to determine the carrier lifetime. Their sample was excited and probed high in the conduction band (at 620 nm), however, so interpretation of the result as the carrier lifetime is not entirely straightforward. It is much more straightforward to interpret absorption spectra in terms of the carrier distribution functions, so we have performed transient absorption spectroscopy of the band-edge region of LT GaAs to determine directly both the carrier relaxation and lifetime.

Experimental

The samples consisted of nominally 1 μm LT GaAs, sandwiched between a 2.4-μm Al_{0.39}Ga_{0.61}As etch-stop and support layer and a 100-Å GaAs cap layer. The LT layers were grown at nominal temperature from 180 to 210 °C for a fixed arsenic pressure of 8 × 10⁻⁶ Torr, and for arsenic pressures of 4 × 10⁻⁶ to 1.5 × 10⁻⁵ Torr for a fixed temperature of 200 °C. The etch stop and cap layers were grown at normal (600 °C) temperature. The sample was annealed for 10 min. at 600 °C after growth. The substrate was removed by a selective etch to allow optical absorption spectroscopy on the LT GaAs layer.

Femtosecond continuum pump-probe techniques were used for the experiments. The laser system was similar to that described in refs. 5 and 6. It produced amplified 100-fs, 10-μJ pulses at 2 kHz, which were used to generate a white light continuum in an 0.5-mm ethylene glycol jet. A 10-nm wide portion of the continuum spectrum centered at 830 nm was selected and amplified to pump the sample. The injected carrier density was estimated to be 10¹⁷ cm⁻³. The probe consisted of the 760-880 nm portion of the continuum. Prisms were used to compensate for the dispersion in the continuum pulse so that the entire probe spectrum arrived at the sample simultaneously (*i.e.* within 100 fs). Differential transmission (DTS) were accumulated on an OMA, where

$$\begin{aligned} DTS &= \frac{\Delta T}{T} = \frac{T(\text{pump on}) - T(\text{pump off})}{T(\text{pump off})} \\ &= \alpha_0 L (f_e + f_h) \end{aligned}$$

$\alpha_0 L$ is the unperturbed absorption spectrum and $f_{e,h}$ are the carrier distribution functions. The experiments were performed at room temperature.

Results

A typical time-resolved DTS for probe delays of -100 fs to +400 fs is shown in Fig. 1. It is interesting to note that the band edge is at 860 nm (1.442 eV), which is slightly blue-shifted from the normal GaAs band edge (1.42 eV). We interpret this shift as being due to strain in the sample arising from the fact that excess arsenic is incorporated into the LT layer during growth

The carrier lifetime was determined by monitoring the amplitude of the differential transmission at the band edge (i.e. 860 nm). A typical decay curve is shown in Fig. 2. The decay curves were fitted using least-squares to a biexponential decay. This biexponential behavior is consistent with previous reflectivity and photoconductivity measurements by other groups [2,4], though the precise lifetimes are somewhat different due in all likelihood to differences in the exact growth conditions for the different samples. These absorption measurements have the advantage that the intraband relaxation dynamics and carrier lifetime effects are clearly resolved. Typically the fast component was around 300 fs and the slow component was around 1.5 ps for this set of samples.

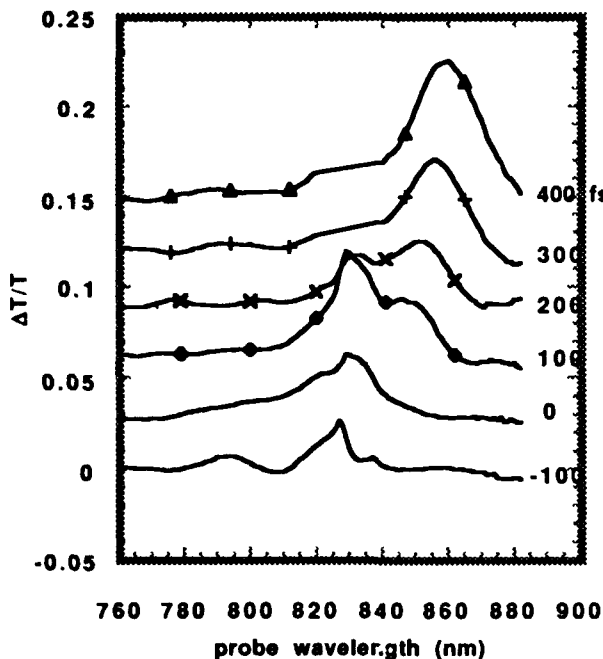


Figure 1. Time-resolved differential absorption spectra near the band edge. The pump pulse is centered at 830 nm.

around 200 °C [7]. The initial hole burning at the pump wavelength due to preferential state filling and the fast relaxation to the band edge are clearly apparent, as in similar experiments on normally grown GaAs [8]. An additional feature of interest is the appearance of a peak below the pump energy at $t = +100$ fs which is due to LO-phonon emission from the initial nonequilibrium electron distribution. This phonon peak is generally not clearly visible in spectra of normally-grown GaAs. The increased appearance of this peak in the LT material is likely due to the ultrafast carrier lifetime. Carrier thermalization has occurred in about 300 fs.

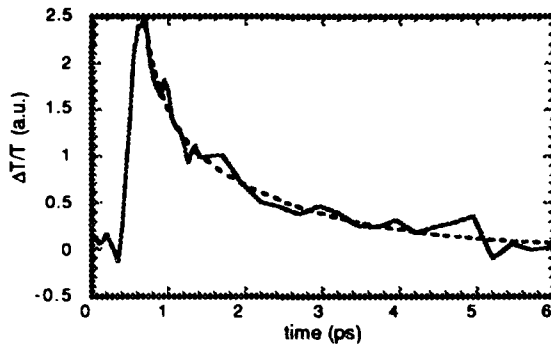


Figure 2. Decay of the absorption saturation at 860 nm. The dashed line is a fitted biexponential decay.

A simple picture of the mechanism responsible for the high resistivity and fast carrier lifetime in this material has been proposed [9]. It has been shown that the effect of lowering the growth temperature is to incorporate excess arsenic into the GaAs crystal [7]. Upon annealing, the excess arsenic forms precipitates which act as "buried" Schottky barriers which can capture the photojected electrons and holes. The density of these precipitates is about 10^{17} cm^{-3} , as determined by TEM. Thus a rough estimate of the capture cross section of the precipitates may then be made from $\sigma = 1/N\tau v$, where N is the density, τ is the lifetime, and v is the thermal velocity. This yields a cross section of about 10^{-12} cm^{-2} , which corresponds rather closely to the precipitate cross-sectional area.

An alternative picture, in which antisite defects (AsGa) that remain in the crystal even after annealing are responsible for the fast lifetime, has also been considered [10]. If we take a capture cross section typical for a deep level, $\sigma = 10^{-13} \text{ cm}^{-2}$, then our experimental lifetimes could be explained by a defect density of about 10^{18} cm^{-3} . This density is not inconsistent with EPR measurements of the defect density in annealed LT GaAs [7], which have a sensitivity limit of 10^{18} cm^{-3} . DLTS measurements, however, have been performed on doped samples grown

and annealed under very similar conditions to those for our (undoped) samples [11]. These measurements show no observable EL2-like defects at the experimental resolution limit (10^{14} cm^{-3}). Hole traps may exist at a density of up to 10^{16} cm^{-3} . The low defect density as determined by DLTS indicates that our results are more consistent with a picture where arsenic precipitates capture both the electrons and holes. Further work, however, is necessary to confirm the precise mechanism responsible for the fast lifetime.

In this model, the shorter carrier lifetimes (as required for many optoelectronic applications) will occur for higher excess arsenic incorporation into the GaAs. When the excess arsenic composition becomes too high, however, the GaAs becomes polycrystalline. Thus the optimal range of MBE parameters yielding fast optical response and good crystal quality is quite narrow. Our experiments were intended to probe the optical response for a series of samples grown near the expected optimal parameters. TEM analysis of our samples showed in fact that only two samples were completely crystalline: one grown at temperature $T=210$ and arsenic pressure $P=4 \times 10^{-6}$, and the other at $T=200$ and $P=8 \times 10^{-6}$. The other samples showed that the LT layer became polycrystalline after several hundred nm growth. As expected, the precipitate density and size increased with decreasing growth temperature, and increased with increasing arsenic pressure. The crystal properties as a function of growth conditions are shown in Table 1.

The carrier lifetimes (i.e. the fast and slow components of the biexponential fit to the band-edge absorption decay) are shown in Fig. 3 as a function of growth temperature, and in Fig. 4 as a function of arsenic pressure. All of the samples show a subpicosecond initial decay, and a "slow" component of around a picosecond. As expected, the decay becomes somewhat faster for lower growth temperature (though the dependence is rather weak over the temperature range studied here). Surprisingly, however, the lifetime increased slightly with decreasing arsenic pressure,

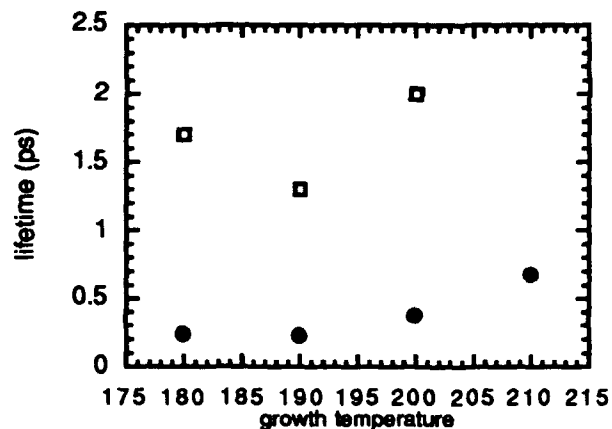


Figure 3. Fast (closed circles) and slow (open squares) components of the band edge decay curves for samples grown at an arsenic pressure of 8×10^{-6} Torr, as a function of substrate temperature.

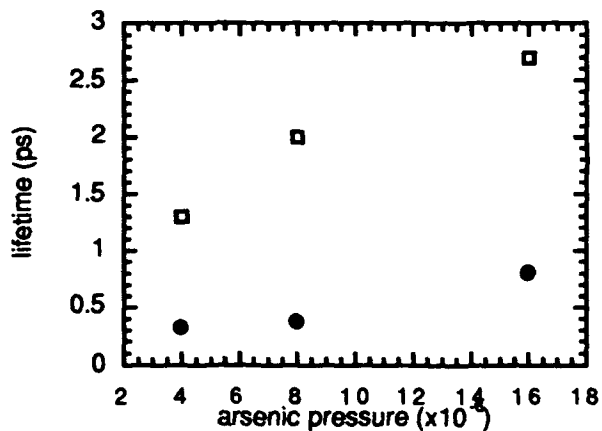


Figure 4. Fast (closed circles) and slow (open squares) components of the band-edge decay curves for samples grown at 200°C as a function of arsenic pressure.

T (°C)	P (Torr)	thickness	diameter
180	8×10^{-6}	320 nm	4.55 nm
190	8×10^{-6}	320 nm	50
200	8×10^{-6}	490 nm	25
210	8×10^{-6}	all (1μm)	5
200	4×10^{-6}	all (1μm)	5
200	1.5×10^{-5}	415 nm	25

Table 1. Thickness of the crystalline part of the LT GaAs layer and arsenic precipitate diameter as a function of substrate temperature and arsenic pressure, as determined by TEM.

despite evidence of increasing excess arsenic with increasing pressure. Nevertheless, it is interesting to note that two of the samples demonstrate at least that it is possible to obtain both fast optical response and good crystalline quality. The optimal range of MBE parameters over which both fast response and good crystallinity may be obtained is evidently quite narrow.

In conclusion, the time-resolved absorption spectrum of LT-grown GaAs pumped near the band edge shows a fast (subpicosecond) response for a series of samples grown near 200°C . We have observed two samples which yield both fast optical response and good crystalline quality. Extensions of this work will include probing the time-dependent distribution

functions that occur in the presence of a very high electric field, in order to elucidate the actual carrier dynamics occurring during photoconductive switching.

Acknowledgment

This work was supported by AFOSR grant URI- 90-0214.

References

1. F.W. Smith, A.R. Calawa, Chang-Lee Chen, M.J. Manfra, and L.J. Mahoney, *IEEE Electron Device Lett.* **9**, 77 (1988).
2. F.W. Smith, *et al.*, *Appl. Phys. Lett.* **54**, 890 (1989).
3. T. Motet, J. Nees, S. Williamson, and G.A. Mourou, (manuscript in preparation).
4. S. Gupta, J. Pamulapati, J. Chwalek, P.K. Bhattacharya, and G. Mourou, in Ultrafast Phenomena VII, ed. by C.B. Harris, E.P. Ippen, G.A. Mourou, and A.H. Zewail, Springer, 1990, p. 297.
5. T. Norris, T. Sizer II, and G. Mourou, *J. Opt. Soc. Am. B* **2**, 613 (1985).
6. I.N. Duling III, T. Norris, T. Sizer II, P. Bado, and G. A. Mourou, *J. Opt. Soc. Am. B* **2**, 616 (1985).
7. M. Kaminska, *et al.*, *Appl. Phys. Lett.* **54**, 1881 (1989).
8. J.L. Oudar, D. Hulin, A. Migus, A. Antonetti, and F. Alexandre, *Phys. Rev. Lett.* **55**, 2074 (1985).
9. A.C. Warren, *et al.*, *Appl. Phys. Lett.* **57**, 1331 (1990).
10. F.W. Smith, Ph.D Thesis, MIT, 1990 (unpublished).
11. W.J. Schaff, Workshop on Low Temperature GaAs buffer layers, San Francisco, CA, April 20 1990.

Comparison of Oxygen Ion- and Proton-Implanted GaAs Photoconductive Switches

Sheng-lung L. Huang, Eve A. Chauchard, and Chi H. Lee

*Electrical Engineering Department, University of Maryland,
College Park, Maryland 20742*

Thane Smith and Timothy T. Lee

COMSAT Laboratories, Clarksburg, Maryland 20871

Thomas R. Joseph

TRW Electronic Systems Group, Redondo Beach, California 90278

Abstract

Oxygen ion and proton implanted GaAs photoconductive (PC) switches which can be used for on-wafer characterization of GaAs MMIC's have been evaluated. The Oxygen switch performed better in terms of switch sensitivity and bandwidth. It has been used to measure the S-parameter of a 3 stage 12 GHz MMIC amplifier. A good agreement between the PC sampling technique and the network analyzer was achieved up to a 40 db dynamic range.

Introduction

On-wafer characterization of MMIC's performed by optoelectronic techniques such as photoconductive sampling or electro-optic sampling is currently investigated by several groups [1,2]. For photoconductive sampling, pulse generation and/or waveform sampling are done by illuminating a photoconductive gap with short laser pulses. In order to integrate monolithically the photoconductive gaps and the device under test, the gaps have to be fabricated with a technology compatible with GaAs MMIC's fabrication technology. In this work, we characterized and compared two such MMIC -compatible photoconductive gaps. The S_{21} parameter of a 3 stage 12 GHz MMIC amplifier is also measured.

For the photoconductive sampling technique, ultrafast carrier lifetime in the gap is required. A

number of approaches [3,4] have been tried to reduce carrier lifetime and achieve a higher bandwidth - sensitivity product. Radiation damaged material is commonly used but a major drawback for this approach is the poor sensitivity due to reduced mobility and reduced number of carriers reaching the contacts. An O^+ implanted switch [5,6] has been developed to improve carrier mobility. This process is compatible with TRW's MMIC fabrication process. We characterized the O^+ implanted GaAs switch and make a comparison with H^+ implanted GaAs switch. We also achieve a good agreement with network analyzer's S_{21} measurement up to a 40 db dynamic range.

Experiment

(i) Device preparation

The same lithographic mask was used for both H^+ and O^+ switches. The starting material is 2" diameter LEC semi-insulating GaAs wafers. For both cases, the metal contacts are formed by the same process. The metal/GaAs contacts are vacuum deposited Cr/Au patterned by lift-off. Electric plating was also used to improve the conductivity of microstrip line.

The H^+ implantation was performed at three energies, 30 keV with a dose of $2 \times 10^{14} \text{ cm}^{-2}$, 75 keV with a dose of $5 \times 10^{14} \text{ cm}^{-2}$, and 120 keV with a dose of 10^{15} cm^{-2} . This was done after the metal contacts

were formed thus the contact metal prevented any damage to the GaAs at the metal/GaAs interface and beneath it. No annealing was done.

The O^+ implantation was performed at two energies, 140 keV with a dose of $5 \times 10^{11} \text{ cm}^{-2}$ and 360 keV with a dose of $1.3 \times 10^{12} \text{ cm}^{-2}$, which are the same as for the TRW oxygen isolation process. It was then annealed at 410°C for 10 minutes after implantation to reduce defects. All these were done before formation of the metal contact to allow on wafer optical probing to be included in the TRW MMIC fabrication process.

(ii) Optical measurement

The laser system is a Coherent CW Mode-locked Nd:YLF laser which generates 50 ps pulses at $1.054 \mu\text{m}$ with a 76 MHz repetition rate. The output is compressed to $3 \sim 5$ ps by a fiber pulse compressor then frequency doubled to $.527 \mu\text{m}$ by a KTP crystal. About 4% of the energy of the green pulses is split to a slow Si detector for normalizing slow variations in laser intensity. The data is then collected using the standard pump - probe PC sampling technique. The schematic diagram is shown in Fig. 1.

We deliberately extend the output time window to 2 ns to achieve the high dynamic range. Since this time window is longer than the time delay available from our delay line, several sets of data were recorded by varying the fixed delay line. Each data set is then compared and calibrated with that recorded at the end of the previous data set. To insure the reliability of connecting data points, each data set has $\frac{2}{3}$ of its points overlap with the previous measurement. The data is shifted, scaled, and interpolated to produce a very high degree of coincidence in the overlapping regions. Finally, a 2 ns time window is achieved.

Due to dark current and difference of sensitivity inherent to the switches, calibration of the acquired data is necessary. The effect of dark current can easily be removed by choosing a new zero level at the beginning of the sampled signal. The switch sensitivity is measured by placing a 1.4 KHz signal with 100 mV peak voltage on the microstrip line, illuminating the switch, and measuring the response at the side line using the lock-in amplifier. Since the photovoltaic signal of the switch will not show up in the AC measurement, using an AC signal source is preferred to using a DC source and chopping the light beam. The absence of the photovoltaic signal allows a more accurate measurement. The cross-correlated data at the input and output ports is then calibrated by scaling the signals proportionately to the sensitivity of the respective switches.

The electrical waveforms generated by the switches were measured by photoconductive sam-

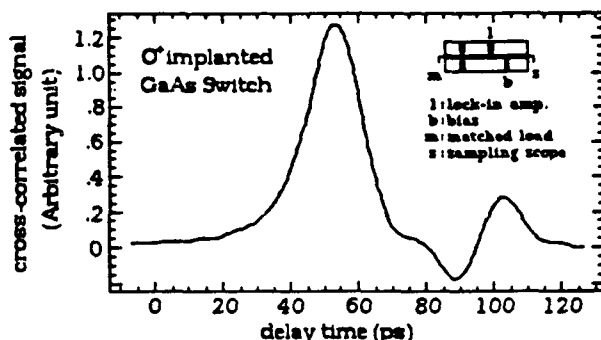


Figure 2. Cross-correlated signal for O^+ implanted switch (measured by photoconductive sampling). The inset shows the device geometry. *l* and *b* indicate the location where the lock-in amplifier and bias voltage were connected.

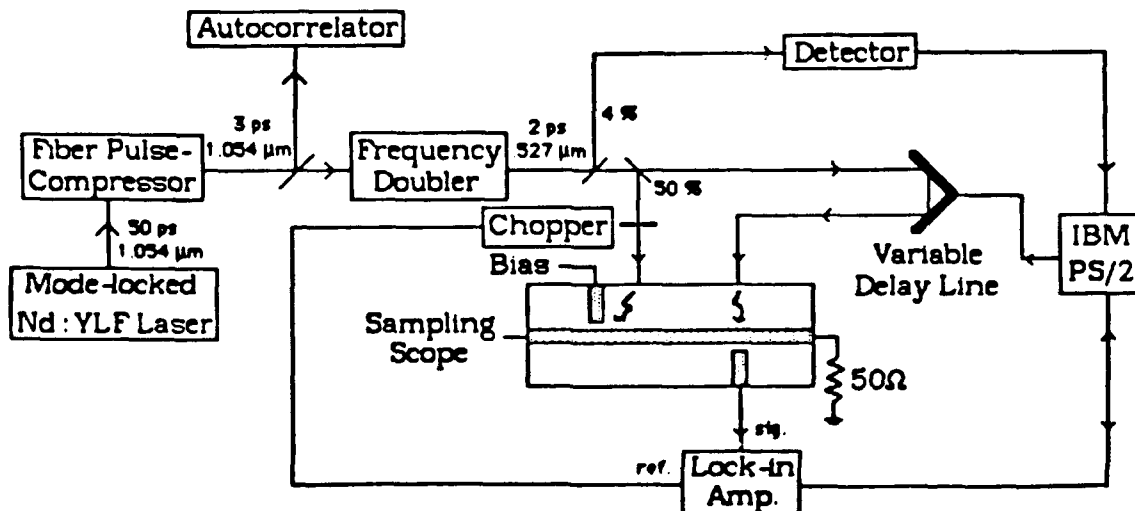


Figure 1. Schematic diagram of PC sampling set-up

pling on devices comprised of four gaps (see inset Fig. 2). This technique yields the cross-correlation of the pulse propagating on the central line and the sampling gap temporal response.

Results

The full width at half maximum of the cross-correlated response of the O^+ switch as shown in Fig. 2 is 19 ps, corresponding to a 14 ps electrical pulse width. It is about three times less than that of the H^+ switch. The implantation with Oxygen ions creates deep level defects which serve as more efficient recombination centers than the defects created by proton implantation.

An interesting feature is the negative peak close to the main pulse for the O^+ switch. This negative signal is neither a reflection from the two ends of the microstrip line nor from the backplane. It is a reflection from the interconnection of the high impedance ($\sim 100 \Omega$) side line to the SMA connector. When the reflected pulse returns to the gap, the photoinduced conductivity is already off but the negative pulse can pass through the gap via gap capacitance. For the H^+ switch, the carrier lifetime is larger than the reflection round trip time, so that the main peak and the negative reflection result in a sharpening of trailing edge of the main pulse. There is also a slight sharpening effect on the O^+ switch. The assumption that the reflection is due to the high impedance side line is verified by putting a small Indium foil on the side line to lower its characteristic impedance to less than 50Ω . As expected, the negative peak becomes positive. The reflected pulse could be suppressed with impedance matched side line. On the other hand, a mismatched side line can be used as pulse forming network to enhance the spectral density of the generated waveform at some specific frequency needed for a device characterization.

Fig. 3 shows that there is a nonlinear dependence between signal peak and bias voltage in the O^+ implanted switch for high bias fields. This effect is not present in the H^+ implanted switch which has severe non-symmetric behavior for positive or negative bias. The nonlinear behavior in the O^+ switch can thus not be attributed to Schottky diode effect. We believe that it is due to impact ionization in the O^+ switch. The photon energy we are using is about 2 eV, which is above the band gap energy, so the generated electrons and holes have initial kinetic energy. Once the carriers kinetic energy has increased to some threshold (approximately 1.5

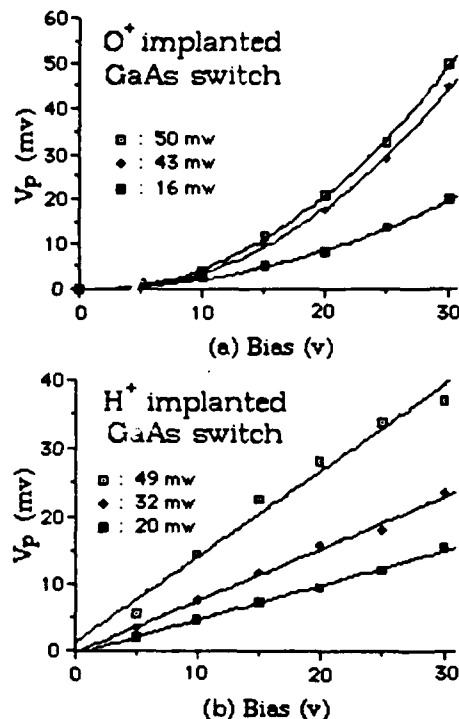


Figure 3. Signal peak vs. Bias (measured by sampling scope and curve-fitted by least-square method) (a) O^+ implanted switch, (b) H^+ implanted switch.

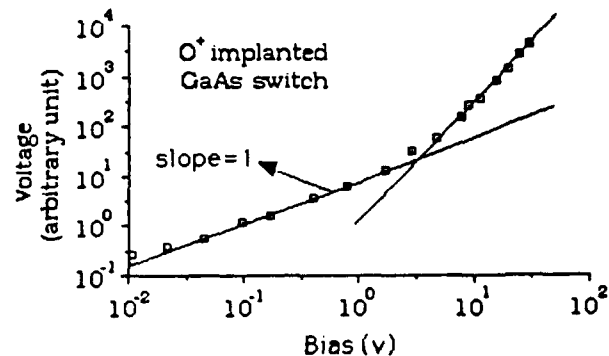


Figure 4. Sampled signal vs. Bias voltage for the O^+ switch. The data points are curve fitted with a slope one straight line at low bias voltage.

times the bandgap energy) due to their acceleration by the applied field, there is chance that impact ionization will happen [7]. For the H^+ switch, a higher density of defect clusters are spread in the gap; they reduce the mean free path of the electrons and holes which can not accumulate enough kinetic energy for impact ionization.

Fig. 4 shows that the non-linear response of the O^+ switch only appears after a bias voltage of 2 Volt: below this threshold of 2 Volts the slope is 1 on this log-log plot. This supports the argument that the non-linear response at higher voltage is due to impact ionization since this phenomena requires a

threshold kinetic energy for carriers. The deviation from slope 1 at very low bias is due to the photovoltaic effect and the noise in the measurement.

The results shown in Figs. 3 and 4 indicate that the O^+ switch would perform well both as a generating gap and as a sampling gap in a device characterization. When the bias is increased to over 25 V, the O^+ switch displays a higher sensitivity and a shorter pulse width compared to the H^+ switch. This shows the superiority of the O^+ switch over the H^+ switch in terms of the bandwidth - sensitivity product. The O^+ switch is capable of generating higher and shorter pulses than the H^+ switch. If the O^+ switch is used as a waveform sampling gap in a device characterization experiment, the sampled signal needs to depend linearly on the voltage amplitude on the line. This condition is fulfilled since the response of the switch is linear at low bias voltages (less than 2V) typical of real MMIC measurements.

It is also observed that with very high intensity (μJ pulse energy on $10 \mu m$ gap with 10 ps pulse width), about three orders of magnitude higher than normally used, the electrical pulse width is broadened by a factor of two. This effect is due to saturation of the defects or traps in the gap. Detailed relaxation processes are still to be elucidated.

We also observe slight pulse width narrowing when the laser power is reduced at the 30 V bias.

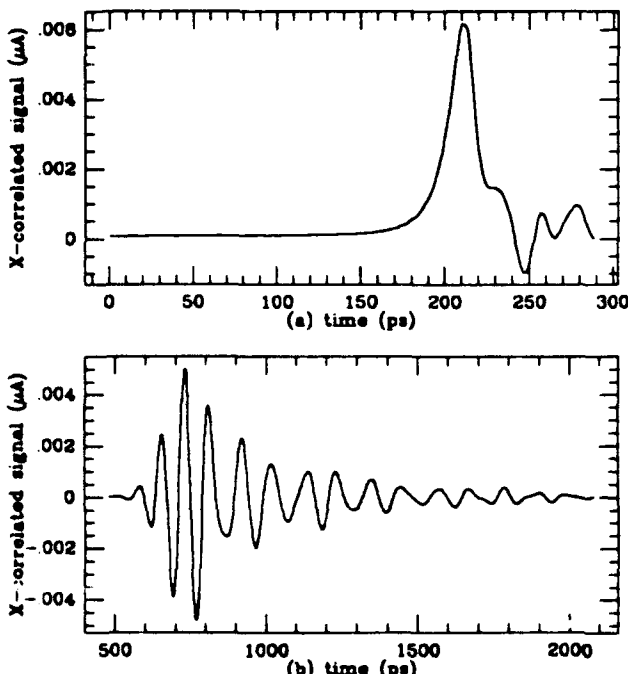


Figure 5. The cross-correlated waveform at (a) Input, (b) Output.

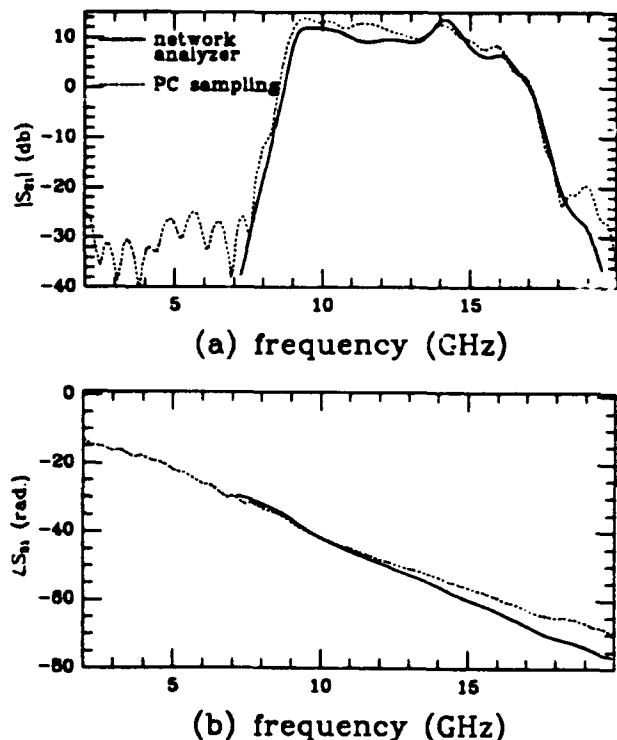


Figure 6. (a) The magnitude of S_{21} , (b) The phase of S_{21} .

This might be due to sweep out effect. With lower laser power, less electrons and holes will be generated, the field in the gap does not collapse as much and it can sweep out the charge carriers.

The measured waveforms for the O^+ switch at input and output ports of the MMIC are shown in Fig. 5. The S_{21} parameter shown in Fig. 6 is obtained from the ratio of the Fourier transform of output waveform to that of input waveform. The optical $|S_{21}|$ shows very good agreement with the result obtained by a network analyzer. Fig. 6 (b) compares the optical and microwave measured phase of S_{21} . The slight difference in the slope of the two curves is due to the difference reference planes of the two measurements.

One important issue which has been overlooked is the limitation of the dynamic range of optoelectronic sampling technique. We use a simple model to explain the dynamic range limitation.

Two distinct features of the PC sampling measurements are evident as shown in Fig. 7. First, the separation of the peaks of the ripples is approximately equal to the inverse of the length of the time window (T). Second, the matching dynamic range increases as the time window increases.

These observations can be explained by the following simple model. Let's consider a sine wave with period t_0 measured by PC sampling with a time window of T . The measured waveform and the magni-

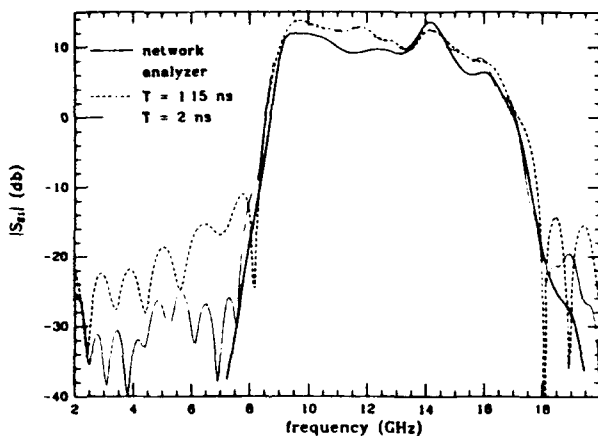


Figure 7. Effect of time windowing.

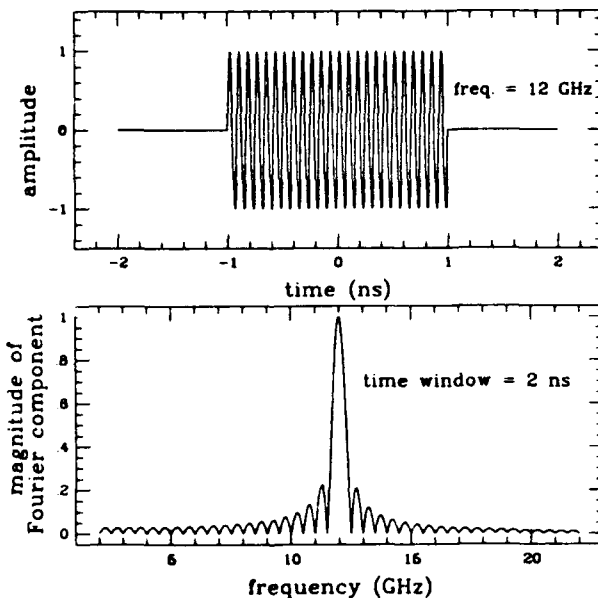


Figure 8. (a) $A(t)$, (b) $A(f)$.

tude of its Fourier transform can be expressed as follows :

$$A(t) = \begin{cases} \sin \frac{2\pi t}{t_0} & ; -\frac{T}{2} < t < \frac{T}{2} \\ 0 & ; \text{elsewhere.} \end{cases}$$

$$|A(f)| = \left| \frac{\sin(\pi f T)}{\pi} \frac{t_0}{1 - f^2 t_0^2} \right|$$

First, it is clear from Fig. 8 that time windowing generates ripples which limits the dynamic range. Second, the distance between two minima is $\frac{1}{f}$ and independent of t_0 . A calculation at two different time windows shows that dynamic range increases when the time window increases (At 5 GHz, the amplitude of ripples is -25 db for $T=1.15$ ns, and -30 db for $T=2$ ns). A more detailed study showed that the next most important limitation on the experimental dynamic range comes from the windowing of the input temporary waveform.

Conclusion

In conclusion, although photoconductive switches are widely used in optical sampling techniques, the detailed carrier dynamics inside the gap is still worthy of further investigation, particularly for GaAs switches compatible with MMIC fabrication processes. We report impact ionization in the O^+ implanted GaAs photoconductive switch, and the subsequent increase in sensitivity of that switch. Additionally, the design of side line can be used as a pulse forming network to enhance the spectral density of the generated pulse at a certain specific frequency in the millimeter wave range. Both switches investigated can be integrated monolithically with GaAs MMIC's allowing for on-wafer measurements. The speed of the O^+ switch is sufficient for S-parameter measurements up to 40 GHz. In this work, a 40 db matching dynamic range compare to network analyzer has also been achieved. The limitation of dynamic range is due to time windowing rather than laser noise.

Acknowledgment

The authors would like to thank Laurence Golob's assistance in taking data. This work was supported in part by MIMIC phase I program under TRW subcontract.

References

1. H-L. Hung, P. Polak-Dingels, K. J. Webb, T. Smith, H. C. Huang, and C. H. Lee, "Millimeter-wave Monolithic Integrated Circuit Characterization by a Picosecond Optoelectronic Technique," IEEE, Microwave Theory Tech., 37, 1223-1231 (1989).
2. K. J. Weingarten, M. J. W. Rodwell, and D. M. Bloom, "Picosecond Optical Sampling of GaAs Integrated Circuit," IEEE J. Quantum Electron., 24, 198-220 (1988).
3. D. H. Auston, Ultrafast Optoelectronics, Ultrashort Laser Pulses and Applications, Springer-Verlag, Edited by W. Kaiser (1988).
4. C. H. Lee, ed., Picosecond Optoelectronic Devices (Academic Press, Orlando, 1984).
5. F. E. Doany, D. Grischkowsky, and C. -C. Chi, "Carrier Lifetime Dependence on Ion Implantation in Silicon", Picosecond Electronics and Optoelectronics II, Edited by F. J. Leonberger, C. H. Lee, F. Capasso, and H. Morkoc (1987).
6. P. N. Favennec, "Semi-insulating layers of GaAs by Oxygen Implantation", Journal of Applied Physics, Vol. 47, 6 (1976).
7. R. S. Muller and T. I. Kamins, Device Electronics for Integrated Circuits (John Wiley & Sons, 2nd ed., 1986), Chap. 4.4.

Femtosecond Refractive and Absorptive Nonlinearities Due to Real Carriers in GaAs

T. Gong and P. M. Fauchet

Laboratory for Laser Energetics, University of Rochester, 250 East River Road, Rochester, New York 14623-1299

The optical properties of GaAs continue to attract interest because of the development of electro-optical and all-optical devices made of III-V semiconductors. The study of ultrafast changes in optical constants (both absorption coefficient and refractive index) is especially important for developing high-speed and high-bit-rate devices. The recent advent of femtosecond lasers has made it possible to observe the changes of optical constants in GaAs on a femtosecond time scale by injection of either real [1-5] or virtual [6] carriers. These measurements provide a unique tool to study hot-carrier relaxation processes and various hot-carrier many-body effects. However, most effort has concentrated on the study of carrier-induced changes of absorption (absorptive nonlinearity). The transient changes of refractive index (refractive or dispersive nonlinearity) could only be deduced from a Kramers-Kronig transformation of the induced changes of absorption over the entire spectrum, which is a complicated procedure especially in the presence of strong nonlinearities on a femtosecond time scale. Since ultrafast changes of the refractive index are very useful for the design of devices using refractive nonlinearities, which have the advantage of low loss and minimal thermal effects, direct and accurate measurements of these changes are necessary.

In this paper we present results of direct femtosecond spectroscopic measurements of the changes of absorption coefficient ($\Delta\alpha$) and especially refractive index (Δn) due to injection of carriers in GaAs. Our results reveal the dynamics of hot-carrier many-body interactions and bring new knowledge on the physics of hot-carrier relaxation. In particular, we observe large

nonlinearities on a femtosecond time scale and will discuss their potential for the design of ultrafast devices.

Our experiments are performed at room temperature using a copper vapor laser amplified colliding pulse mode-locked dye laser, and a pump-probe configuration described in earlier publications [5,7]. Carriers with densities (N) from 10^{17} to 10^{19} cm^{-3} are injected by a pump pulse (80-100 fs) at 620 nm (2 eV). The probe wavelength is tuned between 550 nm and 950 nm. The time-resolved transmission (T) and reflection (R) are measured simultaneously on intrinsic 0.3- μm -thick GaAs films grown by molecular beam epitaxy and mounted on sapphire windows [5,7]. The changes of absorption coefficient ($\Delta\alpha$) and refractive index (Δn) are then calculated from the measured T and R . The time-resolved differential reflection ($\Delta R/R$) is also measured on finely-polished intrinsic, n-type and p-type bulk samples. The change of refractive index is then given by:

$$\Delta n \equiv \frac{n_0^2 - 1}{4} \left(\frac{\Delta R}{R} \right) ,$$

where n_0 is the unperturbed refractive index.

Figure 1(a)-(c) displays the measured spectrum of Δn at different time delays over a wide wavelength region, from below the band gap to above 2 eV for $N \sim 2-3 \times 10^{18} \text{ cm}^{-3}$. The curve in Fig. 1(c) results from a simple calculation under equilibrium conditions [8]. Strong nonlinearities, which cannot be described by this simple theory, appear around the initial excited states and the band edge. Let us first focus on the spectral region around the initial excited states.

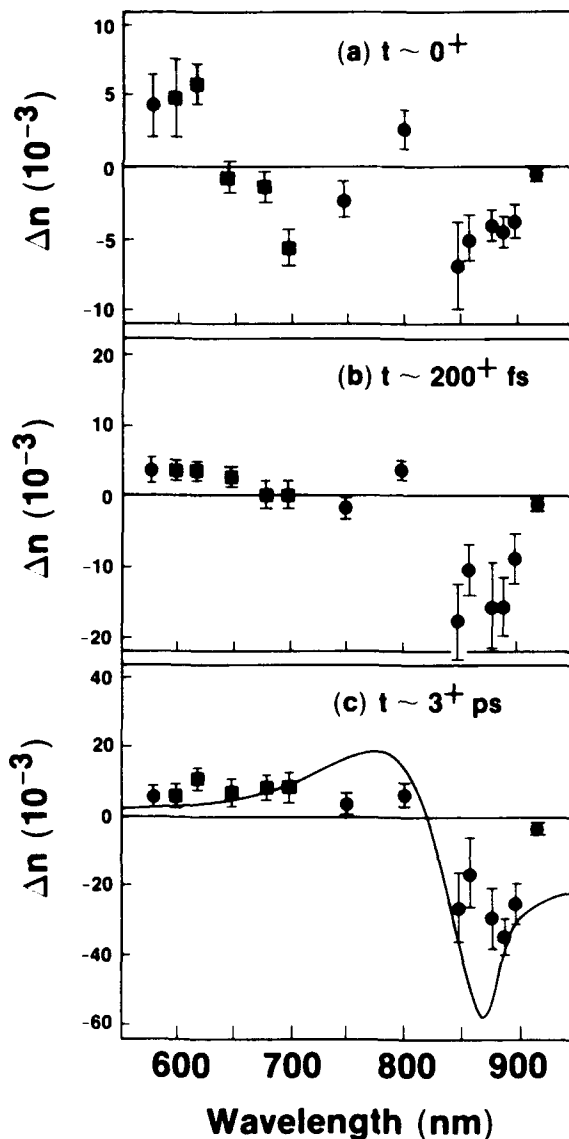


Figure 1. Measured Δn spectrum at different time delays: (a) $t \sim 0^+$; (b) $t \sim 200^+ \text{ fs}$; (c) $t \sim 3^+ \text{ ps}$ for a carrier density $2-3 \times 10^{18} \text{ cm}^{-3}$ injected at 620 nm. ■ are the average values for both intrinsic thin films and bulk samples; ● are the average values for thin films. The error bars are obtained from the standard deviation of the measured values and a conservative estimate of the uncertainty in carrier density. The full line in (c) is obtained from a calculation of Ref. 8 at $N = 3 \times 10^{18} \text{ cm}^{-3}$.

Figure 2 shows the time-resolved differential reflection measured on an intrinsic bulk sample at probe wavelengths from 600 nm to 700 nm. The data at 600 nm and 620 nm exhibit a short-lived positive spike right after carrier injection, whereas the data at 680 nm and 700 nm exhibit a negative spike. No spike is

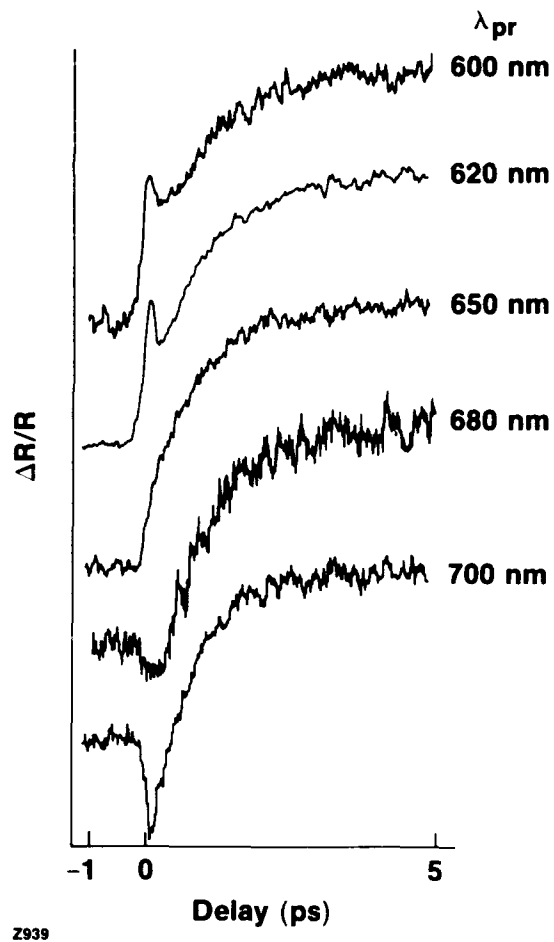


Figure 2. Time-resolved differential reflection ($\Delta R/R$) measured on an intrinsic bulk GaAs sample using probe wavelengths from 600 to 700 nm for a carrier density $2-3 \times 10^{18} \text{ cm}^{-3}$ injected at 620 nm. The traces are displayed with arbitrary normalization for comparison.

observed at 650 nm. The presence of a short-lived spectral resonance around the initial excited states is clearly demonstrated in Fig. 1(a) and Fig. 2. We call this resonance the refractive-index spectral hole burning, because it is related to the absorption spectral hole burning observed by others [1,3]. When a transient nonthermal carrier distribution is generated by the pump pulse, a local decrease of absorption (hole) around the initial excited states appears. The existence of a spectral hole in the imaginary part of the refractive index (absorption) causes a resonance in the real part of the refractive index. If we fit the resonance by a Lorentzian line shape, the FWHM is $\sim 150-200 \text{ meV}$ and the peak is near 650 nm, not at 620 nm, a result confirmed by our induced absorption measurements. Such a relatively large spectral width, which is commensurate with the

result of another absorption spectral hole burning measurement [3], is a strong evidence that carrier-carrier scattering has redistributed electrons through the Γ valley within the pulse width at this carrier density. The origin of the instantaneous red shift of the induced absorption saturation (spectral hole) peak is still under discussion. Possible contributions come from band-gap renormalization [9] and ultrafast redistribution of injected holes [10].

After ~ 200 fs (without deconvolution), the resonance disappears because electrons leave the initial occupied states by carrier-carrier scattering, carrier-phonon scattering and intervalley scattering. The similar gradual rise of Δn on a picosecond time scale in the 580–700 nm spectral region is attributed to bandfilling, which is controlled in part by the slow return of carriers from the satellite valleys. The lack of spectral dependence in this region is expected from the simple theory derived for a cold plasma [8]. However the experimental values appear to be larger than those obtained from this theory, as shown in Fig. 1(c), because the spin-off transitions which monitor the carrier population changes closer to the band edge are not included in this calculation and furthermore, thermalization is not completed in ~ 3 ps.

We also investigate the refractive index spectral hole burning on p-type ($N_{dh} \sim 1.7 \times 10^{18} \text{ cm}^{-3}$) and n-type ($N_{de} \sim 1.3 \times 10^{18} \text{ cm}^{-3}$) GaAs samples and

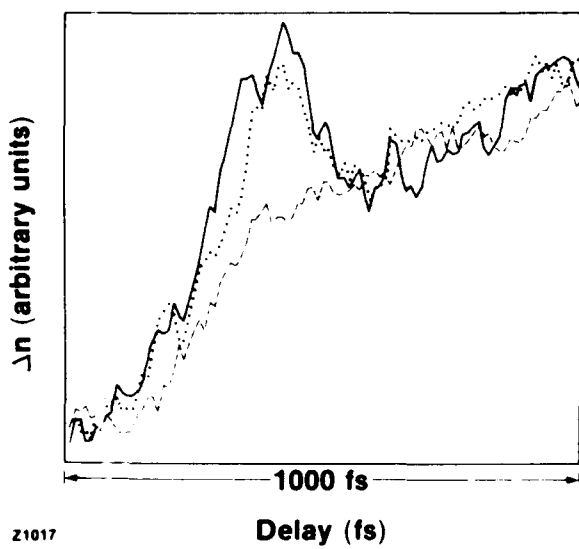


Figure 3. Time-resolved Δn measured on the intrinsic (—), n-type (--) and p-type (....) samples at probe wavelength 620 nm and for a carrier density $3 \times 10^{17} \text{ cm}^{-3}$. All three curves are normalized such that the rise on a picosecond time scale is identical.

compare the results with those for the intrinsic sample. The spectral resonance is similar for the p-type, n-type and intrinsic samples, provided that the injected carrier density is greater than the doping level. At lower carrier densities, the resonance persists in the p-type sample but is strongly reduced in the n-type sample. Figure 3 shows the measured time-resolved changes of the refractive index (Δn) at 620 nm for different samples with an injected carrier density $N \sim 3 \times 10^{17} \text{ cm}^{-3}$. The initial scattering time (with deconvolution) is nearly identical in intrinsic and p-type samples ($\sim 90 \pm 30$ fs), but is about a factor 4 shorter ($\sim 25 \pm 10$ fs) for the n-type sample. This extraordinarily fast initial scattering time in the presence of cold but nondegenerate electrons is attributed to relaxation through the emission of phonon-plasmon coupled modes [11,12]. The estimated scattering time is commensurate with the result of Petersen *et al.* [12], which was deduced at low temperature and with carriers injected 280 meV above the band edge. A qualitatively similar difference between the scattering times of intrinsic and p-type samples on the one hand, and of n-type samples on the other hand, was also observed in GaAs quantum wells [9] in the presence of a degenerate plasma. The surprisingly longer scattering time for the n-type sample at $N > N_{de}$ possibly results from the much higher plasma temperature.

Figure 4 shows the measured time-resolved changes of absorption coefficient ($\Delta\alpha$) at 580 nm for various carrier densities. At this wavelength (and also at 700 nm), the initial transient bleaching is not present in $\Delta\alpha$, because nonthermal carriers are only distributed

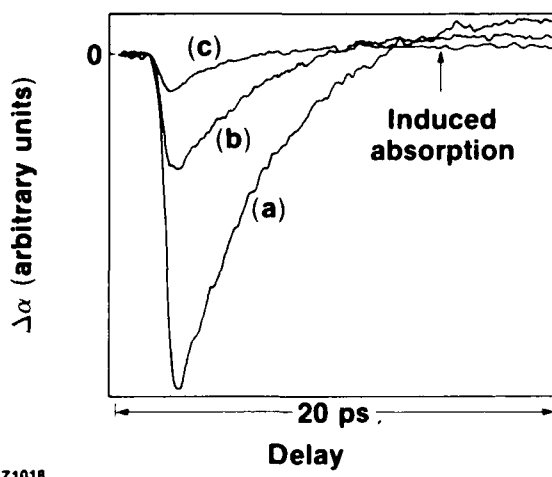


Figure 4. Measured time-resolved $\Delta\alpha$ at 580 nm for various carrier densities $N \sim$: (a) $1 \times 10^{19} \text{ cm}^{-3}$; (b) $4 \times 10^{18} \text{ cm}^{-3}$; (c) $1 \times 10^{18} \text{ cm}^{-3}$.

around the pump-pulse excited states at $t \sim 0$. However, this absorption spectral hole (FWHM ~ 150 –200 meV) brings a transient positive spike in the refractive index at 580 nm that probes the states ~ 140 meV above 2 eV in the Γ valley, and a transient negative spike at 700 nm that probe the states ~ 230 meV below 2 eV in the Γ valley, according to the Kramers-Kronig relation. Therefore the refractive nonlinearity appears more dispersed than the absorptive nonlinearity. The induced absorption on a picosecond time scale is caused by band-gap renormalization due to the relatively cold carriers, which are gathered near the band edge.

Let us now discuss the nonlinearities around the band edge. Figure 5(a) and (b) show the time-resolved changes of the absorption coefficient ($\Delta\alpha$) and refractive index (Δn) for $N \sim 2 \times 10^{18} \text{ cm}^{-3}$ at probe wavelengths of 880, 890, and 900 nm, which are below the initial band-edge, and of 860 nm, which is slightly above the initial band edge. From 880 to 900 nm there is an initial increase in absorption followed by a decrease in absorption, whereas a monotonic decrease in absorption is observed at 860 nm. On the other hand, Δn shows a sharp initial decrease, followed by a much slower variation, at all wavelengths.

When electrons and holes are injected in the conduction and valence bands, they form a quantum mechanical many-body system which can be described adequately only by comprehensive theories. The microscopic origin of the room-temperature near band-edge optical nonlinearities in GaAs has been studied under quasi-equilibrium condition and explained in terms of various many-body effects such as band-gap renormalization, plasma screening of electron-hole interactions and band filling [13]. Figure 6 shows the calculated absorption spectrum (from Ref. 13) around the band edge under different assumptions. Comparison of those curves with our data shown in Fig. 5 support the following conclusions: The induced absorption observed right after carrier excitation at wavelengths below the original band edge is caused by band-gap renormalization and plasma screening of electron-hole interactions due to the hot carriers injected in 2 eV. At 860 nm, the large negative $\Delta\alpha$ produced by plasma screening offsets the small positive $\Delta\alpha$ due to band-gap renormalization. The subsequent decrease of absorption is attributed to band filling. On the other hand, the fast negative changes of refractive index are caused by plasma screening of Sommerfeld continuum states, also predicted by the theory of Ref. 13. The subsequent slower decrease is mainly attributed to band filling

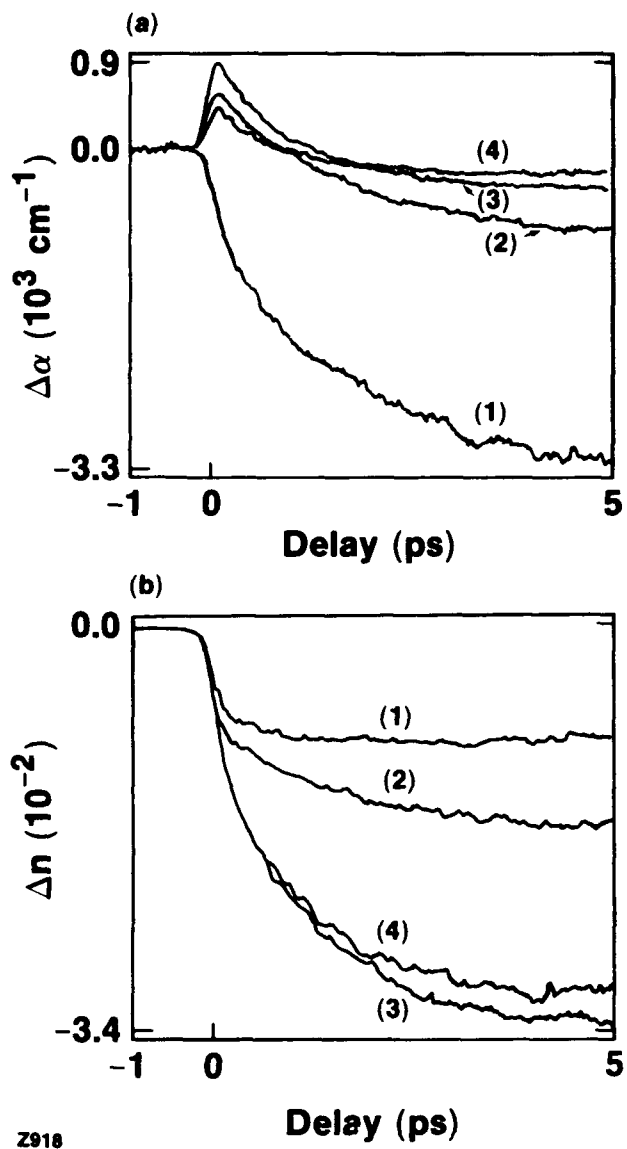


Figure 5. Measured time-resolved $\Delta\alpha$ (a) and Δn (b) for a carrier density $\sim 2 \times 10^{18} \text{ cm}^{-3}$ injected at 620 nm. The probe wavelengths are: (1) 860 nm, (2) 880 nm, (3) 890 nm, (4) 900 nm.

[8,13]. Even though the theory derived for a cold plasma shows a good qualitative agreement with our femtosecond measurements, it does not provide a quantitative fit to our results obtained at $t \sim 0^+$ or $t \sim 3^+$ ps, as shown in Fig. 7. The discrepancy can be traced to the difference between many-body effects due to hot and cold carriers.

Our measurement of femtosecond optical nonlinearities around the band edge at different injected carrier densities [5,14] also bring new knowledge on hot-carrier relaxation processes. In particular, we find

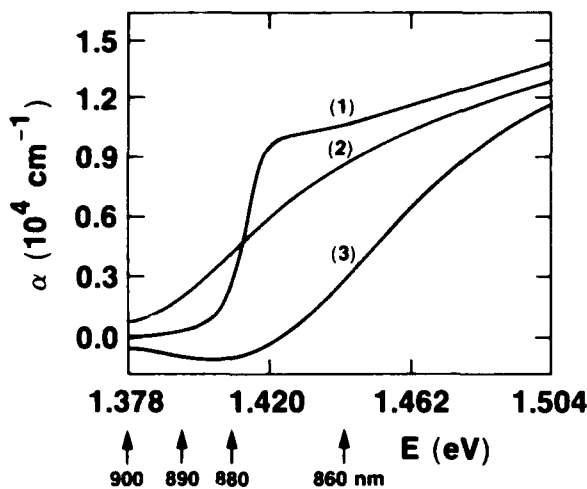


Figure 6. Theoretical calculations of the absorption coefficient (α) around the band-edge from Ref. 13: (1) $N = 10^{15} \text{ cm}^{-3}$; (2) $N = 1.5 \times 10^{18} \text{ cm}^{-3}$, with band-gap renormalization and plasma screening, but without band filling; (3) $N = 1.5 \times 10^{18} \text{ cm}^{-3}$, with band-gap renormalization, plasma screening, and band filling.

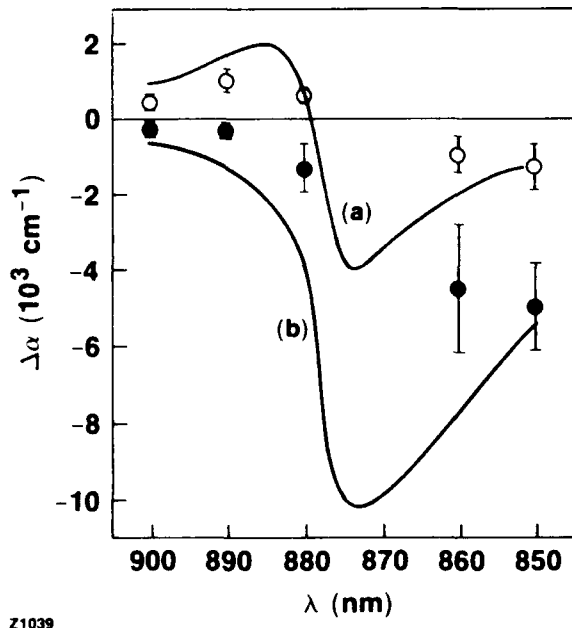


Figure 7. Changes of the absorption coefficient ($\Delta\alpha$) around the band-edge. \circ and \bullet are the experimental data obtained at $t \sim 0^+$ and $t \sim 3^+$ ps for $N \sim 2 \times 10^{18} \text{ cm}^{-3}$. The full curve is the theoretical calculation of Ref. 13 for $N = 1.5 \times 10^{18} \text{ cm}^{-3}$. (a) with band-gap renormalization and plasma screening, but without band filling; (b) with band-gap renormalization, plasma screening and band filling.

that gain occurs in less than 1 ps in a range of wavelengths around the band-edge provided that the injected carrier density is larger than $\sim 3 \times 10^{18} \text{ cm}^{-3}$, and that the time to reach gain is reduced to ~ 300 fs for our highest carrier density ($N \leq 10^{19} \text{ cm}^{-3}$). This observation is a strong evidence for ultrafast band-gap renormalization and also reveals the importance of carrier-carrier scattering and intervalley scattering [14].

Hot-carrier many-body effects in quantum wells have been extensively studied [15-17]. Both experimental measurements [15,16] and theoretical calculations [17] have shown that the effect of plasma screening of excitons is relatively weak in the two-dimensional electron-hole system. The term "screening" has been generally used to describe the effect of free carriers on the excitonic absorption spectrum, but here we only use it to refer to classical screening due to the long-range Coulomb interaction [17]. In that case, exciton bleaching is more strongly governed by K-space filling and short-range exchange effects, resulting from Pauli exclusion principle. Since hot carriers occupy few Bloch states with which excitons (or continuum states for intrinsic GaAs at room temperature) are formed, those K-space effects due to hot carriers should be negligible. Our measurement shows that strong hot-plasma screening of electron-hole interactions in bulk GaAs is really instantaneous within our time-resolution, a result consistent with an earlier measurement by Shank *et al.* [18] at low temperature and with 0.5 ps time resolution.

It is interesting to note that large changes ($> 10^{-2}$) of the refractive index are observed around the band edge on a subpicosecond time scale. These changes, which are comparable to those obtained from cw measurements [8,13], are substantially larger than the changes produced by the Pockels or Franz-Keldysh effects at a field strength of 10^5 V/cm [19]. An all-optical logic gate with 1 ps switch-on time [20] at room temperature was demonstrated in GaAs-AlGaAs quantum wells by using real carrier-induced nonlinearities. Since the change of refractive index per electron-hole pair is only about a factor 2-3 larger in quantum wells (mainly due to exciton bleaching by K-space filling) than in bulk GaAs (mainly due to plasma screening and band filling) [21], similar performance of optical bistable devices using bulk GaAs is expected [20]. Even though devices using real-carrier-induced nonlinearities have a switch-on time almost as short as devices using virtual-carrier-induced nonlinearities [22], the switch-off time, which sets the bit-rate, is much longer in real-carrier-devices

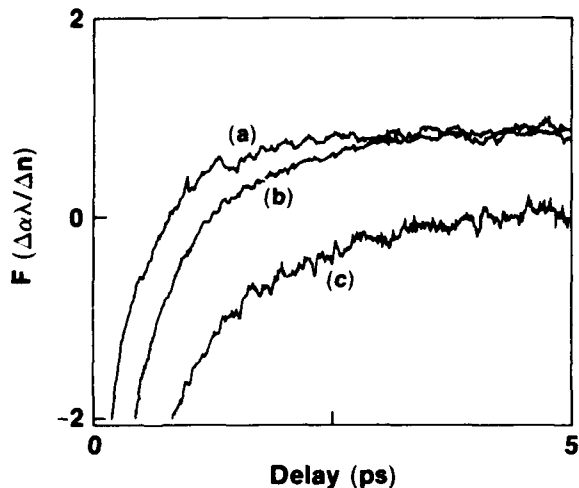


Figure 8. Measured time-resolved figure of merit (F) at 890 nm at various carrier densities $N \sim$: (a) $5 \times 10^{18} \text{ cm}^{-3}$; (b) $2.5 \times 10^{18} \text{ cm}^{-3}$; (c) $1 \times 10^{18} \text{ cm}^{-3}$.

because it usually takes hundreds of picoseconds to remove the carriers.

A figure of merit which is defined as $F = \Delta\alpha\lambda/\Delta n$ is a commonly used device parameter. When $|F| < 1$, the phase of a signal beam is changed more quickly than its amplitude, which makes a device based on the refractive nonlinearity attractive. In Fig. 8 we plot F at 890 nm versus time delay at various carrier densities. The fact that $|F|$ remains smaller than 1 from hundreds of femtoseconds to several picoseconds over a wide range of carrier densities implies that the refractive (dispersive) nonlinearity is dominant at this wavelength. In fact, at 890 nm, the balance among band-gap renormalization, plasma screening and band filling makes $\Delta\alpha$ small, but Δn remains large. This region should be suitable for the design of devices using the refractive nonlinearity, such as phase modulators.

In conclusion, GaAs exhibits ultrafast optical nonlinearities when real carriers are injected by ultrashort laser pulses. Hot-carrier many-body effects such as band-gap renormalization and plasma screening of electron-hole interactions have similarities and differences with those for a cold plasma. The first observation of the refractive index spectral hole burning and further study of such hole burning in different types of samples reveal important carrier scattering physics in the absence and presence of a cold plasma. The large and ultrafast refractive nonlinearities observed around the band-edge are suitable for device applications.

ACKNOWLEDGMENT

The authors thank W. L. Nighan, Jr., D. A. Young, and P. Mertz for technical support, and M. Shayegan and G. Wicks for growing the samples. This work is supported by National Science Foundation under contract ECS-8657263 and the U. S. Army Research Office under contract DAAL03-87-K-0145. T. Gong also acknowledges receipt of a fellowship from the Photonic and Opto-Electronic Materials Advanced Technology Center at Princeton University.

T. Gong is also affiliated with the Department of Electrical Engineering at Princeton University; P. M. Fauchet is also affiliated with the Department of Electrical Engineering at the University of Rochester.

REFERENCES

1. J. L. Oudar, D. Hulin, A. Migus, A. Antonetti, and F. Alexandre, *Phys. Rev. Lett.* **55**, 2074 (1985).
2. A. J. Taylor, D. J. Erskine, and C. L. Tang, *J. Opt. Soc. Am. B* **2**, 663 (1985).
3. R. W. Schoenlein, W. Z. Lin, E. P. Ippen, and J. G. Fujimoto, *Appl. Phys. Lett.* **51**, 1442 (1987).
4. P. C. Becker, H. L. Fragnito, C. H. Brito Cruz, J. Shah, R. L. Fork, J. E. Cunningham, J. E. Henry, and C. V. Shank, *Appl. Phys. Lett.* **53**, 2089 (1988).
5. T. Gong, W. L. Nighan, Jr., and P. M. Fauchet, *Appl. Phys. Lett.* **57**, 2713 (1990).
6. A. Mysyrowicz, D. Hulin, A. Antonetti, A. Migus, W. T. Masselink, and H. Morkoc, *Phys. Rev. Lett.* **56**, 2748 (1986).
7. T. Gong, W. L. Nighan, Jr., and P. M. Fauchet, *SPIE Proceedings* **1268**, 106 (1990).
8. B. R. Bennett, R. A. Soref, and J. A. Del Alamo, *IEEE J. Quantum Electron.* **QE-26**, 113 (1990).
9. W. H. Knox, D. S. Chemla, G. Livescu, J. E. Cunningham, and J. E. Henry, *Phys. Rev. Lett.* **61**, 1290 (1988).
10. C. J. Stanton, D. W. Bailey, and K. Hess, *Phys. Rev. Lett.* **65**, 231 (1990).
11. J. A. Kash, *Phys. Rev. B* **40**, 3455 (1989).
12. C. L. Petersen and S. A. Lyon, *Phys. Rev. Lett.* **65**, 760 (1990).
13. Y. H. Lee, A. Chavez-Prison, S. W. Koch, H. M. Gibbs, S. H. Park, J. Morhange, A. Jeffery, N. Peyghambarian, L. Banyai, A. C. Gossard, and W. Wiegmann, *Phys. Rev. Lett.* **57**, 2446 (1986).

14. P. M. Fauchet, T. Gong, P. J. Kelly, and J. F. Young, submitted to the 7th International Conference on Hot Carriers in Semiconductors, Japan, 1991.
15. W. H. Knox, R. L. Fork, M. C. Downer, D. A. B. Miller, D. S. Chemla, and C. V. Shank, *Phys. Rev. Lett.* **54**, 1306 (1985).
16. W. H. Knox, C. Hirlmann, D. A. B. Miller, J. Shah, D. S. Chemla, and C. V. Shank, *Phys. Rev. Lett.* **56**, 1191 (1986).
17. S. Schmitt-Rink, D. S. Chemla and D. A. B. Miller, *Phys. Rev. B* **32**, 6601 (1985).
18. C. V. Shank, R. L. Fork, R. F. Leheny, and J. Shah, *Phys. Rev. Lett.* **42**, 112 (1979).
19. B. R. Bennett and R. A. Soref, *IEEE J. Quantum Electron.* **QE-23**, 2159 (1987).
20. A. Migus, A. Antonetti, D. Hulin, A. Mysyrowicz, H. M. Gibbs, N. Peyghambarian, and J. L. Jewell, *Appl. Phys. Lett.* **46**, 70 (1985).
21. S. W. Koch, N. Peyghambarian, and H. M. Gibbs, *J. Appl. Phys.* **63**, R1 (1988).
22. D. Hulin, A. Mysyrowicz, A. Antonetti, A. Migus, W. T. Masselink, H. Morkoc, H. M. Gibbs, and N. Peyghambarian, *Appl. Phys. Lett.* **49**, 749 (1986).

Digest Summaries

PICOSECOND SUPERCONDUCTIVE ELECTRONICS

T. Van Duzer

Department of Electrical Engineering and Computer Sciences
and the Electronics Research Laboratory
University of California, Berkeley, California 94720

INTRODUCTION

Materials developments during the past several years will facilitate the realization of promises of picosecond electronics with superconductive devices. An increasing number of groups around the world have developed the capability of making all-refractory integrated circuits based on the $\text{Nb}-\text{NbO}_x-\text{Nb}$ Josephson tunnel junction, which has the I-V characteristic shown in Fig. 1a. These devices have excellent

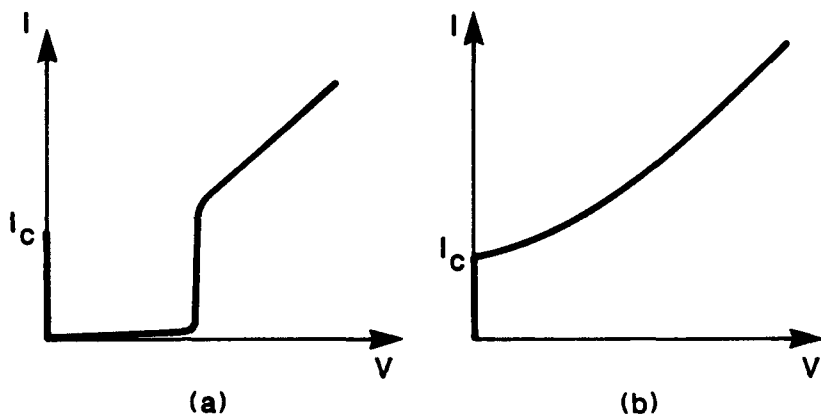


Fig. 1 (a) I-V characteristic for a tunnel junction suitable for voltage-state Josephson logic. (b) I-V characteristic obtained for proximity type junctions with conducting barriers. These are suitable for current-state logic.

and controllable electrical characteristics and are stable both in terms of shelf life and in thermal cycling. Circuits with tens of thousands of logic gates have been made and have shown remarkable electrical performance. It should be borne in mind that in complex electronic circuits with gates that switch with speeds of several picoseconds, the terminal data rates are on the nanosecond scale except in special pipelined situations, such as a shift register. It should also be kept in mind that parasitics limit switch speeds. While the niobium Josephson junctions has a theoretical limiting switching speed of 0.22 ps, the junction capacitance limits the speeds realized to date to slightly more than 1 ps.

Thin films of high temperature oxide superconductors such as YBaCuO have been developed very well during the past three years. It is now almost routine to make very high quality films either by off-axis sputtering or by laser ablation. There have also been a number of realizations of Josephson devices. These are not tunnel junctions, as in the case of the niobium technology, but are so-called proximity effect devices, which have a normal conducting barrier separating the superconductive electrodes. They have an I-V characteristic as shown in Fig. 1b rather than the tunnel junction characteristic of Fig. 1a.

In this paper we will present the current materials situation and show some of the circuits that can be realized with Josephson switching devices having one of the I-V characteristics in Fig. 1. These include such signal processing devices as A/D converters and shift registers and a variety of logic and memory circuits. The circuits employ either voltage-states or current-states. Either type can be made with the tunnel junction but only current-state circuits can be made with junctions having the nonhysteretic I-V characteristics of Fig. 1b.

MATERIALS

Early work on Josephson integrated circuits (notably, in the IBM mainframe computer project) was done using soft metallic superconductors in which alloying was used to make the materials more suitable. The achievable control of device characteristics and stability was not sufficient for large scale integration. Many years had been spent unsuccessfully trying to make satisfactory niobium junctions with native oxide tunneling barriers. The development of the ambient-oxidized-aluminum barrier in the early 1980s led to the ability to make excellent junctions with small spreads of critical currents (maximum zero-voltage currents). This device is the basis for all existing integrated circuit work, except for those using NbN .

There is good reason to want NbN with its 15-16 K transition temperatures for use in infrared detectors for which the cryogenics is already available. The low power dissipation of the Josephson circuits is a desirable feature of signal processing circuits to be combined with the infrared detectors, especially in arrays. The best NbN tunnel junctions use a barrier of MgO , which must be deposited rather than ambient-oxidized as in the case of aluminum used in the niobium junctions. Since it must be deposited as an oxide, thickness (and hence, critical current) uniformity cannot be achieved as well as in the $\text{Nb-NbO}_x\text{Nb}$ technology.

The most highly developed of the oxide superconductors is YBaCuO . This material is highly anisotropic with poor conduction along its c axis and excellent conducting properties along its a-b planes. Films that are c-axis oriented would serve well for interconnects for digital devices. Current work is toward developing the technology to make controllable Josephson devices. The current state of this development

will be discussed. Circuits made with this material would be best operated at no more than about 60 K.

One oxide material (BaKBiO) recently was shown to be usable for making Josephson junctions. It also has the advantage of being isotropic. Its transition temperature is only about 30 K, at best, but this would allow operation at 15-20 K. That greatly relaxes the refrigeration requirement compared with the 4.2 K used for Nb circuits and at the same time allows use of the voltage-state circuit concepts developed for the low-temperature circuits.

CIRCUITS

We will briefly review the state of circuit development, picking out some of the fastest circuits that have either been actually realized or proposed and simulated. These will include the microprocessor circuits developed in the Fujitsu Laboratories, a memory unit developed in the Electrotechnical Laboratory in Japan, some recent flash-type multi-gigahertz A/D concepts, shift register designs that promise clocking at over 50 GHz, and families of digital logic based on current-state circuits that promise speeds higher than can be achieved with voltage-state logic. Some of the devices mentioned can be made with the devices available in high-temperature superconductors.

For more details, the reader is referred to References 1 and 2.

1. T. Van Duzer, "Superconductor Electronic Device Applications," *IEEE J. Quantum Electronics*, vol. 25, pp. 2365-2377, November 1989.
2. T. Van Duzer, "Superconductor Electronics," to appear in *Cryogenics*.

High-Capacity Lightwave Transmission: Ultra-High Speed or Wavelength Multiplexing

Tingye Li
AT&T Bell Laboratories
Crawford Hill Laboratory
Holmdel, New Jersey 07733

The potential total transmission bandwidth of current single-mode optical fibers in the low-loss wavelength regions near $1.3 \mu m$ and $1.55 \mu m$ approaches 50 THz. In order to explore this enormous capacity for the transmission and distribution of future broadband services, the lightwave research community has been pushing the frontiers of high-speed technology to data rates well beyond 10 Gb/s. Long-distance transmission of wavelength-multiplexed channels that run at multi-gigabit-per-second rates have been demonstrated recently using erbium-doped fiber amplifiers as analog (non-regenerative) repeater amplifiers. As fiber dispersion may become the limiting factor that sets the bit-rate-distance product of a long regenerative repeater span containing optical amplifiers, both optical and electronic means for equalizing the effects of fiber dispersion, as well as soliton techniques, are being investigated for operation at multi-gigabit-per-second rates. Thus advances in device technologies and in transmission techniques not only provide enhancements in system performance, but also offer alternatives in system implementation.

This talk will first consider transmission limitations imposed by optical fiber dispersion and nonlinearities, and describe various methods for palliating these effects. Next, multiplexing techniques that enhance transmission capacity will be compared and properties of erbium-doped fiber amplifiers that are relevant to high-capacity transmission will be reviewed. Then, soliton transmission systems that show potential for ultra-long-distance (multi-megameters) applications will be discussed. Finally, technology choices for long-haul applications will be summarized.

Photon-Assisted Resonant Tunneling Through a GaAs/AlGaAs Multiple Quantum Well Structure

Bjorn Jonsson and Ingemar Andersson

Department of Optoelectronics and Electrical Measurements

Chalmers University of Technology

S - 412 96 Goteborg, SWEDEN

Anders Larsson

Center for Space Microelectronics Technology

Jet Propulsion Laboratory / California Institute of Technology

4800 Oak Grove Drive, Pasadena, CA 91109, USA

Thorwald Andersson and Johan Westin

Department of Physics

Chalmers University of Technology

S - 412 96 Goteborg, SWEDEN

Introduction

The use of bandgap engineering techniques to tailor the perpendicular transport characteristics of layered semiconductor structures has resulted in a variety of new phenomena and devices concepts [1]. In particular the coherent interaction of electron waves reflected at interfaces gives rise to resonant tunneling effects which filter electrons of certain energy through the structure. A structure specifically designed for electron energy filtering is the variably spaced superlattice energy filter (VSSEF) in which the quantized states in adjacent quantum wells become aligned under appropriate bias conditions [2].

Device structure

The photoconductive device discussed here is based on intersubband absorption in a GaAs/Al_xGa_{1-x}As multiple quantum well (MQW) structure. The epitaxial structure is shown in

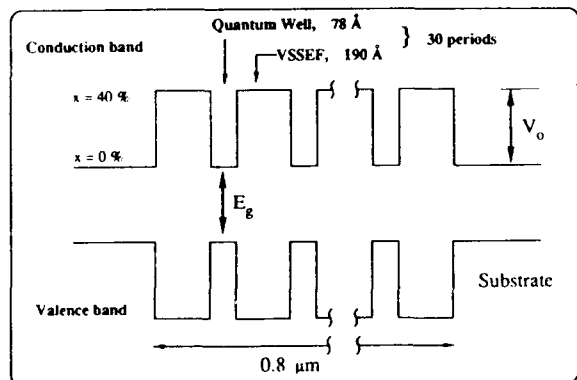
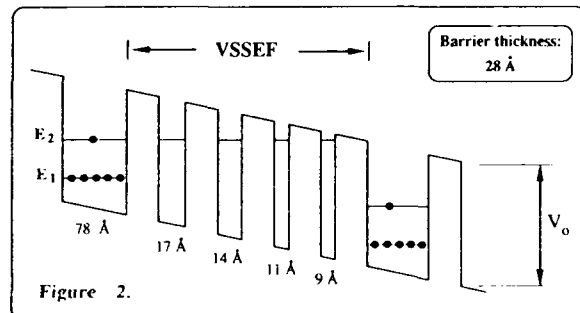


Figure 1. Band diagram showing the epitaxial structure of the detector.



Schematic diagram of the conduction band potential profile with an applied external bias voltage. The location of the energy levels in the quantum wells and the alignment of the energy levels in the VSSEF are illustrated.

Figure 1. The device consists of a total of 30 quantum wells, 78 Å wide, separated by a 190 Å wide VSSEF-structure. From the schematic of the conduction band shown in Figure 2 the principle of operation can easily be understood. Electrons are excited from the ground state energy level E₁ to the second level E₂ by infra-red (IR) radiation. When an appropriate bias voltage is applied to the structure the energy levels in the VSSEF are aligned with the energy level E₂, and the electrons can tunnel out through the structure. The measured photocurrent will hence employ a resonance peak at an appropriate applied electric field (≈ 50 kV/cm).

The MQW-structure used in the experiments was grown by molecular beam epitaxy (MBE) on n-doped GaAs (100). The growth rate of the quantum wells were calibrated by reflection high energy electron diffraction (RHEED) oscillations and the four quantum wells in each VSSEF were 17, 14,

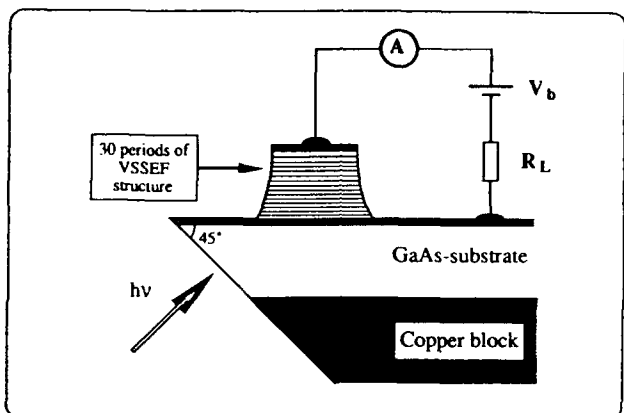


Figure 3.
Experimental setup and illumination principle.

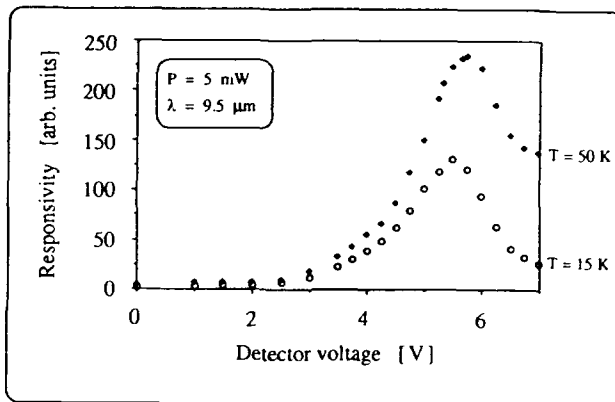


Figure 4.
Detector responsivity as a function of detector voltage, measured at temperatures of 15 K and 50 K.

11, and 9 Å wide, respectively. The $\text{Al}_x\text{Ga}_{1-x}\text{As}$ barriers ($x = 0.4$) were all 28 Å wide. Typical growth rates were 0.8 $\mu\text{m}/\text{h}$ for GaAs. In the center of each of the 78 Å wide quantum wells, a 58 Å thick part was doped with Si.

For measurement purposes, individual detector elements were formed by etching mesas, 90 μm in diameter and 2 μm high. The detector chip was cemented to a copper block and the whole assembly was mounted in a cryostat for low temperature measurements. Figure 3 shows a single device and the electrical connections for the experimental set-up. Conventional bonding techniques were used to connect the device to the bias voltage and the load resistance. This type of intersubband absorption is only sensitive to light with the electric field polarized parallel to the growth direction. In order to maximize both the component of the light with the right polarization incident on the device and the illuminated detector area, the substrate was lapped to an angle of 45°, as indicated in Figure 3.

Experimental results

Measurements were performed on these detector elements, using a CO_2 -laser, with a total output power of approximately 300 mW. The light intensity was attenuated to give approximately 5 mW incident on the area of the device. In order to obtain good sensitivity, the load resistance, R_L was set to 1 $\text{k}\Omega$. To avoid excessive dark currents the bias voltage V_b was adjusted to give detector voltages V_d below 7 V. An optical chopper and lock-in amplifier were used to monitor the changes in the photo-current by measuring the voltage across the load resistance.

The photocurrent versus bias voltage characteristics recorded at two different temperatures are shown in Figure 4. For these measurements the CO_2 -laser was tuned to a wavelength of 9.53 μm . Measurements were also performed for several wavelengths in the interval 9.5 – 10.6 μm . For wavelengths longer than 10.0 μm , corresponding to the separation between the energy levels E_1 and E_2 , the photocurrent response drops rapidly. The curves in Figure 4 show a clear peak at a detector bias voltage V_d of approximately 5.7 V. This peak is believed to be due to alignment of the energy levels in the VSSEF. At higher detector voltages the responsivity drops rapidly indicating a high negative differential resistance. This is a unique feature of the VSSEF device not observed in commonly used photo-detectors. At temperatures of 50 K or less the resonance peak is easily observed. For higher temperatures the peak is, however, smeared out.

Conclusions

We have observed photon-assisted resonant tunneling in a GaAs/AlGaAs VSSEF-structure. Electrons confined in the quantum wells are excited to the second state by intersubband absorption of incident IR radiation. At an appropriate applied electric field the electrons can then tunnel through the VSSEF. This is manifested by the measured peak in the photo-current at a detector voltage of 5.7 V. To our knowledge this is the first time this effect has been observed and it could prove useful for IR-detector applications.

Acknowledgments

This work was supported by the National Swedish Board for Technical Development (STU).

References

- [1] B. F. Levine et al., "GaAs/AlGaAs quantum well long-wavelength infra-red (LWIR) detector with a detectivity comparable to HgCdTe", *Electron. Lett.*, vol 24, No 12, pp 747 – 748, 1988.
- [2] C. J. Summers and K. F. Brennan, "Variably spaced superlattice energy filter, a new device design concept for high-energy electron injection", *Appl. Phys. Lett.*, vol 48, No 12, pp 806 – 808, 1986.

A

Abe, Kathryn, 140
 Allen, S., 104
 Alphonse, G. A., 185
 Andersson, Ingemar, 267
 Andersson, Thorwald, 267
 Andreadakis, N., 185
 Aoshima, Shinichiro, 64, 70
 Auston, D. H., 2
 Axmann, A., 86

B

Bar-Joseph, I., 198, 214, 218
 Bhushan, Manjul, 31
 Bloom, David M., 101, 136
 Bowers, J. E., 92, 104
 Burdge, G., 194

C

Campbell, Arthur B., 119
 Carman, Eric, 140
 Case, Michael, 104, 140
 Chauchard, Eve A., 54, 194, 248
 Chemla, D. S., 198, 214
 Chen, Y. K., 176
 Chen, Yi, 46
 Cho, A. Y., 198, 214
 Chomette, A., 218
 Chou, Stephen Y., 97
 Chu, A. K., 131
 Chwalek, James M., 15
 Clérot, F., 218
 Clifton, B. J., 167
 Comfort, J. H., 110
 Connolly, K. M., 59
 Constantine, P. D., 181
 Cooper, D. J., 181
 Crabbe, E. F., 110
 Crawford, D. L., 92
 Cunningham, Jack E., 24, 40, 210

D

Damen, T. C., 204
 Delfyett, P. J., 185
 Deveaud, B., 218
 Doran, G. E., 40
 Dykaar, D. R., 20

E

Eccleston, R., 223
 El-Ghazaly, S. M., 59
 Elton, D., 181
 Eng, Sverre T., 188

F

Fauchet, P. M., 253
 Federici, J. F., 20
 Ferry, D. K., 126
 Fischer, Paul B., 97
 Florez, L., 185
 Fox, A. M., 210
 Frankel, M. Y., 146
 Franklin, Jeff, 140

G

Gedalyahu, Y., 214
 Giboney, Kirk, 92, 104, 140
 Gigase, Y., 131
 Gmitter, T., 185
 Göbel, Ernst O., 204
 Gong, T., 253
 Goodnick, S. M., 40
 Goossen, Keith W., 31, 161
 Greene, B. I., 20
 Grischkowsky, D., 9, 242
 Grondin, R. O., 59
 Gurvitz, S., 218

H

Hafich, M. J., 92
 Hamm, J. M., 167
 Henderson, D., 79
 Hirano, Isuke, 64
 Huang, Sheng-lung L., 151, 248
 Hülsmann, A., 86
 Hung, Hing-Loi A., 54, 151

J

Jacobson, Dale C., 161
 Jan, W. Y., 210
 Joneckis, L. G., 194
 Jonsson, Björn, 188, 267
 Joseph, Thomas R., 248
 Joshi, R. P., 59

K

Kamegawa, Masayuki, 104, 140
 Kamiya, Takeshi, 36, 75
 Karin, J., 104
 Katzenellenbogen, N., 9, 242
 Kisker, David W., 161
 Klingenstein, M., 86
 Knox, W. H., 40
 Knudson, Alvin R., 119
 Köhler, Klaus, 24, 204, 223
 Kopf, R. F., 20
 Kriman, A. M., 126
 Kuhl, J., 86, 223

L

Lambsdorff, M., 86
 Larsson, Anders, 267
 Lee, Chi H., 54, 151, 194, 248
 Lee, Timothy T., 248
 Leo, Karl, 204
 Levi, A. F. J., 20
 Li, K. D., 101
 Li, Ming G., 54, 151
 Li, Tingye, 265
 Liliental-Weber, Z., 244
 Liu, Yue, 97
 Livescu, G., 210
 Logan, R. A., 176
 Lowery, A. J., 181
 Lyons, W. G., 167

M

Mankiewich, Paul M., 31, 167
 Marshall, I. W., 181
 Mathews, R. H., 167
 McMorrow, Dale, 119
 Melloch, M. R., 242
 Meyerson, B. S., 110
 Miller, D. A. B., 210
 Moglestue, C., 86
 Motet, T., 49
 Mourou, Gerard A., 15, 49, 146
 Myers, David R., 236

N

Nees, John, 46, 49
 Newman, N., 167
 Nguyen, Loi D., 116
 Norris, T. B., 244
 Nuss, Martin C., 24, 31, 161

O

O'Malley, Megan L., 31, 167
 Otsuka, N., 242
 Özbay, Ekmel, 101, 136

P

Patton, G. L., 110
 Pfeiffer, L. N., 20
 Poate, John M., 161

R

Ramaswamy, M., 40
 Regreny, A., 218
 Riaziat, Majid, 156
 Robinson, G. Y., 92
 Roddie, A. G., 79
 Rodwell, M. J. W., 92, 104, 140
 Rosenzweig, J., 86
 Roskos, Hartmut, 24, 31, 161

S

Sankaran, Vasu, 229
 Schäfer, Wilfried, 204
 Schaff, W. J., 244
 Schmitt-Rink, Stefan, 204
 Schneider, Jo., 86
 Sha, W., 244
 Shah, Jagdeep, 24, 204
 Short, Ken T., 161
 Singh, Jasprit, 229
 Sivco, D. L., 198, 214
 Smith, A. J. A., 79
 Smith, P. M., 146
 Smith, Thane, 248
 Song, X. J., 244
 Stoffel, N., 185
 Stork, J. M. C., 110
 Strobel, R., 223
 Sylvestre, P. M., 92

T

Takahashi, Hironori, 64, 70
 Takahashi, Ryo, 75
 Tanbun-Ek, T., 176
 Tell, Ben, 24, 31, 161
 Tsuchiya, Yutaka, 64, 70

V

Valdmanis, J. A., 146
 Van Duzer, T., 262
 Van Zeghbroeck, B., 131

W

Warren, A. C., 242
 Weatherford, Todd R., 119
 Weber, E. R., 244
 Weingarten, Kurt J., 156
 Westin, Johan, 267
 Wey, J. S., 194
 Wey, Y. G., 92
 Whitaker, John F., 15, 146
 White, Alice E., 161

Williamson, Steve, 46, 49

Withers, R. S., 167
 Woodall, J. M., 242
 Woodward, T. K., 198, 214
 Wu, M. C., 176

Y

Yacoby, A., 214
 Yu, Ruai, 104, 140

Z

Zhang, X. -C., 2
 Zhou, J.-R., 126